

Digital Communications over MIMO Channels

Applications to CDMA and Multiple Antenna Systems

Habilitationsschrift

vorgelegt dem Fachbereich 1 (Physik/Elektrotechnik)
der Universität Bremen

von

Dr.-Ing. Volker Kühn



Bremen im Oktober 2004

Preface

Motivation

Mobile radio communications are evolving from pure telephony systems to multimedia platforms offering a variety of services ranging from simple file transfers, audio and video streaming, up to interactive applications. Naturally, these services have different quality of service and bandwidth constraints requiring systems with large flexibility and scalability. Furthermore, bandwidth became an extremely valuable resource emphasizing the need for transmission schemes with high spectral efficiency.

In order to cope with these problems, Code Division Multiple Access (CDMA) was chosen as multiple access scheme in third generation mobile radio systems like UMTS and CDMA 2000. Additionally, multiple antenna systems have recently become a promising candidate that exploit the resource space. On the one hand, Space Division Multiple Access (SDMA) uses multiple antennas at receiver and transmitter to spatially multiplex several data streams and, therefore, increase the spectral efficiency. On the other hand, the link reliability can be improved by beamforming and diversity techniques. As a third component, powerful channel coding like concatenated codes or low density parity check codes allows efficient communications in the vicinity of Shannons channel capacity. Certainly, all mentioned approaches can be combined and incorporated into a single system.

Due to the influence of the mobile radio channel, high spectral efficiencies can only be obtained with sophisticated signal processing either at transmitter or receiver. At the transmitter, a pre-equalization of the channel like Tomlinson-Harashima Precoding allows very simple receiver structures. Derivatives are also applicable in multi-user scenarios (joint transmission) avoiding interference prior to transmission. Moreover, appropriate precoding for multiple transmit antennas and flat fading channels allows the full exploitation of diversity with a simple matched filter at the receiver. All these techniques require a joint preprocessing at a central transmitter, i.e. a coordinated transmission has to be implemented.

Contrarily, the generally asynchronous uplink of a CDMA system consists of spatially separated non-cooperating transmitters and a common base station. In this scenario, a joint preprocessing is not possible and the receiver has to overtake the part of jointly processing the signals. The same situation occurs when multiple antennas are used for spatial multiplexing without channel knowledge at the transmitter. At the first sight, such a multiple antenna system looks quite different from a CDMA uplink concerning the physical implementations. However, using vector notations to derive mathematical models for these systems, it becomes obvious that they are in fact very similar. Both can be described by a mixing matrix leading to a superposition of all transmitted signals. However, the structure of these matrices and their sizes are generally different. Nevertheless, the common task of receivers in both cases is to separate and recover the interfering signals again so that the same detection algorithms can be used.

One aim of this work is to demonstrate the similarity of both approaches. Therefore, a unified description using vector notations and comprising multiple antenna as well as CDMA systems is presented. This model can be generalized to arbitrary vector channels, i.e. channels with multiple inputs and outputs. It is used to derive efficient detection algorithms whose error rate performances are compared by simulations. Furthermore, an information theoretical analysis of CDMA and SDMA systems illuminate ultimate limits and demonstrates the high potential of these concepts. Besides spatial multiplexing, the use of multiple transmit antennas in order to increase the link reliability by diversity concepts (space-time coding) is described. Another focus is the application of error control coding in mobile radio communications. For the example of a CDMA uplink, it is demonstrated that strong codes are an appropriate means to achieve high spectral efficiencies even in the presence of severe multi-user interference.

Structure of Thesis

Chapter 1: Introduction to Digital Communications

The thesis starts with an introduction to digital communication systems. Since the mobile radio channel dominates the design of these systems, its statistical properties are analyzed and appropriate models for frequency selective channels with single as well as multiple inputs and outputs are presented. Afterwards, the basic principles of signal detection and some general expressions for the error rate performance are derived. These results are used in the next section to determine the performance of linear modulation schemes for different channel models. Finally, the principle of diversity is generally discussed. The results are used in subsequent chapters when frequency diversity in CDMA systems and space diversity in multiple antenna systems are explained.

Chapter 2: Information Theory

Chapter 2 deals with the information theoretical analysis of mobile radio systems. Starting with some basic definitions, capacities of the AWGN channel and of fading channels are derived. Especially the difference between ergodic and outage capacity is discussed. The chapter closes with a general derivation of the capacity of multiple-input multiple-output systems without delivering specific results. They are presented for CDMA and SDMA systems in Chapters 4 and 6.

Chapter 3: Forward Error Correction Coding

The third chapter gives a short survey of selected channel coding topics that become relevant in subsequent chapters. Starting with a basic description of linear block and convolutional codes, soft-output decoding algorithms representing an essential ingredient in concatenated coding schemes are derived. Next, the performance of codes is evaluated. On the one hand, the error rate performance is analyzed by the union bound technique exploiting the distance properties of codes. On the other hand, the information processing characteristic (IPC) is based on information theory and allows a comparison with ideal coding schemes. Finally, concatenated codes are considered including turbo decoding and an EXtrinsic Information Transfer (EXIT) charts analysis.

Chapter 4: Code Division Multiple Access

The multiple access scheme CDMA is described in Chapter 4. Besides single-carrier CDMA with the Rake receiver, OFDM-CDMA with different despreading or equalization techniques is also considered. Moreover, the basic differences between uplink and downlink are explained and some examples for spreading sequences are presented. Next, the high performance of low rate coding exploiting the inherent spreading in CDMA systems is demonstrated. The chapter ends with an information theoretical analysis for the CDMA uplink with random spreading.

Chapter 5: Multi-User Detection in CDMA Systems

While the fourth chapter mainly restricts on single-user matched filters, Chapter 5 considers multi-user detection strategies for CDMA systems. After sketching the optimum detectors, low cost linear detectors as well as nonlinear multistage detectors including turbo processing with channel decoding are derived. The chapter closes with a combination of linear pre-processing and nonlinear interference cancellation based on the QL decomposition of the mixing matrix.

Chapter 6: Multiple Antenna Systems

Chapter 6 covers several topics related to multiple antenna systems. It starts with diversity concepts like space-time coding exploiting the basics derived in Chapter 1. Afterwards, the principle of spatial multiplexing is explained. Besides the detection algorithms already described in Chapter 5, a new approach based on the lattice reduction is presented showing a performance close to the optimum maximum likelihood detector. The chapter closes with a brief information theoretical analysis of multiple antenna systems.

Appendices

In Appendix A, some basic derivations concerning the equivalent baseband representation and the moment generating function of Rice fading are presented. Furthermore, it contains tables with frequently used channel models. Appendix B proves the chain rules for entropy and information as well as data processing theorem. Finally, Appendix C presents some basics of linear algebra, Householder reflection and Givens rotation, as well as the LLL algorithm for the lattice reduction.

Notational Remarks

In order to avoid confusion, some notational remarks should be made. Real and imaginary parts of a signal $x(t)$ are denoted by $x'(t)$ and $x''(t)$, respectively. In order to distinguish time-continuous signals and their sampled time-discrete versions, square brackets are used in the time-discrete case leading to $x[k] = x(kT_s)$ with T_s as sampling interval. Moreover, \mathcal{X} represents a stochastic process while $x[k]$ a corresponding sampling functions. Hence, probability mass functions of continuous processes are denoted by $p_{\mathcal{X}}(x)$. The conditional probability mass function $p_{\mathcal{X}|d}(x)$ considers the process \mathcal{X} given a fixed hypothesis d so that it is a function of only a single variable x .

Processes comprising several variables are denoted by $\underline{\mathcal{X}}$. Column vectors, row vectors and matrices are distinguished by \mathbf{x} , $\underline{\mathbf{x}}$, and \mathbf{X} , respectively. A set \mathbb{X} contains all possible values a signal $x[k]$ can take, i.e. $x[k] \in \mathbb{X}$ holds. It can be either an infinite set like \mathbb{Z} , \mathbb{R} , or \mathbb{C} , representing the sets of all integers, real numbers or complex numbers, respectively, or a finite set consisting generally of N symbols $\{X_0, \dots, X_{N-1}\}$.

Bremen, October 2004

Volker Kühn

Contents

Preface	III
1 Introduction to Digital Communications	1
1.1 Basic System Model	1
1.1.1 Introduction	1
1.1.2 Multiple Access Techniques	3
1.1.3 Principle Structure of SISO Systems	6
1.2 Characteristics of Mobile Radio Channels	9
1.2.1 Equivalent Baseband Representation	9
1.2.2 Additive White Gaussian Noise	12
1.2.3 Frequency-Selective Time-Variant Fading	13
1.2.4 Systems with Multiple Inputs and Outputs	18
1.3 Signal Detection	21
1.3.1 Optimal Decision Criteria	21
1.3.2 Error Probability for AWGN Channel	24
1.3.3 Error and Outage Probability for Flat Fading Channels	26
1.4 Digital Linear Modulation	29
1.4.1 Introduction	29
1.4.2 Amplitude Shift Keying (ASK)	30
1.4.3 Quadrature Amplitude Modulation (QAM)	32
1.4.4 Phase Shift Keying (PSK)	35
1.5 Diversity	39

1.5.1	General Concept	39
1.5.2	MRC for Independent Diversity Branches	43
1.5.3	MRC for Correlated Diversity Branches	50
2	Information Theory	55
2.1	Basic Definitions	55
2.1.1	Information, Redundancy and Entropy	55
2.1.2	Conditional, Joint and Mutual Information	57
2.1.3	Extension for Continuous Signals	60
2.1.4	Extension for Vectors and Matrices	61
2.2	Channel Coding Theorem for SISO Channels	62
2.2.1	Channel Capacity	62
2.2.2	Cut-off Rate	64
2.2.3	Gallager Exponent	67
2.2.4	Capacity of the AWGN Channel	69
2.2.5	Capacity of Rayleigh Fading Channel	73
2.2.6	Channel Capacity and Diversity	76
2.3	Channel Capacity of MIMO Systems	79
3	Forward Error Correction Coding	87
3.1	Introduction	87
3.2	Linear Block Codes	90
3.2.1	Description by Matrices	90
3.2.2	Simple Parity Check and Repetition Codes	94
3.2.3	Hamming and Simplex Codes	94
3.2.4	Hadamard-Codes	95
3.2.5	Trellis Representation of Linear Block Codes	96
3.3	Convolutional Codes	97
3.3.1	Structure of Encoder	98
3.3.2	Graphical Description of Convolutional Codes	101
3.3.3	Puncturing Convolutional Codes	102
3.3.4	ML Decoding with Viterbi Algorithm	104

3.4	Soft-Output Decoding of Binary Codes	107
3.4.1	Log-Likelihood Ratios – A Measure of Reliability	107
3.4.2	General Approach for Soft-Output Decoding	110
3.4.3	BCJR Algorithm for Binary Block Codes	113
3.4.4	BCJR Algorithm for Binary Convolutional Codes	116
3.4.5	Soft-Output Decoding for Walsh Codes	118
3.4.6	Implementation in Logarithmic Domain	118
3.5	Performance Evaluation of Linear Codes	121
3.5.1	Distance Properties of Codes	121
3.5.2	Error Rate Performance of Codes	125
3.5.3	Information Processing Characteristic	131
3.6	Concatenated Codes	136
3.6.1	Introduction	136
3.6.2	Performance Analysis for Serial Concatenation	139
3.6.3	Performance Analysis for Parallel Concatenation	144
3.6.4	Turbo Decoding of Concatenated Codes	149
3.6.5	EXIT Charts Analysis of Turbo Decoding	156
4	Code Division Multiple Access	167
4.1	Introduction	167
4.2	Fundamentals	168
4.2.1	Direct-Sequence Spread Spectrum	168
4.2.2	Direct-Sequence CDMA	175
4.2.3	Single-User Matched Filter (SUMF)	180
4.2.4	Spreading Codes	186
4.3	OFDM-CDMA	190
4.3.1	Multi-Carrier Transmission	190
4.3.2	Orthogonal Frequency Division Multiplexing	192
4.3.3	Combining OFDM and CDMA	197
4.4	Low Rate Channel Coding in CDMA Systems	206
4.4.1	Conventional Coding Scheme (CCS)	207
4.4.2	Code-Spread Scheme (CSS)	208

4.4.3	Serially Concatenated Coding Scheme (SCCS)	209
4.4.4	Parallel Concatenated Coding Scheme (PCCS)	213
4.4.5	Influence of MUI on Coding Schemes	215
4.5	Uplink Capacity of CDMA Systems	218
4.5.1	Orthogonal Spreading Codes	219
4.5.2	Random Spreading Codes and Optimum Receiver	220
4.5.3	Random Spreading Codes and Linear Receivers	221
5	Multi-User Detection in CDMA Systems	227
5.1	Optimum Detection	227
5.1.1	Optimum Joint Sequence Detection	228
5.1.2	Optimum Preprocessing and Subsequent Decoding	229
5.1.3	Turbo Detection with Optimum Preprocessing and Decoding	231
5.2	Linear Multi-User Detection	234
5.2.1	Decorrelator (Zero Forcing, ZF)	234
5.2.2	Minimum Mean Squared Error Receiver (MMSE)	238
5.2.3	Linear Parallel Interference Cancellation	242
5.2.4	Linear Successive Interference Cancellation	245
5.3	Nonlinear Iterative Multi-User Detection	247
5.3.1	Nonlinear Devices	247
5.3.2	Uncoded Nonlinear Interference Cancellation	250
5.3.3	Nonlinear Coded Interference Cancellation	257
5.4	Combining Linear MUD and Nonlinear SIC	262
5.4.1	BLAST Detection	262
5.4.2	QL Decomposition for Zero-Forcing Solution	263
5.4.3	QL Decomposition for MMSE Solution	272
5.4.4	Turbo Processing	276
6	Multiple Antenna Systems	279
6.1	Introduction	279
6.2	Multiple Antenna Diversity	280
6.2.1	Receive Diversity	281

6.2.2	Space-Time Transmit Diversity	283
6.2.3	Orthogonal Space-Time Block Codes	287
6.2.4	Space-Time Trellis Codes	298
6.3	Multi-Layer Transmission	310
6.3.1	Channel Knowledge at Transmitter and Receiver	310
6.3.2	Channel Knowledge only at Receiver	313
6.3.3	Performance of Multi-Layer Detection Schemes	315
6.3.4	Lattice Reduction aided Detection	319
6.4	Information Theoretic Analysis	328
A	Channel Models	335
A.1	Equivalent Baseband Representation	335
A.2	Typical Propagation Profiles for Outdoor Mobile Radio Channels .	336
A.3	Moment Generating Function for Ricean Fading	338
B	Derivations for Information Theory	341
B.1	Chain Rule for Entropies	341
B.2	Chain Rule for Information	342
B.3	Data Processing Theorem	342
C	Linear Algebra	343
C.1	Selected Basics	343
C.2	Householder Reflections and Givens Rotation	349
C.3	LLL Lattice-Reduction	351
Abbreviations		357
References		361
Index		379

Chapter 1

Introduction to Digital Communications

1.1 Basic System Model

1.1.1 Introduction

Vector channels or equivalently multiple-input multiple-output (MIMO) channels represent a very general description for a wide range of applications. They incorporate as special cases SISO (Single-Input Single-Output), MISO (Multiple-Input Single-Output) and SIMO (Single-Input Multiple Output) channels. Often, MIMO channels are only associated with multiple antenna systems. However, they are not restricted to this case but can be used in a much broader context, e.g. for any kind of multi-user communication. Therefore, the aim of this work is to study MIMO systems for two specific examples, namely Code Division Multiple Access (CDMA) and multiple antenna systems. Besides a unified description using vector notations, detection algorithms are derived that make the similarity of both systems obvious.

Fig. 1.1.1 illustrates the considered scenario in a very abstract form. Generally, a common channel that may represent a single cell in a cellular network is accessed by N_I inputs and N_O outputs. In this context, the term *channel* is not limited to the physical transmission medium but has a more general meaning and incorporates also parts of a digital communication system. The boundary between transmitter and receiver on the one side and medium on the other side is not strict and depends on the considered scenario. Detailed information about specific descriptions can be found in subsequent chapters.

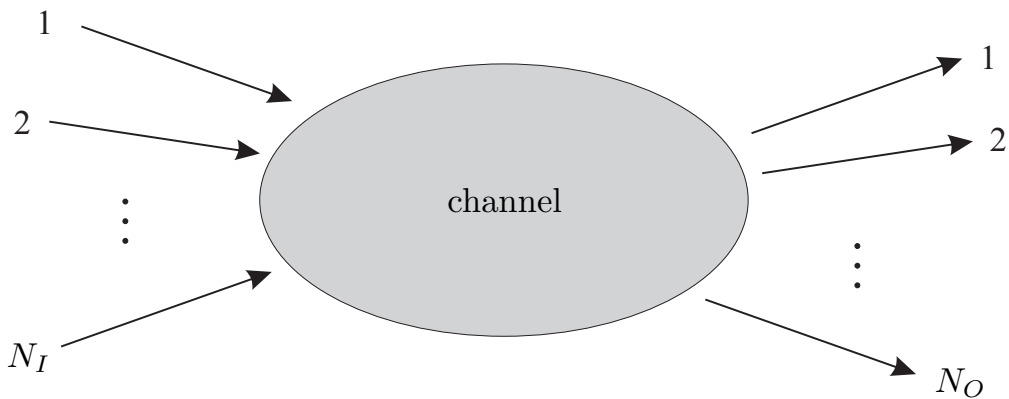


Figure 1.1.1: Principle of multiple access to a common channel

Principally, single-user and multi-user communications are distinguished. In the single-user case, multiple inputs and outputs of a vector channel may correspond to different transmit and receive antennas, carrier frequencies or time slots. Due to the fact that data stems from a single user, intelligent signalling at the transmitter can be performed, e.g. for efficient receiver realizations. In this work, we will restrict on multiple antenna systems that can be used in several ways depending on the channel characteristics and the system requirements. Multiple antennas can be employed for increasing the system's diversity degree [SW94, Ala98, NTSC98, TJC99a] and, therefore, enhance the link performance. The link reliability can also be enhanced by beamforming. Alternatively, several data streams can be multiplexed over spatially separated channels in order to multiply the data rate without increasing bandwidth [Fos96, FG98, GFWV98]. Multiple antenna systems are addressed in Chapter 6.

Contrarily, the $N_I = N_O$ inputs and outputs may correspond to N_U independent user signals in the multi-user case¹. Concerning mobile radio communications, a central base station coordinates the transmissions of uplink and downlink, i.e. from mobile subscribers to the base station and vice versa, respectively. In the downlink, a synchronous transmission can be easily established because all signals originate from the same transmitter. Moreover, knowledge about interactions between different users and their propagation conditions can be exploited at the base station. This allows sophisticated signalling in order to avoid mutual interference and to distribute the total transmit power onto different users efficiently. In many cases, intelligent signalling at the base station coincides with low complexity receivers, being very important for mobile terminals with limited battery power.

However, establishing a synchronous transmission in the uplink requires high efforts because mobile subscribers transmit more or less independently. They communicate only with the base station and not among themselves. In most practical

¹In multi-user scenarios, transmitters and receivers can be as well equipped with multiple antennas leading to multi-user MIMO communications.

cases, they have no information about their influence on other users so that mutual interference cannot be avoided prior to transmission. Hence, effort has to be spent at the base station to compensate this drawback. However, optimal signalling strategies even for the downlink highly depend on the level of knowledge at transmitter and receiver. They are only known for a few special cases and still subject to intensive research.

Looking at the transmission of multiple data streams sharing a common medium, their separation is managed by multiple access techniques regardless whether single- or multi-user communications are considered. In order to ensure a reliable communication, interference between different data streams should be avoided. Ideally, the access on the medium has to be coordinated in a way that different signals are pairwise orthogonal so that no multiple access interference (MAI) disturbs the transmission. However, in most cases, orthogonality cannot be maintained due to the influence of the mobile radio channel. Moreover, the characteristics of the MIMO system highly depend on the specific access techniques.

In order to have a common background, this chapter gives a brief introduction to digital communications. After we have discussed some aspects on multiple-input multiple-output systems, the remaining part of this subsection briefly introduces the most important multiple access schemes and the principle structure of digital communication systems. Next, Section 1.2 is confined to the description of single-input single-output mobile radio channels. Afterwards, some analysis concerning signal detection and the theoretical performance of linear modulation schemes for different transmission channels are presented in Sections 1.3 and 1.4. Finally, Section 1.5 explains the benefits of diversity and delivers basic results for outage and ergodic error probabilities.

1.1.2 Multiple Access Techniques

As explained above, multiple access schemes coordinate the transmission of multiple data streams over a common medium. The description in this section is kept quite general so that it fits to both scenarios, for multi-user communications as well as for the single-user case with several data streams.

Time Division Multiple Access (TDMA)

A quite common multiple access technique is time division multiple access. As the name suggests, the time axis is divided into different time slots according to **Fig. 1.1.2**. Each slot is assigned to a certain data stream whereby a user can also occupy several slots. A defined number of slots build a frame that is repeated periodically. Hence, each user has periodical access to the shared medium. Due to the influence of the transmission channel (cf. Section 1.2) and restrictions of

practical filter design, guard intervals have to be introduced between successive slots in order to avoid interference between them. Within these intervals, no information is transmitted so that they represent redundancy and reduce the spectral efficiency of the communication system.

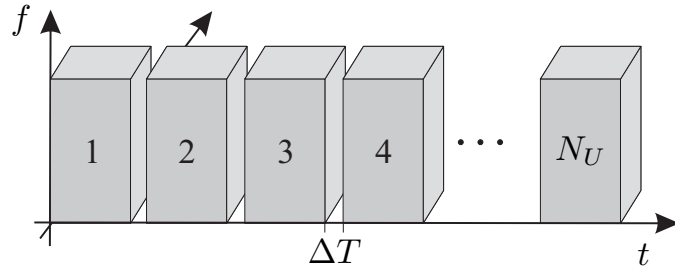


Figure 1.1.2: Principle of Time Division Multiple Access

Frequency Division Multiple Access (FDMA)

Alternatively, the frequency axis can be divided into subbands as illustrated in **Fig. 1.1.3**. The data streams are now distributed on different frequency bands rather than on different time slots. However, in mobile environments, the signals' bandwidths are spread by the Doppler effect so that neighboring subbands interfere. Thus, gaps combatting this effect at the expense of a reduced spectral efficiency are required also for FDMA.

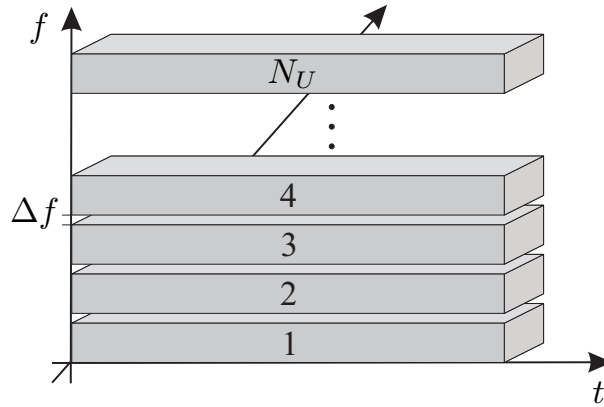


Figure 1.1.3: Principle of Frequency Division Multiple Access

Code Division Multiple Access (CDMA)

In contrast to both preceding schemes code division multiple access allows simultaneous access on the channel in the same frequency range. The basic principle is to

spectrally spread the data streams with specific sequences called spreading codes. The signals can be distinguished by assigning them individual spreading codes. This opens a third dimension as can be seen in **Fig. 1.1.4**. One intuitive choice would lead to orthogonal codes ensuring a parallel transmission of different user signals. However, the transmission channel generally destroys the orthogonality and multi-user interference (MUI) becomes a limiting factor concerning spectral efficiency (cf. Chapters 4 and 5).

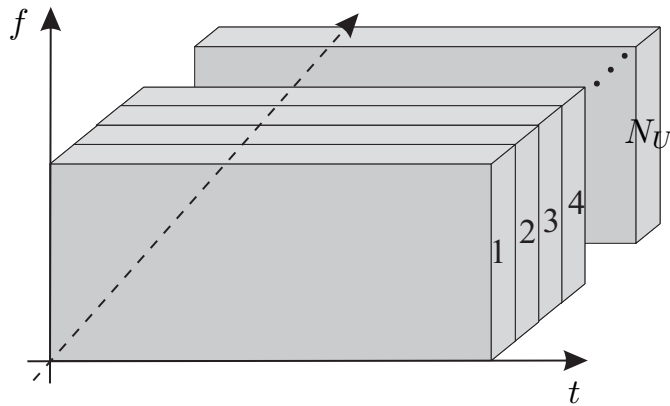


Figure 1.1.4: Principle of Code and Space Division Multiple Access

Space Division Multiple Access (SDMA)

The fourth access scheme exploits the resource space (Fig. 1.1.4 and **Fig. 1.1.5**). Spatially separated data streams can simultaneously access the channel in the same frequency band provided that the locations of transmit and receive antennas are appropriately chosen. In mobile environments, this requirement is difficult to fulfill because users are changing their position during the connection. Therefore, quasi-static scenarios or combinations with the aforementioned access techniques are often considered. Mutual interference is likely to occur also in SDMA systems because transmitter and receiver have no perfect channel knowledge what would be necessary to totally avoid interference.

Naturally, all mentioned access schemes can be combined. The well-known GSM (Global System for Mobile Communications) and DCS-1800 (Digital Cellular System) standards both combine TDMA and FDMA. In UMTS (Universal Mobile Telecommunications System) or IMT-2000 (International Mobile Communications) systems, CDMA is used in connection with TDMA and FDMA [DGNS98, OP98b, TCD⁺98]. While TDMA, FDMA and CDMA have been already used quite a long time, SDMA came up in the last years. This development was pushed by the demand to use assigned licenses for mobile communications as efficiently as possible. Hence, all resources have to be exploited for reaching this goal.

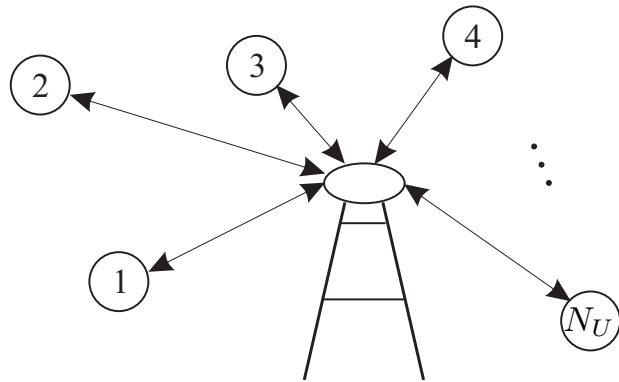


Figure 1.1.5: Principle of Space Division Multiple Access

1.1.3 Principle Structure of SISO Systems

Since the behavior and the properties of a multiple-input multiple-output system highly depend on the characteristics of the underlying SISO systems between each pair of transmit and receive antennas, this subsection describes their principle structure. **Fig. 1.1.6** shows a simplified time-discrete block diagram of a single-input single-output communication link. The time-discreteness is expressed by square brackets and the time indices i , ℓ , and k indicate different symbol rates of the corresponding signals. Neglecting a lot of fundamental components of practical systems like source coding, analog-to-digital conversion etc., the transmitter consists of three blocks being of special interest here: a forward error correction (FEC) encoder, an interleaver Π and a signal mapper. Due to our concentration on digital communications, inputs and outputs of FEC encoder and interleaver are binary while the output of the signal mapper depends on the type of modulation and can take on symbols out of an M -ary alphabet \mathbb{X} . Conventionally, $M = 2^m$ is a power of 2. The receiver comprises the corresponding counterparts of the above mentioned blocks in reverse order. The first block performs some kind of signal processing (SP) – depending on the channel – and the demapping. It is followed by a de-interleaver Π^{-1} and an FEC decoder delivering estimates $\hat{d}[i]$ of the transmitted information bits.

All particular blocks mentioned so far will be subsequently described in more detail. However, some remarks on the time-discrete channel depicted in Fig. 1.1.6 are necessary at this point. In order to simplify the description and to concentrate on the main focus of this work, we declare all time-continuous components of modulator and demodulator as parts of a time-discrete channel model generally described in the equivalent baseband (cf. Section 1.2). Therefore, the only parts of modulator and demodulator that separately appear in Fig. 1.1.6 are the signal mapper and the demapper. These assumptions coincide with a citation of Massey [Mas84]:

'the purpose of the modulation system is to create a good discrete channel from the modulator input to the modulator output, and the purpose of the coding system is to transmit the information bits reliably through this discrete channel at the highest practicable rate.'

However, it is not always easy to strictly separate both devices (e.g. for coded modulation [Ung82, BDMS91]).

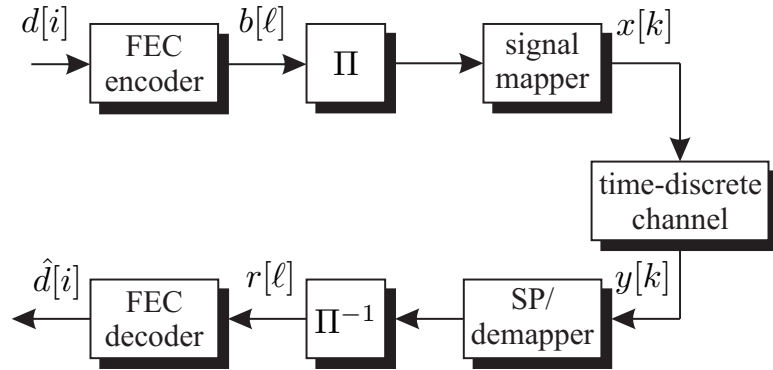


Figure 1.1.6: Principle structure of digital communication systems

Interleaving

Interleaving plays an important role in many digital communication systems for manifold reasons. In the context of mobile radio communications, fading channels often lead to bursty errors, i.e. several successive symbols may be corrupted by deep fades. This has crucial impact on the decoding performance because of its sensitivity to bursty errors (compare decoding of convolutional codes in Chapter 3). In order to overcome this difficulty, interleaving is applied. At the transmitter, an interleaver simply permutes the data stream $b[\ell]$ in a specified way so that the symbols are transmitted in a different order. Consequently, a de-interleaver has to be employed at the receiver re-ordering the symbols back into the original succession. Moreover, we will see in Section 3 that interleaving is also employed in concatenated coding schemes.

Block Interleaver

There exist several types of interleavers. The simplest one is termed block interleaving which divides a sequence into blocks of length L_π . The symbols $b[\ell]$ within each block are then permuted by writing them column-wise into an array consisting of L_{row} rows and L_{col} columns and reading them row by row. An example with $L_{\text{row}} = 3$ and $L_{\text{col}} = 4$ is shown in **Fig. 1.1.7**. The input sequence $b[0], b[1], \dots, b[11]$ becomes due to interleaving

$$b[0], b[3], b[6], b[9], b[1], b[4], b[7] b[10], b[2], b[5], b[8], b[11].$$

It can be recognized that there is a spacing between originally successive symbols of $L_I = 4$. This gap is called interleaving depth. The optimum number of rows and columns and, therefore, the interleaving depth depends on several factors that are discussed in subsequent chapters.

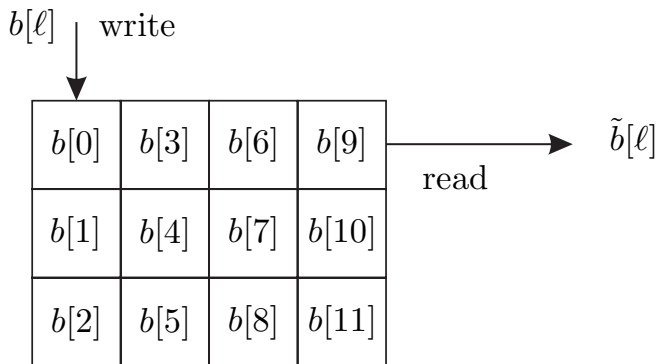


Figure 1.1.7: Structure of block interleaver of length $L_\pi = 12$

Convolutional Interleaving

For the sake of completeness, convolutional interleaving should be mentioned here. It provides the same interleaving depth as block interleaving but with lower delays and smaller memory. However, since this interleaver is not addressed in the sequel, we do not go into further details and refer to [VO79].

Random Interleaving

The application of block interleaving in concatenated coding schemes generally leads to a weak performance. Due to the regular structure of the interleaver it may happen that the temporal distance between pairs of symbols does not change by interleaving resulting in poor distance properties of the entire code (cf. Section 3.6). Therefore, random or pseudo-random interleavers are often applied in this context. Pseudo-random interleavers can be generated by calculating row and column indices with modulo arithmetic. For concatenated coding schemes, interleavers are optimized with respect to the constituent codes.

Interleaving delay

A tight restriction to the total size of interleavers may occur for certain applications such as full duplex speech transmission. Here, delays of some 10 ms are tolerable. Since the interleaver has first to be completely written before it can be read out, its size L_π directly determines the delay $\Delta t = L_\pi \cdot T_s$.

1.2 Characteristics of Mobile Radio Channels

1.2.1 Equivalent Baseband Representation

Wireless channels for mobile radio communications are a challenging medium that require careful system design for reliable transmission. As single-input single-output channels they represent an important building block of vector channels. Therefore, this section describes their time discrete, equivalent baseband representation in more detail. **Fig. 1.2.1** depicts the entire model that comprises all time-continuous analog components even those from transmitter and receiver. The whole structure represents a time-discrete model whose input $x[k]$ is a sequence of generally complex-valued symbols of duration T_s according to some finite symbol alphabet \mathbb{X} . The output sequence $y[k]$ has typically the same rate $1/T_s$ and its symbols are distributed within the complex plane \mathbb{C} .

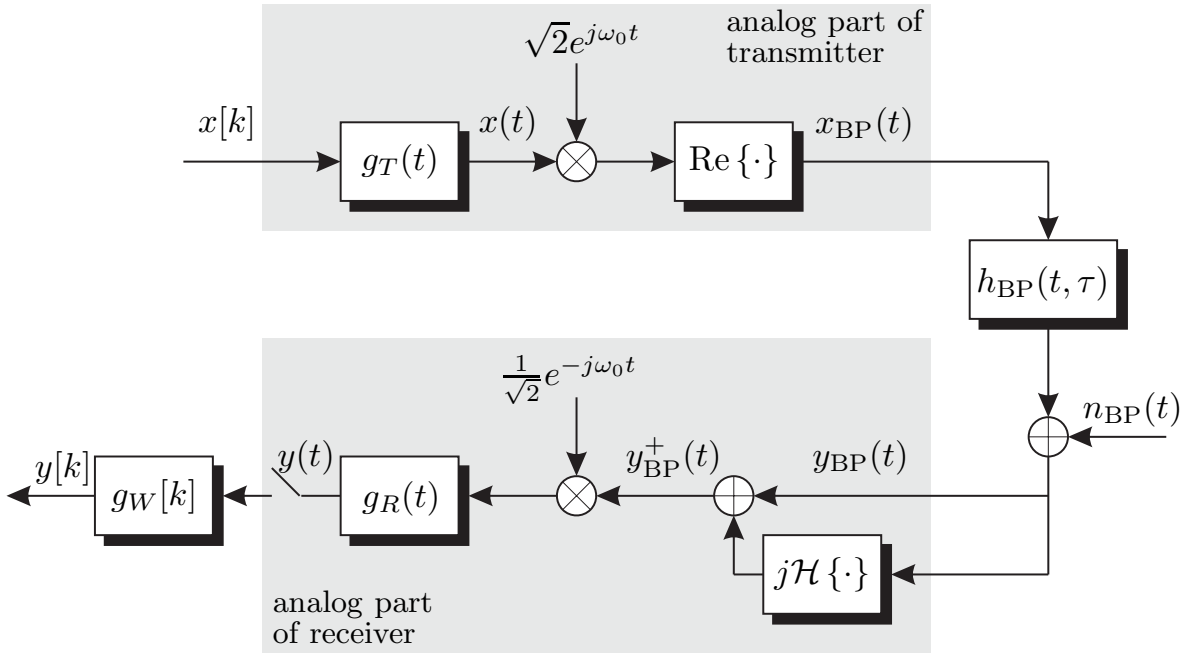


Figure 1.2.1: Structure of the time-discrete, equivalent baseband representation of a mobile radio channel

The input $x[k]$ is transformed by the transmit filter $g_T(t)$ of bandwidth B into a time-continuous, bandlimited signal

$$x(t) = \sum_k x[k] \cdot g_T(t - kT_s) \quad (1.2.1)$$

called complex envelope. Denoting the symbols of the alphabet \mathbb{X} by X_μ and assuming that the energy of the transmit filter impulse response is defined to T_s ²,

²The impulse response $g_T(t)$ itself has no dimension and the time unit stems from integration.

a single symbol $x[k] \cdot g_T(t - kT_s)$ has the average energy

$$E_s = \text{E}\{|X_\mu|^2\} \cdot \int_{-\infty}^{\infty} |g_T(t)|^2 dt := T_s \cdot \text{E}\{|X_\mu|^2\} \quad (1.2.2)$$

resulting in an average power of $\sigma_x^2 = E_s/T_s = \text{E}\{|X_\mu|^2\}$. For zero-mean and independent identically distributed (i.i.d.) symbols $x[k]$, the average spectral density of $x(t)$ is [Kam96]

$$\Phi_{XX}(j\omega) = \frac{1}{T_s} \cdot |G_T(j\omega)|^2 \cdot \text{E}\{|X_\mu|^2\} = \frac{E_s}{T_s^2} \cdot |G_T(j\omega)|^2. \quad (1.2.3)$$

Obviously, it mainly depends on the spectral shape of the transmit filter $g_T(t)$ and not on the kind of modulation scheme. Proceeding towards transmission, the real-valued bandpass signal

$$x_{\text{BP}}(t) = \sqrt{2} \cdot \text{Re}\{x(t) \cdot e^{j\omega_0 t}\} = \sqrt{2} \cdot [x'(t) \cos(\omega_0 t) - x''(t) \sin(\omega_0 t)] \quad (1.2.4)$$

is obtained by shifting $x(t)$ into the bandpass region with the carrier frequency $\omega_0 = 2\pi f_0$ and taking the real part. The factor $\sqrt{2}$ in (1.2.4) keeps the signal power and the symbol energy constant during modulation. The average spectral density of $x_{\text{BP}}(t)$ has the form

$$\Phi_{X_{\text{BP}}X_{\text{BP}}}(j\omega) = \frac{E_s}{2T_s^2} \cdot (|G_T(j\omega - j\omega_0)|^2 + |G_T(j\omega + j\omega_0)|^2). \quad (1.2.5)$$

Besides the shift to $\pm\omega_0$, it differs from $\Phi_{XX}(j\omega)$ by the factor 1/2. **Fig. 1.2.2** sketches the spectral densities for a rectangular shape of $G_T(j\omega)$ with $B = 1/(2T_s)$.

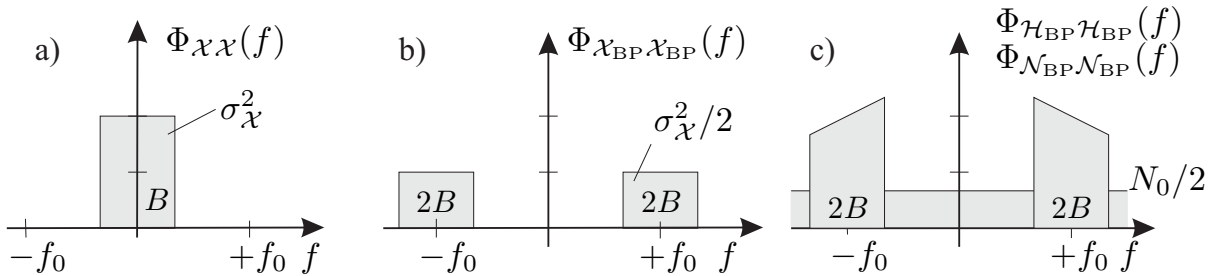


Figure 1.2.2: Power spectral densities for **a)** complex envelope, **b)** bandpass signal and **c)** transmission channel for a rectangular shape of $G_T(j\omega)$

Now, $x_{\text{BP}}(t)$ is transmitted over the mobile radio channel generally represented by its time-variant impulse response $h_{\text{BP}}(t, \tau)$ and an additive noise term $n_{\text{BP}}(t)$ with spectral density $N_0/2$

$$y_{\text{BP}}(t) = h_{\text{BP}}(t, \tau) * x_{\text{BP}}(t) + n_{\text{BP}}(t). \quad (1.2.6)$$

The convolution in (1.2.6) is defined by

$$h_{\text{BP}}(t, \tau) * x_{\text{BP}}(t) = \int_0^\infty h_{\text{BP}}(t, \tau) x_{\text{BP}}(t - \tau) d\tau . \quad (1.2.7)$$

In order to obtain an equivalent baseband representation again, negative frequencies are eliminated with the Hilbert transformation [Kam96, Pro95]

$$\mathcal{H}\{a(t)\} = \int_{-\infty}^{\infty} \frac{a(\tau)}{t - \tau} d\tau \quad \circlearrowleft \quad \mathcal{H}\{A(j\omega)\} = -j \operatorname{sgn}(\omega) A(j\omega) . \quad (1.2.8)$$

Therefore, adding $j\mathcal{H}\{y_{\text{BP}}(t)\}$ to the received signal $y_{\text{BP}}(t)$ yields the complex analytical signal

$$y_{\text{BP}}^+(t) = y_{\text{BP}}(t) + j\mathcal{H}\{y_{\text{BP}}(t)\} \quad \circlearrowleft \quad Y_{\text{BP}}^+(j\omega) = \begin{cases} 2Y_{\text{BP}}(j\omega) & \text{for } \omega > 0 \\ 0 & \text{else} \end{cases} \quad (1.2.9)$$

whose spectrum vanishes for negative frequencies. However, for positive frequencies, the spectrum is doubled or, equivalently, the spectral power density is quadrupled (cf. **Fig. 1.2.3**). Equivalent to the transmitter, the spectral shift back into the baseband is accompanied by a factor $1/\sqrt{2}$ in order to keep the average power constant. Concerning the background noise, this leads to a spectral density of N_0 . As is shown in the Appendix A.1, the output of the receive filter $g_R(t)$ has the form

$$y(t) = g_R(t) * h(t, \tau) * x(t) + n(t) = \sum_k x[k] \cdot \tilde{h}(t, kT_s) + n(t) \quad (1.2.10)$$

where $h(t, \tau) = 1/2 \cdot h_{\text{BP}}^+(t, \tau) e^{-j\omega_0 t}$ and $n(t) = g_R(t) * (n^+(t) e^{-j\omega_0 t} / \sqrt{2})$ denote the equivalent baseband representations of channel impulse response and the filtered background noise, respectively. The filter $\tilde{h}(t, kT_s)$ comprises transmit and receive filter as well as the channel impulse response and represents the channel response on an impulse transmitted at time instance kT_s ³.

In order to obtain the maximum signal to noise ratio at the output of the receive filter, $g_R(t)$ has to be matched to the concatenation of channel impulse response and transmit filter [For72, Kam96], i.e. $g_R(t) = f^*(-t)$ holds with $f(t) = g_T(t) * h(t, \tau)$. However, even if $g_T(t)$ fulfills the first Nyquist criterion [Nyg28], the background noise $n(t)$ is colored by $h(t, \tau)$. Therefore, a prewhitening filter $g_W[k]$ working at the sampling rate $1/T_s$ is required that decorrelates the noise samples $n(t)|_{t=kT_s}$ ⁴. Finally, the time-discrete equivalent baseband channel delivers a

³Note that the second parameter of $\tilde{h}(t, kT_s)$ does not represent delay τ , but the transmission time kT_s .

⁴In practice, the receive filter $g_R(t)$ is only matched to $g_T(t)$ due to lower implementation costs and imperfect knowledge of the channel impulse response.

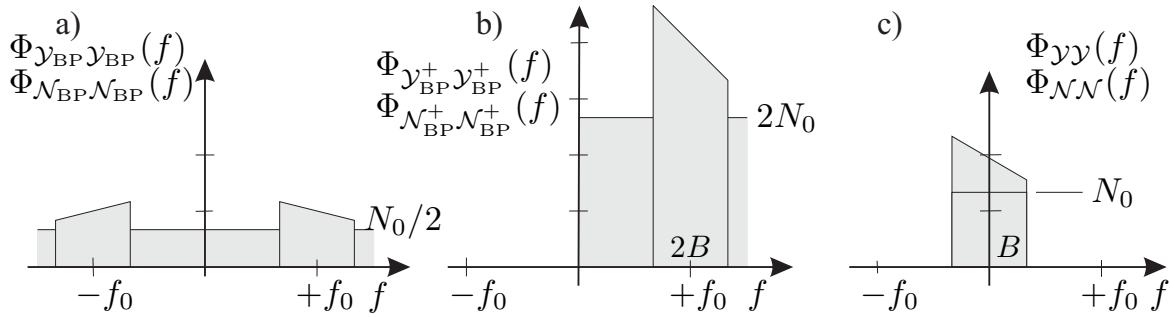


Figure 1.2.3: Power spectral densities for **a)** received bandpass signal, **b)** analytical signal and **c)** received complex envelope

complex-valued signal $y[k] = g_W[k] * y(t)|_{t=kT_s}$ by sampling $y(t)$ at rate $1/T_s$ and filtering it with $g_W[k]$.

Throughout this work, $g_T(t)$ is assumed to be a perfect lowpass filter of bandwidth $B = 1/(2T_s)$. With $g_R(t)$ matched to $h(t, \tau) * g_T(t)$ and a perfect prewhitening filter incorporated into the time discrete channel model $h[k, \kappa]$, the received signal $y[k]$ has the form

$$y[k] = \sum_{\kappa=0}^{L_t} h[k, \kappa] \cdot x[k - \kappa] + n[k] \quad (1.2.11)$$

where L_t denotes the total filter length and $n[k]$ is termed Additive White Gaussian Noise (AWGN). It is described in more detail in the next subsection followed by a description of the frequency-selective fading channel.

1.2.2 Additive White Gaussian Noise

Every data transmission is disturbed by noise stemming from thermal noise, noise of electronic devices and other sources. Due to the superposition of many different statistically independent processes at the receive antenna, the noise $n_{\text{BP}}(t)$ is generally modelled as white and Gaussian distributed. The attribute white describes the flat spectral density that corresponds with uncorrelated successive samples in time domain. For Gaussian distributed samples, this is equivalent with statistical independence. A model reflecting this behavior is the AWGN (Additive White Gaussian Noise) channel. As mentioned in the last section, its two-sided spectral power density $N_0/2$ results in infinite power due to the infinite bandwidth. Therefore, this model gains practical relevance only with a bandwidth limitation, e.g. by filtering with $g_R(t)$.

In this subsection, the channel is assumed to be frequency-nonselective and time invariant so that $h(t, \tau) = \delta(\tau)$ holds and transmit and receive filters are perfect lowpass filters (cf. Fig. 1.2.2 and 1.2.4b). They fulfill the first Nyquist

condition [Nyq28], i.e. their spectra are symmetric with respect to the Nyquist frequency $f_N = 1/(2T_s)$.⁵ Therefore, the sampled equivalent baseband noise $n[k] = n(t)|_{t=kT_s}$ remains white (cf. **Fig. 1.2.4**) [Kam96] and has a spectral density of N_0 (cf. (1.2.9) and Fig. 1.2.3). N_0 is equally distributed onto the real part $n'[k]$ and the imaginary part $n''[k]$ each with a density of $N_0/2$. They are independent of each other resulting in the joint density

$$\begin{aligned} p_{\mathcal{N}}(n) &= p_{\mathcal{N}'}(n') \cdot p_{\mathcal{N}''}(n'') \\ &= \frac{1}{\sqrt{2\pi\sigma_{\mathcal{N}'}^2}} e^{-\frac{n'^2}{2\sigma_{\mathcal{N}'}^2}} \cdot \frac{1}{\sqrt{2\pi\sigma_{\mathcal{N}''}^2}} e^{-\frac{n''^2}{2\sigma_{\mathcal{N}''}^2}} = \frac{1}{\pi\sigma_{\mathcal{N}}^2} e^{-\frac{|n|^2}{\sigma_{\mathcal{N}}^2}} \end{aligned} \quad (1.2.12)$$

of the complex baseband noise. The power of $n(t)$ and, therefore, $n[k]$ is

$$\sigma_{\mathcal{N}}^2 = 2B \cdot N_0 = \frac{N_0}{T_s} = \sigma_{\mathcal{N}'}^2 + \sigma_{\mathcal{N}''}^2 . \quad (1.2.13)$$

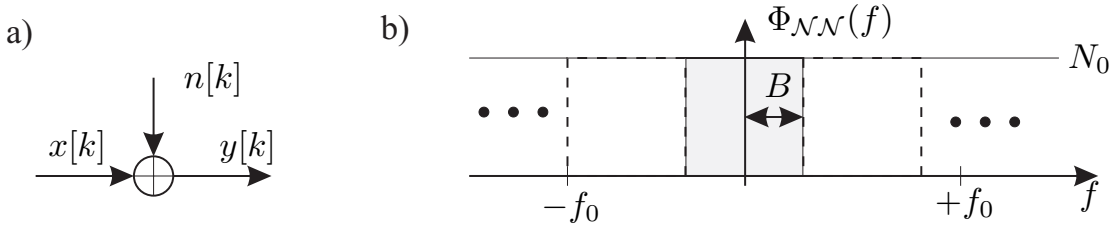


Figure 1.2.4: a) Model and b) spectral density of AWGN channel in the equivalent baseband representation

The perfect lowpass filter $g_R(t) = g_T^*(-t)$ with bandwidth B is matched to $g_T(t)$ [Kam96, Pro95] and maximizes the signal to noise ratio (SNR) at its output. With the signal power $\sigma_{\mathcal{X}}^2 = E_s/T_s$ we obtain the signal to noise ratio

$$SNR = \frac{\sigma_{\mathcal{X}_{BP}}^2}{\sigma_{\mathcal{N}_{BP}}^2} = \frac{\sigma_{\mathcal{X}}^2}{\sigma_{\mathcal{N}}^2} = \frac{E_s/T_s}{N_0/T_s} = \frac{E_s}{N_0} . \quad (1.2.14)$$

as a characteristic measure of the AWGN channel in the baseband as well as in the bandpass regime.

1.2.3 Frequency-Selective Time-Variant Fading

For mobile radio systems, the propagation of radio waves is disturbed by scattering, reflections and shadowing. Generally, many replicas of the same signal arrive at

⁵For perfect lowpass filters, $B = f_N$ and, thus, $B = 1/(2T_s)$ holds, i.e. $2BT_s$ symbols can be transmitted per channel usage.

the receive antenna with different delays, attenuations and phases. Moreover, the channel is time variant due to movements of transmitter or receiver. A channel with N propagation paths can be described by its equivalent baseband impulse response

$$h(t, \tau) = \sum_{\nu=0}^{N-1} h(t, \nu) \cdot \delta(\tau - \tau_\nu), \quad (1.2.15)$$

where t denotes the observation time and $h(t, \nu)$ the complex-valued weighting coefficient corresponding to the ν -th path with delay τ_ν .

Statistical Characterization

Due to the stochastic nature of mobile radio channels they are generally classified by their statistical properties. The autocorrelation function

$$\phi_{\mathcal{H}\mathcal{H}}(\Delta t, \tau) = E\{h^*(t, \tau)h(t + \Delta t, \tau)\} \quad (1.2.16)$$

of $h(t, \tau)$ with respect to t is an appropriate mean for this classification. The faster $\phi_{\mathcal{H}\mathcal{H}}(\Delta t, \tau)$ vanishes in the direction of Δt , the faster is the channel. This relationship can be also expressed in the frequency domain. The Fourier transformation of $\phi_{\mathcal{H}\mathcal{H}}(\Delta t, \tau)$ with respect to Δt yields the scattering function

$$\Phi_{\mathcal{H}\mathcal{H}}(f_d, \tau) = \mathcal{F}\{\phi_{\mathcal{H}\mathcal{H}}(\Delta t, \tau)\}. \quad (1.2.17)$$

The Doppler frequency f_d originates from relative motions between transmitter and receiver. Integrating over τ leads to the Doppler power spectrum

$$\Phi_{\mathcal{H}\mathcal{H}}(f_d) = \int_0^\infty \Phi_{\mathcal{H}\mathcal{H}}(f_d, \tau) d\tau, \quad (1.2.18)$$

describing the power distribution with respect to f_d . The range over which $\Phi_{\mathcal{H}\mathcal{H}}(f_d)$ is almost nonzero is called Doppler bandwidth B_d . It represents a measure for the time variance of the channel and its reciprocal

$$t_c = \frac{1}{B_d} \quad (1.2.19)$$

denotes the coherence time. For $t_c \gg T_s$, the channel is slowly fading, for $t_c \ll T_s$, it changes remarkable during the symbol duration T_s . In the latter case, it is called *time-selective* and *time diversity* (cf. Section 1.4) can be gained when channel coding is applied.

Integrating $\Phi_{\mathcal{H}\mathcal{H}}(f_d, \tau)$ over f_d instead of τ delivers the power delay profile

$$\Phi_{\mathcal{H}\mathcal{H}}(\tau) = \int_{-f_{d \max}}^{f_{d \max}} \Phi_{\mathcal{H}\mathcal{H}}(f_d, \tau) df_d \quad (1.2.20)$$

that describes the power distribution with respect to τ . The coherence bandwidth defined by

$$B_c = \frac{1}{\tau_{\max}} . \quad (1.2.21)$$

represents the bandwidth over which the channel is nearly constant. For *frequency-selective* channels, $B \gg B_c$ holds, i.e. the signal bandwidth B is much larger than the coherence bandwidth and the channel behaves different in different parts of the signal's spectrum. In this case, the maximum delay τ_{\max} is larger than T_s so that successive symbols overlap resulting in linear channel distortions called intersymbol interference (ISI). If the coefficients $h[k, \kappa]$ in the time domain are statistically independent, frequency diversity is obtained (cf. Section 1.4). For $B \ll B_c$, the channel is *frequency-nonselctive*, i.e. its spectral density is constant within the considered bandwidth (*flat fading*). Examples for different power delay profiles can be found in Appendix A.2.

Modelling Mobile Radio Channels

Typically, frequency-selective channels are modelled with time-discrete FIR filters (finite impulse response) following the WSSUS approach (wide sense stationary uncorrelated scattering) [Sch89, Höh92]. According to (1.2.11), the signal is passed through a tapped-delay-line and weighted at each tap with complex channel coefficients $h[k, \kappa]$ as shown in **Fig. 1.2.5**.

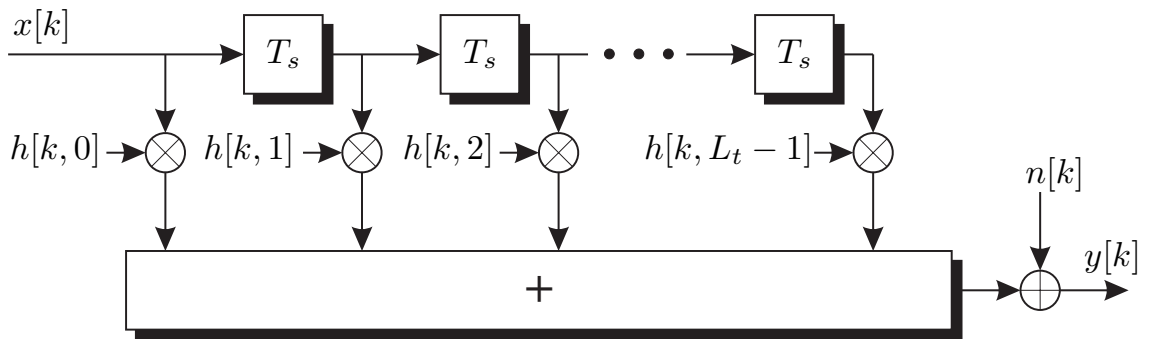


Figure 1.2.5: Tapped-delay-line model of frequency-selective channel with L_t taps

Although the coefficients comprise transmit and receive filter as well as the channel impulse response $h(t, \tau)$ and the pre-whitening filter $g_W[k]$, (as stated in Section 1.2.1), they are assumed to be statistically independent (uncorrelated scattering). The length $L_t = \lceil \tau_{\max}/T_s \rceil$ of the filter depends on the ratio of maximum channel delay τ_{\max} and symbol duration T_s . Thus, the delay axis is divided into equidistant intervals and the e.g. n_κ propagation paths falling into the κ -th interval compose the coefficient

$$h[k, \kappa] = \sum_{i=0}^{n_\kappa-1} e^{j2\pi f_{d,i} k T_s + j\varphi_i} \quad (1.2.22)$$

with φ_i as initial phase of the i -th component. The power distribution among the taps according to the power delay profiles described in Appendix A.2 (tables A.2.1 and A.2.3) is modelled with the distribution of the delays κ . The more delays fall into a certain interval, the higher is the power associated with this interval. Alternatively, a constant number of n propagation paths for each tap can be assumed. In this case,

$$h[k, \kappa] = \rho_\kappa \cdot \sum_{i=0}^{n-1} e^{j2\pi f_{d,i} k T_s + j\varphi_i} \quad (1.2.23)$$

holds and the power distribution is taken into account by adjusting the parameters ρ_κ .

The Doppler frequencies in (1.2.22) and (1.2.23) depend on the relative velocity v between transmitter and receiver, the speed of light c_0 and the carrier frequency f_0

$$f_d = \frac{v}{c_0} \cdot f_0 \cdot \cos \alpha. \quad (1.2.24)$$

In (1.2.24), α represents the angle between the direction of arrival of the examined propagation path and the receiver's movement. Therefore, its distribution determines also that of f_d leading to Table A.2.2. The classical Jakes distribution for $\tau < 0.5 \mu s$ is obtained for isotropic radiations without line of sight connection (cf. **Fig. 1.2.6**). Maximum and minimum Doppler frequencies occur for $\alpha = 0^\circ$ and $\alpha = 180^\circ$, respectively, and determine the Doppler bandwidth $B_d = 2f_{d \max}$.

In the sequel, we focus on the statistics of a single channel coefficient and, therefore, drop the indices k and κ . For a large number of propagation paths per tap, real and imaginary parts of \mathcal{H} are statistically independent and Gaussian distributed stochastic processes and the whole magnitude is Rayleigh distributed

$$p_{|\mathcal{H}|}(\xi) = \begin{cases} 2\xi/\sigma_{\mathcal{H}}^2 \cdot \exp(-\xi^2/\sigma_{\mathcal{H}}^2) & \xi \geq 0 \\ 0 & \text{else} \end{cases} \quad (1.2.25)$$

with mean $E_{\mathcal{H}}\{|h|\} = \sqrt{\pi\sigma_{\mathcal{H}}^2}/2$. In (1.2.25), $\sigma_{\mathcal{H}}^2$ denotes the average power of \mathcal{H} which is chi-squared distributed with two degrees of freedom

$$p_{|\mathcal{H}|^2}(\xi) = \begin{cases} 1/\sigma_{\mathcal{H}}^2 \cdot \exp(-\xi/\sigma_{\mathcal{H}}^2) & \xi \geq 0 \\ 0 & \text{else} \end{cases}. \quad (1.2.26)$$

The phase is uniformly distributed in $[-\pi, \pi]$.

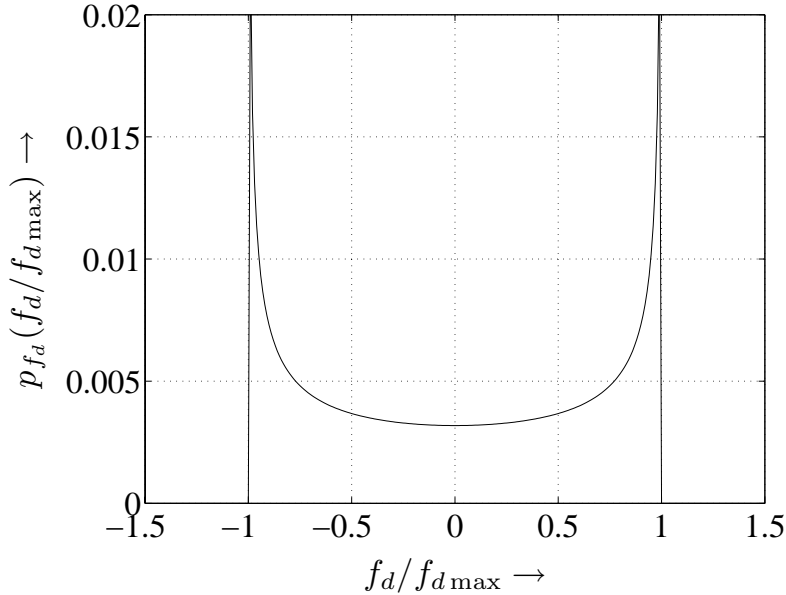


Figure 1.2.6: Distribution of Doppler frequencies for isotropic radiations (Jakes spectrum)

If a line-of-sight (LoS) connection exists between transmitter and receiver, the total power P of the channel coefficient h is shared among a constant LoS and a Rayleigh fading component with variance $\sigma_{\mathcal{H}}^2$. The power ratio between both parts is called *Rice factor* $K = \sigma_{\text{LoS}}^2/\sigma_{\mathcal{H}}^2$. Hence, the LoS component has a power of $\sigma_{\text{LoS}}^2 = K\sigma_{\mathcal{H}}^2$ and the channel coefficient becomes

$$h = \sqrt{\sigma_{\mathcal{H}}^2 \cdot K} + \alpha \quad (1.2.27)$$

with total power $P = (1 + K)\sigma_{\mathcal{H}}^2$. The fading process α consists of real and imaginary parts that are statistically independent zero-mean Gaussian processes each with variance $\sigma_{\mathcal{H}}^2/2$. As shown in [Pro95], the magnitude of \mathcal{H} is Ricean distributed

$$p_{|\mathcal{H}|}(\xi) = \begin{cases} 2\xi/\sigma_{\mathcal{H}}^2 \cdot \exp(-\xi^2/\sigma_{\mathcal{H}}^2 - K) \cdot I_0(2\xi\sqrt{K/\sigma_{\mathcal{H}}^2}) & \xi \geq 0 \\ 0 & \text{else} . \end{cases} \quad (1.2.28)$$

In (1.2.28), $I_0(\cdot)$ denotes the zeroth-order modified Bessel function of first kind [BB99]. Concerning the squared magnitude, we obtain the density

$$p_{|\mathcal{H}|^2}(\xi) = \begin{cases} 1/\sigma_{\mathcal{H}}^2 \cdot \exp(-\xi/\sigma_{\mathcal{H}}^2 - K) \cdot I_0(2\sqrt{\xi K/\sigma_{\mathcal{H}}^2}) & \xi \geq 0 \\ 0 & \text{else} . \end{cases} \quad (1.2.29)$$

The phase is no longer uniformly distributed.

Fig. 1.2.7a shows some Rice distributions for a constant fading variance $\sigma_{\mathcal{H}}^2 = 1$ and varying Rice factor K . For $K = 0$, the direct component vanishes and we

obtain pure Rayleigh fading. In **Fig. 1.2.7b**, the total average power is fixed to $P = 1$ and $\sigma_{\mathcal{H}}^2 = P/(K + 1)$ is adjusted with respect to K . For a growing Rice factor, the probability density function becomes more narrow and reduces to a Dirac impulse for $K \rightarrow \infty$. This extreme case corresponds to the AWGN channel.

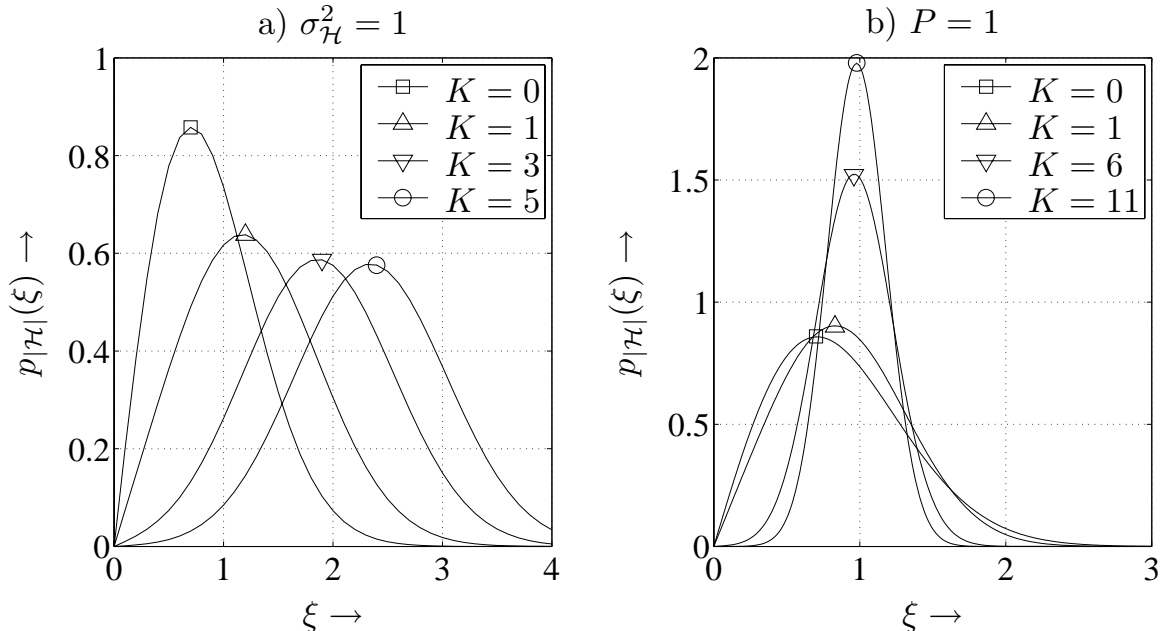


Figure 1.2.7: Rayleigh and Rice distributions for different Rice factors K

The reason for discussing especially the above channels is that they represent somehow extreme propagation conditions. The AWGN channel represents the best case because noise contributions can never be avoided perfectly. The frequency-nonselective Rayleigh fading channel describes the worst case scenario. Finally, Rice fading can be interpreted as a combination of both, where the Rice factor K adjusts the ratio between AWGN and fading parts.

1.2.4 Systems with Multiple Inputs and Outputs

So far, this section described systems with only a single input and a single output. Now, we extend the scenario to multiple-input and multiple-output (MIMO) systems that have already been introduced in Section 1.1.1. However, we restrict here to a general description. Concrete communication systems are treated in Chapters 4 - 6.

According to Fig. 1.1.1, the MIMO system consists of N_I inputs and N_O outputs. Based on (1.2.11), the output of a frequency-selective SISO channel can be described by

$$y[k] = \sum_{\kappa=0}^{L_t-1} h[k, \kappa] \cdot x[k - \kappa] + n[k].$$

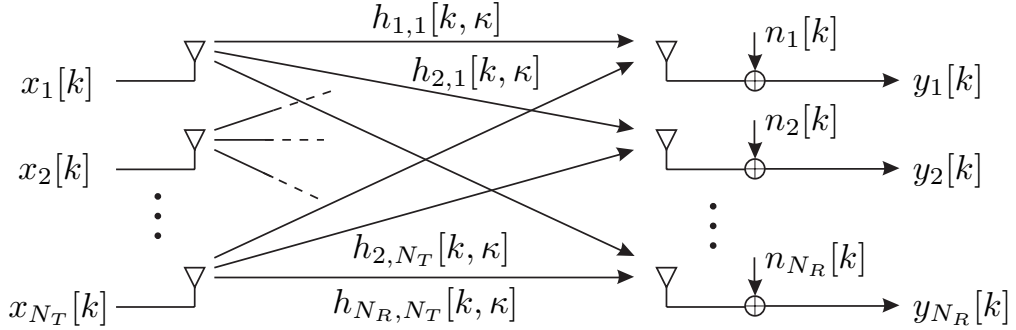


Figure 1.2.8: General structure of frequency-selective MIMO channel

This relationship has now to be extended for MIMO systems. As a consequence, N_I signals $x_\mu[k]$, $1 \leq \mu \leq N_I$, form the input of our system at each time instance k and we obtain N_O output signals $y_\nu[k]$, $1 \leq \nu \leq N_O$. Each pair (μ, ν) of inputs and outputs is connected by a channel impulse response $h_{\nu,\mu}[k, \kappa]$ as depicted in **Fig. 1.2.8**. Therefore, the ν -th output at time instance k can be expressed as

$$y_\nu[k] = \sum_{\mu=1}^{N_I} \sum_{\kappa=0}^{L_t-1} h_{\nu,\mu}[k, \kappa] \cdot x_\mu[k - \kappa] + n_\nu[k] \quad (1.2.30)$$

where L_t denotes the largest number of taps among all contributing channels. Exploiting vector notations by comprising all output signals $y_\nu[k]$ into a column vector $\mathbf{y}[k]$ and all input signals $x_\mu[k]$ into a column vector $\mathbf{x}[k]$, (1.2.30) becomes

$$\mathbf{y}[k] = \sum_{\kappa=0}^{L_t-1} \mathbf{H}[k, \kappa] \cdot \mathbf{x}[k - \kappa] + \mathbf{n}[k]. \quad (1.2.31)$$

In (1.2.31), the channel matrix has the form

$$\mathbf{H}[k, \kappa] = \begin{bmatrix} h_{1,1}[k, \kappa] & \cdots & h_{1,N_I}[k, \kappa] \\ \vdots & \ddots & \vdots \\ h_{N_O,1}[k, \kappa] & \cdots & h_{N_O,N_I}[k, \kappa] \end{bmatrix}. \quad (1.2.32)$$

Finally, we can combine the L_t channel matrices $\mathbf{H}[k, \kappa]$ to obtain a single matrix $\mathbf{H}[k] = [\mathbf{H}[k, 0] \cdots \mathbf{H}[k, L_t - 1]]$. With the new input vector $\mathbf{x}_{L_t}[k] = [\mathbf{x}[k]^T \cdots \mathbf{x}[k - L_t + 1]^T]^T$ we obtain

$$\mathbf{y}[k] = \mathbf{H}[k] \cdot \mathbf{x}_{L_t}[k] + \mathbf{n}[k]. \quad (1.2.33)$$

In previous sections dealing with SISO systems, channels were always assumed to be non-dissipative, i.e. $E\{\sum_{\kappa} |h_{\nu,\mu}[k, \kappa]|^2\} = 1$ holds. For MIMO systems, this assumption can be generally applied too. However, there are some specific scenarios like space diversity concepts that are treated differently. Here, the same information is transmitted and received with several antennas (cf. Section 6.2). In order to emphasize the diversity gain, an appropriate normalization is necessary violating the above assumption. In most cases, error rates are depicted versus the measure E_b/N_0 depending on the average received energy per information bit. For further details please refer to the corresponding sections. Generally, all noise terms added at the outputs of the MIMO system have the same average power as in the SISO case.

As already mentioned, the impulse responses $h_{\nu,\mu}[k, \kappa]$ comprise channel influence as well as transmit and receive filter. More generally, (1.2.33) can describe a system that covers not only the properties of the channel but a larger part of the entire system. Therefore, $\mathbf{H}[k]$ may be replaced by a system matrix $\mathbf{S}[k]$ as done in Chapters 4 and 5. The structure of $\mathbf{S}[k]$ highly depends on the kind of communication system and, especially, on the chosen multiple access technique.

Fig. 1.2.9 illustrates the structure of $\mathbf{S}[k]$ for different scenarios. The gray shaded boxes represent nonzero elements. Certainly, the design goal is to obtain a strictly diagonal matrix for $\kappa = 0$ and zero matrices for $\kappa > 0$. In this case, the data streams are mutually orthogonal so that no multiple access interference exists. Furthermore, no intersymbol interference disturbs the transmission. For frequency-selective fading channels, this best case can only be achieved by Orthogonal Frequency Division Multiplexing (OFDM) or Orthogonal Frequency Division Multiple Access (OFDMA). Due to the insertion of a cyclic prefix called guard interval, interference between successive symbols can be avoided (see Section 4.3).

Classical multiple access schemes like TDMA and FDMA can also perfectly separate different data streams by assigning them different time slots or carrier frequencies, respectively. However, both suffer from intersymbol interference requiring appropriate equalization. Concerning CDMA and SDMA, different implementations exist (Chapter 4 and 5). As single carrier schemes, they suffer from multiple access as well as intersymbol interference. However, in combination with OFDM, the second penalty can be overcome and only multiple access interference (MAI) has to be combatted.

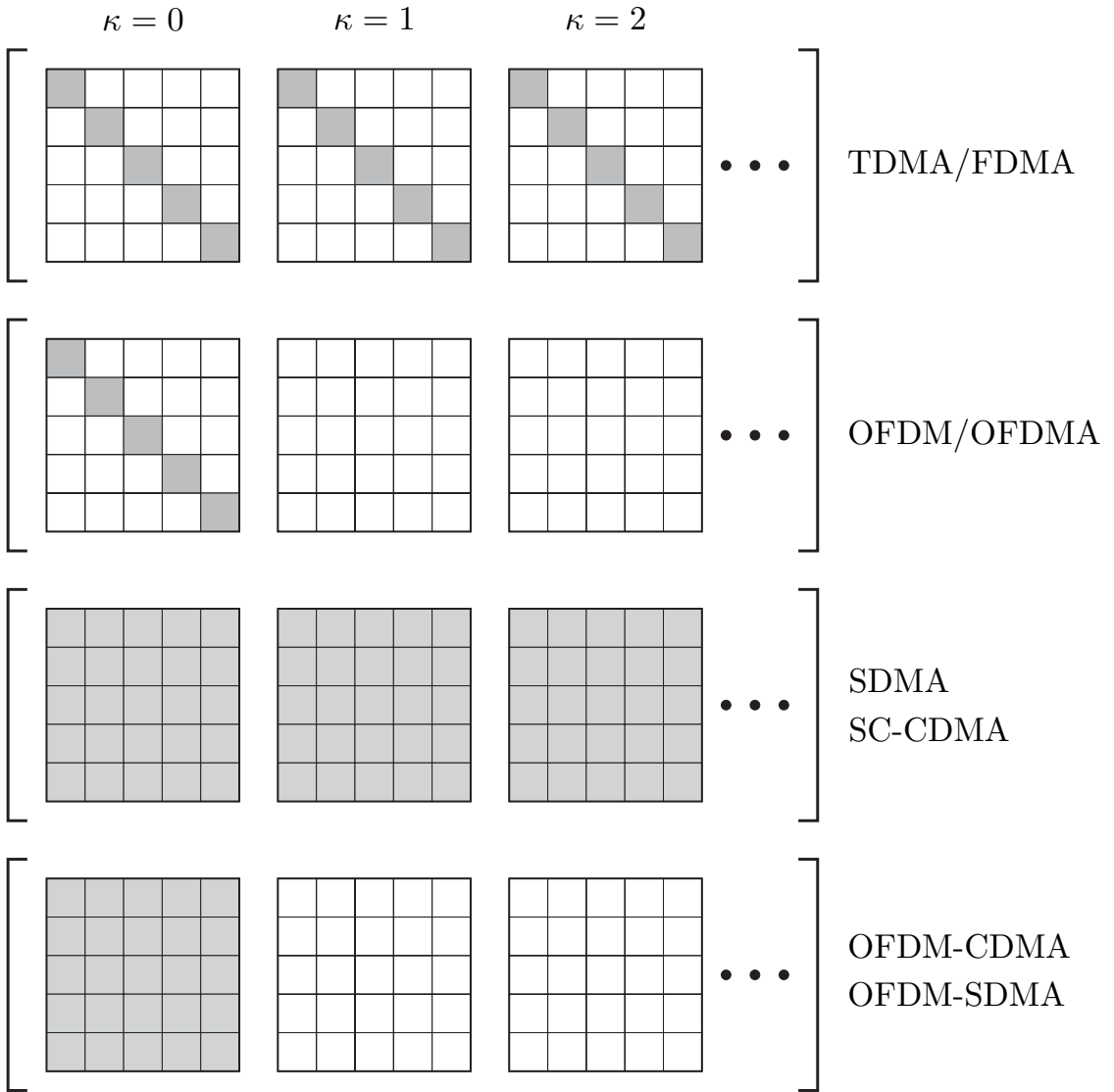


Figure 1.2.9: Illustration of structure of system matrix $\mathbf{S}[k, \kappa]$ for different scenarios

1.3 Signal Detection

1.3.1 Optimal Decision Criteria

This section briefly introduces some basic principles of signal detection. Concrete algorithms for special systems are described in the corresponding sections. We assume a frame-wise transmission, i.e. a sequence \mathbf{x} consisting of L_x discrete, independent, identically distributed (i.i.d.) symbols $x[k]$ is transmitted over a channel as discussed in the last section. Moreover, we restrict to an uncoded transmission while the detection of coded sequences is subject to Chapter 3. The received sequence is denoted by \mathbf{y} and comprises L_x symbols $y[k]$.

Sequence Detection

For frequency-selective channels, \mathbf{y} suffers from ISI and has to be equalized at the receiver. The optimum decision rule for general channels with respect to the frame error probability P_f looks for the sequence $\tilde{\mathbf{x}}$ that maximizes the *a posteriori* probability $\Pr\{\underline{\mathcal{X}} = \tilde{\mathbf{x}} | \mathbf{y}\}$, i.e. the probability that $\tilde{\mathbf{x}}$ was transmitted under the constraint that \mathbf{y} was received. Applying Bayes' rule⁶

$$\Pr\{\underline{\mathcal{X}} = \tilde{\mathbf{x}} | \underline{\mathcal{Y}} = \mathbf{y}\} = p_{\underline{\mathcal{Y}}|\tilde{\mathbf{x}}}(\mathbf{y}) \cdot \frac{\Pr\{\underline{\mathcal{X}} = \tilde{\mathbf{x}}\}}{p_{\underline{\mathcal{Y}}}(\mathbf{y})}. \quad (1.3.1)$$

we obtain the *maximum a posteriori (MAP) sequence detector*

$$\hat{\mathbf{x}} = \operatorname{argmax}_{\tilde{\mathbf{x}} \in \mathbb{X}^{L_x}} \Pr\{\tilde{\mathbf{x}} | \mathbf{y}\} = \operatorname{argmax}_{\tilde{\mathbf{x}} \in \mathbb{X}^{L_x}} [p_{\underline{\mathcal{Y}}|\tilde{\mathbf{x}}}(\mathbf{y}) \cdot \Pr\{\tilde{\mathbf{x}}\}] \quad (1.3.2)$$

where \mathbb{X}^{L_x} denotes the set of sequences with length L_x and symbols $x[k] \in \mathbb{X}$.

It illustrates that the sequence MAP detector takes into account the channel influence by $p_{\underline{\mathcal{Y}}|\tilde{\mathbf{x}}}(\mathbf{y})$ as well as *a priori* probabilities $\Pr\{\tilde{\mathbf{x}}\}$ of possible sequences. It has to be emphasized that $p_{\underline{\mathcal{Y}}|\tilde{\mathbf{x}}}(\mathbf{y})$ is a probability density function since \mathbf{y} is distributed continuously. Contrarily, $\Pr\{\tilde{\mathbf{x}} | \mathbf{y}\}$ represents a probability because \mathbf{y} now serves as a hypothesis and not as a random variable.

If either $\Pr\{\tilde{\mathbf{x}}\}$ is not known *a priori* to the receiver or all sequences are uniformly distributed resulting in a constant $\Pr\{\tilde{\mathbf{x}}\}$, we obtain the *maximum likelihood sequence detector*

$$\hat{\mathbf{x}} = \operatorname{argmax}_{\tilde{\mathbf{x}} \in \mathbb{X}^{L_x}} p_{\underline{\mathcal{Y}}|\tilde{\mathbf{x}}}(\mathbf{y}). \quad (1.3.3)$$

Under these assumptions, it represents the optimal detector minimizing P_f . Since the symbols $x[k]$ in $\tilde{\mathbf{x}}$ are elements of a discrete set \mathbb{X} (cf. Section 1.4), the detectors in (1.3.2) and (1.3.3) solve a combinatorial problem that can not be fixed by gradient methods. An exhaustive search within the set of all possible sequences $\tilde{\mathbf{x}} \in \mathbb{X}^{L_x}$ requires a computational effort that grows exponentially with $|\mathbb{X}|$ and L_x and is prohibitive for most practical cases. An efficient algorithm for an equivalent problem – the decoding of convolutional codes (cf. Section 3.4) – was found by Viterbi in 1967 [Vit67]. Forney showed in [For72] that the Viterbi algorithm is optimal for detecting sequences in the presence of ISI. OFDM (Orthogonal Frequency Division Multiplexing) and CDMA systems offer different solutions for sequence detection in ISI environments. They are described in Chapter 4.

⁶For notational simplicity, $p_{\underline{\mathcal{Y}}|\underline{\mathcal{X}} = \mathbf{x}}(\mathbf{y})$ is simplified to $p_{\underline{\mathcal{Y}}|\mathbf{x}}(\mathbf{y})$ and equivalently $\Pr\{\underline{\mathcal{X}} = \mathbf{x}\}$ to $\Pr\{\tilde{\mathbf{x}}\}$. The term $p_{\underline{\mathcal{Y}}}(\mathbf{y})$ can be neglected because it does not depend on $\tilde{\mathbf{x}}$.

Symbol-by-Symbol Detection

While the Viterbi algorithm minimizes the error probability when detecting sequences, the optimal *symbol-by-symbol MAP detector*

$$\begin{aligned}\hat{x}[k] &= \operatorname{argmax}_{X_\mu \in \mathbb{X}} \Pr\{\mathcal{X}[k] = X_\mu \mid \mathbf{y}\} = \operatorname{argmax}_{X_\mu \in \mathbb{X}} \sum_{\substack{\tilde{\mathbf{x}} \in \mathbb{X}^{L_x} \\ \tilde{x}[k] = X_\mu}} \Pr\{\underline{\mathcal{X}} = \tilde{\mathbf{x}} \mid \mathbf{y}\} \\ &= \operatorname{argmax}_{X_\mu \in \mathbb{X}} \sum_{\substack{\tilde{\mathbf{x}} \in \mathbb{X}^{L_x} \\ \tilde{x}[k] = X_\mu}} p_{\underline{\mathcal{Y}}|\tilde{\mathbf{x}}}(\mathbf{y}) \cdot \Pr\{\tilde{\mathbf{x}}\}\end{aligned}\quad (1.3.4)$$

minimizes the symbol error probability P_s . Obviously, the difference compared to (1.3.2) is the fact that all sequences $\tilde{\mathbf{x}}$ with $\tilde{x}[k] = X_\mu$ contribute to the decision and not only the most probable one. Both approaches need not deliver the same decisions as the following example demonstrates. Consider a sequence $\mathbf{x} = [x[0], x[1]]$ of length $L_x = 2$ with binary symbols $x[k] \in \{X_0, X_1\}$. The conditional probabilities $\Pr\{\tilde{\mathbf{x}} \mid \mathbf{y}\} = \Pr\{\tilde{x}[0], \tilde{x}[1] \mid \mathbf{y}\}$ are exemplarily summarized in Table 1.3.1.

Table 1.3.1: Illustration of sequence and symbol-by-symbol MAP detection

$\Pr\{\tilde{x}[0], \tilde{x}[1] \mid \mathbf{y}\}$	$\tilde{x}[1] = X_0$	$\tilde{x}[1] = X_1$	$\Pr\{\tilde{x}[0] \mid \mathbf{y}\}$
$\tilde{x}[0] = X_0$	0.26	0.27	0.53
$\tilde{x}[0] = X_1$	0.25	0.22	0.47
$\Pr\{\tilde{x}[1] \mid \mathbf{y}\}$	0.51	0.49	

While the MAP sequence detector delivers the sequence $\hat{\mathbf{x}} = [X_0, X_1]$ with the highest a posteriori probability $\Pr\{\tilde{\mathbf{x}} \mid \mathbf{y}\} = 0.27$, the symbol-by-symbol detector decides in favor to

$$\Pr\{\mathcal{X}[0] = X_\mu \mid \mathbf{y}\} = \sum_{X_\nu \in \mathbb{X}} \Pr\{\mathcal{X}[0] = X_\mu, \mathcal{X}[1] = X_\nu \mid \mathbf{y}\}$$

(and an equivalent expression for $x[1]$) resulting in the decisions $\hat{x}[0] = \hat{x}[1] = X_0$. However, the difference between both approaches is only visible at low signal to noise ratios and vanishes at low error rates.

Again, for unknown a priori probability or uniformly distributed sequences, the corresponding *symbol-by-symbol maximum likelihood detector* is obtained by

$$\hat{x}[k] = \operatorname{argmax}_{X_\mu \in \mathbb{X}} p_{\underline{\mathcal{Y}}|\mathcal{X}[k]=X_\mu}(\mathbf{y}) = \operatorname{argmax}_{X_\mu \in \mathbb{X}} \sum_{\substack{\tilde{\mathbf{x}} \in \mathbb{X}^{L_x} \\ \tilde{x}[k] = X_\mu}} p_{\underline{\mathcal{Y}}|\tilde{\mathbf{x}}}(\mathbf{y}) . \quad (1.3.5)$$

Memoryless Channels

For memoryless channels like AWGN and flat fading channels and i.i.d. symbols $x[k]$, the a posteriori probability $\Pr\{\tilde{x} \mid \mathbf{y}\}$ can be factorized into $\prod_k \Pr\{\tilde{x}[k] \mid y[k]\}$. Hence, the detector no longer needs to consider the whole sequence but can decide symbol by symbol. In this case, the time index k can be dropped and (1.3.4) becomes

$$\hat{x} = \operatorname{argmax}_{X_\mu \in \mathbb{X}} \Pr\{\mathcal{X} = X_\mu \mid y\}. \quad (1.3.6)$$

Equivalently, the maximum likelihood detector in (1.3.5) reduces to

$$\hat{x} = \operatorname{argmax}_{X_\mu \in \mathbb{X}} p_{\mathcal{Y}|X_\mu}(y). \quad (1.3.7)$$

1.3.2 Error Probability for AWGN Channel

This section shall describe the general way how to determine probabilities of decision errors. The derivations are restricted to memoryless channels but can be extended to channels with memory or trellis-coded systems. In these cases, vectors instead of symbols have to be considered. For a simple AWGN channel, $y = x + n$ holds and the probability density function $p_{\mathcal{Y}|X_\mu}(y)$ in (1.3.7) has the form

$$p_{\mathcal{Y}|X_\mu}(y) = \frac{1}{\pi\sigma_N^2} \cdot e^{-|y - X_\mu|^2 / \sigma_N^2} \quad (1.3.8)$$

(cf. (1.2.12)). With (1.3.8), a geometrical interpretation of the ML detector in (1.3.7) shows that the symbol X_μ out of \mathbb{X} that minimizes the squared Euclidean distance $|y - X_\mu|^2$ is determined. Let us now define the decision region

$$\mathbb{D}_\mu = \{y \mid |y - X_\mu|^2 < |y - X_\nu|^2 \quad \forall X_\nu \neq X_\mu\} \quad (1.3.9)$$

for symbol X_μ comprising all symbols $y \in \mathbb{C}$ whose Euclidean distance to X_μ is smaller than to any other symbol $X_\nu \neq X_\mu$. The complementary set is denoted by $\overline{\mathbb{D}}_\mu$. Assuming that X_μ was transmitted, a detection error occurs for $y \notin \mathbb{D}_\mu$ or equivalently $y \in \overline{\mathbb{D}}_\mu$. The complementary set can be expressed with the union $\overline{\mathbb{D}}_\mu = \bigcup_{\nu \neq \mu} \overline{\mathbb{D}}_{\mu,\nu}$ of the sets

$$\overline{\mathbb{D}}_{\mu,\nu} = \{y \mid |y - X_\mu|^2 > |y - X_\nu|^2\} \quad (1.3.10)$$

containing all symbols y whose Euclidean distance to a concrete X_ν is smaller than to X_μ . This does not mean that X_ν has the smallest distance of all symbols to $y \in \overline{\mathbb{D}}_{\mu,\nu}$. The symbol error probability can now be approximated by the well-known union bound [Pro95]

$$\begin{aligned}
P_s(X_\mu) &= \Pr \{y \in \overline{\mathbb{D}}_\mu\} = \Pr \left\{y \in \bigcup_{\nu \neq \mu} \overline{\mathbb{D}}_{\mu,\nu}\right\} \\
&\leq \sum_{\nu \neq \mu} \Pr \{y \in \overline{\mathbb{D}}_{\mu,\nu}\}. \tag{1.3.11}
\end{aligned}$$

The equality in (1.3.11) holds if and only if the sets $\overline{\mathbb{D}}_{\mu,\nu}$ are disjoint. The upper (union) bound simplifies the calculation remarkably because in many cases it is much easier to determine the pairwise sets $\overline{\mathbb{D}}_{\mu,\nu}$ than to exactly describe the decision region \mathbb{D}_μ . Substituting $y = X_\mu + n$ in (1.3.10) yields

$$\begin{aligned}
\Pr\{\mathcal{Y} \in \overline{\mathbb{D}}_{\mu,\nu}\} &= \Pr \{|Y - X_\mu|^2 > |Y - X_\nu|^2\} = \Pr \{|\mathcal{N}|^2 > |X_\mu - X_\nu + \mathcal{N}|^2\} \\
&= \Pr \left\{ \underbrace{\operatorname{Re} \{(X_\mu - X_\nu) \cdot \mathcal{N}^*\}}_{\eta} < \underbrace{-\frac{1}{2}|X_\mu - X_\nu|^2}_{\xi} \right\} \tag{1.3.12}
\end{aligned}$$

In (1.3.12), η is now a zero-mean Gaussian distributed random variable with variance $\sigma_\eta^2 = |X_\mu - X_\nu|^2 \sigma_{\mathcal{N}}^2 / 2$ and ξ a constant. This leads to the integral

$$\Pr\{\mathcal{Y} \in \overline{\mathbb{D}}_{\mu,\nu}\} = \frac{1}{\sqrt{\pi|X_\mu - X_\nu|^2 \sigma_{\mathcal{N}}^2}} \int_{-\infty}^{-|X_\mu - X_\nu|^2/2} e^{-\frac{\eta^2}{|X_\mu - X_\nu|^2 \sigma_{\mathcal{N}}^2}} d\eta \tag{1.3.13}$$

that is not solvable in closed form. With the complementary error function [BB99, BSMM00]

$$\operatorname{erfc}(x) = \frac{2}{\sqrt{\pi}} \int_x^\infty e^{-\xi^2} d\xi = 1 - \frac{2}{\sqrt{\pi}} \int_0^x e^{-\xi^2} d\xi = 1 - \operatorname{erf}(x). \tag{1.3.14}$$

we obtain the pairwise error probability between symbols X_μ and X_ν

$$\Pr\{\mathcal{Y} \in \overline{\mathbb{D}}_{\mu,\nu}\} = \frac{1}{2} \cdot \operatorname{erfc} \left(\sqrt{\frac{|X_\mu - X_\nu|^2}{4\sigma_{\mathcal{N}}^2}} \right). \tag{1.3.15}$$

Next, we normalize the squared Euclidean distance $|X_\mu - X_\nu|^2$ to the average symbol power $\sigma_{\mathcal{X}}^2$

$$\Delta_{\mu,\nu}^2 = \frac{|X_\mu - X_\nu|^2}{\sigma_{\mathcal{X}}^2} = \frac{|X_\mu - X_\nu|^2}{E_s/T_s} \tag{1.3.16}$$

so that the average error probability can be calculated with (1.2.14) to

$$\begin{aligned}
P_s &= \operatorname{E} \{P_s(X_\mu)\} = \sum_{X_\mu} P_s(X_\mu) \cdot \Pr\{X_\mu\} \\
&\leq \frac{1}{2} \sum_{X_\mu} \Pr\{X_\mu\} \cdot \sum_{X_\nu \neq X_\mu} \operatorname{erfc} \left(\sqrt{\left(\frac{\Delta_{\mu,\nu}}{2}\right)^2 \cdot \frac{E_s}{N_0}} \right). \tag{1.3.17}
\end{aligned}$$

Equation (1.3.17) shows that the symbol error rate solely depends on the squared Euclidean distance between competing symbols and the signal to noise ratio E_s/N_0 . Examples are presented for various linear modulation schemes in Section 1.4.

1.3.3 Error and Outage Probability for Flat Fading Channels

Ergodic Error Probability

For non-dispersive channels, the transmitted symbol x is weighted with a complex-valued channel coefficient h and $y = hx + n$ holds. Assuming perfect channel state information (CSI) at the receiver, i.e. h is perfectly known, we obtain

$$\begin{aligned} \Pr\{\mathcal{Y} \in \overline{\mathbb{D}}_{\mu,\nu} \mid h\} &= \Pr\{|y - hX_\mu|^2 > |y - hX_{\nu \neq \mu}|^2\} \\ &= \frac{1}{2} \cdot \operatorname{erfc}\left(\sqrt{\left(\frac{\Delta_{\mu,\nu}}{2}\right)^2 \cdot |h|^2 \frac{E_s}{N_0}}\right). \end{aligned} \quad (1.3.18)$$

Therefore, the symbol error probability is itself a random variable depending on the instantaneous channel energy $|h|^2$. The ergodic symbol error rate can be obtained by calculating the expectation of (1.3.18) with respect to $|h|^2$. A convenient way exploits the relationship

$$\frac{1}{2} \cdot \operatorname{erfc}(x) = \frac{1}{\pi} \cdot \int_0^{\pi/2} \exp\left[-\frac{x^2}{\sin^2 \Theta}\right] d\Theta \quad \text{for } x > 0 \quad (1.3.19)$$

which can be derived by changing from cartesian to polar coordinates [SA00]. Applying (1.3.19) in (1.3.18), reversing the order of integration and performing the substitution $s = -(\Delta_{\mu,\nu}/2)^2 E_s / N_0 / \sin^2(\theta)$ leads to

$$\begin{aligned} \mathbb{E}_{\mathcal{H}} \left\{ \Pr\{\mathcal{Y} \in \overline{\mathbb{D}}_{\mu,\nu} \mid h\} \right\} &= \int_0^\infty \frac{1}{\pi} \int_0^{\pi/2} p_{|\mathcal{H}|^2}(\xi) \\ &\quad \times \exp\left[-\xi \frac{(\Delta_{\mu,\nu}/2)^2 E_s / N_0}{\sin^2(\theta)}\right] d\xi d\theta \\ &= \frac{1}{\pi} \int_0^{\pi/2} \int_0^\infty \exp(\xi s) \cdot p_{|\mathcal{H}|^2}(\xi) d\xi d\theta. \end{aligned} \quad (1.3.20)$$

The inner integral in (1.3.20) describes the moment generating function (MGF)

$$\mathcal{M}_{|\mathcal{H}|^2}(s) = \int_0^\infty p_{|\mathcal{H}|^2}(\xi) \cdot e^{s\xi} d\xi \quad (1.3.21)$$

of the random process $|\mathcal{H}|^2$ [Pap65, SA00]. Using the MGF is a very general concept that will be used again in Section 1.5 when dealing with diversity. For the Rayleigh fading channel, the squared magnitude is chi-squared distributed with 2 degrees of freedom so that $\mathcal{M}_{|\mathcal{H}|^2}(s)$ has the form

$$\mathcal{M}_{|\mathcal{H}|^2}(s) = \int_0^\infty \frac{1}{\sigma_{\mathcal{H}}^2} e^{-\xi/\sigma_{\mathcal{H}}^2} \cdot e^{s\xi} d\xi = \frac{1}{1 - s\sigma_{\mathcal{H}}^2}. \quad (1.3.22)$$

The subsequent integration with respect to θ can be solved in closed-form. It yields for a non-dissipative channel with $\sigma_{\mathcal{H}}^2 = 1$

$$\begin{aligned} \mathbb{E}_{\mathcal{H}} \{ \Pr \{ \mathcal{Y} \in \overline{\mathbb{D}}_{\mu,\nu} \mid h \} \} &= \frac{1}{\pi} \int_0^{\pi/2} \frac{\sin^2(\theta)}{\sin^2(\theta) + (\Delta_{\mu,\nu}/2)^2 E_s/N_0} d\theta \\ &= \frac{1}{2} \left(1 - \sqrt{\frac{(\Delta_{\mu,\nu}/2)^2 E_s/N_0}{1 + (\Delta_{\mu,\nu}/2)^2 E_s/N_0}} \right). \end{aligned} \quad (1.3.23)$$

In Appendix A.3 it is shown that the MGF of \mathcal{H} for a Ricean distribution with $P = 1$ has the form

$$\mathcal{M}_{|\mathcal{H}|^2}(s) = \frac{1+K}{1+K-s} \cdot \exp \left[\frac{sK}{1+K-s} \right]. \quad (1.3.24)$$

Here, no closed-form expression is available for

$$\mathbb{E}_{\mathcal{H}} \{ \Pr \{ \mathcal{Y} \in \overline{\mathbb{D}}_{\mu,\nu} \mid h \} \} = \frac{1}{\pi} \int_0^{\pi/2} \mathcal{M}_{|\mathcal{H}|^2} \left(-\frac{(\Delta_{\mu,\nu}/2)^2 E_s/N_0}{\sin^2(\theta)} \right) d\theta. \quad (1.3.25)$$

However, (1.3.25) can be easily computed numerically with arbitrary precision. Equivalent to the procedure for the AWGN channel the union bound in (1.3.11) can be applied to obtain an upper bound of the average error probability.

A comparison of (1.3.15) with (1.3.23) shows that the exponential decay of the error rate for the AWGN channel is replaced by a much lower slope. This can also be observed in **Fig. 1.3.1** illustrating the error rate probabilities for a binary antipodal modulation scheme with equiprobable symbols. For small K , the Ricean fading channel behaves similar to the pure Rayleigh fading channel without line of sight component. With growing K , the LoS component becomes more and more dominating leading finally for $K \rightarrow \infty$ to the AWGN case. Principally, fading channels require much higher signal to noise ratios as the AWGN channel in order to achieve the same error rates.

Outage Probability

For many applications, the ergodic error probability is not the most important parameter. Instead, a certain transmission quality represented by e.g. a target

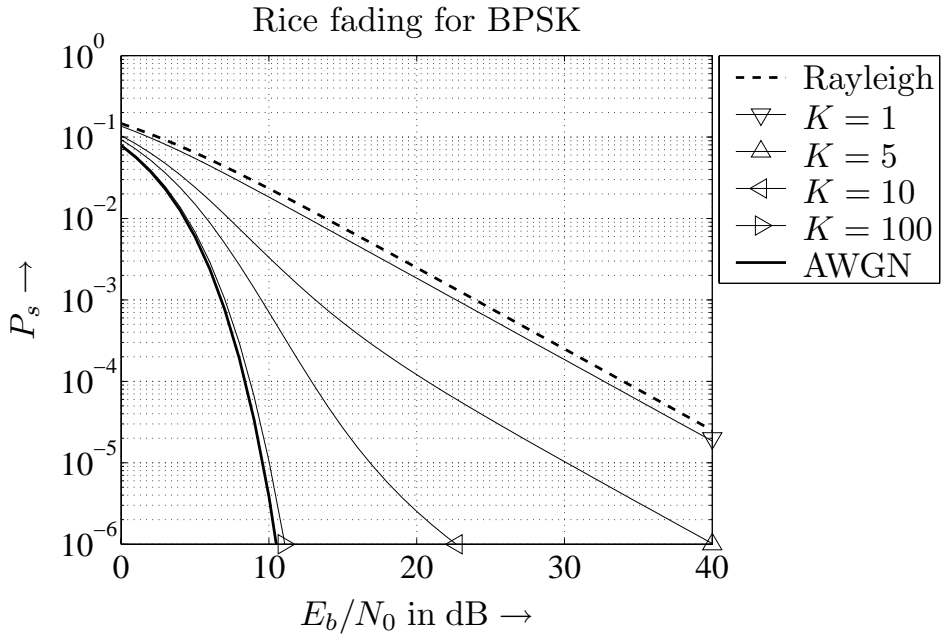


Figure 1.3.1: Symbol error probability for BPSK and transmission over AWGN, Rayleigh and Rice fading channels with different Rice factors K

error rate P_t , has to be guaranteed to a predefined percentage. Therefore, the outage probability P_{out} , i.e. the probability that a certain error rate can not be achieved, is important. For the frequency-nonselective Rayleigh fading channel, P_{out} describes the probability that the instantaneous signal to noise ratio $\gamma = |h|^2 \cdot E_s/N_0$ falls below a predefined threshold γ_t

$$P_{\text{out}} = \Pr\{|H|^2 \cdot E_s/N_0 < \gamma_t\} = \int_0^{\frac{\gamma_t}{E_s/N_0}} p_{|H|^2}(\xi) d\xi = 1 - \exp\left[-\frac{\gamma_t}{E_s/N_0}\right]. \quad (1.3.26)$$

Hence, the outage probability can be calculated by defining a target error rate P_t , determining the required signal to noise ratio γ_t and insert it into (1.3.26). For a binary antipodal modulation scheme with equiprobable symbols, **Fig. 1.3.2** illustrates the outage probability for different target error rates. It can be observed that the higher the quality constraints (low P_t), the higher the outage probability. For $10 \log_{10}(E_s/N_0) = 20$ dB, an error rate of $P_t = 10^{-5}$ can only be achieved to 91%, i.e. $P_{\text{out}} \approx 0.09$, while $P_t = 10^{-1}$ can be ensured to nearly 99.8% ($P_{\text{out}} \approx 8 \cdot 10^{-3}$). For an outage probability of $P_{\text{out}} = 10^{-2}$, a gap of nearly 10 dB exists between $P_t = 0.1$ and $P_t = 10^{-5}$.

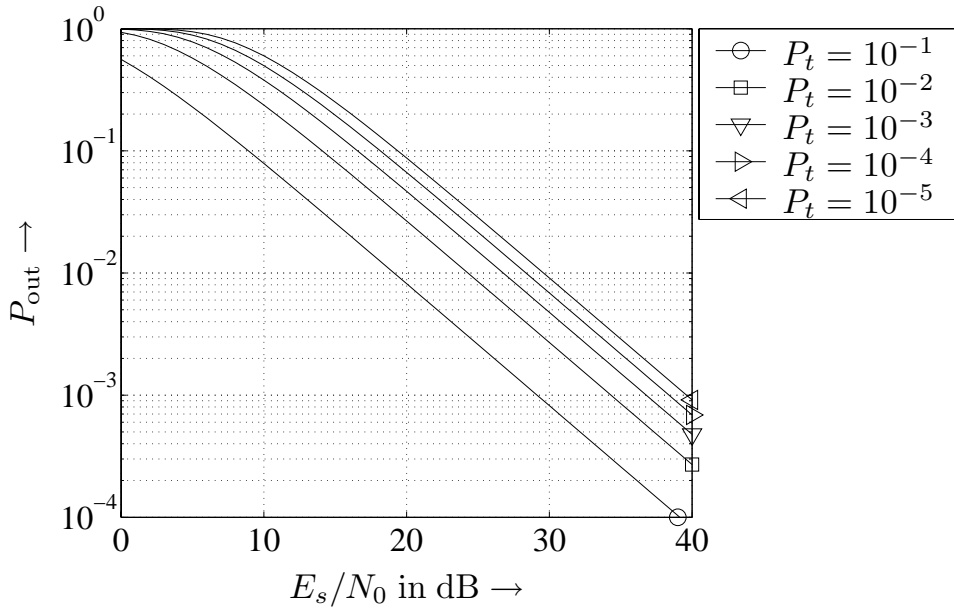


Figure 1.3.2: Outage probability for BPSK, a frequency-nonselective Rayleigh fading channel and different target error rates P_t

1.4 Digital Linear Modulation

1.4.1 Introduction

The analysis and investigations presented in this work are based on linear digital modulation schemes, i.e. the modulator has no memory. Their performances are analyzed in this section for different channels. As before, we always assume perfect lowpass filters $g_T(t)$ and $g_R(t)$ at transmitter and receiver. Therefore, the description focusses on the time-discrete equivalent baseband signal $x[k]$ with average symbol energy E_s at the channel input (cf. Figures 1.1.6 and 1.2.1).

The modulator just performs a simple mapping and successively extracts m -bit out of $b(\ell)$ and maps the m -tuple $\tilde{b}[k] = [b[mk] \dots b[m(k+1)-1]]$, $k = \lfloor l/m \rfloor$, onto one of $M = 2^m$ possible symbols X_μ . They form the signal alphabet $\mathbb{X} = \{X_0, \dots, X_{M-1}\}$ that depends on the type of modulation. Without loss of generality, all symbols are assumed to be equally likely and the average symbol energy is defined to

$$T_s \mathbb{E}\{|X_\mu|^2\} = \frac{T_s}{M} \sum_{\mu=0}^{M-1} |X_\mu|^2 = E_s . \quad (1.4.1)$$

Attention has to be payed when modulation schemes with different alphabet sizes are compared. In order to draw a fair comparison, the different numbers of bits per symbol have to be considered. This is done by calculating the performance

with respect to the average energy per bit $E_b = E_s/m$. In this case, the signal to noise ratio is expressed by the measure E_b/N_0 rather than by E_s/N_0 .

Mapping Strategies

While the symbol error rate (cf. following subsections) only depends on the geometrical arrangement of the symbols as well as the signal to noise ratio, the bit error rate is also affected by the specific mapping of the m -tuples $\tilde{\mathbf{b}}[k]$ onto the symbols X_μ . In many cases, Gray mapping is applied ensuring that neighboring symbols differ only in one bit. This results in a minimum bit error probability if the error events are dominated by mixing up neighboring symbols at the receiver (what is true in most cases). We obtain a tight approximation

$$P_b \approx \frac{1}{m} P_s . \quad (1.4.2)$$

Alternatively, natural mapping just enumerates the symbols (counterclockwise for PSK, starting with the smallest phase) and assigns them the binary representations of their numbers. For both mapping strategies, the exact solution of the bit error rate requires the consideration of the specific error probabilities $\Pr\{y \in \overline{\mathbb{D}}_{\mu,\nu}\}$ between two competing symbols X_μ and X_ν and the corresponding number $w_{\mu,\nu}$ of differing bits concerning their binary presentations. We obtain

$$P_b = \sum_{X_\mu} \Pr\{X_\mu\} \cdot \sum_{X_\nu \neq X_\mu} w_{\mu,\nu} \cdot \Pr\{Y \in \overline{\mathbb{D}}_{\mu,\nu}\} . \quad (1.4.3)$$

1.4.2 Amplitude Shift Keying (ASK)

If the amplitude of real-valued symbols bears the information, the modulation is called Amplitude Shift Keying (ASK). Alternatively, it is also termed Pulse Amplitude Modulation (PAM). In order to have equal distances between neighboring symbols (**Fig. 1.4.1**), the amplitudes are chosen to

$$X_\mu = (2\mu + 1 - M) \cdot e \quad \text{for } 0 \leq \mu < M .$$

The parameter e has to be determined such that (1.4.1) is fulfilled leading to

$$\frac{T_s}{M} \sum_{\mu=0}^{M-1} [(2\mu + 1 - M)e]^2 \stackrel{!}{=} E_s \quad \Rightarrow \quad e = \sqrt{\frac{3}{M^2 - 1} \cdot \frac{E_s}{T_s}} \quad (1.4.4)$$

and a minimum normalized squared Euclidean distance of

$$\Delta_0^2 = \frac{(2e)^2}{E_s/T_s} = \frac{12}{M^2 - 1} . \quad (1.4.5)$$

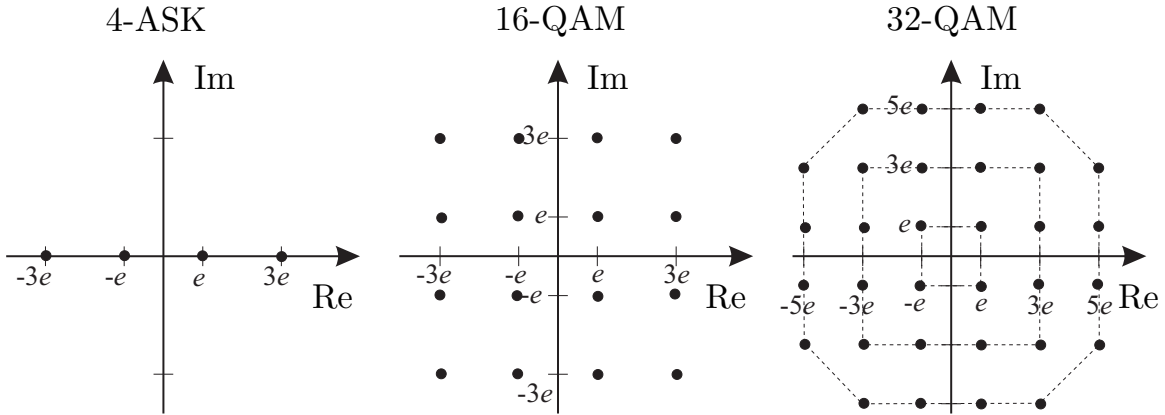


Figure 1.4.1: Symbol alphabets of linear amplitude modulation ($e = \sqrt{E_s/T_s/5}$ for 4-ASK, $e = \sqrt{E_s/T_s/10}$ for 16-QAM and $e = \sqrt{E_s/T_s/20}$ for 32-QAM)

Performance for AWGN Channel

The symbol error probability, i.e. the probability that a wrong symbol is detected at the receiver, can be easily calculated without the union bound. An error occurs if the real part of the noise $n'[k]$ exceeds half of the distance $2e$ between neighboring symbols. Therefore, the inner sum in (1.3.17) has only to be evaluated for two adjacent symbols, i.e. for the smallest Euclidean distance. While the most outer symbols have only one neighbor they can be mixed up with, the inner symbols have two competing neighbors. For equiprobable symbols, this fact can be considered by weighting the symbol specific error rates with the number of competing neighbors resulting in a total weight $(2(M-2) + 2)/M = 2(M-1)/M$. Therefore, (1.4.5) and the derivation in Section 1.3 yield an average error probability

$$P_s^{M\text{-ASK}} = \frac{M-1}{M} \cdot \operatorname{erfc} \left(\sqrt{\frac{3E_s}{(M^2-1)N_0}} \right) \quad (1.4.6a)$$

$$= \frac{M-1}{M} \cdot \operatorname{erfc} \left(\sqrt{\frac{3mE_b}{(M^2-1)N_0}} \right). \quad (1.4.6b)$$

The bit error probabilities can be determined by applying (1.4.2) or (1.4.3).

Performance for Flat Rayleigh Fading Channel

According to the second part of Section 1.3 and the argumentation above, the symbol error probability for a frequency-nonselective Rayleigh fading channel is obtained by applying (1.3.20) for $\Delta_{\mu,\nu} = \Delta_0$ and appropriate weighting

$$P_s^{M\text{-ASK}} = \frac{M-1}{M} \cdot \left(1 - \sqrt{\frac{3E_s/N_0}{M^2 - 1 + 3E_s/N_0}} \right). \quad (1.4.7)$$

Fig. 1.4.2 shows results for M -ASK and transmission over an AWGN and a frequency-nonselective Rayleigh fading channel. Obviously, the performance degrades with increasing M due to decreasing Euclidean distances between the symbols for constant average signal energy E_s . While the error rate shows an exponential decay for the AWGN channel, the slope is nearly linear for the flat Rayleigh fading channel. Therefore, in order to achieve the same average performance for fading channels, the transmit power has to be remarkably higher than for the AWGN channel. For 2-ASK and $P_s = 10^{-4}$, this gap is larger than 25 dB and grows for lower error rates. An appropriate mean to bridge this divide is the application of error correcting codes as explained in Chapter 3.

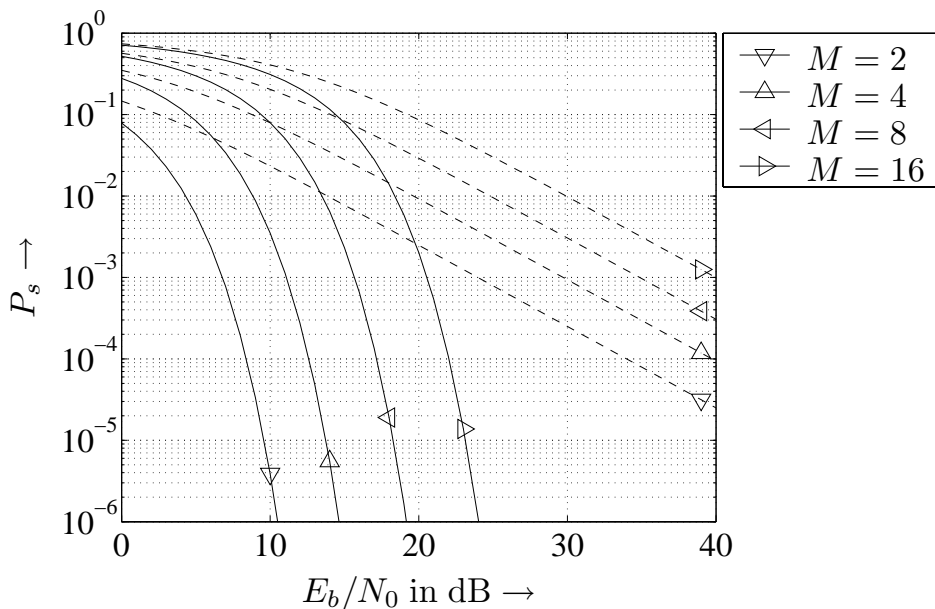


Figure 1.4.2: Symbol error rates for M -ASK and transmission over an AWGN channel (—) and a frequency-nonselective Rayleigh fading channel (---)

1.4.3 Quadrature Amplitude Modulation (QAM)

For quadrature amplitude modulation (QAM), real and imaginary parts of a symbol can be chosen independently from each other. Hence, $m' = m/2$ bits are mapped onto both, real and imaginary symbol parts according to a real-valued M' -ASK with $M' = 2^{m'}$. The combination of both parts results in a square arrangement, e.g. a 16-QAM with $m' = 2$ (see Fig. 1.4.1). Adapting the condition in (1.4.1) to QAM yields

$$\frac{T_s}{M'} \sum_{\mu=0}^{M'-1} \sum_{\nu=0}^{M'-1} (2\mu+1-M')^2 e^2 + (2\nu+1-M')^2 e^2 = 2T_s \sum_{\mu=0}^{M'-1} (2\mu+1-M')^2 e^2 \stackrel{!}{=} E_s .$$

Due to $M = M'^2$, the parameter e for M -QAM can be calculated to

$$e = \sqrt{\frac{3}{2(M-1)} \cdot \frac{E_s}{T_s}} \quad (1.4.8)$$

and the minimum squared Euclidean distance is

$$\Delta_0^2 = \frac{(2e)^2}{E_s/T_s} = \frac{6}{M-1} . \quad (1.4.9)$$

Without going into further details, it has to be mentioned that combinations of ASK and PSK are possible. As an example, Fig. 1.4.1 shows the 32-QAM modulation scheme.

Performance for AWGN Channel

The symbol error rate for M -QAM can be immediately derived because real and imaginary parts represent \sqrt{M} -ASK schemes and can be detected independently. Hence, a correct decision is made if and only if both components are detected correctly. Since the signal energy E_s is equally distributed among real and imaginary parts, we can use (1.4.6a) with $E_s|_{\sqrt{M}-\text{ASK}} = E_s|_{M-\text{QAM}}/2$ to obtain the error probabilities for both parts. The total error probability for M -QAM becomes

$$\begin{aligned} P_s^{M-\text{QAM}} &= 1 - \left[1 - P_s^{\sqrt{M}-\text{ASK}} \left(\frac{E_s/2}{N_0} \right) \right]^2 \\ &= 2P_s^{\sqrt{M}-\text{ASK}} \left(\frac{E_s/2}{N_0} \right) - \left[P_s^{\sqrt{M}-\text{ASK}} \left(\frac{E_s/2}{N_0} \right) \right]^2 . \end{aligned} \quad (1.4.10)$$

The squared error probability in (1.4.10) can be neglected for high signal to noise ratios resulting with $m' = m/2$ in an upper bound

$$P_s^{M-\text{QAM}} < 2 \frac{\sqrt{M}-1}{\sqrt{M}} \operatorname{erfc} \left(\sqrt{\frac{3}{2(M-1)} \frac{E_s}{N_0}} \right) \quad (1.4.11a)$$

$$= 2 \frac{\sqrt{M}-1}{\sqrt{M}} \operatorname{erfc} \left(\sqrt{\frac{3m}{2(M-1)} \frac{E_b}{N_0}} \right) . \quad (1.4.11b)$$

Fig. 1.4.3 illustrates the results for various QAM schemes. The dotted lines represent the exact solution while solid and dashed lines show the results of the upper bound. Concerning the AWGN channel, a noticeable difference between exact solution and approximation can only be observed at high error rates above 10^{-1} .

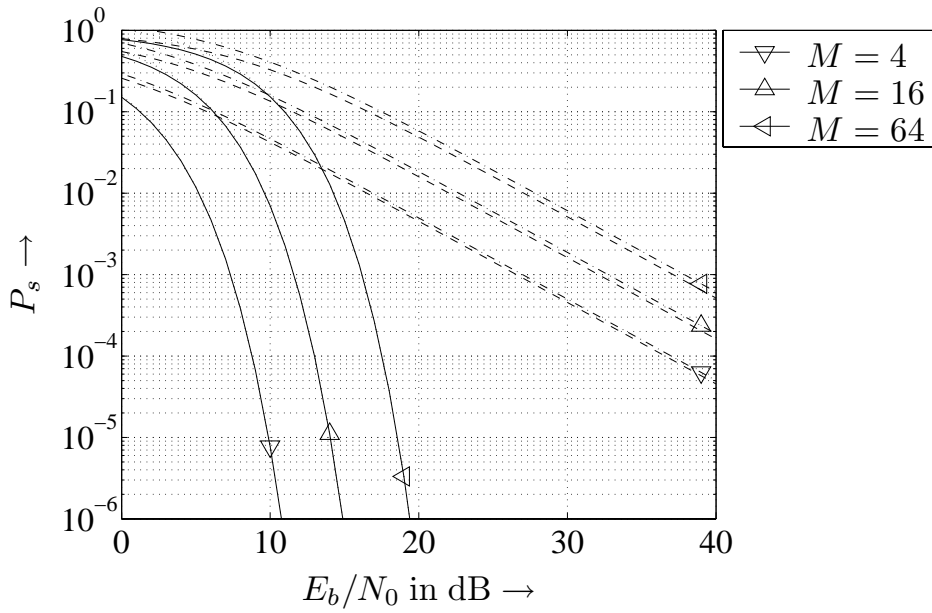


Figure 1.4.3: Symbol error probabilities for M -QAM and transmission over an AWGN channel (—) and a frequency-nonselective Rayleigh fading channel (---), approximations indicated by (- - -)

Performance for Flat Rayleigh Fading Channel

According to the procedure described in the last section, the ergodic symbol error probability for a frequency-nonselective Rayleigh fading channel must be determined by solving

$$\begin{aligned} P_s^{M-\text{QAM}} &= \mathbb{E}_{\mathcal{H}} \{ P_s^{M-\text{QAM}}(h) \} \\ &= \mathbb{E}_{\mathcal{H}} \left\{ 2P_s^{\sqrt{M}-\text{ASK}}(h) - [P_s^{\sqrt{M}-\text{ASK}}(h)]^2 \right\}. \end{aligned} \quad (1.4.12)$$

The expectation of the linear term is already known from M -ASK. Replacing properly M by \sqrt{M} and E_s by $E_s/2$ in (1.4.7) delivers

$$2 \mathbb{E}_{\mathcal{H}} \left\{ P_s^{\sqrt{M}-\text{ASK}}(h) \right\} = 2 \frac{\sqrt{M}-1}{\sqrt{M}} \cdot (1-\alpha) \quad \text{with} \quad \alpha = \sqrt{\frac{3E_s/N_0}{2(M-1)+3E_s/N_0}}.$$

Calculating the expectation of the squared term requires the relationship

$$\left[\frac{1}{2} \operatorname{erfc}(x) \right]^2 = \frac{1}{\pi} \int_0^{\pi/4} \exp \left[-\frac{x^2}{\sin^2 \Theta} \right] d\Theta \quad (1.4.13)$$

given in [SA00]. Exploiting (1.4.13) provides the closed-form solution

$$\left(\frac{\sqrt{M} - 1}{\sqrt{M}} \right)^2 \cdot \left[1 - \frac{4}{\pi} \alpha \tan^{-1} \left(\frac{1}{\alpha} \right) \right] .$$

The combination of both parts finally leads to the solution

$$P_s^{\text{QAM}} = 2 \frac{\sqrt{M} - 1}{\sqrt{M}} \cdot (1 - \alpha) - \left(\frac{\sqrt{M} - 1}{\sqrt{M}} \right)^2 \cdot \left[1 - \frac{4}{\pi} \alpha \cdot \tan^{-1} \left(\frac{1}{\alpha} \right) \right] . \quad (1.4.14)$$

Again, an upper bounded is obtained by dropping the second part of (1.4.14)

$$P_s^{\text{QAM}} < 2 \frac{\sqrt{M} - 1}{\sqrt{M}} \cdot \left(1 - \sqrt{\frac{3E_s/N_0}{2(M-1) + 3E_s/N_0}} \right) . \quad (1.4.15)$$

As illustrated in Fig. 1.4.3, a small gap between the exact solution and its approximation remains over the whole SNR range. Again, a higher spectral efficiency is obtained with growing M at the expense of a larger error rate.

Outage Probability

The outage probability can be numerically evaluated by exploiting (1.4.11a) in order to determine the relation between γ_t and P_t . The obtained thresholds γ_t can be inserted into (1.3.26) leading to the results depicted in **Fig. 1.4.4**. P_{out} increases as expected with growing M . For an outage probability of 1%, signal to noise ratios of 24.3 dB, 25.5 dB and 28.4 dB are required for 4-QAM, 16-QAM and 64-QAM, respectively.

1.4.4 Phase Shift Keying (PSK)

For M -ary Phase Shift Keying (PSK), M symbols are arranged on a circle with radius $\sqrt{E_s/T_s}$ resulting in a constant symbol energy. The bits compose in m -tuples $\tilde{\mathbf{b}}[k]$ determining the symbols' phases that are generally multiples of $2\pi/M$. Alternatively, an offset of π/M can be chosen as shown in **Fig. 1.4.5** for QPSK and 8-PSK. Binary Phase Shift Keying (BPSK) for $M = 2$ and Quaternary Phase Shift Keying (QPSK) for $M = 4$ represent special cases because they can be

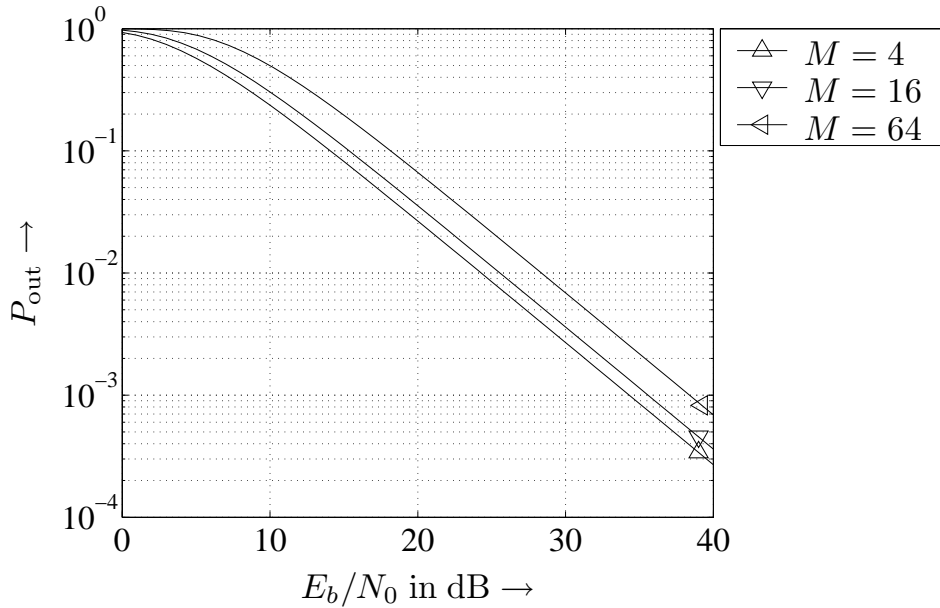


Figure 1.4.4: Outage probability for M -QAM and transmission over a frequency-nonselective Rayleigh fading channel, $P_t = 10^{-3}$

assigned to the class of amplitude modulation schemes, too (2-ASK and 4-QAM, respectively). Their symbol alphabets are also shown in Fig. 1.4.5. For $M > 4$, real and imaginary parts are not independent from each other and have to be detected simultaneously. If the symbols are numbered counterclockwise, the normalized squared Euclidean distance between two symbols X_μ and X_ν is

$$\Delta_{\mu,\nu}^2 = \frac{|X_\mu - X_\nu|^2}{E_s/T_s} = 4 \sin^2 \left((\mu - \nu) \frac{\pi}{M} \right). \quad (1.4.16)$$

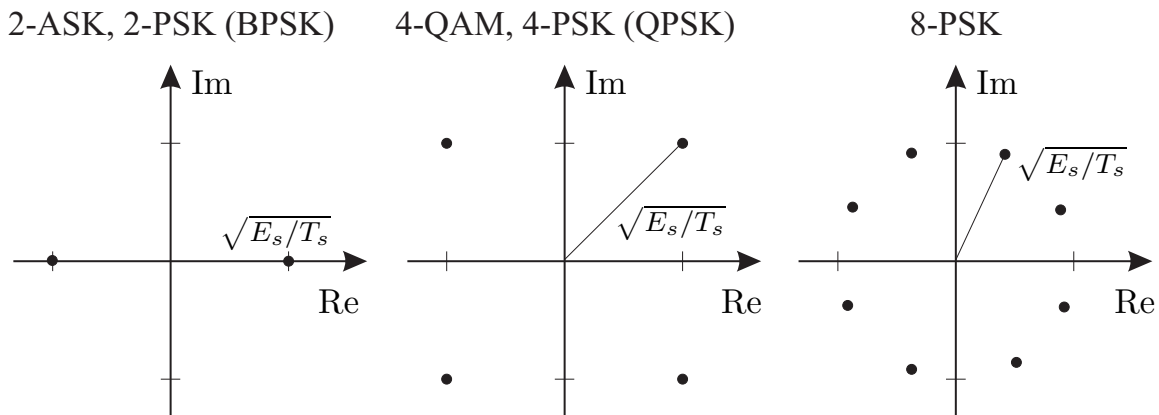


Figure 1.4.5: Symbol alphabets of digital phase modulation

The exact symbol error probability can generally not be expressed in closed form. Except for some special cases, it has to be calculated by numerical integration or approximated by the union bound, cf. (1.3.11). In the sequel, we focus again on a coherent reception for the AWGN and the flat Rayleigh fading channel.

Performance for AWGN Channel

Since BPSK with $M = 2$ is a special case of ASK, the error probability can be calculated with (1.4.6a) leading to

$$P_s^{\text{BPSK}} = \frac{1}{2} \cdot \operatorname{erfc} \left(\sqrt{\frac{E_s}{N_0}} \right). \quad (1.4.17)$$

QPSK can be interpreted as two parallel BPSK schemes with the same E_b/N_0 . Therefore, the bit error probabilities are identical

$$P_b^{\text{QPSK}} = \frac{1}{2} \cdot \operatorname{erfc} \left(\sqrt{\frac{E_b}{N_0}} \right) = \frac{1}{2} \cdot \operatorname{erfc} \left(\sqrt{\frac{E_s}{2N_0}} \right) \quad (1.4.18)$$

while the symbol error probability for QPSK (following the same argumentation as for QAM) is upper bounded by

$$P_s^{\text{QPSK}} = \operatorname{erfc} \left(\sqrt{\frac{E_b}{N_0}} \right) - \left[\frac{1}{2} \cdot \operatorname{erfc} \left(\sqrt{\frac{E_b}{N_0}} \right) \right]^2 < \operatorname{erfc} \left(\sqrt{\frac{E_b}{N_0}} \right). \quad (1.4.19)$$

Concerning $M > 4$, closed-form expressions are not available and the union bound can be applied. Substituting (1.4.16) into (1.3.17) yields the upper bound

$$P_s^{\text{PSK}} < \frac{1}{2} \sum_{\mu=1}^{M-1} \operatorname{erfc} \left(\sin(\mu\pi/M) \cdot \sqrt{\frac{E_s}{N_0}} \right). \quad (1.4.20)$$

A simple approximation stems from the fact that the error probability is dominated by those decisions that mix up neighboring symbols with squared Euclidean distance $4 \sin(\pi/M) E_s / T_s$. Inserting (1.4.16) for $|\mu - \nu| = 1$ into (1.3.15) and taking into account that each symbol has two competing neighbors with equal error probability, we obtain with (1.4.17) a tight approximation [Pro95, Kam96]

$$P_s^{\text{PSK}} \approx \operatorname{erfc} \left(\sin(\pi/M) \cdot \sqrt{\frac{E_s}{N_0}} \right) = \operatorname{erfc} \left(\sin(\pi/M) \cdot \sqrt{m \frac{E_b}{N_0}} \right). \quad (1.4.21)$$

Arbitrary accuracy can be obtained by numerically solving the integral [Cra91, SA00]

$$P_s^{\text{PSK}} = \frac{1}{\pi} \cdot \int_0^{(M-1)/M\pi} \exp \left[-\frac{\sin^2(\pi/M)}{\sin^2(\theta)} \cdot m \frac{E_b}{N_0} \right]. \quad (1.4.22)$$

Performance for Flat Rayleigh Fading Channel

For Rayleigh fading channels, the closed-form expression

$$P_s^{M\text{-PSK}} = \frac{M-1}{M} - \gamma \left[\frac{1}{2} + \frac{1}{\pi} \tan^{-1} (\gamma \cot(\pi/M)) \right] \quad (1.4.23)$$

with

$$\gamma = \sqrt{\frac{\sin^2(\pi/M)E_s/N_0}{1 + \sin^2(\pi/M)E_s/N_0}}$$

can be found in [SA00]. For BPSK with $M = 2$, (1.4.23) reduces to the well-known form

$$P_s^{\text{BPSK}} = \frac{1}{2} \cdot \left[1 - \sqrt{\frac{E_s/N_0}{1 + E_s/N_0}} \right], \quad (1.4.24)$$

and for QPSK ($M = 4$)

$$P_s^{\text{QPSK}} = \frac{3}{4} - \frac{1}{\pi} \sqrt{\frac{E_s/N_0}{2 + E_s/N_0}} \cdot \cot^{-1} \left(-\sqrt{\frac{E_s/N_0}{2 + E_s/N_0}} \right) \quad (1.4.25)$$

is obtained [Pro95]. As before, a simple approximation can be found by considering only the smallest Euclidean distance leading to

$$P_s^{\text{PSK}} \approx 1 - \sqrt{\frac{\sin^2(\pi/M)E_s/N_0}{1 + \sin^2(\pi/M)E_s/N_0}}. \quad (1.4.26)$$

The corresponding results are illustrated in **Fig. 1.4.6**. For the AWGN channel and $M > 4$, the error probabilities obtained by (1.4.21) and (1.4.22) are nearly identical and differ only at very low signal to noise ratios below 0 dB (not in the scope of Fig. 1.4.6). The same holds for (1.4.23) and (1.4.26) for the Rayleigh fading channel. While the union bound provides also tight results in the AWGN case, it is rather weak for the Rayleigh fading channel (not shown in Fig. 1.4.6). Therefore, the simple approximation looking only at the nearest neighbors should be preferred.

Outage Probability

In the same way as described for M -QAM, (1.4.22) can be used to determine γ_t for a specified target error rate P_t . **Fig. 1.4.7** shows the corresponding results obtained by inserting γ_t into (1.3.26). As expected, P_{out} increases with growing M .

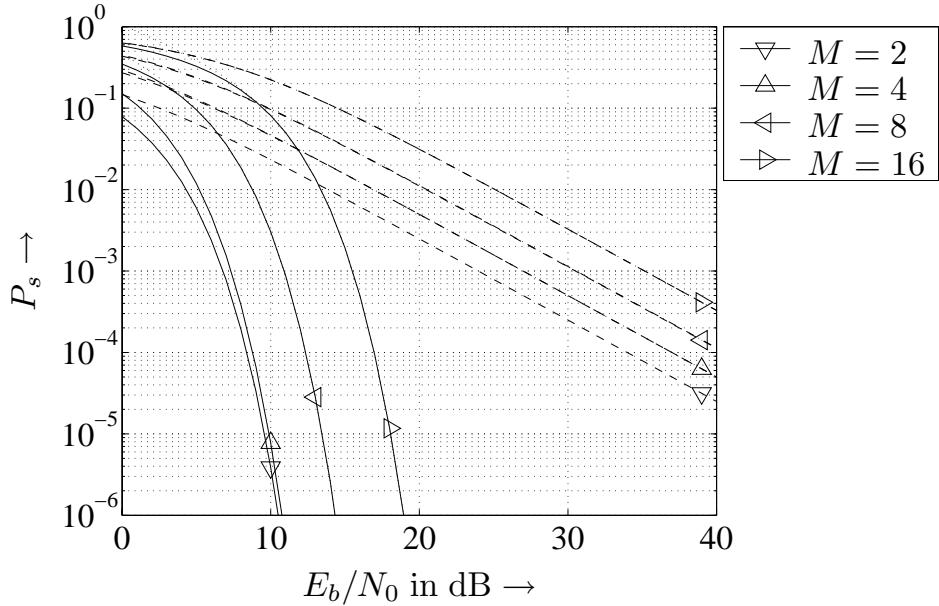


Figure 1.4.6: Symbol error probabilities for M -PSK and transmission over an AWGN channel (—), union bound (···), and a frequency-nonselective Rayleigh fading channel (- - -), approximation (- . -)

1.5 Diversity

1.5.1 General Concept

The previous section illustrated the influence of flat fading channels on the error rate performance. The instantaneous signal to noise ratio $\gamma[k] = |h[k]|^2 \cdot E_s/N_0$ at the receiver's input is a random variable according to the statistics of the current channel coefficient $h[k]$. Low SNRs caused by deep fades cannot be compensated by good channel states resulting in a significantly increased error rate.

In order to overcome or at least lower the fading's influence, the probability of deep fades has to be reduced. This can be accomplished by diversity concepts where several replicas of a signal $x[k]$ are transmitted over different frequency-nonselective channels $h_\ell[k]$, $1 \leq \ell \leq D$. In order to perform fair comparisons between systems with different diversity degrees, the total transmitted energy is fixed and equally distributed on the channels. According to Fig. 1.5.1, the received signal can be expressed with

$$y_\ell[k] = h_\ell[k] \cdot \frac{x[k]}{\sqrt{D}} + n_\ell[k] \quad \Leftrightarrow \quad \mathbf{y}[k] = \frac{x[k]}{\sqrt{D}} \cdot \mathbf{h}[k] + \mathbf{n}[k]. \quad (1.5.1)$$

For mutually independent channels, the probability that all $|h_\ell[k]|^2$ are simultaneously very small is much lower than the probability for a single channel. The described scenario may be obtained by using D receive antennas and one transmit antenna.

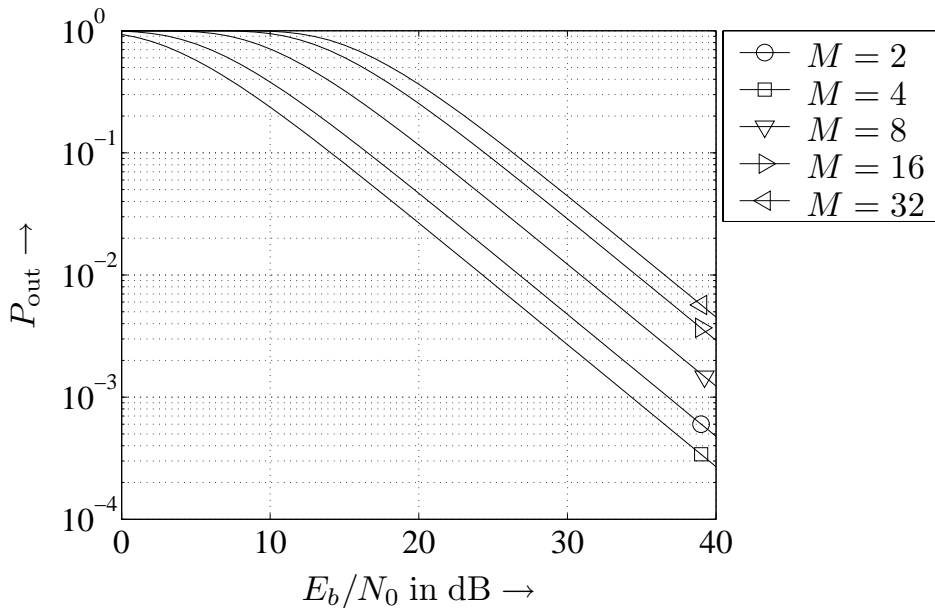


Figure 1.4.7: Outage probability P_{out} for M -PSK, a frequency-nonselective Rayleigh fading channel and a target symbol error rate $P_t = 10^{-3}$

Therefore, a communication system should be designed in a way to exploit as much diversity as possible. If the transmission channel itself provides diversity this can be used by appropriate receiver structures. However, for non-diversity channels, it is possible to artificially introduce diversity into the system. There exist several sources diversity can originate from.

- **frequency diversity:**

If the channel behaves frequency-selective (cf. Section 1.2), its transfer function influences different parts of the signal's spectrum diversely. Hence, diversity is obtained in the frequency domain that can be exploited by appropriate receiver structures. For CDMA systems, the Rake receiver (cf. Subsection 4.2.1 on page 172) exploits frequency diversity by combining different propagation paths being separable in time [Pro95]. In coded OFDM systems, the decoding process averages over carriers associated with different channel coefficients [DKK99a]. Even conventional equalizers like the Viterbi equalizer or linear FIR filter exploit frequency diversity (not the decision feedback equalizer). Finally, frequency diversity can be artificially introduced by operating with different carriers separated by at least the coherence bandwidth of the channel.

- **time diversity:**

If the channel varies in time the application of FEC (Forward Error Correction) coding yields diversity provided that a code word or a coded sequence is longer than the coherence time of the channel. In this case, decoding performs a kind of averaging over good and bad channel states.

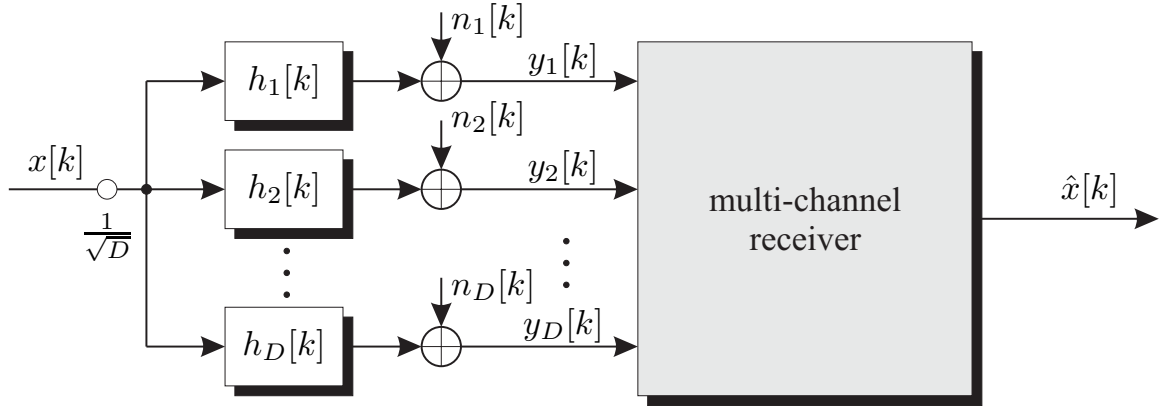


Figure 1.5.1: Illustration of D -fold diversity reception

- **space diversity:**

Recently, systems using multiple antennas at transmitter or receiver gained much interest. For antenna separations larger than several wavelengths, the channels can be assumed to be independent so that diversity is obtained even for frequency-nonselective and quasi static channels. Hence, the space is used to artificially enhance the diversity degree.

- **polarization diversity:**

If antennas support different polarizations, this can be used for polarization diversity. However, we will restrict in this context to the first three cases.

The diversity degree highly depends on the correlation among the contributing channels and their power distribution. The highest degree will be obtained by statistically independent channels with equal average power. Further analysis will be presented in the sequel.

Combining methods

Receiving several replicas of the same signal requires some kind of combining in order to obtain a single representation of the desired symbol. There exist different combining methods depending on the level of channel knowledge at the receiver.

- **Maximum Ratio Combining (MRC):**

Maximum ratio combining achieves the maximum signal to noise ratio at the receiver's output by weighting each received replica $y_j[k]$ by the corresponding complex conjugate channel coefficient $h_j^*[k]$ and successive summation. Therefore, this method requires the knowledge of amplitudes and phases of all involved channels and requires a scanning and tracking for all components. Due to this knowledge, MRC is not restricted to PSK but also

applicable for multi-amplitude signals like QAM. However, it is sensitive to channel estimation errors.

- **Equal Gain Combining (EGC):**

With equal gain combining, only the phase rotations for each $y_j[k]$ are compensated, the magnitudes remain unchanged. This method only requires the phases of all channel coefficients, not the magnitudes. However, due to missing knowledge of the channels' magnitudes, this technique is not suited for ASK and QAM modulation and it performs worse than MRC.

- **Square Law Combining (SLC):**

If the channel is highly time varying and its phase cannot be estimated accurately, square law combining of orthogonally modulated signals is an appropriate method to exploit diversity. Here, the squared magnitudes of the received signals are simply added resulting in a noncoherent receiver. This techniques can only be applied for orthogonal signaling schemes.

- **Selection Combining (SC):**

Selection combining represents the simplest combining method because it selects only a subset of all replicas for further processing and neglects all remaining signals. This reduces the computational costs and may lead even to a better performance than MRC because channels with very low SNR cannot be estimated accurately and contribute much noise.

We will focus in the sequel on maximum ratio combining as the optimum strategy with respect to the error rate performance for perfect channel knowledge.

Maximum Ratio Combining

The optimum solution for a detection problem of a system as described in (1.5.1) is obtained by applying a maximum likelihood detector

$$\hat{x}[k] = \underset{x}{\operatorname{argmax}} \ln p_{\mathcal{Y}|x}(\mathbf{y}[k]) = \underset{x}{\operatorname{argmin}} \left\| \mathbf{y}[k] - \frac{x[k]}{\sqrt{D}} \mathbf{h}[k] \right\|^2. \quad (1.5.2)$$

Setting the partial derivation of (1.5.2) with respect to $x^*[k]$ to zero leads to the optimum receiver structure

$$\begin{aligned} \hat{x}[k] &= \frac{\sqrt{D}}{\|\mathbf{h}[k]\|^2} \mathbf{h}^H[k] \cdot \mathbf{y}[k] = \frac{\sqrt{D}}{\|\mathbf{h}[k]\|^2} \cdot \sum_{\ell=1}^D h_\ell^*[k] \cdot y_\ell[k] \\ &= x[k] + \frac{\sqrt{D}}{\|\mathbf{h}[k]\|^2} \cdot \sum_{\ell=1}^D h_\ell^*[k] \cdot n_\ell[k]. \end{aligned} \quad (1.5.3)$$

As described above, the received diversity components are weighted with the complex conjugate channel coefficients, summed and appropriately weighted (weighting is only necessary for multi-amplitude modulation). The instantaneous signal to noise ratio can be determined by calculating the expectation with respect to $x[k]$ and $n_\ell[k]$

$$\gamma[k] = \frac{\mathbb{E}\{|\mathcal{X}|^2\} \cdot \left[\sum_{\ell=1}^D |h_\ell[k]|^2\right]^2}{\mathbb{E}_{\mathcal{N}}\left\{\sum_{\ell=1}^D h_\ell^*[k]\mathcal{N}_\ell[k] \cdot \sum_{j=1}^D h_j[k]\mathcal{N}_j^*[k]\right\} \cdot D}.$$

Taking into account that the noise samples are mutually independent, i.e. $\mathbb{E}\{\mathcal{N}_i[k]\mathcal{N}_{j \neq i}^*[k]\} = 0$, we obtain

$$\gamma[k] = \frac{\sigma_{\mathcal{X}}^2}{D\sigma_{\mathcal{N}}^2} \cdot \sum_{\ell=1}^D |h_\ell[k]|^2 = \frac{E_s}{DN_0} \cdot \sum_{\ell=1}^D |h_\ell[k]|^2 = \sum_{\ell=1}^D \gamma_\ell[k]. \quad (1.5.4)$$

Hence, the 'global' signal to noise ratio $\gamma[k]$ is obtained by simply summing the 'local' ratios $\gamma_\ell[k]$ each with a mean $\bar{\gamma}_\ell = \sigma_{\mathcal{H}_\ell}^2 E_s / N_0 / D$.

1.5.2 MRC for Independent Diversity Branches

If the channel coefficients in all branches are mutually independent and identically distributed (i.i.d.), $\gamma[k]$ is chi-squared distributed with $2D$ degrees of freedom [SA00, BSMM00]

$$p_\gamma(\xi) = \frac{\xi^{D-1}}{(D-1)! \cdot \bar{\gamma}_\ell^D} \cdot e^{-\xi/\bar{\gamma}_\ell} = \frac{D^D \xi^{D-1}}{(D-1)! (E_s/N_0)^D} \cdot e^{-\frac{\xi D}{E_s/N_0}} \quad (1.5.5)$$

instead of two degrees of freedom for the 'local' ratios $\gamma_\ell[k]$ (cf. Section 1.2). The second equality in (1.5.5) holds for non-dissipative channels with $\sigma_{\mathcal{H}}^2 = 1$. Numerical results for are shown in **Fig. 1.5.2**. With growing diversity degree D , the instantaneous signal to noise ratio concentrates more and more to E_s/N_0 and the SNR variations (influence of the fading) become smaller. For $D \rightarrow \infty$, the AWGN channel without any fading is obtained.

Outage probability

In order to analyze the outage probability for maximum ratio combining i.i.d. diversity paths, the distribution given in (1.5.5) has to be integrated according to (1.3.26)

$$P_{\text{out}} = \int_0^{\gamma_t} p_\gamma(\xi) d\xi. \quad (1.5.6)$$

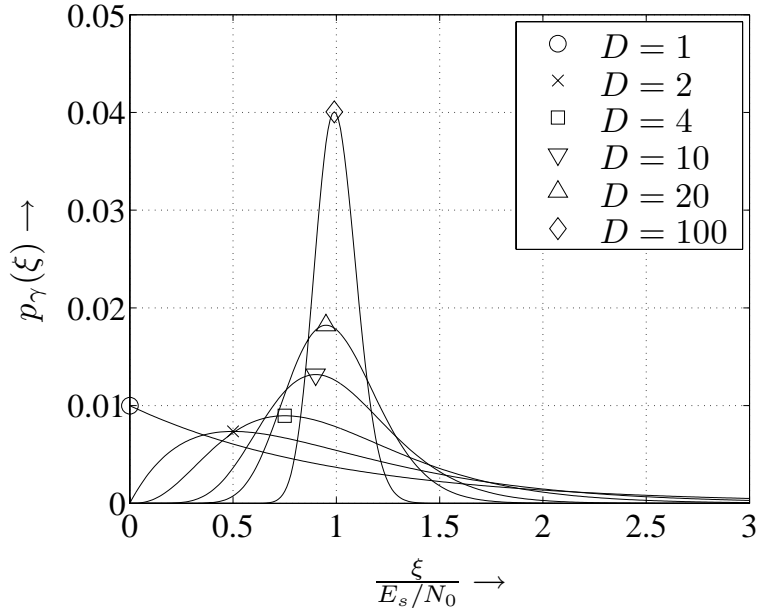


Figure 1.5.2: Probability density functions of $\gamma[k]$ for different diversity degrees D and i.i.d. diversity channels

However, γ is now chi-squared distributed with $2D$ degrees of freedom. Hence, an analytical solution is hard to obtain and the easiest way is to perform the integration in (1.5.6) numerically. For BPSK, Fig. 1.5.3 shows the corresponding results. The left diagram shows P_{out} versus E_b/N_0 for a fixed target error rate of $P_t = 10^{-3}$. Obviously, P_{out} decreases with growing signal to noise ratio as well as with increasing diversity degree D . For high D , $p_\gamma(\xi)$ is essentially nonzero in a very narrow region and, hence, small changes in E_b/N_0 cause tremendous changes in P_{out} resulting in a very steep slope of the curves. Fig. 1.5.3 b) shows the results for a fixed $10 \log_{10}(E_b/N_0) = 12$ dB.

Ergodic Error Probability for MRC

Equivalent to the derivations in Section 1.4, the expectation of the instantaneous error probability with respect to $\gamma[k]$ has to be determined. An exact solution for BPSK and i.i.d. diversity branches can be found in [Pro95]

$$P_s = \left(\frac{1-\mu}{2} \right)^D \cdot \sum_{\ell=0}^{D-1} \binom{D-1+\ell}{\ell} \cdot \left(\frac{1+\mu}{2} \right)^\ell \quad \text{with} \quad \mu = \sqrt{\frac{\bar{\gamma}}{1+\bar{\gamma}}} . \quad (1.5.7)$$

The parameter $\bar{\gamma}$ denotes the average SNR in each branch. In order to get a better illustration of (1.5.7), we derive a simple approximation for $\bar{\gamma} \gg 1$. In this case, the application of a Taylor series expansion shows that $(1+\mu)/2 \approx 1$ and

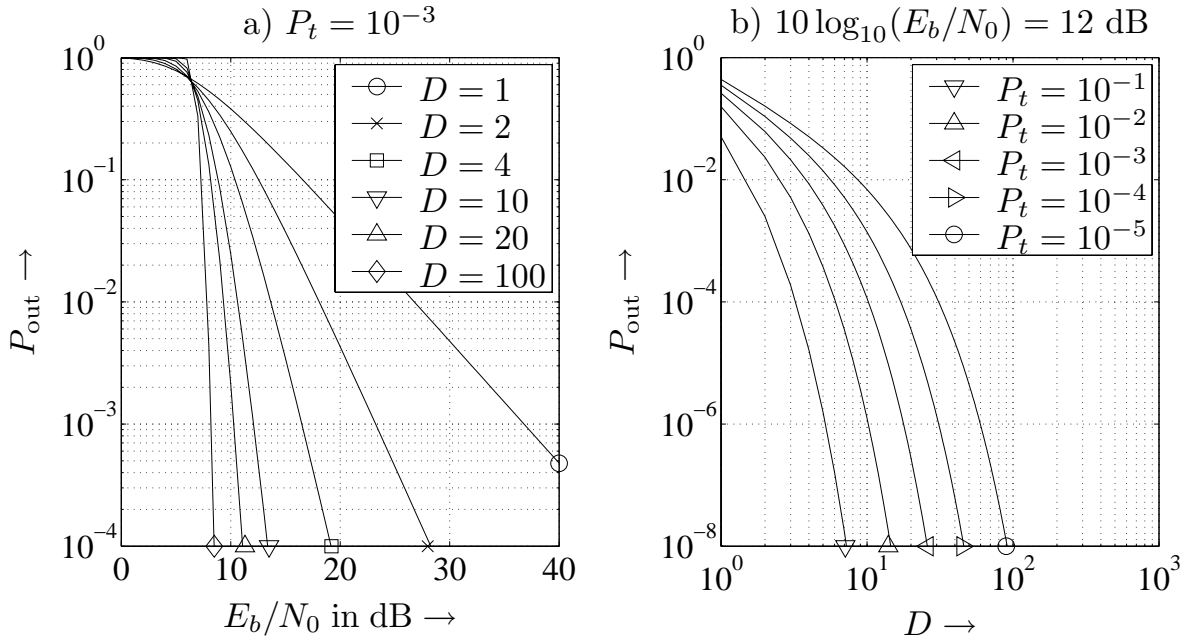


Figure 1.5.3: Outage probabilities for BPSK and i.i.d. Rayleigh fading channels
a) a target error rate of $P_t = 10^{-3}$ and **b)** $10 \log_{10}(E_b/N_0) = 12$ dB

$(1 - \mu)/2 \approx 1/(4\bar{\gamma})$ hold. Therefore, with the relation [Pro95]

$$\sum_{\ell=0}^{D-1} \binom{D-1+\ell}{\ell} = \binom{2D-1}{D} \quad (1.5.8)$$

the symbol error rate can be approximated for large signal to noise ratios by

$$P_s \approx \left(\frac{1}{4\bar{\gamma}} \right)^D \cdot \binom{2D-1}{D} = \left(\frac{D}{4E_s/N_0} \right)^D \cdot \binom{2D-1}{D}. \quad (1.5.9)$$

Obviously, P_s is proportional to the D -th power of the reciprocal of the signal to noise ratio. Since error rate curves are scaled logarithmically, their slope will be dominated by the diversity degree D at high SNRs. This will be demonstrated later in this section.

However, the expression given in (1.5.7) becomes computationally expensive and numerically difficult for high diversity degrees. A more convenient approach especially for unequal power distributions can be obtained by exploiting the alternative representation of the complementary error function already introduced in (1.3.19). This method can be easily applied to arbitrary modulation schemes and unequal power distributions. Moreover, it can be modified in order to cope also the case of correlated diversity branches.

We start with statistically independent diversity branches, i.e. the joint density $p_{\gamma_1 \dots \gamma_D}(\xi_1 \dots \xi_D)$ can be factorized into marginal densities $p_{\gamma_\ell}(\xi_\ell)$. This results

in

$$\begin{aligned} P_s &= \text{E}_\gamma \{P_s(\gamma)\} = \text{E}_{\gamma_1 \dots \gamma_D} \{P_s(\gamma_1 + \dots + \gamma_D)\} \\ &= \int_0^\infty \dots \int_0^\infty P_s(\gamma_1 + \dots + \gamma_D) \cdot p_{\gamma_1}(\xi_1) \dots p_{\gamma_D}(\xi_D) d\xi_1 \dots d\xi_D \quad (1.5.10) \end{aligned}$$

where the integrals in (1.5.10) can be solved separately. Resuming the last section and exploiting the alternative representation of the complementary error function in (1.3.19), it turns out that a unique, parameterized expression for all linear modulation schemes can be found⁷

$$P_s(\gamma) = a \cdot \int_0^b \exp \left[-\frac{c \cdot \gamma}{\sin^2(\theta)} \right] d\theta . \quad (1.5.11)$$

The parameters a , b and c are defined as

$$M - \text{ASK} : \begin{cases} a = \frac{2}{\pi} \cdot \frac{M-1}{M} \\ b = \frac{\pi}{2} \\ c = \frac{3}{M^2-1} \end{cases} \quad (1.5.12a)$$

$$M - \text{QAM} : \begin{cases} a = \frac{4}{\pi} \cdot \frac{\sqrt{M}-1}{\sqrt{M}} \\ b = \frac{\pi}{2} \\ c = \frac{3}{M-1} \end{cases} \quad (1.5.12b)$$

$$M - \text{PSK} : \begin{cases} a = \frac{1}{\pi} \\ b = \pi \cdot \frac{M-1}{M} \\ c = \sin^2(\pi/M) . \end{cases} \quad (1.5.12c)$$

Inserting (1.5.11) into (1.5.10) and reversing the order of integration leads to

$$\begin{aligned} P_s &= \int_0^\infty \dots \int_0^\infty a \int_0^b \exp \left[-\frac{c \cdot (\xi_1 + \dots + \xi_D)}{\sin^2(\theta)} \right] d\theta \cdot p_{\gamma_1}(\xi_1) \dots p_{\gamma_D}(\xi_D) d\xi_1 \dots d\xi_D \\ &= a \int_0^b \prod_{\ell=1}^D \int_0^\infty \exp \left[-\frac{c \cdot \xi_\ell}{\sin^2(\theta)} \right] \cdot p_{\gamma_\ell}(\xi_\ell) d\xi_\ell d\theta . \quad (1.5.13) \end{aligned}$$

⁷For M -QAM, (1.5.11) represents only an approximation because the quadratic term is neglected.

From the derivations in Section 1.3 it is already known that the substitution $s = -c/\sin^2(\theta)$ in the inner integrals of (1.5.13) leads to the moment generating functions

$$\mathcal{M}_{\gamma_\ell}(s) = \int_0^\infty p_{\gamma_\ell}(\xi_\ell) \cdot e^{s\xi_\ell} d\xi_\ell \quad (1.5.14)$$

of the random processes γ_ℓ [Pap65, SA00]. Therefore, as an important intermediate result, the ergodic error probability can be calculated by numerically solving

$$P_s = a \int_0^b \prod_{\ell=1}^D \mathcal{M}_{\gamma_\ell} \left(\frac{-c}{\sin^2(\theta)} \right) d\theta \stackrel{\text{i.i.d.}}{=} a \int_0^b \mathcal{M}_\gamma^D \left(\frac{-c}{\sin^2(\theta)} \right) d\theta \quad (1.5.15)$$

where the second equality in (1.5.15) holds for identically distributed branches.

Ergodic Error Probability for Rayleigh Fading Channel

Inserting the MGF in (1.3.22) for Rayleigh fading channels with chi-squared distributed γ_ℓ results in the following expression for D -fold diversity and statistically independent channels

$$P_s = a \int_0^b \prod_{\ell=1}^D \frac{\sin^2(\theta)}{\sin^2(\theta) + c\bar{\gamma}_\ell} d\theta \stackrel{\text{i.i.d.}}{=} a \int_0^b \left(\frac{D \sin^2(\theta)}{D \sin^2(\theta) + cE_s/N_0} \right)^D d\theta. \quad (1.5.16)$$

Due to the agreement that the transmit power is uniformly distributed onto all diversity paths, the average SNR per path for identically distributed branches is $\bar{\gamma}_\ell = E_s/N_0/D$ leading to the second equality in (1.5.16). For Ricean fading, the MGF of (1.3.24) has to be inserted.

Fig. 1.5.4 shows the results for BPSK and equally distributed branches. As already explained, with increasing diversity degree D , the error rates decrease due to smaller variations of the global signal to noise ratio. In the limit for $D \rightarrow \infty$, the performance of an AWGN channel is obtained. This asymptotic case is normally not of practical interest because channel estimation becomes a critical task due to local SNRs that tend to zero when D goes to infinity.

The largest gains are obtained at high signal to noise ratios where the slopes of the curves are determined by D . For illustration, the dashed lines represent the results obtained with (1.5.9). It can be seen that this approximation is quite tight for high SNR and low diversity degrees. However, for low SNR and especially for high D it becomes very loose. For $D > 10$, the bound is only tight for error rates that are beyond the scope of practical systems.

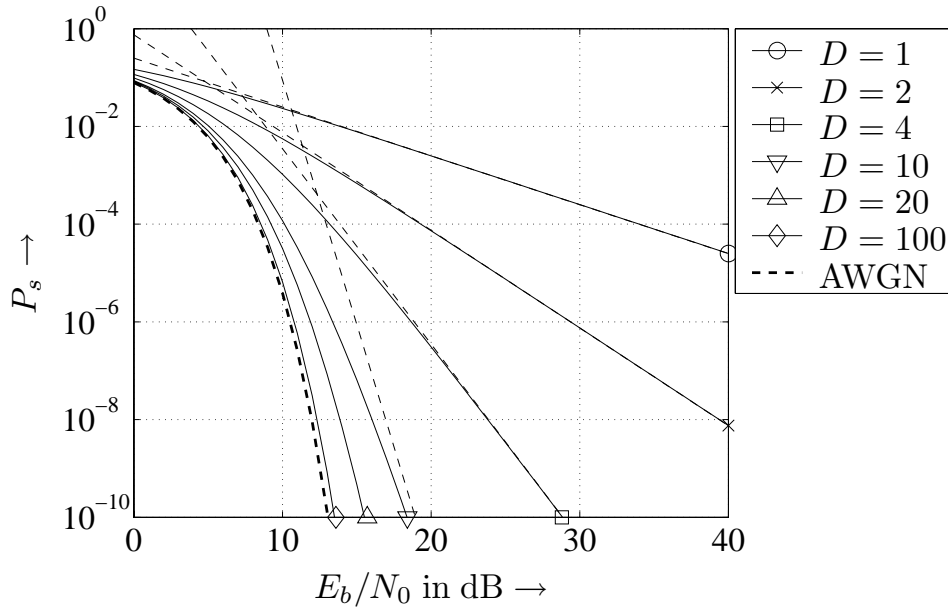


Figure 1.5.4: Symbol error probabilities for transmission of BPSK over i.i.d. Rayleigh fading channels with different diversity degrees D , dashed lines for asymptotic approximation with (1.5.9)

Fig. 1.5.5 illustrates the symbol error rates for a fixed $10 \log_{10}(E_b/N_0) = 12$ dB for different modulation schemes. For $D = 100$, the AWGN performance is nearly approached. However, the largest gain is already obtained for $D < 100$, especially when the error rate for an AWGN channel is quite high.

Ergodic Error Probability for Ricean Fading Channel

Scenarios in which transmit and receive antennas have a direct line-of-sight connection suffer less from fading. However, even in these cases diversity improves the system performance. The improvement depends of course on the Rice factors of the contributing transmission paths. In Appendix A.3 the moment generating function for Ricean fading is derived.

$$\mathcal{M}_{|\mathcal{H}|^2}(s) = \frac{K+1}{K+1-sP} \cdot \exp \left[\frac{sKP}{(K+1)-sP} \right]. \quad (1.5.17)$$

Inserting (1.5.17) into (1.5.15) and applying the substitution $s = -c/\sin^2(\theta)$ allows the numerical computation of the ergodic error probability.

Fig. 1.5.6 shows the error rate performance of a system with D i.i.d. Rice fading channels for different Rice factors K . The average power was fixed to $P = 1$ leading to different variances $\sigma_{\mathcal{H}}^2$ for different Rice factors K . From the left diagram it can be seen that – as expected – the Rice fading channel outperforms the Rayleigh fading channel for all D and a strong LoS part with $K = 10$. For $D = 10$

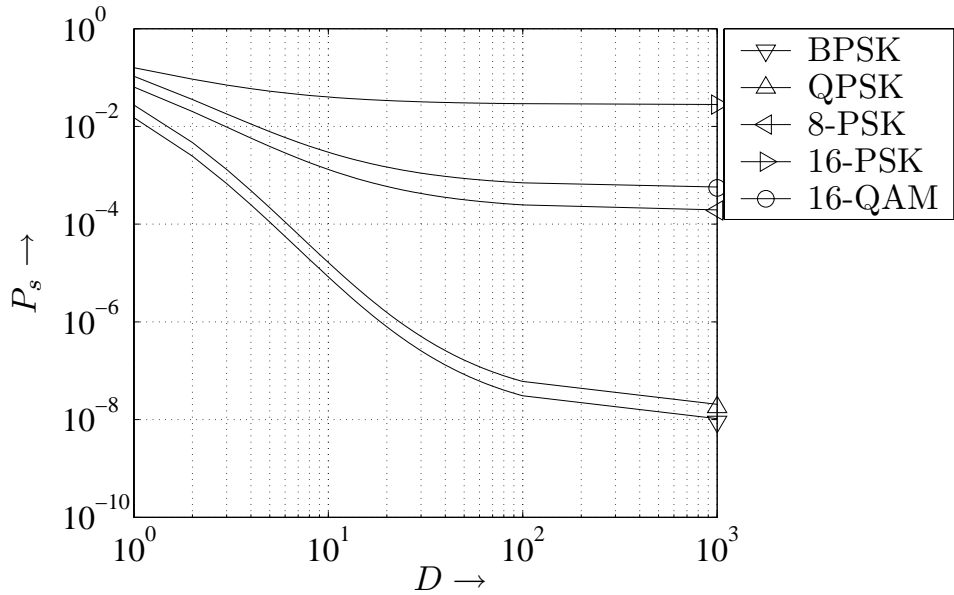


Figure 1.5.5: Symbol error probabilities versus diversity degree D for different modulation schemes at $10 \log_{10}(E_b/N_0) = 12$ dB for i.i.d. Rayleigh fading channels

the AWGN curve can be approached for Ricean fading while the Rayleigh fading channel loses more than 5 dB.

From Fig. 1.5.6b it becomes obvious that the diversity gain decreases with growing K . For small K , i.e. weak LoS components, diversity gains known from Rayleigh fading are possible. For $K \rightarrow \infty$, the performance of the AWGN channel is reached even without diversity. Hence, diversity concepts are only an appropriate mean in severe fading environments.

Unequal Power Distributions

If the power is not equally distributed among the different transmission paths, the first expression in (1.5.16) with different $\bar{\gamma}_\ell$, has to be used. Without loss of generality, it can be assumed that the paths are arranged in descending order with respect to their average power $\sigma_{\mathcal{H}_\ell}^2$ and that the average total power is restricted to D^8 resulting in an overall average SNR

$$\bar{\gamma} = \sum_{\ell=1}^D \bar{\gamma}_\ell = \frac{E_s}{DN_0} \cdot \sum_{\ell=1}^D \sigma_{\mathcal{H}_\ell}^2 = \frac{E_s}{N_0} \quad (1.5.18)$$

⁸This assumption coincides with the i.i.d. case where $\sigma_{\mathcal{H}_\ell}^2 \equiv 1$ holds.

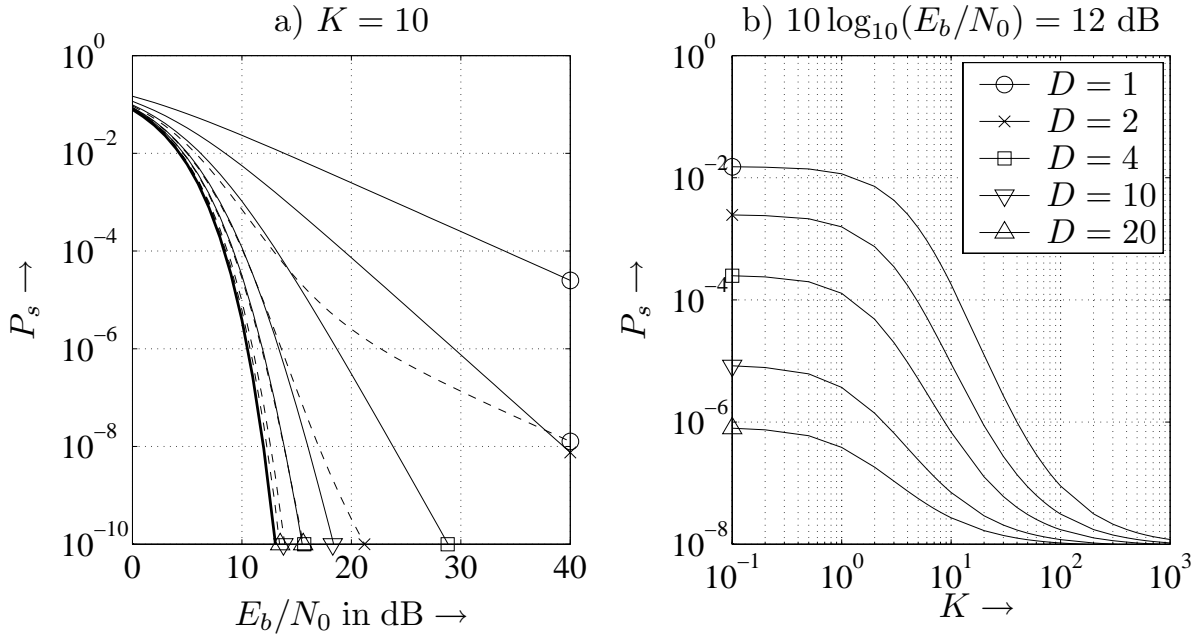


Figure 1.5.6: Symbol error probabilities for i.i.d. Rayleigh and Rice fading channels
a) versus E_b/N_0 for $K = 10$ (- - - Rice, — Rayleigh), **b)** versus K at $10 \log_{10}(E_b/N_0) = 12 \text{ dB}$

after maximum ratio combining. For a linear decay of $\sigma_{\mathcal{H}_\ell}^2$, we obtain the slope $\delta = -2/(D+1)$ and the powers of the contributing channels become

$$\bar{\gamma}_\ell = \frac{E_s}{DN_0} \cdot \delta \cdot (D - \ell) = \frac{2E_s/N_0}{D+1} \cdot \left(1 - \frac{\ell-1}{D}\right) \quad \text{with } 1 \leq \ell \leq D. \quad (1.5.19)$$

From (1.5.19) we obtain the i.i.d. case with $\delta = 0$. For an exponential decay, the signal to noise ratios are determined by

$$\bar{\gamma}_\ell = C \cdot \frac{E_s}{N_0} \cdot \exp(\ell\delta/D) \quad \text{with } 1 \leq \ell \leq D \quad (1.5.20)$$

with $\delta < 0$ and C as a normalization factor. **Fig. 1.5.7** shows the results for BPSK. The best performance is obtained for i.i.d. channels. A linear decay leads to a slight degradation, while the exponential decays with $\delta \geq 5$ lose considerably. The reason is that, with growing δ , the power is concentrated on a single fading channel and, thus, thwarting the diversity effect. At an error rate of $P_s = 10^{-4}$, the exponential profile with $\delta = 10$ needs $D = 20$ paths for obtaining an equivalent diversity degree as in the case of i.i.d. branches with $D = 5$. For $\delta = 100$, approximately 200 paths are required.

1.5.3 MRC for Correlated Diversity Branches

If the different diversity branches are mutually dependent, the factorization of the probability density in (1.5.10) cannot be performed anymore and solving the

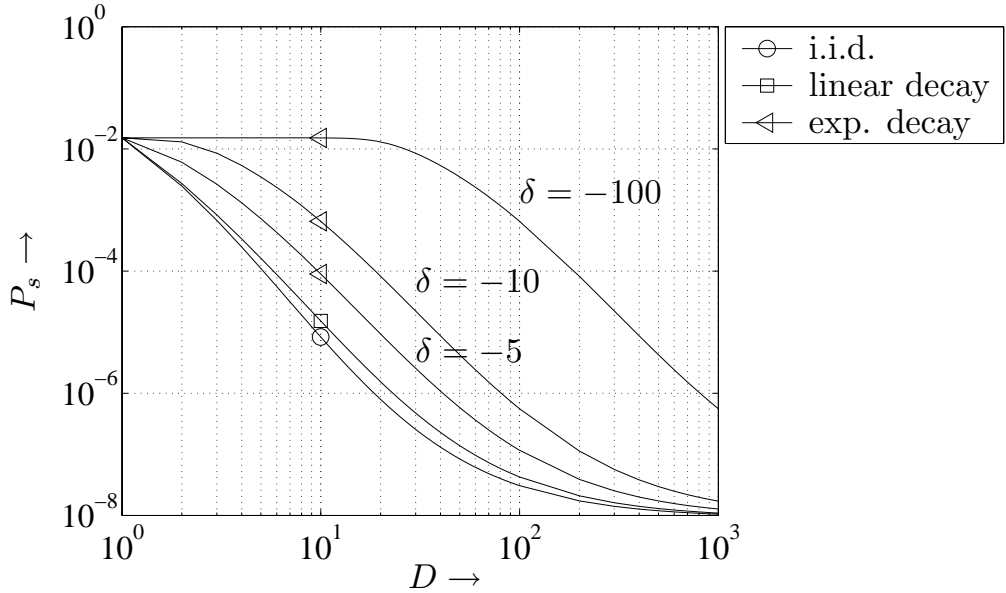


Figure 1.5.7: Symbol error probabilities versus diversity degree D for BPSK and different power profiles at $10 \log_{10}(E_b/N_0) = 12$ dB

integral becomes a difficult task. Generally, the correlations between different channels can be expressed by a correlation matrix

$$\Phi_{\mathcal{H}\mathcal{H}} = \begin{bmatrix} \sigma_{\mathcal{H}_1}^2 & \sigma_{\mathcal{H}_1}\sigma_{\mathcal{H}_2}\rho_{1,2} & \cdots & \sigma_{\mathcal{H}_1}\sigma_{\mathcal{H}_D}\rho_{1,D} \\ \sigma_{\mathcal{H}_1}\sigma_{\mathcal{H}_2}\rho_{2,1} & \sigma_{\mathcal{H}_2}^2 & \cdots & \sigma_{\mathcal{H}_2}\sigma_{\mathcal{H}_D}\rho_{2,D} \\ \vdots & \vdots & \ddots & \vdots \\ \sigma_{\mathcal{H}_1}\sigma_{\mathcal{H}_D}\rho_{D,1} & \sigma_{\mathcal{H}_2}\sigma_{\mathcal{H}_D}\rho_{D,2} & \cdots & \sigma_{\mathcal{H}_D}^2 \end{bmatrix} \quad (1.5.21)$$

whose elements are $\Phi_{\mu,\nu} = E\{h_\mu h_\nu^*\} = \sigma_{\mathcal{H}_\mu}\sigma_{\mathcal{H}_\nu}\rho_{\mu,\nu}$. The coefficient $\rho_{\mu,\nu}$ describes the correlation between the channel coefficients h_μ and h_ν normalized on $\sigma_{\mathcal{H}_\mu}\sigma_{\mathcal{H}_\nu}$. Due to $\rho_{\mu,\mu} = 1$, the main diagonal consists of the powers $\sigma_{\mathcal{H}_\mu}^2$ of the different channels.

A solution of the integral in (1.5.10) can be derived by the well-known Karhunen-Loëve transformation [Kam96, Mer99]. It linearly transforms the vector \mathbf{h} with correlated elements h_μ into a vector \mathbf{w} whose elements w_μ are then uncorrelated. Since the channel coefficients are assumed to be complex Gaussian distributed, they are also statistically independent. The matrix $\mathbf{Q} = [\mathbf{q}_1 \cdots \mathbf{q}_D]$ describing this linear transformation simply consists of the eigenvectors \mathbf{q}_μ of $\Phi_{\mathcal{H}\mathcal{H}}$. Therefore, we only have to solve the eigenvalue problem

$$\Phi_{\mathcal{H}\mathcal{H}}\mathbf{q}_\mu = \lambda_\mu \mathbf{q}_\mu \quad \Rightarrow \quad \det(\Phi_{\mathcal{H}\mathcal{H}} - \lambda \mathbf{I}_D) = 0 \quad (1.5.22)$$

delivering the eigenvalue decomposition $\Phi_{\mathcal{H}\mathcal{H}} = \mathbf{Q}^H \boldsymbol{\Lambda} \mathbf{Q}$. The diagonal matrix $\boldsymbol{\Lambda}$ contains the eigenvalues λ_μ of $\Phi_{\mathcal{H}\mathcal{H}}$. Since \mathbf{Q} is a unitary matrix, the transformation is performed by

$$\mathbf{h} = \mathbf{Q} \cdot \mathbf{w} \quad \Rightarrow \quad \mathbf{w} = \mathbf{Q}^{-1} \cdot \mathbf{h} = \mathbf{Q}^H \cdot \mathbf{h} \quad (1.5.23)$$

resulting in $E\{\mathbf{w}\mathbf{w}^H\} = E\{\mathbf{Q}^H \mathbf{h} \mathbf{h}^H \mathbf{Q}\} = \mathbf{Q}^H \Phi_{\mathcal{H}\mathcal{H}} \mathbf{Q} = \mathbf{Q}^H \mathbf{Q}^H \Lambda \mathbf{Q} \mathbf{Q} = \Lambda$. Hence, we obtain D independent equivalent channels with coefficients w_μ and average powers λ_μ . For these equivalent channels, (1.5.15) can be directly applied again by inserting the corresponding moment generating functions. For Rayleigh fading channels, we obtain the expression

$$P_s = a \int_0^b \prod_{\ell=1}^D \quad \text{with} \quad \gamma_\ell = \lambda_\ell \cdot \frac{E_s}{DN_0} . \quad (1.5.24)$$

Obviously, only nonzero eigenvalues contribute to the product in (1.5.24) and the effective diversity degree becomes smaller for correlated channels.

Constant correlations between equal power paths

In the sequel, the influence of correlations between different paths will be illustrated for a specific example. We assume that all channels have the same average power, i.e. $\sigma_{\mathcal{H}}^2 = \sigma_{\mathcal{H}_1}^2 = \dots = \sigma_{\mathcal{H}_D}^2$, and that the correlation between pairs of diversity branches is constant for all pairs, i.e. $\rho_{\mu,\nu} = \rho$ for all $\mu \neq \nu$. Hence, the correlation matrix becomes

$$\Phi_{\mathcal{H}\mathcal{H}} = \sigma_{\mathcal{H}}^2 \cdot \begin{bmatrix} 1 & \rho & \cdots & \rho \\ \rho & 1 & \cdots & \rho \\ \vdots & \vdots & \ddots & \vdots \\ \rho & \rho & \cdots & 1 \end{bmatrix} \quad (1.5.25)$$

and the argument of the determinant in (1.5.22) has the form

$$\begin{bmatrix} a & b & b & \cdots & b \\ b & a & b & \cdots & b \\ \vdots & & & \ddots & \vdots \\ b & b & \cdots & b & a \end{bmatrix}$$

whose determinant is $(a - b)^{D-1}[a + b(D - 1)]$ [SA00]. Substituting $a = \sigma_{\mathcal{H}}^2 - \lambda$ and $b = \sigma_{\mathcal{H}}^2 \rho$ yields the expression

$$(\sigma_{\mathcal{H}}^2 - \lambda - \sigma_{\mathcal{H}}^2 \rho)^{D-1}[\sigma_{\mathcal{H}}^2 - \lambda + \sigma_{\mathcal{H}}^2 \rho(D - 1)] = 0 .$$

The solutions are the $(D - 1)$ -fold zero $\lambda_1 = \sigma_{\mathcal{H}}^2(1 - \rho)$ and the single zero $\lambda_2 = \sigma_{\mathcal{H}}^2(1 + \rho(D - 1))$. For $\sigma_{\mathcal{H}}^2 = 1$, inserting these eigenvalues into (1.5.24) delivers the ergodic error probability

$$P_s = a \int_0^b \frac{1}{\left(1 + \frac{cE_s/N_0(1-\rho)}{D \sin^2(\theta)}\right)^{D-1}} \frac{1}{1 + \frac{cE_s/N_0(1+\rho(D-1))}{D \sin^2(\theta)}} d\theta . \quad (1.5.26)$$

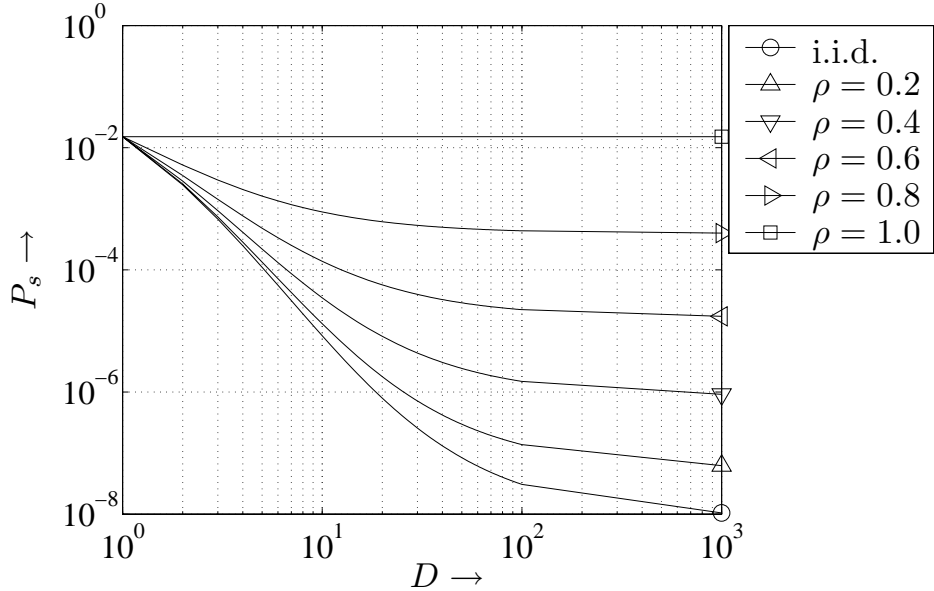


Figure 1.5.8: Symbol error probabilities versus diversity degree D for BPSK, identically distributed channels and varying correlation coefficient ρ at $10 \log_{10}(E_b/N_0) = 12$ dB

A check on plausibility shows the well-known result of i.i.d. diversity branches for $\rho = 0$, and the non-diversity case with $D = 1$ for $\rho = 1$ (total correlation). **Fig. 1.5.8** illustrates the corresponding results. Similar to unequal power distributions among the contributing paths, correlation decreases the benefits of diversity. For $\rho = 0.4$, the error rate hardly falls below 10^{-6} even for $D = 1000$. This error rate is already achieved with $D = 19$ for i.i.d. channels, i.e. the effective diversity degree is only 19. For $\rho = 1$, i.e. totally correlated channels, no diversity gain can be exploited.

Chapter 2

Information Theory

This section briefly introduces Shannon's information theory which was founded in 1948 and represents the basis for all communication systems. Although we make use of this theory only with respect to communication systems, it can be applied in a much broader context, e.g. for the analysis of stock markets [SW93]. Furthermore, we concentrate on the channel coding theorem and do not address the topics source coding and cryptography.

The channel coding theorem delivers ultimate bounds on the efficiency of communication systems. Hence, we can evaluate the performance of practical systems and algorithms. However, the theorem is not constructive in the sense that it tells us how to improve a system. In the sequel, we first have to introduce some definitions.

2.1 Basic Definitions

2.1.1 Information, Redundancy and Entropy

In order to obtain a tool for evaluating communication systems, the term *information* must be mathematically defined and quantified. We assume a random process \mathcal{X} that can take on values out of a finite alphabet \mathbb{X} consisting of elements X_μ with probabilities $\Pr\{X_\mu\}$. By intuition, the information $I(X_\mu)$ of a symbol X_μ should fulfill the following conditions.

1. The information of an event is always nonnegative, i.e. $I(X_\mu) \geq 0$.
2. The information of an event depends on its probability, i.e. $I(X_\mu) = f(\Pr\{X_\mu\})$. Additionally, the information of a rare event should be larger than that of a frequently occurring event.

3. For statistically independent events X_μ and X_ν with $\Pr\{X_\mu, X_\nu\} = \Pr\{X_\mu\} \cdot \Pr\{X_\nu\}$, the common information of both events should be the sum of the individual contents, i.e. $I(X_\mu, X_\nu) = I(X_\mu) + I(X_\nu)$.

Comprising conditions 2 and 3 leads to the relation $f(\Pr\{X_\mu\} \cdot \Pr\{X_\nu\}) = f(\Pr\{X_\mu\}) + f(\Pr\{X_\nu\})$. The only function that fulfills this condition is the logarithm. Hence the information of an event or a symbol X_μ is defined by [Sha48]

$$I(X_\mu) = \log_2 \frac{1}{\Pr\{X_\mu\}} = -\log_2 \Pr\{X_\mu\}. \quad (2.1.1)$$

Since digital communication systems are based on the binary representation of symbols, the logarithm to base 2 is generally used and $I(X_\mu)$ is measured in *bit*. However, different definitions exist using e.g. the natural logarithm (*nat*) or the logarithm to base 10 (*Hartley*). The average information of the process \mathcal{X} is called entropy and defined by

$$\bar{I}(\mathcal{X}) = E\{I(X_\mu)\} = - \sum_{\mu} \Pr\{X_\mu\} \cdot \log_2 \Pr\{X_\mu\}. \quad (2.1.2)$$

The entropy of an alphabet represents the minimum average number of bits that are needed to represent the alphabet in binary form. Finding encoding schemes reaching this goal is generally nontrivial and subject to source or entropy coding. It can be shown that the entropy becomes maximum for equally likely symbols X_μ . In this case, $\bar{I}_{\max}(\mathcal{X}) = \sum_{\mu} 2^{-k} \cdot \log_2 2^k = k$ bit for an alphabet consisting of 2^k elements. Hence, $0 \leq \bar{I}(\mathcal{X}) \leq \log_2 |\mathbb{X}|$ holds.

For an alphabet consisting of only two elements with probabilities $\Pr\{X_1\} = P_e$ and $\Pr\{X_2\} = 1 - P_e$ we obtain the binary entropy function

$$\bar{I}_2(P_e) = -P_e \cdot \log_2(P_e) - (1 - P_e) \cdot \log_2(1 - P_e). \quad (2.1.3)$$

It is depicted in **Fig. 2.1.1**. Obviously, the entropy reaches its maximum $\bar{I}_{\max} = 1$ bit for the highest uncertainty at $\Pr\{X_1\} = \Pr\{X_2\} = P_e = 0.5$. It is zero for $P_e = 0$ and $P_e = 1$ because the symbols are already a priori known and do not contain any information. Moreover, the entropy is a concave function with respect to P_e . This is a very important property that holds also for more than two variables.

A practical interpretation of the entropy can be obtained from the rate distortion theory [CT91]. It states that the minimum number of bits necessary for representing an event x of the process \mathcal{X} without losing information is exactly $\bar{I}(\mathcal{X})$. Fewer bits lead to distortions. The difference between the average number \bar{m} of bits needed for a concrete implementation and the entropy is called redundancy

$$R = \bar{m} - \bar{I}(\mathcal{X}) \quad ; \quad r = \frac{\bar{m} - \bar{I}(\mathcal{X})}{\bar{I}(\mathcal{X})}. \quad (2.1.4)$$

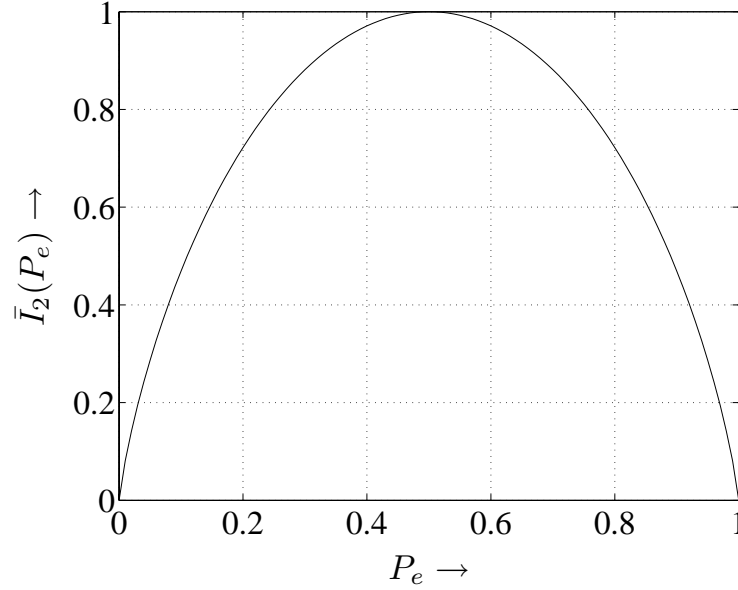


Figure 2.1.1: Binary entropy function

In (2.1.4), R and r denote the absolute and the relative redundancy, respectively. Therefore, the aim of lossless source coding is to find coding schemes that need as few bits as possible to represent a random variable. One very famous scheme is for example the Huffmann code.

2.1.2 Conditional, Joint and Mutual Information

Since the scope of this work is the communication between two or more subscribers, we have to consider at least two processes \mathcal{X} and \mathcal{Y} with symbols $X_\mu \in \mathbb{X}$ and $Y_\nu \in \mathbb{Y}$, respectively. The first process represents the transmitted data, the second the corresponding received data. Hence, the channel is supposed to have discrete input and output symbols and it can be statistically described by the joint probabilities $\Pr\{X_\mu, Y_\nu\}$ or, equivalently, by the conditional probabilities $\Pr\{Y_\nu | X_\mu\}$, $\Pr\{X_\mu | Y_\nu\}$ and the a priori probabilities $\Pr\{X_\mu\}$, $\Pr\{Y_\nu\}$. Following the definitions of the last section, the joint information of two events $X_\mu \in \mathbb{X}$ and $Y_\nu \in \mathbb{Y}$ is

$$I(X_\mu, Y_\nu) = \log_2 \frac{1}{\Pr\{X_\mu, Y_\nu\}} = -\log_2 \Pr\{X_\mu, Y_\nu\}. \quad (2.1.5)$$

Consequently, the joint entropy of both processes is given by

$$\bar{I}(\mathcal{X}, \mathcal{Y}) = E\{I(\mathcal{X}, \mathcal{Y})\} = - \sum_{\mu} \sum_{\nu} \Pr\{X_\mu, Y_\nu\} \cdot \log_2 \Pr\{X_\mu, Y_\nu\}. \quad (2.1.6)$$

Fig. 2.1.2 illustrates the relationships between different kinds of entropies. Besides $\bar{I}(\mathcal{X})$, $\bar{I}(\mathcal{Y})$ and $\bar{I}(\mathcal{X}, \mathcal{Y})$ already known from the previous definitions, three

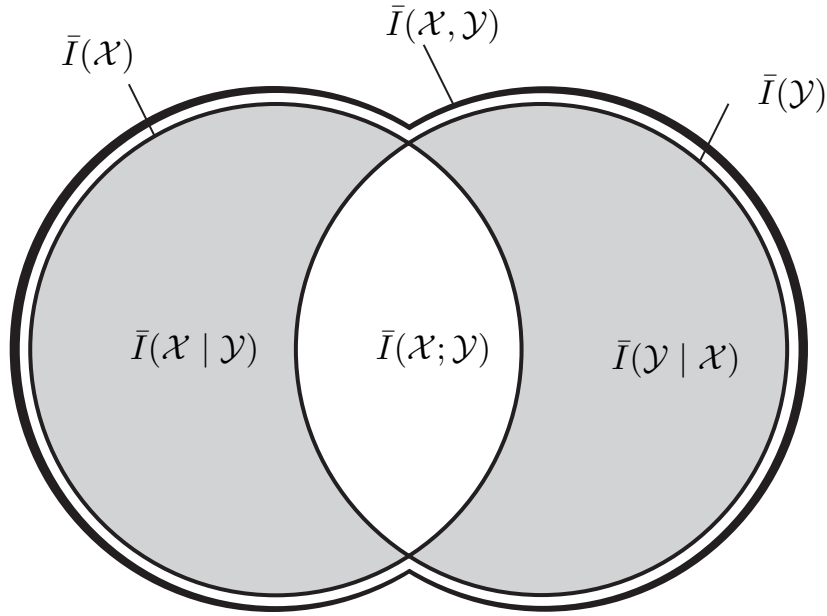


Figure 2.1.2: Illustration of entropies for two processes

further important entropies exist. At the receiver, y is totally known and the term $\bar{I}(\mathcal{X} | y)$ represents the information of \mathcal{X} that is not part of y . Averaging over all possible outputs $Y_\nu \in \mathbb{Y}$ delivers the *equivocation*, i.e. information that was lost during transmission

$$\begin{aligned}\bar{I}(\mathcal{X} | \mathcal{Y}) &= \sum_{Y_\nu} \Pr\{Y_\nu\} \cdot \bar{I}(\mathcal{X} | \mathcal{Y} = Y_\nu) \\ &= - \sum_{\mu} \sum_{\nu} \Pr\{X_\mu, Y_\nu\} \cdot \log_2 \Pr\{X_\mu | Y_\nu\}. \quad (2.1.7)\end{aligned}$$

From Fig. 2.1.2, we recognize that $\bar{I}(\mathcal{X} | \mathcal{Y})$ equals the difference between the joint entropy $\bar{I}(\mathcal{X}, \mathcal{Y})$ and the sinks entropy $\bar{I}(\mathcal{Y})$. Equivalently, we can write $\bar{I}(\mathcal{X}, \mathcal{Y}) = \bar{I}(\mathcal{X} | \mathcal{Y}) + \bar{I}(\mathcal{Y})$ leading to the general chain rule for entropies.

Chain Rule for Entropies

In Appendix B.1, it is shown that the entropy's chain rule [CT91]

$$\bar{I}(\mathcal{X}_1, \mathcal{X}_2 \dots, \mathcal{X}_n) = \sum_{i=1}^n \bar{I}(\mathcal{X}_i | \mathcal{X}_{i-1} \dots, \mathcal{X}_1) \quad (2.1.8)$$

holds for a set of random variables $\mathcal{X}_1, \mathcal{X}_2, \dots, \mathcal{X}_n$, up to \mathcal{X}_n , belonging to a joint probability $\Pr\{\mathcal{X}_1, \mathcal{X}_2, \dots, \mathcal{X}_n\}$.

Contrarily, $\bar{I}(\mathcal{Y} \mid \mathcal{X})$ represents information of \mathcal{Y} that is not contained in \mathcal{X} . Therefore, it cannot stem from the source \mathcal{X} and is termed *irrelevance*.

$$\begin{aligned}\bar{I}(\mathcal{Y} \mid \mathcal{X}) &= \bar{I}(\mathcal{X}, \mathcal{Y}) - \bar{I}(\mathcal{X}) = \sum_{X_\mu} \Pr\{X_\mu\} \cdot \bar{I}(\mathcal{Y} \mid \mathcal{X} = X_\mu) \\ &= - \sum_{\mu} \sum_{\nu} \Pr\{X_\mu, Y_\nu\} \cdot \log_2 \Pr\{Y_\nu \mid Y_\mu\}\end{aligned}\quad (2.1.9)$$

Naturally, the average information of a process \mathcal{X} cannot be increased by some knowledge about \mathcal{Y} so that

$$\bar{I}(\mathcal{X} \mid \mathcal{Y}) \leq \bar{I}(\mathcal{X}) \quad (2.1.10)$$

holds. Equality in (2.1.10) is obtained for statistically independent processes.

The most important entropy $\bar{I}(\mathcal{X}; \mathcal{Y})$ is called *mutual information* and describes the average information common to \mathcal{X} and \mathcal{Y} . According to Fig. 2.1.2, it can be determined by

$$\bar{I}(\mathcal{X}; \mathcal{Y}) = \bar{I}(\mathcal{X}) - \bar{I}(\mathcal{X} \mid \mathcal{Y}) = \bar{I}(\mathcal{Y}) - \bar{I}(\mathcal{Y} \mid \mathcal{X}) = \bar{I}(\mathcal{X}) + \bar{I}(\mathcal{Y}) - \bar{I}(\mathcal{X}, \mathcal{Y}) . \quad (2.1.11)$$

The mutual information is exactly the term that has to be maximized in order to design a communication system with the highest possible spectral efficiency. The maximum mutual information that can be obtained is called *channel capacity* and will be derived for special cases in subsequent sections. Inserting (2.1.2) and (2.1.6) into (2.1.11) yields

$$\begin{aligned}\bar{I}(\mathcal{X}; \mathcal{Y}) &= \sum_{\mu} \sum_{\nu} \Pr\{X_\mu, Y_\nu\} \cdot \log_2 \frac{\Pr\{X_\mu, Y_\nu\}}{\Pr\{X_\mu\} \cdot \Pr\{Y_\nu\}} \\ &= \sum_{\mu} \Pr\{X_\mu\} \sum_{\nu} \Pr\{Y_\nu \mid X_\mu\} \log_2 \frac{\Pr\{Y_\nu \mid X_\mu\}}{\sum_l \Pr\{Y_\nu \mid X_l\} \Pr\{X_l\}} .\end{aligned}\quad (2.1.12)$$

As can be seen, the mutual information depends on the conditional probabilities $\Pr\{Y_\nu \mid X_\mu\}$ determined by the channel and the a priori probabilities $\Pr\{X_\mu\}$. Hence, the only parameter that can be optimized for a given channel in order to maximize the mutual information is the statistics of the input alphabet.

Chain Rule for Information

If the mutual information depends on a signal or parameter z , (2.1.11) changes to $\bar{I}(\mathcal{X}; \mathcal{Y} \mid \mathcal{Z}) = \bar{I}(\mathcal{X} \mid \mathcal{Z}) - \bar{I}(\mathcal{X} \mid \mathcal{Y}, \mathcal{Z})$. This leads directly to the general chain rule for information [CT91] (cf. Appendix B.2)

$$\bar{I}(\mathcal{X}_1, \dots, \mathcal{X}_n; \mathcal{Z}) = \sum_{i=1}^n \bar{I}(\mathcal{X}_i; \mathcal{Z} \mid \bar{I}(\mathcal{X}_{i-1}, \dots, \mathcal{X}_1)) \quad (2.1.13)$$

For only two random variables \mathcal{X} and \mathcal{Y} , (2.1.13) becomes

$$\begin{aligned}\bar{I}(\mathcal{X}, \mathcal{Y}; \mathcal{Z}) &= \bar{I}(\mathcal{X}, \mathcal{Y}) - \bar{I}(\mathcal{X}, \mathcal{Y} | \mathcal{Z}) \\ &= \bar{I}(\mathcal{X}; \mathcal{Z}) + \bar{I}(\mathcal{Y}; \mathcal{Z} | \mathcal{X}) = \bar{I}(\mathcal{Y}; \mathcal{Z}) + \bar{I}(\mathcal{X}; \mathcal{Z} | \mathcal{Y}).\end{aligned}\quad (2.1.14)$$

From (2.1.14), we can learn that first detecting x from z and subsequently y – now for known x – leads to the same mutual information as starting with y and proceeding with the detection of x . As a consequence, the detection order of x and y has no influence from the information theoretic point of view. However, this presupposes an error-free detection of the first signal that can usually not be ensured in practical systems resulting in error propagation.

Data Processing Theorem

With (2.1.13), the data processing theorem can now be derived. Imagine a Markovian chain $\mathcal{X} \rightarrow \mathcal{Y} \rightarrow \mathcal{Z}$ of three random processes \mathcal{X} , \mathcal{Y} and \mathcal{Z} , i.e. \mathcal{Y} depends on \mathcal{X} and \mathcal{Z} depends on \mathcal{Y} but \mathcal{X} and \mathcal{Z} are mutually independent for known y . Hence, $\bar{I}(\mathcal{X}; \mathcal{Z} | y) = 0$ holds. With $\bar{I}(\mathcal{Y}; \mathcal{Z} | x) \geq 0$ (cf. Appendix B.3), we obtain

$$\bar{I}(\mathcal{X}; \mathcal{Z}) \leq \bar{I}(\mathcal{X}; \mathcal{Y}) \quad \text{and} \quad \bar{I}(\mathcal{X}; \mathcal{Z}) \leq \bar{I}(\mathcal{Y}; \mathcal{Z}). \quad (2.1.15)$$

If \mathcal{Z} is a function of \mathcal{Y} , (2.1.15) states that information of \mathcal{X} obtained from \mathcal{Y} cannot be increased by some processing of \mathcal{Y} leading to \mathcal{Z} . Equality holds if \mathcal{Z} is a *sufficient statistics* of \mathcal{Y} .

2.1.3 Extension for Continuous Signals

If the random process \mathcal{X} consists of continuously distributed values, the probabilities $\Pr\{X_\mu\}$ of the last subsection have to be transformed into probability densities $p_{\mathcal{X}}(x)$. Consequently, all sums become integrals and the *differential entropy* is defined by

$$\bar{I}_{\text{diff}}(\mathcal{X}) = - \int_{-\infty}^{\infty} p_{\mathcal{X}}(x) \cdot \log_2 p_{\mathcal{X}}(x) dx = \text{E}\{-\log_2 p_{\mathcal{X}}(x)\}. \quad (2.1.16)$$

Contrarily to the definition of the last subsection, the differential entropy is not restricted to be nonnegative. Hence, the aforementioned interpretation is not valid anymore. Nevertheless, $\bar{I}_{\text{diff}}(\mathcal{X})$ can still be used for the calculation of mutual information and channel capacity which will be demonstrated in Section 2.2.

For a real random variable with a constant probability density $p_{\mathcal{X}}(x) = 1/(2a)$ in the range $|x| \leq a$, a is a positive real constant, the differential entropy has the value

$$\bar{I}_{\text{diff}}(\mathcal{X}) = \int_{-a}^a \frac{1}{2a} \cdot \log_2(2a) dx = \log_2(2a). \quad (2.1.17)$$

For a real random variable with Gaussian density

$$p_{\mathcal{X}}(x) = \frac{1}{\sqrt{2\pi\sigma_{\mathcal{X}}^2}} \cdot \exp\left(-\frac{(x - \mu_{\mathcal{X}})^2}{2\sigma_{\mathcal{X}}^2}\right),$$

we obtain

$$\bar{I}_{\text{diff}}(\mathcal{X}) = \frac{1}{2} \cdot \log_2(2\pi e \sigma_{\mathcal{X}}^2). \quad (2.1.18a)$$

If the random process is circularly symmetric complex, i.e. real and imaginary parts are independent with powers $\sigma_{\mathcal{X}'}^2 = \sigma_{\mathcal{X}''}^2 = \sigma_{\mathcal{X}}^2/2$, the probability density function has the form

$$p_{\mathcal{X}}(x) = p_{\mathcal{X}'}(x') \cdot p_{\mathcal{X}''}(x'') = \frac{1}{\pi\sigma_{\mathcal{X}}^2} \cdot \exp\left(-\frac{|x - \mu_{\mathcal{X}}|^2}{\sigma_{\mathcal{X}}^2}\right).$$

In this case, the entropy is

$$\bar{I}_{\text{diff}}(\mathcal{X}) = \log_2(\pi e \sigma_{\mathcal{X}}^2). \quad (2.1.18b)$$

Comparing (2.1.18a) and (2.1.18b), we observe that the differential entropy of a complex Gaussian random variable equals the joint entropy of two independent real Gaussian variables with halved variance.

2.1.4 Extension for Vectors and Matrices

When dealing with vector channels that have multiple inputs and outputs, we use vector notations as described in Section 1.2.4. Therefore, we now comprise n random variables $x_1 \dots x_n$ of the process \mathcal{X} into the vector \mathbf{x} . With the definition of the joint entropy in (2.1.6), we obtain

$$\begin{aligned} \bar{I}(\underline{\mathcal{X}}) &= - \sum_{\mathbf{x} \in \mathbb{X}^n} \Pr\{\mathbf{x}\} \cdot \log_2 \Pr\{\mathbf{x}\} \\ &= - \sum_{\nu_1=1}^{|\mathbb{X}|} \dots \sum_{\nu_n=1}^{|\mathbb{X}|} \Pr\{X_{\nu_1}, \dots, X_{\nu_n}\} \cdot \log_2 \Pr\{X_{\nu_1}, \dots, X_{\nu_n}\}. \end{aligned} \quad (2.1.19)$$

Applying now recursively the chain rule for entropies in (2.1.8) leads to an upper bound

$$\bar{I}(\underline{\mathcal{X}}) = \sum_{\mu=1}^n \bar{I}(\mathcal{X}_\mu | x_1, \dots, x_{\mu-1}) \leq \sum_{\mu=1}^n \bar{I}(\mathcal{X}_\mu) \quad (2.1.20)$$

where equality holds exactly for statistically independent processes \mathcal{X}_μ . Following the last subsection, the differential entropy for real random vectors becomes

$$\bar{I}_{\text{diff}}(\underline{\mathcal{X}}) = - \int_{\mathbb{R}^n} p_{\underline{\mathcal{X}}}(\mathbf{x}) \cdot \log_2 p_{\underline{\mathcal{X}}}(\mathbf{x}) d\mathbf{x} = \mathbb{E}\{-\log_2 p_{\underline{\mathcal{X}}}(\mathbf{x})\} \quad (2.1.21)$$

Under the restriction $\|\mathbf{x}\| \leq a$, a is a positive real constant, the entropy is maximized for a uniform distribution. Analogue to Section 2.1.1, we obtain

$$p_{\underline{\mathcal{X}}}(\mathbf{x}) = \begin{cases} 1/V_n(a) & \text{for } \|\mathbf{x}\| \leq a \\ 0 & \text{else} \end{cases} \quad \text{with} \quad V_n(a) = \frac{2\pi^{n/2}a^n}{n\Gamma(n/2)}, \quad (2.1.22)$$

i.e. the probability density function describes the surface of a ball in the n -dimensional space. The gamma function in (2.1.22) is defined by $\Gamma(x) = \int_0^\infty t^{x-1}e^{-t}dt$ [Gra00]. It becomes $\Gamma(n) = (n-1)!$ and $\Gamma(n-\frac{1}{2}) = (2n)!\sqrt{\pi}/(n! \cdot 2^{2n})$ for $n = 1, 2, 3, \dots$. The expectation in (2.1.21) now delivers

$$\bar{I}_{\text{diff}}(\underline{\mathcal{X}}) = \log_2 \left(\frac{2\pi^{n/2}a^n}{n\Gamma(n/2)} \right). \quad (2.1.23)$$

Contrarily, for a given covariance matrix $\Phi_{\underline{\mathcal{X}}\underline{\mathcal{X}}} = E_{\underline{\mathcal{X}}} \{\mathbf{x}\mathbf{x}^H\}$ of a real-valued process $\underline{\mathcal{X}}$, the maximum entropy is achieved by a multivariate Gaussian density

$$p_{\underline{\mathcal{X}}}(\mathbf{x}) = \frac{1}{\sqrt{\det(2\pi\Phi_{\underline{\mathcal{X}}\underline{\mathcal{X}}})}} \cdot \exp \left(-\frac{\mathbf{x}^T \Phi_{\underline{\mathcal{X}}\underline{\mathcal{X}}}^{-1} \mathbf{x}}{2} \right) \quad (2.1.24)$$

and amounts to

$$\bar{I}_{\text{diff}}(\underline{\mathcal{X}}) = \frac{1}{2} \cdot \log_2 \det(2\pi e \Phi_{\underline{\mathcal{X}}\underline{\mathcal{X}}}). \quad (2.1.25)$$

For complex elements of \mathbf{x} with the same variance $\sigma_{\mathcal{X}}^2$, the Gaussian density becomes

$$p_{\underline{\mathcal{X}}}(\mathbf{x}) = \frac{1}{\sqrt{\det(\pi\Phi_{\underline{\mathcal{X}}\underline{\mathcal{X}}})}} \cdot \exp \left(-\mathbf{x}^H \Phi_{\underline{\mathcal{X}}\underline{\mathcal{X}}}^{-1} \mathbf{x} \right), \quad (2.1.26)$$

and the corresponding entropy has the form

$$\bar{I}_{\text{diff}}(\underline{\mathcal{X}}) = \log_2 \det(\pi e \Phi_{\underline{\mathcal{X}}\underline{\mathcal{X}}}), \quad (2.1.27)$$

if real and imaginary parts are statistically independent.

2.2 Channel Coding Theorem for SISO Channels

2.2.1 Channel Capacity

This section describes the channel capacity and the channel coding theorem defined by Shannon. **Fig. 2.2.1** depicts the simple system model. An FEC encoder that is explained in more detail in Chapter 3 maps k data symbols represented by the vector \mathbf{d} onto a vector \mathbf{x} of length n , i.e. the code rate is $R_c = k/n$. The vector \mathbf{x} is transmitted over the channel resulting in the output vector \mathbf{y} of same length

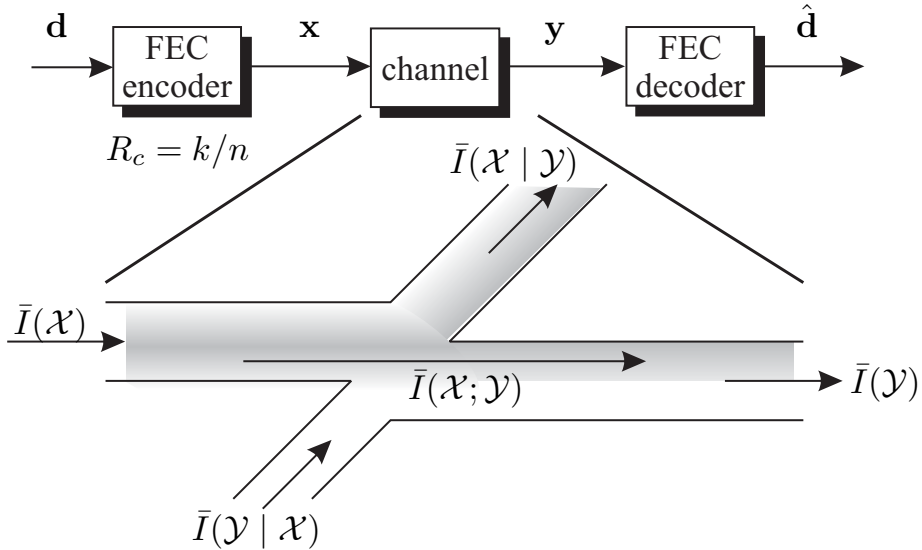


Figure 2.2.1: Simple model of a communication system

n . Finally, the FEC decoder tries to recover \mathbf{d} based on the observation \mathbf{y} and the knowledge of the code's structure.

As already mentioned in Section 2.1.2, the mutual information $\bar{I}(\mathcal{X}; \mathcal{Y})$ is the crucial parameter that has to be maximized. According to (2.1.11), it only depends on the conditional probabilities $\Pr\{Y_\nu | X_\mu\}$ and the a priori probabilities $\Pr\{X_\mu\}$. Since the $\Pr\{Y_\nu | X_\mu\}$ are given by the channel characteristics and can hardly be influenced, the mutual information can only be maximized by properly adjusting $\Pr\{X_\mu\}$. Therefore, the channel capacity C describes the maximum mutual information

$$C = \sup_{\Pr\{\mathcal{X}\}} \sum_{\mu} \sum_{\nu} \Pr\{Y_\nu | X_\mu\} \cdot \Pr\{X_\mu\} \cdot \log_2 \frac{\Pr\{Y_\nu | X_\mu\}}{\sum_l \Pr\{Y_\nu | X_l\} \cdot \Pr\{X_l\}} \quad (2.2.1)$$

obtained for optimally choosing the source statistics $\Pr\{\mathcal{X}\}$.¹ It can be shown that the mutual information is a concave function with respect to $\Pr\{\mathcal{X}\}$. Hence, only one maximum exists that can be determined by the sufficient conditions

$$\frac{\partial C}{\partial \Pr\{X_\mu\}} = 0 \quad \forall \quad X_\mu \in \mathbb{X}. \quad (2.2.2)$$

Due to the use of the logarithm to base 2, C is measured in [bits/channel use] or [bits/s/Hz]. In many practical systems, the statistics of the input alphabet is fixed or the effort for optimizing it is prohibitively high. Therefore, uniformly distributed input symbols are often assumed and the expression

¹If the maximum capacity is really reached by a certain distribution, the supremum can be replaced by the maximum operator.

$$\bar{I}(\mathcal{X}; \mathcal{Y}) = \log_2 |\mathcal{X}| + \frac{1}{|\mathcal{X}|} \cdot \sum_{\mu} \sum_{\nu} \Pr\{Y_{\nu} | X_{\mu}\} \cdot \log_2 \frac{\Pr\{Y_{\nu} | X_{\mu}\}}{\sum_l \Pr\{Y_{\nu} | X_l\}}. \quad (2.2.3)$$

is called channel capacity although the maximization with respect to $\Pr\{\mathcal{X}\}$ is missing. The first term in (2.2.3) represents $\bar{I}(\mathcal{X})$, the second the negative equivocation $\bar{I}(\mathcal{X} | \mathcal{Y})$.

The famous channel coding theorem of Shannon states that at least one code of rate $R_c \leq C$ exists for which an error-free transmission can be ensured. The theorem assumes perfect MAP or maximum likelihood decoding (cf. Section 1.3) and the code's length may be arbitrary long. However, the theorem does not show a way to find this code. For $R_c > C$ it can be shown that an error-free transmission is impossible even with tremendous effort [CT91].

For continuously distributed signals, the probabilities (2.2.1) have to be replaced by corresponding densities and the sums by integrals. In the case of a discrete signal alphabet and a continuous output, we obtain the expression

$$C = \sup_{\Pr\{\mathcal{X}\}} \int_{\mathbb{Y}} \sum_{\mu} p_{\mathcal{Y}|X_{\mu}}(y) \cdot \Pr\{X_{\mu}\} \cdot \log_2 \frac{p_{\mathcal{Y}|X_{\mu}}(y)}{\sum_l p_{\mathcal{Y}|X_l}(y) \cdot \Pr\{X_l\}} dy. \quad (2.2.4)$$

2.2.2 Cut-off Rate

Up to this point, no expression addressing the error rate attainable for a certain code rate R_c and codeword length n was achieved. This drawback can be overcome with the cut-off rate and the corresponding Bhattacharyya bound. We denote valid codewords by \mathbf{x} and the code representing the set of all codewords as Γ . Furthermore, we assume that $\mathbf{x} \in \Gamma$ of length n was transmitted and define its decision region $\mathbb{D}(\mathbf{x})$ such that the decoder decides correctly for all received vectors $\mathbf{y} \in \mathbb{D}(\mathbf{x})$. For a discrete output alphabet of the channel, the error probability of \mathbf{x} can be expressed by

$$P_w(\mathbf{x}) = \sum_{\mathbf{y} \notin \mathbb{D}(\mathbf{x})} \Pr\{\mathbf{y} | \mathbf{x}\} = \sum_{\substack{\mathbf{x}' \in \Gamma \\ \mathbf{x}' \neq \mathbf{x}}} \sum_{\mathbf{y} \in \mathbb{D}(\mathbf{x}')} \Pr\{\mathbf{y} | \mathbf{x}\}. \quad (2.2.5)$$

For all $\mathbf{y} \in \mathbb{D}(\mathbf{x}')$, $\Pr\{\mathbf{y} | \mathbf{x}'\}$ is larger than $\Pr\{\mathbf{y} | \mathbf{x}\}$ and

$$\Pr\{\mathbf{y} | \mathbf{x}'\} \geq \Pr\{\mathbf{y} | \mathbf{x}\} \quad \Rightarrow \quad \sqrt{\frac{\Pr\{\mathbf{y} | \mathbf{x}'\}}{\Pr\{\mathbf{y} | \mathbf{x}\}}} \geq 1 \quad (2.2.6)$$

holds. The multiplication of (2.2.5) with (2.2.6) and the extension of the inner sum in (2.2.5) to all possible received words $\mathbf{y} \in \mathbb{Y}^n$ leads to an upper bound

$$\begin{aligned} P_w(\mathbf{x}) &\leq \sum_{\substack{\mathbf{x}' \in \Gamma \\ \mathbf{x}' \neq \mathbf{x}}} \sum_{\mathbf{y} \in \mathbb{D}(\mathbf{x}')} \Pr\{\mathbf{y} \mid \mathbf{x}\} \cdot \sqrt{\frac{\Pr\{\mathbf{y} \mid \mathbf{x}'\}}{\Pr\{\mathbf{y} \mid \mathbf{x}'\}}} \\ &\leq \sum_{\substack{\mathbf{x}' \in \Gamma \\ \mathbf{x}' \neq \mathbf{x}}} \sum_{\mathbf{y} \in \mathbb{Y}^n} \sqrt{\Pr\{\mathbf{y} \mid \mathbf{x}\} \cdot \Pr\{\mathbf{y} \mid \mathbf{x}'\}}. \end{aligned} \quad (2.2.7)$$

The computational costs for calculating (2.2.7) are too high for practical systems because the number of codewords and especially the number of possible received words is very large. Moreover, we do not know a good code yet and we are not interested in the error probabilities of single codewords \mathbf{x} . Hence, we calculate the average over all possible codes Γ , i.e. we determine $E\{P_w(\mathbf{x})\}$ with respect to $\Pr\{\underline{\mathcal{X}}\}$ where \mathbf{x} is not restricted to be an element of Γ but $\mathbf{x} \in \mathbb{X}^n$ holds. In order to reach this goal, we assume that \mathbf{x} and \mathbf{x}' are identically distributed and independent² so that $\Pr\{\mathbf{x}, \mathbf{x}'\} = \Pr\{\mathbf{x}\} \cdot \Pr\{\mathbf{x}'\}$ holds. The expectation of the square root in (2.2.7) becomes

$$\begin{aligned} \sqrt{\Pr\{\mathbf{y} \mid \mathbf{x}\} \cdot \Pr\{\mathbf{y} \mid \mathbf{x}'\}} &= \sum_{\mathbf{x} \in \mathbb{X}^n} \sum_{\mathbf{x}' \in \mathbb{X}^n} \sqrt{\Pr\{\mathbf{y} \mid \mathbf{x}\} \cdot \Pr\{\mathbf{y} \mid \mathbf{x}'\}} \cdot \Pr\{\mathbf{x}\} \cdot \Pr\{\mathbf{x}'\} \\ &= \sum_{\mathbf{x} \in \mathbb{X}^n} \sqrt{\Pr\{\mathbf{y} \mid \mathbf{x}\}} \cdot \Pr\{\mathbf{x}\} \cdot \sum_{\mathbf{x}' \in \mathbb{X}^n} \sqrt{\Pr\{\mathbf{y} \mid \mathbf{x}'\}} \cdot \Pr\{\mathbf{x}'\} \\ &= \left(\sum_{\mathbf{x} \in \mathbb{X}^n} \sqrt{\Pr\{\mathbf{y} \mid \mathbf{x}\}} \cdot \Pr\{\mathbf{x}\} \right)^2. \end{aligned} \quad (2.2.8)$$

Since (2.2.8) does no longer depend on \mathbf{x}' , the outer sum in (2.2.7) becomes a constant factor $2^k - 1$ that can be approximated with $R_c = k/n$ by 2^{nR_c} . We obtain [CT91]

$$\begin{aligned} P_w = E\{P_w(\mathbf{x})\} &< 2^{nR_c} \cdot \sum_{\mathbf{y} \in \mathbb{Y}^n} \left(\sum_{\mathbf{x} \in \mathbb{X}^n} \sqrt{\Pr\{\mathbf{y} \mid \mathbf{x}\}} \cdot \Pr\{\mathbf{x}\} \right)^2 \\ &= 2^{nR_c + \log_2 \sum_{\mathbf{y} \in \mathbb{Y}^n} \left(\sum_{\mathbf{x} \in \mathbb{X}^n} \sqrt{\Pr\{\mathbf{y} \mid \mathbf{x}\}} \cdot \Pr\{\mathbf{x}\} \right)^2}. \end{aligned} \quad (2.2.9)$$

²This assumption includes also codes that map different information words onto the same codeword leading to $\mathbf{x} = \mathbf{x}'$. Since the probability of these codes is very low, their contribution to the ergodic error rate is rather small.

In order to minimize the average error probability, the second part of the exponent in (2.2.9) has to be minimized. Defining the cut-off rate to

$$R_0 = \max_{\Pr\{\underline{\mathcal{X}}\}} \left[-\frac{1}{n} \cdot \log_2 \left(\sum_{\mathbf{y} \in \mathbb{Y}^n} \left(\sum_{\mathbf{x} \in \mathbb{X}^n} \sqrt{\Pr\{\mathbf{y} \mid \mathbf{x}\}} \cdot \Pr\{\mathbf{x}\} \right)^2 \right) \right], \quad (2.2.10)$$

depending only on the conditional probabilities $\Pr\{\mathbf{y} \mid \mathbf{x}\}$ of the channel, we obtain an upper bound for the minimum average error rate

$$\min_{\Pr\{\underline{\mathcal{X}}\}} \mathbb{E}\{P_w\} < 2^{-n(R_0 - R_c)} = 2^{-n \cdot E_B(R_c)}. \quad (2.2.11)$$

In (2.2.11), $E_B(R_c) = R_0 - R_c$ denotes the Bhattacharyya error exponent. This result demonstrates that arbitrary low error probabilities can be achieved for $R_0 > R_c$. If the code rate R_c approaches R_0 , the length n of the code has to be increased infinitely for an error free transmission. Furthermore, (2.2.11) now allows an approximation of error probabilities for finite codeword lengths.

Based on the channel coding theorem, R_0 is always smaller than the channel capacity C . For $R_0 < R_c < C$, the bound in (2.2.11) cannot be applied. Moreover, due to the introduction of the factor in (2.2.6) the bound becomes very loose for large number of codewords.

For memoryless channels, the vector probabilities can be factorized into symbol probabilities simplifying the calculation of (2.2.10) tremendously. Applying the distributive law, we finally obtain

$$R_0 = \max_{\Pr\{\mathcal{X}\}} \left[-\log_2 \left(\sum_{y \in \mathbb{Y}} \left(\sum_{x \in \mathbb{X}} \sqrt{\Pr\{y \mid x\}} \cdot \Pr\{x\} \right)^2 \right) \right]. \quad (2.2.12)$$

Continuously Distributed Output

In [BB99, page 633], an approximation of R_0 is derived for the AWGN channel with a discrete input \mathbb{X} and a continuously distributed output. The derivation starts with calculating the average error probability and finally delivers the result in (2.2.11). Using our notation, we obtain

$$R_0 = \log_2(|\mathbb{X}|) - \log_2 \left(1 + \frac{1}{|\mathbb{X}|} r(\mathbb{X}, N_0) \right) \quad (2.2.13)$$

with

$$r(\mathbb{X}, N_0) = \min_{\Pr\{\mathcal{X}\}} |\mathbb{X}|^2 \cdot \sum_{\mu=1}^{|\mathbb{X}|} \sum_{\nu=1}^{|\mathbb{X}|} \Pr\{X_\mu\} \Pr\{X_\nu\} \exp \left[-\frac{|X_\mu - X_\nu|^2}{4N_0} \right]. \quad (2.2.14)$$

However, performing the maximization is a difficult task so that a uniform distribution of \mathbb{X} is often assumed. In this case, the factor in front of the double sum and the a priori probabilities eliminate each other.

2.2.3 Gallager Exponent

In order to tighten the bound of Bhattacharyya, Gallager introduced an optimization parameter $\rho \in [0, 1]$ leading to the expression

$$\begin{aligned} P_w = \text{E}\{P_w(\mathbf{x})\} &< 2^{\rho n R_c} \cdot \sum_{\mathbf{y} \in \mathbb{Y}^n} \left(\sum_{\mathbf{x} \in \mathbb{X}^n} \Pr\{\mathbf{y} \mid \mathbf{x}\}^{\frac{1}{1+\rho}} \cdot \Pr\{\mathbf{x}\} \right)^{1+\rho} \\ &= 2^{\rho n R_c + \log_2 \sum_{\mathbf{y} \in \mathbb{Y}^n} \left(\sum_{\mathbf{x} \in \mathbb{X}^n} \Pr\{\mathbf{y} \mid \mathbf{x}\}^{\frac{1}{1+\rho}} \cdot \Pr\{\mathbf{x}\} \right)^{1+\rho}}. \end{aligned} \quad (2.2.15)$$

Similar to the definition of the cut-off rate in (2.2.10) we can now define the Gallager function

$$E_0(\rho, \Pr\{\underline{\mathcal{X}}\}) = -\frac{1}{n} \cdot \log_2 \left(\sum_{\mathbf{y} \in \mathbb{Y}^n} \left(\sum_{\mathbf{x} \in \mathbb{X}^n} \Pr\{\mathbf{y} \mid \mathbf{x}\}^{\frac{1}{1+\rho}} \cdot \Pr\{\mathbf{x}\} \right)^{1+\rho} \right). \quad (2.2.16)$$

Comparing (2.2.8) with (2.2.16), it becomes obvious that the bounds of Gallager and Bhattacharyya are identical for $\rho = 1$ and $R_0 = \max_{\Pr\{\underline{\mathcal{X}}\}} E_0(1, \Pr\{\underline{\mathcal{X}}\})$ holds. The average symbol error probability in (2.2.11) becomes

$$P_w < 2^{-n(E_0(\rho, \Pr\{\underline{\mathcal{X}}\}) - \rho \cdot R_c)}. \quad (2.2.17)$$

For memoryless channels, the Gallager function can be simplified to

$$E_0(\rho, \Pr\{\mathcal{X}\}) = -\log_2 \left(\sum_{y \in \mathbb{Y}} \left(\sum_{x \in \mathbb{X}} \Pr\{y \mid x\}^{\frac{1}{1+\rho}} \cdot \Pr\{x\} \right)^{1+\rho} \right). \quad (2.2.18)$$

With the Gallager exponent

$$E_G(R_c) = \max_{\Pr\{\mathcal{X}\}} \max_{\rho \in [0, 1]} (E_0(\rho, \Pr\{\mathcal{X}\}) - \rho \cdot R_c) \quad (2.2.19)$$

we finally obtain the minimum error probability

$$\min_{\Pr\{\mathcal{X}\}} P_w < 2^{-n \cdot E_G(R_c)}. \quad (2.2.20)$$

We now want to discuss the curve sketching of $E_G(R_c)$. By partial derivation with respect to ρ it can be shown that $E_0(\rho, \Pr\{\mathcal{X}\})$ increases monotonically with

$\rho \in [0, 1]$ from 0 to its maximum R_0 . Furthermore, fixing ρ in (2.2.19) leads to a straight line of $E_G(R_c)$ with slope $-\rho$. Hence, we have an array of straight lines – one for each ρ – and each of them is determined by searching the optimum statistics $\Pr\{\mathcal{X}\}$. The Gallager exponent is finally obtained by finding the maximum among all lines for each code rate R_c .

This procedure is illustrated in **Fig. 2.2.2**. The critical rate

$$R_{\text{crit}} = \left. \frac{\partial}{\partial \rho} E_0(\rho, \Pr\{\mathcal{X}\}) \right|_{\rho=1} \quad (2.2.21)$$

represents the maximum rate for which $\rho = 1$ is the optimal choice. It is important to mention that $\Pr\{\mathcal{X}\}$ in (2.2.21) already represents the optimal choice for a maximal rate. In the range $0 < R_c \leq R_{\text{crit}}$ the parameterization by Gallager does not affect the result and $E_G(R_c)$ equals the Bhattacharyya exponent $E_B(R_c)$ given in (2.2.11). Hence, the cut-off rate can be used for approximating the error probability. For $R_c > R_{\text{crit}}$, the Bhattacharyya bound cannot be applied anymore and we have to use the tighter Gallager bound with $\rho < 1$.

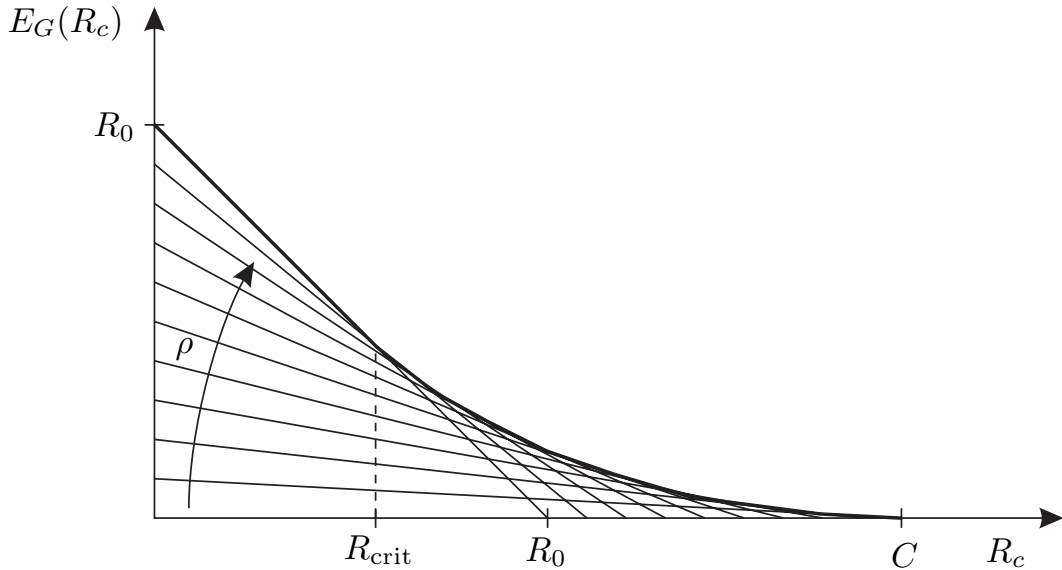


Figure 2.2.2: Curve sketching of Gallager exponent $E_G(R_c)$

According to (2.2.20), we can achieve arbitrary low error probabilities by appropriately choosing n as long as $E_G(R_c) > 0$ holds. The maximum rate for which an error-free transmission can be ensured is reached at the point where $E_G(R_c)$ crosses the axis. It can be shown that this point is obtained for $\rho \rightarrow 0$ resulting in

$$R_{\max} = \lim_{\rho \rightarrow 0} \frac{E_0(\rho, \Pr\{\mathcal{X}\})}{\rho} = \max_{\Pr\{\mathcal{X}\}} \bar{I}(\mathcal{X}; \mathcal{Y}) = C. \quad (2.2.22)$$

Therefore, the maximum rate for which an error-free transmission can be ensured is exactly the channel capacity C (what was already stated in the channel coding

theorem). Transmitting at $R_c = C$ requires an infinite codeword length $n \rightarrow \infty$. For the sake of completeness, it has to be mentioned that an expurgated exponent $E_x(\rho, \Pr\{\mathcal{X}\})$ with $\rho \geq 1$ exists leading to tighter results than the Gallager exponent for rates below $R_{\text{ex}} = \frac{\partial}{\partial \rho} E_x(\rho, \Pr\{\mathcal{X}\})|_{\rho=1}$ [CT91].

2.2.4 Capacity of the AWGN Channel

AWGN Channel with Gaussian Distributed Input

In this and the next section we discuss the recent results for some practical channels. We start with the equivalent baseband representation of the AWGN channel already depicted in Fig. 1.2.4. If the generally complex input and output signals are continuously distributed, differential entropies have to be used. Since the information in \mathcal{Y} for known \mathcal{X} can only stem from the noise \mathcal{N} , the mutual information illustrated in Fig. 2.2.1 has the form

$$\bar{I}_{\text{diff}}(\mathcal{X}; \mathcal{Y}) = \bar{I}_{\text{diff}}(\mathcal{Y}) - \bar{I}_{\text{diff}}(\mathcal{Y} | \mathcal{X}) = \bar{I}_{\text{diff}}(\mathcal{Y}) - \bar{I}_{\text{diff}}(\mathcal{N}). \quad (2.2.23)$$

The maximization of (2.2.23) with respect to $p_{\mathcal{X}}(x)$ affects only the term $\bar{I}_{\text{diff}}(\mathcal{Y})$ because the background noise cannot be influenced. For statistically independent processes \mathcal{X} and \mathcal{N} , the corresponding powers can simply be added $\sigma_{\mathcal{Y}}^2 = \sigma_{\mathcal{X}}^2 + \sigma_{\mathcal{N}}^2$ and, hence, fixing the transmit power directly fixes $\sigma_{\mathcal{Y}}^2$. According to Section 2.1.3, the maximum mutual information for a fixed power is obtained for a Gaussian distributed process \mathcal{Y} . However, this can only be achieved for a Gaussian distribution of \mathcal{X} . Hence, we have to substitute (2.1.18b) into (2.2.23). Inserting the results of Section 1.2.2 ($\sigma_{\mathcal{X}}^2 = 2BE_s$ and $\sigma_{\mathcal{N}}^2 = 2BN_0$) we obtain the channel capacity

$$\begin{aligned} C^{2-\text{dim}} &= \log_2(\pi e \sigma_{\mathcal{Y}}^2) - \log_2(\pi e \sigma_{\mathcal{N}}^2) \\ &= \log_2 \left(\frac{\sigma_{\mathcal{X}}^2 + \sigma_{\mathcal{N}}^2}{\sigma_{\mathcal{N}}^2} \right) = \log_2 \left(1 + \frac{E_s}{N_0} \right). \end{aligned} \quad (2.2.24)$$

If only the real part of \mathcal{X} is used for data transmission, the bits transmitted per channel usage is halved. However, we have to take into account that only the real part of the noise disturbs the transmission so that the effective noise power is also halved ($\sigma_{\mathcal{N}'}^2 = \frac{1}{2}\sigma_{\mathcal{N}}^2 = BN_0$). If the transmit power remains unchanged ($\sigma_{\mathcal{X}'}^2 = \sigma_{\mathcal{X}}^2 = 2BE_s$), (2.2.24) becomes

$$C^{1-\text{dim}} = \frac{1}{2} \cdot \log_2(\pi e \sigma_{\mathcal{Y}'}^2) - \frac{1}{2} \cdot \log_2(\pi e \sigma_{\mathcal{N}'}^2) = \frac{1}{2} \cdot \log_2 \left(1 + 2 \frac{E_s}{N_0} \right). \quad (2.2.25)$$

In many cases, the evaluation of systems in terms of a required E_s/N_0 leads not to a fair comparison. This is especially the case when the number of channel symbols transmitted per information bit varies. Therefore, a better comparison is obtained

by evaluating systems with respect to the required energy E_b per information bit. For binary modulation schemes with $m = 1$, it is related to E_s by

$$k \cdot E_b = n \cdot E_s \implies E_s = \frac{k}{n} \cdot E_b = R_c \cdot E_b \quad (2.2.26)$$

because the FEC encoder does not add or remove any energy. Substituting E_s in (2.2.24) and (2.2.25) delivers

$$C^{2-\text{dim}} = \log_2 \left(1 + R_c \frac{E_b}{N_0} \right), \quad C^{1-\text{dim}} = \frac{1}{2} \cdot \log_2 \left(1 + 2R_c \frac{E_b}{N_0} \right).$$

Since the highest spectral efficiency is obtained for $R_c = C$, these equations only implicitly determine C . We can resolve them with respect to E_b/N_0 and obtain the common result

$$\frac{E_b}{N_0} = \frac{2^{2C} - 1}{2C}. \quad (2.2.27)$$

For $C \rightarrow 0$, the required E_b/N_0 does not tend to 0 but to a finite value

$$\lim_{C \rightarrow 0} \frac{E_b}{N_0} = \lim_{C \rightarrow 0} \frac{2^{2C} \cdot \ln 2 \cdot 2}{2} = \ln 2 \doteq -1.59 \text{ dB}. \quad (2.2.28)$$

Hence, no error-free transmission is possible below this ultimate bound. **Fig. 2.2.3** illustrates the channel capacity for the AWGN channel with Gaussian input. Obviously, real and complex-valued transmissions have the same capacity for $E_s/N_0 \rightarrow 0$ or, equivalently, $E_b/N_0 \rightarrow \ln 2$. For larger signal to noise ratios, the complex system has a higher capacity because it can transmit twice as many bits per channel use than the real-valued system. This advantage affects the capacity linearly while the drawback of a halved signal to noise ratio compared to the real-valued system has only a logarithmic influence. Asymptotically, doubling the signal to noise ratio (3 dB step) increases the capacity by 1 bit/s/Hz for the complex case.

AWGN Channel with Discrete Input

Unfortunately, no closed-form expressions exist for discrete input alphabets and (2.2.4) has to be evaluated numerically. Due to the reasons discussed on page 64 we assume a uniform distribution of \mathcal{X}

$$C = \log_2(|\mathcal{X}|) + \frac{1}{|\mathcal{X}|} \cdot \int_{\mathbb{Y}} \sum_{\mu} p_{\mathcal{Y}|X_{\mu}}(y) \cdot \log_2 \frac{p_{\mathcal{Y}|X_{\mu}}(y)}{\sum_l p_{\mathcal{Y}|X_l}(y)} dy. \quad (2.2.29)$$

An approximation of the cut-off rate was already presented in (2.2.13).

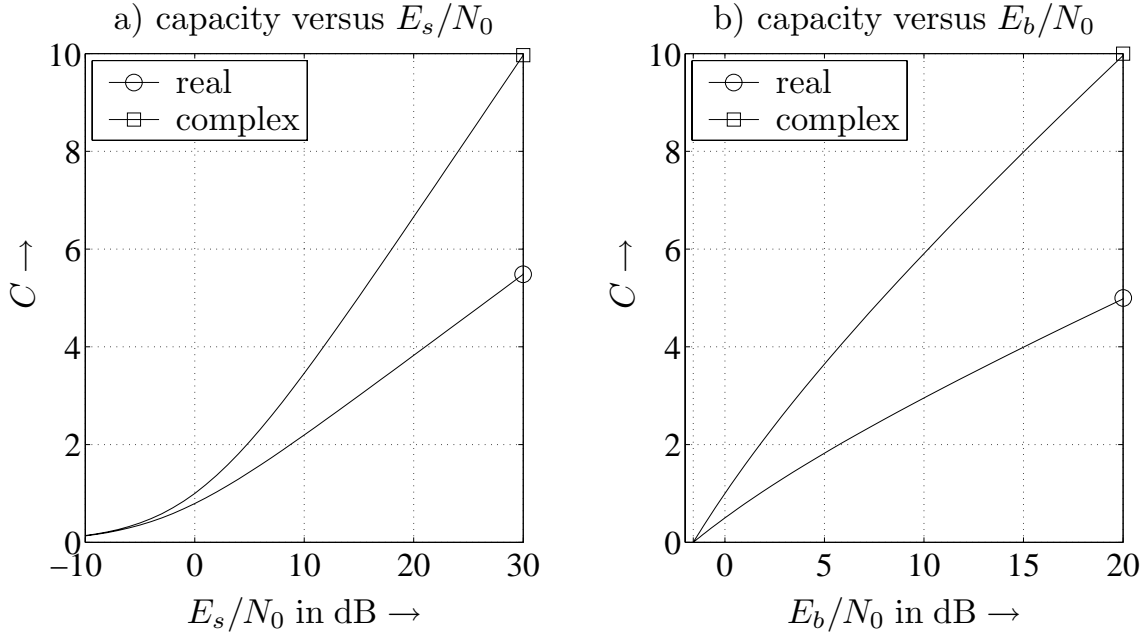


Figure 2.2.3: Channel capacities for AWGN channel with Gaussian distributed input

Fig. 2.2.4 shows the channel capacities for the AWGN channel and different PSK schemes. Obviously, for very low signal to noise ratios $E_s/N_0 \rightarrow 0$, no difference between discrete input alphabets and a continuously Gaussian distributed input can be observed. However, for higher SNR, the Gaussian input represents an upper bound that cannot be reached by discrete modulation schemes. Their maximum capacity is limited to the number of bits transmitted per symbol ($\log_2 |\mathcal{X}|$). Since BPSK consists of real symbols ± 1 , its capacity is upper bounded by that of a continuously Gaussian distributed real input and the highest spectral efficiency that can be obtained is 1 bit/s/Hz. The other schemes have to be compared to a complex Gaussian input. For very high signal to noise ratios, the uniform distribution is optimum again since the maximum capacity reaches exactly the number of bits per symbol.

Regarding ASK and QAM schemes, approximating a Gaussian distribution of the alphabet by *signal shaping* can improve the mutual information although it need not to be the optimum choice. The maximum gain is determined by the power ratio of uniform and Gaussian distribution if both have the same differential entropy. With (2.1.17) and (2.1.18a) for real-valued transmissions we obtain

$$\log_2(2a) = \frac{1}{2} \log_2(2\pi e \sigma_{\mathcal{X}}^2) \quad \Rightarrow \quad \sigma_{\mathcal{X}}^2 = \frac{2a^2}{\pi e}. \quad (2.2.30)$$

Since the average power for the uniform distributed signal is

$$\int_{-\infty}^{\infty} p_{\mathcal{X}}(x)x^2 dx = \int_{-a}^a \frac{x^2}{2a} dx = \left. \frac{x^3}{6a} \right|_{-a}^a = \frac{a^2}{3},$$

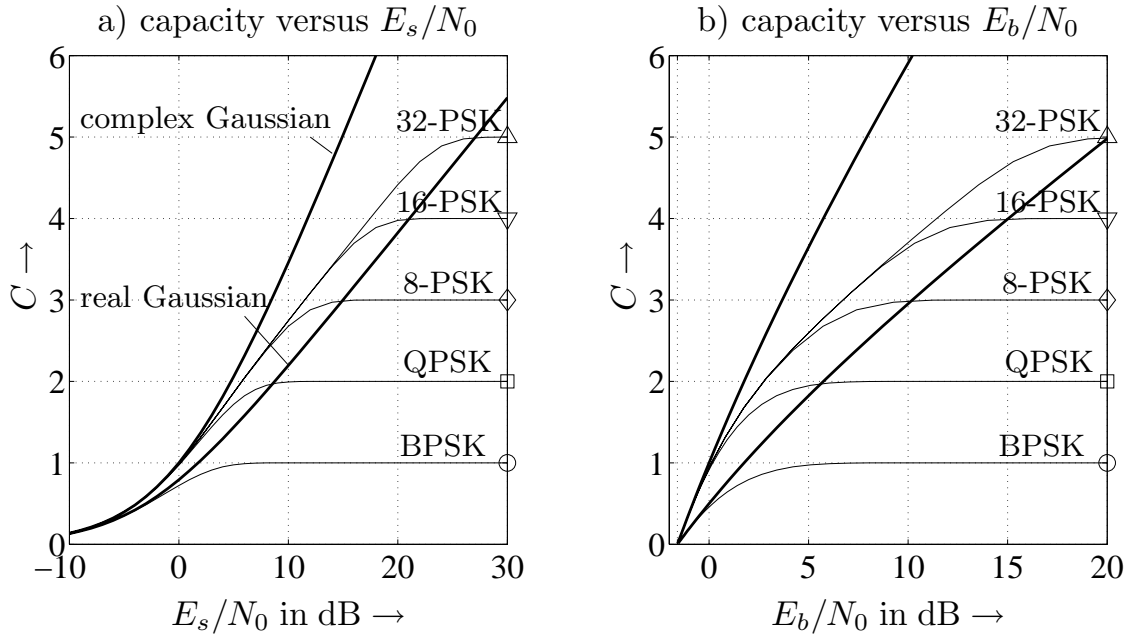


Figure 2.2.4: Capacity of AWGN channel for different PSK constellations

the power ratio between uniform and Gaussian distributions for identical entropies becomes with (2.2.30)

$$\frac{a^2/3}{\sigma_x^2} = \frac{a^2/3}{2a^2/(pe)} = \frac{\pi e}{6} \rightarrow 1.53 \text{ dB} . \quad (2.2.31)$$

Hence, we can save 1.53 dB transmit power when changing from a uniform to a Gaussian distribution without loss of entropy. The distribution of the discrete signal alphabet has the form [FWH98]

$$\Pr\{X_\mu\} = K(\lambda) \cdot e^{-\lambda|X_\mu|^2} \quad (2.2.32)$$

where $K(\lambda)$ must be chosen appropriately to fulfill the condition $\sum_\mu \Pr\{X_\mu\} = 1$. The parameter $\lambda \geq 0$ has to be optimized for each signal to noise ratio. For $\lambda = 0$, the uniform distribution with $K(0) = |\mathbb{X}|^{-1}$ is obtained. **Fig. 2.2.5** depicts the corresponding results. We observe that these small alphabet sizes with 16 and 64 symbols allow only little gains, e.g. 1 dB for 64-QAM. As mentioned before, for high signal to noise ratios, λ tends to zero resulting in a uniform distribution achieving the highest possible mutual information.

The last aspect in this subsection addresses the influence of quantization on the capacity. Quantizing the output of an AWGN channel leads to a model with discrete inputs and outputs that can be fully described by the conditional probabilities $\Pr\{Y_\nu | X_\mu\}$. They depend on the signal to noise ratio of the channel and certainly on the quantization thresholds. We will concentrate in the sequel on BPSK modulation. A hard decision at the output delivers the binary symmetric channel (BSC). Its capacity can be calculated by

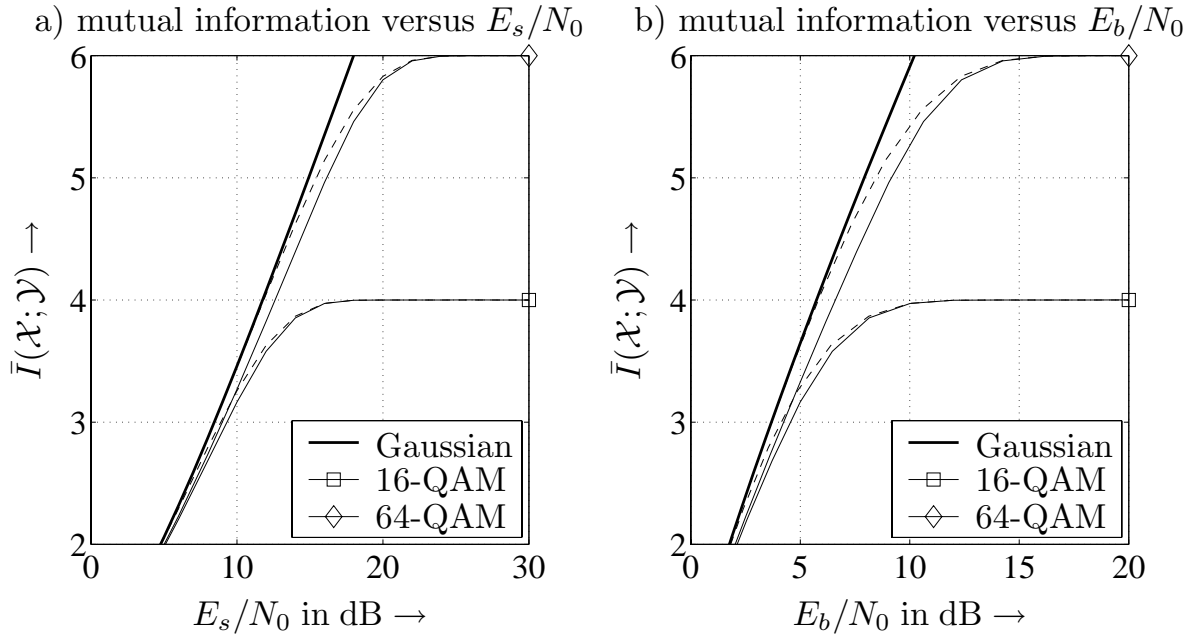


Figure 2.2.5: Capacity of AWGN channel for different QAM constellations (solid lines: uniform distribution, dashed lines: Gaussian distribution)

$$C = 1 + P_s \log_2(P_s) + (1 - P_s) \log_2(1 - P_s) = 1 - \bar{I}_2(P_s) \quad (2.2.33)$$

where $P_s = \frac{1}{2} \operatorname{erfc}(\sqrt{E_s/N_0})$ denotes the symbol error probability. Generally, we obtain 2^q output symbols Y_ν for a q -bit quantization. The quantization thresholds have to be chosen such that the probabilities $\Pr\{Y_\nu \mid X_\mu\}$ with $1 \leq \mu \leq |\mathbb{X}|$ and $1 \leq \nu \leq 2^q$ maximize the mutual information. **Fig. 2.2.6** shows the corresponding results. On the one hand, the loss due to a hard decision prior to decoding can be up to 2 dB, i.e. the minimum E_b/N_0 for which an error-free transmission is principally possible is approximately 0.4 dB. On the other hand, a 3-bit quantization loses only slightly compared to the continuous case. For high signal to noise ratios, the influence of quantization is rather small.

2.2.5 Capacity of Rayleigh Fading Channel

In Section 1.3.3 we discussed the error probability for frequency-nonselective fading channels and recognized that the error rate itself is a random variable depending on the instantaneous fading coefficient h . For the derivation of channel capacities we encounter the same situation. Again, we can distinguish between an ergodic capacity representing the average capacity among all channel states and an outage capacity C_{out} representing the capacity that cannot be reached with an outage probability P_{out} . For the sake of simplicity, we restrict the derivation on complex Gaussian distributed inputs because there exist no closed-form expressions for

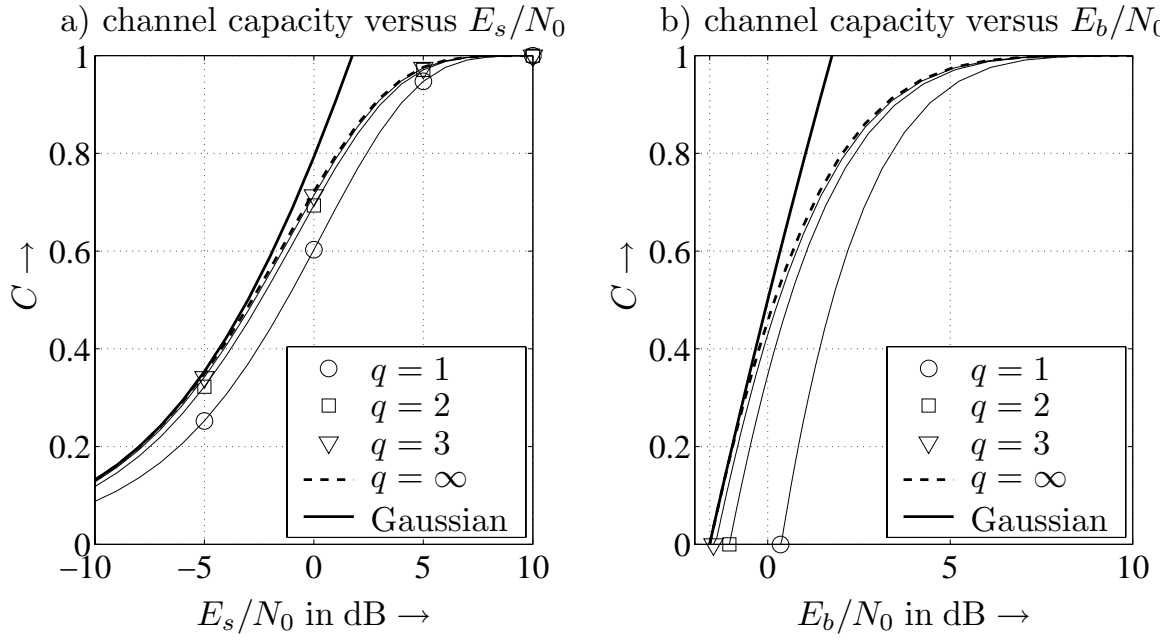


Figure 2.2.6: Capacity of AWGN channel for BPSK and different quantization levels

discrete signal alphabets. Starting with the result of the previous section we obtain the instantaneous capacity

$$C(h) = \log_2 \left(1 + |h|^2 \cdot \frac{E_s}{N_0} \right) \quad (2.2.34)$$

that depends on the actual channel coefficient h . Averaging (2.2.34) with respect to $p_{|\mathcal{H}|^2}(\xi)$ delivers the ergodic channel capacity

$$\bar{C} = \mathbb{E}_{\mathcal{H}}\{C(h)\} = \mathbb{E}_{\mathcal{H}} \left\{ \log_2 \left(1 + |h|^2 \cdot \frac{E_s}{N_0} \right) \right\}. \quad (2.2.35)$$

In order to compare the capacities of fading channels with that of the AWGN channel, we have to apply Jensen's inequality [CT91]. Since $C(h)$ is a concave function, it states

$$\mathbb{E}_{\mathcal{X}}\{f(x)\} \leq f(\mathbb{E}_{\mathcal{X}}\{x\}). \quad (2.2.36)$$

For convex functions, ' \leq ' has to be replaced by ' \geq '. Moving the expectation in (2.2.35) into the logarithm leads to

$$\bar{C} = \mathbb{E}_{\mathcal{H}} \left\{ \log_2 \left(1 + |h|^2 \cdot \frac{E_s}{N_0} \right) \right\} \leq \log_2 \left(1 + \mathbb{E}_{\mathcal{H}}\{|h|^2\} \cdot \frac{E_s}{N_0} \right). \quad (2.2.37)$$

From (2.2.37) we see immediately that the capacity of a fading channel with average power $\sigma_{\mathcal{H}}^2 = \mathbb{E}_{\mathcal{H}}\{|h|^2\} = 1$ is always smaller than that of an AWGN channel with same average signal to noise ratio.

Ergodic Capacity

We now want to calculate the ergodic capacity for concrete fading processes. If $|\mathcal{H}|$ is Rayleigh distributed, we know from Section 1.2 that $|h|^2$ is chi-squared distributed with two degrees of freedom. According to Section 1.3.3, we have to insert $p_{|\mathcal{H}|^2}(\xi) = 1/\sigma_{\mathcal{H}}^2 \cdot \exp(-\xi/\sigma_{\mathcal{H}}^2)$ into (2.2.35). Applying the partial integration technique and substituting $(\xi - N_0/E_s)/\sigma_{\mathcal{H}}^2$, we obtain

$$\begin{aligned}\bar{C} &= \int_0^\infty \log_2 \left(1 + \xi \frac{E_s}{N_0} \right) \cdot \frac{1}{\sigma_{\mathcal{H}}^2} \cdot e^{-\xi/\sigma_{\mathcal{H}}^2} d\xi \\ &= \log_2(e) \cdot \exp \left(\frac{1}{\sigma_{\mathcal{H}}^2 E_s / N_0} \right) \cdot \text{expint} \left(\frac{1}{\sigma_{\mathcal{H}}^2 E_s / N_0} \right)\end{aligned}\quad (2.2.38)$$

where $\text{expint}(x) = \int_x^\infty e^{-t}/t dt$ denotes the exponential integral function [Gra00]. **Fig. 2.2.7** shows a comparison between the capacities of AWGN and flat Rayleigh fading channels. For sufficiently large SNR, the curves are parallel and we can observe a loss due to fading of roughly 2.5 dB. Compared with the BER loss of approximately 17 dB in the uncoded case, this loss is rather small. It can be explained by the fact that the channel coding theorem presupposes infinite long codewords allowing the decoder to exploit a high diversity gain. This leads to a small loss in capacity compared to the AWGN channel. Astonishingly, the ultimate limit of -1.59 dB is the same for AWGN and Rayleigh fading channel.

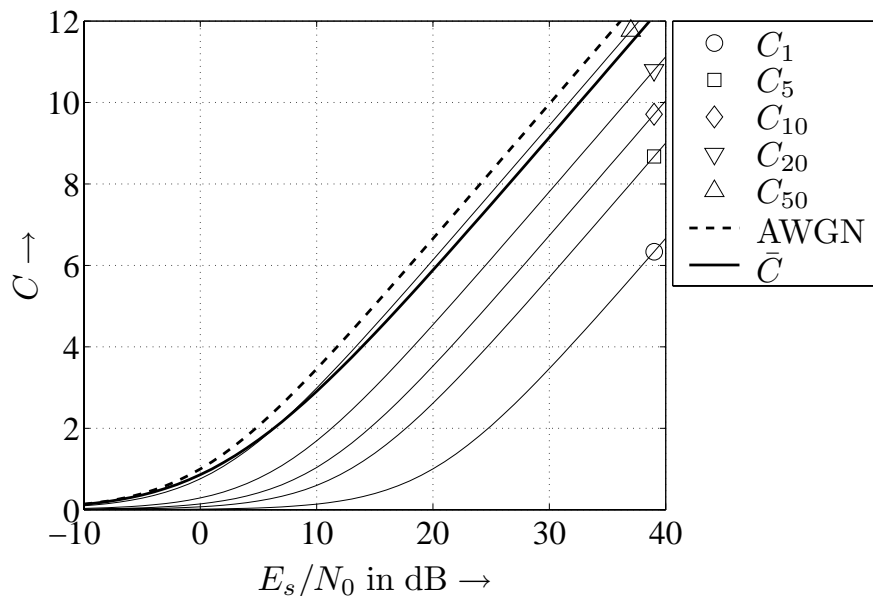


Figure 2.2.7: Ergodic and outage capacity of flat Rayleigh fading channels for Gaussian input versus E_b/N_0 (C_p denotes the outage capacity for $P_{\text{out}} = p$)

Outage Probability and Outage Capacity

With the same argumentation as in Section 1.3 we define now the outage capacity C_{out} with the corresponding outage probability P_{out} . The latter one describes the probability that the instantaneous capacity $C(h)$ falls below a threshold C_{out} .

$$P_{\text{out}} = \Pr\{C(h) < C_{\text{out}}\} = \Pr\left\{\log_2\left(1 + |h|^2 \cdot \frac{E_s}{N_0}\right) < C_{\text{out}}\right\} \quad (2.2.39)$$

Inserting the density $p_{|H|^2}(\xi)$ with $\sigma_H^2 = 1$ into (2.2.39) leads to

$$P_{\text{out}} = \Pr\left\{|h|^2 < \frac{2^{C_{\text{out}}} - 1}{E_s/N_0}\right\} = 1 - \exp\left(\frac{1 - 2^{C_{\text{out}}}}{E_s/N_0}\right). \quad (2.2.40)$$

Resolving the last equation with respect to C_{out} yields

$$C_{\text{out}} = \log_2\left(1 - E_s/N_0 \cdot \ln(1 - P_{\text{out}})\right). \quad (2.2.41)$$

Conventionally, C_{out} is written as C_p where $p = P_{\text{out}}$ determines the corresponding outage probability. **Fig. 2.2.7** shows the outage capacities for different values of P_{out} . For $P_{\text{out}} = 0.5$, the corresponding capacity C_{50} reached with a probability of only 50% is close to the ergodic capacity \bar{C} . For smaller P_{out} , i.e. the instantaneous capacity must be available to a higher percentage, C_{out} decreases dramatically. At a spectral efficiency of 6 bit/s/Hz, the loss in terms of E_b/N_0 amounts to nearly 8 dB for $P_{\text{out}} = 0.1$ and roughly 18 dB for $P_{\text{out}} = 0.01$.

Fig. 2.2.8 depicts the outage probability versus the outage capacity for different values E_s/N_0 . As expected for high signal to noise ratios, large capacities can be achieved with very low outage probability. However, P_{out} grows rapidly with decreasing E_s/N_0 . The asterisks denote the outage probability of the ergodic capacity C . As could already be observed in Fig. 2.2.7, it is close to 0.5.

2.2.6 Channel Capacity and Diversity

As explained in the last subsection, the instantaneous channel capacity is a random variable itself depending on the squared magnitude of the actual channel coefficient h . Since $|h|^2$ varies over a wide range, the capacity also has a large variance. Besides the ergodic capacity \bar{C} , the outage capacity C_{out} is an appropriate measure for the channel quality. From Section 1.5 we know that diversity reduces this variance and, therefore, also reduces the outage probability of the channel. Assuming that a signal x is transmitted over D statistically independent channels with coefficients h_ℓ , $1 \leq \ell \leq D$, the instantaneous capacity after maximum ratio combining becomes

$$C(h) = \log_2\left(1 + \sum_{\ell=1}^D |h_\ell|^2 \frac{E_s}{DN_0}\right) = \log_2\left(1 + |h|^2 \frac{E_s}{DN_0}\right). \quad (2.2.42)$$

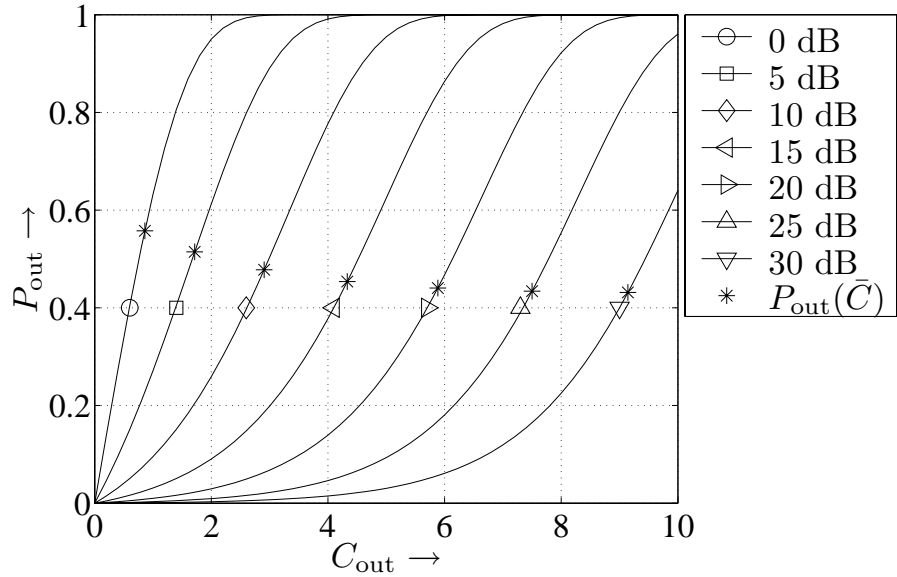


Figure 2.2.8: Outage probability of flat Rayleigh fading channels for Gaussian input

The only difference to (2.2.34) is that the signal to noise ratio is weighted with a new random variable $|h|^2$ which is chi-squared distributed with $2D$ degrees of freedom (instead of 2). The probability density $p_\gamma(\xi)$ of the variable $\gamma = \sum_{\ell=1}^D |h_\ell|^2 E_s / N_0 / D$ was already presented in (1.5.5) on page 43. The ergodic capacity is obtained by averaging $C(h)$ in (2.2.42) with respect to $p_\gamma(\xi)$. Solving numerically the integral

$$\bar{C} = \int_0^\infty \log_2 \left(1 + \xi \frac{E_s}{DN_0} \right) \cdot \frac{D^D \xi^{D-1}}{(D-1)! (E_s/N_0)^D} \cdot e^{-\frac{\xi D}{E_s/N_0}} d\xi \quad (2.2.43)$$

leads to the results shown in **Fig. 2.2.9**. We have assumed independent Rayleigh fading channels with uniform power distribution. As expected, the ergodic capacity grows with increasing D . While the largest gains are obtained for the transition from $D = 1$ to $D = 2$, a higher diversity degree only leads to minor improvements. Asymptotically, the capacity of the AWGN channel is reached for $D \rightarrow \infty$. Nearly no differences can be observed for $D = 50$.

Concerning the outage probability, (2.2.39) has to be calculated for $|h|^2 = \sum_{\ell=1}^D |h_\ell|^2$. Resolving (2.2.39) with respect to $|h|^2$ and inserting the chi-squared distribution with $2D$ degrees of freedom from (1.5.5) yields

$$P_{\text{out}} = \Pr \left\{ |h|^2 < \frac{2^{C_{\text{out}}} - 1}{E_s/N_0/D} \right\} = \frac{1}{(D-1)!} \cdot \int_0^{\frac{2^{C_{\text{out}}} - 1}{E_s/N_0/D}} \xi^{D-1} \cdot e^{-\xi} d\xi. \quad (2.2.44)$$

The integral in (2.2.44) is often referred to as incomplete Gamma function because the upper limit is finite. The obtained outage probabilities are illustrated in

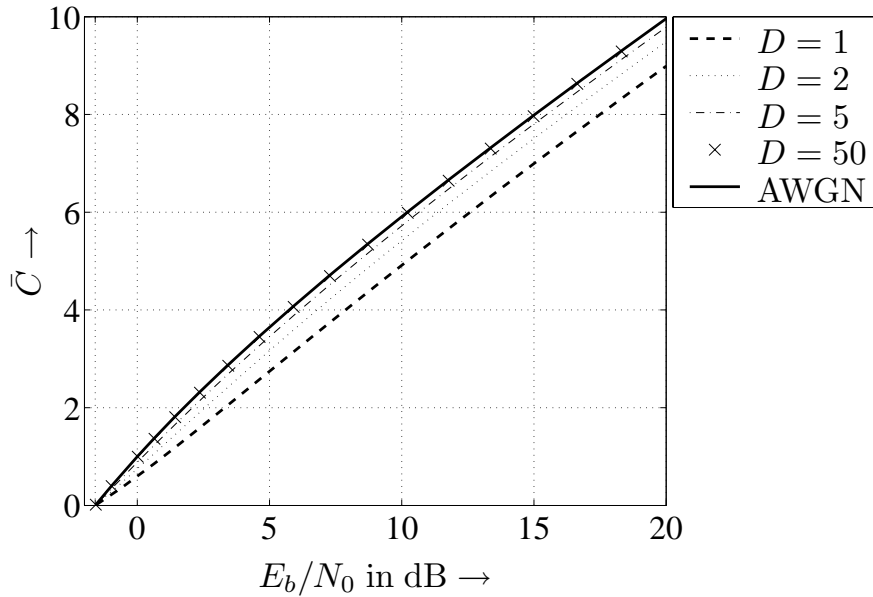


Figure 2.2.9: Ergodic capacity for Rayleigh fading channels with different diversity degree

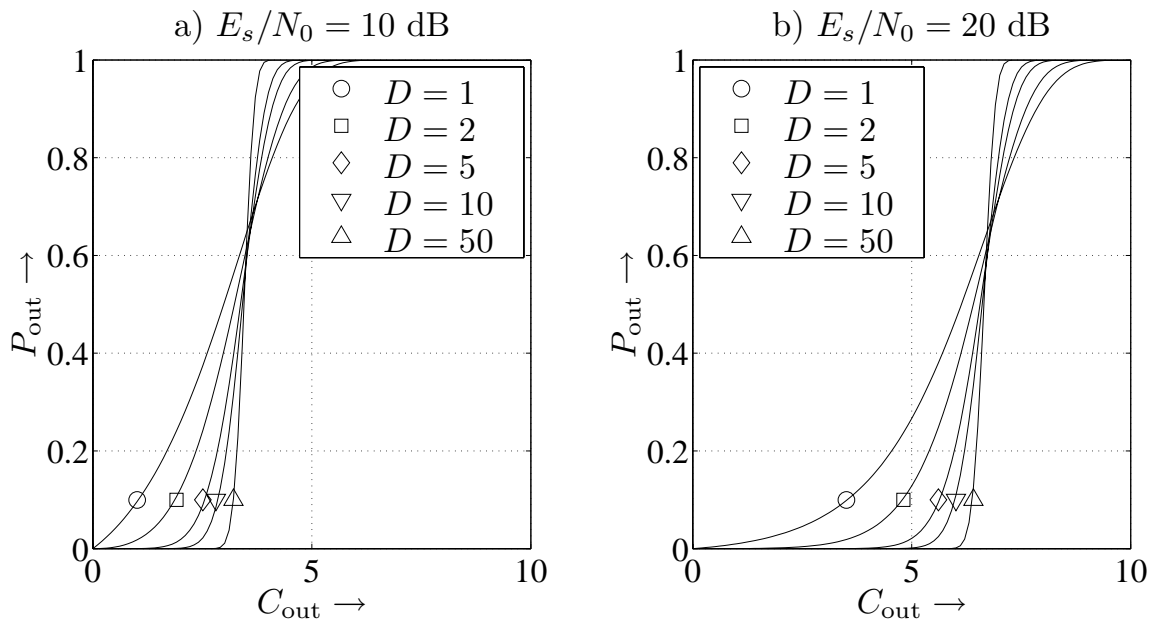


Figure 2.2.10: Outage probability of flat Rayleigh fading channels for Gaussian input

Fig. 2.2.10 versus the corresponding outage capacities. For low outage probabilities, e.g. $P_{\text{out}} = 0.1$, diversity increases the outage capacity, i.e. larger capacities can be guaranteed with a certain probability. The gains become bigger for high signal to noise ratios (compare $E_s/N_0 = 10$ dB and $E_s/N_0 = 20$ dB). However, for $P_{\text{out}} > 0.7$, the relations are reversed and large diversity degrees lead to higher outage probabilities. This behaviour is not astonishing because diversity reduces

the variations of the SNR, i.e. very low SNRs occur less frequently as well as very high SNRs. Therefore, very high capacities much above the ergodic capacity \bar{C} occur more seldom for large D resulting in high outage probabilities. Nevertheless, these cases are pathological because outage probabilities above 0.7 are generally not relevant in practical systems.

Finally, **Fig. 2.2.11** depicts C_{out} versus E_s/N_0 for different diversity degrees D and outage probabilities P_{out} . We see that diversity can dramatically increase the outage capacity especially for large E_s/N_0 . Moreover, the largest gains are obtained for transitions between small D and for low outage probabilities.

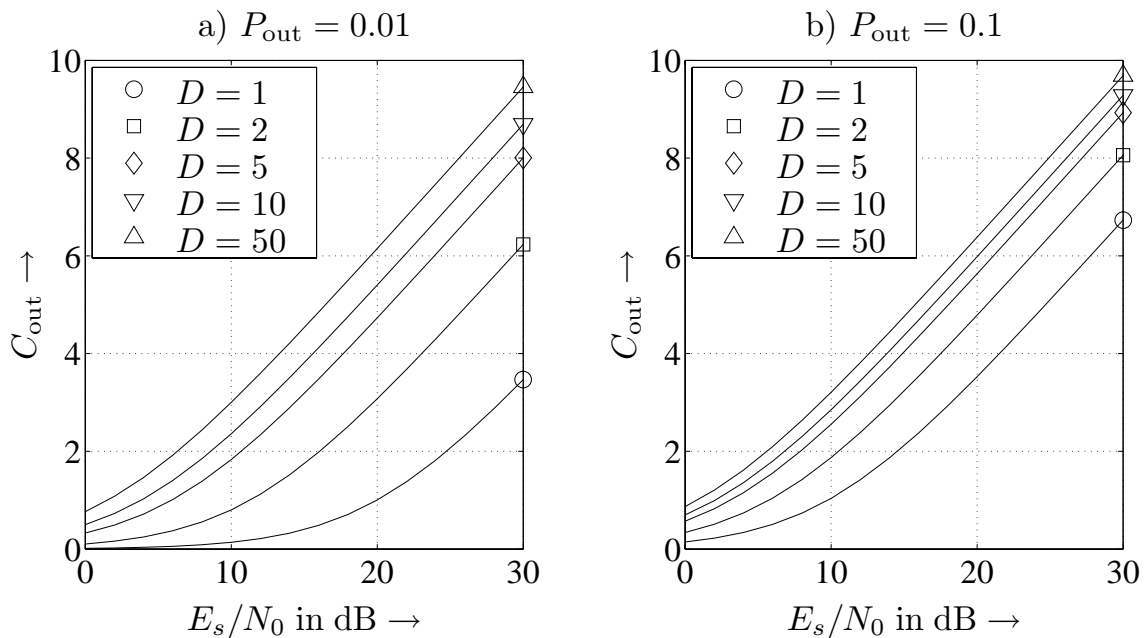


Figure 2.2.11: Outage probability of flat Rayleigh fading channels for Gaussian input

2.3 Channel Capacity of MIMO Systems

As already explained earlier, MIMO systems can be found in a wide range of applications. The specific scenario very much affects the structure and the statistical properties of the system matrix given in (1.2.31). In Section 1.2.4 some examples for the structure of this matrix were presented. Therefore, general statements concerning the ergodic or the outage capacity of arbitrary MIMO systems cannot be derived. In fact, only a common approach for calculating the instantaneous capacity, given a system matrix \mathbf{S} that is not further specified, will be explained here. This approach is later adapted to specific transmission scenarios like CDMA, SDMA or space-time coding.

In the sequel, we will restrict ourselves to frequency-nonselective fading channels. Since we focus on the instantaneous capacity $C(\mathbf{S})$ we can neglect the time index k . The general system model with N_I inputs and N_O outputs was already described in (1.2.31) as

$$\mathbf{y} = \mathbf{S} \cdot \mathbf{x} + \mathbf{n}. \quad (2.3.1)$$

The channel matrix \mathbf{H} is replaced by the $N_O \times N_I$ system matrix \mathbf{S} because it represents not only the channel but may also comprise other parts of the transmission system like spreading in CDMA systems. The coefficients $S_{\nu,\mu}$ of \mathbf{S} describe the transmission between the μ -th input and the ν -th output. For the sake of simplicity, Gaussian distributed input signals and perfect channel state information at the receiver are assumed. The assumption of a Gaussian input leads to an upper bound of the capacity for discrete input alphabets.

The only difference to SISO systems is that we have to deal with vectors instead of scalars. Adapting (2.2.23) to the MIMO case described in (2.3.1), we obtain

$$\bar{I}(\underline{\mathcal{X}}; \underline{\mathcal{Y}} | \mathbf{S}) = \bar{I}_{\text{diff}}(\underline{\mathcal{Y}} | \mathbf{S}) - \bar{I}_{\text{diff}}(\underline{\mathcal{N}}). \quad (2.3.2)$$

Using now vector notations and the definitions given in Sections 2.1.3 and 2.1.4, the instantaneous mutual information becomes

$$\bar{I}(\underline{\mathcal{X}}; \underline{\mathcal{Y}} | \mathbf{S}) = \log_2 \det(\pi e \Phi_{\underline{\mathcal{Y}} \underline{\mathcal{Y}}}) - \log_2 \det(\pi e \Phi_{\underline{\mathcal{N}} \underline{\mathcal{N}}}). \quad (2.3.3)$$

Next, we have to address the covariance matrices for the received signal \mathbf{y} and the noise \mathbf{n} . Taking into account (2.3.1) and assuming mutually independent noise contributions at the N_O outputs of the system, we obtain

$$\Phi_{\underline{\mathcal{Y}} \underline{\mathcal{Y}}} = E_{\underline{\mathcal{X}}, \underline{\mathcal{N}}} \{ (\mathbf{S}\mathbf{x} + \mathbf{n}) \cdot (\mathbf{S}\mathbf{x} + \mathbf{n})^H \} = \mathbf{S} \Phi_{\underline{\mathcal{X}} \underline{\mathcal{X}}} \mathbf{S}^H + \Phi_{\underline{\mathcal{N}} \underline{\mathcal{N}}} \quad (2.3.4a)$$

and

$$\Phi_{\underline{\mathcal{N}} \underline{\mathcal{N}}} = \sigma_{\mathcal{N}}^2 \cdot \mathbf{I}_{N_O}. \quad (2.3.4b)$$

The insertion of (2.3.4a) and (2.3.4b) into (2.3.3) yields

$$\bar{I}(\underline{\mathcal{X}}; \underline{\mathcal{Y}} | \mathbf{S}) = \log_2 \left(\frac{\det \Phi_{\underline{\mathcal{Y}} \underline{\mathcal{Y}}}}{\det \Phi_{\underline{\mathcal{N}} \underline{\mathcal{N}}}} \right) = \log_2 \det \left(\mathbf{I}_{N_O} + \frac{1}{\sigma_{\mathcal{N}}^2} \mathbf{S} \Phi_{\underline{\mathcal{X}} \underline{\mathcal{X}}} \mathbf{S}^H \right). \quad (2.3.5)$$

In order to reduce the vector notation to a set of independent scalar equations, we now apply the singular value decomposition (SVD) (see Appendix C.3 and [GvL93]) to the system matrix

$$\mathbf{S} = \mathbf{U}_S \cdot \boldsymbol{\Sigma}_S \cdot \mathbf{V}_S^H. \quad (2.3.6)$$

In (2.3.6), \mathbf{U}_S and \mathbf{V}_S are square unitary matrices (see Appendix C.3), i.e. the relations $\mathbf{U}_S \mathbf{U}_S^H = \mathbf{U}_S^H \mathbf{U}_S = \mathbf{I}_{N_O}$ and $\mathbf{V}_S \mathbf{V}_S^H = \mathbf{V}_S^H \mathbf{V}_S = \mathbf{I}_{N_I}$ hold. The diagonal matrix $\boldsymbol{\Sigma}_S$ contains the singular values σ_i of \mathbf{S} . For $N_I < N_O$, it has the form

$$\boldsymbol{\Sigma}_S = \begin{pmatrix} \sigma_1 & & 0 \\ & \ddots & \\ 0 & & \sigma_{N_I} \\ \mathbf{0} & \dots & \mathbf{0} \end{pmatrix} \quad \text{for } N_I < N_O , \quad (2.3.7a)$$

while

$$\boldsymbol{\Sigma}_S = \begin{pmatrix} \sigma_1 & 0 & \mathbf{0} \\ & \ddots & \mathbf{0} \\ 0 & \sigma_{N_O} & \mathbf{0} \end{pmatrix} \quad \text{for } N_I > N_O \quad (2.3.7b)$$

holds for $N_I > N_O$. The rank r of \mathbf{S} is limited to the minimum of N_I and N_O , i.e. $r \leq \min(N_I, N_O)$. The application of the SVD to (2.3.5) results in

$$\begin{aligned} \bar{I}(\underline{\mathcal{X}}; \underline{\mathcal{Y}} | \mathbf{S}) &= \log_2 \det \left(\mathbf{I}_{N_O} + \frac{1}{\sigma_{\mathcal{N}}^2} \mathbf{U}_S \boldsymbol{\Sigma}_S \mathbf{V}_S^H \boldsymbol{\Phi}_{\underline{\mathcal{X}} \underline{\mathcal{X}}} \mathbf{V}_S \boldsymbol{\Sigma}_S^H \mathbf{U}_S^H \right) \\ &= \log_2 \det \left(\mathbf{U}_S (\mathbf{I}_{N_O} + \frac{1}{\sigma_{\mathcal{N}}^2} \boldsymbol{\Sigma}_S \mathbf{V}_S^H \boldsymbol{\Phi}_{\underline{\mathcal{X}} \underline{\mathcal{X}}} \mathbf{V}_S \boldsymbol{\Sigma}_S^H) \mathbf{U}_S^H \right) \\ &= \log_2 \det \left(\mathbf{I}_{N_O} + \frac{1}{\sigma_{\mathcal{N}}^2} \boldsymbol{\Sigma}_S \mathbf{V}_S^H \boldsymbol{\Phi}_{\underline{\mathcal{X}} \underline{\mathcal{X}}} \mathbf{V}_S \boldsymbol{\Sigma}_S^H \right) \end{aligned} \quad (2.3.8)$$

The second equality holds because the determinant of a matrix does not change due to the multiplication with unitary matrices. We now have to distinguish two special cases concerning the kind of channel knowledge at the transmitters.

No Cooperation between MIMO Inputs

First, we assume that the different inputs of the MIMO system do not or cannot cooperate with each other. This might be the case in the uplink of a CDMA system where mobile subscribers can only communicate with a base station and not among themselves. Moreover, if no channel knowledge is available, it is impossible to adapt the signal vector \mathbf{x} onto the channel properties. In these cases, no optimization of $\boldsymbol{\Phi}_{\underline{\mathcal{X}} \underline{\mathcal{X}}}$ with respect to \mathbf{S} is possible and the best strategy is to transmit N_I independent data streams with equal power E_s/T_s . Hence, the covariance matrix of \mathbf{x} becomes $\boldsymbol{\Phi}_{\underline{\mathcal{X}} \underline{\mathcal{X}}} = E_s/T_s \cdot \mathbf{I}_{N_I}$ and the mutual information in (2.3.8) already represents the channel capacity ($\sigma_{\mathcal{N}}^2 = N_0/T_s$)

$$\begin{aligned} C(\mathbf{S}) &= \log_2 \det \left(\mathbf{I}_{N_O} + \frac{E_s}{N_0} \boldsymbol{\Sigma}_S \boldsymbol{\Sigma}_S^H \right) \\ &= \log_2 \left[\prod_{\nu=1}^r \left(1 + \lambda_{\nu} \frac{E_s}{N_0} \right) \right] = \sum_{\nu=1}^r \log_2 \left(1 + \lambda_{\nu} \frac{E_s}{N_0} \right) . \end{aligned} \quad (2.3.9)$$

The coefficients $\lambda_\nu = \sigma_\nu^2$ in (2.3.9) denote the squared nonzero singular values of \mathbf{S} or, equivalently, the eigenvalues of $\mathbf{S}^H \mathbf{S}$. The interpretation of (2.3.9) shows that we sum up the capacities of r independent sub-channels with different powers λ_ν . These sub-channels represent the eigenmodes of the channel described by \mathbf{S} . The ergodic capacity is obtained by calculating the expectation of (2.3.9) with respect to the λ_ν .

Cooperation among MIMO Inputs

If the transmitters are allowed to cooperate and if they have knowledge about the instantaneous system matrix \mathbf{S} , we can do better than simply transmitting independent data streams with equal power over the N_I inputs. According to (2.3.9), the eigenmodes of \mathbf{S} represent independent sub-systems that do not interact. Applying the eigenvalue decomposition to the covariance matrix of \mathbf{x} that still has to be determined yields

$$\Phi_{\underline{\mathcal{X}} \underline{\mathcal{X}}} = \mathbb{E}\{\mathbf{x}\mathbf{x}^H\} = \mathbf{V}_X \mathbf{P} \mathbf{V}_X^H \quad (2.3.10)$$

where $\mathbf{P} = \text{diag}(P_\nu)$ denotes a diagonal matrix with powers P_ν on the main diagonal. The maximum mutual information can be obtained by choosing $\mathbf{V}_X = \mathbf{V}_S$. Inserting (2.3.10) into (2.3.8) then leads to

$$\begin{aligned} \bar{I}(\underline{\mathcal{X}}; \underline{\mathcal{Y}} | \mathbf{S}) &= \log_2 \det \left(\mathbf{I}_{N_O} + \frac{1}{\sigma_N^2} \boldsymbol{\Sigma}_S \mathbf{V}_S^H \mathbf{V}_S \mathbf{P} \mathbf{V}_S^H \mathbf{V}_S \boldsymbol{\Sigma}_S^H \right) \\ &= \log_2 \det \left(\mathbf{I}_{N_O} + \frac{1}{\sigma_N^2} \boldsymbol{\Sigma}_S \mathbf{P} \boldsymbol{\Sigma}_S^H \right) = \sum_{\nu=1}^r \log_2 \left(1 + \lambda_\nu \frac{P_\nu}{\sigma_N^2} \right). \end{aligned} \quad (2.3.11)$$

Hence, we fully exploit the eigenmodes of the system \mathbf{S} with a transmit vector $\mathbf{x} = \mathbf{V}_S \tilde{\mathbf{x}}$ where $\tilde{\mathbf{x}}$ is isotropic, i.e. it has no preferred direction. The multiplication with the unitary matrix \mathbf{V}_S does not change its statistical properties but rotates the coordinate system. Particularly, it is important that the total power of $\underline{\mathcal{X}}$ does not change so that $\sigma_{\underline{\mathcal{X}}}^2 = \sigma_{\tilde{\mathcal{X}}}^2$ holds.

However, in order to maximize $\bar{I}(\underline{\mathcal{X}}; \underline{\mathcal{Y}} | \mathbf{S})$ we still have to find the optimal power levels P_ν for the data streams x_ν . Since only r nonzero singular values of \mathbf{S} exist, we would waste power by choosing $P_\nu > 0$ for $r < \nu \leq N_I$. Therefore, power is spent only for those sub-channels with $\sigma_\nu > 0$. For these r channels, we have to solve the following convex optimization problem

$$\max_{P_1 \dots P_r} \sum_{\nu=1}^r \log_2 \left(1 + \lambda_\nu \frac{P_\nu}{\sigma_N^2} \right) \quad \text{with} \quad P_\nu \geq 0 \quad \text{and} \quad \sum_{\nu=1}^r P_\nu = N_I \cdot \frac{E_s}{T_s}. \quad (2.3.12)$$

The first expression in (2.3.12) has to be maximized while the second and third

ones represent necessary conditions. By using the Lagrange function

$$L(P_1, \dots, P_r, \mu_1, \dots, \mu_r, \xi) = - \sum_{\nu=1}^r \log_2 \left(1 + \lambda_\nu \frac{P_\nu}{\sigma_N^2} \right) - \mu_\nu P_\nu + \xi \cdot P_\nu , \quad (2.3.13)$$

we obtain the necessary and sufficient Karush-Kuhn-Tucker conditions [CT91]

$$\text{a)} \quad \frac{\partial L}{\partial P_\nu} = 0 , \quad \text{b)} \quad \mu_\nu \geq 0 , \quad \text{c)} \quad \mu_\nu \cdot P_\nu = 0 \quad \text{for } 1 \leq \nu \leq r . \quad (2.3.14)$$

First, the partial derivation of L with respect to P_ν yields

$$\frac{\partial L}{\partial P_\nu} = - \frac{\log_2(e) \lambda_\nu / \sigma_N^2}{1 + \lambda_\nu P_\nu / \sigma_N^2} - \mu_\nu + \xi = 0 . \quad (2.3.15)$$

Resolving this with respect to μ_ν and exploiting condition b) in (2.3.14), we obtain

$$\mu_\nu = \xi - \frac{\log_2(e) \lambda_\nu / \sigma_N^2}{1 + \lambda_\nu P_\nu / \sigma_N^2} \geq 0 \iff P_\nu \geq \frac{\log_2(e)}{\xi} - \frac{\sigma_N^2}{\lambda_\nu} \quad (2.3.16)$$

Next, we have to apply the third Karush-Kuhn-Tucker condition often termed *complementary slackness*. It states that μ_ν has to be zero as long as the power $P_\nu > 0$ holds and that μ_ν can become arbitrary large for $P_\nu = 0$. Hence, inserting the left hand side of (2.3.16) into condition c) of (2.3.14), results in

$$P_\nu \cdot \left(\xi - \frac{\log_2(e) \lambda_\nu / \sigma_N^2}{1 + \lambda_\nu P_\nu / \sigma_N^2} \right) = 0 \iff P_\nu = 0 \vee P_\nu = \frac{\log_2(e)}{\xi} - \frac{\sigma_N^2}{\lambda_\nu} \quad (2.3.17)$$

We have to distinguish the two cases

$$\begin{aligned} \frac{\log_2(e)}{\xi} &> \frac{\sigma_N^2}{\lambda_\nu} &\implies P_\nu &= \frac{\log_2(e)}{\xi} - \frac{\sigma_N^2}{\lambda_\nu} > 0 \\ \frac{\log_2(e)}{\xi} &\leq \frac{\sigma_N^2}{\lambda_\nu} &\implies P_\nu &= 0 . \end{aligned}$$

Finally, the unknown variable ξ is chosen such that the total power constraint is fulfilled and

$$\sum_{\nu=1}^r P_\nu = \sum_{\nu=1}^r \left(\frac{\log_2(e)}{\xi} - \frac{\sigma_N^2}{\lambda_\nu} \right) = N_I \cdot \frac{E_s}{T_s} \quad (2.3.18)$$

must hold. The procedure is typically known as *waterfilling* and illustrated in **Fig. 2.3.1**. It can be interpreted as pouring water into a vessel with a bumpy ground. Naturally, the water surface is flat. Therefore, at those positions with a high ground level, the water column is rather small while it is high for deep ground levels. Moreover, it may happen for low water levels that the ground is not totally

covered leading to a zero water column. The heights of the water columns represent the different power levels, the heights of the vessel ground the inverse signal to noise ratios of the equivalent channels. Hence, the higher the normalized noise level $\sigma_{\mathcal{N}}^2/\lambda_{\nu}$, the less power is spent to channel ν . With other words, high power is assigned to good channels and only low power to bad channels. If a channel is too bad, it is not used at all ($P_{\nu} = 0$). The higher the total power E_s/T_s , the lower the probability of unused channels.

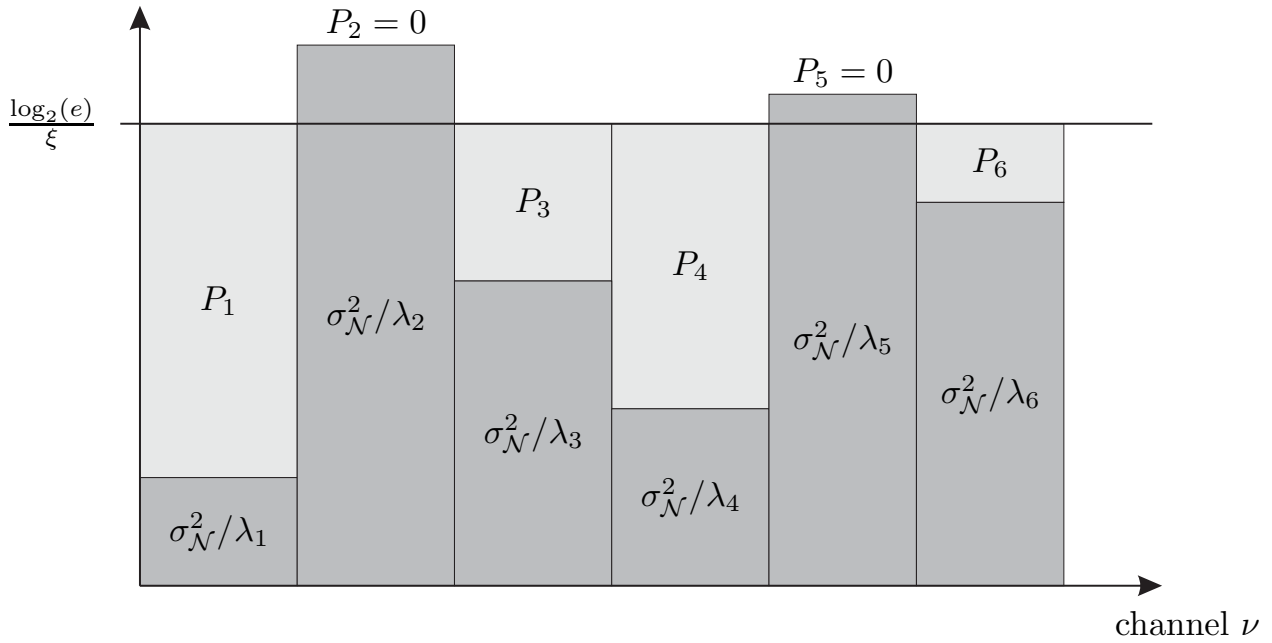


Figure 2.3.1: Principle of waterfilling

These conclusions hold only for Gaussian distributed input signals. For discrete input alphabets, different strategies have to be pursued concerning the power distribution. The reason is that only m bits can be transmitted per symbol for 2^m -ary modulation schemes. Once an error free uncoded transmission is reached on a certain layer, more transmit power does not increase the layer's spectral efficiency unless a different modulations scheme is chosen. The increase in spectral efficiency is quantized leading to different distributions as for the continuous Gaussian case.

Concluding, we can say that without channel knowledge at the transmitter, the best strategy is to transmit N_I independent data streams with equal power. However, if the transmitters have perfect channel state information and are allowed to cooperate, the covariance matrix $\Phi_{\mathcal{X}\mathcal{X}}$ has to be chosen such that the eigenmodes of the channel are exploited and the power levels of the resulting r independent channels have to be adjusted according to the waterfilling principle.

Assuming identical singular-values of the matrix \mathbf{S} , (2.3.9) tells us that the capacity $C(\mathbf{S})$ grows linearly with the rank r of \mathbf{S} . Hence, the capacity of full rank MIMO

systems can be linearly increased with $r = \min\{N_I, N_O\}$, e.g. by using more antennas at transmitter and receiver. Since $C(\mathbf{S})$ grows only logarithmically with the signal to noise ratio, the potential of MIMO systems is much larger.

Similar to scalar Rayleigh fading channels, ergodic and outage capacities can be determined for vector channels. Since we have not considered concrete MIMO systems, examples will be presented in Chapters 4 and 6 dealing with CDMA and multiple antenna systems.

Chapter 3

Forward Error Correction Coding

3.1 Introduction

Principally, we distinguish between three fundamental coding principles: source coding, channel or Forward Error Correction (FEC) coding and cryptography. The task of source coding is to compress the sampled and quantized signal such that a minimum number of bits is needed for representing the originally analog signal in digital form. Codes for cryptography try to cipher a signal so that it can only be interpreted by the desired user and not by third parties.

Contrarily, channel coding pursues a totally different intention. The signal should be protected against transmission errors. This is accomplished by adding redundancy to the information allowing the receiver to detect or even correct transmission errors. Thereby, channel coding works contrarily to source coding which aims to represent a message with as few bits as possible.

Forward Error Correction coding plays an important role in many digital systems, especially in today's mobile communication systems which were not realizable without coding. Indeed, FEC codes are applied in standards like GSM (*Global System for Mobile Communications*) [MP92], UMTS (*Universal Mobile Telecommunication System*) [OP98b, SH99, HT02, LWN02] and Hiperlan/2 or IEEE802.11. Thereby, channel coding is not restricted to communications but can also be found in storage applications. In this area, compact disks, digital versatile disks, DAT tapes and hard disks in personal computers use FEC strategies.

Since the majority of digital communication systems transmit binary data out of the finite field $\text{GF}(2) = \{0, 1\}$ [PW72, Bla83, LC04], we only consider binary codes throughout this work. Moreover, we restrict the derivations in this chapter to a block-wise BPSK transmission over frequency-nonselective channels with perfect channel state information at the receiver. Based on these assumptions and the principle system structure illustrated in Fig. 1.1.6, we obtain the model in **Fig. 3.1.1**. First, the encoder collects k information bits out of the data stream $d[i]$ and build a vector \mathbf{d} . Second, it maps this vector onto a new vector \mathbf{b} of length $n > k$. The resulting data stream $b[\ell]$ is interleaved, BPSK modulated and transmitted over the channel. The frequency nonselective channel consists of a single coefficient $h[\ell]$ per time instance and the additive white Gaussian noise component $n[\ell]$.

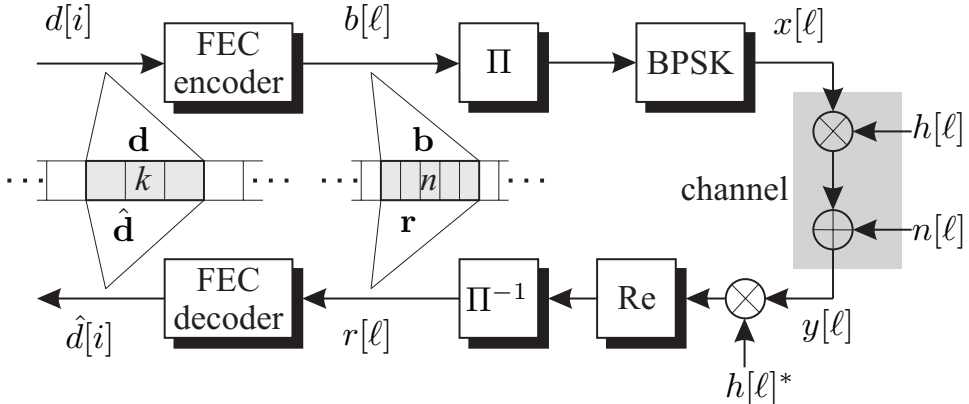


Figure 3.1.1: Structure of coded communication system

According to Section 1.3.1, the optimum ML sequence detector determines that code sequence $\hat{\mathbf{b}}$ with the largest conditional probability density $p_{\underline{\mathcal{Y}}|\hat{\mathbf{b}}}(\mathbf{y})$. Equivalently, we can also estimate the sequence \mathbf{x} because BPSK simply maps a bit in \mathbf{b} onto a binary symbol in \mathbf{x} .¹ Since the logarithm is a strictly monotone function, we obtain

$$\hat{\mathbf{x}} = \underset{\tilde{\mathbf{x}}}{\operatorname{argmax}} p_{\underline{\mathcal{Y}}|\tilde{\mathbf{x}}}(\mathbf{y}) = \underset{\tilde{\mathbf{x}}}{\operatorname{argmax}} \ln p_{\underline{\mathcal{Y}}|\tilde{\mathbf{x}}}(\mathbf{y}) . \quad (3.1.1)$$

For frequency-nonselective fading channels with $y[\ell] = h[\ell] \cdot x[\ell] + n[\ell]$, the conditional densities $p_{\underline{\mathcal{Y}}|\tilde{\mathbf{x}}}(\mathbf{y})$ can be factorized

$$p_{\underline{\mathcal{Y}}|\tilde{\mathbf{x}}}(\mathbf{y}) = \prod_{\ell} p_{\mathcal{Y}|\tilde{x}[\ell]}(y[\ell]) \quad \text{with} \quad p_{\mathcal{Y}|\tilde{x}[\ell]}(y[\ell]) = \frac{1}{\pi \sigma_{\mathcal{N}}^2} \cdot \exp \left(-\frac{|y[\ell] - h[\ell]\tilde{x}[\ell]|^2}{\sigma_{\mathcal{N}}^2} \right)$$

where $\sigma_{\mathcal{N}}^2$ denotes the power of the complex noise. Inserting the conditional probability density into (3.1.1) leads to

¹In the sequel, the influence of the interleaver is neglected.

$$\begin{aligned}\hat{\mathbf{x}} &= \operatorname{argmin}_{\tilde{\mathbf{x}}} \sum_{\ell} |y[\ell] - h[\ell] \cdot \tilde{x}[\ell]|^2 = \operatorname{argmax}_{\tilde{\mathbf{x}}} \sum_{\ell} \tilde{x}[\ell] \cdot \operatorname{Re} \{h^*[\ell] \cdot y[\ell]\} \\ &= \operatorname{argmax}_{\tilde{\mathbf{x}}} \sum_{\ell} \tilde{x}[\ell] \cdot r[\ell].\end{aligned}\tag{3.1.2}$$

Therefore, the optimum receiver can be split into two parts. First, the matched filter weights the received symbols $y[\ell]$ with the corresponding conjugate complex channel coefficients $h^*[\ell]$ and – for BPSK – extracts the real parts. On the one hand, this corrects the phase shifts induced by the channel. On the other hand, the attenuation of the magnitudes of $y[\ell]$ ensures an optimal combining in the subsequent decoding process that determines the codeword $\hat{\mathbf{x}}$ with the maximum correlation to the obtained sequence \mathbf{r} . Hence, it performs a kind of maximum ratio combining like the diversity reception in Section 1.5.1 so that decoding can exploit time-diversity in time-selective environments.

As mentioned above, encoding simply means mapping a vector of k binary symbols onto another vector consisting of n symbols. Due to this assignment which must be bijective, only 2^k vectors out of 2^n possible vectors are used as codewords. In other words, the encoder selects a k -dimensional subspace out of an n -dimensional vector space. A proper choice allows the detection and even the correction of transmission errors. The ratio

$$R_c = \frac{k}{n},\tag{3.1.3}$$

is called code rate and describes the relative amount of information in a codeword. Consequently, the absolute redundancy is $n - k$, the relative redundancy $(n - k)/n = 1 - R_c$.

We strictly distinguish between the *code* Γ representing the set of codewords (k -dimensional subspace) and the *encoder* [Bos99]. The latter one just performs the mapping between \mathbf{d} and \mathbf{b} . Systematic encoding means that the information bits in \mathbf{d} are explicitly contained in \mathbf{b} , e.g. the encoder appends some additional bits to \mathbf{d} . If information bits and redundant bits cannot be distinguished in \mathbf{b} , the encoding is called nonsystematic.

Optimizing a code means to arrange a set of codewords in the n -dimensional space such that certain properties are optimal. There exist different criteria for improving the performance of the entire coding scheme. Generally, the pair-wise Hamming distances between codewords are maximized and the corresponding number of pairs with a certain distance is minimized [Fri96, JZ98, Bos99, LC04]. A different approach focusses on the mutual information between encoder input and decoder output being the basis of information theory. Especially for concatenated codes, this approach seems to be well suited for predicting the performance of codes accurately [tB00a, tB00b, tB01c, HHFJ02]. However, the optimization of codes is highly nontrivial and still an unsolved problem in the general case.

Similar to Section 1.3.2 where the squared Euclidean distance between symbols determined the error rate performance, there exist an equivalent measure for codes. The Hamming distance $d_H(\mathbf{a}, \mathbf{b})$ denotes the number of differing symbols between the codewords \mathbf{a} and \mathbf{b} . For binary codes, Hamming distance and Euclidean distance are equivalent measures. The minimum distance d_{\min} of a code, i.e. the minimum Hamming distance that can occur between any pair of codewords, determines number of correctable and detectable errors. An (n, k, d_{\min}) code² can certainly correct

$$t = \left\lfloor \frac{d_{\min} - 1}{2} \right\rfloor \quad (3.1.4a)$$

errors and detect

$$t' = d_{\min} - 1 \quad (3.1.4b)$$

errors. In (3.1.4a), $\lfloor x \rfloor$ denotes the largest integer smaller than x . Sometimes a code may correct or detect even more errors, but this cannot be ensured. Concerning convolutional codes, the minimum Hamming distance is called free distance d_f . In Subsection 3.5.3, the distance properties of codes are discussed in more detail.

Since channel coding is only one topic among many others in this thesis, it restricts to explain the basic principles of encoding and decoding and to present some basic codes. Further information can be found in [CC81, Bla83, JZ98, Bos99, LC04]. The next two sections describe some basics of linear block codes and convolutional codes. Afterwards, soft-output decoding algorithms are derived being a substantial part of turbo decoding structures. Next, Section 3.5 analyzes the error rate performance of codes before the last section explains fundamentals of concatenated codes and 'turbo' decoding that became a world-wide research topic in 1993.

3.2 Linear Block Codes

3.2.1 Description by Matrices

Linear block codes represent a huge family of practically important codes. This section describes some basic properties of block codes and considers selected examples. As already mentioned, we restrict on binary codes whose symbols are elements of $GF(2)$. Consequently, the rules of finite algebra have to be applied. Concerning the definitions of finite groups, fields, and vector spaces, we refer to [Bos99]. All additions and multiplications have to be performed modulo 2 which is denoted by \oplus and \otimes , respectively. In contrast to hard decision decoding that generally exploits the algebraic structure of a code, there exist also soft-in soft-out

²This is a commonly used notation for a code of length n with k information bits and a minimum Hamming distance d_{\min} .

decoders that are of special interest in concatenated schemes and will be derived in Section 4.4.

Generator Matrix

A (n, k) linear block code can be completely described by a generator matrix \mathbf{G} consisting of k rows and n columns. Each information word is represented by a row vector $\underline{\mathbf{d}} = [d_1, \dots, d_k]$ of length k and assigned to a codeword $\underline{\mathbf{b}} = [b_1, \dots, b_n]$ of length n by³

$$\underline{\mathbf{b}} = \underline{\mathbf{d}} \otimes \mathbf{G} \quad \text{with} \quad \mathbf{G} = \begin{bmatrix} G_{1,1} & \dots & G_{1,n} \\ \vdots & & \vdots \\ G_{k,1} & \dots & G_{k,n} \end{bmatrix}. \quad (3.2.1)$$

The code Γ represents the set of all 2^k codewords and is defined to

$$\Gamma = \{\underline{\mathbf{d}} \otimes \mathbf{G} \mid \underline{\mathbf{d}} \in \text{GF}(2)^k\} \quad (3.2.2)$$

where $\text{GF}(2)^k$ denotes the k -dimensional vector space where each dimension can take values out of $\text{GF}(2)$. The codeword $\underline{\mathbf{b}}$ can be interpreted as linear combination of the rows of \mathbf{G} where the symbols in $\underline{\mathbf{d}}$ are the coefficients of this combination. Due to the assumed linearity and the completeness of the code space, all rows of \mathbf{G} represent valid codewords. Therefore, they span the code space, i.e. they form its basis.

Elementary Matrix Operations

Resorting the columns of \mathbf{G} leads to a different succession of the symbols in a codeword. Codes that emanate from each other by resorting their symbols are called *equivalent codes*. Although the mapping $\underline{\mathbf{d}} \rightarrow \underline{\mathbf{b}}$ is different for equivalent codes, their distance properties (see also Section 3.5.3) are still the same. However, the capability of detecting or correcting burst errors can be destroyed.

Concerning the rows of \mathbf{G} , the following operations are allowed without changing the code.

1. Resorting of rows
2. Multiplication of a row with a scalar according to the finite algebra rules
3. Linear combination of rows

³In many text books, row vectors are commonly used to describe information and codewords. Unless otherwise stated, we define vectors as column vectors. In order to avoid confusion and to keep conformity to literature, we underline row vectors $\underline{\mathbf{d}}$ and denote column vectors by \mathbf{d} .

By applying the above listed operations, each generator matrix can be put into the Gaussian normal form

$$\mathbf{G} = [\mathbf{I}_k \mid \mathbf{P}] . \quad (3.2.3)$$

In (3.2.3), \mathbf{I}_k represents the $k \times k$ identity matrix and \mathbf{P} a parity matrix with k rows and $n - k$ columns. Generator matrices of this form describe systematic encoders because the multiplication of $\underline{\mathbf{d}}$ with the left part of \mathbf{G} results in $\underline{\mathbf{d}}$ again. The rest of the codeword represents redundancy and is generated by linear combining subsets of bits in $\underline{\mathbf{d}}$.

Parity Check Matrix

Equivalently to the generator matrix, the $(n - k) \times n$ parity check matrix \mathbf{H} can be used to describe an encoder. Assuming a structure of \mathbf{G} as given in (3.2.3), it has the form

$$\mathbf{H} = [-\mathbf{P}^T \mid \mathbf{I}_{n-k}] . \quad (3.2.4)$$

The minus sign in (3.2.4) can be neglected for binary codes. Obviously, the relation

$$\mathbf{G} \otimes \mathbf{H}^T = [\mathbf{I}_k \quad \mathbf{P}] \otimes \begin{bmatrix} -\mathbf{P} \\ \mathbf{I}_{n-k} \end{bmatrix} = [-\mathbf{P} \oplus \mathbf{P}] = \mathbf{0} . \quad (3.2.5)$$

always holds regardless whether \mathbf{G} and \mathbf{H} have the Gaussian normal form or not. Since the rows of \mathbf{G} form the basis of the code space,

$$\underline{\mathbf{b}} \otimes \mathbf{H}^T = \mathbf{0}, \quad (3.2.6)$$

is valid for all $\underline{\mathbf{b}} \in \Gamma$, i.e. the rows in \mathbf{H} are orthogonal to all codewords in Γ . Hence, the code Γ represents the null space concerning \mathbf{H} and can be expressed by

$$\Gamma = \{ \underline{\mathbf{b}} \in \text{GF}(2)^n \mid \underline{\mathbf{b}} \otimes \mathbf{H}^T = \mathbf{0} \} . \quad (3.2.7)$$

Dual Code

Based on the above properties, the usage \mathbf{H} instead of \mathbf{G} for encoding leads to a code Γ^\perp whose elements are orthogonal to Γ . It is called *dual code* and defined by

$$\Gamma^\perp = \left\{ \tilde{\underline{\mathbf{b}}} \in \text{GF}(2)^n \mid \tilde{\underline{\mathbf{b}}}^T \otimes \underline{\mathbf{b}} = 0 \quad \forall \quad \underline{\mathbf{b}} \in \Gamma \right\} . \quad (3.2.8)$$

The codewords of Γ^\perp are obtained by $\tilde{\underline{\mathbf{b}}} = \underline{\mathbf{d}} \otimes \mathbf{H}$ with $\underline{\mathbf{d}} \in \text{GF}(2)^{n-k}$. Due to the dimension of \mathbf{H} , the dual code has the same length as Γ but consist of 2^{n-k} elements. This fact can be exploited for decoding. If $n - k \ll k$ holds, it may be advantageous to perform the decoding via the dual code and not with the original one [Off96].

Syndrome Decoding

The parity check matrix can be used to detect and correct transmission errors. We assume that the symbols of the received codeword $\underline{\mathbf{r}} = \underline{\mathbf{b}} \oplus \underline{\mathbf{e}}$ have been already hard decided, and $\underline{\mathbf{e}}$ denote the error pattern with nonzero elements at erroneous positions. The syndrome is defined by

$$\underline{\mathbf{s}} = \underline{\mathbf{r}} \otimes \mathbf{H}^T = (\underline{\mathbf{b}} \oplus \underline{\mathbf{e}}) \otimes \mathbf{H}^T = \underline{\mathbf{b}} \otimes \mathbf{H}^T \oplus \underline{\mathbf{e}} \otimes \mathbf{H}^T = \underline{\mathbf{e}} \otimes \mathbf{H}^T \quad (3.2.9)$$

and represents a vector consisting of $n - k$ elements. We see from (3.2.9) that it is independent of the transmitted codeword and depends only on the error pattern. For $\underline{\mathbf{s}} = \mathbf{0}_{1 \times n-k}$, the transmission was error-free or the error pattern was a valid codeword ($\underline{\mathbf{e}} \in \Gamma$). In the latter case, the error is not detectable and the decoder fails.

If a binary (n, k, d_{\min}) code should be able to correct t errors, each possible error pattern has to be uniquely assigned to a syndrome. Hence, the following *Hamming bound* or *sphere packing bound* is obtained:

$$2^{n-k} \geq \sum_{r=0}^t \binom{n}{r}. \quad (3.2.10)$$

Equality holds for *perfect codes* which have exactly as much redundancy as necessary for correcting all error patterns with $w_H(\underline{\mathbf{e}}) \leq t$. This corresponds to the densest possible packing of codewords in the n -dimensional space. Only very few perfect codes are known today. One example are Hamming codes described subsequently.

Since the code consists of 2^k out of 2^n possible elements of the n -dimensional vector space, there exist much more error patterns ($2^n - 2^k$) than syndromes. Therefore, decoding principles like standard array decoding or syndrome decoding [Bos99, LC04] group error vectors $\underline{\mathbf{e}}$ leading to the same syndrome $\underline{\mathbf{s}}_\mu$ into a coset

$$\mathbb{M}_\mu = \{\underline{\mathbf{e}} \in \text{GF}(2)^n \mid \underline{\mathbf{e}} \otimes \mathbf{H}^T = \underline{\mathbf{s}}_\mu\}. \quad (3.2.11)$$

For each coset \mathbb{M}_μ with $\mu = 0, \dots, 2^{n-k} - 1$, a coset leader $\underline{\mathbf{e}}_\mu$ is determined which generally has the minimum Hamming weight among all elements of \mathbb{M}_μ . Syndromes and coset leaders are stored in a lookup table. After the syndrome $\underline{\mathbf{s}}$ has been calculated, the table is scanned for the corresponding coset leader. Finally, the error correction is performed by subtracting the coset leader from the received codeword

$$\hat{\underline{\mathbf{b}}} = \underline{\mathbf{r}} \oplus \underline{\mathbf{e}}_\mu. \quad (3.2.12)$$

This decoding scheme represents the optimum maximum likelihood hard-decision decoding. Unlike the direct approach of (3.1.2) which compares all possible codewords with the received vector, the exponential dependency between decoding

complexity and the cardinality of the code is broken by exploiting the algebraic code structure. More sophisticated decoding principles like soft-in soft-out decoding are presented in Section 3.4.

3.2.2 Simple Parity Check and Repetition Codes

The simplest form of encoding is to repeat each information bit $n - 1$ times. Hence, an $(n, 1, n)$ Repetition Code (RP) with code rate $R_c = 1/n$ is obtained which consists of only 2 codewords, the all-zero and the all-one word.

$$\Gamma = \left\{ \underbrace{[0 \cdots 0]}_n, \underbrace{[1 \cdots 1]}_n \right\}$$

Since the two codewords differ in all n bits, the minimum distance amounts to $d_{\min} = n$. The generator and parity check matrices have the form

$$\mathbf{G} = [1 \mid 1 \cdots 1] \quad \mathbf{H} = \left[\begin{array}{c|ccc} 1 & 1 & & \\ \vdots & & \ddots & \\ 1 & & & 1 \end{array} \right]. \quad (3.2.13)$$

As the information bit d is simply repeated, the multiplication of $\underline{\mathbf{b}}$ with \mathbf{H}^T results in the modulo-2-addition of d with each of its replicas which yields of cause the all-zero vector.

The corresponding dual code is the $(n, n - 1, 2)$ Single Parity Check (SPC) code. The generator matrix equals \mathbf{H} in (3.2.13) except that the order of identity and parity part has to be reversed. We recognize that the encoding is systematic and the column consisting only of ones delivers the sum over all $n - 1$ information bits. Hence, the encoder appends a single parity bit so that all codewords have an even Hamming weight. Obviously, the minimum distance is $d_{\min} = 2$ and the code rate $R_c = (n - 1)/n$.

3.2.3 Hamming and Simplex Codes

Hamming codes are probably the most famous codes that can correct single errors ($t = 1$) and detect double errors ($t' = 2$). They have always a minimum distance of $d_{\min} = 3$ whereby the code rate tends to unity for $n \rightarrow \infty$.

Definition:

A binary $(n, k, 3)$ Hamming code of order r has the block length $n = 2^r - 1$ and encodes $k = n - r = 2^r - r - 1$ information bits. The columns of \mathbf{H} represent all binary numbers of length r between 1 and $2^r - 1$.

Hamming codes are *perfect codes*, i.e. the number of syndromes equals exactly the number of correctable error patterns. For $r = 2, 3, 4, 5, 6, 7, \dots$, there exist the following binary (n, k) Hamming codes: $(3,1)$, $(7,4)$, $(15,11)$, $(31,26)$, $(63,57)$, $(127,120)$ etc. As an example, generator and parity check matrices of the $(7, 4)$ Hamming code are given in systematic form.

$$\mathbf{G} = \left[\begin{array}{cccc|ccc} 1 & 0 & 0 & 0 & 0 & 1 & 1 \\ 0 & 1 & 0 & 0 & 1 & 0 & 1 \\ 0 & 0 & 1 & 0 & 1 & 1 & 0 \\ 0 & 0 & 0 & 1 & 1 & 1 & 1 \end{array} \right]; \quad \mathbf{H} = \left[\begin{array}{cccc|ccc} 0 & 1 & 1 & 1 & 1 & 0 & 0 \\ 1 & 0 & 1 & 1 & 0 & 1 & 0 \\ 1 & 1 & 0 & 1 & 0 & 0 & 1 \end{array} \right] \quad (3.2.14)$$

The dual code obtained by using \mathbf{H} as the generator matrix is called *Simplex code*. It consists of $2^{n-k} = 2^r$ codewords and has the property that all rows of \mathbf{H} and, therefore, all codewords have the constant weight $w_H(\underline{\mathbf{b}}) = 2^{r-1}$ (except the all-zero word). The name simplex stems from the geometrical property that all codewords have the same mutual Hamming distance $d_H(\underline{\mathbf{b}}, \underline{\mathbf{b}}') = 2^{r-1}$.

3.2.4 Hadamard-Codes

Hadamard codes can be constructed from simplex codes by extending all codewords with a preceding zero [Bos99]. This results in a generator matrix whose structure is identical to that of the corresponding simplex code except an additional first column containing only zeros. Hence, the columns of \mathbf{G} consist of all possible binary numbers between 0 and $2^k - 1$. Hadamard codes have the parameters $n = 2^r$ and $k = r$ so that there exist $M = 2^r$ codewords of length $n = M$. The code rate amounts to $R_c = r/2^r = \log_2(M)/M$. For $k = 3$ and $M = 8$, we obtain the generator matrix

$$\mathbf{G} = \left[\begin{array}{ccccccccc} 0 & 1 & 0 & 1 & 0 & 1 & 0 & 1 \\ 0 & 0 & 1 & 1 & 0 & 0 & 1 & 1 \\ 0 & 0 & 0 & 0 & 1 & 1 & 1 & 1 \end{array} \right]. \quad (3.2.15)$$

Since the columns of \mathbf{G} contain all possible vectors with weight 1, \mathbf{G} represents a systematic encoder although it has not the Gaussian normal form. Therefore, the information bits are distributed within the codeword at positions $\mu = 2^{-(l+1)}M$ with $0 \leq l < k$. Moreover, the property of simplex codes that all pairs of codewords have identical Hamming distances is retained. This distance amounts to $d = 2^{r-1}$.

The so-called Hadamard matrix \mathbf{B}_H comprises all codewords. It can be recursively constructed with

$$\mathbf{B}_{H,m} = \left[\begin{array}{cc} \mathbf{B}_{H,m-1} & \mathbf{B}_{H,m-1} \\ \mathbf{B}_{H,m-1} & \overline{\mathbf{B}}_{H,m-1} \end{array} \right] \quad (3.2.16)$$

where $\overline{\mathbf{B}}_H$ and \mathbf{B}_H are complementary matrices, i.e. zeros and ones are exchanged. If $\mathbf{B}_{H,0} = 1$ is used for the initialization, we obtain Hadamard codes whose block

lengths $n = 2^r$ are a power of 2. With a different initialization, also codes whose block length are multiples of 12 or 20 can be constructed.

The application of BPSK maps the logical bits onto antipodal symbols by $x_\nu = 1 - 2b_\nu$. This leads to orthogonal Walsh sequences that are used in CDMA systems for spectral spreading (see Chapter 4). They can also be employed as orthogonal modulation schemes [SG91, Pro95, Ben96].

An important advantage of Hadamard codes is the fact that they can be very efficiently ML decoded. The direct approach in (3.1.2) correlates the received word with all possible codewords and subsequently determines the maximum. The correlation can be efficiently implemented by the Fast Hadamard transformation. This linear transformation is similar to the well-known Fourier transformation and exploits symmetries of a butterfly structure. Moreover, the received symbols are only multiplied with ± 1 allowing very efficient implementations.

3.2.5 Trellis Representation of Linear Block Codes

Like convolutional codes that will be introduced in the next section, linear block codes can be graphically described by trellis diagrams [Wol78, Off96]. This representation bases on the parity check matrix $\mathbf{H} = [\mathbf{h}_1 \cdots \mathbf{h}_n]$. The number of states depends on the length of the vectors \mathbf{h}_ν and equals 2^{n-k} . A state is described by a vector $\mathbf{s} = [s_1, \dots, s_{n-k}]^T$ with the binary elements $s_\nu \in \text{GF}(2)$. If \mathbf{s}' denotes the preceding state at time instance $\nu - 1$ and \mathbf{s} the successive state at time instance ν , we obtain the following description for a state transitions

$$\mathbf{s} = \mathbf{s}' \oplus b_\nu \cdot \mathbf{h}_\nu , \quad 1 \leq \nu \leq n . \quad (3.2.17)$$

At the beginning ($\nu = 0$), we start with $\mathbf{s}' = \mathbf{0}$. Hence, the state remains unchanged for $b_\nu = 0$ and changes for $b_\nu = 1$. From (3.2.6), we can directly see that the linear combination of the columns \mathbf{h}_ν taking the coefficients from a codeword $\underline{\mathbf{b}} \in \Gamma$ results in the all-zero vector $\mathbf{0}$. Therefore, the corresponding trellis is terminated, i.e. it starts and ends in the all-zero-state.

Fig. 3.2.1 shows the trellis for a (7,4,3) Hamming code with a parity check matrix of the last section in systematic form. Obviously, two branches leave each state during the first four transitions representing the information part of the codewords. The parity bits are totally determined by the information word and, therefore, only one branch leaves each state during the last three transitions leading finally back to the all-zero-state. The trellis representation of block codes can be used for soft-in soft-output decoding, e.g. with the BCJR algorithm presented in Section 3.4.

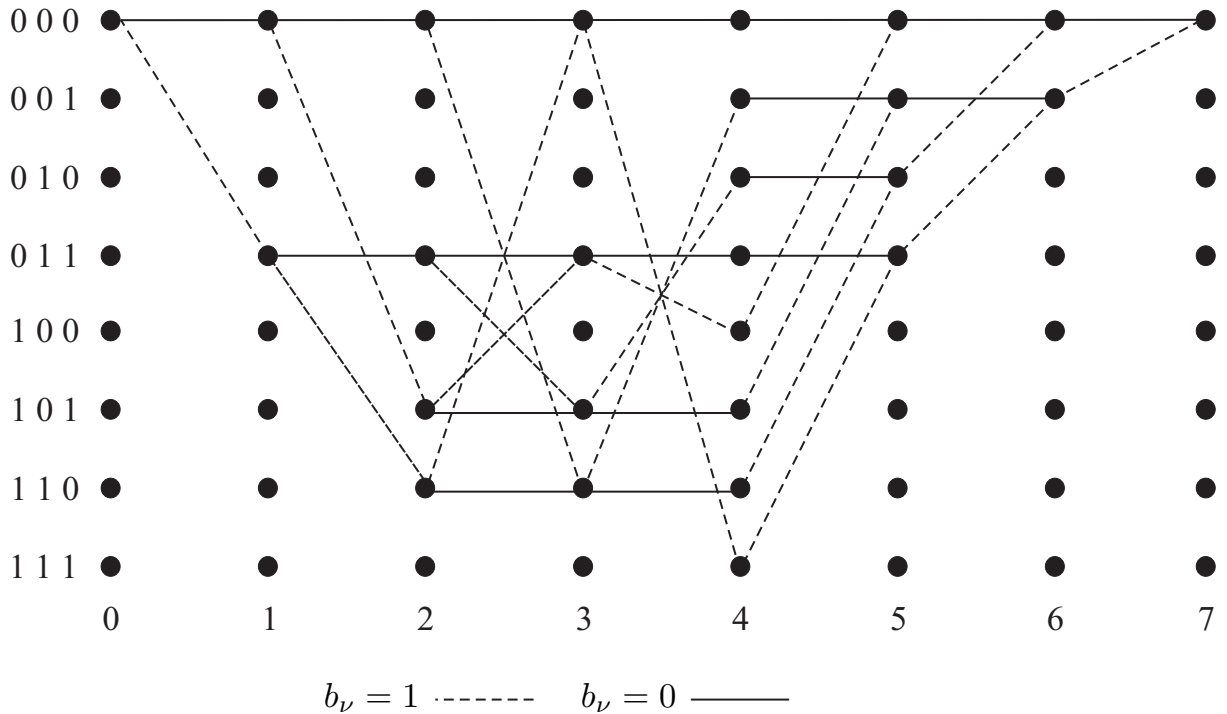


Figure 3.2.1: Trellis representation for $(7,4,3)$ -Hamming code from Section 3.2.4

3.3 Convolutional Codes

Convolutional codes are employed in many modern communication systems and belong to the class of linear codes. Their breakthrough came with the development of the Viterbi algorithm [Vit67], an efficient algorithm for maximum likelihood decoding. It has the ability of processing soft inputs instead of hard decision inputs which is a major advantage over many block codes. Contrarily to the large number of block codes, only few convolutional codes are relevant in practice. Moreover, they have very simple structures and can be graphically described by finite state and trellis diagrams.

There exists a duality between block and convolutional codes. On the one hand, convolutional codes have memory so that successive codewords are not independent from each other and sequences instead of single codewords have to be processed at the decoder. Therefore, block codes can be interpreted as special convolutional codes without memory. On the other hand, we always consider finite sequences in practice. Hence, we can imagine a whole sequence as a single codeword so that convolutional codes are a special implementation of block codes. Generally, it depends on the kind of application which interpretation is better suited. The minimum Hamming distance of convolutional codes is termed free distance and denotes by d_f .

3.3.1 Structure of Encoder

Convolutional codes exist for a variety of code rates $R_c = k/n$. However, codes with $k = 1$ are employed in most systems because this reduces the decoding effort and higher rates can be easily obtained by appropriate puncturing (cf. Section 3.3.3). Therefore, we restrict the description to rate $1/n$ codes. Hence, the input vector of the encoder reduces to a scalar $d[i]$ and successive codewords $\underline{\mathbf{b}}[i]$ consisting of n bits are correlated. Due to $R_c = 1/n$, the bit rate is multiplied with n as indicated by the time index ℓ in Fig. 3.1.1. Here, we comprise n code bits belonging to an information bit $d[i]$ to a codeword $\underline{\mathbf{b}}[i] = [b_1[i], \dots, b_n[i]]$ that obviously has the same rate and time index as $d[i]$.

The encoder can be implemented by a linear shift register as depicted in **Fig. 3.3.1**. Besides the code rate, another important parameter is the constraint length L_c describing the number of clock pulses an information bit affects the output. The larger L_c and, thus, the register memory, the better is the performance of a code. However, we will see that this coincides with an exponential increase in decoding complexity.

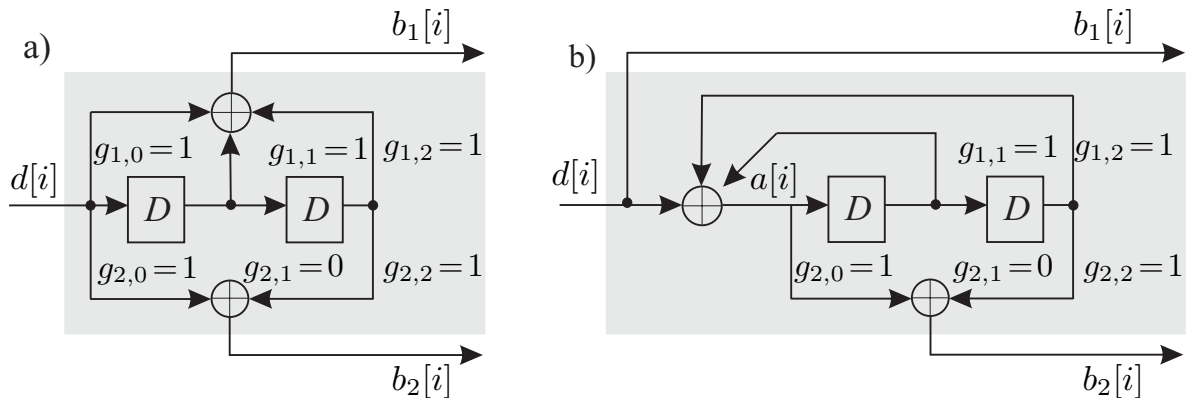


Figure 3.3.1: Structure of convolutional encoders with $R_c = 1/2$ and $L_c = 3$
a) Nonrecursive encoder with $g_1(D) = 1 + D + D^2$ and $g_2(D) = 1 + D^2$
b) Recursive encoder with $g_1(D) = 1$ and $g_2(D) = (1+D^2)/(1+D+D^2)$

We refer to the simple example in Fig. 3.3.1 for explaining the principle encoding process. At each clock pulse, one information bit $d[i]$ is fed into the register whose elements are linearly combined by modulo-2-adders. They deliver $n = 2$ outputs $b_\nu[i]$, $\nu = 1, 2$, at each clock pulse building the codeword $\underline{\mathbf{b}}[i]$. Hence, the encoder has a code rate $R_c = 1/2$ and a memory of 2 so that $L_c = 2 + 1 = 3$ holds. The optimal encoder structure, i.e. the connections between register elements and adders cannot be obtained with algebraic tools but has to be determined by a computer aided code search. Possible performance criteria are the distance spectrum or the IOWEF that will be described in Section 3.5. Tables of optimum codes for various code rates and constraint lengths can be found in [Pro95, JZ98].

Nonrecursive Nonsystematic Encoders

Principally, we distinguish between recursive and nonrecursive structures resembling to infinite impulse response (IIR) and finite impulse response (FIR) filters, respectively. Obviously, the nonrecursive encoder in Fig. 3.3.1a is nonsystematic since none of the coded output bits permanently equals $d[i]$. For a long time, only nonsystematic nonrecursive (NSC) encoders have been employed because no good systematic encoders without feedback exist. This is a difference to linear block codes that show the same error rate performance for systematic and nonsystematic encoders.

The linear combining of the register contents is described by n generators that are assigned to the n encoder outputs. Each generator g_ν comprises L_c scalars $g_{\nu,\mu} \in \text{GF}(2)$, $\mu = 0, \dots, L_c - 1$. A nonzero scalar $g_{\nu,\mu}$ indicate a connection between register element μ and the ν -th modulo-2-adder while the connection is missing for $g_{\nu,\mu} = 0$. Using a polynomial presentation, we obtain the ν -th output⁴

$$b_\nu[i] = \sum_{\mu=0}^{L_c-1} d[i - \mu] \cdot g_{\nu,\mu} \pmod{2} \Rightarrow b_\nu(D) = d(D) \otimes g_\nu(D) \quad (3.3.1)$$

with

$$g_\nu(D) = \sum_{\mu=0}^{L_c-1} g_{\nu,\mu} \cdot D^\mu. \quad (3.3.2)$$

Since the multiplication of polynomials is equivalent to the convolution of the corresponding sequences, the coded sequence $b_\nu[i]$ is generated by convolving the input sequence $d[i]$ with the ν -th generator. This explains the naming of convolutional codes. For the example in Fig. 3.3.1a, we obtain

$$\begin{aligned} g_1(D) &= g_{1,0} + g_{1,1}D + g_{1,2}D^2 = 1 + D + D^2 \\ g_2(D) &= g_{2,0} + g_{2,1}D + g_{2,2}D^2 = 1 + D^2. \end{aligned}$$

Vector notations as well as octal or decimal representations can be used alternatively. For a generator polynomial $g(D) = 1 + D + D^3$ we obtain

$$\underline{\mathbf{g}} = [g_0 \ g_1 \ g_2 \ g_3] = [1 \ 1 \ 0 \ 1] \hat{=} 11_{10} \hat{=} 15_8.$$

Concerning the decimal notation, the coefficient g_0 always denotes the least significant bit (LSB), g_{L_c-1} consequently the MSB leading to $1 + 2 + 8 = 11$. For octal notation, 3-bit-tupels are formed starting from the right hand side resulting in $[1 \ 0 \ 1] = 5_8$. If less than three bits remain, zeros are preceded to the left.

⁴The symbol \otimes denotes the multiplication according to the rules in $\text{GF}(2)$.

Recursive Systematic Encoders

With the first presentation of 'Turbo Codes' in 1993 [BGT93], recursive systematic convolutional (RSC) encoders have found great attention. Although they have been already known much earlier, their importance for concatenated codes became obvious since that time. Recursive encoders have an IIR structure and are mainly used as systematic encoders although this is not mandatory. The structure of RSC encoders can be derived from their nonrecursive counterparts by choosing one of the polynomials as denominator. For codes with $n = 2$, we can choose $g_1(D)$ as well as $g_2(D)$ for the feedback. In **Fig. 3.3.1b**, $g_1(D)$ was used and we obtain the modified generator polynomials

$$\tilde{g}_1(D) = 1 \quad (3.3.3a)$$

$$\tilde{g}_2(D) = \frac{g_2(D)}{g_1(D)} = \frac{1 + D^2}{1 + D + D^2} \quad (3.3.3b)$$

and the output bits

$$\tilde{b}_1(D) = \tilde{g}_1(D) \otimes d(D) = d(D) \quad (3.3.4a)$$

$$\tilde{b}_2(D) = \tilde{g}_2(D) \otimes d(D) = g_2(D) \otimes a(D) . \quad (3.3.4b)$$

The polynomial $a(D) = d(D)/g_1(D)$ in (3.3.4b) represent the input of the shift register depicted in Fig. 3.3.1b. Since D represents a delay operator, we obtain the following temporal relationship

$$a(D) \otimes [1 + D + D^2] = d(D) \Leftrightarrow a[i] = d[i] \oplus a[i - 1] \oplus a[i - 2] .$$

From this, the recursive encoder structure becomes obvious. The assumption $g_{1,0} = 1$ does not restrict the generality and leads to

$$a[i] = d[i] \oplus \sum_{\mu=1}^{L_c-1} g_{1,\mu} \cdot a[i - \mu] \mod 2 . \quad (3.3.5)$$

For notational simplicity, we neglect the tilde in the sequel and denote also recursive polynomials by $g_\nu(D)$. It has to be mentioned that nonrecursive nonsystematic codes and their recursive systematic counterparts have the same distance spectra $A(D)$. However, the mapping between input and output sequence and, thus, the IOWEF $A(W, D)$ is different (see Subsection 3.5.3). Recursive codes have due to their IIR structure an infinite impulse response i.e. they require a minimum input weight of $w = 2$ to obtain a finite output weight. This is one important property that predestines them for the application in concatenated coding schemes (cf. Section 3.6).

Termination of Convolutional Codes

In practical systems we always have sequences of finite length, e.g. they consist of N codewords. Due to the memory of the encoder, the decoder cannot decide on the basis of single codewords but has to consider the entire sequence or even larger parts of it. Hence, a decoding delay occurs because a certain part of the received sequence has to be processed until a reliable decision of the first bits can be made (see Viterbi decoding). This leads directly to a problem that the last bits of a sequence cannot be reliably estimated if the decoder does not know the final state of the encoder (truncated codes). In order to overcome this difficulty, $L_c - 1$ tail bits are appended to the information sequences forcing the encoder to end in a predefined state, conventionally the all-zero-state. With this knowledge, the decoder is enabled to estimate the last bits very reliably.

Since tail bits does not bear any information but represent redundancy, they reduces the code rate R_c . For a sequence consisting of N codewords we obtain

$$R_c^{\text{tail}} = \frac{N}{n \cdot (N + L_c - 1)} = R_c \cdot \frac{N}{N + L_c - 1}. \quad (3.3.6)$$

For $N \gg L_c$, the reduction of R_c can be neglected.

A different approach to allow reliable detection of all bits without reducing the code rate are tailbiting codes. They initialize the encoder with its final state. The decoder only knows that initial and final state are identical but it does not know the state itself. A detailed description can be found in [CFV99].

3.3.2 Graphical Description of Convolutional Codes

Since the encoder can be implemented by a shift register, it represents a finite state machine. This means that its output only depends on the input and the actual state but not on preceding states. The number of possible states is determined by the length of the register (memory) and amounts to 2^{L_c-1} in the binary case. **Fig. 3.3.2** shows the state diagrams of the nonrecursive and the recursive examples of Fig. 3.3.1. Due to $L_c = 3$, both encoders have four states. The transitions between them are labelled with the associated information bit $d[i]$ and the generated code bits $b_1[i], \dots, b_n[i]$. Hence, the state diagram totally describes the encoder.

Although the state diagram fully describes a convolutional code, it does not contain a temporal component which is necessary for decoding. This missing part is delivered by the trellis diagram shown in **Fig. 3.3.3**. It stems from the state diagram by arranging the states vertically as nodes and repeat them horizontally to illustrate the time axis. The state transitions are represented by branches labelled with the corresponding input and output bits. Generally, the encoder is initialized

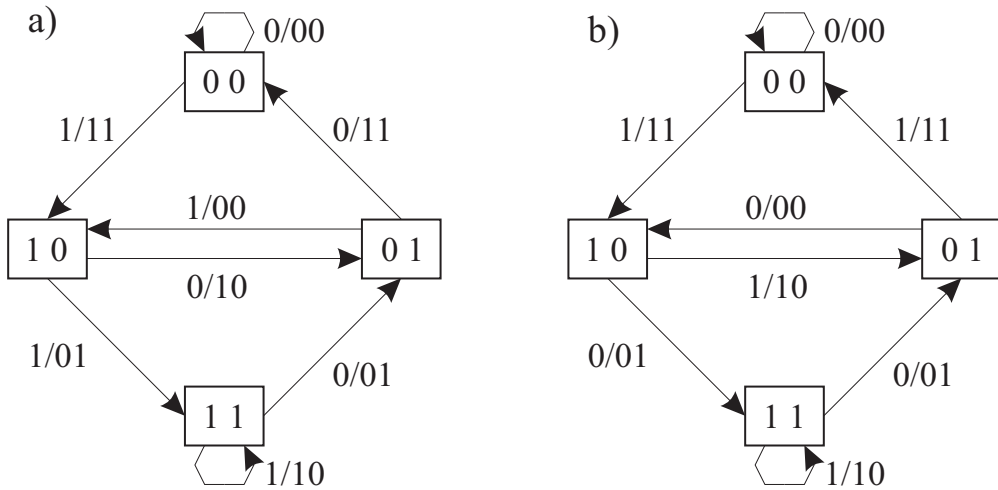


Figure 3.3.2: Finite state diagrams of convolutional codes with

$$\mathbf{a}) \quad g_1(D) = 1 + D + D^2 \text{ and } g_2(D) = 1 + D^2$$

$$\mathbf{b}) \quad g_1(D) = 1 \text{ and } g_2(D) = (1 + D^2)/(1 + D + D^2)$$

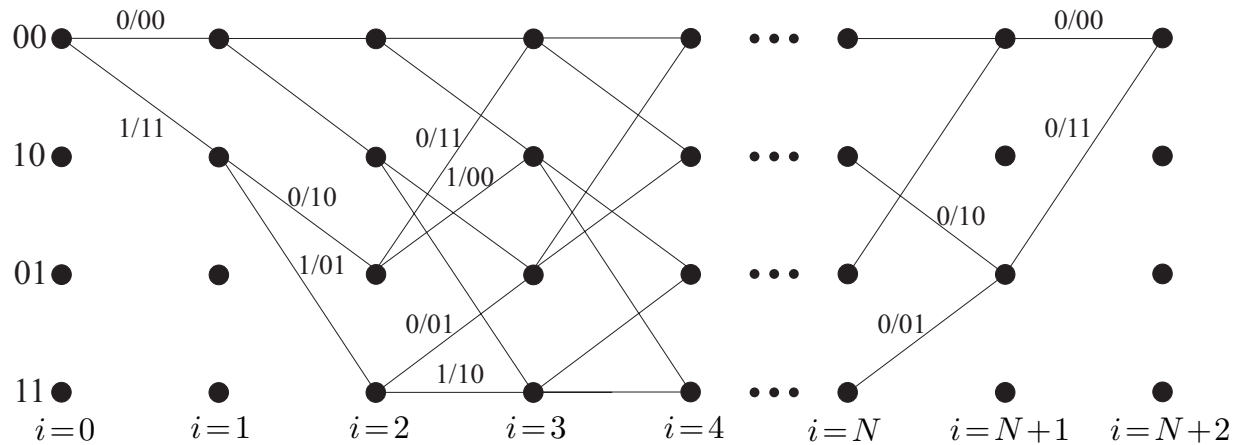


Figure 3.3.3: Trellis diagram for nonrecursive convolutional code with

$$g_1(D) = 1 + D + D^2 \text{ and } g_2(D) = 1 + D^2$$

with zeros so that we start in the all-zero-state. After L_c steps, the trellis is fully developed, i.e. two branches leave each state and every state is reached by two branches.

3.3.3 Puncturing Convolutional Codes

In modern communication systems, adaptivity is an important feature. In the context of link adaptation, the code rate as well as the modulation scheme are adjusted with respect to the channel quality. During good transmission conditions, weak codes with large R_c are sufficient so that high data rates can be transmitted with little redundancy. In bad channel states, strong FEC codes are required and

R_c is decreased. Moreover, Unequal Error Protection (UEP) adjusts the code rate with respect to the importance of different information parts [Hag89]. Finally, the concept of incremental redundancy when transmission errors have been detected in Automatic Repeat Request (ARQ) schemes uses variations of the code rate [Hag88].

A popular way for adapting the code rate is puncturing. Although puncturing can be applied to any code, we restrict to the description for convolutional codes. The basic principle is that after encoding, only a subset of the code bits is transmitted while the others are suppressed. This decreases the number of transmitted bits and, therefore, increases the code rate. Besides its flexibility, a major advantage of puncturing is that it does not affect the decoder so that a lot of code rates can be achieved with only a single hardware implementation of the decoder.

Principally, the optimum subset of bits to be transmitted has to be adapted to the specific mother code and can only be found by a computer aided code search. In practice, puncturing is performed periodically where one period comprises L_P codewords. A pattern in form of a matrix \mathbf{P} determines the transmitted and suppressed bits during one period. This matrix consists of n rows and L_P columns with binary elements $p_{\mu,\nu} \in \text{GF}(2)$

$$\mathbf{P} = \begin{pmatrix} p_{1,1} & p_{1,2} & \cdots & p_{1,L_P} \\ p_{2,1} & p_{2,2} & \cdots & p_{2,L_P} \\ \vdots & \vdots & & \vdots \\ p_{n,1} & p_{n,2} & \cdots & p_{n,L_P} \end{pmatrix} = (\mathbf{p}_1 \ \mathbf{p}_2 \ \cdots \ \mathbf{p}_{L_P}) . \quad (3.3.7)$$

The columns \mathbf{p}_ν contain the puncturing pattern for certain time instance and are periodically assigned to successive codewords $\mathbf{b}[i] = [b_1[i] \dots b_n[i]]$ with $\nu = (i \bmod L_P) + 1$. A zero at the μ -th position indicates that the μ -th bit is suppressed while a one indicates that the bit is transmitted.

Generally, \mathbf{P} contains $l + L_P$ ones with $1 \leq l \leq (n - 1) \cdot L_P$, i.e. only $l + L_P$ bits are transmitted instead of $n \cdot L_P$ without puncturing. Hence, the code rate amounts to

$$R'_c = \frac{L_P}{L_P + l} \quad (3.3.8)$$

and can vary in the interval

$$\frac{L_P}{L_P \cdot n} = \frac{1}{n} \leq R'_c \leq \frac{L_P}{L_P + 1} . \quad (3.3.9)$$

Certainly, puncturing reduces the performance of the mother code because the Hamming distances between codewords are decreased. However, it can be shown that punctured codes are as good as nonpunctured codes of the same rate.

Catastrophic Convolutional Codes

Puncturing has to be applied carefully because it can generate catastrophic codes. These codes are not suited for error protection because they can generate infinite long sequences with finite weight that do not merge with the all-zero-sequence. Due to the linearity of convolutional codes this means that a finite number of transmission errors can cause an infinite number of decoding errors which leads to a performance degradation due to coding. There exist some sufficient criteria for NSC encoders allowing the recognition of catastrophic codes. Systematic encoders are principally not catastrophic.

- All generator polynomials have a common factor.
- A closed loop with zero weight exists in the finite state diagram (except the loop in the all-zero-state).
- All modulo-2-adders have an even number of connections. This leads to a loop in the all-one-state with zero weight.

3.3.4 ML Decoding with Viterbi Algorithm

A major advantage of convolutional codes is the possibility to perform an efficient soft-input maximum likelihood decoding while this is often too complex for block codes⁵. We focus in this section on the classical Viterbi algorithm delivering hard decision outputs as estimates of the information bits. In Section 3.4, we address algorithms that provide reliability information for each decision and are therefore suited for decoding concatenated codes.

In the sequel, we assume that no a priori information of the information bits $d[i]$ is available and that all information sequences are equally likely. In this case, maximum likelihood decoding (MLD) is the optimum decoding approach. Since convolutional encoder deliver sequences of codewords $\mathbf{b}[i]$ that are not uncorrelated, we have to modify the ML decision rule in (3.1.2) slightly. If a sequence \mathbf{x} consists of N codewords $\mathbf{x}[i]$ each of n code bits $x_\nu[i]$, we obtain

$$\hat{\mathbf{x}} = \underset{\tilde{\mathbf{x}}}{\operatorname{argmax}} \sum_{i=0}^{N-1} \sum_{\nu=1}^n \tilde{x}_\nu[i] \cdot r_\nu[i]. \quad (3.3.10)$$

According to (3.3.10), we have to sum the incremental metrics $\sum_{\nu=1}^n \tilde{x}_\nu[i] \cdot r_\nu[i]$ for all sequences and decide in favor to that one with the largest (cumulative) path metric. This is obviously impractical because the number of possible sequences

⁵Standard array and syndrome decoding for linear block codes perform maximum likelihood decoding with hard decision input.

grows exponentially with their lengths. Since convolutional encoders are finite state machines, their output at a certain time instance only depends on the input and the current state. Hence, they represent Markov models of first order, i.e. the history of previous states is meaningless if we know the last state. Performing the decoding on the basis of the trellis diagram now leads to the famous Viterbi algorithm whose complexity depends only linearly on the sequence length N [Pro95, Kam96, KK01].

We now briefly describe the Viterbi algorithm based on the trellis segment in **Fig. 3.3.4**. We assume that the encoder and decoder start both in the all-zero-state. Preceding states are denoted by \mathbf{s}' and successive states by \mathbf{s} . They represent the register content, e.g. $\mathbf{s} = [1 \ 0]$. To simplify notation, we define the set $\Upsilon = \text{GF}(2)^{L_c - 1}$ containing all possible states \mathbf{s} . For our example with four states, we obtain $\Upsilon = \{[00], [01], [10], [11]\}$. Moreover, the set $\Upsilon_{\mathbf{s}}$ comprises all states \mathbf{s}' for which a transition to state \mathbf{s} exists.

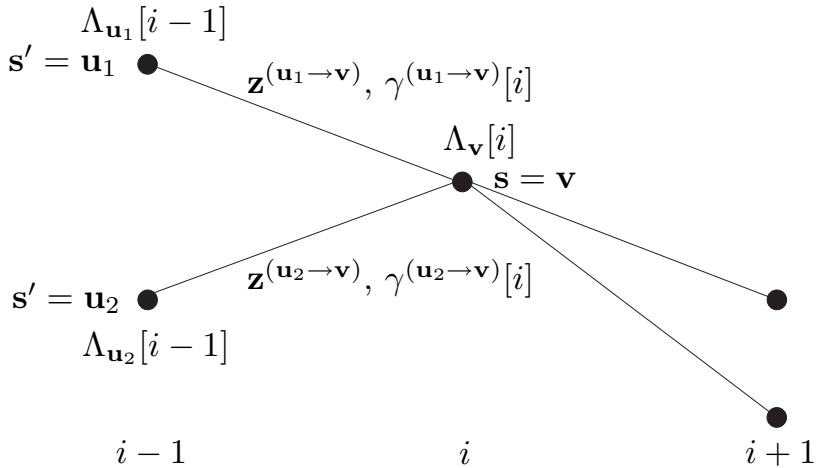


Figure 3.3.4: Segment of trellis diagram for illustration of Viterbi algorithm

Viterbi Algorithm

- ① Start in the all-zero-state of the trellis at time instance $i = 0$ and initialize the cumulative path metrics $\Lambda_{\mathbf{s}'}[i = 0] = \mathbf{0}$ of all states $\mathbf{s}' \in \Upsilon$.
- ② At time instance i , calculate incremental metrics (branch metrics)

$$\gamma^{(\mathbf{s}' \rightarrow \mathbf{s})}[i] = \sum_{\nu=1}^n r_{\nu}[i] \cdot z_{\nu}^{(\mathbf{s}' \rightarrow \mathbf{s})}, \quad (3.3.11)$$

for all $\mathbf{s}' \in \Upsilon_{\mathbf{s}}$ and $\mathbf{s} \in \Upsilon$ where $z_{\nu}^{(\mathbf{s}' \rightarrow \mathbf{s})} = \pm \sqrt{E_s/T_s}$ denotes the ν -th code symbol of transition $\mathbf{s}' \rightarrow \mathbf{s}$.

- ③ Add incremental metrics of ② to cumulative metrics of corresponding states at time instance $i - 1$: $\Lambda_{\mathbf{s}'}[i - 1] + \gamma^{(\mathbf{s}' \rightarrow \mathbf{s})}[i]$ with $\mathbf{s}' \in \Upsilon_s$ and $\mathbf{s} \in \Upsilon$.
- ④ At each state \mathbf{s} , choose path with the largest cumulative metric and discard the competing path:

$$\Lambda_{\mathbf{s}}[i] = \max_{\mathbf{s}' \in \Upsilon_s} \left\{ \Lambda_{\mathbf{s}'}[i - 1] + \gamma^{(\mathbf{s}' \rightarrow \mathbf{s})}[i] \right\}$$

Due to the Markov property, we just have to consider one preceding time instance. Once we have chosen the best path among those arriving at a state \mathbf{s} , all other paths cannot outperform the best path in the future and are discarded. Therefore, the computational complexity grows only linearly with the sequence length N .

- ⑤ Repeat procedure from ② until all N received codewords $\mathbf{r}[i]$ have been processed.
- ⑥ Determine survivor at end of trellis diagram:
 - *Terminated trellis*: Continue procedure for $L_c - 1$ tail bit and determine path with best metric $\Lambda_0[N + L_c - 1]$ in all-zero-state.
 - *Truncated trellis*: Determine path with best global cumulative metric $\Lambda_{\mathbf{s}}[N]$ with $\mathbf{s} \in \Upsilon$.
- ⑦ Estimates of the information bits are delivered by tracing back the survivor determined in ⑥.

According to the above procedure, a whole sequence has to be processed until estimates of the information bits are available. However, for a continuous transmission or very long blocks this leads to long delays that may not be acceptable for certain applications. Moreover, limited memory in the decoder may require to process shorter parts of the block. It has been shown that reliable decisions of a bit $d[i]$ can be made when a subsequence from $\mathbf{r}[i]$ to $\mathbf{r}[i + K]$ with sufficiently large K has been processed. A rule of thumb states that the decision depth K has to be approximately five times the constraint length L_c [HJ71]. After processing K steps, early parts of competing paths have merged with high probability and the decision is reliable.

Punctured Codes

Prior to decoding, positions of punctured bits have to be filled with dummy bits. Assuming an antipodal transmission, zeros can be inserted. Looking at (3.3.10), we recognize that $r_\nu[i] = 0$ does not affect the incremental metric. However, puncturing reduces the Hamming distances between code sequences. Therefore, the decision depth K has to be increased [Hag88] in order to keep decision reliable.

3.4 Soft-Output Decoding of Binary Codes

In the last decade, tremendous effort has been spent to analyze and design concatenated codes. As will be shown in Sections 3.6.2 and 3.6.3, the analytical performance analysis often presupposes an optimum maximum likelihood decoding of the entire which is infeasible in most practical systems. Instead, a concatenation of distinct decoders mutually exchanging information was found to be a suboptimum but practical solution. In order to avoid a loss of information by hard decision decoding, algorithms that process and provide soft information for each bit are required.

The optimum soft-in soft-out decoder would deliver a list of a posteriori probabilities, one for each possible codeword. Since the number of codewords for practical codes can easily even exceeds the number of atoms in space, this is an infeasible approach. Instead, the generally trellis based decoders work on a symbol-by-symbol basis and deliver soft information for each bit separately.

In this section, we first define an appropriate measure of reliability and then proceed with deriving soft-output decoding algorithms for block codes and convolutional codes. For the sake of simplicity, we always assume BPSK modulated signals according to Section 1.4 and a memoryless channel.

3.4.1 Log-Likelihood Ratios – A Measure of Reliability

Since the information is represented by a random process \mathcal{B} , a suitable soft information is of course the probability $\Pr\{\mathcal{B} = b\}$. BPSK maps the coded bits b onto antipodal signals x by $x = (1 - 2b)\sqrt{E_s/T_s}$, i.e. $b = 0$ corresponds to $x = +\sqrt{E_s/T_s}$ and $b = 1$ to $x = -\sqrt{E_s/T_s}$. Due to the restriction on the binary case, $\Pr\{b = 0\} + \Pr\{b = 1\} = 1$ holds, i.e. we have only one independent parameter and the entire information is already contained either in $\Pr\{b = 0\}$ or $\Pr\{b = 1\}$. Hence, we can also use the logarithmic ratio of the probabilities leading to the log-likelihood ratio (LLR)

$$L(b) = L(x) = \ln \frac{\Pr\{b = 0\}}{\Pr\{b = 1\}} = \ln \frac{\Pr\{x = +\sqrt{E_s/T_s}\}}{\Pr\{x = -\sqrt{E_s/T_s}\}} \quad (3.4.1)$$

as an appropriate measure of reliability for b [Hag96b]. The sign of $L(b)$ determines the hard decision while the magnitude denotes the reliability. The larger the difference between $\Pr\{b = 0\}$ and $\Pr\{b = 1\}$ the larger is the magnitude of their ratio. If $b = 1$ and $b = 0$ are equally likely, a decision is totally random (unreliable) and $L(b) = 0$ holds. Since the logarithm is a strictly monotone function, we can also calculate probabilities from the LLR's. Resolving (3.4.1) with respect to $\Pr\{b = 0 | r\}$ and $\Pr\{b = 1 | r\}$ results in

$$\Pr\{b = v\} = \frac{e^{-v \cdot L(b)}}{1 + e^{-L(b)}} \text{ with } v \in \{0, 1\} \quad (3.4.2a)$$

for the logical variable b and in

$$\Pr\{x = X\} = \frac{1}{1 + e^{-\operatorname{sgn}(X) \cdot L(x)}} \text{ with } X \in \left\{ +\sqrt{E_s/T_s}, -\sqrt{E_s/T_s} \right\} \quad (3.4.2b)$$

for antipodal signals. The probability for a correct decision is determined in the following way. For $b = 0$ we obtain the true data if $L(\hat{b})$ is positive, i.e.

$$\Pr\{\hat{b} = b \mid b = 0\} = \frac{1}{1 + e^{-L(\hat{b})}} = \frac{e^{|L(\hat{b})|}}{1 + e^{|L(\hat{b})|}} \text{ for } L(\hat{b}) > 0 .$$

Equivalently, $L(\hat{b})$ has to be negative for $b = 1$

$$\Pr\{\hat{b} = b \mid b = 1\} = \frac{1}{1 + e^{L(\hat{b})}} = \frac{1}{1 + e^{-|L(\hat{b})|}} = \frac{e^{|L(\hat{b})|}}{1 + e^{|L(\hat{b})|}} \text{ for } L(\hat{b}) < 0 .$$

Combining both expressions finally yields

$$\Pr\{\hat{b} = b\} = \frac{e^{|L(\hat{b})|}}{1 + e^{|L(\hat{b})|}} . \quad (3.4.3)$$

Moreover, the expectation of a decision for the antipodal signal x becomes with (3.4.2b)

$$\begin{aligned} \mathbb{E}\{\hat{x}\} &= \sum_{X=\pm\sqrt{\frac{E_s}{T_s}}} X \cdot \Pr\{\hat{x} = X\} = \sqrt{\frac{E_s}{T_s}} \cdot \left(\frac{e^{L(\hat{x})}}{1 + e^{L(\hat{x})}} - \frac{1}{1 + e^{L(\hat{x})}} \right) \\ &= \sqrt{\frac{E_s}{T_s}} \cdot \tanh(L(\hat{x})/2) . \end{aligned} \quad (3.4.4)$$

For uniformity, we refer in the following derivation to the logical values '0' and '1'. However, equivalent expressions can be obtained with antipodal signals $\pm\sqrt{E_s/T_s}$. Looking at the transmission of information, a decision is based on the matched filter output r . According to the MAP criterion in Section 1.3 we have to choose that \hat{b} that maximizes the a posteriori probability

$$\hat{b} = \operatorname{argmax}_{v \in \{0, 1\}} \Pr\{b = v \mid r\} .$$

Replacing the probabilities in (3.4.1) by a posteriori probabilities and applying Bayes' rule we obtain

$$L(\hat{b}) = L(b \mid r) = \ln \frac{\Pr\{b = 0 \mid r\}}{\Pr\{b = 1 \mid r\}} = \underbrace{\ln \frac{p_{\mathcal{R}|b=0}(r)}{p_{\mathcal{R}|b=1}(r)}}_{L(r \mid b)} + \underbrace{\ln \frac{\Pr\{b = 0\}}{\Pr\{b = 1\}}}_{L_a(b)} . \quad (3.4.5)$$

Hence, the log-likelihood ratio in (3.4.5) consists for an uncoded transmission of two components. The term $L(r|b)$ depends on the channel statistics $p_{\mathcal{R}|b}(r)$ and, therefore, only on the matched filter output r . Contrarily, $L_a(b)$ is independent from r and represents a priori knowledge about the bit b .

The log-likelihood ratio can be very easily calculated for memoryless channels like AWGN and flat Rayleigh fading channels depicted in Fig. 3.1.1. Inserting the conditional probability densities into (3.4.5) results in

$$L(r | x) = 4 \frac{E_s}{N_0} \tilde{r} = 4|h|^2 \underbrace{\frac{E_s}{N_0}}_{L_{ch}} \tilde{y} \quad \text{with} \quad \tilde{y} = \frac{y}{\sqrt{E_s/T_s}}. \quad (3.4.6)$$

In (3.4.6), \tilde{r} is a normalized version of the matched filter output $r = \operatorname{Re}\{h^* \cdot y\}$ with unit average power of the information part equivalent to the definition of \tilde{y} . Hence, the log-likelihood ratio is directly obtained from the matched filter output \tilde{r} except some appropriate scaling with the signal to noise ratio E_s/N_0 . Equivalently, the normalized channel output \tilde{y} can be directly weighted with the channel reliability L_{ch} that depends on E_s/N_0 as well as the channel gain $|h|^2$. As a consequence, it is natural to use log-likelihood ratios in subsequent decoding algorithms as they are provided by matched filtering. For this goal we need an appropriate algebra called *L-Algebra* [Hag96b].

As already known from block and convolutional codes, the parity check bits are generated by modulo-2-sums of certain information bits d_i . In order to calculate the LLR of a parity bit, we look at a simple single parity check code with two statistically independent information bits $b_1 = d_1$, $b_2 = d_2$ and the parity bit $b_3 = d_1 \oplus d_2$. The LLR $L(x_3)$ is given by

$$\begin{aligned} L(b_3) &= L(d_1 \oplus d_2) = \ln \frac{\Pr\{b_3 = 0\}}{\Pr\{b_3 = 1\}} \\ &= \ln \frac{\Pr\{d_1 = 0\} \cdot \Pr\{d_2 = 0\} + \Pr\{d_1 = 1\} \cdot \Pr\{d_2 = 1\}}{\Pr\{d_1 = 0\} \cdot \Pr\{d_2 = 1\} + \Pr\{d_1 = 1\} \cdot \Pr\{d_2 = 0\}}. \end{aligned}$$

Rearranging the probabilities such that we obtain likelihood ratios $\Pr\{d = 0\}/\Pr\{d = 1\}$ and applying the relationships $\tanh(x/2) = (e^x - 1)/(e^x + 1)$ as well as $\ln[(1+x)/(1-x)] = 2 \operatorname{artanh}(x)$ yields

$$L(d_3) = 2 \operatorname{artanh}(\lambda_1 \cdot \lambda_2) \quad \text{with} \quad \lambda_\mu = \tanh(L(d_\mu)/2). \quad (3.4.7)$$

By complete induction techniques it can be shown that (3.4.7) can be generalized for N independent variables

$$L(d_1 \oplus \dots \oplus d_N) = 2 \operatorname{artanh} \left(\prod_{\mu=1}^N \tanh(L(d_\mu)/2) \right) \quad (3.4.8)$$

With (3.4.8), we now have a rule for calculating the LLR of a sum of statistically independent random variables.

An approximation with lower computational complexity can be derived by exploiting the behavior of the tanh function. It saturates at ± 1 for arguments with large magnitude and has a nearly linear shape with a slope of 1 at the origin. Therefore, large magnitudes at the input result in a multiplication with ± 1 while the input with the smallest magnitude mainly determines the magnitude of the output. Hence, we obtain the approximation

$$L(d_1 \oplus \cdots \oplus d_N) \approx \min_{\mu}(|L(d_{\mu})|) \cdot \prod_{\mu=1}^N \operatorname{sgn}(L(d_{\mu})) . \quad (3.4.9)$$

3.4.2 General Approach for Soft-Output Decoding

In a first step, we derive a direct approach for calculating in a symbol-by-symbol manner log-likelihood ratios for each information bit. Therefore, we consider an encoder that maps the information vector $\mathbf{d} = [d_1, \dots, d_k]^T$ onto the codeword $\mathbf{b} = [b_1, \dots, b_n]^T$ consisting of n bits. After BPSK modulation, the vector \mathbf{x} is transmitted. Based on the matched filter output $\mathbf{r} = [r_1, \dots, r_n]^T$ we now have to determine $L(d_{\mu} | \mathbf{r})$. In the context of concatenated codes, we will see later that it is necessary to calculate LLR's $L(b_{\nu} | \mathbf{r})$ of coded bits as well. This can be accomplished by simply replacing the targeted d_{μ} with the desired code bit b_{ν} in the following derivation.

According to the symbol-by-symbol MAP criterion of Section 1.3, the a posteriori probability $\Pr\{\mathcal{X} = x | \mathbf{r}\}$ represents an appropriate soft information containing all available information. Since we consider a binary transmission, the random variable \mathcal{X} can take only two different values and the log-likelihood ratio of the corresponding probabilities also comprises the entire information.

$$L(\hat{d}_{\mu}) = \ln \frac{\Pr\{d_{\mu} = 0 | \mathbf{r}\}}{\Pr\{d_{\mu} = 1 | \mathbf{r}\}} = \ln \frac{p_{\mathcal{D}_{\mu}, \underline{\mathcal{R}}}(d_{\mu} = 0, \mathbf{r})}{p_{\mathcal{D}_{\mu}, \underline{\mathcal{R}}}(d_{\mu} = 1, \mathbf{r})} . \quad (3.4.10)$$

The probability densities in nominator and denominator can be extended by exploiting the relation $\Pr\{b_{\mu} = v\} = \sum_{\mathbf{b}, b_{\mu} = v} \Pr\{\mathbf{b}\}$. In order to obtain the separation into $d_{\mu} = 0$ and $d_{\mu} = 1$, we divide the code space Γ into two sets of equal size, namely $\Gamma_{\mu}^{(0)}$ comprising all codewords whose μ -th information bit is zero and $\Gamma_{\mu}^{(1)}$ with all remaining codewords corresponding to $d_{\mu} = 1$. This results in

$$L(\hat{d}_{\mu}) = \ln \frac{\sum_{\mathbf{b} \in \Gamma_{\mu}^{(0)}} p_{\underline{\mathcal{B}}, \underline{\mathcal{R}}}(\mathbf{b}, \mathbf{r})}{\sum_{\mathbf{b} \in \Gamma_{\mu}^{(1)}} p_{\underline{\mathcal{B}}, \underline{\mathcal{R}}}(\mathbf{b}, \mathbf{r})} = \ln \frac{\sum_{\mathbf{b} \in \Gamma_{\mu}^{(0)}} p_{\underline{\mathcal{R}}|\mathbf{b}}(\mathbf{r}) \cdot \Pr\{\mathbf{b}\}}{\sum_{\mathbf{b} \in \Gamma_{\mu}^{(1)}} p_{\underline{\mathcal{R}}|\mathbf{b}}(\mathbf{r}) \cdot \Pr\{\mathbf{b}\}} . \quad (3.4.11)$$

For memoryless channels, the conditional probability densities can be factorized into n terms

$$p_{\underline{\mathcal{R}}|\mathbf{b}}(\mathbf{r}) = \prod_{\nu=1}^n p_{\mathcal{R}_\nu|b_\nu}(r_\nu) .$$

Moreover, a codeword \mathbf{b} is totally determined by the corresponding information word \mathbf{d} . Since the information bits are assumed to be statistically independent, $\Pr\{\mathbf{b}\} = \Pr\{\mathbf{d}\} = \prod_{\mu=1}^k \Pr\{d_\mu\}$ holds and we obtain

$$L(\hat{d}_\mu) = \ln \frac{\sum_{\mathbf{b} \in \Gamma_\mu^{(0)}} \prod_{\nu=1}^n p_{\mathcal{R}_\nu|b_\nu}(r_\nu) \cdot \prod_{\nu=1}^k \Pr\{d_\nu\}}{\sum_{\mathbf{b} \in \Gamma_\mu^{(1)}} \prod_{\nu=1}^n p_{\mathcal{R}_\nu|b_\nu}(r_\nu) \cdot \prod_{\nu=1}^k \Pr\{d_\nu\}} . \quad (3.4.12)$$

If we consider systematic encoders with $d_\mu = b_\mu$ for $1 \leq \mu \leq k$, the terms corresponding to $\nu = \mu$ in the products of nominator and denominator are constant. Hence, $p_{\mathcal{R}_\mu|b_\mu}(r_\mu)$ as well as $\Pr\{d_\mu\}$ can be extracted yielding

$$L(\hat{d}_\mu) = L(r_\mu | d_\mu) + L_a(d_\mu) + \ln \underbrace{\frac{\sum_{\mathbf{b} \in \Gamma_\mu^{(0)}} \prod_{\substack{\nu=1 \\ \nu \neq \mu}}^n p_{\mathcal{R}_\nu|b_\nu}(r_\nu) \cdot \prod_{\substack{\nu=1 \\ \nu \neq \mu}}^k \Pr\{d_\nu\}}{\sum_{\mathbf{b} \in \Gamma_\mu^{(1)}} \prod_{\substack{\nu=1 \\ \nu \neq \mu}}^n p_{\mathcal{R}_\nu|b_\nu}(r_\nu) \cdot \prod_{\substack{\nu=1 \\ \nu \neq \mu}}^k \Pr\{d_\nu\}}}_{L_e(\hat{d}_\mu)} . \quad (3.4.13)$$

Equation (3.4.13) shows that $L(\hat{d}_\mu)$ consists for systematic encoding of three parts: the intrinsic information

$$L(r_\mu | d_\mu) = \ln \frac{p_{\mathcal{R}_\mu|d_\mu=0}(r_\mu)}{p_{\mathcal{R}_\mu|d_\mu=1}(r_\mu)} = 4 \frac{E_s}{N_0} r_\mu \quad (3.4.14a)$$

obtained from the weighted matched filter output of the symbol d_μ itself, the a priori information

$$L_a(d_\mu) = \ln \frac{\Pr\{d_\mu = 0\}}{\Pr\{d_\mu = 1\}} \quad (3.4.14b)$$

that is already known from the uncoded case and as a third part $L_e(\hat{d}_\mu)$. This last component does not depend on the μ -th bit itself but on all other bits of a codeword. Therefore, it is called *extrinsic information*. For memoryless channels, all three parts are independent from each other so that the LLR's can simply be summed. The extrinsic information is responsible for the coding gain since it exploits the structure of the code. In the case of nonsystematic encoding, extrinsic and intrinsic components cannot be separated. However, soft-output decoding is still possible.

Since the log-likelihood values $L(r_\mu | b_\mu)$ are scaled versions of the matched filter output, it would be desirable to express (3.4.13) by these LLR's instead of probability densities. The a priori probabilities can be substituted by (3.4.2a) and for the conditional probability densities

$$\begin{aligned} p_{\mathcal{R}_\nu | b_\nu}(r_\nu) &= \Pr\{b_\nu | r_\nu\} \cdot \frac{p_{\mathcal{R}_\nu}(r_\nu)}{\Pr\{b_\nu\}} \\ &= \frac{\exp[-b_\nu L(b_\nu | r_\nu)]}{1 + \exp[-L(b_\nu | r_\nu)]} \cdot \frac{1 + \exp[-L_a(b_\nu)]}{\exp[-b_\nu L_a(b_\nu)]} \cdot p_{\mathcal{R}_\nu}(r_\nu) \\ &= \frac{\exp[-b_\nu L(r_\nu | b_\nu)]}{1 + \exp[-L(b_\nu | r_\nu)]} \cdot [1 + \exp[-L_a(b_\nu)]] \cdot p_{\mathcal{R}_\nu}(r_\nu) \quad (3.4.15) \end{aligned}$$

holds. It has to be emphasized that the LLR's $L_a(b_\nu)$ and $L(r_\nu | b_\nu)$ do not depend on the concrete b_ν but only on the ratio of probabilities corresponding to the two possible values of b_ν . Hence, inserting (3.4.15) into (3.4.13) allows the cancellation of all terms independent of b_ν . We obtain

$$L_e(\hat{d}_\mu) = \ln \frac{\sum_{\mathbf{b} \in \Gamma_\mu^{(0)}} \prod_{\substack{\nu=1 \\ \nu \neq \mu}}^n \exp[-b_\nu L(r_\nu | b_\nu)] \cdot \prod_{\substack{\nu=1 \\ \nu \neq \mu}}^k \exp[-b_\nu L_a(b_\nu)]}{\sum_{\mathbf{b} \in \Gamma_\mu^{(1)}} \prod_{\substack{\nu=1 \\ \nu \neq \mu}}^n \exp[-b_\nu L(r_\nu | b_\nu)] \cdot \prod_{\substack{\nu=1 \\ \nu \neq \mu}}^k \exp[-b_\nu L_a(b_\nu)]}. \quad (3.4.16)$$

With the definition

$$L(b_\nu; r_\nu) = \begin{cases} L(r_\nu | b_\nu) + L_a(b_\nu) & \text{for } 1 \leq \nu \leq k \\ L(r_\nu | b_\nu) & \text{for } k < \nu \leq n \end{cases} \quad (3.4.17)$$

(3.4.13) becomes

$$L(\hat{d}_\mu) = L(r_\mu | d_\mu) + L_a(d_\mu) + \ln \frac{\sum_{\mathbf{b} \in \Gamma_\mu^{(0)}} \prod_{\substack{\nu=1 \\ \nu \neq \mu}}^n \exp[-b_\nu L(b_\nu; r_\nu)]}{\sum_{\mathbf{b} \in \Gamma_\mu^{(1)}} \prod_{\substack{\nu=1 \\ \nu \neq \mu}}^n \exp[-b_\nu L(b_\nu; r_\nu)]} \quad (3.4.18a)$$

$$= L(r_\mu | d_\mu) + L_a(d_\mu) + \ln \frac{\sum_{\mathbf{x} \in \Gamma_\mu^{(+1)}} \prod_{\substack{\nu=1 \\ \nu \neq \mu}}^n \exp[x_\nu L(b_\nu; r_\nu)/2]}{\sum_{\mathbf{x} \in \Gamma_\mu^{(-1)}} \prod_{\substack{\nu=1 \\ \nu \neq \mu}}^n \exp[x_\nu L(b_\nu; r_\nu)/2]}. \quad (3.4.18b)$$

Equation (3.4.18a) demonstrates that we only need the scaled matched filter outputs and the a priori LLR's for each bit in order to determine the extrinsic information. An equivalent expression is obtained by using antipodal symbols $x_\nu = \pm 1$

instead of logical bits $b_\nu \in \{0, 1\}$. The relationship $b_\nu = (1 - x_\nu)/2$ leads to (3.4.18b). However, a direct implementation of (3.4.18a) or (3.4.18b) requires a prohibitive computational effort because the number of codewords $\mathbf{b} \in \Gamma_\mu^{(0,1)}$ over which we have to sum in nominator and denominator becomes excessively high for codes with reasonable cardinality. For example, the (255,247,3)-Hamming code consists of $2^{247} = 2.3 \cdot 10^{74}$ codewords.

It is possible to perform the decoding with the dual code (see page 92). This leads to lower computational costs if the cardinality of the dual code is much smaller than of the original code [Off96]. A different possibility is the representation of the code by its trellis diagram. In the following subsections, we present trellis based symbol-by-symbol decoding algorithms for linear block codes and convolutional codes as well as simplified versions operating in the logarithmic domain.

3.4.3 BCJR Algorithm for Binary Block Codes

Basically, the algorithm to be presented now is not restricted to decoding purposes but can be generally applied for estimating a posteriori LLR's in systems represented by a trellis diagram. Hence, it can be used for decoding convolutional and linear block codes as well as for the equalization of dispersive channels [BCJR74, LVS95, DJB95, Jor00]. The so-called BCJR algorithm was presented for the first time in 1972 by Bahl, Cocke, Jelinek and Raviv [BCJR72]. The savings in computational complexity compared to a direct implementation of (3.4.18a) are based on the fact that the encoder can be interpreted as a Markov process of first order (compare Viterbi decoder on page 104).

We start the derivation for binary linear block codes by going back to (3.4.10) and we focus on soft-output decoding the information bit d_μ , i.e. estimating $L(\hat{d}_\mu)$. Looking at the trellis representation of linear block codes (rf. Section 3.2.5), d_μ initiates a transition from a state \mathbf{s}' at time instance $\mu - 1$ to a state \mathbf{s} at time μ . The set of all possible transitions $\{\mathbf{s}', \mathbf{s}\}$ can be separated into two subsets, those corresponding to $d_\mu = 0$ and those associated with $d_\mu = 1$. Moreover, \mathbf{r} can be divided into three parts: the vector $\mathbf{r}_{k < \mu}$ comprising all received symbols before time instance μ , the symbol r_μ and the vector $\mathbf{r}_{k > \mu}$ containing all symbols received after time instance μ . With this, (3.4.10) becomes⁶

$$L(\hat{d}_\mu) = \ln \frac{\sum_{\substack{\{\mathbf{s}', \mathbf{s}\} \\ d_\mu=0}} p(\mathbf{s}', \mathbf{s}, \underline{\mathbf{r}})}{\sum_{\substack{\{\mathbf{s}', \mathbf{s}\} \\ d_\mu=1}} p(\mathbf{s}', \mathbf{s}, \underline{\mathbf{r}})} = \ln \frac{\sum_{\substack{\{\mathbf{s}', \mathbf{s}\} \\ d_\mu=0}} p(\mathbf{s}', \mathbf{s}, \underline{\mathbf{r}}_{k < \mu}, r_\mu, \underline{\mathbf{r}}_{k > \mu})}{\sum_{\substack{\{\mathbf{s}', \mathbf{s}\} \\ d_\mu=1}} p(\mathbf{s}', \mathbf{s}, \underline{\mathbf{r}}_{k < \mu}, r_\mu, \underline{\mathbf{r}}_{k > \mu})}. \quad (3.4.19)$$

⁶For notational simplicity, we deviate from the conventional notation and simplify $p_{\underline{\mathcal{S}'}, \underline{\mathcal{S}}, \underline{\mathcal{R}}}(\mathbf{s}', \mathbf{s}, \mathbf{r})$ to $p(\mathbf{s}', \mathbf{s}, \mathbf{r})$.

If LLR's of coded bits b_ν are to be calculated, d_μ has to be replaced in (3.4.19) by b_ν . The probability density functions in nominator and denominator can be factorized by the chain rule

$$\begin{aligned} p(\mathbf{s}', \mathbf{s}, \mathbf{r}_{k<\mu}, r_\mu, \mathbf{r}_{k>\mu}) &= p(\mathbf{r}_{k>\mu} \mid \mathbf{s}', \mathbf{s}, \mathbf{r}_{k<\mu}, r_\mu) \\ &\quad \cdot p(\mathbf{s}, r_\mu \mid \mathbf{s}', \mathbf{r}_{k<\mu}) \cdot p(\mathbf{s}', \mathbf{r}_{k<\mu}). \end{aligned} \quad (3.4.20)$$

Since the encoder can be modelled as a Markov process of first order, the first term in (3.4.20) can be rewritten as

$$\beta_\mu(\mathbf{s}) := p(\mathbf{r}_{k>\mu} \mid \mathbf{s}', \mathbf{s}, \mathbf{r}_{k<\mu}, r_\mu) = p(\mathbf{r}_{k>\mu} \mid \mathbf{s}) \quad (3.4.21)$$

because the history described by \mathbf{s}' , $\mathbf{r}_{k<\mu}$ and r_μ is irrelevant once \mathbf{s} is known. Illustratively, $\beta_\mu(\mathbf{s})$ represents the probability that the sequence $\mathbf{r}_{k>\mu}$ will be received if we start at time instance μ from state \mathbf{s} . The second factor in (3.4.20) can be simplified in the same way. Once the state \mathbf{s}' at time $\mu - 1$ is known, the sequence $\mathbf{r}_{k<\mu}$ is obsolete. The probability density has the form

$$\gamma_\mu(\mathbf{s}', \mathbf{s}) := p(\mathbf{s}, r_\mu \mid \mathbf{s}') = p(r_\mu \mid \mathbf{s}', \mathbf{s}) \cdot \Pr\{\mathbf{s} \mid \mathbf{s}'\}. \quad (3.4.22)$$

Hence, it comprises the conditional probability density of the flat fading channel

$$p(r_\mu \mid \mathbf{s}', \mathbf{s}) = \frac{1}{\sqrt{\pi|h_\mu|^2 \sigma_N^2}} \cdot \exp\left(-\frac{(r_\mu - |h_\mu|^2 z^{(\mathbf{s}' \rightarrow \mathbf{s})})^2}{|h_\mu|^2 \sigma_N^2}\right). \quad (3.4.23)$$

and the a priori probability $\Pr\{d_\mu\} = \Pr\{\mathbf{s} \mid \mathbf{s}'\}$ of a bit d_μ associated with a transition from \mathbf{s}' to \mathbf{s} . According to Section 3.3.4, $z^{(\mathbf{s}' \rightarrow \mathbf{s})} = \pm \sqrt{E_s/T_s}$ in (3.4.23) denotes the code symbol corresponding to the transition from \mathbf{s}' to \mathbf{s} . If a priori knowledge is available in the form of $L_a(d_\mu)$, we obtain

$$\Pr\{\mathbf{s} \mid \mathbf{s}'\} = \begin{cases} (1 + \exp[-L_a(d_\mu)])^{-1} & \text{for } d_\mu = 0 \\ (1 + \exp[L_a(d_\mu)])^{-1} & \text{for } d_\mu = 1 \\ 0 & \text{transition does not exist.} \end{cases} \quad (3.4.24)$$

Finally, we define the joint probability density

$$\alpha_{\mu-1}(\mathbf{s}') := p(\mathbf{s}', \mathbf{r}_{k<\mu}). \quad (3.4.25)$$

Inserting (3.4.21), (3.4.23) and (3.4.25) into (3.4.20) leads to

$$L(\hat{d}_\mu) = \ln \frac{\sum_{\substack{(\mathbf{s}', \mathbf{s}) \\ d_\mu=0}} \alpha_{\mu-1}(\mathbf{s}') \cdot \gamma_\mu(\mathbf{s}', \mathbf{s}) \cdot \beta_\mu(\mathbf{s})}{\sum_{\substack{(\mathbf{s}', \mathbf{s}) \\ d_\mu=1}} \alpha_{\mu-1}(\mathbf{s}') \cdot \gamma_\mu(\mathbf{s}', \mathbf{s}) \cdot \beta_\mu(\mathbf{s})}. \quad (3.4.26)$$

Hence, the terms in the sums of (3.4.26) can be split into three parts: $\alpha_{\mu-1}(\mathbf{s}')$ covers the past $k < \mu$, $\gamma_\mu(\mathbf{s}', \mathbf{s})$ represents the presence and $\beta_\mu(\mathbf{s})$ the future $k > \mu$. The probability densities $\alpha_{\mu-1}(\mathbf{s}')$ and $\beta_\mu(\mathbf{s})$ can be calculated recursively.

$$\begin{aligned}\alpha_\mu(\mathbf{s}) &= p(\mathbf{s}, \mathbf{r}_{k<\mu+1}) = \sum_{\mathbf{s}'} p(\mathbf{s}', \mathbf{s}, \mathbf{r}_{k<\mu}, r_\mu) \\ &= \sum_{\mathbf{s}'} \gamma_\mu(\mathbf{s}', \mathbf{s}) \cdot \alpha_{\mu-1}(\mathbf{s}')\end{aligned}\quad (3.4.27)$$

$$\begin{aligned}\beta_{\mu-1}(\mathbf{s}') &= p(\mathbf{r}_{k>\mu-1} | \mathbf{s}') = \frac{1}{\Pr\{\mathbf{s}'\}} \sum_{\mathbf{s}} p(\mathbf{s}', \mathbf{s}, \mathbf{r}_\mu, \mathbf{r}_{k>\mu}) \\ &= \sum_{\mathbf{s}} \gamma_\mu(\mathbf{s}', \mathbf{s}) \cdot \beta_\mu(\mathbf{s})\end{aligned}\quad (3.4.28)$$

From (3.4.27) we see that $\alpha_\mu(\mathbf{s})$ can be calculated successively by a forward recursion because $\alpha_\mu(\mathbf{s})$ at time instance μ depends on the preceding values $\alpha_{\mu-1}(\mathbf{s}')$ at time instance $\mu - 1$. Equivalently, $\beta_{\mu-1}(\mathbf{s}')$ is determined by a backward recursion. The calculations are illustrated in **Fig. 3.4.1** showing a trellis segment with forward and backward recursion.

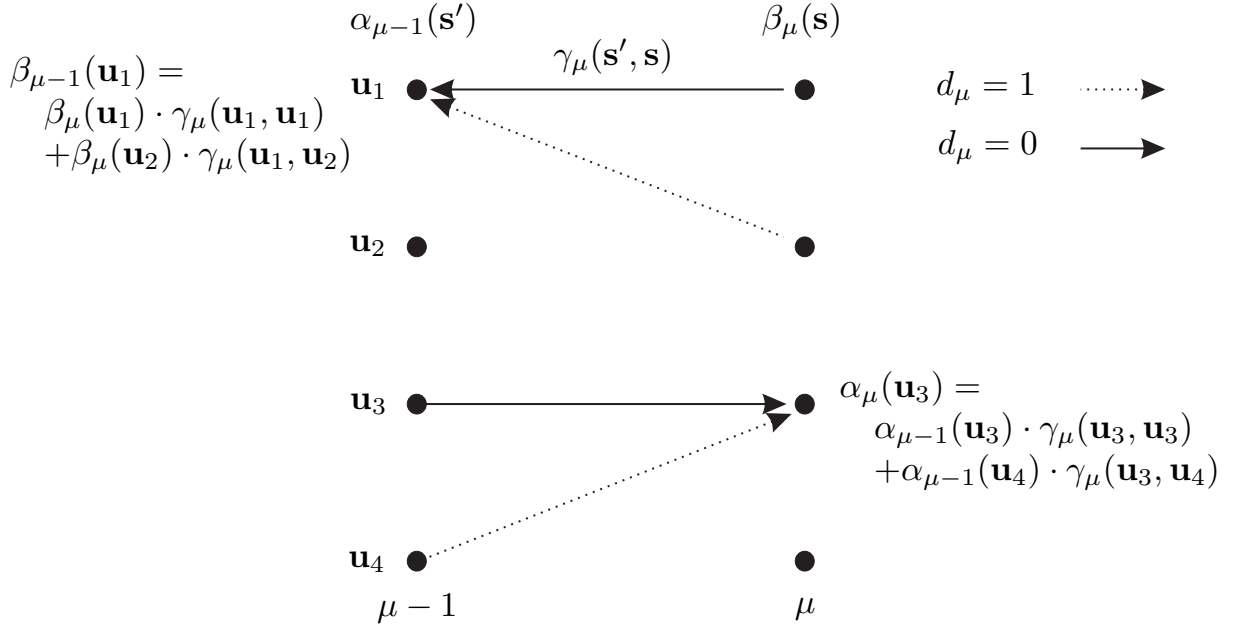


Figure 3.4.1: Section of trellis diagram for explanation of BCJR algorithm

Initialization

A recursive calculation always requires an initialization at the beginning of the procedure. Computing $\gamma_\mu(\mathbf{s}', \mathbf{s})$ and $\alpha_\mu(\mathbf{s})$ in the forward recursion is similar to

the conventional Viterbi algorithm except that no paths are discarded. At time instance $\mu = 0$, the trellis starts in the all-zero-state with the initialization

$$\alpha_0(\mathbf{s}') = \begin{cases} 1 & \text{for } \mathbf{s}' = \mathbf{0} \\ 0 & \text{for } \mathbf{s}' \neq \mathbf{0} \end{cases}. \quad (3.4.29)$$

Since block codes are represented by a terminated trellis, we end again in the all-zero-state. This leads to the initialization

$$\beta_n(\mathbf{s}) = \begin{cases} 1 & \text{for } \mathbf{s} = \mathbf{0} \\ 0 & \text{for } \mathbf{s} \neq \mathbf{0} \end{cases}. \quad (3.4.30)$$

Extended Battail Algorithm

The decoding algorithm can be simplified for linear block codes. Using the bits b_μ of a codeword $\mathbf{b} \in \Gamma$ as coefficients for linear combining the columns \mathbf{h}_μ of the parity check matrix \mathbf{H} always leads to the all-zero vector. Since the trellis representation of linear block codes also bases on the linear combination of \mathbf{h}_μ , each codeword corresponds to a certain paths through the trellis starting and ending in the all-zero state. Resolving (3.2.6) with respect to the μ th component, we obtain

$$\sum_{\nu=1}^n b_\nu \cdot \mathbf{h}_\nu \mod 2 = \mathbf{0} \quad \Rightarrow \quad b_\mu \cdot \mathbf{h}_\mu = \sum_{\substack{\nu=1 \\ \nu \neq \mu}}^n b_\nu \cdot \mathbf{h}_\nu \mod 2. \quad (3.4.31)$$

Hence, skipping the μ -th column in \mathbf{H} leads to a trellis with two possible final states. For $b_\mu = 0$, the trellis ends in the all-zero-state, for $b_\mu = 1$ it is the state $\mathbf{s} = \mathbf{h}_\mu$. **Fig. 3.4.2** illustrates the modified trellis of the Hamming code when the second column $\mathbf{h}_2 = [1 \ 0 \ 1]^T$ of \mathbf{H} is skipped (compare Fig. 3.2.1).

The extended Battail algorithm exploits this relationship and avoids a backward recursion. The extrinsic information can be calculated by [Off96]

$$L_e(\hat{d}_\mu) = \ln \alpha_n(\mathbf{0}) - \ln \alpha_n(\mathbf{h}_\mu). \quad (3.4.32)$$

Therefore, only a forward recursion similar to the Viterbi algorithm has to be performed for each bit to be estimated.

3.4.4 BCJR Algorithm for Binary Convolutional Codes

This subsection describes a symbol-by-symbol soft-output decoding algorithm for binary convolutional codes. Since most parts of the algorithm are identical to the last section, we mention only the differences. Contrarily to linear block codes, successive codewords are not mutually independent. Hence, an information sequence

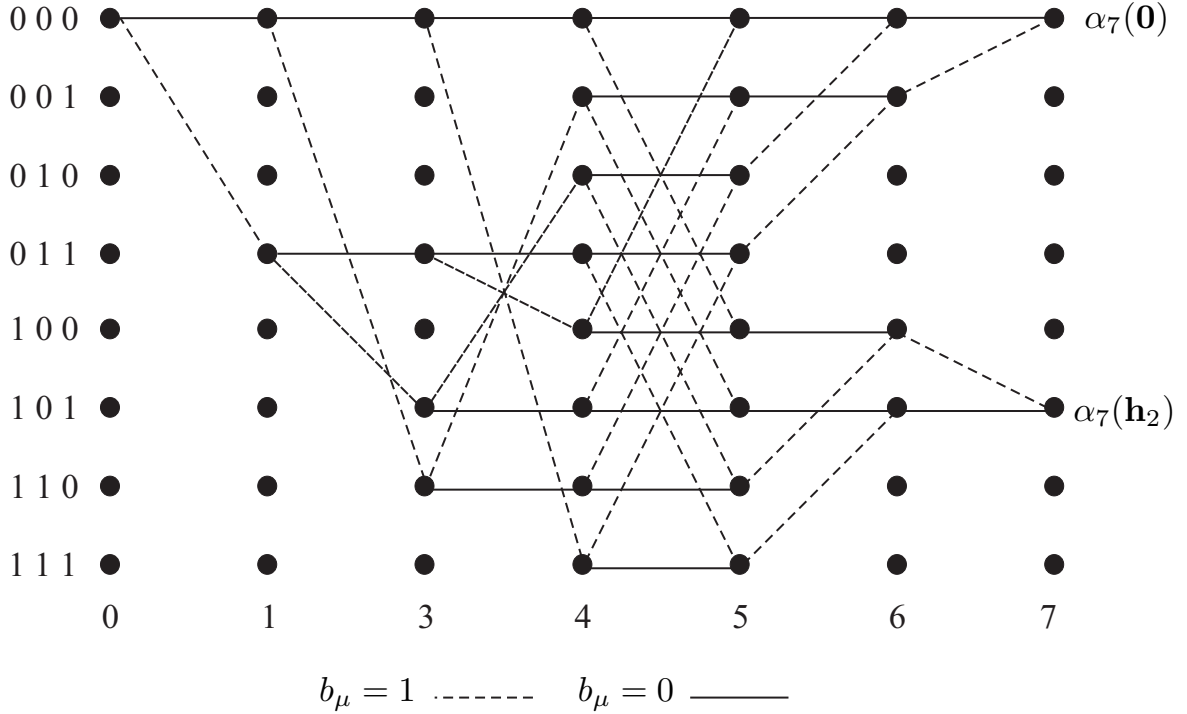


Figure 3.4.2: Modified trellis diagram of (7,4) Hamming code, second column $\mathbf{h}_2 = [1 \ 0 \ 1]^T$ of \mathbf{H} skipped

\mathbf{d} is mapped by the encoder onto a code sequence $\mathbf{b} = [\mathbf{b}[0]^T \cdots \mathbf{b}[N-1]^T]^T$ consisting of codewords $\mathbf{b}[i] = [b_1[i] \cdots b_n[i]]^T$. Consequently, the decoder processes the whole received sequence $\mathbf{r} = [\mathbf{r}[0]^T \cdots \mathbf{r}[N-1]^T]^T$ at the matched filter output instead of single codewords $\mathbf{r}[i]$.

The main difference concerns the calculation of the incremental metrics in (3.4.23), i.e. the conditional probability density of the channel. Since each segment of the trellis corresponds now to an n -bit codeword, the incremental metric becomes

$$p(\mathbf{r}[i] | \mathbf{s}', \mathbf{s}) = \prod_{\mu=1}^n \frac{1}{\sqrt{\pi |h_\mu[i]|^2 \sigma_N^2}} \cdot \exp \left(-\frac{(r_\mu[i] - |h_\mu[i]|^2 z_\mu^{(\mathbf{s}' \rightarrow \mathbf{s})})^2}{|h_\mu[i]|^2 \sigma_N^2} \right). \quad (3.4.33)$$

According to Section 3.3.4, $\mathbf{z}^{(\mathbf{s}' \rightarrow \mathbf{s})}$ denotes the codeword corresponding to the state transition $(\mathbf{s}', \mathbf{s})$. The variables $\alpha_{i-1}(\mathbf{s}')$, $\gamma_i(\mathbf{s}', \mathbf{s})$ and $\beta_i(\mathbf{s})$ are calculated in the same way as for linear block codes.

Initialization

For a terminated trellis, the same initialization as introduced in the last section can be applied. If the trellis is truncated and the last state of the encoder not known to the receiver, two different initializations of the backward recursion are

possible. On the one hand, we can use the results of the forward recursion resulting in

$$\beta_N(\mathbf{s}) = \alpha_N(\mathbf{s}) . \quad (3.4.34)$$

On the other hand, $\beta_N(\mathbf{s})$ can be set to a constant value for all $1 \leq \mathbf{s} \leq 2^{L_c-1}$

$$\beta_N(\mathbf{s}) = 2^{1-L_c} . \quad (3.4.35)$$

3.4.5 Soft-Output Decoding for Walsh Codes

Symbol-by-symbol soft-output decoding algorithm of Walsh codes can be efficiently implemented by the Fast Hadamard Transform (FHT). Unifying the three terms in (3.4.18a) into a single expression and exchanging the order of the product and the exponential function yields

$$L(\hat{d}_\mu) = \ln \frac{\sum_{\mathbf{b} \in \Gamma_\mu^{(0)}} \exp \left[- \sum_{\nu=1}^n b_\nu \cdot L(b_\nu; r_\nu) \right]}{\sum_{\mathbf{b} \in \Gamma_\mu^{(1)}} \exp \left[- \sum_{\nu=1}^n b_\nu \cdot L(b_\nu; r_\nu) \right]} \quad (3.4.36a)$$

$$= \ln \frac{\sum_{\mathbf{b} \in \Gamma_\mu^{(0)}} \exp [-\text{FHT}\{L(\mathbf{b}; \mathbf{r})\}]}{\sum_{\mathbf{b} \in \Gamma_\mu^{(1)}} \exp [-\text{FHT}\{L(\mathbf{b}; \mathbf{r})\}]} . \quad (3.4.36b)$$

From (3.4.36a) we see that each possible codeword $\mathbf{b} \in \Gamma$ has to be correlated with the LLR's $L(b_\nu; r_\nu)$ (inner sums in nominator and denominator). While this requires in general a computational effort that grows proportional to M^2 , an efficient implementation exists for Walsh codes. Applying the FHT reduces these costs by a factor down to $M \log_2(M)$ what is equivalent to the FFT algorithm. Summarizing, soft-output decoding of Walsh codes is performed by dividing the FHT outputs into two sets and inserting them into (3.4.36b).

3.4.6 Implementation in Logarithmic Domain

Regarding the implementation of the BCJR algorithm on a specific hardware, it is beneficial to perform all calculations in the logarithmic domain. This circumvents problems with the numerical representation of very large or very small numbers. Moreover, multiplications are transformed into additions reducing the computational costs remarkably. Since we generally assume Gaussian distributed background noise, the natural logarithm is predestinated.

Without loss of generality we restrict to binary codes so that only two branches leave each state \mathbf{s}' and arrive at each state \mathbf{s} . Looking at the derivations in the

previous sections, we recognize that the arguments of the logarithm are always sums. The following transformation allows us to simplify the logarithm of sums.

$$\ln(e^{x_1} + e^{x_2}) = \max[x_1, x_2] + \ln\left(1 + e^{-|x_1 - x_2|}\right) \quad (3.4.37)$$

Obviously, the expression on the left hand side is mainly transformed into a maximum search. The correction term $\ln(1 + \exp(-|x_1 - x_2|))$ only depends on the absolute difference between x_1 and x_2 and can be easily quantized. This enables the use of simple lookup tables avoiding the computation of exponential and logarithmic functions. Equation (3.4.37) can also be recursively applied to more than two terms, i.e. we start with the first two terms, then apply (3.4.37) to the intermediate result and the third term etc. [RVH95].

Using the notation for convolutional codes, the transformation of the incremental metric in (3.4.33) into the logarithmic domain delivers

$$\begin{aligned} \bar{\gamma}_i(\mathbf{s}', \mathbf{s}) &= \ln[\gamma_i(\mathbf{s}', \mathbf{s})] \\ &= C[i] - \sum_{\mu=1}^n \frac{(r_\mu[i] - |h_\mu[i]|^2 z_\mu^{(\mathbf{s}' \rightarrow \mathbf{s})})^2}{|h_\mu[i]|^2 \sigma_N^2} + \ln(\Pr\{\mathbf{s} \mid \mathbf{s}'\}) \end{aligned} \quad (3.4.38)$$

where $C[i]$ is independent from concrete state transitions and can therefore be neglected. Furthermore, calculating the square in the nominator of (3.4.38), we recognize that $r_\mu[i]^2$ and $(|h_\mu[i]|^2 z_\mu^{(\mathbf{s}' \rightarrow \mathbf{s})})^2$ do not differ for different state transitions and can also be cancelled. Consequently, we obtain

$$\begin{aligned} \bar{\gamma}_i(\mathbf{s}', \mathbf{s}) &= \sum_{\mu=1}^n 2 \frac{z_\mu^{(\mathbf{s}' \rightarrow \mathbf{s})} r_\mu[i]}{\sigma_N^2} + \ln(\Pr\{\mathbf{s} \mid \mathbf{s}'\}) \\ &= \sum_{\mu=1}^n \frac{1}{2} L(r_\mu[i] \mid b_\mu) z_\mu^{(\mathbf{s}' \rightarrow \mathbf{s})} + \ln(\Pr\{\mathbf{s} \mid \mathbf{s}'\}) \end{aligned} \quad (3.4.39)$$

Hence, only a sum of log-likelihood ratios has to be calculated rather than probability densities. The a priori probabilities in (3.4.39) can be substituted by applying (3.4.2a) and (3.4.37)

$$\begin{aligned} \ln(\Pr\{\mathbf{s} \mid \mathbf{s}'\}) &= -\ln\left(1 + e^{\pm L_a(d[i])}\right) \\ &= -\max[0, \pm L_a(d[i])] + \ln\left(1 + e^{-|L_a(d[i])|}\right). \end{aligned} \quad (3.4.40)$$

In (3.4.40), the plus sign holds for the transition $(\mathbf{s}' \rightarrow \mathbf{s})$ corresponding to an information bit $d[i] = 0$, and, consequently the minus sign for $d[i] = 1$. For $\bar{\alpha}_i(\mathbf{s}) = \ln[\alpha_i(\mathbf{s})]$ and $\bar{\beta}_{i-1}(\mathbf{s}') = \ln[\beta_{i-1}(\mathbf{s}')]$ we obtain the expressions

$$\begin{aligned}\bar{\alpha}_i(\mathbf{s}) &= \ln \sum_{\mathbf{s}'} \exp \left[\ln (\gamma_i(\mathbf{s}', \mathbf{s}) \cdot \alpha_{i-1}(\mathbf{s}')) \right] \\ &= \max_{\mathbf{s}'} [\bar{\gamma}_i(\mathbf{s}', \mathbf{s}) + \bar{\alpha}_{i-1}(\mathbf{s}')] + \ln \left(1 + e^{-|\Delta[i]|} \right)\end{aligned}\quad (3.4.41)$$

and

$$\begin{aligned}\bar{\beta}_{i-1}(\mathbf{s}') &= \ln \sum_{\mathbf{s}} \exp \left[\ln (\gamma_i(\mathbf{s}', \mathbf{s}) \cdot \beta_i(\mathbf{s})) \right] \\ &= \max_{\mathbf{s}} [\bar{\gamma}_i(\mathbf{s}', \mathbf{s}) + \bar{\beta}_i(\mathbf{s})] + \ln \left(1 + e^{-|\Delta[i]|} \right).\end{aligned}\quad (3.4.42)$$

In (3.4.41) and (3.4.42), $\Delta[i]$ denotes the difference between those terms the maximum is taken from. Looking at the last equations and assuming that the correction term is obtained by a lookup table, it becomes obvious that no exponential or logarithmic functions have to be calculated. All multiplications are transformed into additions and all additions into maximizations. Therefore, the computational costs are reduced remarkably without loss in performance. This version of the BCJR algorithm is often called log-MAP [RHV97].

An approximation of the BCJR algorithm which reduces the computational complexity additionally is obtained if the correction terms are neglected. This results in the so-called Max-Log-MAP algorithm. It can be shown that the hard decision of its output values equals the output of the Viterbi decoder [RVH95]. The whole output can be described by

$$\begin{aligned}L(\hat{d}[i]) &= \max_{\substack{(\mathbf{s}', \mathbf{s}) \\ d[i]=0}} [\bar{\alpha}_{i-1}(\mathbf{s}') + \bar{\gamma}_i(\mathbf{s}', \mathbf{s}) + \bar{\beta}_i(\mathbf{s})] \\ &\quad - \max_{\substack{(\mathbf{s}', \mathbf{s}) \\ d[i]=1}} [\bar{\alpha}_{i-1}(\mathbf{s}') + \bar{\gamma}_i(\mathbf{s}', \mathbf{s}) + \bar{\beta}_i(\mathbf{s})].\end{aligned}\quad (3.4.43)$$

Concerning the initialization,

$$\alpha_0(\mathbf{s}') = \begin{cases} 0 & \text{for } \mathbf{s}' = \mathbf{0} \\ -\infty & \text{for } \mathbf{s}' \neq \mathbf{0} \end{cases}\quad (3.4.44)$$

and

$$\beta_N(\mathbf{s}) = \begin{cases} 0 & \text{for } \mathbf{s} = \mathbf{0} \\ -\infty & \text{for } \mathbf{s} \neq \mathbf{0} \end{cases}\quad (3.4.45)$$

holds for a terminated trellis. In case of a truncated trellis, $\beta_N(\mathbf{s}) \equiv \mathbf{0}$ can be used. There exist also an extension of the Viterbi algorithm that delivers soft outputs. The so-called Soft-Output Viterbi Algorithm (SOVA) is described in [HH89].

3.5 Performance Evaluation of Linear Codes

3.5.1 Distance Properties of Codes

The performance of a code is only asymptotically determined by its minimum Hamming distance d_{\min} , i.e. for high signal to noise ratios. For low and medium SNRs the whole distance spectrum, i.e. all distances that can occur between pairs of codewords, has to be considered. Determining the distance spectrum of a code may become very demanding especially for extremely long codes. A simplification occurs for linear codes allowing us to restrict the comparison of each codeword $\mathbf{b} \in \Gamma$ with the all-zero-word instead of calculating its Hamming distances to all other words in Γ . The distance to the all-zero-word is obtained by simply counting the nonzero symbols in \mathbf{b} , and, therefore, determining its Hamming weight $w_H(\mathbf{b})$. The whole spectrum of a code can be expressed by the polynomial

$$A(D) = \sum_{\mathbf{b} \in \Gamma} D^{w_H(\mathbf{b})} = \sum_{d=0}^n A_d \cdot D^d = 1 + \sum_{d=d_{\min}}^n A_d \cdot D^d. \quad (3.5.1)$$

The coefficients A_d represent the number of codewords \mathbf{b} with weight $w_H(\mathbf{b}) = d$. Therefore, the relation $\sum_{d=0}^n A_d = 2^k = |\Gamma|$ holds, i.e. the sum of all coefficients A_d equals the number of codewords. For convolutional codes, A_d describes the number of code sequences with weight d . Minimum weight and distance spectrum solely depend on the code and not on the encoder.

If concatenated codes are considered or the bit error rate has to be determined, the so-called IOWEF (Input Output Weight Enumerating Function) [BM96b, BM96a, BMDP96] is of importance. It not only reflects the weight d of the coded bits but also the weight w of the corresponding information bits. Therefore, it describes the input and output relationship of the encoder. The IOWEF is obtained by simply counting the number of nonzero symbols for each pair of input and output vectors of the encoder leading to a two-dimensional polynomial

$$A(W, D) = \sum_{w=0}^k \sum_{d=0}^n A_{w,d} \cdot W^w D^d = 1 + \sum_{w=1}^k \sum_{d=d_{\min}}^n A_{w,d} \cdot W^w D^d. \quad (3.5.2)$$

In (3.5.2), $A_{w,d}$ denote the number of codewords with weight d and weight w of the associated information vector \mathbf{d} . Certainly, $\sum_w A_{w,d} = A_d$ holds. Especially for concatenated codes, we need conditional IOWEF's that are restricted to only a single input weight w

$$A(w, D) = \sum_{d=0}^n A_{w,d} \cdot D^d \quad (3.5.3)$$

or a single output weight d

$$A(W, d) = \sum_{w=0}^k A_{w,d} \cdot W^w . \quad (3.5.4)$$

Finally, calculating the bit error probability requires the coefficients

$$C_d = \frac{1}{k} \cdot \frac{\partial}{\partial W} A(W, d) \Big|_{W=0} = \sum_{w=1}^k \frac{w}{k} \cdot A_{w,d} \quad (3.5.5)$$

because they represent the average number of nonzero information bits including all sequences with output weight d .

IOWEF for some Linear Block Codes

As already mentioned, it is a demanding task to determine the IOWEF $A(W, D)$ or even $A(D)$ for arbitrary codes. Only for distinct or very simple codes, closed form expressions are known. Here, we illustrate distance spectra and IOWEF for some linear block codes considered in this thesis. Starting with the $(n, 1, n)$ -repetition code from page 94, we recall that it consists only of two codewords, the all-zero-word and the all-one-word with weight n . Hence, the distance spectrum has the form $A(D) = 1 + D^n$ and the IOWEF becomes $A(W, D) = 1 + WD^n$.

Looking at the $(n, n - 1, 2)$ -single parity check code of Subsection 3.2.2, we know that only even weights occur. Since $\binom{n-1}{w}$ denotes the number of possibilities to arrange w ones in the information part of length $k = n - 1$, we obtain the IOWEF

$$A(W, D) = \sum_{w=0}^{n-1} \binom{n-1}{w} \cdot W^w \cdot D^{\lfloor \frac{w+1}{2} \rfloor \cdot 2} \quad (3.5.6)$$

where $\lfloor x \rfloor$ denotes the largest integer smaller than x . The distance spectrum becomes

$$A(D) = \sum_{d=0}^{\lfloor \frac{n-1}{2} \rfloor} \binom{n}{2d} \cdot D^{2d} + \begin{cases} 0 & \text{for } n \text{ is odd} \\ D^n & \text{for } n \text{ is even} . \end{cases} \quad (3.5.7)$$

Next, we look at the Simplex code with $n = 2^r - 1$ and $k = r$. All its codewords have a Hamming weight of $w_H(\mathbf{b}) = 2^{r-1}$ (except the all-zero-word). Hence, the distance spectrum has the form

$$A(D) = 1 + (2^r - 1) \cdot D^{2^{r-1}} \quad (3.5.8)$$

and the IOWEF becomes

$$A(W, D) = 1 + \sum_{w=1}^{k=r} \binom{r}{w} \cdot W^w D^{2^{r-1}} . \quad (3.5.9)$$

Since the Hadamard code of Subsection 3.2.4 has been obtained by extending each codeword of the Simplex code by a preceding zero, their distance spectra and IOWEFs are identical.

Finally, we consider the Hamming code of order r that is the dual code of the Simplex code. Distance spectrum of dual codes are related to each other by the MacWilliams identity [PW72, Bla83, Fri96]

$$A^\perp(D) = 2^{-k} \cdot (1 + D)^n \cdot A\left(\frac{1 - D}{1 + D}\right) \quad (3.5.10)$$

where n and k are given by the original (n,k) -code Γ . In our case, the Simplex code serves as original code with $n = 2^r - 1$ and $k = r$. Applying (3.5.10) to (3.5.8) yields

$$A(D) = (1 - 2^{-r}) \cdot (1 - D)(1 - D^2)^{2^{r-1}-1} + 2^{-r} \cdot (1 + D)^{2^r-1} \quad (3.5.11a)$$

$$= \frac{n}{n+1} \cdot (1 - D)(1 - D^2)^{\frac{n-1}{2}} + \frac{1}{n+1} \cdot (1 + D)^n \quad (3.5.11b)$$

for the Hamming code.

IOWEF for Convolutional Codes

We now have a look at the IOWEF of convolutional codes. We start the derivation with the modification of the finite state diagram from Fig. 3.3.2a by cutting the self-loop in the all-zero-state. Defining the all-zero-state as starting and ending point results in a structure depicted in **Fig. 3.5.1**. Each branch is labelled with a polynomial denoting the input weight w and the output weight d of the corresponding state transition. The weight of a sequence of successive transitions is calculated by multiplying their polynomial terms. The whole IOWEF is obtained by summing the polynomials of all possible paths starting and ending in the all-zero-state.

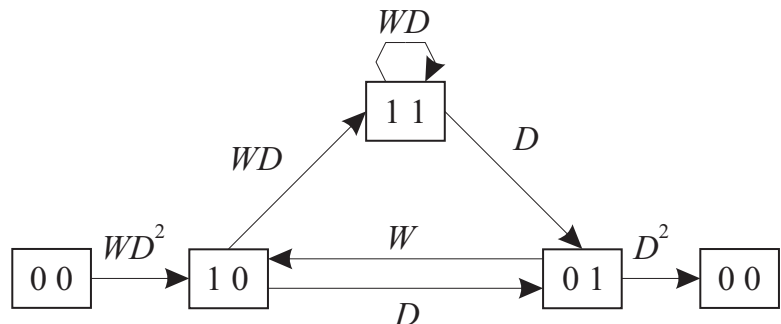


Figure 3.5.1: Modified trellis diagram for determining IOWEF of convolutional code from Fig. 3.3.2a

First, we consider a continuous data transmission with only a single divergence from the all-zero sequence. The above mentioned procedure can be mathematically described by a series of the form

$$A(W, D) = \sum_{i=0}^{\infty} \underline{\mathbf{a}}_{\setminus\{0\}} \cdot \underline{\mathbf{\Xi}}_{\setminus\{0\}}^i \cdot \underline{\mathbf{b}}_{\setminus\{0\}}, \quad (3.5.12)$$

where the matrix

$$\underline{\mathbf{\Xi}}_{\setminus\{0\}} = \begin{bmatrix} 0 & W & 0 \\ D & 0 & WD \\ D & 0 & WD \end{bmatrix} \quad (3.5.13)$$

comprises the labels of all possible state transitions excluding the all-zero-state. An element $\Xi_{\nu\mu}$ represents the label of the transition from state ν into state μ where the indices are the decimal representations of the state vectors \mathbf{s}' and \mathbf{s} consisting of binary elements. For example, the second row describes the branches leaving state $\mathbf{s}' = [1 0]^T$, i.e. $\Xi_{21} = D$ belongs to the transition to state $\mathbf{s} = [0 1]^T$ with zero input weight and an output weight of one and $\Xi_{23} = WD$ to the transition to state $\mathbf{s} = [1 1]^T$. Since a self-loop does not exist in state $\mathbf{s}' = [1 0]^T$, $\Xi_{22} = 0$ holds. According to Fig. 3.5.1, we start from the all-zero state always with a transition into state $\mathbf{s} = [1 0]^T$ with label WD^2 . This is ensured by the row vector $\underline{\mathbf{a}}_{\setminus\{0\}} = [0 \ WD^2 \ 0]$. Equivalently, we reach the all-zero-state only from state $\mathbf{s}' = [0 1]^T$ with label D^2 described by vector $\underline{\mathbf{b}}_{\setminus\{0\}} = [D^2 \ 0 \ 0]^T$. For a practical implementation, the series is truncated after a certain number of transitions.

For concatenated codes, we have to regard a block-wise transmission and especially multiple divergences from the all-zero-sequence. This can be accomplished by extending the matrix in (3.5.13). Including all transitions from and into the all-zero-state, we obtain

$$\mathbf{\Xi} = \begin{bmatrix} 1 & 0 & WD^2 & 0 \\ D^2 & & & \\ 0 & \mathbf{\Xi}_{\setminus\{0\}} & & \\ 0 & & & \end{bmatrix} = \begin{bmatrix} 1 & 0 & WD^2 & 0 \\ D^2 & 0 & W & 0 \\ 0 & D & 0 & WD \\ 0 & D & 0 & WD \end{bmatrix} \quad (3.5.14)$$

and the modified vectors $\underline{\mathbf{a}} = [1 \ 0 \ 0 \ 0]$ and $\underline{\mathbf{b}} = [1 \ 0 \ 0 \ 0]^T$.

Fig. 3.5.2 shows the coefficients A_d and C_d for two convolutional codes with constraint lengths $L_c = 4$ and $L_c = 9$ and a common code rate $R_c = 1/2$. Obviously, A_d and C_d increase exponentially with the distance d . The free distance of a code corresponds to the first nonzero coefficient A_d (excluding the all-zero-word) and amounts to $d_f = 6$ for the $L_c = 4$ code and $d_f = 12$ for $L_c = 9$. Hence, d_f becomes larger for increasing constraint length L_c .

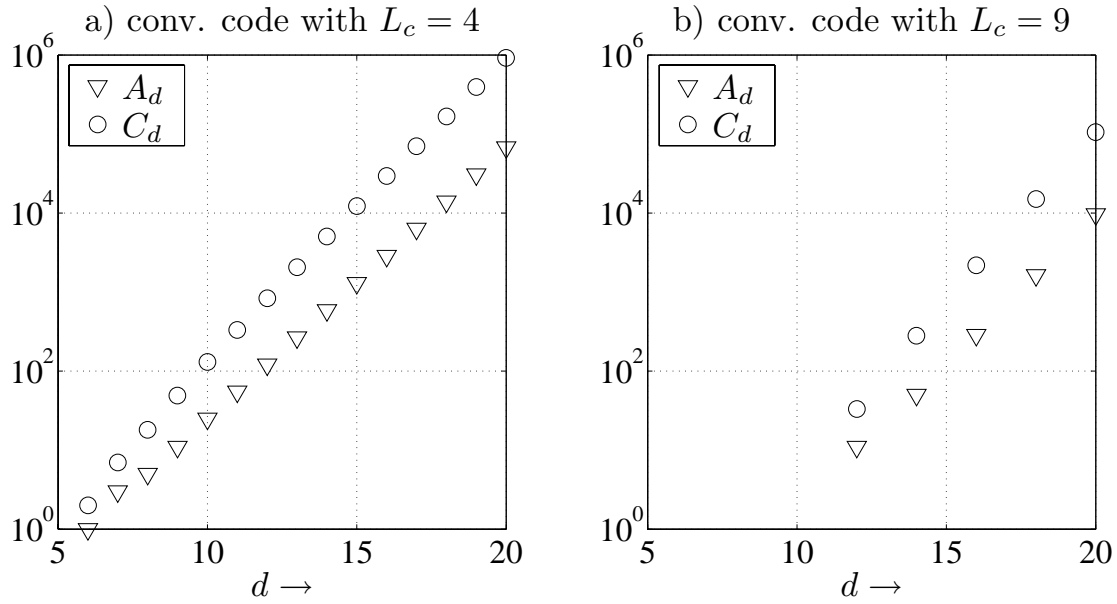


Figure 3.5.2: Coefficients A_d and C_d for different convolutional codes [Pro95]
a) $g_1 = 17_8$ and $g_2 = 15_8$, **b)** $g_1 = 561_8$ and $g_2 = 753_8$

3.5.2 Error Rate Performance of Codes

The analytical evaluation of the error rate performance of codes is based on the maximum likelihood detection already described in Section 3.1. Since a codeword consists of n symbols, the detection cannot be performed symbol-wise but has to consider the whole codeword. For convolutional codes, n has to be replaced by the total number nN of symbols in a sequence. Since we restrict to BPSK, the vectors \mathbf{b} and \mathbf{x} are linearly related to each other and can be used equivalently. The derivation will be divided into 2 parts: We start with the AWGN channel and succeed with flat fading channels.

Error Rate Performance for AWGN Channel

Without loss of generality, we assume that we transmit the all-zero-word $\mathbf{b} = \mathbf{0}_{n \times 1}$, i.e. $\mathbf{x}^{(0)} = [\sqrt{E_s/T_s} \cdots \sqrt{E_s/T_s}]^T$ holds. The matched filter output has the form

$$\mathbf{r} = \text{Re}\{\mathbf{y}\} = \mathbf{x}^{(0)} + \mathbf{n}' \quad (3.5.15)$$

where $\mathbf{n}' = \text{Re}\{\mathbf{n}\}$ contains the Gaussian distributed noise samples with zero mean and the variance $\sigma_{\mathcal{N}'}^2 = N_0/(2T_s)$. According to Section 3.1, the optimum detector in (3.1.2) determines the word \mathbf{x} with the largest conditional density $p_{\mathcal{R}|\mathbf{x}}(\mathbf{r})$. The set

$$\mathbb{M}_{0,i} = \{\mathbf{r} \mid p_{\mathcal{R}|\mathbf{x}^{(i)}}(\mathbf{r}) > p_{\mathcal{R}|\mathbf{x}^{(0)}}(\mathbf{r})\} = \{\mathbf{r} \mid \mathbf{r}^T \mathbf{x}^{(i)} > \mathbf{r}^T \mathbf{x}^{(0)}\} \quad (3.5.16)$$

comprises all received vectors $\mathbf{r} = [r_1 \cdots r_n]^T$ that have a larger conditional probability with respect to $\mathbf{x}^{(i)}$ than to the true $\mathbf{x}^{(0)}$. Therefore, these vectors would lead to a wrong decision. Rewriting the inner product in (3.5.16) and inserting (3.5.15) delivers the pairwise error probability⁷

$$\begin{aligned} \Pr\{\mathbf{x}^{(0)} \rightarrow \mathbf{x}^{(i)}\} &= \Pr\{\mathbf{r} \in \mathbb{M}_{0,i} \mid \mathbf{x}^{(0)}\} \\ &= \Pr\left\{\sum_{\nu=1}^n r_\nu x_\nu^{(0)} < \sum_{\nu=1}^n r_\nu x_\nu^{(i)}\right\} \\ &= \Pr\left\{\sum_{\nu=1}^n (x_\nu^{(0)} - x_\nu^{(i)}) n'_\nu < -\sum_{\nu=1}^n (x_\nu^{(0)} - x_\nu^{(i)}) x_\nu^{(0)}\right\}. \end{aligned} \quad (3.5.17)$$

Due to the assumption $x_\nu^{(0)} \equiv \sqrt{E_s/T_s}$ the differences between $x_\nu^{(0)}$ and $x_\nu^{(i)}$ take only the values 0 and $2\sqrt{E_s/T_s}$. Since $\mathbf{x}^{(0)}$ and $\mathbf{x}^{(i)}$ differ in exactly $d_H(\mathbf{x}^{(0)}, \mathbf{x}^{(i)})$ positions, the left hand side of the inequality in (3.5.17) describes a zero mean Gaussian distributed variable η with variance $\sigma_\eta^2 = 4d_H(\mathbf{x}^{(0)}, \mathbf{x}^{(i)})\sigma_{N'}^2 E_s/T_s$. The right hand side has the constant value $-2d_H(\mathbf{x}^{(0)}, \mathbf{x}^{(i)})E_s/T_s$. Equivalent to (1.3.15), we obtain with the pairwise error probability

$$P_d = \Pr\{\mathbf{x}^{(0)} \rightarrow \mathbf{x}^{(i)}\} = \frac{1}{2} \cdot \operatorname{erfc}\left(\sqrt{d_H(\mathbf{x}^{(0)}, \mathbf{x}^{(i)}) \cdot E_s/N_0}\right). \quad (3.5.18)$$

for two codewords $\mathbf{x}^{(0)}$ and $\mathbf{x}^{(i)}$ with Hamming distance $d_H(\mathbf{x}^{(0)}, \mathbf{x}^{(i)})$. An average error probability for $\mathbf{x}^{(0)}$ can be obtained by calculating (3.5.18) for the union over all sets $\mathbb{M}_{0,i}$ for $i \neq 0$. However, it may become very difficult to exactly determine $\cup_i \mathbb{M}_{0,i}$. A good approximation yields the well-known union bound [Pro95, Bos99]

$$\begin{aligned} P_e(\mathbf{x}^{(0)}) &= \Pr\left\{\mathbf{r} \in \bigcup_{i=1}^{2^k-1} \mathbb{M}_{0,i} \mid \mathbf{x}^{(0)}\right\} \leq \sum_{i=1}^{2^k-1} \Pr\left\{\mathbf{r} \in \mathbb{M}_{0,i} \mid \mathbf{x}^{(0)}\right\} \\ &\leq \frac{1}{2} \sum_{i=1}^{2^k-1} \operatorname{erfc}\left(\sqrt{d_H(\mathbf{x}^{(0)}, \mathbf{x}^{(i)}) \frac{E_s}{N_0}}\right) \end{aligned} \quad (3.5.19)$$

where the equality holds if and only if all sets $\mathbb{M}_{0,i}$ are disjoint. Due to the linearity of the considered codes, (3.5.19) is not only valid for a specific $\mathbf{x}^{(0)}$ but represents the general probability of a decoding failure. The argument of the complementary error function only depends on the Hamming distances and the signal to noise ratio. Therefore, instead of running over all competing codewords or sequences, we can simply use the distance spectrum defined in (3.5.1) to rewrite (3.5.19)

⁷We apply the same simplifications as in footnote 6 on page 22.

$$P_e \leq \frac{1}{2} \sum_{d=d_{\min}}^n A_d \cdot \operatorname{erfc} \left(\sqrt{d \frac{E_s}{N_0}} \right) = \sum_{d=d_{\min}}^n A_d \cdot P_d . \quad (3.5.20)$$

Regarding bit error probabilities, we have to consider the specific mapping of information vectors \mathbf{d} onto code vectors \mathbf{b} or, equivalently, \mathbf{x} . This can be accomplished by replacing the coefficients A_d in (3.5.20) by C_d defined in (3.5.5). We obtain

$$P_b \leq \frac{1}{2} \sum_{d=d_{\min}}^n C_d \cdot \operatorname{erfc} \left(\sqrt{d \frac{E_s}{N_0}} \right) = \frac{1}{2} \sum_{d=d_{\min}}^n C_d \cdot \operatorname{erfc} \left(\sqrt{d R_c \frac{E_b}{N_0}} \right) . \quad (3.5.21)$$

The union bound approximation of the bit error rate for an NSC code with generators $g_1 = 15_8$ and $g_2 = 17_8$ is illustrated in **Fig. 3.5.3**. The results have been obtained from (3.5.21) by replacing n as upper limit of the summation by the parameter d_{\max} . For high signal to noise ratios, the asymptotic performance is dominated by the minimum Hamming distance d_f as can be seen from $d_{\max} = d_{\min} = d_f$. For medium signal to noise ratios, also higher Hamming distances have to be included. However, for small SNR's, the union bound diverges for large d_{\max} as the comparison with the simulation results show.

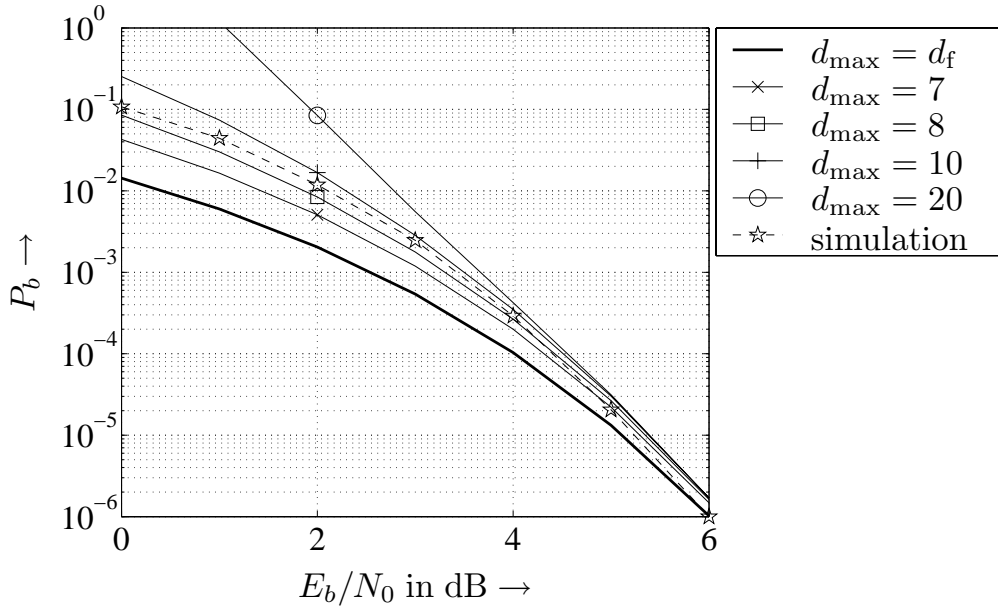


Figure 3.5.3: Bit error probabilities for convolutional code with $g_1 = 15_8$ and $g_2 = 17_8$ and different maximum distances considered for union bound (AWGN)

Fig. 3.5.4 shows the bit error rates for convolutional codes with different constraint length L_c . Obviously, the performance increases with growing memory. However, also the decoding costs grow exponentially with the constraint length. Hence, a trade-off between performance and complexity has to be found. Since the

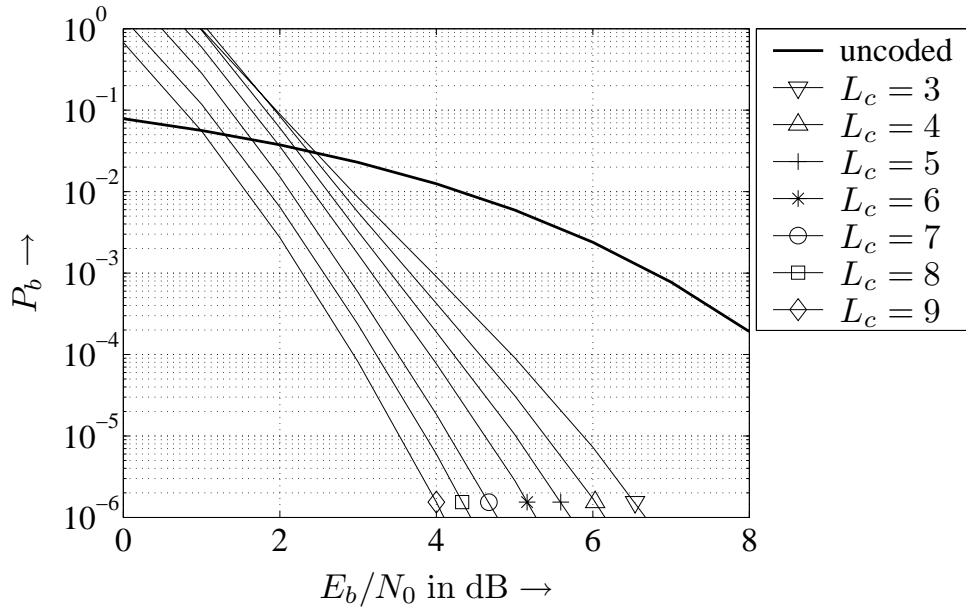


Figure 3.5.4: Bit error probabilities for convolutional codes of different constraint lengths [Pro95] and AWGN channel (union bound)

additional gains are getting smaller for growing L_c , it is questionable if Shannon's channel capacity of can be reached by simply enlarging the memory of convolutional codes. Concerning this goal, concatenated codes presented in Section 3.6 are more promising.

Error Rate Performance for Flat Fading Channels

For flat fading channels, only the pairwise error probability has to be recalculated. Each symbol x_ν is weighted with a complex channel coefficient h_ν of unit average power. Assuming that the coefficients are perfectly known to the receiver, the output of the matched filter has the form

$$r_\nu = h_\nu^* \cdot y_\nu = |h_\nu|^2 x_\nu^{(0)} + \operatorname{Re} \{h_\nu^* n_\nu\} = |h_\nu|^2 x_\nu^{(0)} + \tilde{n}_\nu \quad (3.5.22)$$

and the probability in (3.5.17) becomes

$$\begin{aligned} \Pr\{\mathbf{r} \in \mathbb{M}_{0,i} \mid \mathbf{x}^{(0)}, \mathbf{h}\} \\ = \Pr \left\{ \sum_{\nu=1}^n (x_\nu^{(0)} - x_\nu^{(i)}) \tilde{n}_\nu < - \sum_{\nu=1}^n (x_\nu^{(0)} - x_\nu^{(i)}) |h_\nu|^2 x_\nu^{(0)} \right\}. \end{aligned} \quad (3.5.23)$$

Again, the differences between $x_\nu^{(0)}$ and $x_\nu^{(i)}$ take only the values 0 and $2\sqrt{E_s/T_s}$. We define now the set \mathbb{L} of those indices ν for which $x_\nu^{(0)}$ and $x_\nu^{(i)}$ differ. Obviously, \mathbb{L} consists of $d_H(\mathbf{x}^{(0)}, \mathbf{x}^{(i)})$ elements. The right hand side of the inequality in

(3.5.23) has the constant value $-2E_s/T_s \sum_{\nu \in \mathbb{L}} |h_\nu|^2$. Since the noise is circularly symmetric, the left hand side is a zero mean Gaussian distributed variable η with variance

$$\sigma_\eta^2 = 4 \frac{E_s}{T_s} \cdot \frac{\sigma_N^2}{2} \cdot \sum_{\nu \in \mathbb{L}} |h_\nu|^2 = 2 \frac{E_s N_0}{T_s^2} \cdot \sum_{\nu \in \mathbb{L}} |h_\nu|^2 . \quad (3.5.24)$$

We obtain the pairwise error probability

$$\Pr\{\mathbf{x}^{(0)} \rightarrow \mathbf{x}^{(i)} \mid \mathbf{h}\} = \frac{1}{2} \cdot \operatorname{erfc} \left(\sqrt{\sum_{\nu \in \mathbb{L}} |h_\nu|^2 \cdot E_s / N_0} \right) . \quad (3.5.25)$$

Determining its expectation requires averaging over all contributing channel coefficients h_ν with $\nu \in \mathbb{L}$. We distinguish two cases.

Block Fading Channel

For a block fading channel where all n symbols of a codeword are affected by the same channel coefficient $h_\nu = h$, the sum in (3.5.25) becomes $d_H(\mathbf{x}^{(0)}, \mathbf{x}^{(i)}) \cdot |h|^2$. In this case, we have to average over a single coefficient and can exploit the results of Section 1.3. For a Rayleigh fading channel with $\sigma_h^2 = 1$, we obtain

$$P_d = \Pr\{\mathbf{x}^{(0)} \rightarrow \mathbf{x}^{(i)}\} = \frac{1}{2} \left[1 - \sqrt{\frac{d_H(\mathbf{x}^{(0)}, \mathbf{x}^{(i)}) E_s / N_0}{1 + d_H(\mathbf{x}^{(0)}, \mathbf{x}^{(i)}) E_s / N_0}} \right] . \quad (3.5.26)$$

Inserting (3.5.26) into the right hand side of (3.5.20) provides the ergodic error probability $P_e \leq \sum_{d=d_{\min}}^n A_d \cdot P_d$. However, the union bound technique applied on convolutional codes and block fading channels does only converge for extremely high signal to noise ratios. Even for SNR's in the range of 20 dB - 30 dB, the results are not meaningful at all.

Perfectly Interleaved Channel

If the channel is perfectly interleaved, the coefficients h_ν are statistically independent from each other and identically distributed. In this case, we use again the equivalent expression for the complementary error function already known from Section 1.3 and (3.5.25) becomes

$$\Pr\{\mathbf{x}^{(0)} \rightarrow \mathbf{x}^{(i)} \mid \mathbf{h}\} = \frac{1}{\pi} \cdot \int_0^{\pi/2} \exp \left[\frac{\sum_{\nu \in \mathbb{L}} |h_\nu|^2 \cdot E_s / N_0}{\sin^2(\theta)} \right] d\theta . \quad (3.5.27)$$

The ergodic error probability has to be calculated by averaging (3.5.27) with respect to the set of channel coefficients h_ν for $\nu \in \mathbb{L}$. This procedure was already applied for diversity reception in Section 1.3. Hence, it becomes obvious that

coding over time-selective channels can exploit diversity. The achievable diversity degree depends on the coherence time of the channel and the data rate. We denote the process comprising $d_H(\mathbf{x}^{(0)}, \mathbf{x}^{(i)})$ channel coefficients by $\underline{\mathcal{H}}$. The moment generating function $\mathcal{M}_{|\underline{\mathcal{H}}|^2}(s)$ of the squared magnitudes $|h_\nu|^2$, $\nu \in \mathbb{L}$, requires a multivariate integration which can be separated into single integrations for i.i.d. coefficients h_ν . With

$$\mathcal{M}_{|\underline{\mathcal{H}}|^2}(s) = \int_0^\infty e^{s\xi} \cdot p_{|\underline{\mathcal{H}}|^2}(\xi) d\xi = \left[\int_0^\infty e^{s\xi} \cdot p_{|\mathcal{H}|^2}(\xi) d\xi \right]^{d_H(\mathbf{x}^{(0)}, \mathbf{x}^{(i)})}. \quad (3.5.28)$$

and the substitution $s = -\frac{E_s/N_0}{\sin^2(\theta)}$ we finally obtain

$$\Pr\{\mathbf{x}^{(0)} \rightarrow \mathbf{x}^{(i)}\} = \frac{1}{\pi} \cdot \int_0^{\pi/2} \left[\mathcal{M}_{|\mathcal{H}|^2} \left(-\frac{E_s/N_0}{\sin^2(\theta)} \right) \right]^{d_H(\mathbf{x}^{(0)}, \mathbf{x}^{(i)})} d\theta. \quad (3.5.29)$$

Inserting the results already known for Rayleigh fading with $\sigma_{\mathcal{H}}^2 = 1$ (cf. (1.3.22)) and Rice fading with $P = 1$ (cf. (1.3.24)) finally leads to the union bound approximations

$$P_e^{\text{Rayleigh}} \leq \frac{1}{\pi} \sum_{d=d_{\min}}^n A_d \cdot \int_0^{\pi/2} \left(\frac{\sin^2(\theta)}{\sin^2(\theta) + \sigma_{\mathcal{H}}^2 E_s / N_0} \right)^d d\theta \quad (3.5.30)$$

$$P_e^{\text{Rice}} \leq \frac{1}{\pi} \sum_{d=d_{\min}}^n A_d \cdot \int_0^{\pi/2} \left(\frac{(1+K) \sin^2(\theta)}{(1+K) \sin^2(\theta) + E_s / N_0} \right)^d \cdot \exp \left[-\frac{d K E_s / N_0}{(1+K) \sin^2(\theta) + E_s / N_0} \right] d\theta, \quad (3.5.31)$$

respectively. Again, bit error probabilities are obtained by replacing the coefficients A_d in by C_d defined in (3.5.5).

The corresponding error probability curves are depicted in **Fig. 3.5.5a** for a Rayleigh fading channel and convolutional codes of different constraint lengths. Since the free distance d_f of a code determines the diversity degree for perfect interleaved fading channels, the slopes of the curves become steeper with increasing L_c and, thus, growing d_f . In order to evaluate the diversity degree of each code, the dashed lines represent the theoretical steepness for the associated diversity order d_f . Obviously, the solid lines are parallel to the dashed lines indicating the same slope.

In **Fig. 3.5.5b**, the results for a half-rate code with $L_c = 4$ and a Rice fading channel with unit power P are depicted. As expected, the AWGN performance is approached for increasing Rice factor K . **Fig. 3.5.6** demonstrates the tightness of the union bound for medium and high signal to noise ratios. At low SNR's, it diverges and different bounding techniques should be preferred.

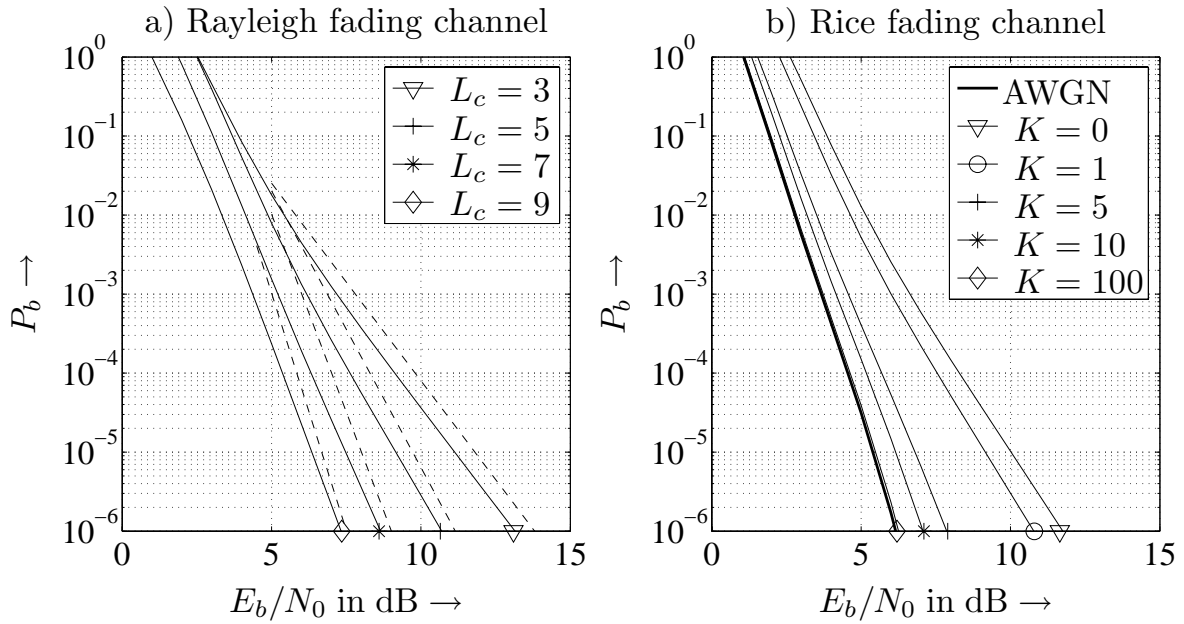


Figure 3.5.5: Bit error probabilities for convolutional codes (union bound)

- a) Different constraint lengths and Rayleigh fading channel
- b) $g_1 = 15_8$ and $g_2 = 17_8$ and Rice fading channels

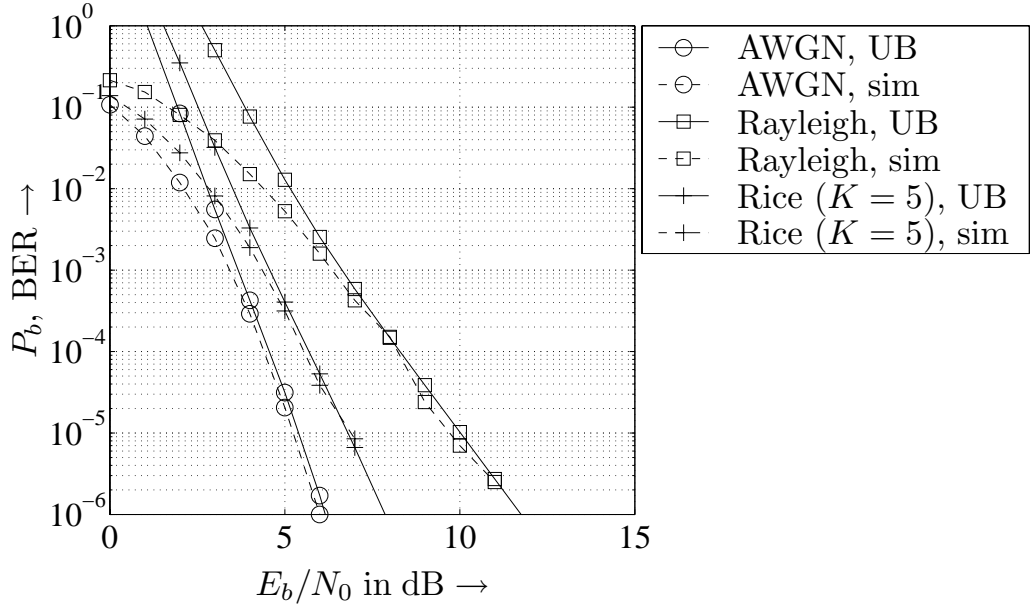


Figure 3.5.6: Comparison of union bound and simulation for convolutional code with $g_1 = 15_8$ and $g_2 = 17_8$ and different channels

3.5.3 Information Processing Characteristic

Applying the union bound to evaluate the error rate performance of codes always assumes optimal maximum likelihood decoding. However, especially for concatenated codes (cf. Section 3.6), optimum decoding is not feasible and non-optimum

techniques like turbo decoding have to be applied. In order to verify the performance of encoder and (sub-optimum) decoder pairs the mutual information can be used [tB01c, HHFJ02].

Simplifying the system given in Fig. 3.1.1 directly leads to a model presented in **Fig. 3.5.7**. For the sake of simplicity, we restrict our analysis to the AWGN channel. Without loss of generality, we choose a sequence \mathbf{d} consisting of N_d information bits. This sequence is encoded with a code rate $R_c = N_d/N_x$ and BPSK modulated, i.e. we transmit a sequence \mathbf{x} of N_x BPSK symbols over the channel. At the receiver, the matched filtered sequence \mathbf{r} is decoded delivering $\tilde{\mathbf{d}}$. For the moment, the interleaver/de-interleaver pair is neglected. The sequences \mathbf{d} , \mathbf{x} , \mathbf{r} , and $\tilde{\mathbf{d}}$ are samples of the corresponding processes $\underline{\mathcal{D}}$, $\underline{\mathcal{X}}$, $\underline{\mathcal{R}}$, and $\tilde{\underline{\mathcal{D}}}$.

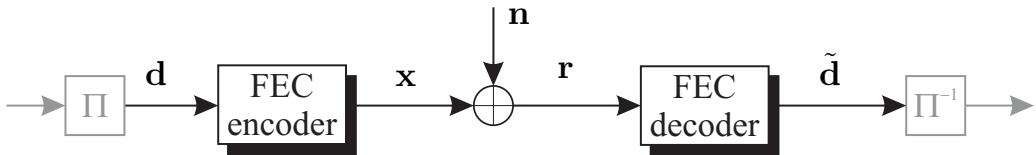


Figure 3.5.7: Simplified model of communication system

The optimality of a code and a corresponding encoder decoder pair can be evaluated by comparing the mutual information $\bar{I}_{\text{diff}}(\underline{\mathcal{D}}; \tilde{\underline{\mathcal{D}}})$ between the encoder input and the decoder output with the mutual information $\bar{I}_{\text{diff}}(\underline{\mathcal{X}}; \underline{\mathcal{R}})$ between input and matched filter output. The larger this difference, the larger is the sub-optimality of the encoder-decoder pair.

From the data processing theorem (cf. Section 2.1) we know already that signal processing cannot increase capacity and $\bar{I}_{\text{diff}}(\underline{\mathcal{D}}; \tilde{\underline{\mathcal{D}}}) \leq \bar{I}_{\text{diff}}(\underline{\mathcal{X}}; \underline{\mathcal{R}})$ is always true. Since the mutual information depends on the length of the transmitted sequence, it is preferable to define the Information Processing Characteristic (IPC) [HHFJ02]

$$\text{IPC}(C) = \frac{1}{N_d} \cdot \bar{I}_{\text{diff}}(\underline{\mathcal{D}}; \tilde{\underline{\mathcal{D}}}) \quad (3.5.32)$$

as an appropriate measure. It describes the average information common to the information $\underline{\mathcal{D}}$ and its estimates $\tilde{\underline{\mathcal{D}}}$. Hence, it can take values between zero and one. As the noise is white and stationary and since we transmit N_x BPSK symbols, $\bar{I}_{\text{diff}}(\underline{\mathcal{X}}; \underline{\mathcal{R}}) = N_x \cdot C$ equals N_x times the channel capacity C and we obtain the relationship

$$\text{IPC}(C) = \frac{1}{N_d} \cdot \bar{I}_{\text{diff}}(\underline{\mathcal{D}}; \tilde{\underline{\mathcal{D}}}) \leq \frac{1}{N_d} \cdot \bar{I}_{\text{diff}}(\underline{\mathcal{X}}; \underline{\mathcal{R}}) = \frac{N_x}{N_d} \cdot C = \frac{C}{R_c}. \quad (3.5.33)$$

Equation (3.5.33) illustrates that the IPC is upper bounded by the ratio of channel capacity and code rate. A perfect coding scheme with an optimum decoder can achieve at most equality resulting in

$$\text{IPC}_{\text{ideal}}(C) = \min[1, C/R_c] \quad (3.5.34)$$

because we can transmit at most 1 bit/symbol for BPSK (the IPC cannot exceed one). The larger the ratio C/R_c , the better is the coding scheme. Codes that reach Shannon's channel capacity achieve $\text{IPC}(C = R_c) = 1$. Furthermore, it is shown in [HHFJ02] that a perfect coding scheme does not benefit from soft-output decoding, i.e. $\bar{I}_{\text{diff}}(\mathcal{D}; \tilde{\mathcal{D}}) = \bar{I}_{\text{diff}}(\mathcal{D}; \hat{\mathcal{D}})$.

For practical codes, $\bar{I}_{\text{diff}}(\underline{\mathcal{D}}; \underline{\mathcal{D}})$ and, thus, also $\text{IPC}(C)$ are hard to determine due to the generally nonlinear behavior of the decoder. An optimum decoding algorithm providing a posteriori probabilities $\Pr\{\mathbf{x}^{(i)} \mid \mathbf{r}\}$ for each possible code sequence $\mathbf{x}^{(i)}$ would not lose any information. Although this requires prohibitively high computational costs, we can determine the corresponding IPC by applying the entropy's chain rule (cf. (2.1.8))

$$\begin{aligned} \bar{I}_{\text{diff}}(\underline{\mathcal{D}}; \underline{\mathcal{R}}) &= \bar{I}_{\text{diff}}(\mathcal{D}_1; \underline{\mathcal{R}}) + \bar{I}_{\text{diff}}(\mathcal{D}_2; \underline{\mathcal{R}} \mid \mathcal{D}_1) \\ &\quad + \cdots + \bar{I}_{\text{diff}}(\mathcal{D}_{N_d}; \underline{\mathcal{R}} \mid \mathcal{D}_1 \cdots \mathcal{D}_{N_d-1}). \end{aligned} \quad (3.5.35)$$

In [HHFJ02] it is shown that $\bar{I}_{\text{diff}}(\mathcal{D}_i; \underline{\mathcal{R}} \mid \mathcal{D}_1 \cdots \mathcal{D}_{i-1}) = \bar{I}_{\text{diff}}(\mathcal{D}_1; \underline{\mathcal{R}})$ holds leading to $\bar{I}_{\text{diff}}(\underline{\mathcal{D}}; \underline{\mathcal{R}}) = N_d \cdot \bar{I}_{\text{diff}}(\mathcal{D}_1; \underline{\mathcal{R}})$. Therefore, we obtain the mutual information for optimum sequence decoding by applying symbol-by-symbol decoding and restricting the IPC analysis only on the first information bit d_1 of a sequence.

$$\begin{aligned} \text{IPC}(C) &= \bar{I}_{\text{diff}}(\mathcal{D}_1; \underline{\mathcal{R}}) = \bar{I}_{\text{diff}}(\mathcal{D}_1; \tilde{\mathcal{D}}_1) \\ &= 1 + \frac{1}{2} \cdot \int_{-\infty}^{\infty} \sum_{\mu=0}^1 p_{\tilde{\mathcal{D}}_1 \mid \mathcal{D}_1=\mu}(\xi) \cdot \log_2 \frac{p_{\tilde{\mathcal{D}}_1 \mid \mathcal{D}_1=\mu}(\xi)}{\sum_{\nu=0}^1 p_{\tilde{\mathcal{D}}_1 \mid \mathcal{D}_1=\nu}(\xi)} d\xi \end{aligned} \quad (3.5.36)$$

Hence, we simply have to carry out a simulation with the BCJR algorithm performing an optimum symbol-by-symbol soft-output decoding, estimating $p_{\tilde{\mathcal{D}}_1 \mid \mathcal{D}_1=i}(\xi)$ for $i \in \{0, 1\}$ by determining the corresponding histograms for the first bit d_1 at the decoder output and insert the obtained parameters into (3.5.36). This leads to much better results than the exploitation of all bits d_i because the decoder knows the initial state of the trellis allowing very reliable estimates of the first bit.

The results are shown in **Fig. 3.5.8a**. The curve for the ideal coding scheme is obtained from (3.5.34) showing that the IPC depends linearly on C until C reaches R_c . For $C < R_c$, soft output sequence decoding of convolutional codes nearly achieves the performance of an ideal coding scheme (bold line). Although an error free transmission is impossible in this region, the observed behavior is of special interest in the context of concatenated codes because the constituent codes with code rates $R_{c,i} > C$ are operating above capacity. Only the overall rate of the concatenated code is below the channel capacity. In the region $0.4R_c \leq C \leq 0.7R_c$, a small gap to the ideal coding scheme occurs while for $C \geq 0.7R_c$, the optimum performance is reached again.

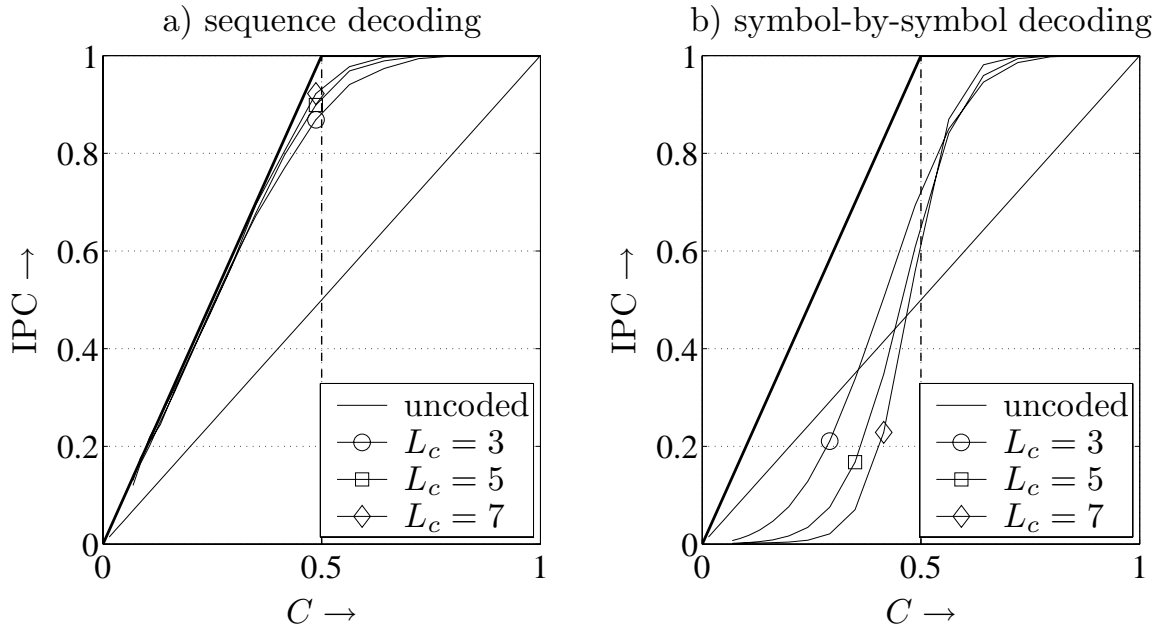


Figure 3.5.8: IPC charts for different nonsystematic nonrecursive convolutional encoding with $R_c = 1/2$ (bold line represents ideal coding scheme)
a) optimum sequence soft-output decoding
b) optimum symbol-by-symbol soft-output decoding with BCJR

For symbol-by-symbol soft-output decoding, we have to assume perfect interleaving before encoding and after decoding that destroys the memory in the end-to-end system (see gray colored interleavers in Fig. 3.5.7). Since the $\tilde{\mathcal{D}}_i$ are now mutually independent, the entropy's chain rule in (3.5.35) becomes

$$\sum_{i=1}^{N_d} \bar{I}_{\text{diff}}(\mathcal{D}_i; \tilde{\mathcal{D}}_i) = N_d \cdot \bar{I}_{\text{diff}}(\mathcal{D}; \tilde{\mathcal{D}}) \leq \bar{I}_{\text{diff}}(\underline{\mathcal{D}}; \tilde{\mathcal{D}}) \quad (3.5.37)$$

where the inequality holds because memory increases capacity. Consequently, the IPC for symbol-by-symbol decoding is obtained by extending (3.5.36) to all information bits d_i , $1 \leq i \leq N_d$ resulting in

$$\bar{I}_{\text{diff}}(\mathcal{D}; \tilde{\mathcal{D}}) = 1 + \frac{1}{2} \cdot \int_{-\infty}^{\infty} \sum_{\mu=0}^1 p_{\tilde{\mathcal{D}}|\mathcal{D}=\mu}(\xi) \cdot \log_2 \frac{p_{\mathcal{D}|\mathcal{D}=\mu}(\xi)}{\sum_{\nu=0}^1 p_{\mathcal{D}|\mathcal{D}=\nu}(\xi)} d\xi. \quad (3.5.38)$$

The results are shown in **Fig. 3.5.8b**. A comparison with Fig. 3.5.8a illuminates the high loss due to symbol-by-symbol decoding. The performance of the optimum coding scheme is not reached over a large range of capacities $C < 0.7$. If the capacity C is smaller than the code rate R_c , the performance becomes even worse than in the uncoded case. Furthermore, we can observe a point of intersection for codes with different constraint lengths roughly at $0.55 C$. Hence, weaker codes

perform better for low C . Only for larger capacities, strong codes can benefit from their better error correcting capabilities.

Fig. 3.5.9a illustrates the results obtained for recursive systematic encoding and symbol-by-symbol MAP decoding. Since no soft-output sequence decoding is performed, we also have a high loss compared to the optimum coding scheme. However, we perform always better than for an uncoded transmission. This is a major difference to nonsystematic nonrecursive encoding. It has to be mentioned that the curves for all RSC codes intersect exactly at $C = R_c = 0.5$.

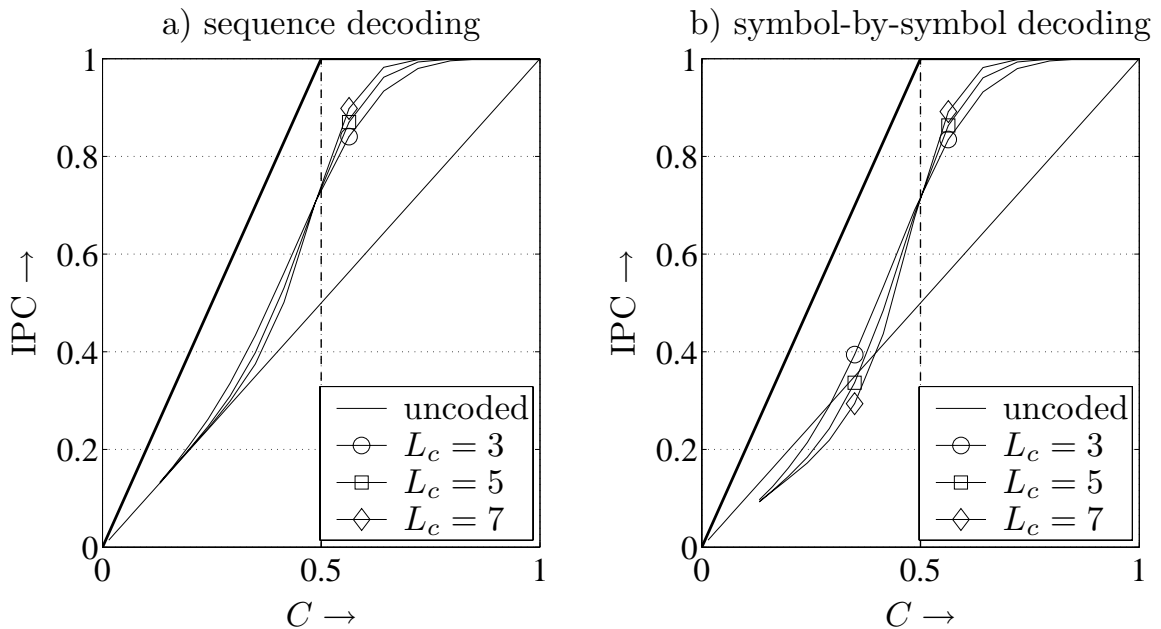


Figure 3.5.9: IPC charts for different systematic recursive convolutional encoding with $R_c = 1/2$ (bold line represents ideal coding scheme)

- a) optimum symbol-by-symbol soft-output decoding with BCJR
- b) symbol-by-symbol soft-output decoding with Max-Log-MAP

Finally, suboptimum symbol-by-symbol Max-Log-MAP decoding as depicted in **Fig. 3.5.9b** loses a little compared to the optimum BCJR algorithm, mainly at low capacities. In this area, the performance is slightly worse than in uncoded case.

Summarizing, we can state that memory increases the performance of convolutional codes in the high SNR regime because the free distance dominates the error probability. Contrarily, for low SNR and, hence, small channel capacity C , the results of this subsection show that low-memory (weak) codes are superior. This behavior will be of importance in the next section because the constituent codes of a concatenated scheme often operate in the area $C < R_c$.

3.6 Concatenated Codes

3.6.1 Introduction

Reviewing the results of the last section, especially Figures 3.5.4 and 3.5.5a, it seems to be questionable if Shannon's channel capacity can be reached by simply increasing the constraint length of convolutional codes. Moreover, the computational decoding complexity increases exponentially with the encoders memory leading quickly to impractical computational costs. Also the described linear block codes are not suited to reach the ultimate limit⁸.

A different approach for reaching the channel capacity was found by Forney in 1966 [For66]. He concatenated several simple codes with the aim to increase the overall performance while maintaining moderate decoding costs. In 1993, concatenated codes obtained great attention with the presentation of so-called *Turbo Codes* [BGT93]. These originally half-rate codes represent a parallel concatenation of two convolutional codes that are decoded iteratively and approach Shannon's capacity up to a small gap of 0.5 dB. At that time, this was a phenomenal performance that pushed worldwide research activities in the area of concatenated codes.

Meanwhile, a lot of research has been done in this field [BM96a, BM96b, Hag96b, RHV97, BDMP98, tB01b, tB01c] and the basic understanding becomes better. Woven codes [LBB98, FBZS01, JJB04] have also shown exceptional performance. More generally, the concatenation with the corresponding decoding principle is not restricted to FEC codes but can be applied to a variety of concatenated systems like modulation and coding [HL99], coding and equalization [BF98] or coding and multi-user (multi-layer) detection [Küh03, SWK03, HtB03].



Figure 3.6.1: Serial code concatenation

Principally, we distinguish between parallel and serial concatenated codes. A serial concatenation of N codes with rates $R_{c,i} = k_i/n_i$ is depicted in **Fig. 3.6.1**. Each encoder processes the entire data stream of the preceding encoder where successive encoders C_i and C_{i+1} are separated by an individual interleavers Π_i . As we will see in the next subsection, the interleaver plays a crucial role in concatenating codes. The entire code rate is simply the product of the rates of all contributing codes

⁸An exception are Low Density Parity Check (LDPC) codes [Gal63]. They belong to the class of linear block codes and show a capacity achieving performance. However, they lie outside the scope of this book.

$$R_c = \prod_{i=1}^N R_{c,i} . \quad (3.6.1)$$

The corresponding decoders are arranged in reverse order with the corresponding de-interleavers in between. However, as will be shown later, the signal flow is not one-directional but decoders may also feed back information to preceding instances.

Contrarily, each encoder processes the same information bits in the case of a parallel concatenation (**Fig. 3.6.2**). However, the orders of the encoders' input bits are different due to the interleaving. This results in sub-streams at the encoder outputs that are not only permuted but nearly independent. They are finally multiplexed resulting in a total code rate of

$$R_c = \frac{k}{n_1 + \cdots + n_N} = \frac{1}{\frac{1}{R_{c,1}} + \cdots + \frac{1}{R_{c,N}}} . \quad (3.6.2)$$

Concerning the decoding process, we refer at the moment to the following sections.

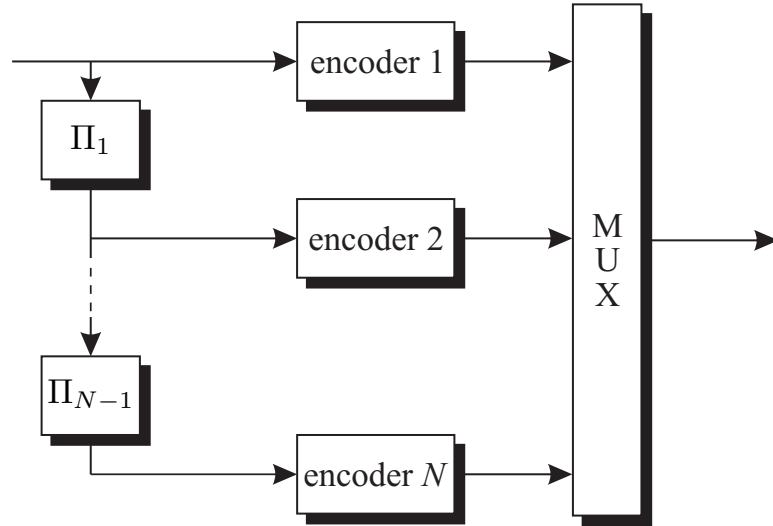


Figure 3.6.2: Parallel code concatenation

For the sake of simplicity, we restrict in the sequel on two concatenated codes. Therefore, only one interleaver is employed and its index can be omitted. In the case of a serial concatenation, encoder 1 is denoted as the outer encoder, and, consequently, encoder 2 as the inner encoder.

Since concatenated codes comprise several components, a lot of parameters have to be optimized. Questions like the distribution of the code rates among the encoders or the order of strong and weak codes for a serial concatenation have

to be answered. Besides the constituent codes, the interleaver represents a key component. Investigations in the last years have shown that random or pseudo-random interleaving is superior to simple block interleaving in many cases [BP95, JHJ01, HTZ03, HTZ04].

In order to analyze the bit error rate performance of concatenated codes analytically, we can apply the union bound given in (3.5.21)

$$P_b \leq \frac{1}{2} \cdot \sum_{d=d_{\min}}^n C_d \cdot \operatorname{erfc} \left(\sqrt{dR_c \frac{E_b}{N_0}} \right) .$$

Determining the coefficients C_d requires knowledge of the IOWEF (3.5.2)

$$A(W, D) = \sum_{w=0}^k \sum_{d=0}^n A_{w,d} \cdot W^w D^d$$

of the concatenated code. An exact calculation of the IOWEF is a demanding task or even impossible because the number of states of the underlying super-trellis becomes extremely high and concatenated codes are time variant due to the inherent interleaving. A simplified analysis was derived in [BM96b, BM96a, BDMP98] based on the concept of a uniform interleaver.

A uniform interleaver is a theoretical device that covers all possible permutations of a sequence with a certain length L_π . All permutations are equally likely so that they are weighted with $\binom{L_\pi}{w}^{-1}$ where w denotes the weight of the permuted sequence. Therefore, the uniform interleaver represents an average interleaver and, consequently, we will obtain an average IOWEF of the concatenated code. **Fig. 3.6.3** illustrates an example of a uniform interleaver of length $L_\pi = 4$ for a sequence with weight $w = 2$.

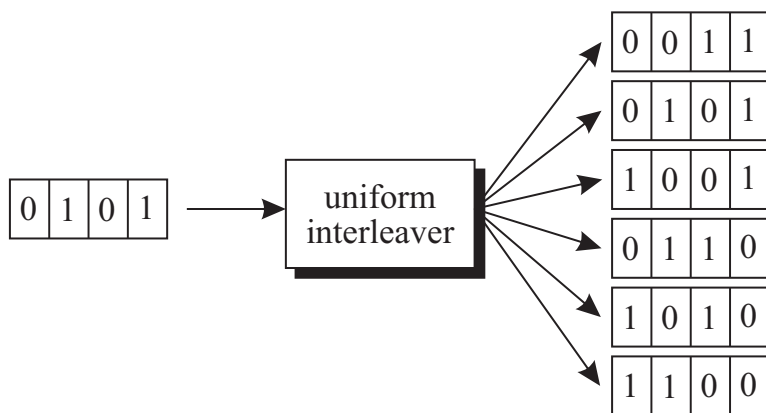


Figure 3.6.3: Illustration of uniform interleaver of length $L_\pi = 4$ and an input sequence with weight $w = 2$

The next two sections analyze the error rate performance of concatenated codes by exploiting the input output weight enumerating function (IOWEF) and the union bound technique. In the previous sections we saw already that the union bound diverges at low signal-to-noise ratios, i.e. exactly in that region where concatenated codes are intended to operate. Hence, it seems to be questionable if the results obtained with the union bound technique are meaningful. Furthermore, the application of the union bound presupposes an optimal maximum likelihood decoding of the concatenated code. As we will see in Section 3.6.4, this solution is generally not feasible and sub-optimum iterative approaches are applied.

However, comparisons between analytical and simulation results have shown a good consistency for not too low signal to noise ratios, i.e. code rates above the cut-off rate of the channel [BDMP98]. Therefore, at least the asymptotic behavior can be predicted with the union bound. Approaching the channel capacity at very low SNRs, so-called EXIT charts presented in Section 3.6.5 allow more accurate predictions taking into account the iterative decoding approach.

3.6.2 Performance Analysis for Serial Concatenation

As mentioned above, we focus only on the concatenation of two constituent codes depicted in **Fig. 3.6.4**. The introduction of the uniform interleaver decouples both component codes so that all possible sequences with a certain weight l at the output of the outer encoder are mapped onto all possible input sequences with weight l of the inner encoder. Therefore, the IOWEF of the entire code is obtained by multiplying the conditioned IOWEF's of the constituent codes according to [BDMP98]

$$A^{\text{ser}}(W, D) = \sum_l \frac{A_1(W, l) \cdot A_2(l, D)}{\binom{L_\pi}{l}} = \sum_w \sum_d A_{w,d}^{\text{ser}} \cdot W^w D^d. \quad (3.6.3)$$

From (3.6.3) we see that the output weight of the outer encoder equals the input weight of the inner encoder. Averaging over all possible permutations requires the division by $\binom{L_\pi}{l}$, i.e. the number of possibilities to arrange l ones in a block of length L_π . The coefficients C_d are obtained by

$$C_d = \sum_w \frac{w}{L_\pi \cdot R_{c,1}} \cdot A_{w,d}^{\text{ser}}. \quad (3.6.4)$$

Concerning the concatenation of block codes we have to consider the particularity that the interleaver length L_π may cover several codewords of inner and outer code. Hence, the IOWEF's inserted in (3.6.3) have to be extended to describe a set of statistically independent (parallel) codewords. Assuming that L_π is m_1 times as large as the codeword length n_1 of the outer code, the resulting IOWEF is simply the m_1 -th power of $A_1(W, D)$

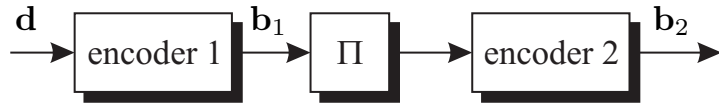


Figure 3.6.4: Serial concatenation of two codes

$$A_1^{m_1}(W, D) = [A_1(W, D)]^{m_1} . \quad (3.6.5)$$

If the interleaver additionally comprises m_2 information words of the inner encoder C_2 , the overall IOWEF becomes

$$A^{\text{ser}}(W, D) = \sum_l \frac{A_1^{m_1}(W, l) \cdot A_2^{m_2}(l, D)}{\binom{L_\pi}{l}} = \sum_w \sum_d A_{w,d}^{\text{ser}} \cdot W^w D^d . \quad (3.6.6)$$

For convolutional codes this case is generally irrelevant because the sequence length matches the interleaver size.

Code Design

Without further derivations, we now present some guidelines concerning the design of serial concatenated codes based on the results obtained from (3.6.3) and the union bound in (1.3.11). Detailed derivations can be found in [BDMP98, BMDP96, KK01].

1. The inner code should always be a recursive convolutional code. Only in this case a gain is obtained by increasing the interleaver size especially at low signal-to-noise ratios.
2. The effective distance d_{eff} of the inner code should be as large as possible. It is defined as the minimum Hamming weight of all codewords whose input weight amounts to $w_H(\mathbf{d}) = 2$. This constraint can be fulfilled by choosing a recursive convolutional code whose feedback polynomial is prime.
3. Another criterion that partly contradicts the last one states that sequences with an input weight 3 of the inner encoder have large influence on the error rate performance. Hence, for an odd minimum distance of the outer code, a feedback polynomial of the inner code containing the factor $1 + D$ is often advantageous.
4. The free distance of the outer code should be as large as possible because it represents the input weight of the inner encoder. This ensures a large interleaving gain.

5. The number of sequences with $w_H(\mathbf{b}_1) = d_f$ and their input weights should be minimized for the outer code. This generally leads to the choice of non-recursive convolutional codes as outer codes.

All these guidelines are valid for code rates below the cut-off rate [BDMP98]. For codes working above the cut-off rate, i.e. at extremely low SNRs, different guidelines may be valid. They are discussed in Section 3.6.5.

Example: Serial Concatenated Convolutional Codes

We now illustrate the performance for an example of two serially concatenated convolutional codes. As constituent codes, we have chosen half-rate codes with constraint length $L_c = 4$. They are punctured appropriately in order to obtain an overall code rate of $R_c = 1/2$. **Fig. 3.6.5a** shows the structure of the nonrecursive nonsystematic encoder with the generator polynomials $g_1(D) = 1 + D + D^3$ and $g_2(D) = 1 + D + D^2 + D^3$. It is used as outer encoder. **Fig. 3.6.5b** depicts one of the two possible recursive systematic encoders with $g_2(D) = (1+D+D^2+D^3)/(1+D+D^3)$. Alternatively the encoder with $g_2(D) = (1+D+D^3)/(1+D+D^2+D^3)$ (not depicted) is used as inner encoder. Moreover, random interleavers of different lengths are employed.

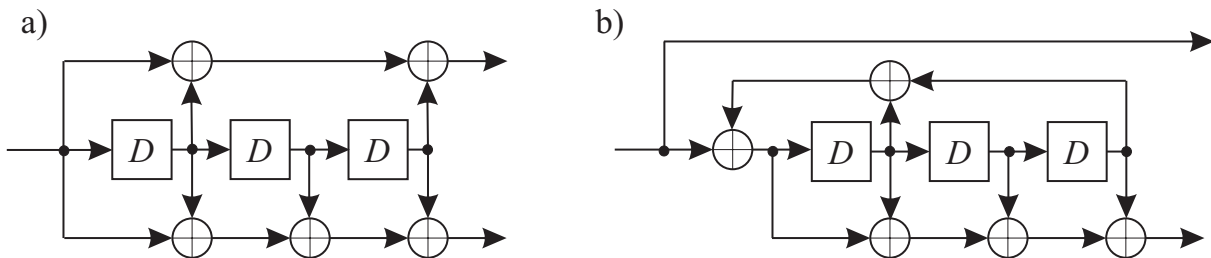


Figure 3.6.5: a) NSC encoder with $g_1(D) = 1 + D + D^3$, $g_2(D) = 1 + D + D^2 + D^3$
b) RSC encoder with $g_2(D) = (1 + D + D^2 + D^3)/(1 + D + D^3)$

The concatenation is compared to a conventional half-rate NSC code with constraint length $L_c = 9$. This specific choice allows for similar decoding complexities. As a measure for decoding complexity the number of states in the trellis is used. In Subsection 3.6.4, it will be explained that decoding is performed iteratively. Assuming that the Max-Log-MAP algorithm requires twice as many operations as the Viterbi algorithm due to forward and backward processing of the trellis and taking into account that two constituent codes have to be decoded, we can carry out 8 decoding iterations for a trellis with 8 states ($L_c = 4$) to have the same complexity as for a single $L_c = 9$ code ($256 \text{ states}/(2 \cdot 2 \cdot 8 \text{ states}) = 8 \text{ iterations}$). Code parameters of the considered serial concatenations are summarized in **Table 3.6.1** where R'_c denotes the code rate after puncturing.

Table 3.6.1: Parameters of serial code concatenations

name	outer NSC code C_1	inner RSC code C_2	puncturing
SC1	$L_c = 4, R'_c = 2/3$ $g_1(D) = 1 + D + D^2 + D^3$ $g_2(D) = 1 + D + D^3$	$L_c = 4, R'_c = 3/4$ $g_1(D) = 1$ $g_2(D) = \frac{1+D+D^3}{1+D+D^2+D^3}$	$\mathbf{P}_1 = \begin{bmatrix} 1 & 0 \\ 1 & 1 \end{bmatrix}$ $\mathbf{P}_2 = \begin{bmatrix} 1 & 1 & 0 \\ 1 & 0 & 1 \end{bmatrix}$
SC2	$L_c = 4, R'_c = 2/3$ $g_1(D) = 1 + D + D^2 + D^3$ $g_2(D) = 1 + D + D^3$	$L_c = 4, R'_c = 3/4$ $g_1(D) = 1$ $g_2(D) = \frac{1+D+D^2+D^3}{1+D+D^3}$	$\mathbf{P}_1 = \begin{bmatrix} 1 & 0 \\ 1 & 1 \end{bmatrix}$ $\mathbf{P}_2 = \begin{bmatrix} 1 & 1 & 0 \\ 1 & 0 & 1 \end{bmatrix}$
SC3	$L_c = 4, R'_c = 3/4$ $g_1(D) = 1 + D + D^2 + D^3$ $g_2(D) = 1 + D + D^3$	$L_c = 4, R'_c = 2/3$ $g_1(D) = 1$ $g_2(D) = \frac{1+D+D^3}{1+D+D^2+D^3}$	$\mathbf{P}_1 = \begin{bmatrix} 1 & 1 & 0 \\ 1 & 0 & 1 \end{bmatrix}$ $\mathbf{P}_2 = \begin{bmatrix} 1 & 0 \\ 1 & 1 \end{bmatrix}$
NSC	$L_c = 9, R_c = 1/2, g_1 = 561_8, g_2 = 753_8$		

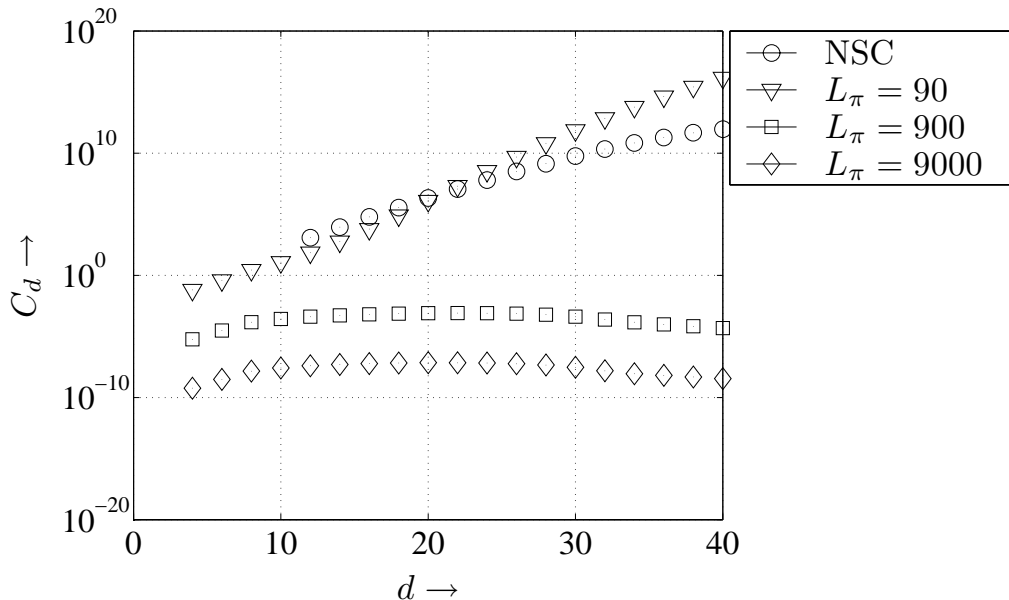
**Figure 3.6.6:** Coefficients C_d for NSC code ($g_1 = 561_8, g_2 = 753_8$) and serial concatenation SC1 for different interleaver sizes

Fig. 3.6.6 illustrates the coefficients C_d obtained from (3.6.4). The outer NSC code was punctured to $R_{c,1} = 2/3$ and the inner code to $R_{c,2} = 3/4$. Obviously, the concatenated codes have a much smaller minimum Hamming distance than the $L_c = 9$ code. Due to the puncturing, the free distances of the constituent codes have been largely reduced resulting in an overall minimum Hamming distance⁹ of only 3. Contrarily, the NSC code with $L_c = 9$ has a free distance of $d_f = 12$ and,

⁹Be aware that this is only an average minimum distance due to the uniform interleaving. A lot of permutations exist that lead to larger minimum distances. This is expressed by the coefficients C_d being much smaller than 1.

therefore, a better asymptotical performance. However, with increasing interleaver size, the average number of sequences with a low Hamming weight becomes very small, i.e. only few interleavers will cause sequences with low weight. Hence, it should be possible to find at least one interleaver with high minimum distance.

Moreover, at low signal-to-noise ratios, the coefficients C_d have even as much impact on the error rate performance than the distance d itself. This is approved in **Fig. 3.6.7** showing the bit error probability of the considered codes. Increasing the interleaver size results in a remarkable gain even at low signal-to-noise ratios. However, the minimum distance cannot be increased by larger interleavers, only the average number of sequences with small Hamming weight is lowered. Asymptotically, the convolutional code with $L_c = 9$ outperforms the serial concatenation due to its larger free distance. A comparison for very low SNR's is not possible due to the inaccuracy of the union bound in this area. Additionally, we see that the code SC1 whose feedback polynomial contains the term $1+D$ performs slightly better than the code SC2 with a prime feedback polynomial. This, was already stated in requirement 3 of the code design.

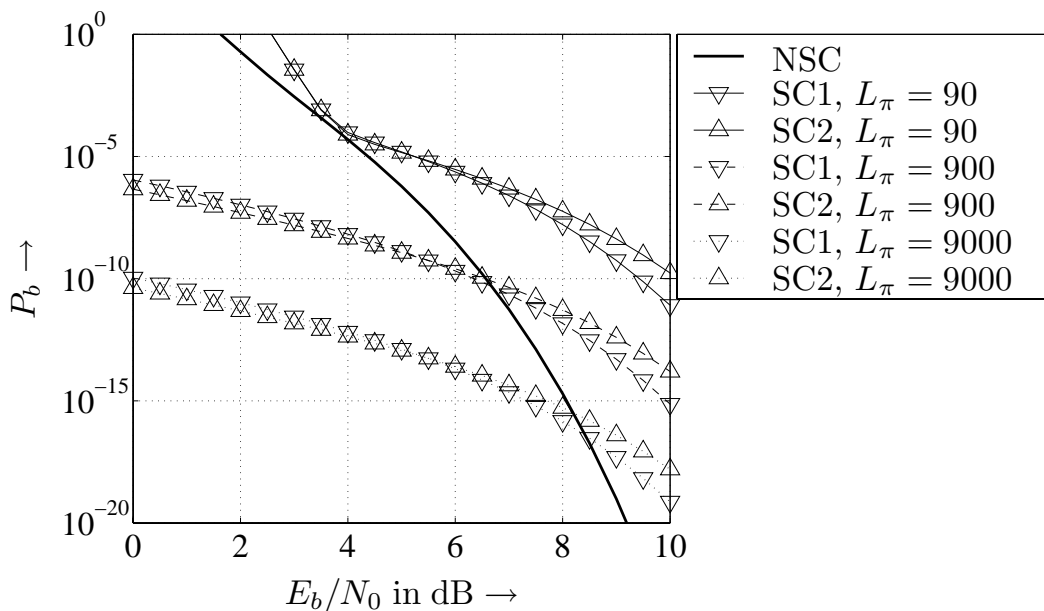


Figure 3.6.7: Error rate performance of NSC code and serial concatenations SC1 and SC2 for different interleaver lengths

Finally, **Fig. 3.6.8** demonstrates the effect when the code rates of inner and outer codes are exchanged. This is accomplished by simply exchanging the puncturing. It has to be mentioned that the exchange of code rates affects also the interleaver size because the overall codeword length was assumed to be constant. It can be seen that the puncturing scheme for SC1 (outer rate $R_{c,1} = 2/3$, inner rate $R_{c,2} = 3/4$) shows a better performance at low and medium signal to noise ratios. Hence, the union bound tells us that it is better to have a strong outer code with

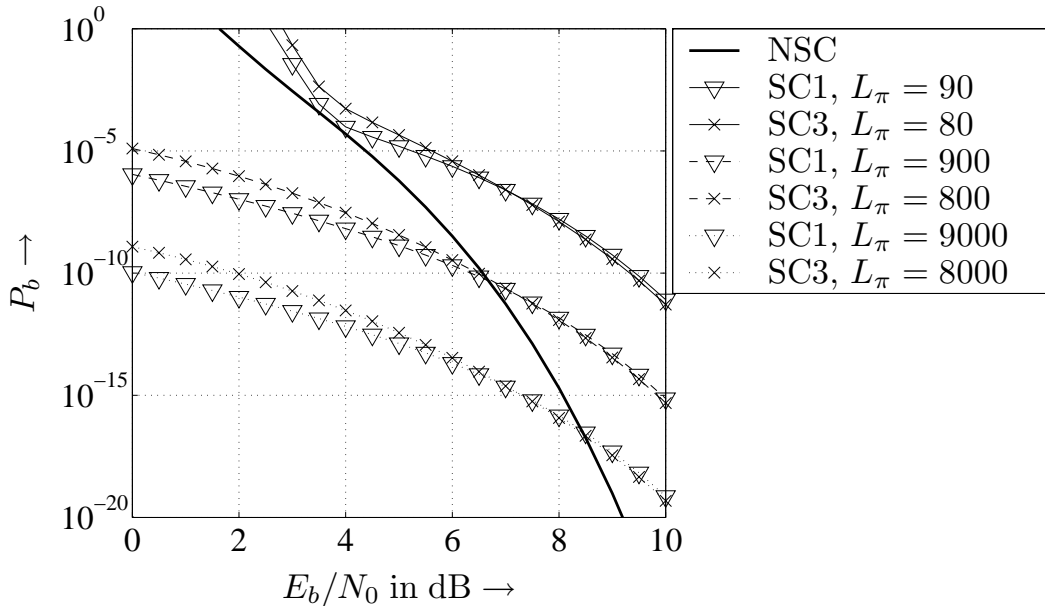


Figure 3.6.8: Error rate performance of NSC code and serial concatenations SC1 and SC3 for different interleaver lengths

high minimum distance than a strong inner code. Please be aware that maximum likelihood decoding is assumed.

3.6.3 Performance Analysis for Parallel Concatenation

Parallel concatenated codes pushed the development of general code concatenation very much. The most famous representative are turbo codes presented the first time in 1993 by Berrou, Glavieux and Thitimajshima [BGT93, BG93]. They approached Shannon's capacity within 0.5 dB for a half-rate code initiating a worldwide boom. Besides the choice of important encoder ingredients like RSC codes and the specific interleaver structure, the iterative decoding strategy is responsible for the big success of turbo codes. Meanwhile, a lot of research in the area of concatenated codes has been done in the last decade and the gap to Shannon's channel capacity was closed up to 0.1 dB [tB00b].

We focus in the sequel on the description of turbo codes, i.e. the concatenation of systematic constituent encoders¹⁰. The corresponding structure for a parallel concatenation of two codes is shown in Fig. 3.6.9. Since each information bit should be transmitted at most once, \mathbf{d} can be directly fed to the puncturing device. Hence each encoder only generates additional parity bits \mathbf{b}_1 and \mathbf{b}_2 . In order to adjust the entire code rate, appropriate puncturing of \mathbf{d} , \mathbf{b}_1 and \mathbf{b}_2 may be performed. Finally, the resulting sequences are multiplexed to a vector \mathbf{b} .

¹⁰Generally, also the parallel concatenation of nonsystematic encoders is possible [CMCT00].

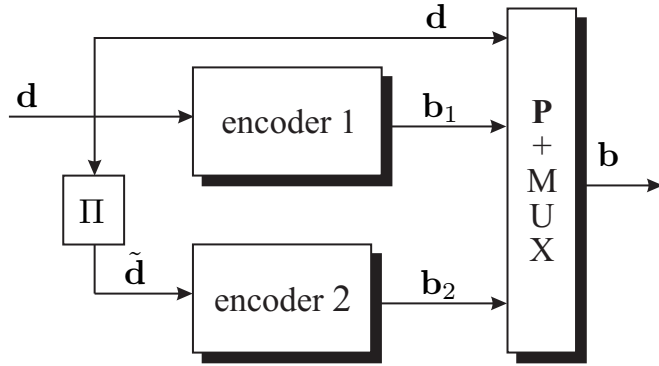


Figure 3.6.9: Parallel concatenation of two codes for systematic encoding

In contrast to the serial concatenation, all parallel arranged encoders obtain the same information bits just in different orders. Hence, the weight of their input sequences is always the same. Moreover, the encoder outputs contain only parity bits. Their weights are denoted by p and we obtain the conditional IOWEF

$$A(w, P) = \sum_p A_{w,p} \cdot P^p, \quad (3.6.7)$$

where $A_{w,p}$ denotes the number of sequences with an input weight w and a parity weight p . The entire Hamming weight of a sequence amounts to $d = w + p$. Using the uniform interleaver, we obtain the conditional IOWEF of the parallel concatenation

$$A^{\text{par}}(w, P) = \frac{A_1(w, P) \cdot A_2(w, P)}{\binom{L_\pi}{w}} = \sum_p A_{w,p}^{\text{par}} \cdot P^p. \quad (3.6.8)$$

By multiplying the conditional IOWEFs $A_1(w, P)$ and $A_2(w, P)$, we ensure that all output sequences with the same input weight w are combined. Uniform interleaving is now performed only with the information bits leading to the normalization with $\binom{L_\pi}{w}$. In order to determine the coefficients C_d in (3.6.8), we have to take into account that the information bits may be punctured as well. Denoting the weight of the punctured information bits with \tilde{w} , we obtain

$$C_d = \sum_{\tilde{w}+p=d} \frac{w}{L_\pi} \cdot A_{w,p}^{\text{par}}, \quad (3.6.9)$$

where the sum runs over all pairs (\tilde{w}, p) whose sum equals the entire Hamming weight $d = \tilde{w} + p$.

Code Design

As in the case of the serial concatenation, some guidelines exist for the code construction. Since the target of concatenating code was the construction of powerful

codes on the basis of simple constituent encoders, convolutional codes with small constraint length are mainly employed. Although codes with large memory may also show a good performance [CMCT00], they contradict the requirement of a feasible decoding effort. Furthermore, it can be shown that the bit error rate behaves asymptotically like

$$P_b \sim L_\pi^{1-w_{\min}} \implies P_b \sim L_\pi^{-1} \text{ for } w_{\min} = 2 \quad (3.6.10)$$

where w_{\min} represents the minimum input weight of an encoder to obtain an output sequence with finite weight. Obviously, $w_{\min} = 2$ holds for RSC codes (cf. page 98) so that the error rate decreases when the interleaver is enlarged. This is not true for nonrecursive codes ($w_{\min} = 1$). Hence, RSC codes are used as constituent codes in a parallel concatenation. Moreover, codes with rate $1/n$ are preferred because higher rates can be easily achieved by appropriate puncturing.

Finally, the effective distance d_{eff} (cf. page 140) has to be maximized rather than the free distance d_f . From this it can be shown that the feedback polynomial should be prime.

Besides the constituent codes, the interleaver has also deep impact on the performance. First of all, it has to avoid that both encoders deliver simultaneously output sequences with low weight. In that case, the minimum Hamming distance of the entire code would be small. Hence, if the first encoder outputs a low weight sequence, the information bits should be permuted in such a way that the output of the second encoder has a large weight. Therefore, the interleaver directly influences the distance spectrum of the concatenated code¹¹.

Example: Turbo Codes

We now illustrate the performance of parallel concatenated codes for the example of a turbo code. As constituent codes, we have chosen the same convolutional codes as in Subsection 3.6.2. They are both punctured to the rate $R_{c,1} = R_{c,2} = 2/3$ yielding an entire code rate¹² of $R_c = 1/2$. The turbo codes are compared to a conventional half-rate NSC code with constraint length $L_c = 9$ due to a similar decoding complexity. All configurations are listed in **Table 3.6.2**.

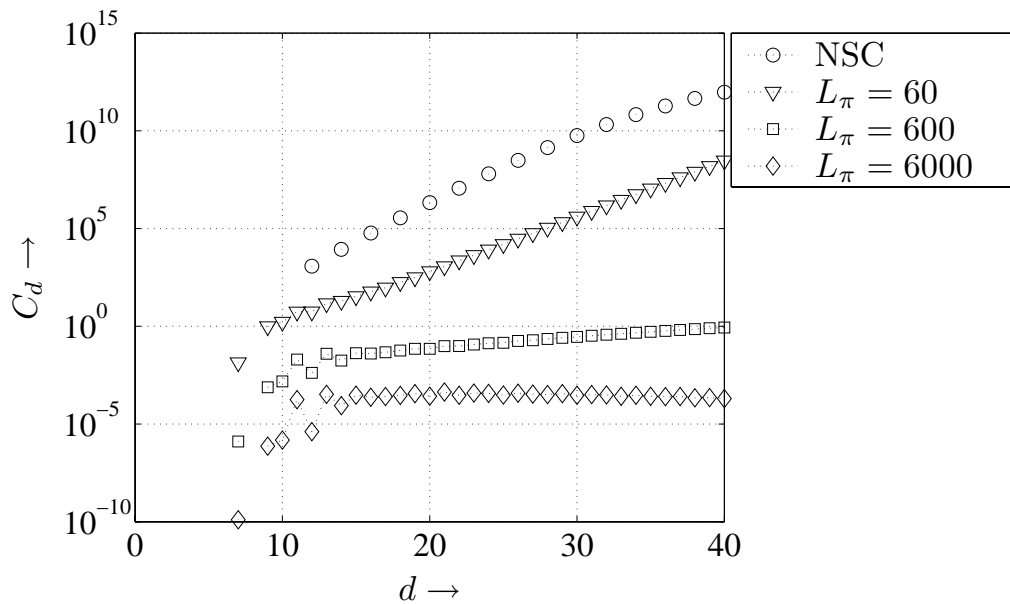
Fig. 3.6.10 illustrates the coefficients C_d . As in the case of the serial concatenation, the coefficients become smaller with increasing interleaver size. Hence, sequences with low weight occur less frequently and the performance at low signal-to-noise ratios is expected to be better for turbo codes. Asymptotically, the min-

¹¹This cannot be observed for the uniform interleaver that comprises all possible permutations.

¹²Both component codes have the same code rate of $2/3$ only if the information bits are assigned to both encoders outputs although they are transmitted only once. If they are assigned to only one constituent code, this has the rate $2/3$ while the remaining code transmits only 1 parity bit per two information bits ($R_{c,2} = 2$).

Table 3.6.2: Parameters of parallel code concatenations

name	constituent code	puncturing
PC1	$L_c = 4, R'_c = 2/3, g_1(D) = 1, g_2(D) = \frac{1+D+D^2+D^3}{1+D+D^3}$	$\mathbf{P} = \begin{bmatrix} 1 & 0 \\ 1 & 1 \\ 0 & 1 \end{bmatrix}$
PC2	$L_c = 4, R'_c = 2/3, g_1(D) = 1, g_2(D) = \frac{1+D+D^3}{1+D+D^2+D^3}$	$\mathbf{P} = \begin{bmatrix} 1 & 0 \\ 1 & 1 \\ 0 & 1 \end{bmatrix}$
PC3	$L_c = 4, R'_c = 2/3, g_1(D) = 1, g_2(D) = \frac{1+D+D^2+D^3}{1+D+D^3}$	$\mathbf{P} = \begin{bmatrix} 1 & 1 \\ 1 & 0 \\ 0 & 1 \end{bmatrix}$
NSC	$L_c = 9, R_c = 1/2, g_1 = 561_8, g_2 = 753_8$	

**Figure 3.6.10:** Coefficients C_d for NSC code and turbo code PC1 for different interleaver lengths

imum distance dominates and the $L_c = 9$ convolutional code will outperform the turbo code.

Based on the coefficients shown in Fig. 3.6.10, **Fig. 3.6.11** depicts the bit error rate performance of the turbo code. As expected, the performance increases for larger interleavers. The NSC code is outperformed at low SNRs while the slope of its BER curve is higher for large SNRs leading to a better asymptotic performance. Furthermore, we observe a large gap between the codes PC1 and PC2. PC1 clearly outperforms PC2 due to its prime feedback polynomial¹³. This illustrates the importance of requirement 2 of the code design.

¹³The feedback polynomial of PC2 can be factorized to $1 + D + D^2 + D^3 = (1 + D)(1 + D^2)$.

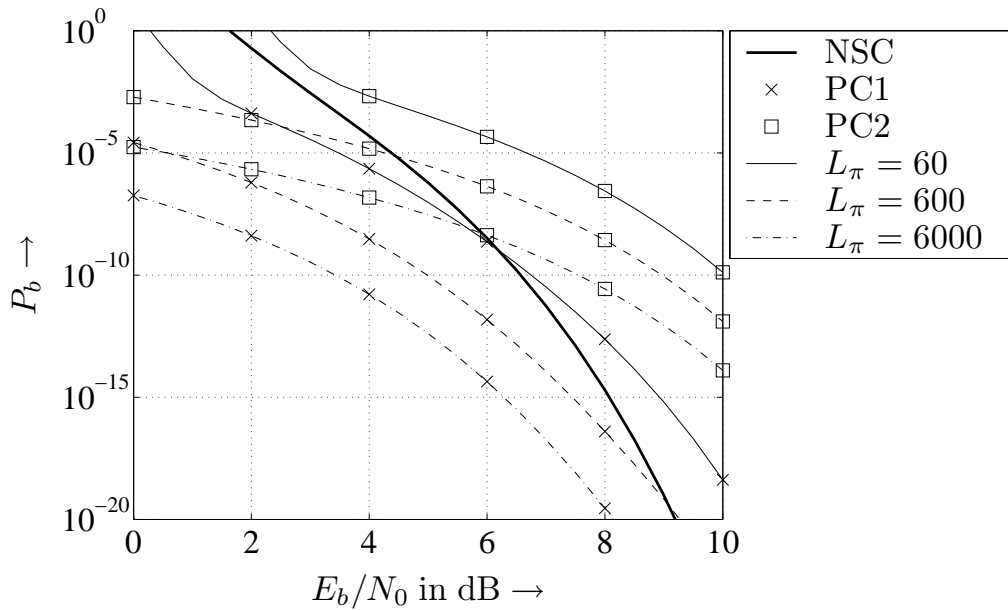


Figure 3.6.11: Error rate performance NSC code and of half-rate turbo codes PC1 and PC2

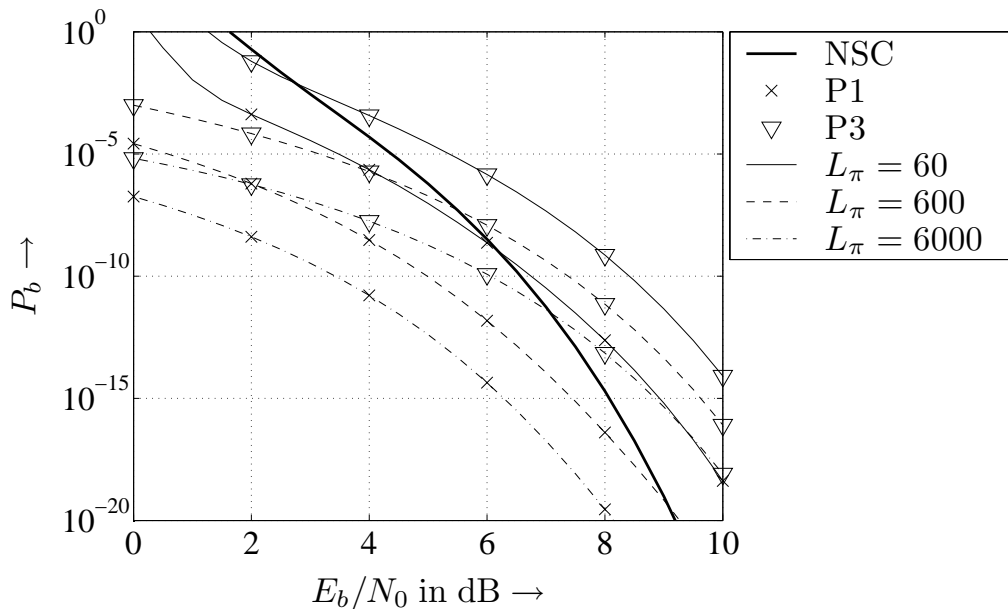


Figure 3.6.12: Error rate performance of NSC code and half-rate turbo codes PC1 and PC3

Fig. 3.6.12 compares different puncturing schemes for the turbo code. Obviously, P3 puncturing only the parity bits leads to a worse performance. The scheme P1 also punctures some systematic information bits and, thus, keeps more of the redundancy of the code. This ensures a higher minimum distance (8 instead of 7) as well as a fewer sequences with low weight leading to a better overall performance.

Comparison of Serial and Parallel Concatenation

Fig. 3.6.13 illustrates the comparison of serial and parallel concatenated codes for the examples discussed in the last subsections. All codes have the overall rate $R_c = 1/2$ and the interleaver lengths were chosen such that the codeword lengths are identical for serial and parallel concatenations. It can be seen that for small codeword lengths, the parallel concatenation clearly shows the best performance. For large interleavers, the serial concatenation seems to be superior at low and medium SNR while the parallel concatenation shows a lower asymptotical error rate at high signal to noise ratios.

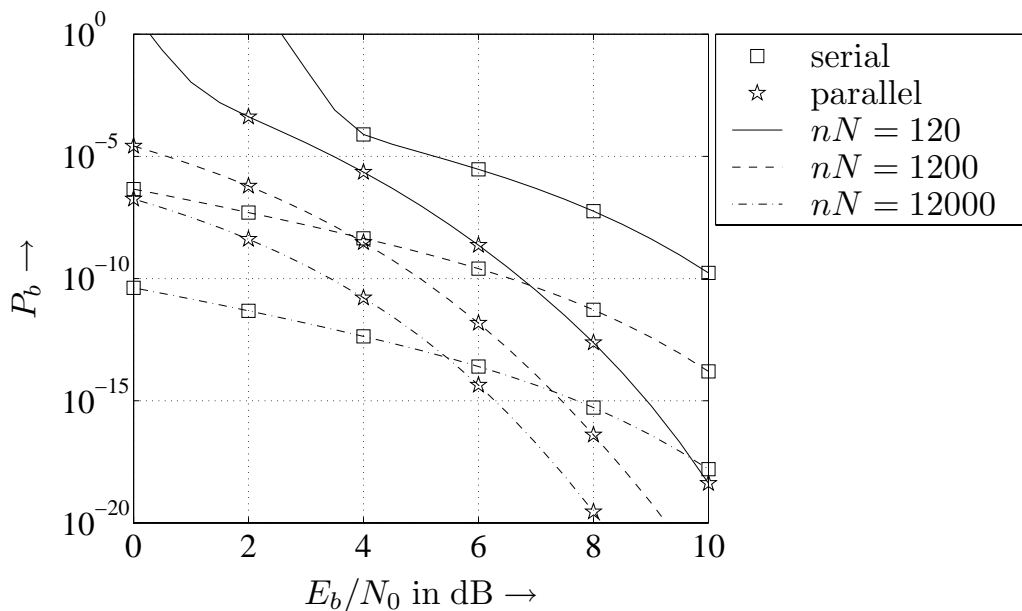


Figure 3.6.13: Comparison of best serial concatenation (SC1) and best parallel concatenation (PC1) for half-rate codes and different codeword lengths

3.6.4 Turbo Decoding of Concatenated Codes

As already mentioned before, the specific decoding of concatenated codes plays a major role for their success. Since optimal maximum likelihood decoding of the entire code is infeasible, we try to approach this solution iteratively by decoding all contributing codes separately. The key idea behind this approach is that the interleaver decouples the concatenated codes so that the extrinsic information obtained by the two decoders can be assumed to be mutually independent. Hence, exchanging extrinsic information between the involved decoders may improve the overall performance leading hopefully to a near maximum likelihood estimate.

Iterative Decoding for Serial Concatenations

We start our description with the serial concatenation according to Fig. 3.6.1. The corresponding decoder structure employs soft-in soft-out symbol-by-symbol decoders like the BCJR algorithm for each constituent code and is depicted in **Fig. 3.6.14**. The first iteration of the process starts with the inner decoder 2 delivering the LLR $L_2^{(1)}(\hat{\mathbf{b}}_1)$ whose de-interleaved version represents the input $L_{a,1}^{(1)}(\hat{\mathbf{b}}_1)$ of the outer decoder 1. This decoder now provides estimates $L_1^{(1)}(\hat{\mathbf{d}})$ of the information bits as well as log-likelihood ratios of the coded bits

$$L_1^{(1)}(\hat{\mathbf{b}}_1) = L_{a,1}^{(1)}(\hat{\mathbf{b}}_1) + L_{e,1}^{(1)}(\hat{\mathbf{b}}_1). \quad (3.6.11)$$

From (3.6.11) we see that the LLRs consist of the input signal itself and the extrinsic part $L_{e,1}^{(1)}(\hat{\mathbf{b}}_1)$ which is extracted by subtracting $L_{a,1}^{(1)}(\hat{\mathbf{b}}_1)$ from $L_1^{(1)}(\hat{\mathbf{b}}_1)$. The interleaved extrinsic LLR is fed back as a priori information $L_{a,2}^{(1)}(\hat{\mathbf{b}}_1)$ to decoder 2 for the second iteration¹⁴.

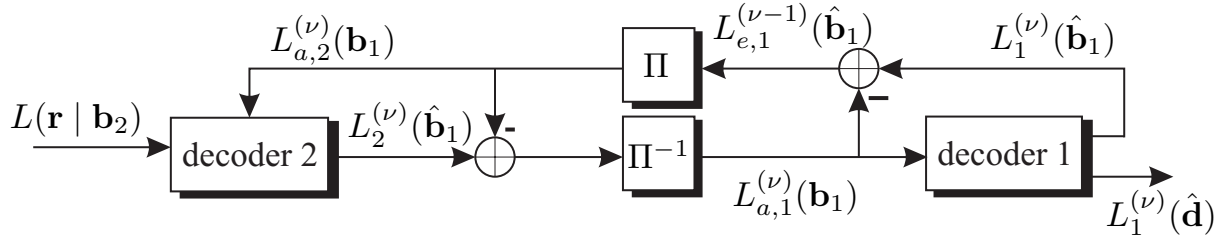


Figure 3.6.14: Iterative decoding of two serial concatenated codes

Now, the second iteration starts with an improved decoder 2 that can also exploit the a priori information $L_{a,2}^{(2)}(\hat{\mathbf{b}}_1)$ according to (3.4.37) and (3.4.39). As shown in (3.4.13) for systematic encoding, its output generally consists of three parts

$$L_2^{(\nu)}(\hat{\mathbf{b}}_1) = L_{\text{ch}} \cdot \mathbf{r}_s + L_{a,2}^{(\nu)}(\hat{\mathbf{b}}_1) + L_{e,2}^{(\nu)}(\hat{\mathbf{b}}_1) \quad (3.6.12)$$

where \mathbf{r}_s only contains the received systematic symbols. Since $L_{a,2}^{(\nu)}(\hat{\mathbf{b}}_1)$ was generated by $L_{e,1}^{(\nu-1)}(\hat{\mathbf{b}}_1)$ of decoder 1, it must not be delivered back to the outer decoder but has to be subtracted prior to the de-interleaving resulting in

$$L_{a,1}^{(\nu)}(\hat{\mathbf{b}}_1) = L_2^{(\nu)}(\hat{\mathbf{b}}_1) - L_{a,2}^{(\nu)}(\hat{\mathbf{b}}_1). \quad (3.6.13)$$

Repeating the described procedure multiple times results in an iterative decoding scheme from which the name *turbo codes* can be explained because it resembles the principle of a turbo engine.

¹⁴In a serial concatenation, the coded bits of the outer code are the information bits of the inner code.

We now present some simulation results for the same constituent codes listed in Table 3.6.1 and a simple AWGN channel. Unless otherwise stated, decoding with the Max-Log-MAP algorithm is performed. First, **Fig. 3.6.15** shows the bit error rates for different decoding iterations and an interleaver size of $L_\pi = 80$ bits. Obviously, the error rate decreases continuously with each additional iteration. However, the incremental gain becomes smaller and smaller because the correlation among the extrinsic LLRs gets larger with each iteration step. These correlations can be reduced by increasing the length of the interleaver. For $E_b/N_0 > 4$ dB, the union bound is very tight and can be approached by the iterative decoding scheme.

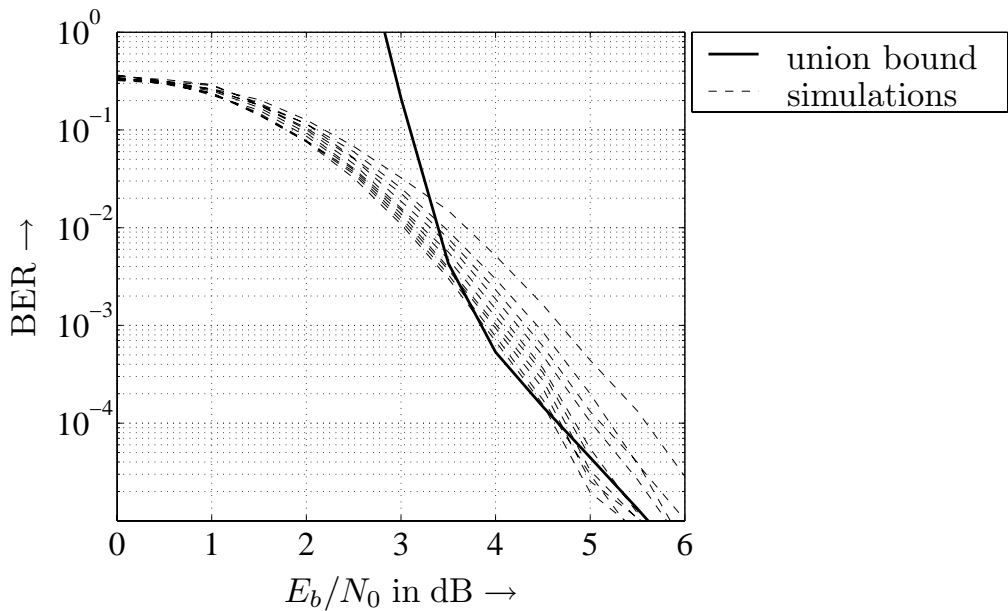


Figure 3.6.15: Illustration of performance improvements by iterative decoding of serial concatenation SC3 and a random interleaver of length $L_\pi = 80$

Fig. 3.6.16 illustrates the influence of the interleaver size L_π . As can be seen, the gains by additional decoding iterations become larger with increasing L_π because the above mentioned correlations are reduced. For $L_\pi = 8000$, a bit error rate of 10^{-5} is obtained at $E_b/N_0 = 2$ dB. Decreasing the interleaver length to $L_\pi = 800$ requires a signal to noise ratio of roughly $E_b/N_0 = 3$ dB for achieving the same performance. For $L_\pi = 80$, the error rate is reached for $E_b/N_0 = 5$ dB.

Fig. 3.6.17 compares different puncturing schemes to achieve a total code rate of $1/2$. Contrarily to Fig. 3.6.8, keeping the inner code stronger with a rate $2/3$ and puncturing the outer code to a rate $3/4$ (scheme SC3) leads to better results than with scheme SC1. Finally, **Fig. 3.6.18** shows the comparison of Log-MAP and Max-Log-MAP decoding algorithms. It can be seen that the difference in the first iteration is neglectable while it becomes larger and larger in subsequent iterations. In the sixth iteration, the loss due to the Max-Log-MAP algorithm is 0.5 dB.

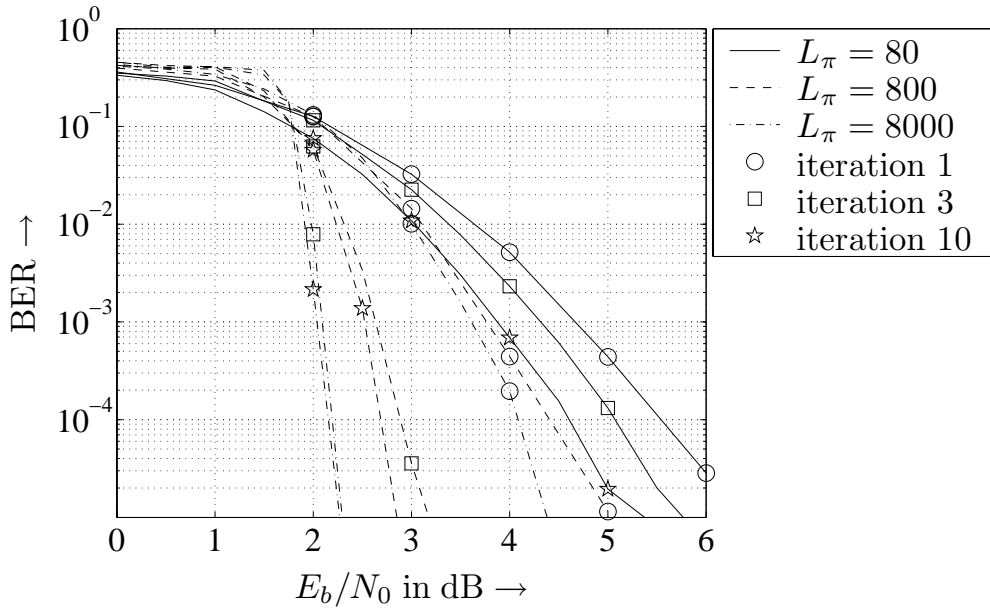


Figure 3.6.16: Comparison of different interleaver lengths for serial concatenation SC3

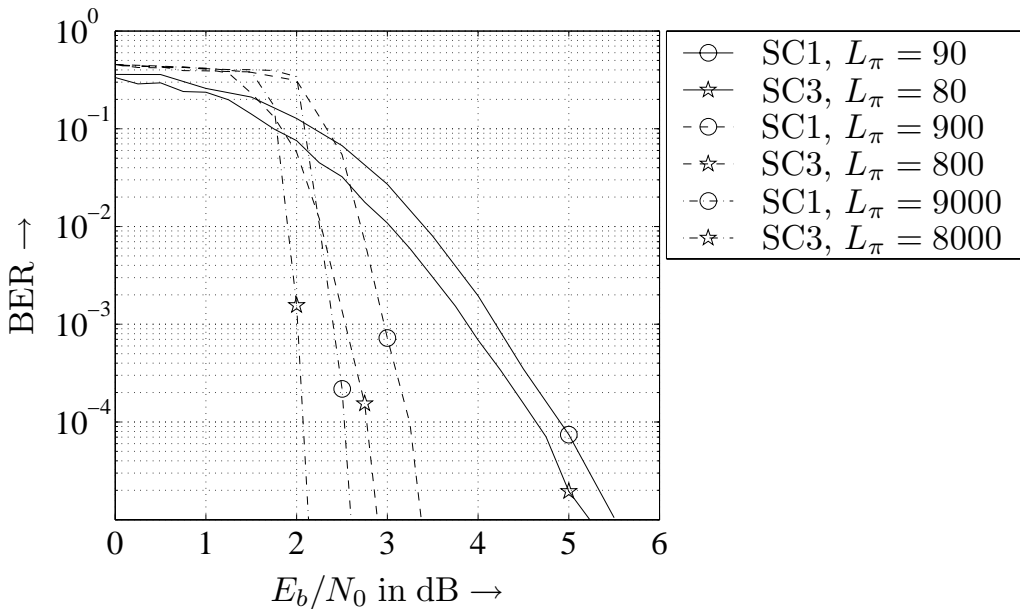


Figure 3.6.17: Comparison of puncturing schemes SC1 and SC3 for different interleaver lengths

Iterative Decoding for Parallel Concatenations

Concerning the parallel concatenation, both constituent encoders process the same information bits but in different orders. Consequently, the corresponding decoders estimate the same bits. However, their estimation is based on different parity bits that are decoupled due to the interleaver. As in the case of the serial concatenation, the extrinsic information at the decoder outputs is extracted and exchanged

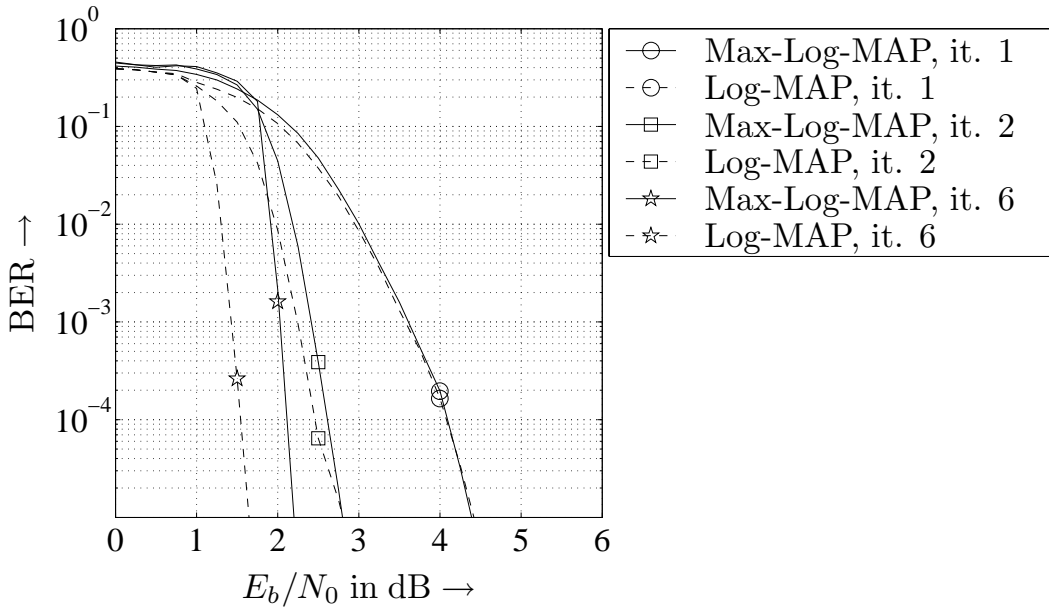


Figure 3.6.18: Comparison of Max-Log-MAP and Log-MAP for serial concatenation SC3 with $L_\pi = 8000$

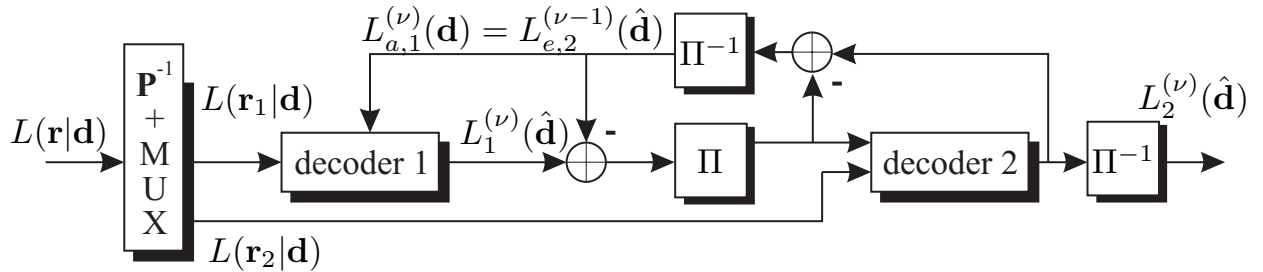


Figure 3.6.19: Iterative decoding of two parallel concatenated codes

between the decoders. **Fig. 3.6.18** shows the decoder structure. First, the received symbols are distributed to the corresponding decoders (MUX) and dummy bits are inserted at positions of punctured bits (\mathbf{P}^{-1}). The iterative process then starts with decoder 1 providing LLRs of the information bits

$$L_1^{(1)}(\hat{\mathbf{d}}) = L(\mathbf{r}_1 | \mathbf{d}) + L_{e,1}^{(1)}(\hat{\mathbf{d}}).$$

The systematic part¹⁵ as well as the extrinsic information are fed to decoder 2 which additionally receives LLRs $L(\mathbf{r}_2 | \mathbf{d})$ of the parity bits generated by encoder 2. The extrinsic information is extracted, de-interleaved and fed back as a priori knowledge $L_{a,1}^{(2)}(\hat{\mathbf{d}}) = L_{e,2}^{(1)}(\hat{\mathbf{d}})$ to decoder 1. Now, the second iteration starts with an improved decoder output

¹⁵Since the systematic information bits are an explicit part of the decoder's output, they can be provided via decoder 1.

$$L_1^{(2)}(\hat{\mathbf{d}}) = L(\mathbf{r}_1 \mid \mathbf{d}) + L_{a,1}^{(2)}(\mathbf{d}) + L_{e,1}^{(2)}(\hat{\mathbf{d}}). \quad (3.6.14)$$

exploiting the a priori information. As in the case for serial concatenated codes, the extrinsic information is extracted in each iteration and supplied as a priori knowledge to the opposite decoder. The a priori LLR $L_{a,1}(\hat{\mathbf{d}})$ stems from decoder 2 and has to be eliminated before passing the signal again to decoder 2. Performing these steps several times leads to the well-known turbo decoding.

We now discuss some simulation results for different turbo coding schemes listed in Table 3.6.2. The interleaver is chosen randomly following the concept of uniform interleaving. Unless otherwise mentioned, decoding is performed with the Max-Log-MAP algorithm.

First, **Fig. 3.6.20** show the bit error rates for a turbo code with $L_\pi = 60$. Puncturing is performed in a way that the parity bits of both encoders are transmitted alternately, i.e. the information bits are always transmitted. Obviously, the gains after the third iteration become very small for this little interleaver. The union bound is reached for $E_b/N_0 = 2.5$ dB. Note that this does not mean that the performance of an overall maximum likelihood decoder is achieved because the union bound represents only an upper bound that can be underrun as depicted in Fig. 3.6.20.

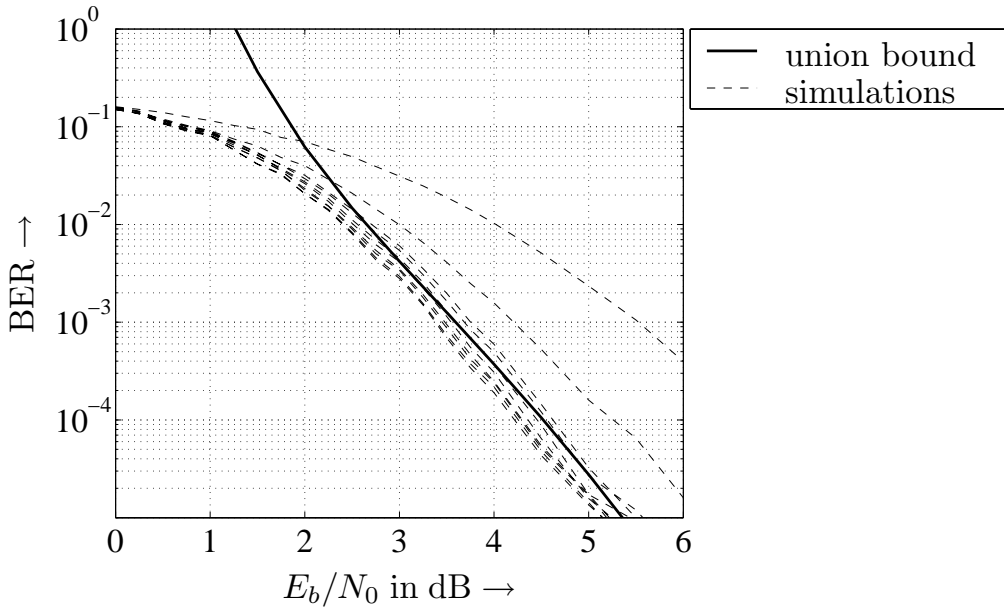


Figure 3.6.20: Illustration of performance improvements by iterative decoding for turbo code PC3, interleaver size $L_\pi = 60$

Fig. 3.6.21 shows the turbo code's performance for different interleaver lengths. While the interleaver size has nearly no impact in the first iteration, large differences can be observed for subsequent decoding iterations. The longer the interleavers the higher are the additional gains for successive iterations. This behavior

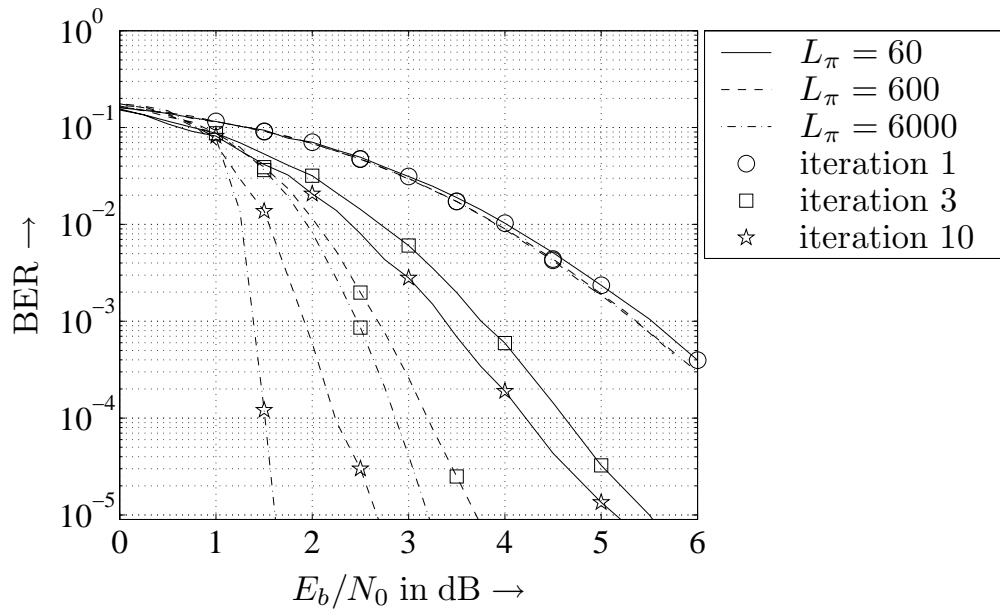


Figure 3.6.21: Comparison of turbo code P3 performance for different interleaver lengths

can be explained by the fact that large interleavers ensure a better decoupling of the a priori information, i.e. the assumption of uncorrelated successive symbols $L_a(d_i)$ is better fulfilled for large interleavers. Hence, a gain of 1.5 dB between the third and tenth iteration is obtained for $L_\pi = 6000$ and only 1 dB for $L_\pi = 600$.

Since the systematic information bits are transmitted only once for classical turbo codes, the question arises if puncturing is applied only to the parity bits or also to the information bits. The analysis with the union bound in Section 3.6.3 delivered the result that puncturing information bits is superior because the code's structure is maintained. **Fig. 3.6.22** shows the corresponding results obtained by Monte-Carlo simulations. We see that the union bound results cannot be confirmed. Obviously, puncturing only the parity bits leads to a better first iteration and a faster convergence of the iterative process. Asymptotically, it seems that the gap can be decreased. The systematic information bits help the decoder especially at low signal to noise ratios. This was also observed in [tB00b] where *code doping* is applied for ensuring a convergence of the iterative process. Moreover, puncturing an information bit affects both codes simultaneously while puncturing a parity bit has impact only on the generating constituent code.

Finally, serial and parallel concatenations should be compared. From **Fig. 3.6.23** we can conclude that the parallel concatenation of the considered convolutional code outperforms the serial one for all three interleaver lengths. Especially at very low SNRs the turbo code starts with lower error rates and, thus, reaches the waterfall region where the bit error rate decreases rapidly earlier. However, this result cannot be generalized to all possible serial and parallel concatenations.

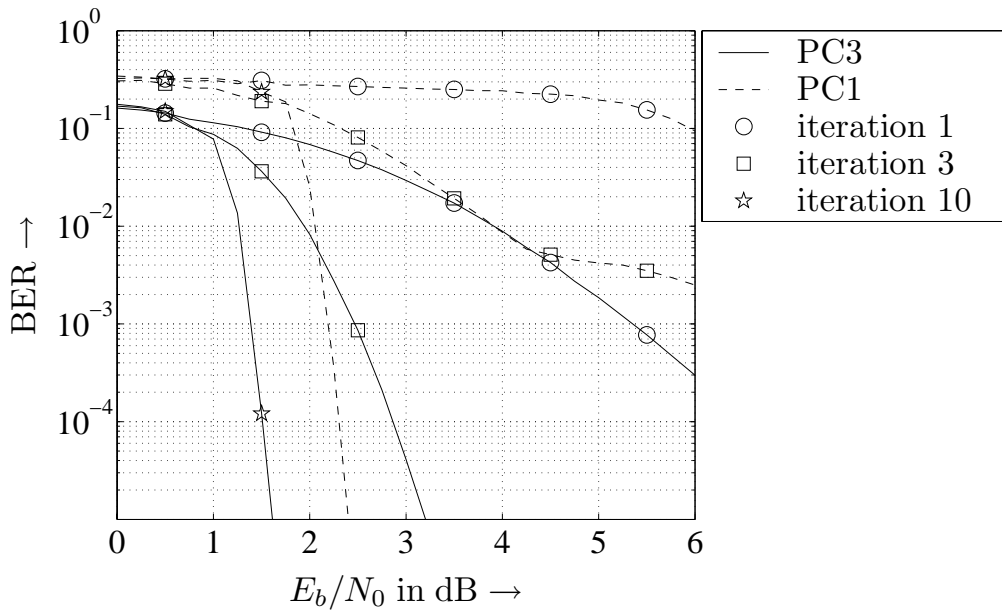


Figure 3.6.22: Comparison of different puncturing schemes PC1 and PC2 for turbo codes, $L_\pi = 6000$

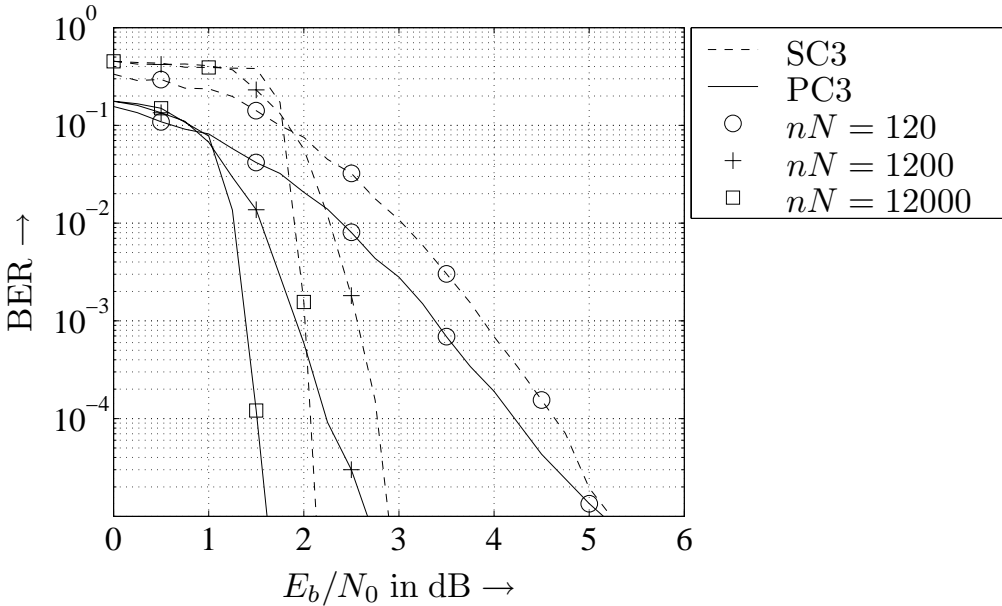


Figure 3.6.23: Comparison of serial and parallel concatenated convolutional codes for different interleaver lengths and 10 decoding iterations

3.6.5 EXIT Charts Analysis of Turbo Decoding

The above analysis focused on the distance properties of concatenated codes and approximated the bit error rate performance with the union bound. However, this technique assumes an optimum maximum likelihood decoding that is not feasible in practice. Moreover, the union bound diverges at very low SNR, i.e. exactly in the region of interest when approaching channel capacity. Realizing that the basic principle of turbo decoding is the exchange of extrinsic information,

ten Brink developed a new analysis tool based on so-called EXtrinsic Information Transfer (EXIT) charts [tB00a, tB00b, tB01a, tB01b, tB01c]. With this approach, the iterative nature of the decoding process is taken into consideration and the performance of concatenated codes can be tightly predicted. Alternative solutions like density evolution [DDP01] etc. are less accurate. However, the use of mutual information presupposes infinite long sequences (interleavers) that are impossible in practice. Nevertheless, results will demonstrate that this technique accurately predicts the true performance.

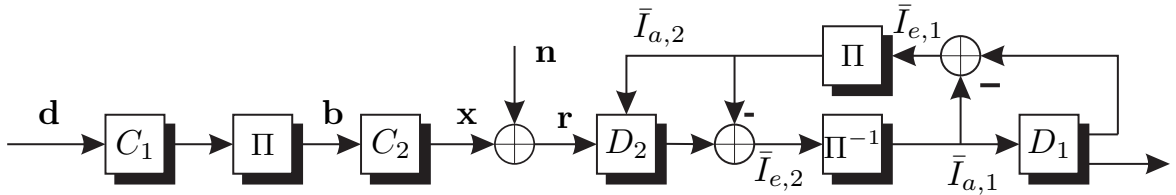


Figure 3.6.24: Simplified system model for serial code concatenation

The basic idea behind this semi-analytical approach is to determine the decoder's input-output relationship with respect to the mutual a priori information \bar{I}_a and the mutual extrinsic information \bar{I}_e . At this point, we have to distinguish serial and parallel concatenations. We start with the serial code concatenation that is depicted once again in **Fig. 3.6.24**. The inner decoder D_2 processes the channel output \mathbf{r} as well as the a priori LLRs $L_{a,2}(\mathbf{b})$ (compare Fig. 3.6.14) provided by the outer decoder D_1 . The information part contained in $L_{a,2}(\mathbf{b})$ that is common to the true code bits \mathbf{b} is the mutual a priori information (see also definition of mutual information in Section 2.1.2)

$$\bar{I}_{a,2} = \bar{I}(\mathbf{b}; L_{a,2}(\mathbf{b})) = \bar{I}_{e,1}. \quad (3.6.15)$$

The second equality holds because the amount of information does not change by permutations. The mutual extrinsic information at the output of D_2

$$\bar{I}_{e,2} = \bar{I}(\mathbf{b}; L_{e,2}(\hat{\mathbf{b}})) = f(E_s/N_0, \bar{I}_{a,2}) = f(C, \bar{I}_{a,2}) \quad (3.6.16)$$

depends on both inputs and can be expressed as a function of the channel capacity C (or equivalently E_s/N_0) and $\bar{I}_{a,2}$. With the above argumentation we obtain

$$\bar{I}_{a,1} = \bar{I}_{e,2}. \quad (3.6.17)$$

Contrarily, the outer decoder D_1 processes only the output of the inner decoder, it has no direct access to the channel output. Therefore, it is independent of the signal to noise ratio and the mutual information of its extrinsic output $L_{e,1}(\hat{\mathbf{b}})$

$$\bar{I}_{e,1} = \bar{I}(\mathbf{b}; L_{e,1}(\hat{\mathbf{b}})) = f(\bar{I}_{a,1}) \quad (3.6.18)$$

is only a function of $\bar{I}_{a,1}$.

Looking at the parallel code concatenation depicted in **Fig. 3.6.25**, we have similar relationships. However, a slight difference appears in that both decoders have access to the channel output so that their outputs are both functions of the signal to noise ratio as well as the a priori information. Moreover, the mutual information is always related to the information bits \mathbf{d} instead of the code bits \mathbf{b} because the decoders exchange information with respect to \mathbf{d} . We obtain

$$\bar{I}_{e,1} = \bar{I}(\mathbf{d}; L_{e,1}(\hat{\mathbf{d}})) = f(E_s/N_0, \bar{I}_{a,1}) = f(C, \bar{I}_{a,2}) \quad (3.6.19)$$

$$\bar{I}_{e,2} = \bar{I}(\mathbf{d}; L_{e,2}(\hat{\mathbf{d}})) = f(E_s/N_0, \bar{I}_{a,2}) = f(C, \bar{I}_{a,2}) \quad (3.6.20)$$

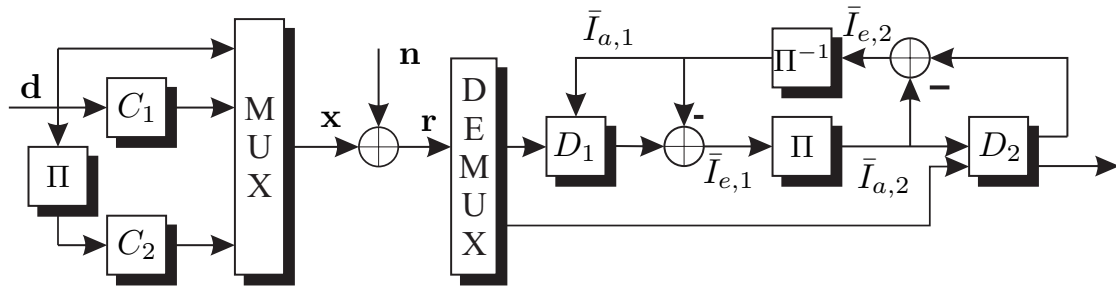


Figure 3.6.25: Simplified system model for parallel code concatenation

Next, we have to answer the question how to determine the mutual information \bar{I}_e and \bar{I}_a . We follow the semi-analytical approach of ten Brink [tB01c] where \bar{I}_a is obtained by modelling the a priori LLRs $L_a(d_\mu)$ at the decoder inputs as Gaussian distributed random variables. The motivation comes from the assumption that the extrinsic information at the output of a decoders is Gaussian distributed. Although this is only approximately true after some iterations, the results justify the assumption. According to (3.4.6) on page 109, the LLR of a signal $y = x + n$ with binary $x = \pm 1$ has the form

$$L(y) = L_{\text{ch}} \cdot y = L_{\text{ch}} \cdot (x + n) = \frac{2}{\sigma_{N'}^2} \cdot x + \frac{2}{\sigma_{N'}^2} \cdot n \quad (3.6.21)$$

where n denotes white Gaussian noise with variance $\sigma_{N'}^2 = N_0/2/T_s$. Due to $x = \pm 1$, $\sigma_x^2 = E_s/T_s = 1$ holds and $L_{\text{ch}} = 2/\sigma_{N'}^2$ is obtained. Obviously, the mean of this LLR for fixed x is $2/\sigma_{N'}^2$, while its variance amounts to

$$\sigma_{N_a}^2 = E \left\{ \left(\frac{2}{\sigma_{N'}^2} \right)^2 \cdot n^2 \right\} = \left(\frac{2}{\sigma_{N'}^2} \right)^2 \cdot \sigma_{N'}^2 = \frac{4}{\sigma_{N'}^2}. \quad (3.6.22)$$

Comparing (3.6.22) with the mean we recognize that the latter is half of the variance [tB01c]. Since x is antipodal but d_μ and b_μ are unipolar, we define

the new variable $a_\mu = 1 - 2d_\mu$ or $a_\mu = 1 - 2b_\mu$ depending on the considered concatenation. Hence, can model the Gaussian distributed LLR by

$$L_a(\mathbf{a}) = \frac{\sigma_{\mathcal{N}_a}^2}{2} \cdot \mathbf{a} + \mathbf{n}_a . \quad (3.6.23)$$

From (3.6.23) we see that the artificially generated a priori LLR is created by taking the true data \mathbf{a} – based on either the information bits or the code bits –, weighting them with $\sigma_{\mathcal{N}_a}^2/2$ and adding white Gaussian noise \mathbf{n}_a with zero mean and variance $\sigma_{\mathcal{N}_a}^2$.

According to (2.2.29) on page 70, the average mutual information between equiprobable binary symbols a_μ and the a priori LLRs is defined to

$$\bar{I}_a = 1 + \frac{1}{2} \cdot \sum_{\alpha=\pm 1} \int_{-\infty}^{\infty} p_{\mathcal{N}_a}(\xi - \alpha A) \log_2 \left(\frac{p_{\mathcal{N}_a}(\xi - \alpha A)}{p_{\mathcal{N}_a}(\xi - A) + p_{\mathcal{N}_a}(\xi + A)} \right) d\xi \quad (3.6.24)$$

with $A = \sigma_{\mathcal{N}_a}^2/2$. Inserting the Gaussian distribution into (3.6.24) and exploiting the integrand's symmetry yields

$$\bar{I}_a = 1 - \int_{-\infty}^{\infty} \frac{1}{\sqrt{2\pi\sigma_{\mathcal{N}_a}^2}} \cdot \exp \left[-\frac{(\xi - \sigma_{\mathcal{N}_a}^2/2)^2}{2\sigma_{\mathcal{N}_a}^2} \right] \log_2 (1 + e^{-\xi}) d\xi . \quad (3.6.25)$$

Equation (3.6.25) shows that $\bar{I}_a = f(\sigma_{\mathcal{N}_a}^2)$ is only a function of the a priori variance $\sigma_{\mathcal{N}_a}^2$. Since this function is monotonically increasing as depicted in **Fig. 3.6.26**, the variance of \mathcal{N}_a can be determined by $\sigma_{\mathcal{N}_a}^2 = f^{-1}(\bar{I}_a)$. Hence, the a priori information is modelled according to (3.6.23) where the noise variance $\sigma_{\mathcal{N}_a}^2$ is chosen according to the given \bar{I}_a .

Due to the nonlinear behavior of soft-in soft-out decoding algorithms, the mutual extrinsic information cannot be calculated analytically. Hence, simulations have to be carried out for measuring the conditional histograms $\hat{p}_{\mathcal{Z}|a=\pm 1}(z)$ of the extrinsic information $z_\mu = L_e(a_\mu)$ at the decoder output. The average extrinsic information is obtained by solving

$$\bar{I}_e = 1 + \frac{1}{2} \cdot \sum_{\alpha=\pm 1} \int_{-\infty}^{\infty} \hat{p}_{\mathcal{Z}|a=\alpha}(z) \log_2 \left(\frac{\hat{p}_{\mathcal{Z}|a=\alpha}(z)}{\hat{p}_{\mathcal{Z}|a=+1}(z) + \hat{p}_{\mathcal{Z}|a=-1}(z)} \right) dz \quad (3.6.26)$$

numerically.

Fig. 3.6.27 shows the relationship $\bar{I}_e = f(E_s/N_0, \bar{I}_e)$ for a systematic recursive convolutional code and an AWGN channel with different signal-to-noise-ratios. The decoder processes both, the output of the AWGN channel as well as a priori

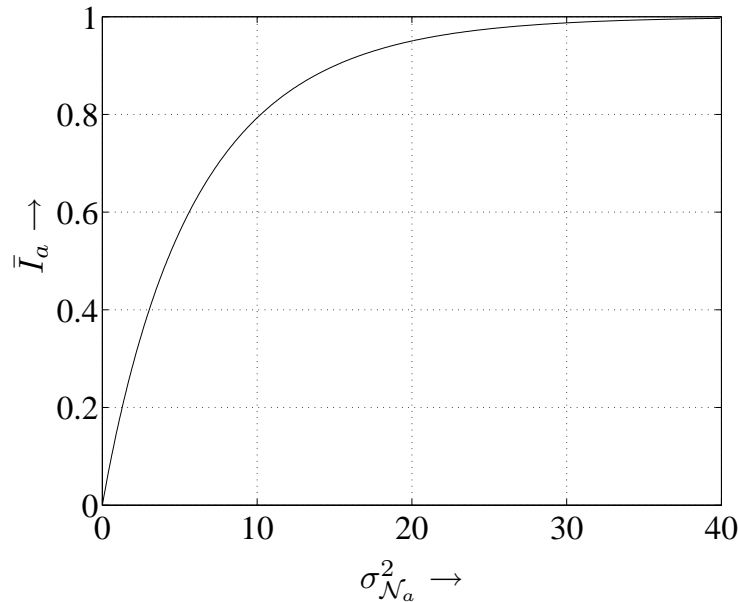


Figure 3.6.26: Relationship between $\sigma_{\mathcal{N}_a}^2$ and the mutual a priori information \bar{I}_a

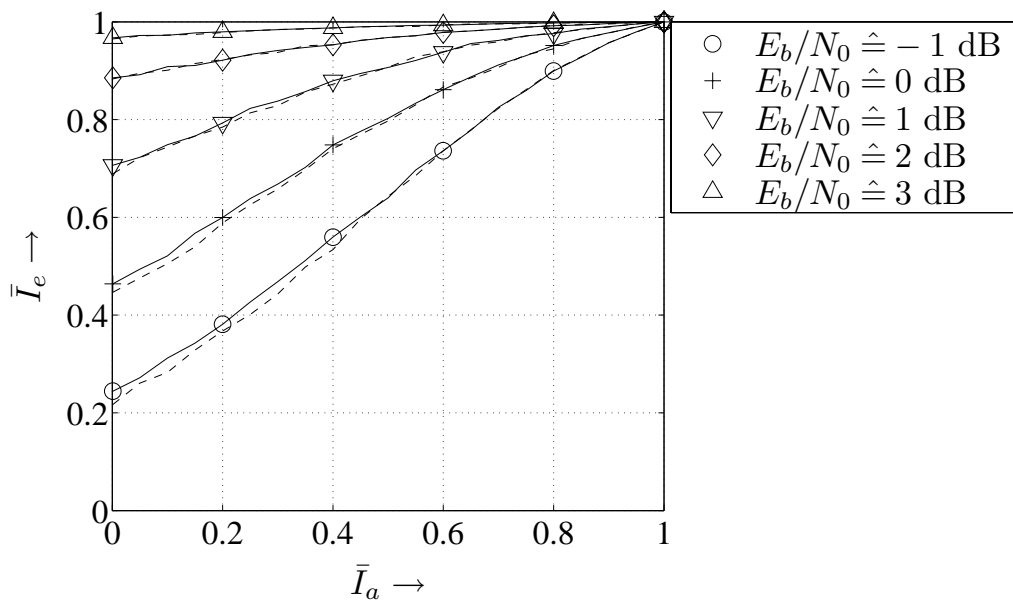


Figure 3.6.27: Mutual extrinsic versus mutual a priori information for RSC code with $g_1(D) = 1$, $g_2(D) = (1 + D + D^3)/(1 + D + D^2 + D^3)$ and AWGN, MAP algorithm: solid line, Max-Log-MAP algorithm: dashed line

LLRs with specified \bar{I}_a . Obviously, the mutual extrinsic information increases with growing SNR and \bar{I}_a . If the a priori information is certain, i.e. $\bar{I}_a = 1$, the extrinsic information at the decoder output is reliable too regardless of the channel quality. Contrarily, for high SNR, nearly no a priori information is needed for good decoding results. Moreover, the Max-Log-MAP algorithm seems to lose only at very low signal-to-noise-ratios and for small mutual a priori information.

Fig. 3.6.28a compares the results for different convolutional codes if only a priori information is provided to the decoder, e.g. the outer decoder in a serial concatenation. Astonishingly, all curves intersect at the point (0.5, 0.5). Up to now, no explanation was found for this behavior. On the left hand side of this intersection point, stronger codes with large constraint length L_c perform worse than codes with small L_c . Moreover, the mutual extrinsic information is smaller than the mutual a priori information at the decoder's input. On the right hand side, the relations change and strong codes perform better. Here, \bar{I}_e exceeds \bar{I}_a .

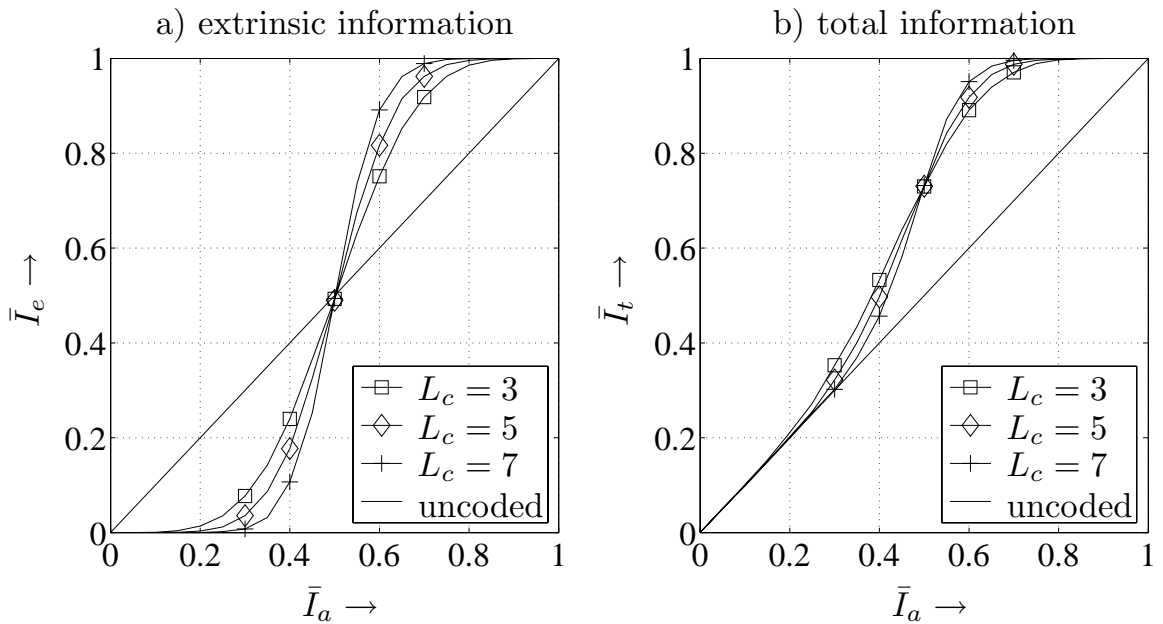


Figure 3.6.28: Mutual extrinsic (a) and total (b) information versus mutual a priori information for RSC codes with different L_c , AWGN channel and MAP decoding

In **Fig. 3.6.28b**, the total mutual information $\bar{I}_t = \bar{I}(\mathbf{b}; L(\hat{\mathbf{b}}))$ based on $L(\hat{\mathbf{b}}) = L_a(\mathbf{b}) + L_e(\hat{\mathbf{b}})$ at the decoder's output is depicted. There is still the intersection at $\bar{I}_a = 0.5$. Additionally, it becomes obvious that the decoder always provides a (possibly very small) improvement compared to the uncoded case. Comparing Figs. a) and b) we observe that the sum of $L_a(\mathbf{b})$ and $L_e(\hat{\mathbf{b}})$ does not result in a sum of the corresponding mutual information \bar{I}_a and \bar{I}_e . Instead, $L(\hat{\mathbf{b}})$ has to be directly used to determine \bar{I}_t or an approximation called *information combining* [LHHH03, LHH04] can be applied.

Serial Concatenation

The basic idea behind EXIT charts is that extrinsic information provided by one constituent decoder is used in the turbo decoding process as a priori information for the other decoder. A graphical illustration of this process is obtained by drawing

the trajectories of inner and outer code into one diagram and exchanging abscissa and ordinate for the outer code. This leads to an EXtrinsic Information Transfer (EXIT) chart like the one depicted in **Fig. 3.6.29**. It shows the trajectories of an outer NSC code punctured to $R_{c,1} = 3/4$ and an inner RSC code with rate $R_{c,2} = 2/3$ resulting in an overall code rate of $R_c = 1/2$. Be aware that the signal to noise ratio $E_s/N_0 = R_c E_b/N_0$ at the input of the inner decoder is adjusted according to the overall code rate R_c and not to the individual rate $R_{c,2}$.

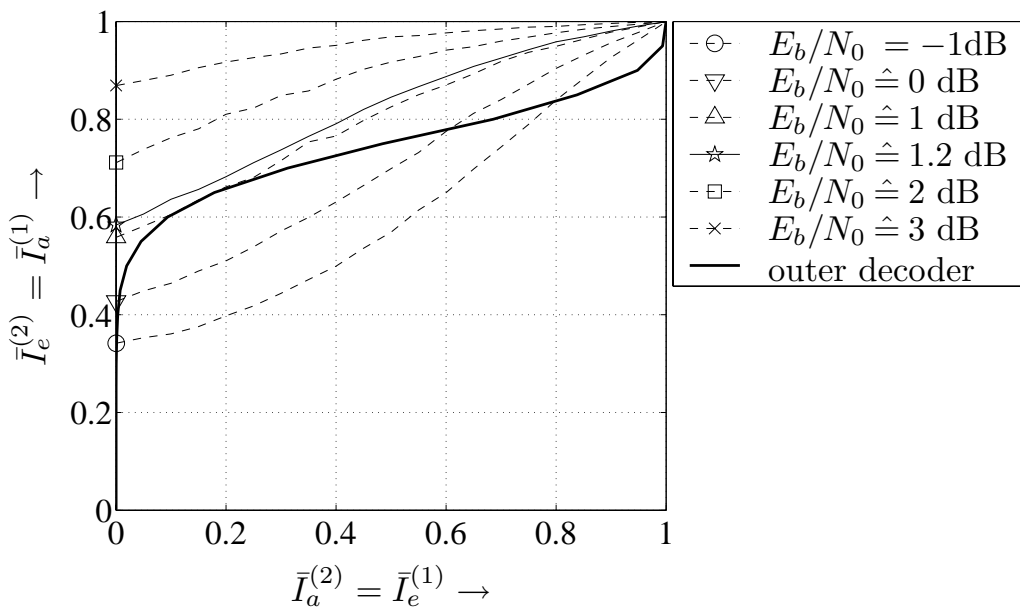


Figure 3.6.29: EXIT chart for serial concatenation of outer NSC code and inner RSC code as used in Fig. 3.6.18, AWGN channel and MAP decoding

The bold solid curve of the outer code does not depend on the signal-to-noise ratio while the dashed curves of the inner code strongly depend on the SNR. It can be seen that the curves touch for $E_b/N_0 = 1$ dB (\triangle). For larger E_b/N_0 , e.g. solid line with pentagon for $E_b/N_0 = 1.2$ dB, the dashed curves lie above the solid one and a gap opens through which the decoding process can converge. Only in this case the a priori information leads to an increased extrinsic information so that reliability is improved in each iteration.

The convergence of the turbo decoding process is demonstrated in **Fig. 3.6.30** for $E_b/N_0 = 1.2$ dB. The squares indicate the mutual extrinsic information $\bar{I}_{e,2} = \bar{I}_{a,1}$ at the output of the inner decoder, the pentagons the mutual extrinsic information $\bar{I}_{e,1} = \bar{I}_{a,2}$ at the output of the outer decoder. Obviously, the inner decoder starts without any a priori information ($\bar{I}_{a,2}^{(1)} = 0$) and delivers $\bar{I}_{e,2}^{(1)} \approx 0.58$. This extrinsic information is exactly the a priori information $\bar{I}_{a,1}^{(1)}$ of the outer decoder, that provides $\bar{I}_{e,1}^{(1)} = 0.07$. This becomes the a priori information of the inner decoder in the second iteration that delivers $\bar{I}_{e,2}^{(2)} \approx 0.61$ and so on.

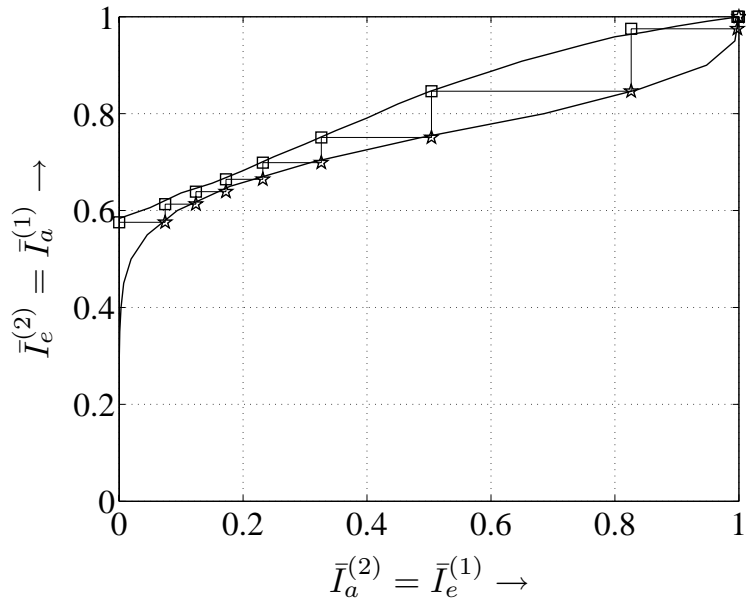


Figure 3.6.30: EXIT chart for serial concatenation of outer NSC and inner RSC code as used in Fig. 3.6.18, AWGN channel with $E_b/N_0 = 1.2$ dB and MAP decoding

Due to the tunnel between the trajectories, the mutual extrinsic information always increases from iteration to iteration and finally approaches $\bar{I}_{e,1} = \bar{I}_{e,2} = 1$. If the trajectories intersect before the point $(\bar{I}_a, \bar{I}_e) = (1, 1)$, the iterative decoding process gets stuck and convergence is lost. The larger the gap, the less iterations are needed until convergence, but the larger is also the gap to Shannon's channel capacity. Hence, for large interleavers, EXIT charts represent a suitable mean for predicting the convergence behavior for iterative decoding of concatenated codes. Moreover, it is possible to design codes whose decoding trajectories match to each other so that a very narrow tunnel leads to the point $(\bar{I}_a, \bar{I}_e) = (1, 1)$. In [tB00b] a serial concatenated code is presented that approaches Shannon's channel capacity within a gap of 0.1 dB.

Fig. 3.6.31 shows the results obtained with the Max-Log-MAP decoder. Astonishingly, the trajectories do not tightly predict the true behavior of the turbo decoder for $E_b/N_0 = 1.8$ dB. Although the decoder slowly converges to $(\bar{I}_a, \bar{I}_e) = (1, 1)$, the trajectories predict a faster convergence. For smaller E_b/N_0 , convergence cannot be achieved anymore although predicted. The reason for this discrepancy is the assumption that each decoder is assumed to obtain true LLR's. In fact, they are only provided with approximations of LLR's delivered by suboptimum Max-Log-MAP decoders.

At higher signal-to-noise-ratios, e.g. $E_b/N_0 = 2$ dB, the true decoding behavior matches again the trajectories' prediction. Hence, EXIT charts based on the Max-Log-MAP algorithm are not suited for the determination of the minimum required E_b/N_0 in order to ensure convergence.

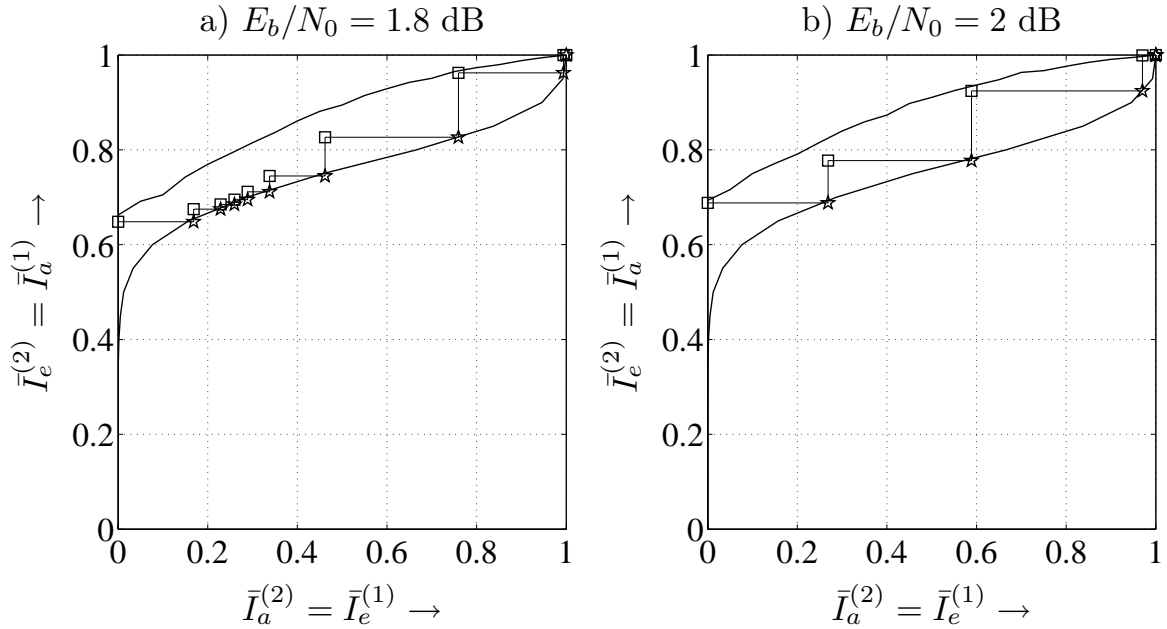


Figure 3.6.31: EXIT chart for serial concatenation of outer NSC and inner RSC code as used in Fig. 3.6.18, AWGN channel and Max-Log-MAP decoding

Parallel Concatenation

The analysis for parallel code concatenations is depicted in **Fig. 3.6.32**. The left diagram shows the results for symbol-by-symbol MAP decoding. Obviously, the prediction tightly matches the true turbo decoding behavior. In Fig. 3.6.32b, it can be seen that the turbo decoder gets stuck when the Max-Log-MAP algorithm is applied although the trajectories predict convergence. As already explained for the serial concatenation, the reason for this failure is that the assumptions made for the EXIT charts analysis are not fulfilled when employing the Max-Log-MAP decoder.

One assumption was that log-likelihood ratios represent the extrinsic information that is exchanged between the decoders. The Max-Log-MAP does not deliver exact LLRs but only approximations (see page 120) and the predicted convergence cannot be achieved. In order to verify this explanation, **Fig. 3.6.33a** shows the results for Max-Log-MAP decoding if the a priori information is provided by an additionally introduced MAP decoder. We recognize that convergence is obtained. Contrarily, **Fig. 3.6.33b** shows the results for MAP decoding when the a priori information is provided by a Max-Log-MAP decoder. In this case, the iterative decoding scheme does not converge. From this, we can conclude that for low SNR's when the trajectories come close to each other, optimum MAP decoding is crucial because the extrinsic information delivered by the Max-Log-MAP decoder leads to a significant loss avoiding convergence.

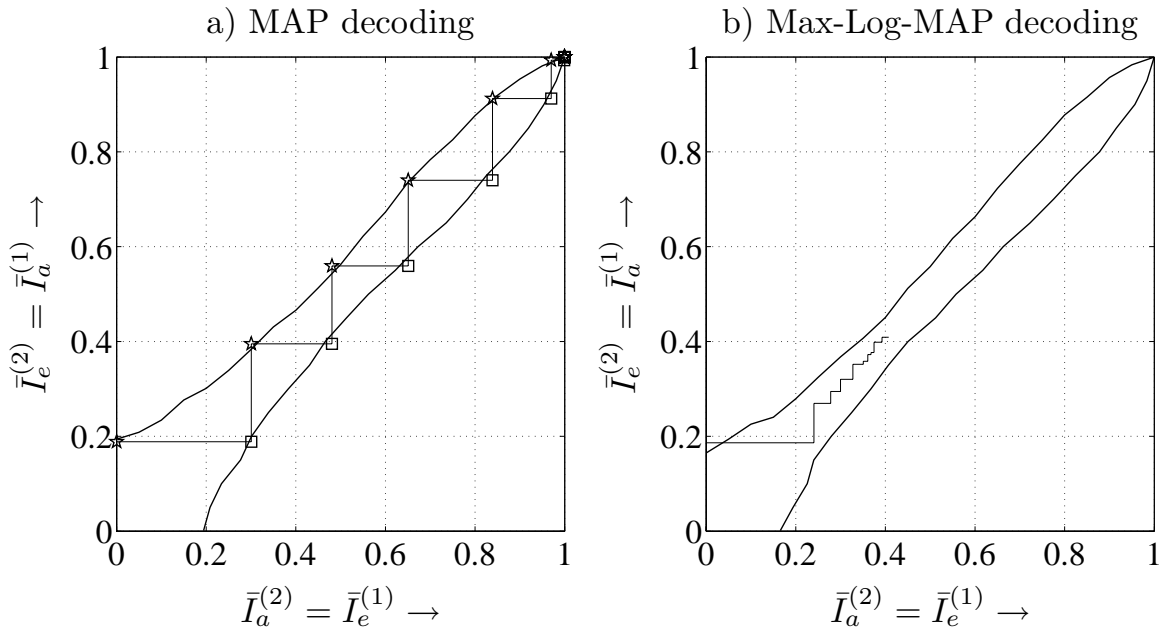


Figure 3.6.32: EXIT chart for parallel concatenation of two RSC codes as used in Fig. 3.6.22 (P1), AWGN channel with $E_b/N_0 = 1$ dB

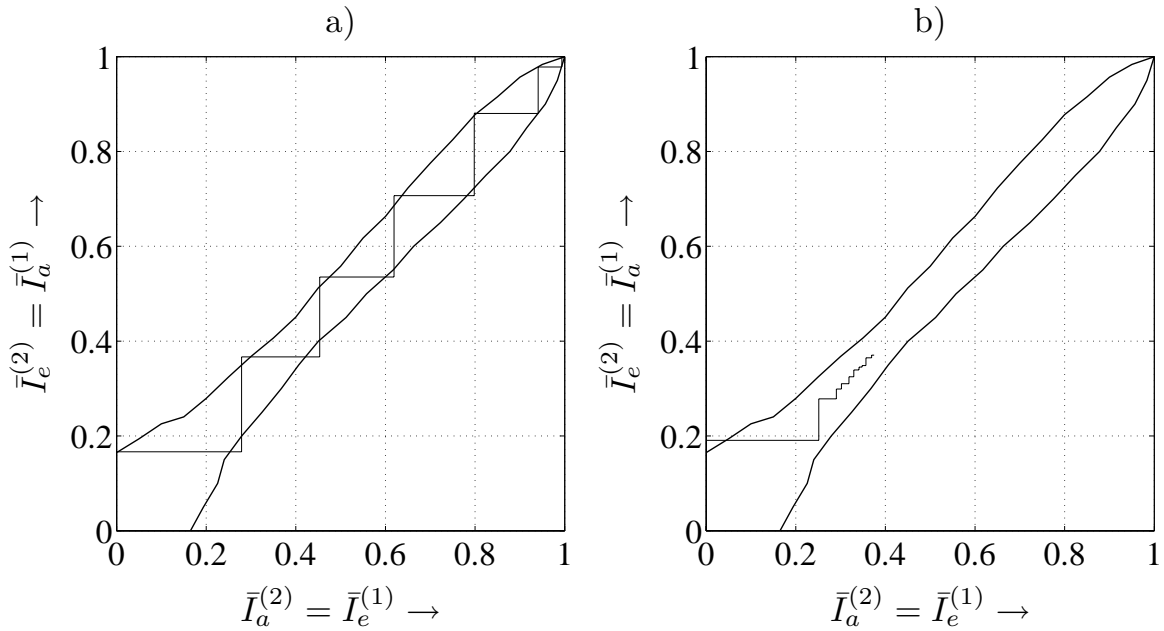


Figure 3.6.33: EXIT chart for parallel concatenation of two RSC codes as used in Fig. 3.6.22, AWGN channel and with $E_b/N_0 = 1$ dB

- a) Max-Log-MAP decoding with a priori information by MAP decoder
- b) MAP decoding with a priori information by Max-Log-MAP decoder

Chapter 4

Code Division Multiple Access

4.1 Introduction

In Section 1.1.2 we introduced different multiple access techniques. Contrarily to time and frequency division multiple access schemes, each user occupies the whole time-frequency domain in CDMA systems. The signals are separated with spreading codes which are used for artificially increasing the signal bandwidth beyond the necessary value. Therefore, CDMA systems incorporate spread spectrum techniques like frequency hopping, direct-sequence spread spectrum or chirp techniques [Pro95]. Despread can only be performed with knowledge of the employed spreading code.

For a long time, CDMA or spread spectrum techniques were restricted to military applications. Meanwhile, they found their way into mobile radio communications and have been established in several standards. The IS95 standard [GJP⁺91, SG91] in the USA employs CDMA as well as the UMTS [TCD⁺98, HT02] and IMT2000 [DGNS98, OP98a, OP98b] standards. Many reasons exist for using CDMA, e.g. spread spectrum signals show a high robustness against multipath propagation. Further advantages are more related to cellular aspects of communication systems.

Due to the simultaneous transmission in the same frequency band, appropriate correlation properties of the spreading codes are needed allowing the signal separation at the receiver. However, these properties are generally destroyed by the influence of the mobile radio channel. Especially the frequency selectivity has severe impact on broadband signals. As a consequence, multi-user interference occurs and limits

the system performance. Contrarily to TDMA and FDMA systems where each time slot and each frequency band can be occupied only once, CDMA does not have this strict limitation. Although the interference grows with each additional user and degrades the performance, this degradation is 'graceful' and not abrupt as for TDMA and FDMA.

Multi-user interference can be combatted in two different ways. On the one hand, interference is simply treated as additional white Gaussian noise and mitigated by strong error control coding (see Chapter 3 and Section 4.4) [Dek00, KDK00b]. On the other hand, multi-user detection strategies try to cancel or suppress the interference [Ver98, HT00, VS99, TH99, SM99, ARAS99, Kle96, Mos96] and are discussed in Chapter 5.

In this chapter, we describe the general concept of CDMA systems. We will explain the way of spreading, discuss the correlation properties of spreading codes and demonstrate the limited performance of a single-user matched filter (SUMF). Moreover, the principle differences between uplink and downlink transmission are described. Additionally, the combination of OFDM (Orthogonal Frequency Division Multiplexing) and CDMA (OFDM-CDMA) as an example of multi-carrier CDMA (MC-CDMA) is compared to the classical single-carrier CDMA (SC-CDMA).

For the sake of simplicity, we restrict to a chip-level based system model. Hence, the whole system works at the chip rate $1/T_c$ and the channel model from Fig. 1.2.5 includes the impulse shaping filters at transmitter and receiver. Furthermore, this model implies a perfect synchronization at the receiver.

4.2 Fundamentals

4.2.1 Direct-Sequence Spread Spectrum

The spectral spreading inherent in any CDMA system can be performed in several ways, e.g. frequency hopping, chirp techniques. We concentrate here on the widely-used direct-sequence spreading where the information bearing signal is directly multiplied with the spreading code. Further information can be found in [PSM82, ZP85, CM88, PMS91, Pro95, Vit95, GV97, SH99]. For the moment, we consider an uncoded system but the description can be easily extended to coded systems. **Fig. 4.2.1** shows the principle structure of a direct-sequence spread spectrum (DS-SS) system.

The generally complex-valued symbols $a[\ell]$ at the output of the signal mapper are multiplied with a spreading code $c[\ell, k]$. The resulting signal is

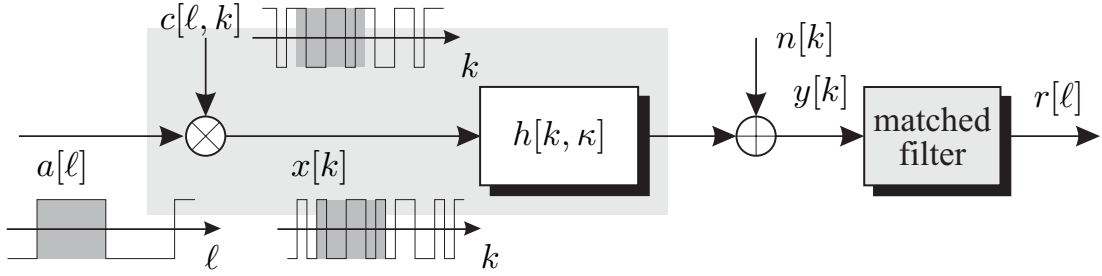


Figure 4.2.1: Structure of direct-sequence spread spectrum system

$$x[k] = \sum_{\ell} a[\ell] \cdot c[\ell, k] \quad \text{with} \quad c[\ell, k] = \begin{cases} \pm 1 & \text{for } \ell N_s \leq k < (\ell + 1)N_s \\ 0 & \text{else} \end{cases} \quad (4.2.1)$$

where the chip index k runs N_s times faster than the symbol index ℓ . Since the $c[\ell, k]$ is nonzero only in the interval $[\ell N_s, (\ell+1)N_s[$, spreading codes of consecutive symbols do not overlap. The spreading factor N_s is often termed processing gain G_p and denotes the number of chips $c[\ell, k]$ multiplied with a single symbol $a[\ell]$. In coded systems, G_p includes also the code rate R_c and, hence, describes the ratio between the durations of an information bit (T_b) and a chip (T_c)

$$G_p = \frac{T_b}{T_c} = \frac{T_s}{R_c \cdot T_c} = \frac{N_s}{R_c}. \quad (4.2.2)$$

This definition is of special interest in systems with varying code rates and spreading factors as discussed in Section 4.4. The processing gain describes the ability to suppress interfering signals. The larger G_p , the higher is the suppression.

In the sequel, we restrict to binary spreading sequences, i.e. the chips take the values $\pm 1/\sqrt{N_s}$ because they are commonly used in practical systems. Hence, the signal to noise ratio per chip is N_s times smaller than for a symbol $a[\ell]$ and $E_s/N_0 = N_s \cdot E_c/N_0$ holds. Since the local generation of spreading codes at transmitter and receiver has to be easily established, feedback shift registers providing periodical sequences are often used (see Section 4.2.4). We distinguish short codes and long codes. The period of short codes equals exactly the spreading factor N_s , i.e. each symbol $a[\ell]$ is multiplied with the same code. Contrarily, the period of long codes exceeds the duration of one symbol $a[\ell]$ so that different symbols are multiplied with different segments of a long sequence. For notational simplicity, we refer to short codes unless otherwise stated. In Fig. 4.2.1, spreading with short codes for $N_s = 7$ is illustrated by showing the signals $a[\ell]$, $c[\ell, k]$ and $x[k]$.

Fig. 4.2.2 shows the power spectral densities of $a[\ell]$ and $x[k]$ for a spreading factor $N_s = 4$, an oversampling factor of $w = 8$ and rectangular pulses of the chips. Obviously, the densities have a $(\sin(x)/x)^2$ shape and the main lobe of $x[k]$

is four times broader than that of $a[\ell]$. However, the total power of both signals is still the same, i.e. spreading does not affect the signals power. Hence, the power spectrum density around the origin is larger for $a[\ell]$.

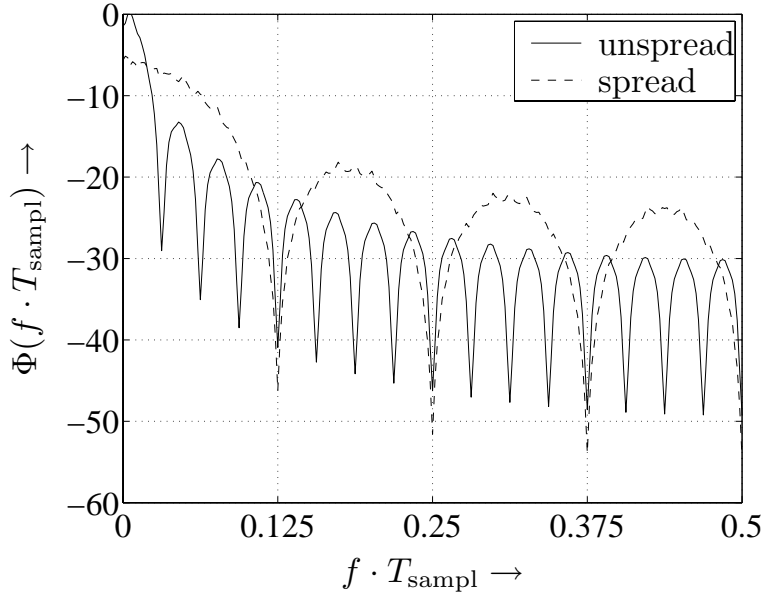


Figure 4.2.2: Power spectral densities of original and spread signal for $N_s = 4$

Receiver for Frequency Nonselective Fading

For the sake of simplicity, we explain the despreading first for frequency-nonselective channels, i.e.

$$y[k] = h[k] \cdot x[k] + n[k] = \sum_{\ell} a[\ell] \cdot h[k] c[\ell, k] + n[k] = \sum_{\ell} a[\ell] \cdot s[\ell, k] + n[k] \quad (4.2.3)$$

represents the received signal. The product $s[\ell, k] = h[k] \cdot c[\ell, k]$ of spreading code and channel coefficient is called signature.¹ At the receiver, the filter that maximizes the signal to noise ratio has to be matched to $s[\ell, k]$, i.e. $g_{\text{MF}}[\ell, k] = s^*[\ell, (\ell + 1)N_s - k]$ holds. The convolution of $y[k]$ with $g_{\text{MF}}[k]$ now yields

$$\begin{aligned} \tilde{r}[k] &= \sum_{k'=\ell N_s}^{(\ell+1)N_s-1} y[k'] \cdot g_{\text{MF}}[\ell, k - k'] \\ &= \sum_{k'=\ell N_s}^{(\ell+1)N_s-1} y[k'] \cdot s^*[\ell, k' + (\ell + 1)N_s - k]. \end{aligned} \quad (4.2.4)$$

¹For frequency-selective channels, the signature is defined more generally on page 171 as the convolution between $h[k, \kappa]$ and $s[\ell, k]$. For flat fading channels considered here, the convolution reduces to a simple multiplication.

If the channel is constant during N_s samples what is generally fulfilled in practice, $h[k]$ can be expressed by $h[\ell]$ and the signature becomes $s[\ell, k] = h[\ell] \cdot c[\ell, k]$. Sampling $\tilde{r}[k]$ in (4.2.4) at $k = (\ell + 1)N_s$ after all N_s chips of the ℓ -th symbol $a[\ell]$ have been received, simply delivers the correlation between $y[k]$ and $s[\ell, k]$ within one symbol duration $T_s = N_s T_c$. Therefore, the optimum receiver is a correlator sampled at symbol rate $1/T_s$

$$\begin{aligned}
r[\ell] &= \tilde{r}[k] \Big|_{k=(\ell+1)N_s} = \sum_{k'=\ell N_s}^{(\ell+1)N_s-1} y[k'] \cdot s^*[\ell, k'] \\
&= \sum_{k'=\ell N_s}^{(\ell+1)N_s-1} (h[\ell]c[\ell, k']a[\ell] + n[k']) \cdot h[\ell]^* \cdot c[\ell, k'] \\
&= |h[\ell]|^2 \cdot \sum_{k'=\ell N_s}^{(\ell+1)N_s-1} a[\ell] \cdot \underbrace{c[\ell, k']^2}_{=1/N_s} + h[\ell]^* \cdot \sum_{k'=\ell N_s}^{(\ell+1)N_s-1} n[k'] \cdot c[\ell, k'] \\
&= |h[\ell]|^2 \cdot a[\ell] + \tilde{n}[\ell]. \tag{4.2.5}
\end{aligned}$$

The matched filter delivers the original symbol $a[\ell]$ weighted with the squared magnitude $|h[\ell]|^2$ of the channel coefficient and disturbed by white Gaussian noise with zero mean and variance $\sigma_{\mathcal{N}}^2 = |h[\ell]|^2 \cdot \sigma_{\mathcal{N}}^2$. Since this is the same result as for narrow-band transmission, spread spectrum gives no advantage in single-user systems with flat fading channels.

Receiver for Frequency Selective Fading

The broadened spectrum leads in many cases to a frequency-selective behavior of the mobile radio channel. For appropriately chosen spreading codes no equalization is necessary and the matched filter is still a suited mean. First, we redefine the signature as the convolution of spreading code and channel impulse response

$$s[\ell, k] = c[\ell, k] * h[\ell, k] = \sum_{\kappa=0}^{L_t-1} h[\ell, \kappa] \cdot c[\ell, k - \kappa]. \tag{4.2.6}$$

In contrast to the spreading code itself, the length of the signature now exceeds N_s samples, and successive symbols interfere. Correlating the received signal $y[k]$ with the signature $s[\ell, k]$ yields after some manipulations

$$\begin{aligned}
r[\ell] &= \sum_{k=\ell N_s}^{(\ell+1)N_s+L_t-1} s[\ell, k]^* \cdot y[k] \\
&= \sum_{\kappa=0}^{L_t-1} h[\ell, L_t - 1 - \kappa]^* \cdot \sum_{k=\ell N_s+L_t-1}^{(\ell+1)N_s+L_t-2} y[k - \kappa] \cdot c[\ell, k - L_t + 1] \tag{4.2.7}
\end{aligned}$$

Implementing (4.2.7) directly leads to the well-known Rake receiver that was originally introduced by Price and Green in 1958 [PG58]. It represents the matched receiver for spread spectrum communications over frequency-selective channels. From **Fig. 4.2.3** we recognize that it basically consists of a parallel concatenation of several correlators also called fingers each synchronized to a dedicated propagation path. The received signal $y[k]$ is first delayed in each finger by $0 \leq \kappa < L_t$, then weighted with the spreading code (with a constant delay $L_t - 1$) and integrated over a spreading period. Notice that integration starts after $L_t - 1$ samples have been received, i.e. even the most delayed replica $h[\ell, L_t - 1] \cdot x[k - L_t + 1]$ is going to be sampled. Next, the branch signals are weighted with the complex conjugated channel coefficients and summed. Therefore, the Rake receiver maximum ratio combines the propagation paths and fully exploits diversity (see Section 1.5) provided by the frequency-selective channel.

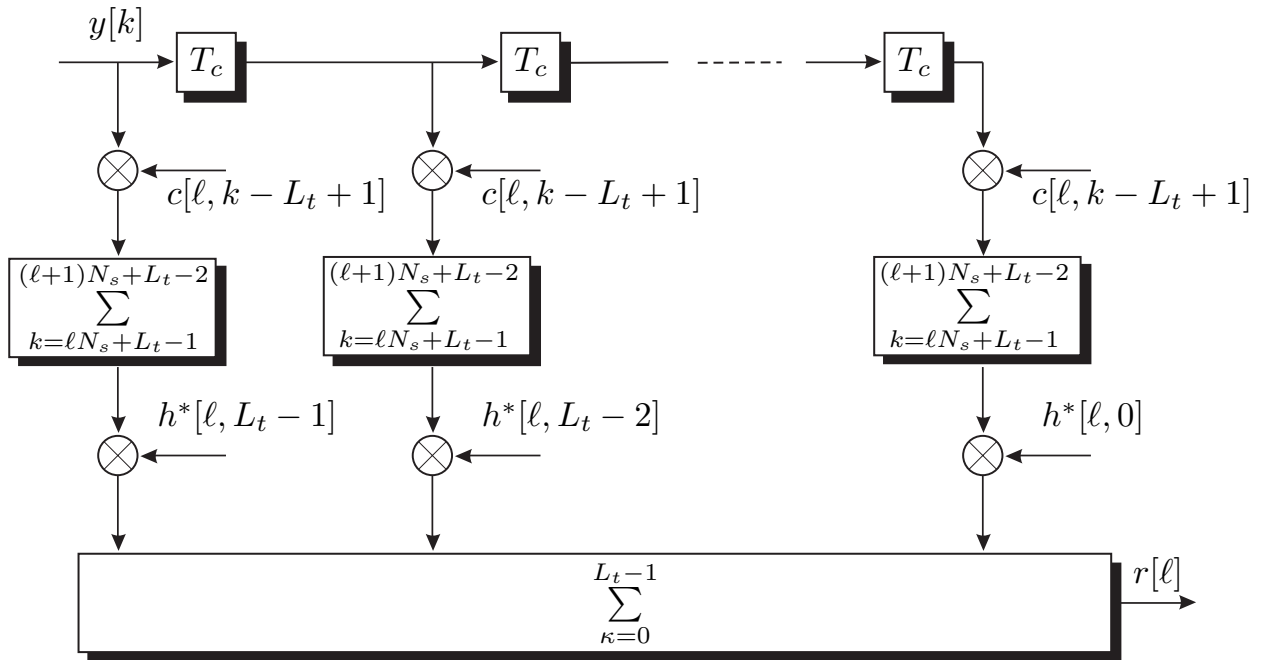


Figure 4.2.3: Structure of Rake receiver as parallel concatenation of several correlators

All components of the Rake receiver perform linear operations and their succession can be changed. This may reduce the computational costs of an implementation that depend on the specific hardware and the system parameters like spreading factor, maximum delay and number of Rake fingers. A possible structure is shown in **Fig. 4.2.4**. The tapped delay line represents a filter matched only to the channel impulse response and not to the whole signature. We need only a single correlator at the filter output to perform the despreading.

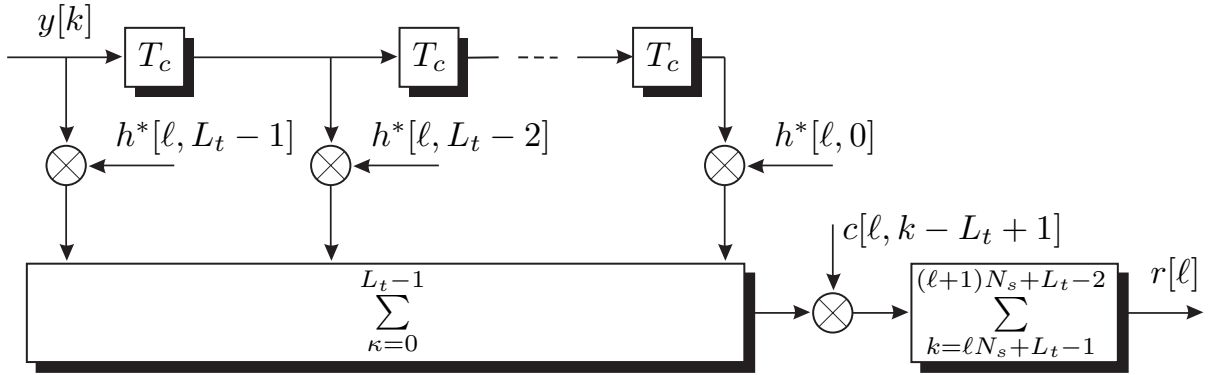


Figure 4.2.4: Structure of Rake receiver as parallel concatenation of several correlators

Next, we have to consider the output signal $r[\ell]$ in more detail. Inserting

$$y[k] = \sum_{\ell} a[\ell] \cdot s[\ell, k] + n[k]$$

into (4.2.7) yields

$$r[\ell] = \sum_{\kappa=0}^{L_t-1} h[\ell, L_t - 1 - \kappa]^* \cdot \sum_k \left(\sum_{\ell'} a[\ell'] \cdot s[\ell', k - \kappa] + n[k - \kappa] \right) \cdot c[\ell, k - L_t + 1].$$

Since the signatures $s[\ell, k]$ exceed the duration of one symbol, symbols at $\ell' = \ell \pm 1$ overlap with $a[\ell]$ and cause intersymbol interference. These signal parts are comprised in a term ISI so that we can focus in the sequel on $\ell' = \ell$. Moreover, the noise contribution at the Rake output is denoted by $\tilde{n}[\ell]$. We obtain with $s[\ell, k] = \sum_{\kappa} h[\ell, \kappa] \cdot c[\ell, k - \kappa]$

$$\begin{aligned} r[\ell] &= \text{ISI} + \tilde{n}[\ell] + a[\ell'] \cdot \sum_{\kappa=0}^{L_t-1} \sum_{\kappa'=0}^{L_t-1} h[\ell, L_t - 1 - \kappa]^* \cdot h[\ell, \kappa'] \\ &\quad \cdot \sum_{k=\ell N_s + L_t - 1}^{(\ell+1)N_s + L_t - 2} c[\ell, k - \kappa - \kappa'] \cdot c[\ell, k - L_t + 1]. \end{aligned} \quad (4.2.8)$$

The last sum in (4.2.9) represents the autocorrelation $\phi_{CC}[\ell, \kappa + \kappa' - (L_t - 1)]$ of the spreading code $c[\ell, k]$. The substitution $\kappa \rightarrow L_t - 1 - \kappa$ finally results in

$$\begin{aligned} r[\ell] &= a[\ell'] \cdot \sum_{\kappa=0}^{L_t-1} \sum_{\kappa'=0}^{L_t-1} h[\ell, L_t - 1 - \kappa]^* \cdot h[\ell, \kappa'] \cdot \phi_{CC}[\ell, \kappa' - \kappa] + \text{ISI} + \tilde{n}[\ell] \\ &= r^a[\ell] + r^{\text{ISI}}[\ell] + \tilde{n}[\ell]. \end{aligned} \quad (4.2.9)$$

We see from (4.2.9) that the autocorrelation function of spreading codes influences the output of the Rake receiver. If it is impulse like, i.e. $\phi_{CC}[\ell, \kappa] \approx 0$ for $\kappa \neq 0$, each

branch of the Rake receiver extracts exactly one propagation path and suppresses the other interfering signal components. More precisely, the first (left) finger extracts the path with the largest delay ($h[\ell, L_t - 1]$) because we start integrating at $k = \ell N_s + L_t - 1$ while the last (right) finger detects the path with the smallest delay corresponding to $h[\ell, 0]$. Due to this temporal reversion, all signal components are summed synchronously and the output of the Rake receiver consists of three parts as stated in (4.2.9). The first term

$$r^a[\ell] = \sum_{\kappa=0}^{L_t-1} |h[\ell, \kappa]|^2 \cdot a[\ell] \quad (4.2.10)$$

combines the desired signal parts transmitted over different propagation paths according to the maximum ratio combining principle². This maximizes the signal to noise ratio and delivers a diversity gain. The second term

$$r^{\text{ISI}}[\ell] = \sum_{\kappa=0}^{L_t-1} \sum_{\substack{\kappa'=0 \\ \kappa' \neq \kappa}}^{L_t-1} h^*[\ell, \kappa] h[\ell, \kappa'] \cdot \phi_{CC}[\ell, \kappa - \kappa'] \cdot a[\ell] + \text{ISI} \quad (4.2.11)$$

comprises path crosstalk between different Rake fingers as well as intersymbol interference (ISI) due to imperfect autocorrelation properties of the spreading code³. For random spreading codes and rectangular chip impulses, $\phi_{CC}[\ell, \kappa] \approx \sqrt{1/N_s}$ holds for $\kappa > 0$ and a large spreading factor N_s . Hence, the power of asynchronous signal components is attenuated by the factor $1/N_s$. Path crosstalk can be suppressed best for spreading codes with impulse-like autocorrelation functions.

It has to be mentioned that the Rake fingers need not to be separated by fixed time delays as depicted in Fig. 4.2.3. Since they have to be synchronized onto the channel taps – which are not likely to be spaced equidistantly – the Rake fingers are individually delayed. This requires appropriate synchronization and tracking units at the receiver. Nevertheless, the Rake receiver collects the whole signal energy of all multipath components and maximizes the SNR.

Fig. 4.2.5 shows the bit error rates versus E_b/N_0 for an uncoded single-user DS-CDMA system with random spreading codes of length $N = 16$. The mobile radio channel was assumed to be perfectly interleaved, i.e. successive channel coefficients are independent of each other. The number of channel taps varies between $L_t = 1$ and $L_t = 8$ and their average power is uniformly distributed. Obviously, the performance becomes better with increasing diversity degree $D = L_t$. However, for growing L_t , the difference between the theoretical diversity curves from (1.5.15)

²Compared to (1.5.3), the normalization with $\sum_{\kappa=0}^{L_t-1} |h[\ell, \kappa]|^2$ was neglected.

³The exact expression should consider the case that the data symbol may change during the correlation due to the relative delay $\kappa - \kappa'$. In this case, the even autocorrelation function has to be replaced by the odd ACF defined in (4.2.35) on page 187.

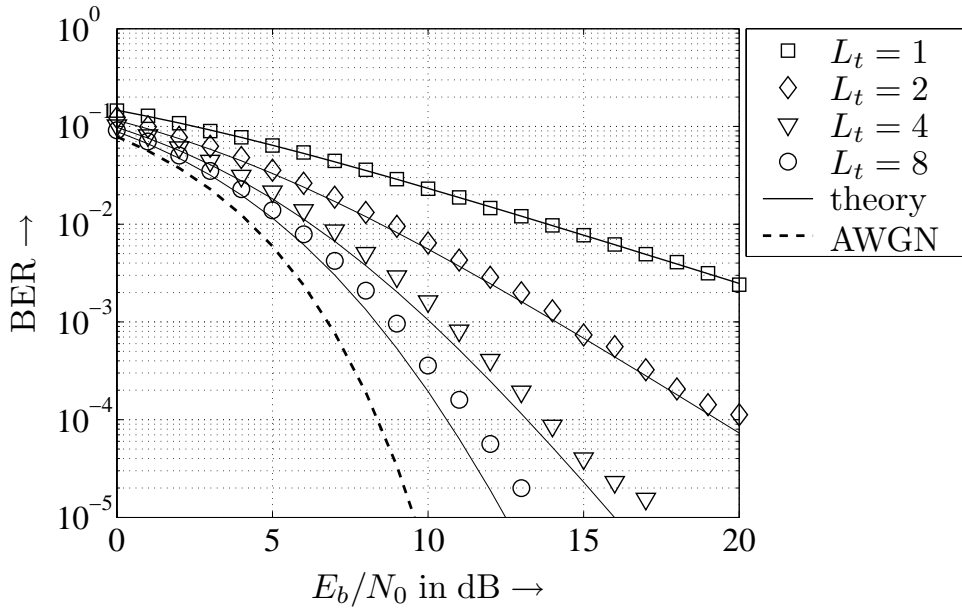


Figure 4.2.5: Illustration of path crosstalk and diversity gain of Rake receiver

and the true BER curves increases as well. This effect is caused by the growing path crosstalk between the Rake fingers due to imperfect autocorrelation properties of the employed spreading codes.

Channel and Rake receiver outputs can also be expressed in vector notations. We comprise all received samples $y[k]$ into a single vector \mathbf{y} and all transmitted symbols $a[\ell]$ into a vector \mathbf{a} . Furthermore, $\mathbf{s}[\ell]$ contains all $N_s + L_t - 1$ samples of the signature $s[\ell, k]$ for $k = \ell N_s, \dots, (\ell + 1)N_s + L_t - 2$. Then, we obtain

$$\mathbf{y} = \mathbf{S} \cdot \mathbf{a} + \mathbf{n}, \quad (4.2.12)$$

where the system matrix \mathbf{S} contains the signatures $\mathbf{s}[\ell]$ as depicted in **Fig. 4.2.6**. Each signature is positioned in an individual column but shifted by N_s samples. Therefore, $L_t - 1$ samples overlap leading to interfering consecutive symbols. For $N_s \gg L_t$, this interference can be neglected. With vector notations, the Rake's output signal in (4.2.7) becomes

$$\mathbf{r} = \mathbf{S}^H \cdot \mathbf{y} = \mathbf{S}^H \mathbf{S} \cdot \mathbf{a} + \mathbf{S}^H \mathbf{n}. \quad (4.2.13)$$

4.2.2 Direct-Sequence CDMA

In code division multiple access schemes, spread spectrum is used for separating signals of different subscribers. This is accomplished by assigning each user u a

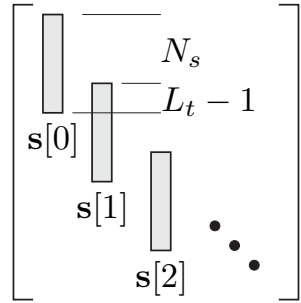


Figure 4.2.6: Structure of system matrix \mathbf{S} for frequency-selective fading

unique spreading code $c_u[\ell, k]$ with $1 \leq u \leq N_U$. The ratio between the number of active users N_U and the spreading factor N_s is denoted as the load

$$\beta = \frac{N_U}{N_s} \quad (4.2.14)$$

of the system. For $\beta = 1$, the system is said to be fully loaded. Assuming an error free transmission, the spectral efficiency η of a system is defined as the average number of information bits transmitted per chip

$$\eta = \frac{N_U}{G_p} = R_c \cdot \frac{N_U}{N_s} = R_c \cdot \beta \quad (4.2.15)$$

and is averaged over all active users. Obviously, spectral efficiency and system load are identical for uncoded systems ($R_c = 1$) while they differ by a factor R_c for coded systems.

Mathematically, the received signal can be conveniently described by using vector notations. Therefore, the system matrix \mathbf{S} in (4.2.12) has to be extended so that it contains the signatures of all users as illustrated in **Fig. 4.2.7**. Each block of the matrix corresponds to a certain time index ℓ and contains the signatures $\mathbf{s}_u[\ell]$ of all users. Due to this arrangement, the vector

$$\mathbf{a} = [a_1[0] \ a_2[0] \ \cdots \ a_{N_U}[0] \ a_1[1] \ a_2[1] \ \cdots]^T \quad (4.2.16)$$

consists of all data symbols of all users in temporal order.

Downlink Transmission

At this point, we have to distinguish between uplink and downlink transmissions. In the downlink depicted in **Fig. 4.2.8**, a central base station or access point transmits the user signals $x_u[k]$ synchronously to the mobile units. Hence, looking at the link between the base station and one certain mobile unit u , all signals are affected by the same channel $h_u[\ell, \kappa]$. Consequently, the signatures of different

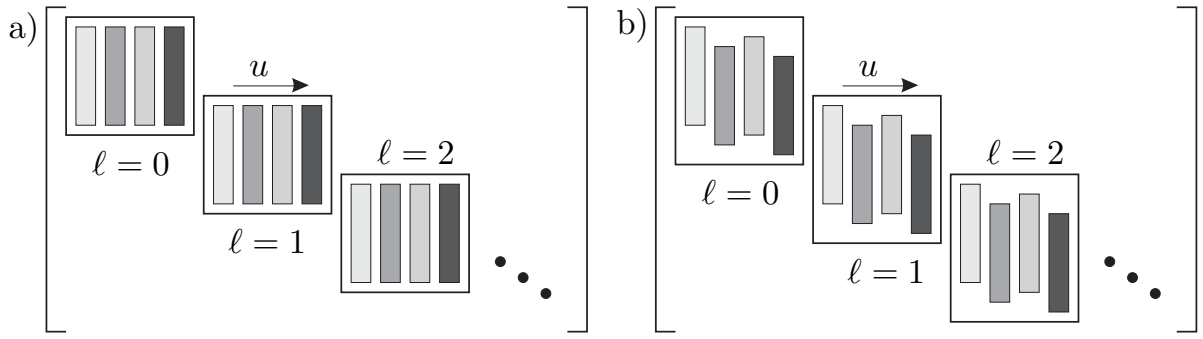


Figure 4.2.7: Structure of system matrix \mathbf{S} for Direct-Sequence CDMA
a) synchronous downlink, **b)** asynchronous uplink

users v distinguish only in the spreading code, i.e. $s_v[\ell, \kappa] = c_v[\ell, \kappa] * h_u[\ell, \kappa]$ holds, and the received signal for user u becomes

$$\mathbf{y}_u = \mathbf{S} \cdot \mathbf{a} + \mathbf{n}_u = \mathbf{T}_{h_u[\ell, \kappa]} \mathbf{C} \cdot \mathbf{a} + \mathbf{n}_u . \quad (4.2.17)$$

In (4.2.17), $\mathbf{T}_{h_u[\ell, \kappa]}$ denotes the convolutional matrix of the time varying channel impulse response $h_u[\ell, \kappa]$ and \mathbf{C} is a block diagonal matrix

$$\mathbf{C} = \begin{pmatrix} \mathbf{C}[0] & & & \\ & \mathbf{C}[1] & & \\ & & \mathbf{C}[2] & \\ & & & \ddots \end{pmatrix} \quad (4.2.18)$$

containing in its blocks $\mathbf{C}[\ell] = [\mathbf{c}_1[\ell] \cdots \mathbf{c}_{N_U}[\ell]]$ the spreading codes $\mathbf{c}_u[\ell] = [c_u[\ell, \ell N_s] \cdots c_u[\ell, (\ell + 1)N_s - 1]]^T$ of all users. This structure simplifies the mitigation of multi-user interference because the equalization of the channel can restore the desired correlation properties of the spreading codes as we will see later.

However, the channels from the common base station to different mobile stations are different, especially the path loss may vary. In order to ensure the demanded quality of service, e.g. a certain SINR at the receiver input, power control strategies are applied. The aim is to transmit only as much power as necessary to obtain the required SINR at the mobile receiver. However, increasing the transmit power of one user also enhances the interference to all other subscribers so that the problem occurs to be a multi-dimensional optimization task.

In the considered downlink, the base station chooses the transmit power according to the requirements of each user and the entire network. Since each user receives the whole bundle of signals, it is likely to happen that the desired signal is disturbed by high power signals whose associated receivers experience poor channel conditions. This imbalance of power levels termed near-far effect represents a

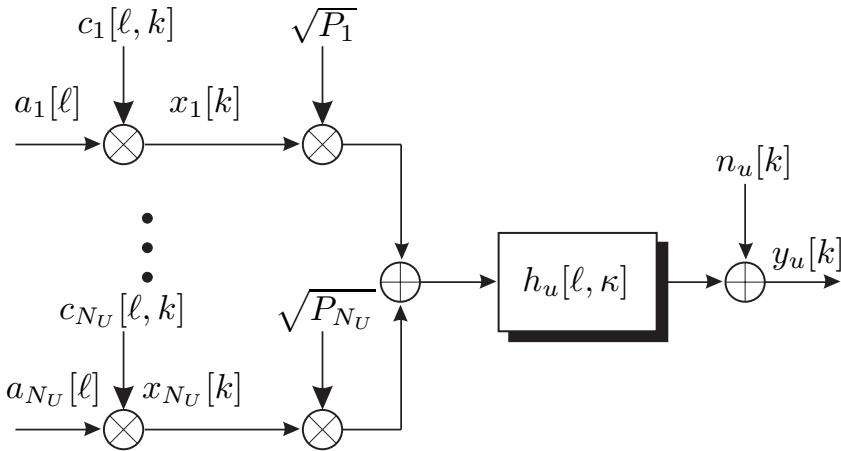


Figure 4.2.8: Structure of downlink for direct-sequence CDMA system

penalty for weak users because they suffer much more under the strong interference. The scenario can be mathematically described by introducing a diagonal matrix \mathbf{P} into (4.2.12) containing the user specific power amplification P_u (see Fig. 4.2.8).

$$\mathbf{y} = \mathbf{SP}^{1/2} \cdot \mathbf{a} + \mathbf{n} \quad (4.2.19)$$

Uplink Transmission

Contrarily, the uplink signals are transmitted asynchronously which is indicated by different starting positions of the signatures $\mathbf{s}_u[\ell]$ within each block as depicted in **Fig. 4.2.7b**. Moreover, the signals are transmitted over individual channels as shown in **Fig. 4.2.9**. Hence, the spreading codes have to be convolved individually with their associated channel impulse responses and the resulting signatures $\mathbf{s}_u[\ell]$ from (4.2.6) are arranged in a matrix \mathbf{S} (see Fig. 4.2.7b).

The main difference compared to the downlink is now that the signals interfering at the base station experienced different path losses because they were transmitted over different channels.⁴ Again, a power control adjusts the power levels P_u of each user such that its required signal to interference plus noise ratio (SINR) is obtained at the receiving base station. However, practical impairments like fast fading channels and an imperfect power control lead to SINR imbalances also in the uplink. Additionally, identical power levels are not likely in environments supporting multiple services with different quality of service constraints. Hence, near-far effects also influence the uplink performance in a CDMA system. Receivers that care about different power levels are called *near-far resistant*. In the context of multi-user detectors, a near-far-resistant receiver will be introduced.

⁴Moreover, inter-cell interference in multi-cell environments have to be considered.

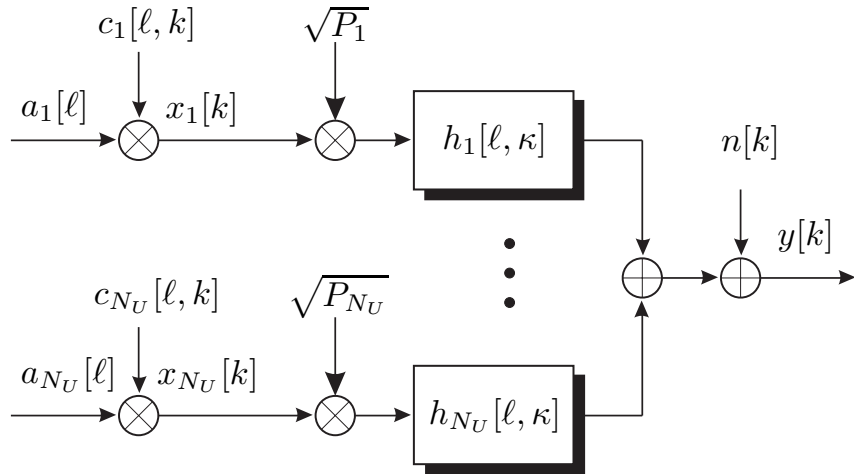


Figure 4.2.9: Structure of uplink for direct-sequence CDMA system

Multi-rate CDMA Systems

As already mentioned in the previous paragraphs, modern communication systems like UMTS or CDMA 2000 are designed to provide a couple of different services, like speech and data transmission as well as multimedia applications. These services require different data rates that can be supported by different means. One possibility is to adapt the spreading factor N_s . Since the chip duration T_c is a constant system parameter, decreasing N_s enhances the data rate while keeping the overall bandwidth constant ($T_c = T_s/N_s \rightarrow B = N_s/T_s$).

However, a large spreading factor corresponds to good interference suppression and subscribers with large N_s are more robust against multi-user interference and path crosstalk. Contrarily, users with low N_s become quite sensitive to interference as can be seen from (4.2.25) and (4.2.29). These correspondences are similar to near-far effects – a small spreading factor is equivalent to a low transmit power and vice versa. Hence, low spreading users need either a higher power level than the interferers, a cell with only a few interferers, or sophisticated detection techniques at the receiver that are insensitive to these effects.

The multi-code technique offers another possibility to support multiple data rates. Instead of decreasing the spreading factor, several spreading codes are assigned to a subscriber demanding high data rates. Of course, this approach consumes resources in terms of spreading codes that can no longer be offered to other users. However, it does not suffer from an increased sensitivity to interference.

A third approach proposed in the UMTS standard and limited to 'hot-spot' scenarios with low mobility is the HSDPA (High Speed Downlink Packet Access) channel. It employs adaptive coding and modulation schemes as well as multiple antenna techniques (cf. Chapter 6). Moreover, the connection is not circuit switched but

packet oriented, i.e. there exist no permanent connection between mobile and base station but data packets are transmitted according to certain scheduling schemes. Due to the variable coding and modulation schemes, an adaption to actual channel conditions is possible but requires slowly fading channels. Contrarily to standard UMTS links, the spreading factor is fixed to $N_s = 16$ and no power control is applied [TS2].

4.2.3 Single-User Matched Filter (SUMF)

The optimum single-user matched filter (SUMF) does not care about other users and treats their interference as additional white Gaussian distributed noise. In frequency-selective environments, the SUMF is simply a Rake receiver. As described earlier, its structure can be mathematically described by correlating \mathbf{y} with the signature of the desired user. Using vector notations, the output for user u is given by

$$\mathbf{r}_u = \mathbf{S}_u^H \cdot \mathbf{y} = \mathbf{S}_u^H \mathbf{S}_u \cdot \mathbf{a}_u + \mathbf{S}_u^H \mathbf{S}_{\setminus u} \cdot \mathbf{a}_{\setminus u} + \mathbf{S}_u^H \cdot \mathbf{n} \quad (4.2.20)$$

where \mathbf{S}_u contains exactly those columns of \mathbf{S} that corresponds to user u (compare Fig. 4.2.6). Consequently, $\mathbf{S}_{\setminus u}$ consists of the remaining columns not associated with u . The same notation holds for \mathbf{a}_u and $\mathbf{a}_{\setminus u}$. The noise $\tilde{\mathbf{n}} = \mathbf{S}_u^H \mathbf{n}$ is now colored with the covariance matrix $\Phi_{\tilde{\mathcal{N}}\tilde{\mathcal{N}}} = E\{\tilde{\mathbf{n}}\tilde{\mathbf{n}}^H\} = \sigma_{\mathcal{N}}^2 \mathbf{S}_u^H \mathbf{S}_u$.

If the signatures in \mathbf{S}_u are mutually orthogonal to those in $\mathbf{S}_{\setminus u}$, then $\mathbf{S}_u^H \mathbf{S}_{\setminus u}$ is always zero and \mathbf{r}_u does not contain any multi-user interference. In that case, the matched filter describes the optimum detector and the performance of a CDMA system would be that of a single-user system with L_t -fold diversity. However, although the spreading codes may be appropriately designed, the mobile radio channel generally destroys any orthogonality. Hence, we obtain multi-user interference (MUI), i.e. symbols of different users interfere. This MUI limits the system performance dramatically. The output of the Rake receiver for user u can be split into four parts

$$r_u[\ell] = r_u^a[\ell] + r_u^{\text{MUI}}[\ell] + r_u^{\text{ISI}}[\ell] + \tilde{n}_u[\ell] \quad (4.2.21)$$

Comparing (4.2.21) with (4.2.9) shows that path crosstalk, ISI and noise are still present, but a fourth term denoting the multiple access interference stemming from other active users now additionally disturbs the transmission. This term can be quantified by

$$r_u^{\text{MUI}}[\ell] = \sum_{\kappa=0}^{L_t-1} \sum_{\substack{v=1 \\ v \neq u}}^{N_U} \sqrt{P_v} \cdot \sum_{\kappa'=0}^{L_t-1} h_u^*[\ell, \kappa] h_v[\ell, \kappa'] \cdot \phi_{C_u C_v}[\ell, \kappa - \kappa'] \cdot a_u[\ell] a_v[\ell] \quad (4.2.22)$$

where the factor P_v adjusts the received power of user v . From (4.2.22) we see that the crosscorrelation function $\phi_{C_u C_v}[\ell, \kappa - \kappa']$ of the spreading codes determines

the influence of MUI. For orthogonal sequences, $r^{\text{MUI}}[\ell]$ vanishes and the matched filter is optimum. Moreover, the SUMF is not near-far resistant because high power levels P_v of interfering users increase the interfering power and, therefore, the error rate.

Assuming a high number of active users, the interference is often modelled as additional Gaussian distributed noise due to the central limit theorem. In this case, the signal to noise ratio defined in (1.2.14) has to be replaced by a signal to interference plus noise ratio (SINR).

$$\text{SNR} = \frac{\sigma_{\mathcal{X}}^2}{\sigma_{\mathcal{N}}^2} \quad \longrightarrow \quad \text{SINR} = \frac{\sigma_{\mathcal{X}}^2}{\sigma_{\mathcal{N}}^2 + \sigma_{\mathcal{I}}^2} \quad (4.2.23)$$

The term $\sigma_{\mathcal{I}}^2$ denotes the interference power, i.e. the denominator in (4.2.23) represents the sum of interference and noise power. Generally, these powers vary in time because they depend on the instantaneous channel conditions. For simplicity, we restrict the following analysis on the AWGN channel. Assuming random spreading codes, the power of each interfering user is suppressed in the average by a factor N_s and

$$\sigma_{\mathcal{I}}^2 = \frac{E_s}{T_s} \cdot \sum_{v \neq u} P_v \cdot \phi_{u,v}^2[0] = \frac{1}{N_s} \cdot \frac{E_s}{T_s} \cdot \sum_{v \neq u} P_v \quad (4.2.24)$$

holds. Next, we illuminate the difference between uplink and downlink especially for real-valued modulation schemes. For the sake of simplicity, we restrict to BPSK and QPSK.

Downlink Transmission for AWGN Channel

We distinguish three cases:

1. No power control and real symbols

If the modulation alphabet contains only real symbols, we consider only the real part of the matched filtered signal and only half of the noise power disturbs the transmission. Hence, $\sigma_{\mathcal{N}'}^2 = N_0/2/T_s$ has to be inserted into (4.2.23) (compare page 13). Without power control, all users experience the same channel in the downlink so that their received power levels $P_v = 1$ are identical. The resulting average SINR for BPSK can be approximated by

$$\text{SINR} \approx \frac{E_s}{N_0/2 + (N_U - 1)E_s/N_s} = \frac{E_b}{N_0/2 + (N_U - 1)E_b/N_s}. \quad (4.2.25)$$

Obviously, enlarging the spreading factor N_s results in a better suppression of interfering signals for fixed N_U . **Fig. 4.2.10** shows the SINR versus the number

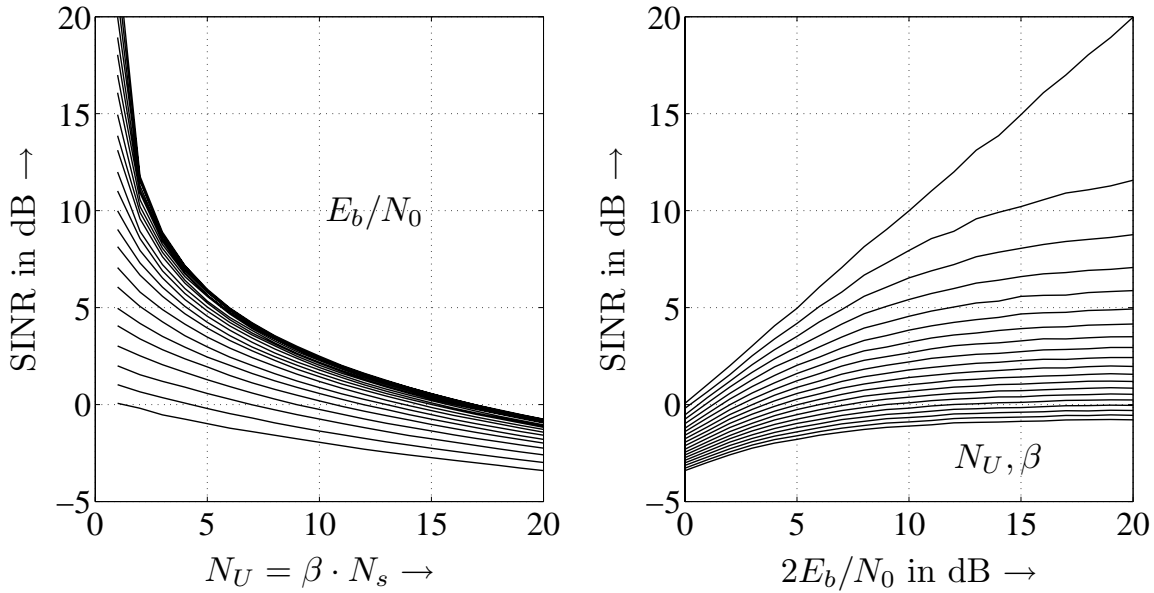


Figure 4.2.10: SINR for downlink of DS-CDMA system with BPSK, random spreading ($N_s = 16$) and AWGN channel, $1 \leq N_U \leq 20$

of active users and versus the $2E_b/N_0^5$. We recognize that the SINR decreases dramatically for growing number of users. For very high loads, the SINR is dominated by the interference and the noise plays only a minor role. This directly affects the bit error probability so that the performance will dramatically degrade.

According to the general result in (1.3.15) on page 25, the error probability becomes

$$P_b = \frac{1}{2} \cdot \operatorname{erfc} \left(\sqrt{\frac{\sigma_{\mathcal{X}}^2}{\sigma_{\mathcal{N}}^2}} \right) = \frac{1}{2} \cdot \operatorname{erfc} \left(\sqrt{\frac{\sigma_{\mathcal{X}}^2}{2\sigma_{\mathcal{N}'}^2}} \right)$$

for BPSK transmission over an AWGN channel. The argument of the complementary error function is half of the effective signal to noise ratio $\sigma_{\mathcal{X}}^2/\sigma_{\mathcal{N}'}^2$, after extracting the real part. Using this result and substituting the SNR by the SINR, we obtain for the considered CDMA system

$$P_b \approx \frac{1}{2} \cdot \operatorname{erfc} \left(\sqrt{\frac{\text{SINR}}{2}} \right) = \frac{1}{2} \cdot \operatorname{erfc} \left(\sqrt{\frac{E_b}{N_0 + 2(N_U - 1)E_b/N_s}} \right). \quad (4.2.26)$$

Fig. 4.2.11 shows the corresponding results. As predicted, the bit error probability increases dramatically with growing system load β . For large β , it is totally dominated by the interference.

⁵For BPSK, $E_b = E_s$ holds. Furthermore, we use the effective signal to noise ratio $2E_b/N_0$ after extracting the real part since this determines the error rate in the single user case.

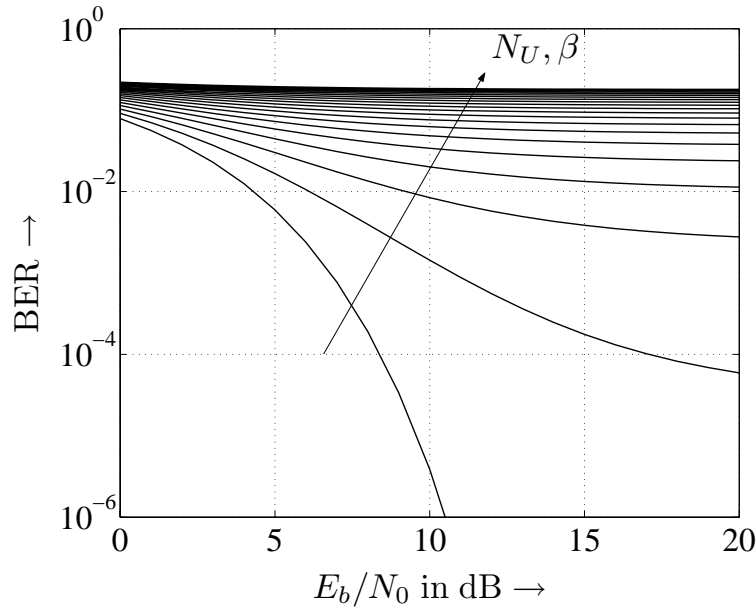


Figure 4.2.11: Bit error probability for downlink of DS-CDMA system with BPSK, random spreading ($N_s = 16$) and an AWGN channel, $1 \leq N_U \leq 20$

2. No power control and complex symbols

If we use a complex QPSK symbol alphabet, the total noise power $\sigma_{\mathcal{N}}^2$ instead of $\sigma_{\mathcal{N}'}^2$ affects the decision and (4.2.25) becomes with $E_s = 2E_b$

$$\text{SINR} \approx \frac{E_s}{N_0 + (N_U - 1)E_s/N_s} = \frac{E_b}{N_0/2 + (N_U - 1)E_b/N_s}. \quad (4.2.27)$$

This is the same expression in terms of E_b as in (4.2.25). Therefore, the bit error rates of inphase and quadrature components equal exactly those of BPSK in (4.2.26) when E_b is used. This result coincides with those presented in Section 1.4.

3. Power control and real symbols

As a last scenario, we look at a BPSK system with power control where the received power of a single user v is much higher than that of the other users ($P_v \gg P_{u \neq v}$). The SINR results in

$$\text{SINR}_u \approx \frac{E_b}{N_0/2 + E_b/N_s \sum_{v \neq u} P_v}. \quad (4.2.28)$$

Fig. 4.2.12 shows the results obtained for $N_U = 3$ users from which one of the interferers varies its power level while the others keep their levels constant. Obviously, the performance degrades dramatically with growing power amplification P_v of user v . For $P_v \rightarrow \infty$, the signal to noise ratio has no influence anymore and the performance is dominated by the interferer. Hence, the SUMF is not near-far resistent.

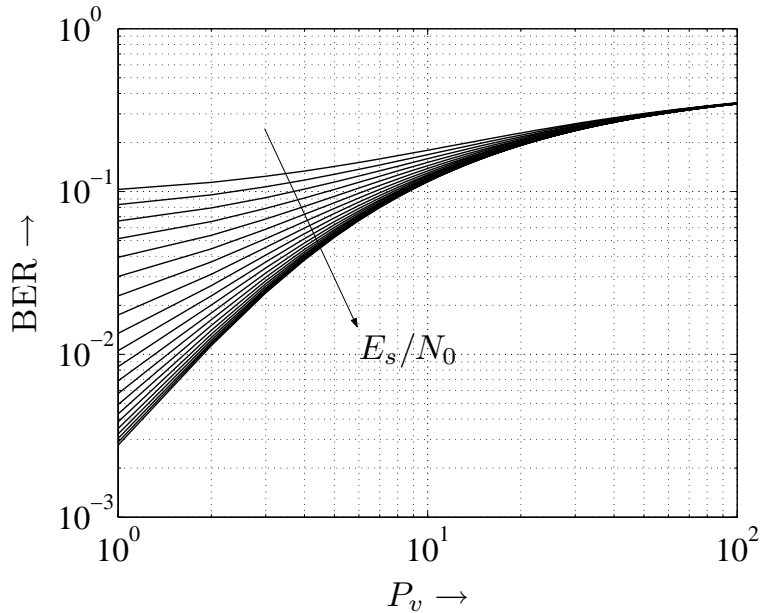


Figure 4.2.12: Bit error probability for downlink of DS-CDMA system with power control, BPSK, random spreading ($N_s = 16$) and an AWGN channel, $N_U = 3$ users

Uplink transmission

The main difference between uplink and downlink transmission is the fact that each user is affected by its individual channel. We now assume a perfect power control that ensures the same power level for all users at the receiver. Note that this differs from the downlink where all users are influenced by the same channel and a power control would result in different power levels. Again, we restrict to the AWGN channel but allow random phase shifts by φ_u on each channel. We distinguish two cases:

1. Real symbols and AWGN channel with random phases

After coherent reception by multiplying with $e^{-j\varphi_u}$, real-valued modulation schemes like BPSK benefit from the fact that the interference is distributed in the complex plane due to $e^{j(\varphi_v - \varphi_u)}$ with $\varphi_v - \varphi_u \neq 0$ while the desired signal is contained only in the real part. Hence, only half of the interfering power affects the real part and the average SINR becomes

$$\text{SINR} \approx \frac{E_s}{N_0/2 + 1/2 \cdot (N_U - 1)E_s/N_s} \stackrel{\text{BPSK}}{=} \frac{2E_b}{N_0 + (N_U - 1)E_b/N_s} . \quad (4.2.29)$$

Fig. 4.2.13 shows the corresponding results for an AWGN channels. A comparison with Fig. 4.2.10 shows that the SINR's are much larger especially for high loads. Concerning the bit error rate performance,

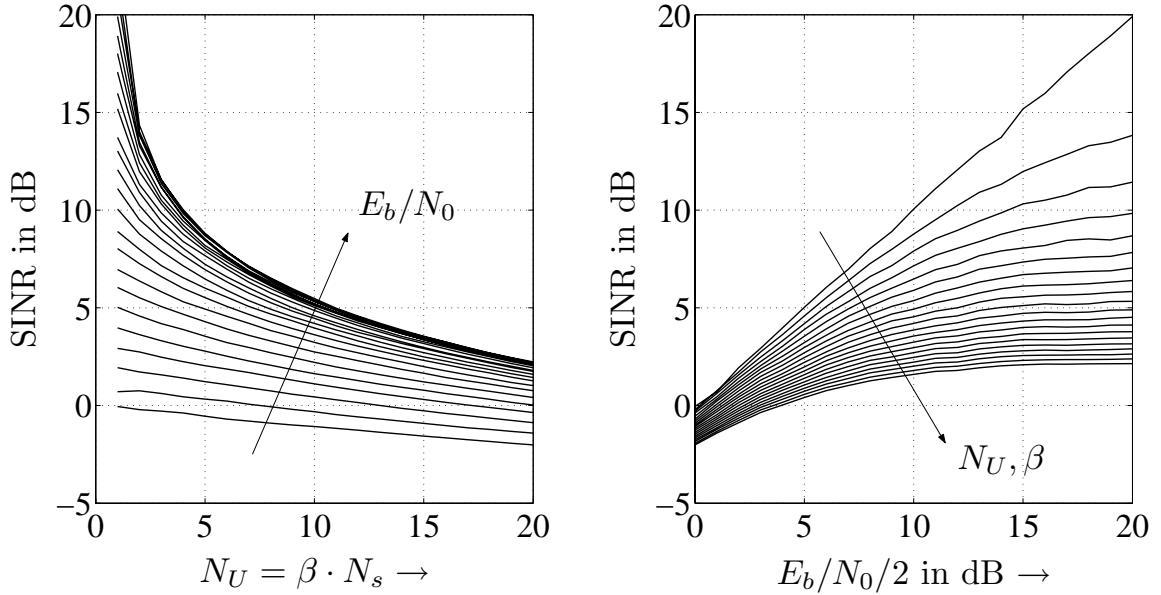


Figure 4.2.13: SINR for uplink of DS-CDMA system with BPSK, random spreading ($N_s = 16$) and AWGN channels with random phases, $1 \leq N_U \leq 20$

$$P_b \approx \frac{1}{2} \cdot \operatorname{erfc} \left(\sqrt{\frac{\text{SINR}}{2}} \right) = \frac{1}{2} \cdot \operatorname{erfc} \left(\sqrt{\frac{E_s}{N_0 + (N_U - 1)E_s/N_s}} \right). \quad (4.2.30)$$

delivers the results depicted in **Fig. 4.2.14**. A comparison with the downlink in Fig. 4.2.11 illustrates the benefits of real-valued modulation schemes in the uplink, too. However, it has to be emphasized that complex modulation alphabets have a higher spectral efficiency, i.e. more bits per symbol can be transmitted.

2. Complex symbols and AWGN channel with random phases

It is straightforward to recognize that the distribution of the interference in the complex plane provides no advantage for complex-valued modulation schemes like QPSK. Therefore, the entire interfering power σ_I^2 disturbs the transmission and the SINR becomes

$$\text{SINR} \approx \frac{E_s}{N_0 + (N_U - 1)E_s/N_s} = \frac{E_b}{N_0/2 + (N_U - 1)E_b/N_s}. \quad (4.2.31)$$

Comparing (4.2.29) with (4.2.31) in terms of E_b we see that BPSK and QPSK behave different in the uplink.

However, it has to be mentioned that orthogonal spreading codes could be employed for synchronous frequency-nonselective channels. In this case, no multi-user interference would disturb the transmission and the above discussion is superficial. Nevertheless, the assumptions simplified the above analysis and the principle differences between uplink and downlink still hold for frequency-selective channels. Concerning a synchronous downlink transmission, even the use of scrambled

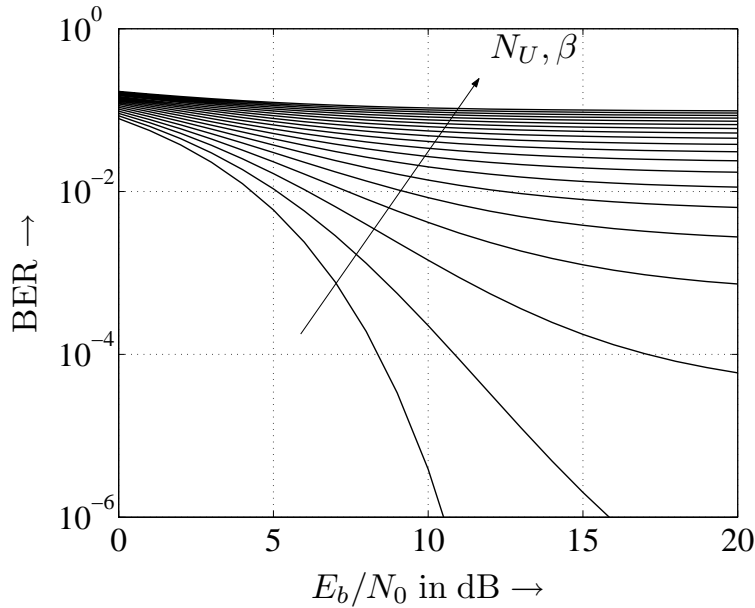


Figure 4.2.14: Bit error probability for uplink of DS-CDMA system with BPSK, random spreading codes ($N_s = 16$) and an AWGN channel with random phases, $1 \leq N_U \leq 20$

orthogonal sequences (see page 188) makes sense because synchronous signal components are perfectly suppressed and an equalization of the single channel would restore orthogonality. For totally asynchronous transmissions, orthogonal codes do generally not lead to any advantage.

We saw that the auto and crosscorrelation properties of spreading codes play a crucial role in CDMA systems. Therefore, the next section briefly introduces some important code families. Afterwards, the performance of a single-user matched filter is discussed in the context of OFDM-CDMA and in coded environments.

4.2.4 Spreading Codes

Requirements for Spreading Codes

As illustrated above the correlation properties of spreading codes have deep impact on the performance of spread spectrum and CDMA systems. In order to simplify notation, we consider the spreading codes $c_u[\ell, k]$ only within one symbol period. Hence, the time variable ℓ is a constant and can be neglected in this section. The even or periodic correlation function for real signals is defined by

$$\phi_{\mathcal{C}_u \mathcal{C}_v}^{\text{even}}[\kappa] = \sum_{k=0}^{N_s-1} c_u[k] c_v[k + \kappa]. \quad (4.2.32)$$

For $u = v$ it represents the even (periodic) autocorrelations function, for $u \neq v$ the even crosscorrelation function. Regarding short codes, $\phi_{\mathcal{C}_u \mathcal{C}_v}[\kappa]$ is itself periodic with a period that equals the spreading factor N_s .

On the one hand, different propagation paths must be separated by the Rake receiver in order to exploit diversity provided by a frequency-selective channel. This requires an impulse-like shape of the autocorrelation function, i.e. $\phi_{\mathcal{C}_u \mathcal{C}_u}[\kappa] \approx 0$ for $\kappa \neq 0$ is desirable. This property is also important for synchronization purposes. On the other hand, interfering users must be suppressed sufficiently by low cross-correlations $\phi_{\mathcal{C}_u \mathcal{C}_{v \neq u}}[\kappa] \approx 0$ for arbitrary κ . Unfortunately, both conditions cannot be fulfilled simultaneously as shown in [SP80]. Hence, a trade-off between autocorrelation and crosscorrelation properties is required. Moreover, a lot of spreading sequences should exist in order to provide many users access to the system.

Regarding the uplink of a CDMA system, the transmission is generally asynchronous. Therefore, changes of the data symbols $a_u[\ell]$ occur during correlation and the definition given in (4.2.32) cannot be applied anymore. In fact, we need the non-periodic correlation function

$$\phi_{\mathcal{C}_u \mathcal{C}_v}^{\text{non}}[\kappa] = \begin{cases} \sum_{k=0}^{N_s-1-\kappa} c_u[k] \cdot c_v[k+\kappa] & 0 \leq \kappa < N_s \\ \sum_{k=0}^{N_s-1+\kappa} c_u[k-\kappa] \cdot c_v[k] & -N_s < \kappa \leq 0 . \end{cases} \quad (4.2.33)$$

With (4.2.33), the even correlation function in (4.2.32) becomes

$$\phi_{\mathcal{C}_u \mathcal{C}_v}^{\text{even}}[\kappa] = \phi_{\mathcal{C}_u \mathcal{C}_v}^{\text{non}}[\kappa] + \phi_{\mathcal{C}_u \mathcal{C}_v}^{\text{non}}[N_s - \kappa] . \quad (4.2.34)$$

Equivalently, the odd correlation function

$$\phi_{\mathcal{C}_u \mathcal{C}_v}^{\text{odd}}[\kappa] = \phi_{\mathcal{C}_u \mathcal{C}_v}^{\text{non}}[\kappa] - \phi_{\mathcal{C}_u \mathcal{C}_v}^{\text{non}}[N_s - \kappa] \quad (4.2.35)$$

describes the correlation between two BPSK modulated signals $u[k]$ and $v[k]$ if they have a mutual delay κ and the information symbol $a[\ell]$ of one signal changes its sign during correlation.

Orthogonal Spreading Codes

Concerning multi-user interference, orthogonal spreading codes would be optimum because they suppress interfering signals perfectly. An example of orthogonal codes are Hadamard codes or Walsh sequences [Wal23, Har64, Har71] that were already introduced as FEC codes in Section 3.2.4. For a synchronous transmission over frequency-nonselective channels, signals can be perfectly separated because

$$\phi_{\mathcal{C}_u^w \mathcal{C}_v^w}[\kappa = 0] = \begin{cases} 1 & u = v \\ 0 & \text{else} \end{cases} \quad (4.2.36)$$

holds. Walsh sequences exist for those lengths N_s for which N_s , $N_s/12$ or $N_s/20$ are powers of 2. The number of Walsh sequences of a given length N_s equals exactly N_s .

Since autocorrelation and crosscorrelation properties cannot be perfect at the same time, we can conclude that the autocorrelation properties of Walsh sequences are rather bad. Moreover, even the crosscorrelation can take quite large values for $\kappa \neq 0$. Hence, for asynchronous transmissions or frequency-selective mobile radio channels, the orthogonality is destroyed and severe interference makes a reliable transmission nearly impossible.

A solution to this problem is to combine Walsh sequences $c_u^w[k]$ with an outer scrambling code $c^s[k]$. This second code does not perform an additional spreading because the duration of its chips is the same as for $c_u^w[k]$. In cellular networks, $c^s[k]$ is usually identical for all users within the same cell [GJP⁺91, DGNS98]. Therefore, the new code

$$c_u[k] = c_u^w[k] \cdot c^s[k] \quad (4.2.37)$$

maintains orthogonality for synchronous signal components and suppresses asynchronous parts like a random code.

Maximum Length Sequences (m-sequences)

In order to have an efficient implementation, spreading codes are often generated by feedback shift registers. **Fig. 4.2.15** shows an example with a register length of $m = 9$. The register can be initialized arbitrary with ± 1 and generates a periodical sequence. If the polynomial $g(D) = g_0 + g_1D + \dots + g_mD^m$ describing the feedback structure of the register is prime, the period of the sequence is maximized to $2^m - 1$ and the register passes through all $2^m - 1$ states except the all-one-state within one period. Therefore, these sequences are termed m-sequences or maximum length sequences.

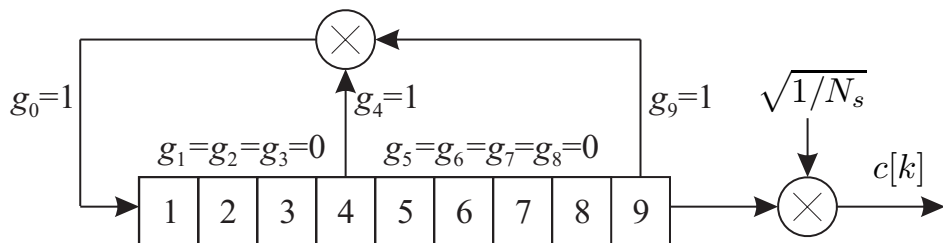


Figure 4.2.15: Feedback shift register of length $m = 9$ for generating an m-sequence with period $= 2^9 - 1 = 511$

One important property of m-sequences is that they have a near optimum autocorrelation function

$$\phi_{\mathcal{C}_u \mathcal{C}_u}^{\text{m-seq}}[\kappa] = \begin{cases} 1 & \text{for } \kappa = 0 \\ -1/N_s & \text{else} \end{cases}. \quad (4.2.38)$$

Hence, they are called quasi-orthogonal since they tightly approach an impulse-like shape. Consequently, asynchronous replicas of the desired signal can be suppressed very good. Concerning the crosscorrelation, m-sequences perform much worse. Moreover, given a certain spreading factor N_s , there exist only a few m-sequences. This dramatically limits the applicability in CDMA systems because only few users could be supported. As an example, there exist only six m-sequences of length $N_s = 31$ whose feedback polynomials are

$$\begin{aligned} g_1(D) &= 1 + D^2 + D^5 & g_2(D) &= 1 + D^3 + D^5 \\ g_3(D) &= 1 + D + D^2 + D^3 + D^5 & g_4(D) &= 1 + D + D^2 + D^4 + D^5 \\ g_5(D) &= 1 + D + D^3 + D^4 + D^5 & g_6(D) &= 1 + D^2 + D^3 + D^4 + D^5. \end{aligned} \quad (4.2.39)$$

Gold Codes

Gold discovered in 1967 that the crosscorrelation between certain pairs of m-sequences take only three different values. Moreover, such preferred pairs can be used to construct a whole family of codes that have the same period as well as the same correlation property [Gol67]. This is accomplished by multiplying the register outputs of the corresponding shift registers as shown in **Fig. 4.2.16**. Different codes are generated by inserting different delays between both registers. The delay n can be adjusted between $n = 0$ and $n = 2^m - 1$. Hence, a set of $2^m + 1$ Gold codes can be constructed on the basis of a preferred pair of m-sequences including the two generating m-sequences itself. **Table 4.2.1** shows preferred pairs of m-sequences for the feedback polynomials listed in (4.2.39). The sequence length is $N_s = 31$ (register length $m = 5$).

	$g_1(D)$	$g_2(D)$	$g_3(D)$	$g_4(D)$	$g_5(D)$	$g_6(D)$
$g_1(D)$			x	x	x	x
$g_2(D)$			x	x	x	x
$g_3(D)$	x	x		x	x	
$g_4(D)$	x	x	x			x
$g_5(D)$	x	x	x			x
$g_6(D)$	x	x		x	x	

Table 4.2.1: Preferred pairs of m-sequences for generation of Gold code with length 31

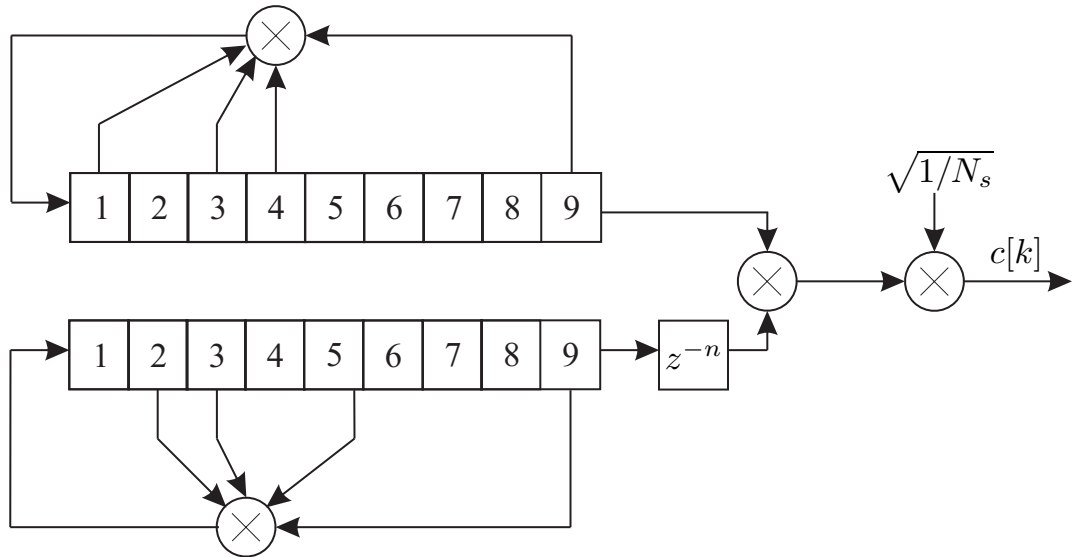


Figure 4.2.16: Pair of feedback shift register of length $m = 9$ for generating a Gold code of length $2^9 - 1 = 511$

Gold codes can also be generated by a single shift register whose length is twice as large as m [PSM82]. Consequently, Gold codes are no maximum length sequences. Furthermore, Gold codes exist only for shift registers whose lengths are not divisible by four. The even crosscorrelation function of Gold codes takes the values

$$\phi_{\mathcal{C}_u \mathcal{C}_v}^{\text{Gold}}[\kappa] = \frac{1}{N_s} \cdot \begin{cases} -1 \\ -2^{\lfloor (m+2)/2 \rfloor} - 1 \\ 2^{\lfloor (m+2)/2 \rfloor} - 1 \end{cases}, \quad (4.2.40)$$

where $\lfloor x \rfloor$ denotes the integer part of x [SP80].

There exist a large number of sequences like Kasami sequences or complex-valued spreading codes that are not addressed in this book. Since the code optimization is not the focus, we often use random codes without any designed correlation properties.

4.3 OFDM-CDMA

4.3.1 Multi-Carrier Transmission

The above sections showed that spreading with sequences having appropriate correlation properties is a suited mean to overcome the frequency selectivity of the transmission channel. Moreover, diversity is gained by separating different propagation paths during despreading and combine them according to the maximum

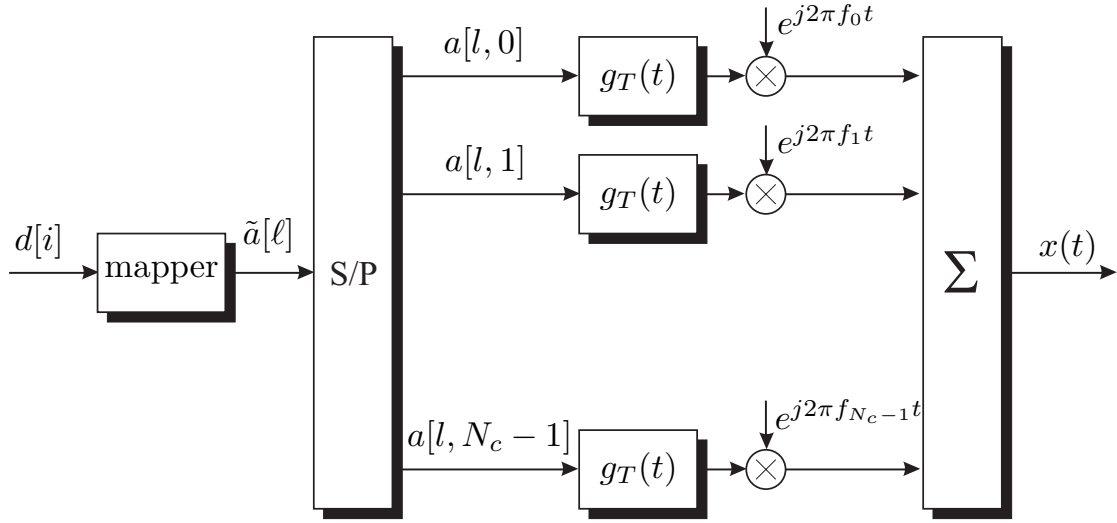


Figure 4.3.1: Structure of multi-carrier transmitter

ratio combining principle (see Rake receiver on page 172). A different way to treat frequency selectivity is to use narrow band signals whose bandwidth B is much smaller than the coherence bandwidth of the channel. In this case, intersymbol interference can be neglected and equalization is carried out by multiplying the received signal with the complex conjugate channel coefficient.

However, a small bandwidth corresponds with large symbol durations and low data rates. In order to overcome this penalty, multiple narrow-band data streams can be transmitted in parallel on different sub-carriers. **Fig. 4.3.1** shows the structure of a multi-carrier transmitter. As in a conventional single-carrier system, the bits $d[i]$ are fed to a linear $M = 2^m$ -ary modulator. Afterwards, the symbols $\tilde{a}[\ell]$ of duration T_s are mapped onto N_c parallel streams $a[l, \mu] = \tilde{a}[lN_c + \mu]$ with $0 \leq \mu < N_c$ where they are lowpass filtered with $g_T(t)$ (refer to Section 1.2). Next, the signals are multiplied with their associated carriers. Note that the frequencies f_μ do not describe the transmission band but still the equivalent baseband, i.e. $-f_{\max} \leq f_\mu \leq +f_{\max}$ holds. The complex baseband signal has the form

$$x_{MC}(t) = \sum_{l=-\infty}^{\infty} \sum_{\mu=0}^{N_c-1} a[l, \mu] \cdot g_T(t - lT_{MC}) \cdot e^{j2\pi f_\mu t}. \quad (4.3.1)$$

The symbol rate of one multi-carrier symbol amounts

$$\frac{1}{T_{MC}} = \frac{1}{N_c \cdot m \cdot T_b} = \frac{1}{N_c \cdot T_s} \quad (4.3.2)$$

and the bandwidth of each sub-stream is N_c times smaller than for a single-carrier transmission.

However, multi-carrier systems also come along with some drawbacks. First, the superposition of N_c independent signals results in a complex envelope $|x(t)|$ that varies over a wide range. This is essentially a problem for power amplifiers. They are designed to work efficiently (with only a few losses) at a defined working point, i.e. a certain magnitude of the signal. If this working point is exceeded, the amplifier loses its linearity and efficiency. Therefore, signals whose magnitudes have a large peak-to-average ratio are often nonlinearly distorted. This leads to a higher error rate performance as well as to out-of-band radiation which is essentially bad in FDMA systems. Additionally, the narrow bandwidth leads to flat fading conditions on each sub-carrier. Therefore, no frequency diversity can be exploited.

4.3.2 Orthogonal Frequency Division Multiplexing

Orthogonal Frequency Division Multiplexing represents a special kind of multi-carrier technique. The first ideas for a multi-carrier transmission are traced back to [Sal67, Wei94] and have been reinvented several times [Bin90, KSTB92]. A practical breakthrough happens with the definition of the European terrestrial Digital Audio Broadcasting (DAB) [HL01]. DAB employs OFDM for the first time in a mobile radio application. Shortly after DAB, the terrestrial Digital Video Broadcasting (DVB-T) was defined also employing OFDM [Rei95, Sch98]. Today, OFDM is used in wireless local area networks (WLAN) according to the HIPERLAN/2 or the IEEE 802.11a standards [Hip99].

OFDM is also applied in wired transmission systems like DSL technologies (digital subscriber line). In this context, the multi-carrier technique is termed Discrete Multi-Tone (DMT).

Transmitter Design

Starting with the above described multi-carrier transmitter, we obtain an OFDM transmitter by using the following specifications. The lowpass filter $g_T(t)$ has a rectangular shape

$$g_T(t) = \begin{cases} 1 & \text{for } 0 \leq t < T_{\text{MC}} \\ 0 & \text{else} \end{cases} \quad (4.3.3)$$

Since the rectangular impulse in (4.3.3) corresponds to the si-function in the frequency domain

$$|G_T(j2\pi f)| = \left| \frac{\sin(2\pi f T_{\text{MC}}/2)}{2\pi f T_{\text{MC}}/2} \right| = |\text{si}(\pi f T_{\text{MC}})|, \quad (4.3.4)$$

the spectrum has equidistant zeros at multiples of $\Delta f = 1/T_{\text{MC}}$. Adjusting now the carrier spacing according to $f_\mu - f_{\mu-1} = \Delta f = 1/T_{\text{MC}}$, the si-functions over-

lap such that a maximum of one sub-carrier coincides with zeros of all other subcarriers. Therefore, the first Nyquist condition is fulfilled in the frequency domain and parallel signals are mutually orthogonal so that no interference disturbs the transmission. This explains the naming 'orthogonal' in OFDM and is illustrated in **Fig. 4.3.2**.

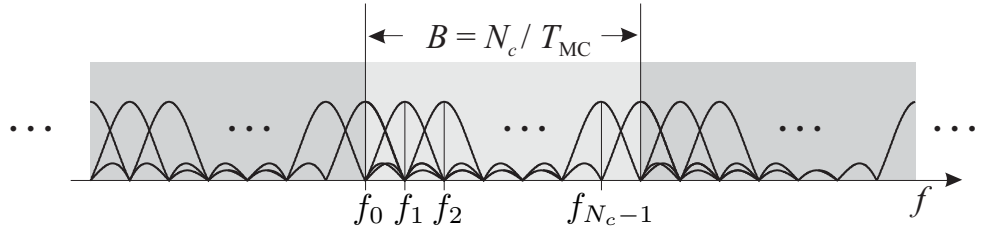


Figure 4.3.2: Spectrum of OFDM transmit signal

In Chapter 1, we derived a time-discrete channel model that is used for subsequent investigations. Therefore, we do not use the time-continuous signal $x_{\text{MC}}(t)$ but a sampled version of it. Inserting (4.3.3) into (4.3.1), we obtain with $f_\mu = \mu/T_{\text{MC}} = \mu/(N_c T_s)$ a time-discrete signal

$$\begin{aligned} x[\ell] &:= x(\ell T_s) = \sum_{\mu=0}^{N_c-1} a[l, \mu] \cdot e^{j2\pi\mu/(N_c T_s)\ell T_s} \\ &= \sum_{\mu=0}^{N_c-1} a[l, \mu] \cdot e^{j2\pi\mu\ell/N_c} = \text{IDFT}_{(\mu)}\{a[l, \mu]\} \end{aligned} \quad (4.3.5)$$

of rate $1/T_s = N_c/T_{\text{MC}}$. The samples in the interval $lN_c \leq \ell < (l+1)N_c$ represent the l -th OFDM symbol of length N_c . Moreover, we recognize from (4.3.5) that the OFDM transmitter can be efficiently implemented with the inverse FFT (Fast Fourier Transform). **Fig. 4.3.3** shows the whole OFDM transmitter.

The Guard Interval

The most important property of OFDM is the orthogonality in time as well as in frequency domain. In the time domain, this is ensured by using non-overlapping rectangular impulses $g_T(t)$, in the frequency domain, the specific spacing of the sub-carriers avoids intercarrier interference. However, this orthogonality is destroyed by frequency-selective channels as depicted in **Fig. 4.3.4**. Without loss of generality, we regard the OFDM symbol at time instance 0 and its direct neighbors. If L_t is the length of channel impulse response, $L_t - 1$ samples of consecutive OFDM symbols overlap due to the post-transient phase. This effect is termed intersymbol interference (ISI) and destroys orthogonality in time. Moreover, the pre-transient phase leads to intercarrier interference (ICI).

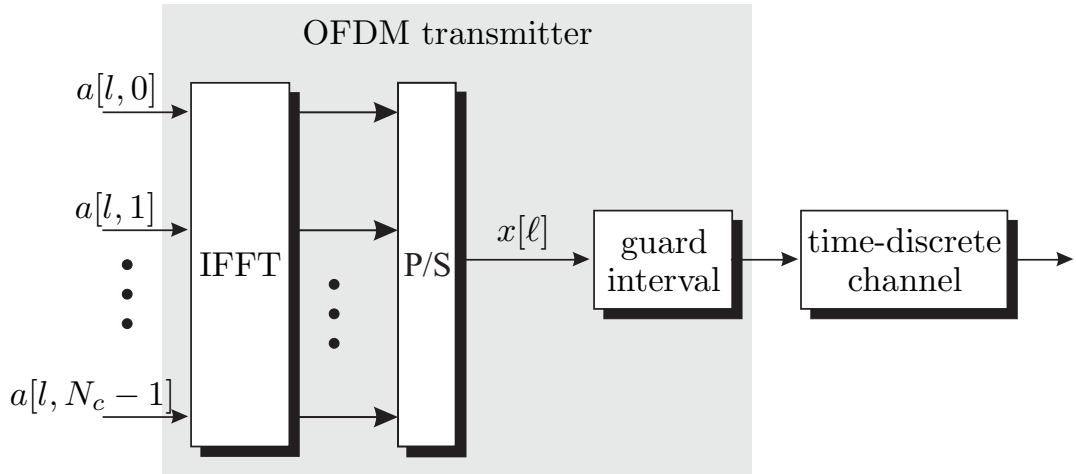


Figure 4.3.3: Structure of OFDM transmitter

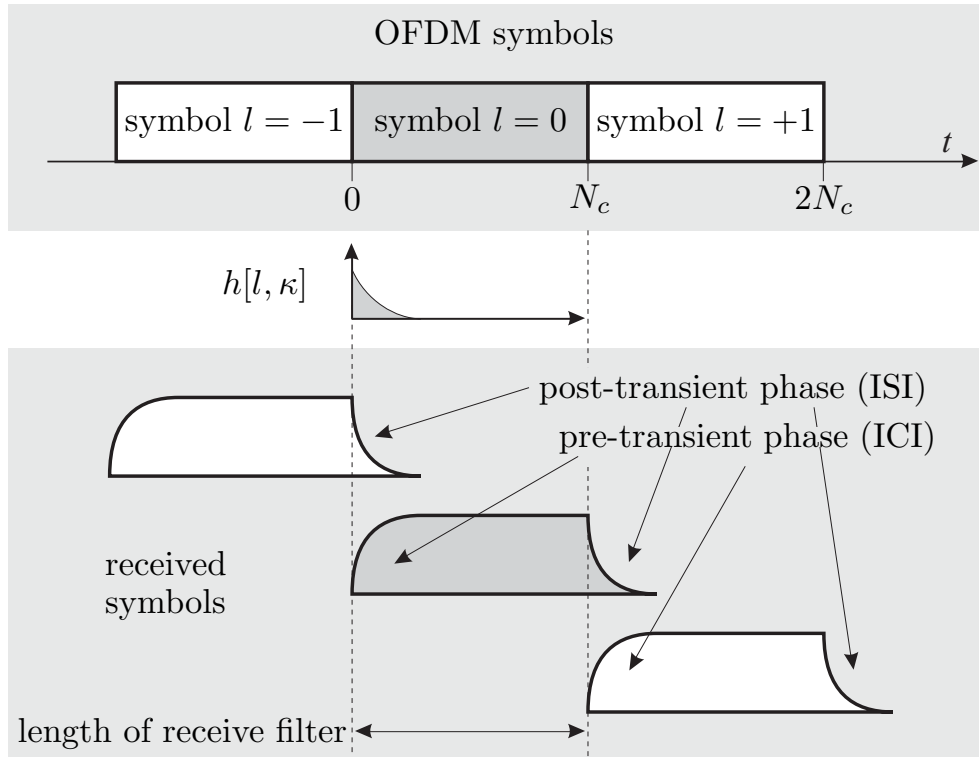


Figure 4.3.4: Influence of frequency-selective channel on OFDM transmission

Orthogonality can be maintained by inserting a cyclic prefix called guard interval in front of each OFDM symbol. Each OFDM symbol will be preceded by its own tail in the interval. This is demonstrated in **Fig. 4.3.5**. If the length of the guard interval N_g is at least as long as the length of the channel impulse response L_t , the post-transient phase of symbol -1 and the pre-transient phase of symbol 0 are restricted to the guard interval and do not affect the core OFDM symbols.

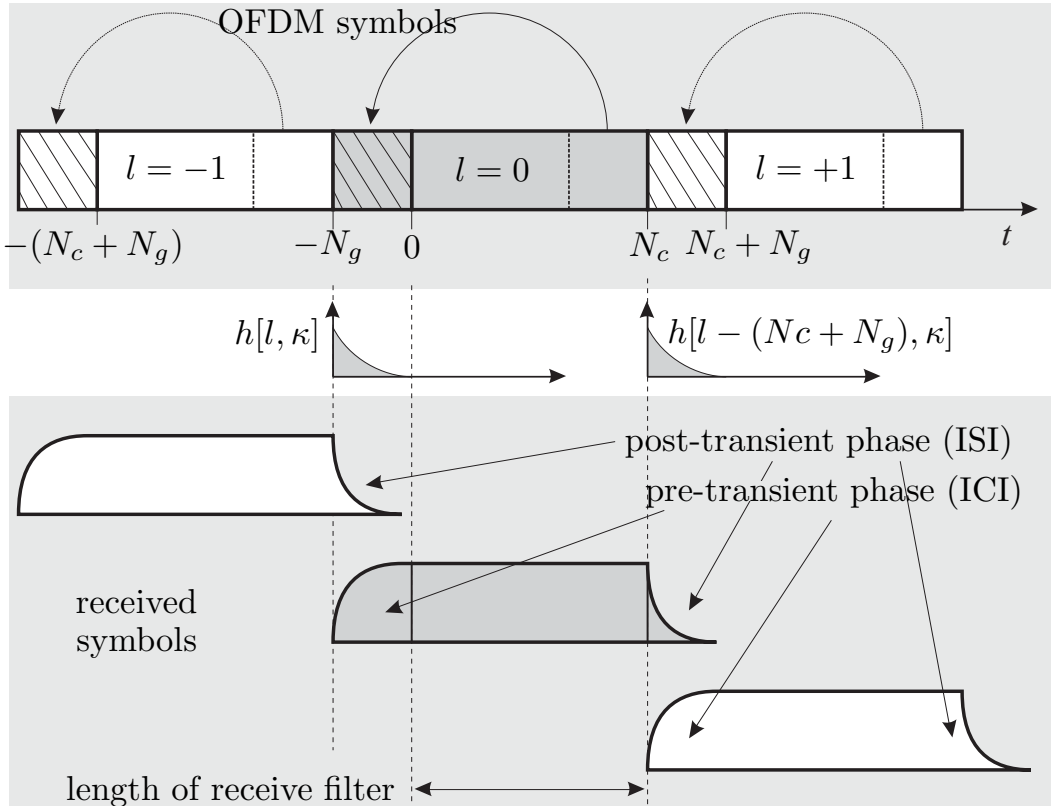


Figure 4.3.5: Effect of guard interval

The insertion of the cyclic prefix results in a cyclic convolution of channel impulse response and OFDM symbol. According to the properties of the discrete Fourier transformation, a cyclic convolution of two signals corresponds to the product of the associated spectra. Hence, for $\kappa_{\max} < N_g$, we obtain

$$\begin{aligned}\tilde{x}[\ell] &= x[\ell] \circledast h[l, \ell - lN_c] \\ \tilde{X}[l, \mu] &= \underbrace{\text{DFT}_{(\ell)}\{x[\ell]\}}_{a[l, \mu]} \cdot \underbrace{\text{DFT}_{(\ell)}\{h[l, \ell]\}}_{H[l, \mu]} = a[l, \mu] \cdot H[l, \mu]\end{aligned}\quad (4.3.6)$$

where \circledast denotes the cyclic convolution with respect to ℓ . We can conclude from (4.3.6) that the symbols $a[l, \mu]$ on each sub-channel are multiplied by a scalar complex channel coefficient $H[l, \mu]$. Therefore, we have flat fading conditions on each subcarrier and no diversity can be gained for uncoded transmissions.

Receiver Design

The above mentioned properties simplify the receiver structure remarkably as depicted in **Fig. 4.3.6**. First, the guard interval is removed and only the core OFDM symbol in the time interval $lN_c \leq \ell < (l + 1)N_c$ is processed. Since this also removes pre-transient and post-transient phases, we have a steady-state within each core symbol and can process successive OFDM symbols independently. Furthermore, orthogonality between subcarriers is maintained. After transforming the core symbol back into the frequency domain, we obtain the received vector at time instance l

$$\begin{aligned} \tilde{y}[\ell] &= x[\ell] \circledast h[l, \ell - lN_c] + \tilde{n}[\ell] \\ &\vdots \\ y[l, \mu] &= H[l, \mu] \cdot a[l, \mu] + n[l, \mu]. \end{aligned} \quad (4.3.7)$$

Due to the cyclic prefix, we have transformed the frequency-selective channel into a flat fading channel on each sub-carrier and the received vector can be described in the frequency domain by

$$\mathbf{y}[l] = \mathbf{H}[l] \cdot \mathbf{a}[l] + \mathbf{n}[l] \quad (4.3.8)$$

where $\mathbf{H}[l] = \text{diag}[H[l, 0] \cdots H[l, N_c - 1]]$ represents a matrix with the transfer function on the main diagonal. The vectors $\mathbf{a}[l]$ and $\mathbf{n}[l]$ contain the information symbols $a[l, \mu]$ and the noise samples $n[l, \mu]$ for $0 \leq \mu < N_c$, respectively. The noise statistics are not affected because the Fourier transformation is orthogonal, i.e. $n[l, \mu]$ is still Gaussian distributed with zero mean and variance $\sigma_n^2 = N_0/T_s$. According to Fig. 4.3.6, equalization is now performed by weighting the symbols $y[l, \mu]$ with scalar equalizer coefficients.

$$\hat{a}[l, \mu] = E[l, \mu] \cdot y[l, \mu] \Leftrightarrow \hat{\mathbf{a}}[l] = \mathbf{E}[l] \cdot \mathbf{y}[l] \quad (4.3.9)$$

In (4.3.9), $\mathbf{E}[l]$ is a diagonal matrix containing the equalizer coefficients $E[l, \mu]$ of each subcarrier.

The main benefit of OFDM is the extremely simple equalization. This advantage is obtained at the expense of a reduced spectral efficiency due to the insertion of the cyclic prefix. Removing the prefix at the receiver results in a violation of the matched filter principle and, consequently, in an SNR loss

$$\delta^2 = 1 - \frac{N_g}{N_c + N_g} = \frac{N_c}{N_c + N_g} = \frac{1}{1 + N_g/N_c}. \quad (4.3.10)$$

Obviously, the SNR loss and, equivalently, the efficiency of OFDM depend on the ratio N_g/N_c , i.e. the fraction of the guard interval compared to the core OFDM symbol. The larger the ratio, the larger the loss. A practical value is $N_g/N_c =$

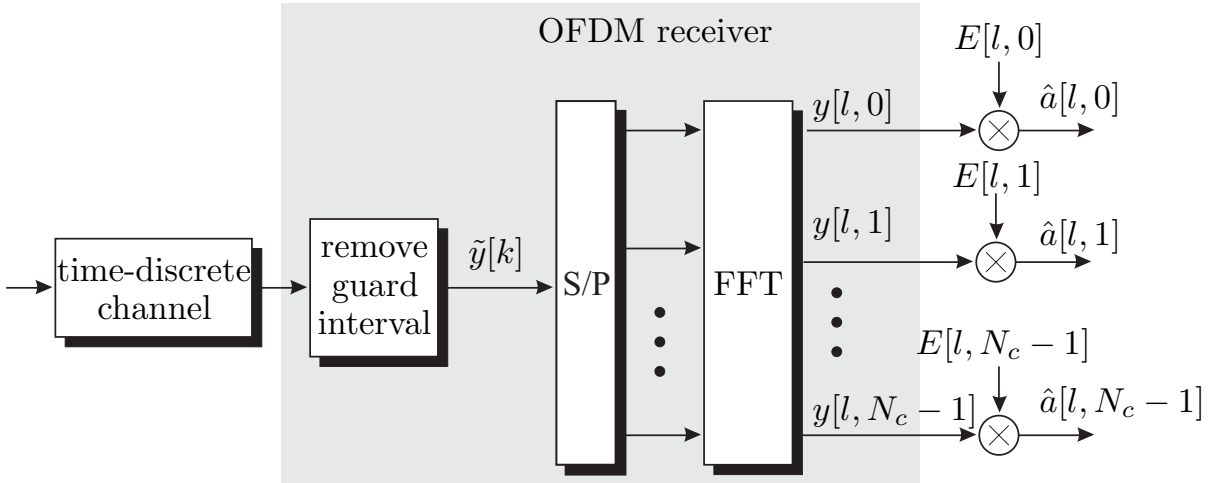


Figure 4.3.6: Structure of OFDM receiver

0.25 resulting in a loss of approximately 1 dB. Since the minimum length of the guard interval is fixed by the channel length L_t , the efficiency can be improved by increasing the number of carriers N_c . However, this also enlarges total symbol duration $N_c + N_g$ which may become critical for time varying channels.⁶ Therefore, we always have to find a compromise between frequency selectivity, time selectivity and spectral efficiency in OFDM systems.

4.3.3 Combining OFDM and CDMA

It is quite obvious that spread spectrum and OFDM represent two opposite techniques to treat frequency-selective channels. While spread spectrum suffers from path crosstalk in the Rake receiver, OFDM has the penalty of a reduced spectral efficiency due to the guard interval. A promising candidate for future mobile radio systems is the combination of both approaches. There exist several possibilities to combine multi-carrier techniques and CDMA [YLF93, FP93, DS93, Van95, Kai98, Dek00]. We restrict to the combination of OFDM and CDMA called OFDM-CDMA with spectral spreading in the frequency domain [Dek00, KDK00b].

Fig. 4.3.7 shows the principal structure of an OFDM-CDMA system. It simply consists of a serial concatenation of the classical direct-sequence spreading part and the block-oriented operating OFDM part. In contrast to single-carrier CDMA, spreading is now performed in frequency domain. This is demonstrated in more detail in **Fig. 4.3.8**. Generally, the serial to parallel converter extracts N_b symbols out of $\tilde{a}_u[\ell]$ that contribute to one OFDM symbol of user u . Each of these symbols is spread by a factor N_s resulting in $N_c = N_b \cdot N_s$ chips modulating the different

⁶It was always assumed that the channel remains constant during one OFDM symbol.

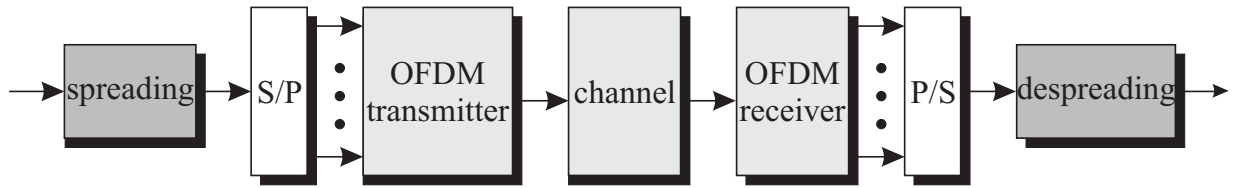


Figure 4.3.7: Structure of OFDM-CDMA system

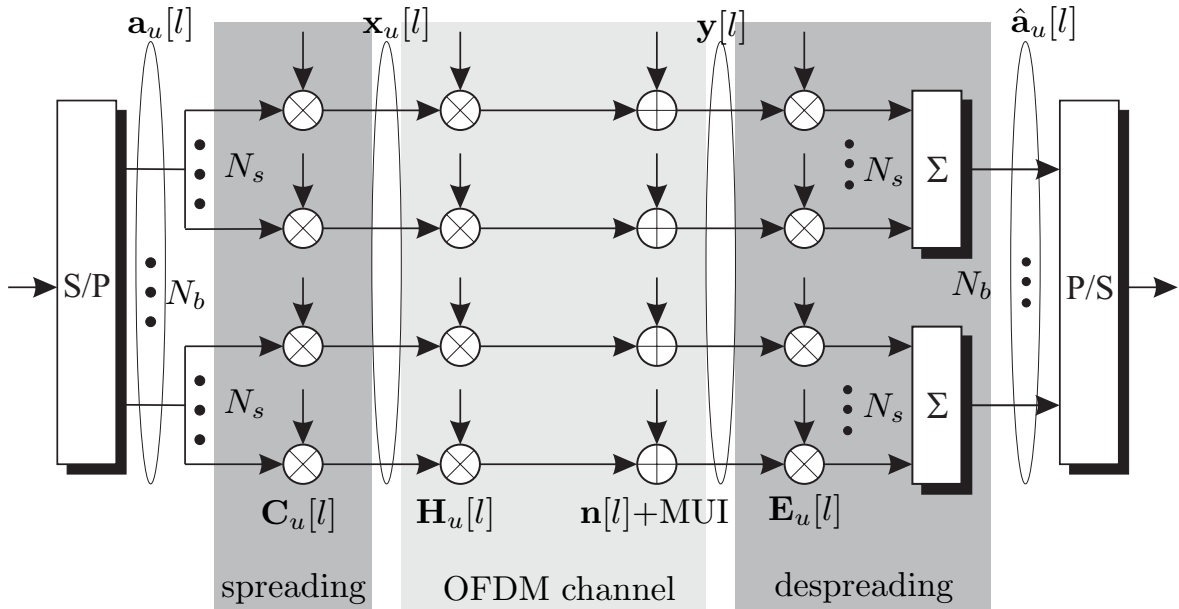


Figure 4.3.8: Alternative description of OFDM-CDMA system

subcarriers. Since these chips represent the input of the IFFT block, spreading takes place in the frequency domain.

Exploiting the OFDM properties derived in the last section, we obtain N_c parallel data streams that are weighted with the coefficients $H_u[l, \mu]$ of the channel transfer function (flat fading) and disturbed by independent noise samples $n[l, \mu]$ as well as multi-user interference. Hence, path crosstalk known from the Rake receiver is avoided at the expense of a reduced spectral efficiency due to the cyclic prefix.

Assuming a quasi synchronous transmission⁷, exactly this prefix enables us to perform simple block oriented signal processing at the receiver because interblock interference is mitigated. Contrarily, single-carrier CDMA requires to consider a sequence of consecutive symbols which mutually interfere. The l -th received OFDM symbol $\mathbf{y}[l] = [y_0[l] \cdots y_{N_c-1}[l]]^T$ has the well-known form

⁷Quasi synchronous means that the maximum mutual delay among all users is limited to the length of the guard interval. In this case, the core OFDM symbols of all users can be processed in a single step and intersymbol interference is mitigated.

$$\mathbf{y}[l] = \mathbf{S}[l] \cdot \mathbf{a}[l] + \mathbf{n}[l], \quad (4.3.11)$$

where $\mathbf{a}[l]$ comprises the symbols of all users contributing to this symbol

$$\mathbf{a}[l] = [a_1[l, 0] \quad \cdots \quad a_1[l, N_b - 1] \quad \cdots \quad a_{N_U}[l, N_b - 1]]^T. \quad (4.3.12)$$

Synchronous Downlink Transmission

As explained before, the downlink is characterized by the fact that all users experience the same channel. Looking at the u -th mobile receiver, the signature matrix $\mathbf{S}[l]$ becomes

$$\mathbf{S}_u[l] = \mathbf{H}_u[l] \cdot \mathbf{C}[l] \quad (4.3.13)$$

with $\mathbf{H}_u[l] = \text{diag}[H_u[l, 0] \cdots H_u[l, N_c - 1]]$ containing the channel transfer function of user u on its diagonal. The spreading matrix $\mathbf{C}[l] = [\mathbf{C}_1[l] \cdots \mathbf{C}_{N_U}[l]]$ concatenates the user-specific matrices

$$\mathbf{C}_u[l] = \begin{bmatrix} \mathbf{c}_u[l, 0] \\ & \ddots \\ & & \mathbf{c}_u[l, N_b - 1] \end{bmatrix} \quad (4.3.14)$$

which consist of vectors $\mathbf{c}_u[l, \mu] = [c_{u,0}[l, \mu] \cdots c_{u,N_s-1}[l, \mu]]^T$ representing the spreading code of user u for symbol $a_u[l, \mu]$. If only a single symbol is mapped onto one OFDM symbol, the matrices $\mathbf{C}_u[l]$ reduce to column vectors.

In multi-rate CDMA systems with various symbol rates and spreading factors, the number N_b of symbols associated with one OFDM symbol and, hence, the length of different spreading code parts $\mathbf{c}_u[l, \mu]$ vary among users. This leads to different structure of the matrices $\mathbf{C}_u[l]$ and a nonsymmetric code matrix $\mathbf{C}[l]$.

At the receiver, we now have to perform the despreading. The specific form of the signature matrix in (4.3.13) allows different very efficient ways for despreading [FK03, HMCK03].

Maximum Ratio Combining (MRC)

According to the classical matched filter, we have to multiply $\mathbf{y}[l]$ with the Hermitian form of $\mathbf{S}_u[l] = \mathbf{H}_u[l] \cdot \mathbf{C}_u[l]$ leading to

$$\mathbf{r}_u[l] = \mathbf{E}_u^{\text{MRC}}[l] \cdot \mathbf{y}[l] = \mathbf{S}_u^H[l] \cdot \mathbf{y}[l] = \mathbf{C}_u^T[l] \cdot \mathbf{H}_u^H[l] \cdot \mathbf{y}[l]. \quad (4.3.15)$$

The multiplication with $\mathbf{H}_u^H[l]$ weights each chip with the corresponding conjugate complex channel coefficient ensuring a coherent reception. The subsequent

despread with $\mathbf{S}_u^H[l]$ performs a maximum ratio combining. Inserting the structure of $\mathbf{y}[l]$ into (4.3.15), the N_b output symbols for user u are obtained by

$$\mathbf{r}_u[l] = \mathbf{C}_u^T[l] \cdot \mathbf{H}_u^H[l] \cdot \mathbf{H}_u[l] \cdot \mathbf{C}_u[l] \cdot \mathbf{a}[l] + \tilde{\mathbf{n}}[l]. \quad (4.3.16)$$

Although this approach maximizes the signal to noise ratio and perfectly exploits diversity, it does not consider multi-user interference which dramatically limits the system performance [Dek00, Kai98]. The diagonal matrix $\mathbf{H}_u^H[l] \cdot \mathbf{H}_u[l]$ between $\mathbf{C}_u^T[l]$ and $\mathbf{C}_u[l]$ in (4.3.16) destroys the orthogonality of the spreading codes because the chips of the spreading codes are weighted with different magnitudes. The performance degradation is the same as in single-carrier CDMA systems.

Orthogonal Restoring Combining (ORC)

However, the influence of multi-user interference can be easily overcome in OFDM-CDMA systems. Restoring the orthogonality is possible by perfectly equalizing the channel also known as zero-forcing (ZF) solution [FK03]. In OFDM based systems, this is easily implemented by dividing each symbol in $\mathbf{y}[l]$ with the corresponding channel coefficient. With $\mathbf{H}_u^{-1}[l] = \text{diag}[H_u^{-1}[l, 0] \cdots H_u^{-1}[l, N_c - 1]]$, we obtain

$$\begin{aligned} \mathbf{r}_u[l] &= \mathbf{E}_u^{\text{ORC}}[l] \cdot \mathbf{y}[l] = \mathbf{C}_u^T[l] \cdot \mathbf{H}_u^{-1}[l] \cdot (\mathbf{H}_u[l] \cdot \mathbf{C}[l] \cdot \mathbf{a}[l] + \mathbf{n}[l]) \\ &= \mathbf{C}_u^T[l] \cdot \mathbf{C}[l] \cdot \mathbf{a}[l] + \mathbf{C}_u^T[l] \cdot \mathbf{H}_u^{-1}[l] \cdot \mathbf{n}[l]. \end{aligned} \quad (4.3.17)$$

If the partial spreading codes $\mathbf{c}_u[l, \mu]$ of different users are mutually orthogonal, $\mathbf{C}_u^T[l] \cdot \mathbf{C}[l] = [\mathbf{0}_{N_b \times (u-1)N_b} \ \mathbf{I}_{N_b} \ \mathbf{0}_{N_b \times (N_U-u)N_b}]$ holds. Hence, the multiplication with $\mathbf{C}_u^T[l]$ suppresses all users except user u and (4.3.17) becomes

$$\mathbf{r}_u[l] = \mathbf{a}_u[l] + \mathbf{C}_u^T[l] \cdot \mathbf{H}_u^{-1}[l] \cdot \mathbf{n}[l]. \quad (4.3.18)$$

We see that the desired symbols $\mathbf{a}_u[l]$ have been perfectly extracted, and only the modified background noise disturbs a decision. However, exactly this background noise is often significantly amplified by restoring orthogonality leading to high error probabilities especially at low signal to noise ratios. This effect is well-known from zero-forcing equalization [Kam96] and linear multi-user detection [Mos96].

A comparison with the linear ZF detector in Subsection 5.2.1 on page 234 shows the following equivalence. For a fully loaded system with $N_s = N_U$, $\mathbf{C}[l]$ is an orthogonal $N_U \times N_U$ matrix. Neglecting time indices, the ZF criterion (4.3.17) delivers with $\mathbf{S} = \mathbf{H}\mathbf{C}$

$$\mathbf{E} = (\mathbf{S}^H \mathbf{S})^{-1} \mathbf{S}^H = \mathbf{C}^{-1} \mathbf{H}^{-1} \mathbf{H}^{-H} \mathbf{C}^{-H} \mathbf{C}^H \mathbf{H}^H = \mathbf{C}^T \mathbf{H}^{-1}. \quad (4.3.19)$$

Obviously, (4.3.19) coincides with $\mathbf{E}_u^{\text{ORC}}[l]$ in (4.3.17). Concerning the downlink, OFDM-CDMA allows a very efficient implementation of the ZF multi-user detector without any matrix inversion.

Equal Gain Combining (EGC)

Two approaches exist that try to find a compromise between interference suppression and low noise amplification. Instead of dividing through a channel coefficient, we could just correct the phase shift and keep the amplitude constant. Hence, all chips experience the same 'gain' resulting in

$$\begin{aligned} \mathbf{r}_u[l] &= \mathbf{E}_u^{\text{EGC}}[l] \cdot \mathbf{y}[l] \\ &= \mathbf{C}_u^T[l] \cdot \begin{bmatrix} \frac{H_u^*[l,0]}{|H_u[l,0]|} \\ \ddots \\ \frac{H_u^*[l,N_c-1]}{|H_u[l,N_c-1]|} \end{bmatrix} (\mathbf{H}_u[l] \cdot \mathbf{C}[l] \cdot \mathbf{a}[l] + \mathbf{n}[l]) \\ &= \mathbf{C}_u^T[l] \cdot \begin{bmatrix} \frac{|H_u[l,0]|^2}{|H_u[l,0]|} \\ \ddots \\ \frac{|H_u[l,N_c-1]|^2}{|H_u[l,N_c-1]|} \end{bmatrix} \cdot \mathbf{C}[l] \cdot \mathbf{a}[l] + \tilde{\mathbf{n}}[l]. \quad (4.3.20) \end{aligned}$$

From (4.3.20) we see that the equalizer coefficients have unit magnitudes so that the noise is not amplified. A second impact is that amplitude variations of the channel transfer function are not emphasized so that the originally perfect correlation properties of the spreading codes become not so bad after equalization as for MRC.

Minimum Mean Squared Error (MMSE)

A second possibility to avoid an amplification of the background noise is to use the minimum mean squared error solution. Starting with the MMSE criterion

$$\mathbb{E} \left\{ \| \mathbf{E}_u \mathbf{y}[l] - \mathbf{a}_u[l] \|^2 \right\} = \mathbb{E} \left\{ \| \mathbf{E}_u (\mathbf{H}_u[l] \mathbf{C}[l] \mathbf{a}[l] + \mathbf{n}[l]) - \mathbf{a}_u[l] \|^2 \right\} \rightarrow \min, \quad (4.3.21)$$

for user u , a solution is obtained by setting the derivation with respect to \mathbf{E}_u^H to zero and solve the equation system. This yields

$$\mathbf{E}_u^{\text{MMSE}}[l] = \mathbf{C}_u^T[l] \cdot \mathbf{H}_u^H[l] \cdot \left(\mathbf{H}_u[l] \cdot \mathbf{H}_u^H[l] + \frac{\sigma_{\mathcal{N}}^2}{\sigma_{\mathcal{A}}^2} \cdot \mathbf{I}_{N_c} \right)^{-1}. \quad (4.3.22)$$

Since $\mathbf{H}_u[l]$ is a diagonal matrix, the application of (4.3.22) results in

$$\begin{aligned} \mathbf{r}_u[l] &= \mathbf{E}_u^{\text{MMSE}}[l] \cdot \mathbf{y}[l] \\ &= \mathbf{C}_u^T[l] \begin{bmatrix} \frac{|H_u[l,0]|^2}{|H_u[l,0]|^2 + \sigma_{\mathcal{N}}^2 / \sigma_{\mathcal{A}}^2} \\ \ddots \\ \frac{|H_u[l,N_c-1]|^2}{|H_u[l,N_c-1]|^2 + \sigma_{\mathcal{N}}^2 / \sigma_{\mathcal{A}}^2} \end{bmatrix} \mathbf{C}[l] \mathbf{a}[l] + \tilde{\mathbf{n}}[l]. \quad (4.3.23) \end{aligned}$$

Obviously, we have to add the ratio between noise power $\sigma_{\mathcal{N}}^2$ and signal power $\sigma_{\mathcal{A}}^2$ to the squared magnitudes in the denominators. This avoids an amplification of the noise at subcarriers with deep fades. For infinite high SNR, $\sigma_{\mathcal{N}}^2/\sigma_{\mathcal{A}}^2 \rightarrow 0$ holds and the MMSE equalization equals the ORC scheme.

Similar to the ORC solution, we can compare (4.3.22) with the linear MMSE multi-user detector on page 239. For a fully loaded system with $N_s = N_U$, $\mathbf{C}[l]$ is an orthogonal $N_U \times N_U$ matrix. The MMSE criterion in (5.2.20) delivers with $\mathbf{S} = \mathbf{H}\mathbf{C}$

$$\begin{aligned}\mathbf{E} &= (\mathbf{S}^H \mathbf{S} + \frac{\sigma_{\mathcal{N}}^2}{\sigma_{\mathcal{A}}^2} \mathbf{I}_{N_U})^{-1} \mathbf{S}^H = (\mathbf{C}^H \mathbf{H}^H \mathbf{H} \mathbf{C} + \frac{\sigma_{\mathcal{N}}^2}{\sigma_{\mathcal{A}}^2} \mathbf{I}_{N_U})^{-1} \mathbf{C}^H \mathbf{H}^H \\ &= \mathbf{C}^{-1} (\mathbf{H}^H \mathbf{H} + \frac{\sigma_{\mathcal{N}}^2}{\sigma_{\mathcal{A}}^2} \mathbf{I}_{N_U})^{-1} \mathbf{C}^{-H} \mathbf{C}^H \mathbf{H}^H \\ &= \mathbf{C}^H (\mathbf{H}^H \mathbf{H} + \frac{\sigma_{\mathcal{N}}^2}{\sigma_{\mathcal{A}}^2} \mathbf{I}_{N_U})^{-1} \mathbf{H}^H.\end{aligned}\quad (4.3.24)$$

Since the channel matrices are diagonal, (4.3.24) and (4.3.22) are identical. Hence, OFDM-CDMA allows a very efficient implementation of the MMSE multi-user detector for the downlink without matrix inversion.

In order to evaluate the performances of the described equalization techniques, we consider the synchronous downlink of an OFDM-CDMA system with BPSK modulation. Scrambled Walsh codes with a spreading factor $N_s = 16$ are employed. The choice of $N_c = 16$ subcarriers results in a mapping of one information bit onto one OFDM symbol. Moreover, a 4-path Rayleigh fading channel is used requiring a guard interval of length $L_t - 1 = 3$ samples. The E_b/N_0 loss due to the insertion of the cyclic prefix has not been considered because it is identical for all equalization schemes.

As we explained earlier, the frequency-selectivity of the channel destroys the Walsh codes' orthogonality and multi-user interference disturbs the transmission. For a load of $\beta = 1/2$, we see from Fig. 4.3.9a that the MMSE approach performs best over the whole range of signal to noise ratios. EGC comes very close to the MMSE solution at low and medium SNRs, but loses up to 3 dB for high signal to noise ratios. MRC perform much worse except in the low SNR regime where the background noise dominates the system reliability. In this area, orthogonal restoring combining represents the worst approach, it can outperform MRC only for SNRs larger than 14 dB due to the noise amplification. None of the equalizing schemes can reach the single-user bound that represents the achievable error rate in the absence of interference.

Fig. 4.3.9b depicts the results for $N_U = 16$, i.e. a fully loaded system with $\beta = 1$. The advantage of the MMSE solution becomes larger. Especially EGC loses a lot and is even outperformed by orthogonal restoring combining at high SNRs.

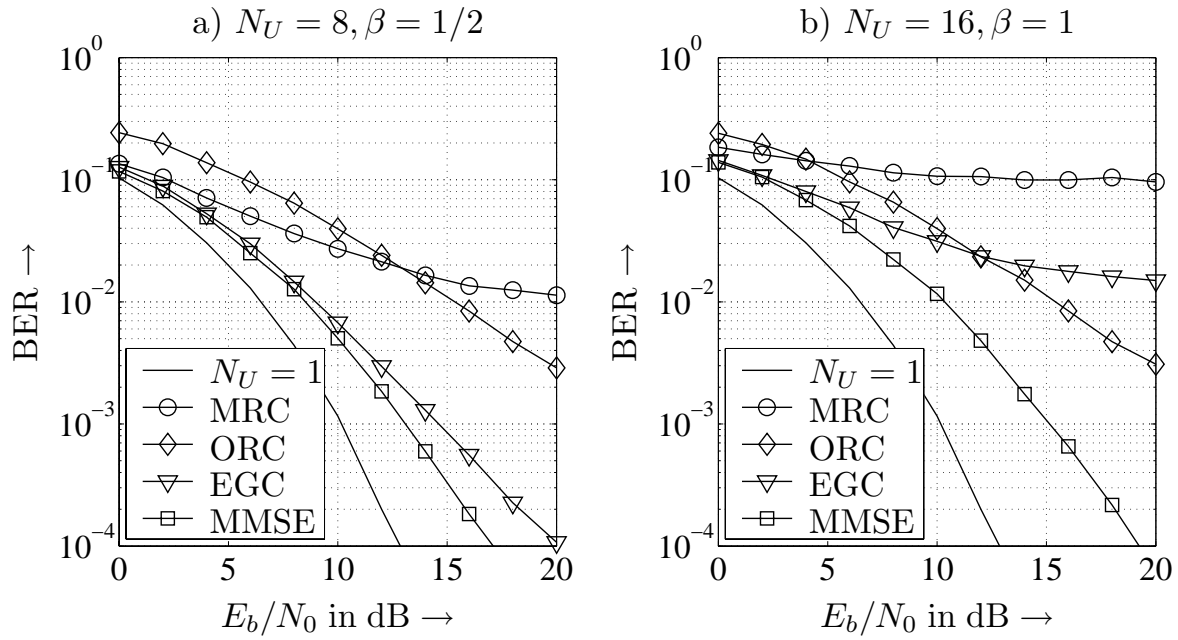


Figure 4.3.9: Error rate performance of OFDM-CDMA system with $G_p = 16$ and different equalization techniques for a 4-path Rayleigh fading channel
a) $N_U = 8$ active users, **b)** $N_U = 16$ active users

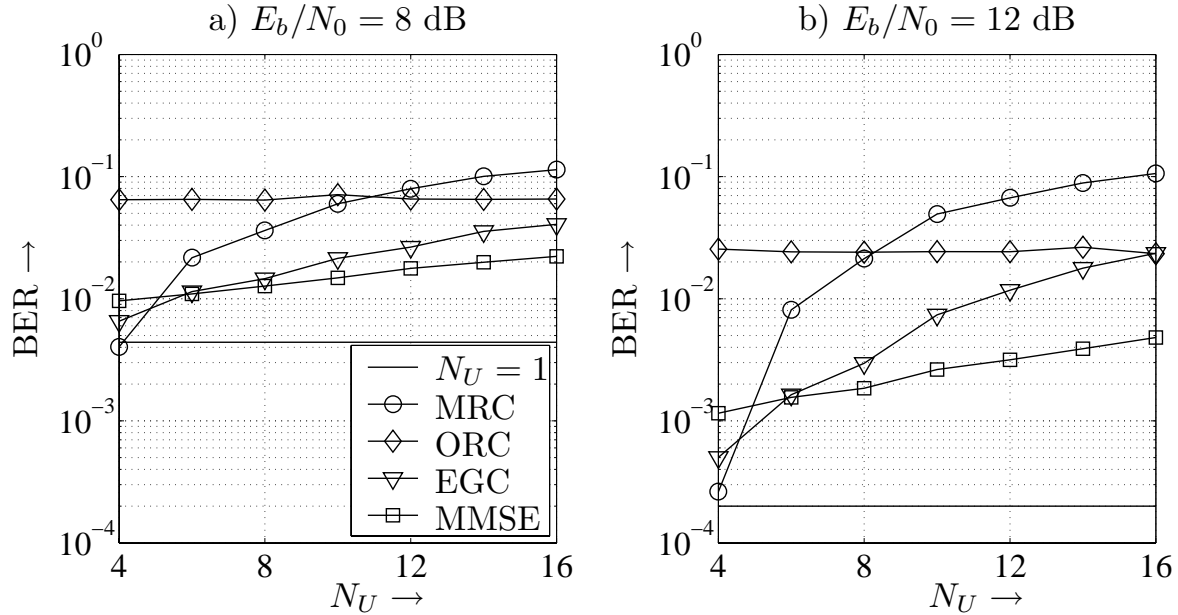


Figure 4.3.10: Error rate performance of OFDM-CDMA system with $G_p = 16$ and different equalization techniques for a 4-path Rayleigh fading channel
a) $E_b/N_0 = 8$ dB, **b)** $E_b/N_0 = 12$ dB

The higher the load, the better is the performance of ORC compared to EGC and MRC because interference becomes the dominating penalty. As will be also shown in Section 5.2, linear multi-user detection schemes are not able to reach the single-user bound for high load.

The discussed effects are confirmed in **Fig. 4.3.10** where the bit error rate is depicted versus the number of users. First, we recognize that ORC is independent of the load β since the whole interference is suppressed. Different signal to noise ratios just lead to a vertical shift of the curve (compare Figs. 4.3.10a and b). Moreover, ORC outperforms MRC and EGC for high loads and SNRs. MMSE equalization shows the best performance except for very low loads. In that region, EGC and especially MRC show a better performances because the interference power is low and optimizing the signal to noise ratio ensures the best performance.

Fig. 4.3.11 points out another interesting aspect that holds also for single-carrier CDMA systems. Since the frequency selectivity destroys the orthogonality of spreading codes, there exist a rivalry between diversity gains and increased multi-user interference. The trade-off depends on the kind of equalization that is applied. For the MMSE equalizer, the diversity gain dominates and the error rate performance is improved for growing L_t . Contrarily, the multi-user interference conceals the diversity effect for equal gain combining and performance degrades for increasing L_t .

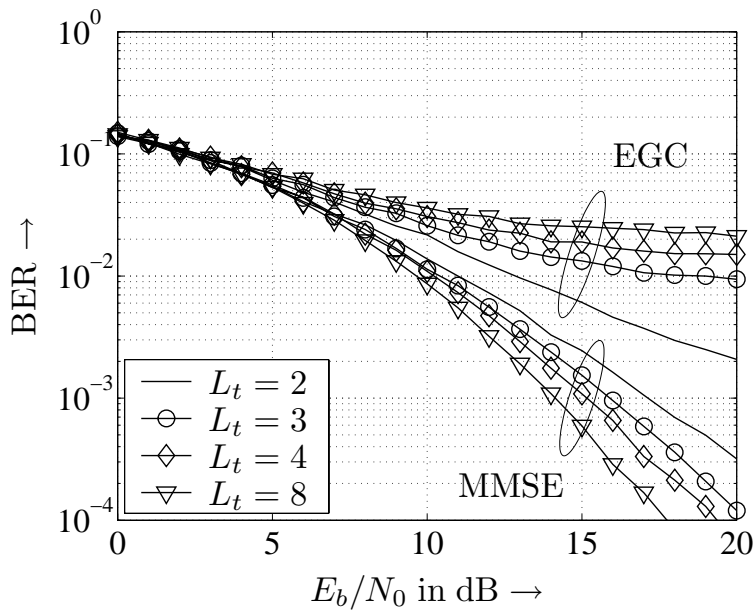


Figure 4.3.11: Error rate performance of OFDM-CDMA system with $G_p = 16$ and $N_U = 16$ for EGC and MMSE equalization and L_t -path Rayleigh fading channels

Quasi-Synchronous Uplink Transmission

Concerning the uplink, an equalization is not as easy because each user is affected by an individual channel. For simplicity, we assume a coarse synchronization ensuring that the maximum delay $\Delta\kappa$ between two users is limited to the length N_g of the guard interval minus the maximum channel delay κ_{\max} .

$$\Delta\kappa \leq N_g - \kappa_{\max} \quad (4.3.25)$$

In this case, a block oriented processing is possible and a single FFT block can transform the OFDM symbols of all users simultaneously into the frequency domain. Hence, the signature matrix $\mathbf{S}[l]$ becomes

$$\mathbf{S}[l] = [\mathbf{s}_1[l] \quad \cdots \quad \mathbf{s}_{N_U}[l]] \quad (4.3.26)$$

with $\mathbf{s}_u[l] = \text{diag}[H_u[l, 0] \cdots H_u[l, N_c - 1]] \cdot \mathbf{c}_u[l]$. The signature of a user is obtained by multiplying the coefficients of the channel transfer function element-wise with the chips of the spreading code. The data vector $\mathbf{a}[l]$ is defined in the same way as described in (4.3.12).

The simple matched filter provides a sufficient statistics, i.e. we do not lose any information and an optimum overall processing is still possible. Hence, despreading with maximum ratio combining has to be applied resulting in

$$\mathbf{r}[l] = \mathbf{E}^{\text{MRC}}[l] \cdot \mathbf{y}[l] = \mathbf{S}^H[l] \cdot \mathbf{y}[l] = \mathbf{S}^H[l] \cdot \mathbf{S}[l] \cdot \mathbf{a}[l] + \mathbf{S}^H[l] \cdot \mathbf{n}[l]. \quad (4.3.27)$$

Due to the non-diagonal structure of $\mathbf{S}^H[l] \cdot \mathbf{S}[l]$, multi-user interference degrades the system performance. This is confirmed by the results shown in **Fig. 4.3.12**. With growing β , error floors occur so that for loads larger than 0.5, a reliable uncoded transmission is not possible. The larger better, the smaller is the influence of the background noise as depicted in diagram b).

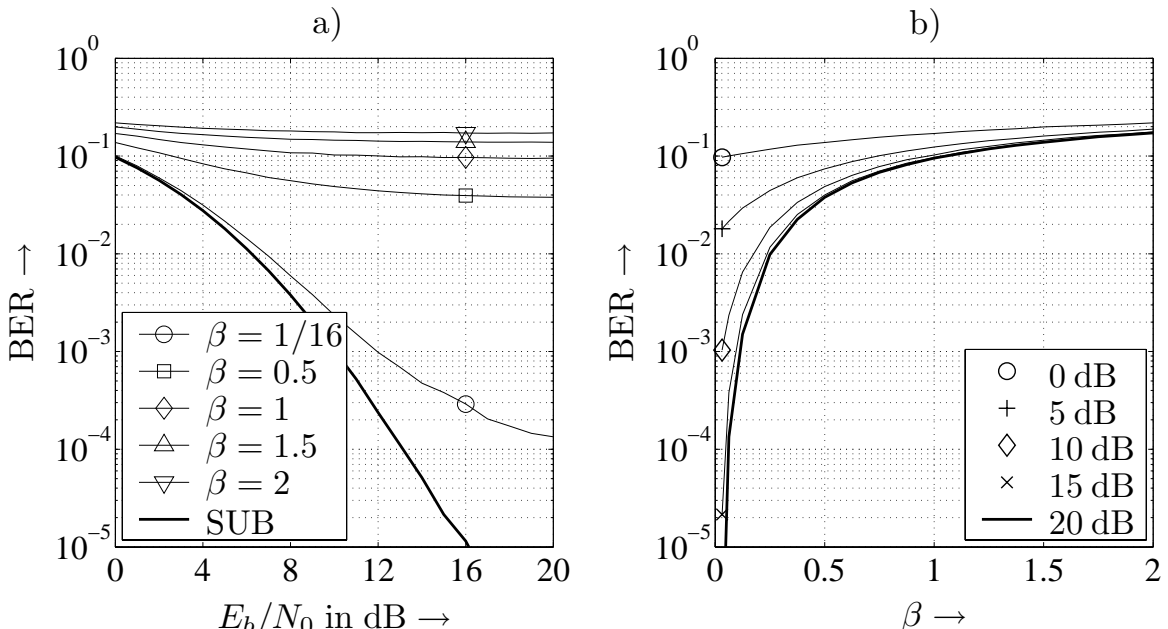


Figure 4.3.12: Error rate performance of OFDM-CDMA uplink with $G_p = 16$, BPSK, and 4-path Rayleigh fading channels

Concluding, we can state that OFDM represents a pretty good technique for synchronous downlink transmissions while the discussed benefits can not be exploited in the uplink. Here, each signal experiences its own channel so that a common equalization is not possible. Moreover, different carrier frequency offsets between transmitter and receiver pairs destroy even the orthogonality between subcarriers of the same user and cause inter-carrier interference. Therefore, more sophisticated detection algorithms as presented in Chapter 5 are required.

4.4 Low Rate Channel Coding in CDMA Systems

The previous sections illustrated that multi-user interference dramatically degrades the system performance. Using OFDM-CDMA in a downlink transmission allows an appropriate equalization that suppresses the interference efficiently. However, this is not possible in an asynchronous uplink transmission. One possibility is the application of multi-user detection techniques that exploit the interference's structure and are discussed in Chapter 5. Alternatively, we can interpret the interference as additional additive white Gaussian noise. This assumption is approximately fulfilled for a large number of users according to the central limit theorem.

It is well-known that noise can be combatted best by strong error correcting codes. One important feature of CDMA systems is the inherent spectral spreading already depicted in Figs. 4.2.1 and 4.2.2. As shown in **Fig. 4.4.1**, this spreading can also be described from Fig. 4.3.8 as simply repeating each symbol $a[\ell]$ N_s times and subsequent scrambling with a user-specific sequence $c[\ell, k]$ [Vit90, FOO98, KDK00b, KDK00b, Dek00]. Scrambling means that the repeated data stream is symbol-wise multiplied with the user-specific sequence without spectral spreading. Therefore, an 'uncoded' CDMA system with direct-sequence spreading can also be interpreted as a system with a scrambled repetition code of low rate $1/N_s$.

The block *matched filter* in Fig. 4.4.1 may describe the OFDM equalizers discussed in Subsection 4.3.2 (Fig. 4.3.8) or a Rake receiver as depicted in Fig. 4.2.4 excluding the summation over N_s chips after the multiplication with $c[\ell, k]$. The summation itself is common to OFDM-CDMA and SC-CDMA systems and is carried out by the *repetition decoder*. If the repetition is counted among the channel coding part of a communication system, only scrambling remains a CDMA-specific task and the system part between channel encoder and decoder depicted in Fig. 4.4.1 can be regarded as a user-specific time-discrete super channel.

However, repetition codes are known to have very poor error correcting capabilities regarding their very low code rate. Hence, the task is to replace them by more powerful low rate FEC codes that perform good at very low signal to noise ratios. This thesis does not claim to present the best code suited to this problem. In

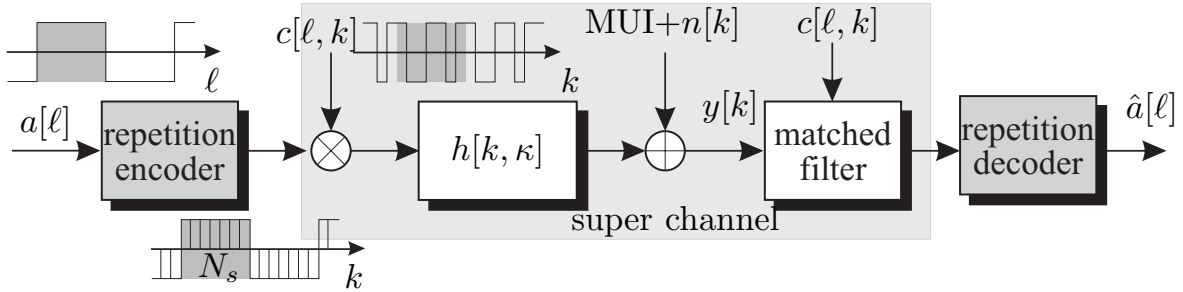


Figure 4.4.1: Illustration of direct-sequence spreading as repetition coding and scrambling

fact, some important aspects concerning the code design are illuminated and the performances of four different coding schemes are compared. Specifically, we look at traditional convolutionally encoded systems where the rates of convolutional and repetition code are exchanged, a code-spread system, and serial as well as parallel code concatenations.

The performance evaluation was carried out for an OFDM-CDMA⁸ uplink with $N_c = 64$ subcarriers and a 4-path Rayleigh fading channel with uniform power delay profile. Successive channel impulse responses are statistically independent, i.e. perfect interleaving in the time domain is assumed. For notational simplicity, we restrict the analysis on BPSK although a generalization to multi-level modulation schemes is straight forward. In the next four subsections, the error rate performance of each coding scheme is analyzed for the single-user case. In Subsection 4.4.5, all schemes are finally compared in multi-user scenarios.

4.4.1 Conventional Coding Scheme (CCS)

The first approach abbreviated CCS does not change the classical direct-sequence spreading and can be interpreted as a concatenation of convolutional code and repetition code. It is illustrated in **Fig. 4.4.2**. The convolutional code is described by its constraint length L_c and the code rate $R_c^{cc} = 1/n$. Subsequent repetition encoding with rate $R_c^{rc} = 1/N_s = n/G_p$ ensures a constant processing gain $G_p = R_c^{-1} = (R_c^{cc} \cdot R_c^{rc})^{-1}$. The influence of different convolutional codes is illuminated by choosing different combinations of R_c^{cc} and R_c^{rc} while their product remains constant. The employed convolutional codes are summarized in Table 4.4.1. They have been found by a nested code search [FOOS98] and represent codes with maximum free distance and minimum number of sequences with weight d_f .

We see from **Fig. 4.4.3** that the performance can be improved by decreasing the code rate. The largest gains are obtained by changing from $R_c^{cc} = 1/2$ to $R_c^{cc} = 1/4$

⁸Similar results can be obtained for SC-CDMA systems. The differences only concern the path crosstalk of the Rake receiver and the E_b/N_0 -loss due to the cyclic prefix for OFDM-CDMA.

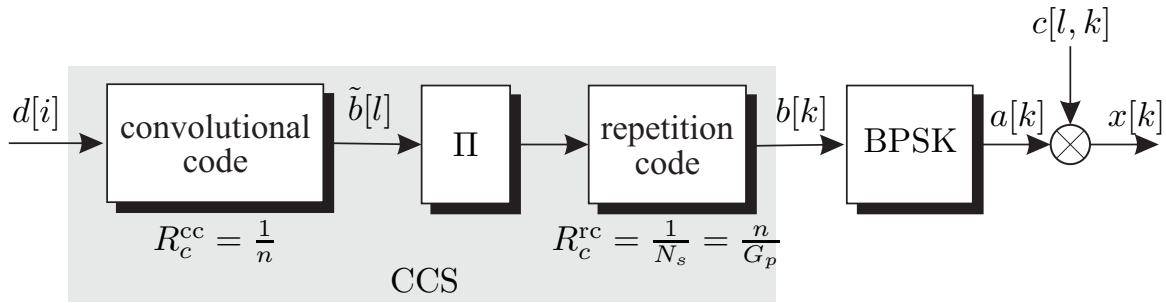


Figure 4.4.2: Conventional coding scheme (CCS) consisting of outer convolutional code, interleaver and inner repetition code

Table 4.4.1: Parameters of coding schemes for OFDM-CDMA system with processing gain $G_p = R_c^{-1} = 64$

	L_c	R_c^{cc}	generators	R_c^{rc}	d_f
CCS 2	7	1/2	133 ₈ , 171 ₈	1/32	10
CCS 4	7	1/4	117 ₈ , 127 ₈ , 155 ₈ , 171 ₈	1/16	20
CCS 8	7	1/8	117 ₈ , 127 ₈ , 155 ₈ , 171 ₈ 135 ₈ , 173 ₈ , 135 ₈ , 145 ₈	1/8	40
CSS	7	1/64	[FOOS98]	1	320

while a further reduction of R_c leads only to minor improvements. The reason is that convolutional codes of very low rate incorporate as well a repetition of parity bits. The contribution of repeated bits becomes larger for decreasing constraint lengths and code rates. Therefore, no large gains can be expected for extremely low rate convolutional codes. This is confirmed by the free distances summarized in Table 4.4.1 that grow in the same way as R_c is reduced.

4.4.2 Code-Spread Scheme (CSS)

Reducing R_c^{cc} to the minimum value of $R_c = 1/G_p$ results in a single very low rate convolutional code and the repetition code is discarded. The corresponding structure of the transmitter is depicted in Fig. 4.4.4. The convolutional encoder already performs the entire spreading so that the coded sequence is directly scrambled with the user-specific sequence. Many ideas of the so-called code-spreading are encapsulated in [Vit90]. In [FOOS98] an enormous number of low rate convolutional codes found by computer search are listed. These codes have a maximum free distance d_f and a minimum number of sequences with weight d_f .

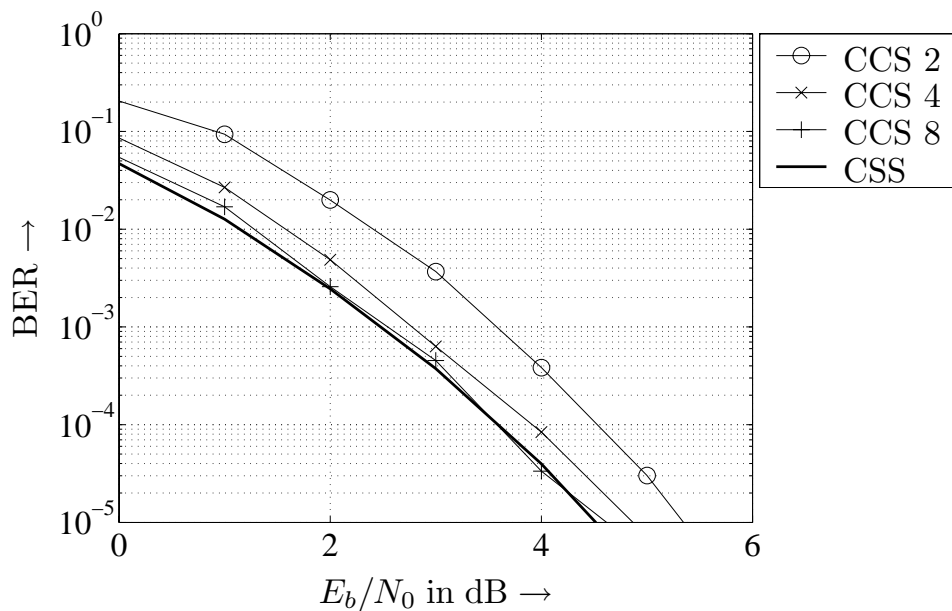


Figure 4.4.3: Performance of single-user OFDM-CDMA system with $N_c = 64$ subcarriers, 4-path Rayleigh fading and different convolutional codes from Table 4.4.1

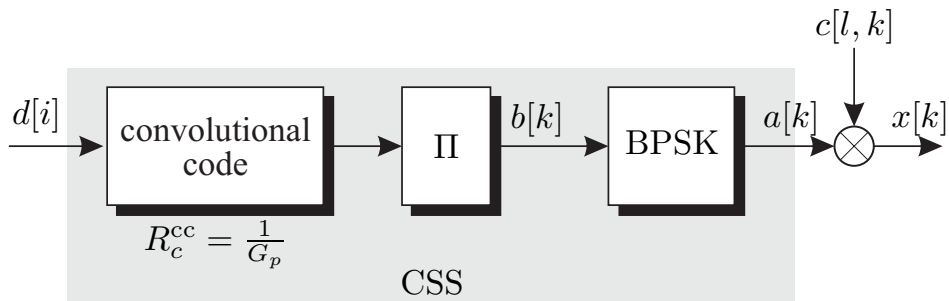


Figure 4.4.4: Code-Spread Scheme (CSS) consisting of single low-rate convolutional code

However, the obtained codes also include a kind of unequal repetition code, i.e. different bits of a code word are repeated unequally [FOOS98]. Therefore, the performance of CSS is comparable to that of CCS's as results in Fig. 4.4.3 show.

4.4.3 Serially Concatenated Coding Scheme (SCCS)

Instead of reducing the code rate of the convolutional code, we know from Section 3.6 that parallel and serial concatenations of very simple component codes lead to extremely powerful codes. Hence, the inner repetition code should be at least partly replaced by a stronger code. Concerning the serial concatenation, we know from Section 3.6 that the inner code should be a recursive convolutional code in order to exploit the benefits of large interleavers [BMDP96].

In the sequel, we consider two different concatenated coding schemes: a serial concatenation of two convolutional codes (SCCC) and a serial concatenation of an outer convolutional code and an inner Walsh code (SCCW). The latter scheme is used in the uplink of IS95 [GJP⁺91, SG91] where Walsh codes are employed as an orthogonal modulation scheme allowing a simple noncoherent demodulation. Although Walsh codes are no recursive convolutional codes, they offer the advantage of a small code rate (large spreading) and low computational decoding costs even for soft-output decoding (see Fast Hadamard Transform in Subsection 3.4.5).

Fig. 4.4.5 shows the structure of the serially concatenated coding scheme. The outer convolutional encoder is followed by an interleaver and the inner code that can be chosen as described above. The final repetition code may be necessary to ensure a constant processing gain. Since we are not interested in interleaver design for concatenated codes, we simply use random interleavers as described in Chapter 3 and vary only the length L_π .

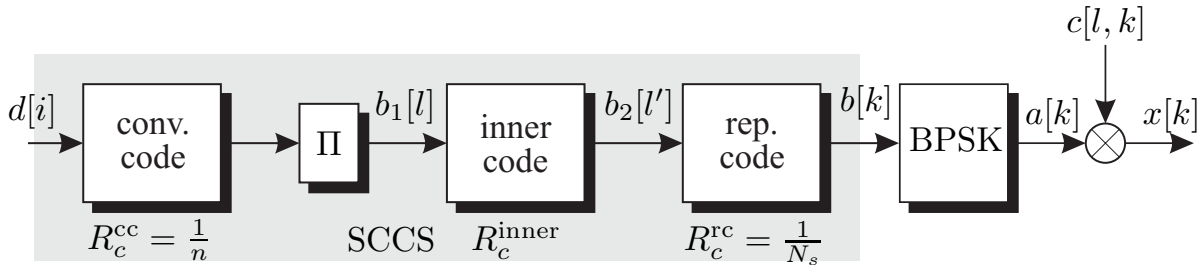


Figure 4.4.5: Structure of serially concatenated coding scheme (SCCS)

The corresponding decoder structure is shown in **Fig. 4.4.6**. First, the received signal is equalized in the frequency domain according to the MRC principle including the descrambling⁹. Next, an integrate-and-dump filter decodes the repetition code and delivers the LLR's $L(\hat{b}_2[l'])$. Now, the iterative decoding process starts with the inner soft-in soft-out decoder. The extrinsic part $L_e(\hat{b}_1[l])$ of its output is deinterleaved and fed to the outer soft-output convolutional decoder. Again, extrinsic information is extracted and fed back as a priori information $L_a(\hat{b}_1[l])$ to the inner decoder. This iterative turbo processing is carried out several times until convergence is obtained (compare Section 3.6).

Due to the high number of parameters, we fix the code rate of the outer convolutional code to $R_c^{cc} = 1/2$. Hence, introducing the inner code affects only the repetition code whose code rate R_c^{rc} increases in the same way as R_c^{inner} decreases (s. Table 4.4.2). Although theoretical analysis tells us that the minimum distance of the outer code should be as large as possible (see page 140), the iterative decoding process benefits from a stronger inner code. This is confirmed by simulation

⁹In single-carrier CDMA, this corresponds to the Rake receiver of Fig. 4.2.4 excluding the summation over N_s chips after the multiplication with $c[\ell, k]$.

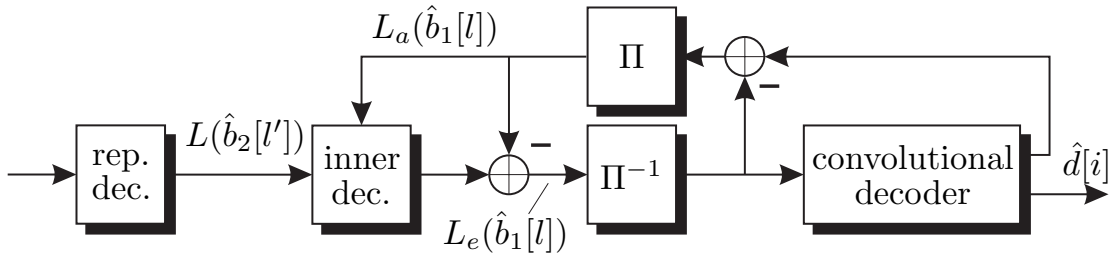


Figure 4.4.6: Decoder structure of serially concatenated coding scheme (SCCS)

results showing that lower rates of the outer convolutional code, e.g. $R_c^{cc} = 1/6$, coming along with higher rates of the inner codes, e.g. $R_c^{rc} = 1$, lead to a significant performance loss. The interleaver Π between the outer convolutional and the inner encoder is a randomly chosen interleaver of length $N = 600$ or $N = 6000^{10}$.

Table 4.4.2: Main parameters of serially concatenated coding schemes (feedback polynomial of recursive convolutional encoders indicated by superscript r)

	outer NSC code, $R_c^{cc} = 1/2$	inner code	rep. code
SCCW 1	$g_1 = 7_8, g_2 = 5_8$	Walsh, $R_c^{wh} = 4/16$	$R_c^{rc} = 1/8$
SCCW 2	$g_1 = 7_8, g_2 = 5_8$	Walsh, $R_c^{wh} = 6/64$	$R_c^{rc} = 1/3$
SCCW 3	$g_1 = 7_8, g_2 = 5_8$	Walsh, $R_c^{wh} = 8/256$	-
SCCW 4	$g_1 = 23_8, g_2 = 55_8$	Walsh, $R_c^{wh} = 6/64$	$R_c^{rc} = 1/3$
SCCW 5	$g_1 = 133_8, g_2 = 171_8$	Walsh, $R_c^{wh} = 6/64$	$R_c^{rc} = 1/3$
SCCC 1	$g_1 = 7_8, g_2 = 5_8$	$g_1 = 7_8, g_2^r = 5_8$	$R_c^{rc} = 1/16$
SCCC 2	$g_1 = 7_8, g_2 = 5_8$	$g_1 = 23_8, g_2 = 27_8$ $g_3^r = 35_8, g_4 = 37_8$	$R_c^{rc} = 1/8$

Fig. 4.4.7 shows the error rate performance of the concatenation of an outer half-rate convolutional code with $L_c = 3$ and different inner Walsh codes (SCCW) and interleaver lengths L_π . We observe that the weakest (shortest) Walsh codes (SCCW 1) perform better for low SNR, i.e. the iterative process converges earlier. For medium SNR, the SCCW 2 system with $M = 64$ represents the best choice and for high SNR, the code with $M = 256$ (SCCW 3) shows the best asymptotical performance. Moreover, increasing the interleaver length from $L_\pi = 600$ to $L_\pi = 6000$ leads to improvements of 0.5 dB for SCCW1, 0.7 dB for SCCW2 and 1 dB for SCCW3. Compared to a single convolutional code with $L_c = 7$,

¹⁰The shorter interleaver may be suited for full duplex speech transmission, while the longer one is restricted to data transmission with weaker delay constraints.

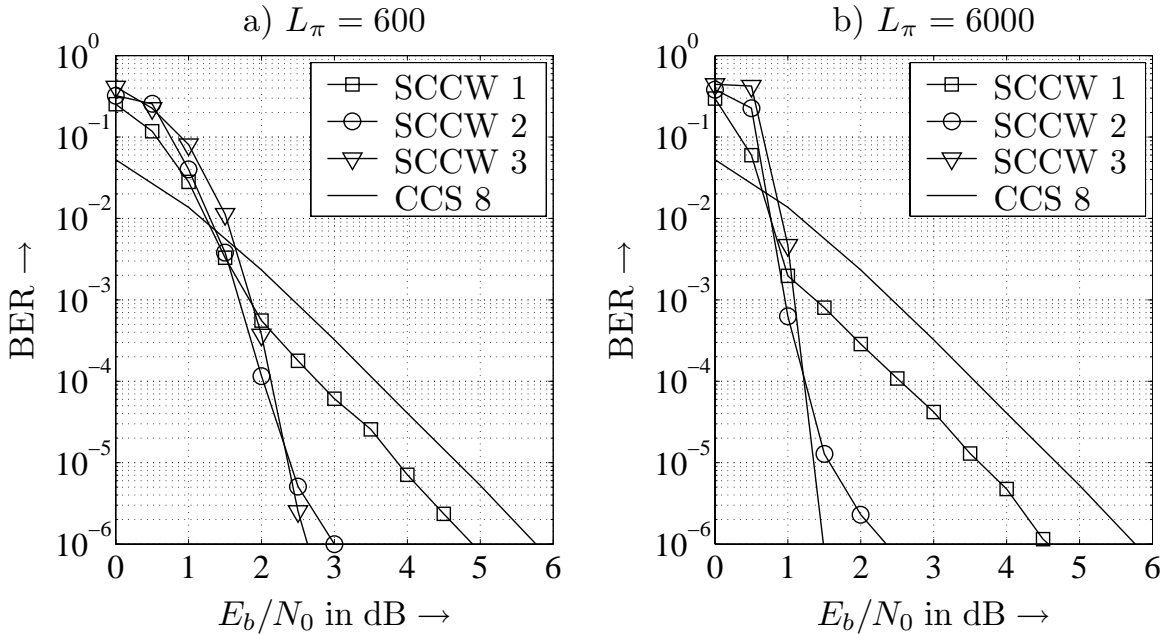


Figure 4.4.7: Performance of SCCW systems with $L_c = 3$ convolutional code for different Walsh codes and interleaver lengths, 10 decoding iterations

the SCCW's perform better for medium and high SNR, but not for extremely low SNR. However, the low SNR regime is exactly the working point for high MUI. This region will be of special interest in Chapter 5 when we consider multi-user detection techniques that include channel coding.

We now choose the $M = 64$ Walsh code as the inner code and vary the constraint length of the outer convolutional code. Obviously, the SCCW 2 system with $L_c = 3$ performs best over a wide range of bit error rates as can be seen from **Fig. 4.4.8a**. Only asymptotically, SCCW 4 and SCCW 5 can benefit from their stronger outer convolutional codes. A comparison of Figs. 4.4.8a and 4.4.8b illustrates that the larger the interleaver, the steeper is the slope of the curves in the waterfall region and the clearer becomes the asymptotic advantage. Since the decoding complexity is much lower for SCCW 2, this scheme represents our favorite among the tested concatenations.

Next, we compare the SCCW 2 scheme with two serially concatenated convolutional codes also listed in Table 4.4.2. The inner code is now a recursive systematic convolutional code. From **Fig. 4.4.9a** we recognize that SCCW 2 performs better down to error rates of 10^{-6} . A stronger inner convolutional code in SCCC 2 cannot increase the performance of the iterative decoding process. Naturally, the code rate of SCCW 2 is much lower than for the SCCC approaches, but since we spread the signals anyway by a fixed processing gain, this is no disadvantage. Hence, low rate coding in CDMA systems can be efficiently accomplished by serially concatenating an outer convolutional code with an inner Walsh code. For very low SNR, the single convolutional code CCS 8 still shows the best performance.

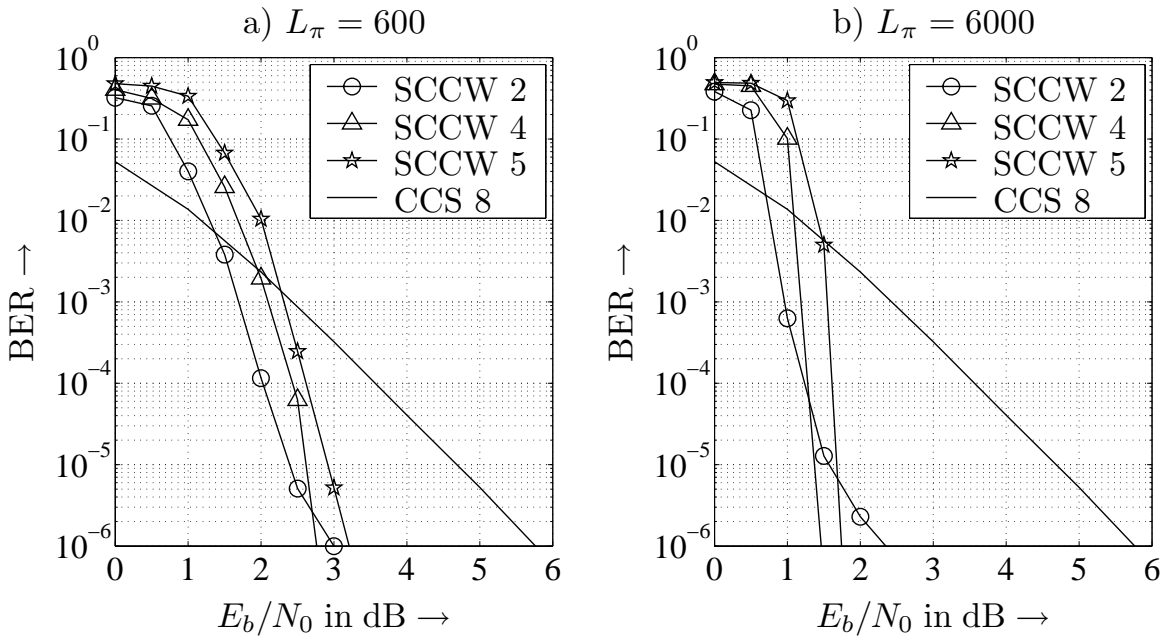


Figure 4.4.8: Performance of SCCW system with $M = 64$ Walsh code for different convolutional codes and interleaver lengths, 10 decoding iterations

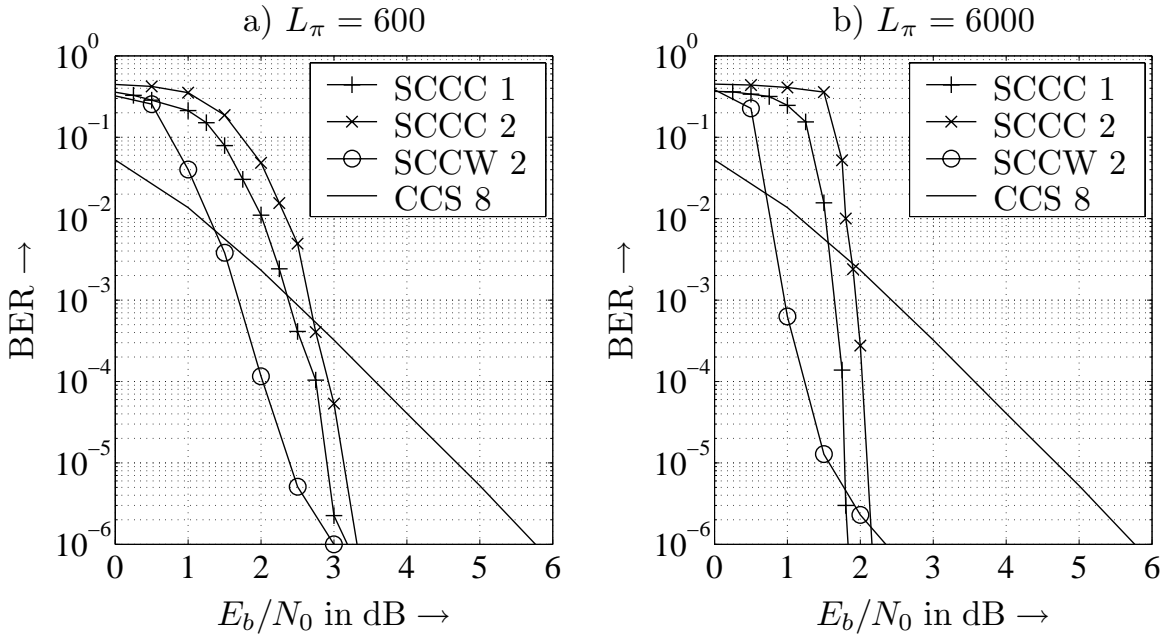


Figure 4.4.9: Performance of SCCC system with different convolutional codes and interleaver lengths, 10 decoding iterations

4.4.4 Parallel Concatenated Coding Scheme (PCCS)

Extremely low rate codes for spread spectrum applications were introduced in [Vit95]. The key idea behind these super-orthogonal codes is to incorporate low rate Walsh codes into the structure of a convolutional encoder. **Fig. 4.4.1** shows

an example using an RSC code with constraint length $L_c = 5$. The inner $L_c - 2 = 3$ register elements are fed to the Walsh encoder of rate $R_c^{\text{wh}} = (L_c - 2)/2^{L_c - 2} = 3/8$. The bits $a[i]$ and $a[i - L_c - 1]$ are added element-wise to the Walsh coded bits $b^{\text{wh}}[l]$. This ensures that not only the original Walsh codewords, but also their binary complements are valid codewords and branches in the trellis leaving the same state are assigned to antipodal codewords. The entire code rate depends on the constraint length of the convolutional code and amounts to

$$R_c^{\text{so}} = \frac{1}{2^{L_c - 2}} = \frac{1}{8} \quad (4.4.1)$$

because each information bit at the encoder input corresponds to $n = 2^{L_c - 2}$ output bits. Naturally, super-orthogonal codes can also be used as constituent codes in a concatenated coding scheme [vWL98]. In fact, we are looking at a parallel concatenated coding scheme (PCCS) according to Fig. 3.6.2 using two super-orthogonal codes as depicted in Fig. 4.4.10. For each information bit, two codewords each of length $n = 8$ are generated yielding a total code rate of the concatenated scheme of $R_c^{\text{PCCS}} = 1/16$. Hence, a repetition code with rate $R_c^{\text{rc}} = 1/4$ is necessary to obtain a desired processing gain of $G_p = 64$.

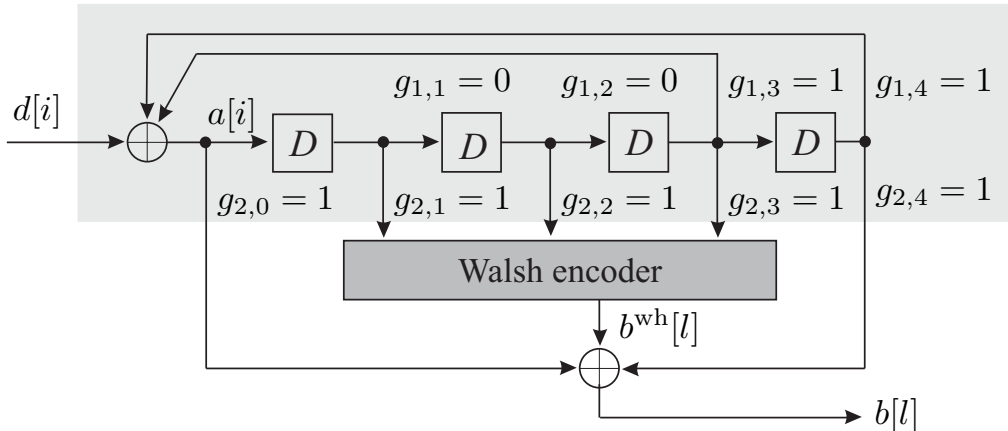


Figure 4.4.10: Encoder structure of super-orthogonal convolutional codes with $L_c = 5$ [Vit95]

At the receiver, appropriate turbo decoding has to be performed. The well-known BCJR algorithm described in Section 3.4.4 has to be extended for super-orthogonal codes. Essentially, we need an incremental metric for each branch in the trellis comparing the hypothesis with the received codeword $\mathbf{y}[i]$. This metric can be obtained by performing a fast Hadamard transform of $\mathbf{y}[i]$ delivering after appropriate scaling a log-likelihood value for each possible Walsh codeword. These LLR's are now used as incremental metrics in the BCJR algorithm.

The results obtained for the above described super-orthogonal code and different interleaver sizes are shown in **Fig. 4.4.11** for a perfectly interleaved 4-path

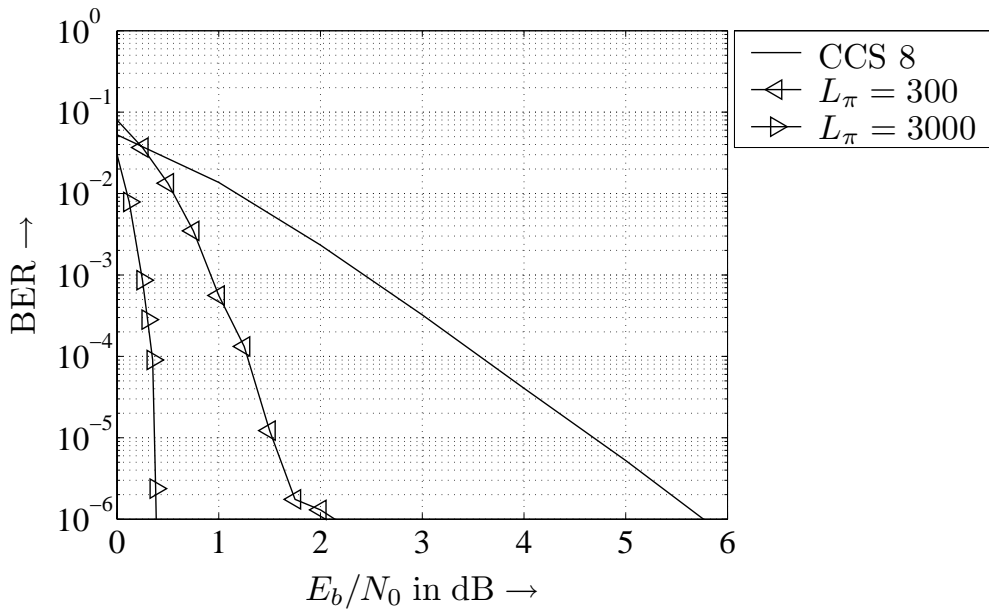


Figure 4.4.11: Performance of parallel concatenated super-orthogonal codes for $N_U = 1$, $G_p = 64$ and different interleaver lengths, 10 decoding iterations

Rayleigh fading channel, a processing gain of $G_p = 64$ and BPSK modulation. Note that frame lengths of 600 bits and 6000 bits for interleaver sizes $L_\pi = 300$ and $L_\pi = 3000$, respectively, are the same as for the SCCS systems because only information bits are permuted in a parallel concatenation. Obviously, PCCS outperforms the conventional convolutional code with rate $R_c^{cc} = 1/8$. At a bit error rate of 10^{-3} , the gains amount to 1.5 dB and 2.2 dB while they increase up to 3.5 dB and more than 5 dB for 10^{-6} . Compared to the serial code concatenations depicted in Fig. 4.4.9, the performance can be improved by approximately 1 dB for the smaller interleaver and by more than 1.5 dB for the larger interleaver at 10^{-6} .

4.4.5 Influence of MUI on Coding Schemes

Finally, we have to analyze the behavior of the coding schemes under the influence of severe multi-user interference. Regardless of the specific coding scheme, it has to be recalled that the processing gain G_p defined in (4.2.2) comprises the spreading factor N_s as well as the code rate R_c , i.e. $G_p = N_s/R_c$ describes the entire spreading including the FEC code. Since we exchange the contribution of channel coding and spreading while keeping G_p constant, the system load $\beta = N_U/N_s$ defined in (4.2.14) varies although N_U and the entire bandwidth are kept constant. For some of the mentioned coding schemes, spreading and coding even cannot be distinguished anymore. Therefore, we will base a comparison on the spectral efficiency defined in (4.2.15) instead of the system load.

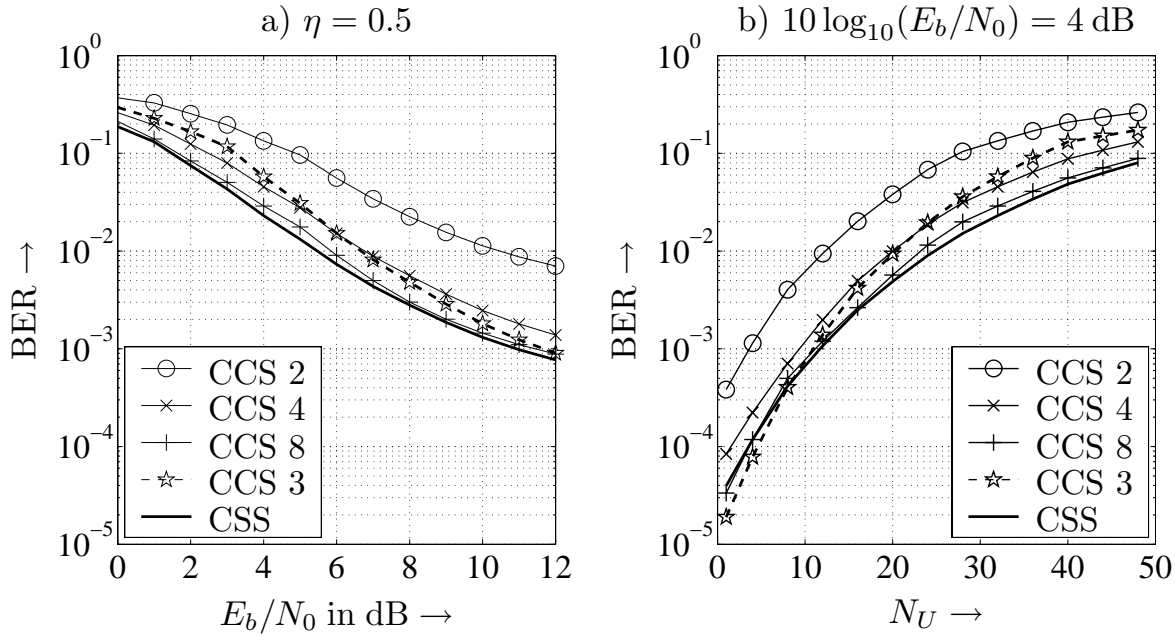


Figure 4.4.12: Performance of OFDM-CDMA system with $N_c = 64$ subcarriers, 4-path Rayleigh fading and different convolutional codes from Table 4.4.1

Fig. 4.4.12a compares the same coding schemes as Fig. 4.4.3, but now for a spectral efficiency of $\eta = N_U/G_p = 32/64 = 1/2$ instead of the single-user case. Note that half rate coded TDMA or FDMA systems as employed in GSM [MP92] can reach at most $\eta = 1/2$ if all time and frequency slots are occupied. Since they represent narrow-band systems without spectral spreading, low rate coding cannot be applied. The ranking of the coding schemes is qualitatively the same. We recognize that a bit error rate of 10^{-3} can only be achieved for the low rate convolutional codes with $R_c^{cc} \leq 1/4$. The half rate code cannot reach this error rate. Lower error probabilities as required for data services cannot be supported for $\eta = 1/2$.

Fig. 4.4.12b illustrates the performances for $10 \log_{10}(E_b/N_0) = 4$ dB versus the number of active users. For this SNR and error rates below 10^{-3} , the convolutional code of rate $R_c^{cc} = 1/2$ can only support four users, while the codes with lower rates support up to 11 users. This corresponds to spectral efficiencies of $\eta = 6.25 \cdot 10^{-2}$ and $\eta = 0.172$, respectively. For higher efficiencies, larger SNRs are required to meet this error rate constraint.

Convolutional codes with higher constraint length as used in UMTS [HT02] can slightly improve the performance. In the UMTS uplink, a code with $L_c = 9$ and rate $R_c^{cc} = 1/3$ is employed. Its performance is also depicted in Fig. 4.4.12 with label 'CCS 3'. Obviously, it performs better for low efficiencies, or, equivalently, at high signal to noise ratios. For $N_U > 10$, it performs worse than CCS8 and CSS, and for $N_U > 24$, even CCS4 is better. Concluding, none of the coding schemes described so far is able to reach a target error rate of 10^{-3} for low SINRs.

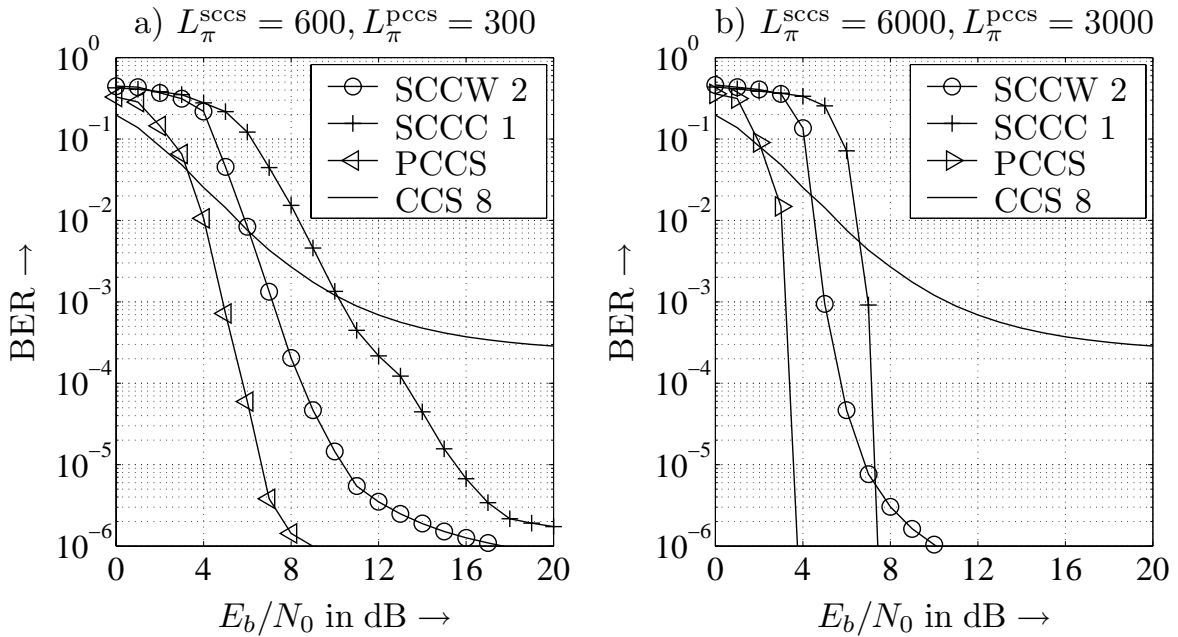


Figure 4.4.13: Performance of concatenated coding schemes for different interleaver lengths, $N_U = 32$ active users, $G_p = 64$ and 10 decoding iterations

Next, we look at the introduced concatenated coding schemes. A comparison with CCS 8 in **Fig. 4.4.13a** shows that all depicted schemes can reach a bit error rate of 10^{-3} while much lower error rates can only be ensured by concatenated schemes. SCCC 1 shows the same performance as the conventional convolutional code, the Walsh coded system SCCW 2 gains about 3 dB compared to them. Parallel concatenated super-orthogonal codes gain additionally 2 dB. At 10^{-5} , the differences become even larger, i.e. SCCW 2 outperforms SCCC1 by 5 dB and PCCS gains 4 dB compared to SCCW 2. All schemes show an error floor starting roughly at 10^{-6} .

For the larger interleaver, **Fig. 4.4.13b** illustrates that all concatenated schemes perform better, especially their error floors move out of the visible area. The parallel concatenated super-orthogonal codes still show the best performance and gain approximately 4 dB compared to the SCCS. For signal to noise ratios larger than 8 dB, SCCC 1 performs better than SCCW 2 while the latter is superior between 4 and 8 dB. Below 2 dB, the conventional convolutional code represents the best choice.

A different visualization in **Fig. 4.4.14** depicts the error rate performance versus the number of active users N_U for a signal to noise ratio of 3 dB. The dramatic performance degradation due to multi-user interference becomes obvious. For this E_b/N_0 value, $L_\pi = 600$ and a target bit error rate of 10^{-3} , the conventional convolutional code and the SCCC 1 scheme can support only up to 6 users while SCCW 2 and PCCS support up to 12 and 20 users, respectively. For the larger interleaver, the Walsh coded system reaches 20 users, SCCC 1 only 13 and PCCS 30 user. For higher SNRs, the relations change and SCCC 1 outperforms SCCW 2.

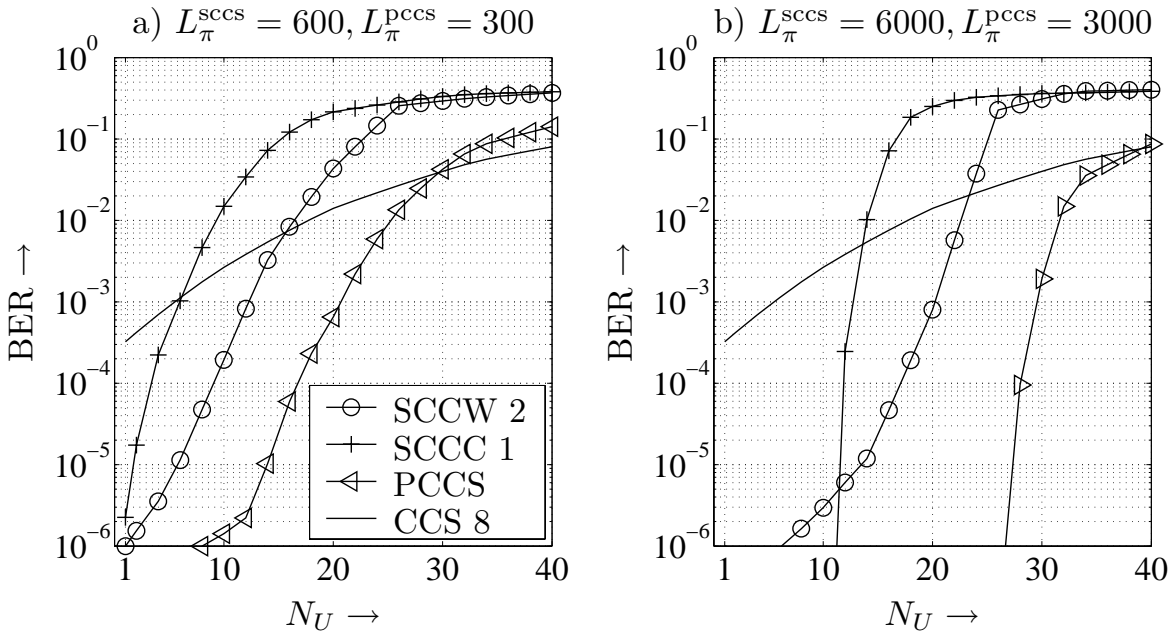


Figure 4.4.14: Performance of concatenated coding schemes for different interleaver lengths, $E_b/N_0 = 3$ dB, $G_p = 64$ and 10 decoding iterations

Due to the waterfall region of concatenated coding schemes, the performance degrades very rapidly with increasing system load while the degradation is rather smooth for the convolutional code. Hence, there exist an area of very low SNR or very high load where conventional convolutional codes outperform concatenated schemes. Although these areas correspond to high error rates that will generally not satisfy certain QoS constraints, they represent the starting point of iterative interference cancellation approaches discussed in Chapter 5. Therefore, we may expect that iterative interference cancellation incorporating FEC decoders converge earlier for convolutional codes than for concatenated codes.

4.5 Uplink Capacity of CDMA Systems

The last section showed that strong error control coding can provide good performance even for highly loaded systems. However, we do not know yet if the sole employment of good codes is the best choice for communications in interference limited environments. Hence, the capacity of CDMA systems assuming a perfect detector at the receiver has to be analyzed in order to determine the maximum achievable spectral efficiency. For the sake of simplicity, we consider the uplink of a synchronous OFDM-CDMA system with real Gaussian inputs and binary spreading codes. Results are presented for an AWGN channel and a 4-paths Rayleigh fading channel with uniform power distribution.

Looking at a single cell environment, the l -th received symbol consists of N_s chips and can be described by

$$\mathbf{y}[l] = \mathbf{S}[l] \cdot \mathbf{a}[l] + \mathbf{n}[l]$$

with $\mathbf{S}[l] = [\mathbf{s}_1[l] \quad \dots \quad \mathbf{s}_{N_U}[l]]$ containing the signatures $\mathbf{s}_u[l]$, $1 \leq u \leq N_U$, of all users in its columns. The capacity $C(\mathbf{S})$ depends on the system matrix \mathbf{S} and the user-specific signal to noise ratios. It represents the total number of information bits that can be reliably transmitted per N_s chips and has to be shared among the active users in this cell. The ergodic capacity is obtained by calculating the expectation $\bar{C} = E\{C(\mathbf{S})\}$. Assuming a totally symmetric situation where all users have identical conditions, the average capacity per user is obtained by

$$C_u = \frac{E\{C(\mathbf{S})\}}{N_U} = \frac{\bar{C}}{N_U}. \quad (4.5.1)$$

The division of \bar{C} by the spreading factor N_s delivers the spectral efficiency

$$\eta = \frac{\bar{C}}{N_s} = \beta \cdot C_u \quad (4.5.2)$$

already defined in (4.2.15). It describes the average number of information bits transmitted per chip and is measured in bits/chip. The relation between both definitions is that (4.5.2) assumes a perfect coding scheme ensuring an error free transmission while (4.2.15) considers a practical code and is always related to a certain target error rate. The definitions can be transferred into one another by replacing C_u with the code rate R_c or, equivalently, \bar{C} with $R_c N_U$. For small β , only few users are active and the spectral efficiency of the system will be low because the large bandwidth is not efficiently used.

4.5.1 Orthogonal Spreading Codes

We start our analysis with orthogonal spreading codes that can be employed for synchronous transmission in frequency-nonselective environments. Therefore, no multi-user interference disturbs the transmission and the user-specific capacity of an AWGN channel with real Gaussian distributed input equals exactly the expression given in (2.2.25)

$$C_{\text{orth.},u} = \frac{1}{2} \cdot \log_2 \left(1 + 2 \frac{E_s}{N_0} \right).$$

It only depends on the signal to noise ratio. The spectral efficiency

$$\eta_{\text{orth.}} = \beta \cdot C_u = \frac{\beta}{2} \cdot \log_2 \left(1 + 2 \frac{E_s}{N_0} \right) \quad \text{for } 0 \leq \beta \leq 1 \quad (4.5.3)$$

grows linearly up to a load of $\beta = 1$ for fixed SNR. Here, all orthogonal binary spreading codes are occupied. For $\beta > 1$, so-called Welch-bounded sequences have to be employed [RM94] with which η stays at a constant level depending on the actual signal to noise ratio [VS99]. It has to be mentioned that the single-user matched filter is the optimum receiver for orthogonal spreading while random codes require much higher computational costs for optimum detection.

4.5.2 Random Spreading Codes and Optimum Receiver

For random spreading codes, the optimum receiver performs joint maximum likelihood decoding of all users (see Chapter 5). Considering the uplink, the mobile units transmit independently from each other, i.e. there is no cooperation among them. Hence, we have to apply (2.3.9) which becomes for a real-valued transmission

$$C(\mathbf{S}) = \frac{1}{2} \cdot \sum_{\nu=1}^r \log_2 \left(1 + 2\lambda_\nu \cdot \frac{E_s}{N_0} \right) = \frac{1}{2} \cdot \sum_{\nu=1}^r \log_2 \left(1 + 2\lambda_\nu \cdot C(\mathbf{S}) \cdot \frac{E_b}{N_0} \right).$$

The eigenvalues λ_ν belong to the matrix $\mathbf{S}[l] \cdot \mathbf{S}^H[l]$. Similar to Chapter 2, we can calculate ergodic and outage capacities. Analytical expressions for the eigenvalue distribution can only be obtained with a large system analysis where N_s and N_U tend to infinity while their ratio $\beta = N_U/N_s$ is constant. Instead, we calculate the ergodic capacities by choosing an appropriate number of system matrices \mathbf{S} , perform an eigenvalue analysis, calculate the instantaneous capacities according to (2.3.9) and average them. User-specific capacities and spectral efficiencies are obtained by applying (4.5.1) and (4.5.2).

The results in **Fig. 4.5.1a** illustrate the user-specific capacities C_u for an AWGN channel and a spreading factor $N_s = 64$. Normal lines correspond to random binary spreading codes while bold lines represent the optimum capacity for orthogonal spreading. In the latter case, no interference disturbs the transmission and $C_{\text{orth.},u}$ does not depend on the load for $\beta \leq 1$. This leads to an upper bound as can be seen in Fig. 4.5.1a. For $\beta > 1$, $C_{\text{orth.},u}$ also degrades because the overall spectral efficiency η shared among all users remains constant leading to $C_{\text{orth.},u} = \eta/\beta$. Concerning random spreading, C_u is largest for few users because the multiple access interference is low. With growing N_U , the interference becomes stronger and stronger and the capacity for each user degrades.

Fig. 4.5.1b illustrates the overall spectral efficiency versus E_b/N_0 . We recognize that η generally increases with growing β because more users are sharing the same medium. This is illustrated by the fact that C_u is approximately halved from 2.5 bits/s/Hz for $\beta = 3/4$ down to 1.3 bits/s/Hz for $\beta = 2$ at $10 \log_{10}(E_b/N_0) = 10$ dB. Hence, the load grows by a factor $2.67 > 2$ and the entire system efficiency increases by a factor 1.4. While these gains are rather large for small β , they reduce

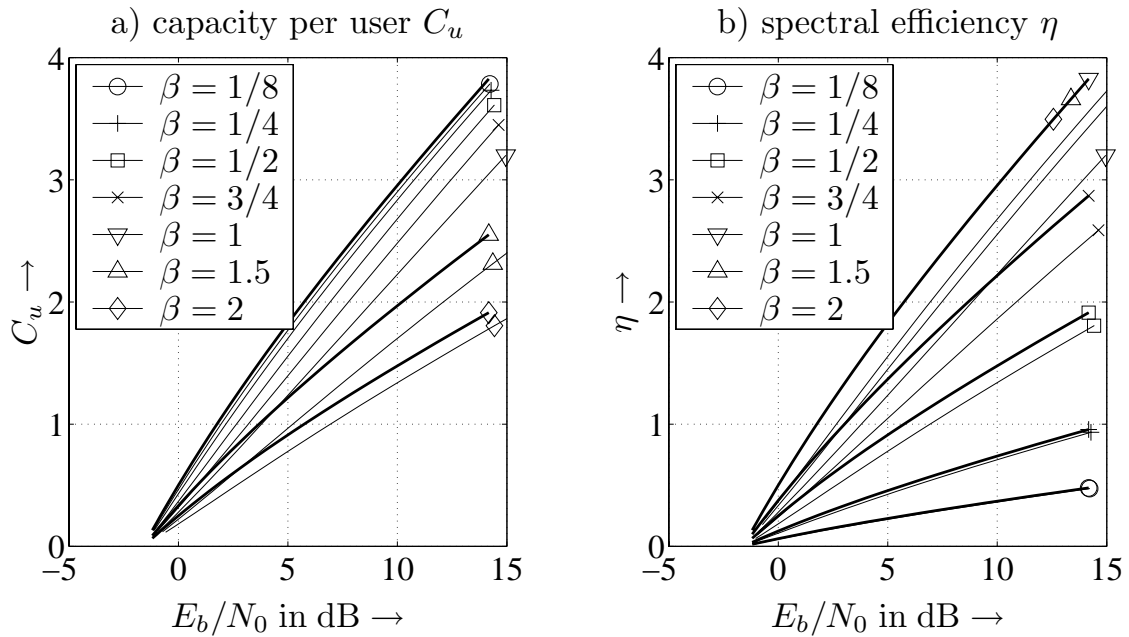


Figure 4.5.1: Ergodic capacity/spectral efficiency of DS-CDMA system with $N_s = 64$ and AWGN channel,
bold lines: orthogonal spreading, normal lines: random spreading

for high loads, e.g. as β approaches two. The efficiencies $\eta_{\text{orth.}}$ for orthogonal codes always represent upper bounds for the random spreading case. As can be seen from Fig. 4.5.1b, $\eta_{\text{orth.}}$ does not grow anymore for $\beta > 1$.

The above described behavior is again depicted in **Fig. 4.5.2** showing C_u and η versus the load β for different signal to noise ratios. While C_u decreases with growing load, the spectral efficiency increases. The curves intersect always for $\beta = 1$ because all users are assumed to have the same SNR so that $C_u = \eta \cdot \beta = \eta$ holds. Comparing Fig. 4.5.2a) with 4.5.2b), we recognize that there is nearly no difference between the AWGN channel and OFDM-CDMA with a 4-path Rayleigh fading channel and uniform power delay profile¹¹.

4.5.3 Random Spreading Codes and Linear Receivers

The results described above hold for optimum signal processing at the receiver or orthogonal spreading codes. However, we explained already that optimal solutions like joint maximum likelihood decoding of all user signals are infeasible in practice. Moreover, the orthogonality is generally destroyed by the influence of the mobile radio channel. Hence, we will discuss in the next chapter suboptimum strategies that perform some kind of preprocessing for separating the users and individual FEC decoding. In this context, we can distinguish linear and non-

¹¹The loss due to the guard interval was neglected.

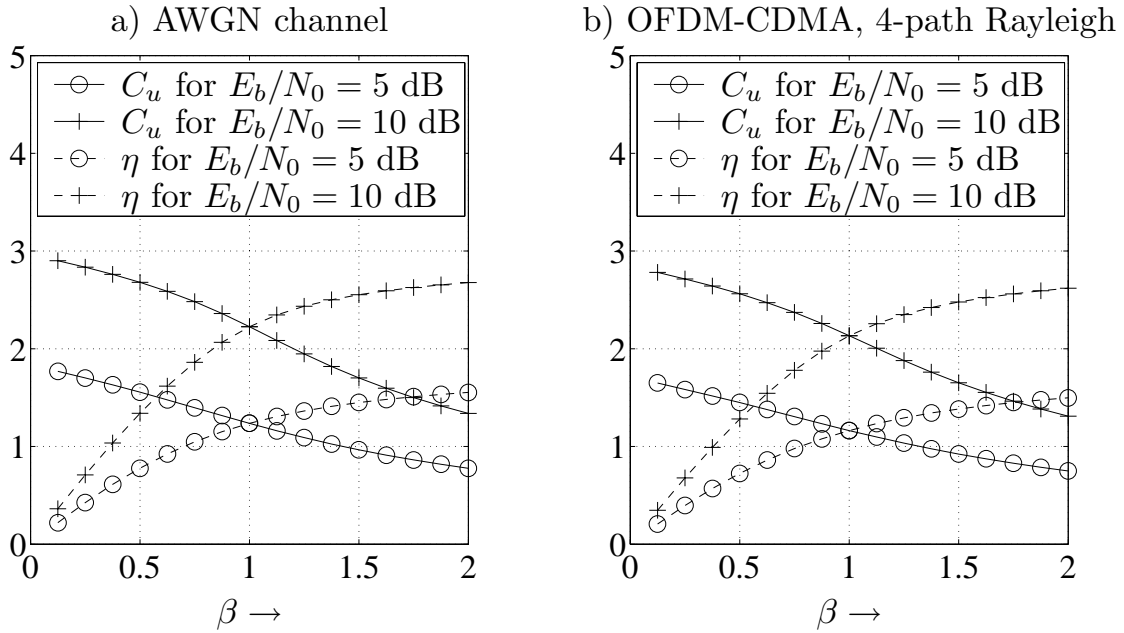


Figure 4.5.2: Ergodic capacity/spectral efficiency of DS-CDMA system with random spreading, $N_s = 64$ and AWGN channel

linear techniques. In order to motivate the next chapter, we consider first the potential of linear preprocessors in terms of spectral efficiency η versus the load β . Specifically, the matched filter as well as zero-forcing (ZF) and MMSE filters with subsequent optimum user specific FEC decoding are analyzed. The following results are extracted from [VS99] where a detailed description of the derivation can be found.

Single-User Matched Filter (SUMF)

We consider again a simple AWGN channel, real-valued Gaussian distributed input signals and random spreading codes for all users. In contrast to orthogonal spreading, the single-user matched filter is not optimum anymore for random spreading codes. In [VS99], it is shown that the user-specific capacity can be expressed by

$$C_{\text{MF},u} = \frac{1}{2} \cdot \log_2 \left(1 + \frac{2E_s/N_0}{1 + 2\beta E_s/N_0} \right). \quad (4.5.4)$$

This result has been obtained by applying a large system analysis where N_U and N_s grow infinitely while their ratio β remains constant. In order to compare different code rates or spreading factors, we have to find an expression depending on E_b/N_0 rather than E_s/N_0 . If each user encodes with a rate $R_c = C_u$, $E_s/N_0 = C_u E_b/N_0$ holds and (4.5.4) becomes an implicit equation

$$C_{\text{MF},u} = \frac{1}{2} \cdot \log_2 \left(1 + \frac{2C_u E_b/N_0}{1 + 2\beta C_u E_b/N_0} \right) = \frac{1}{2} \cdot \log_2(1 + x). \quad (4.5.5)$$

Resolving

$$x = \frac{2C_u E_b / N_0}{1 + 2\beta C_u E_b / N_0} \quad (4.5.6)$$

with respect to N_0/E_b and substituting $C_u = \frac{1}{2} \cdot \log_2(1+x)$ yields

$$\frac{N_0}{E_b} = \log_2(1+x) \cdot \left(\frac{1}{x} - \beta \right) \quad (4.5.7)$$

that has to be numerically solved. The value x can be inserted in (4.5.5) to obtain the $C_{\text{MF},u}$ or the spectral efficiency $\eta_{\text{MF}} = \beta \cdot C_{\text{MF},u}$.

Zero-Forcing Receiver (Decorrelator, ZF)

Although zero-forcing and MMSE filter will be introduced in Sections 5.2.1 and 5.2.2, their principle performance should be analyzed already here. From the large scale analysis ($N_U \rightarrow \infty$, $N_s \rightarrow \infty$, β constant) in [VS99] we obtain

$$C_{\text{ZF},u} = \frac{1}{2} \cdot \log_2 \left(1 + 2(1-\beta) \frac{E_s}{N_0} \right) \quad (4.5.8)$$

and consequently

$$\eta_{\text{ZF}} = \frac{\beta}{2} \cdot \log_2 \left(1 + 2(1-\beta) \frac{E_s}{N_0} \right). \quad (4.5.9)$$

Comparing (4.5.8) with the spectral efficiency for orthogonal codes given in (4.5.3) we observe that the only difference is an SNR loss depending on the load β . Hence, the decorrelator totally removes the interference at the expense of an amplification of the background noise (see Section 5.2.1). This penalty is expressed by the factor $(1-\beta)$ in front of E_s/N_0 .

Minimum Mean Squared Error Filter (MMSE)

Concerning the linear MMSE filter, [VS99] provides the solution

$$C_{\text{MMSE},u} = \frac{1}{2} \cdot \log_2 \left[1 + 2 \frac{E_s}{N_0} - \frac{1}{4} F \left(2 \frac{E_s}{N_0}, \beta \right) \right] \quad (4.5.10)$$

with

$$F(a, b) = \left(\sqrt{a(1+\sqrt{b})^2 + 1} - \sqrt{a(1-\sqrt{b})^2 + 1} \right)^2. \quad (4.5.11)$$

Again, we can apply the substitutions $C = 1/2 \cdot \log_2(1+x)$ and $E_s/N_0 = C_{\text{MMSE},u} \cdot E_b/N_0$ resulting in the implicit equation

$$\begin{aligned} x &= 2C_{\text{MMSE},u} \frac{E_b}{N_0} - \frac{1}{4} F \left(2C_{\text{MMSE},u} \frac{E_b}{N_0}, \beta \right) \\ &= \log_2(1+x) \frac{E_b}{N_0} - \frac{1}{4} F \left(\log_2(1+x) \frac{E_b}{N_0}, \beta \right) \end{aligned} \quad (4.5.12)$$

which has to be solved numerically. The user specific capacity is finally obtained by

$$C_{\text{MMSE},u} = \frac{1}{2} \log_2(1+x) \iff \eta_{\text{MMSE}} = \frac{\beta}{2} \log_2(1+x) \quad (4.5.13)$$

The results for the above analyzed receiver concepts are depicted in **Fig. 4.5.3**. We recognize that the highest efficiency is always obtained for orthogonal spreading codes because no multi-user interference disturbs the transmission and each user experiences a simple AWGN channel. Therefore, the user-specific capacity grows linearly up to a load of $\beta = 1$ for fixed E_b/N_0 . For $\beta > 1$, it stays at a constant level depending on the actual signal to noise ratio.

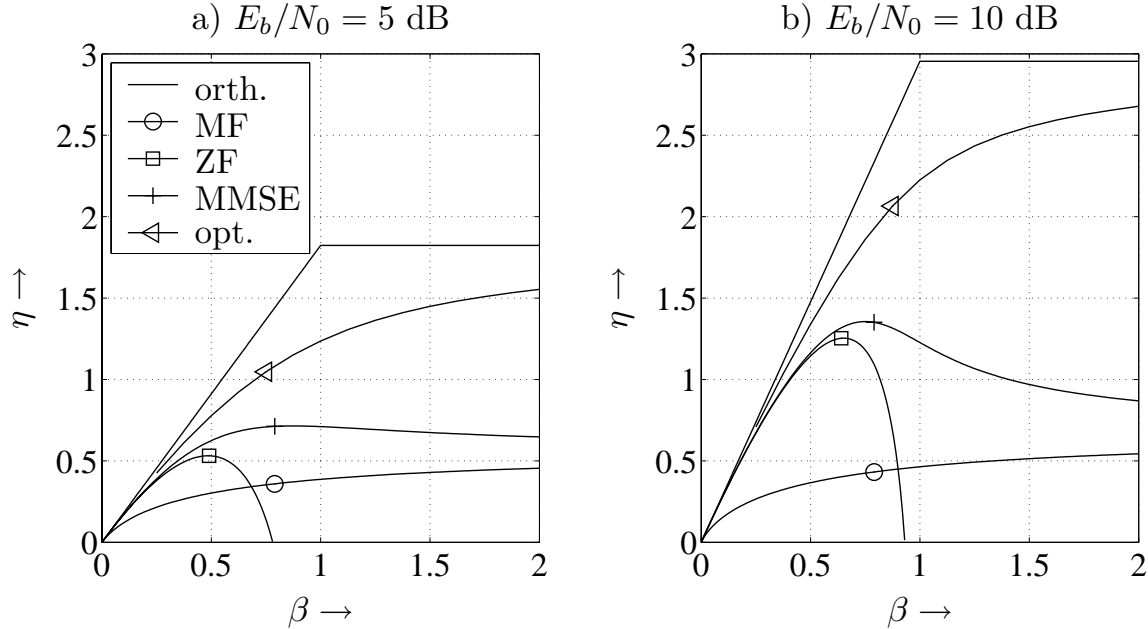


Figure 4.5.3: Ergodic spectral efficiency of DS-CDMA system versus load for $E_b/N_0 = 10$ dB and AWGN channel

For random spreading codes, the spectral efficiency of the optimum receiver performing a joint maximum likelihood decoding of all users was determined as described in Subsection 4.5.2. As expected, it shows the best performance of all multi-user detection techniques. Among the linear receivers, the matched filter

shows only a good performance for very low loads where the background noise dominates the transmission. However, its spectral efficiency increases monotonically with growing β . The decorrelator (ZF) shows near-optimum performance up to a load of approximately $\eta = 0.25$. The load with the highest spectral efficiency depends on the signal to noise ratio because the decorrelator suffers severely from the background noise (compare Figs. 4.5.3a) and b)). For loads above this optimum, its performance degrades dramatically and reaches $\eta_{\text{ZF}} = 0$ below $\beta = 1$. The MMSE receiver overcomes the drawback of amplifying the noise and shows the best performance of all linear schemes.

However, a large gap remains between linear and nonlinear techniques, especially for the matched filter even with optimum channel coding. Therefore, we focus in the next chapter on not only on linear, but also on nonlinear multi-user detection strategies like jointly processing all user signals.

Chapter 5

Multi-User Detection in CDMA Systems

5.1 Optimum Detection

In this chapter, we consider the uplink of a coded DS-CDMA system where a common base station has to detect all incoming signals. This is a major difference to the downlink where the mobile knows generally only its own spreading code and is only interested in its own signal. This requires the application of blind or semiblind multi-user detection techniques [HT00] that are not the focus of this work. A comparison with the detection algorithms for multi-layer space-time transmission [GFWV98, FGVW99, WBR⁺01, BWKK03] presented in Chapter 6 demonstrate the strong equivalence of CDMA systems and multiple antenna systems used for multi-layer transmission.

Regarding the uplink, each user maps an word \mathbf{d}_u consisting of k information bits by appropriate FEC encoding onto a codeword $\mathbf{b}_u = [b_u[0] \cdots b_u[n - 1]]$. After subsequent linear PSK or QAM modulation delivering the sequence \mathbf{a}_u , each symbol $a_u[\ell]$ is spread with a spreading code $\mathbf{c}_u[\ell]$. Since we look at the generally asynchronous uplink, random spreading codes are employed. In short code CDMA systems, $\mathbf{c}_u[\ell]$ is independent of the time index ℓ while it varies from symbol to symbol in long code systems. The obtained sequence \mathbf{x}_u is transmitted over the individual channel with impulse response $\mathbf{h}_u[\ell]$. At the receiver, i.e. a common base station, all transmitted signals are superimposed and additive white Gaussian noise \mathbf{n} is added resulting in

$$\mathbf{y} = \mathbf{H} \cdot \mathbf{x} + \mathbf{n} = \mathbf{S} \cdot \mathbf{a} + \mathbf{n} . \quad (5.1.1)$$

In (5.1.1), $\mathbf{H} = [\mathbf{T}_{\mathbf{h}_1} \cdots \mathbf{T}_{\mathbf{h}_{N_U}}]$ represents a concatenation of several user-specific convolution matrices $\mathbf{T}_{\mathbf{h}_u}$ [Kam96] that cover all time instances of the considered sequence. The vector $\mathbf{x} = [\mathbf{x}_1^T \cdots \mathbf{x}_{N_U}^T]^T$ comprises the spread sequences of all users. According to (4.2.6) on page 171, the convolution of spreading code $\mathbf{c}_u[\ell]$ and channel impulse response $\mathbf{h}_u[\ell]$ can be expressed by the signature $\mathbf{s}_u[\ell]$. This leads to the second part of (5.1.1) where \mathbf{S} comprises the signatures of all users and \mathbf{a} the modulated symbols (compare Section 4.2.2). The vector based notation in (5.1.1) is only of theoretical value because vectors and matrices are generally much too large for implementation issues. Nevertheless, it is well suited for the following analysis.

5.1.1 Optimum Joint Sequence Detection

In the sequel, we assume perfect knowledge of the channel impulse responses and the spreading codes. As already mentioned in Section 1.3, the optimum detector performs a joint maximum a posteriori decoding for all users based on the received sequence \mathbf{y} . Mathematically, this can be expressed by

$$\hat{\mathbf{d}}^{\text{map}} = \underset{\tilde{\mathbf{d}}}{\operatorname{argmax}} \Pr\{\tilde{\mathbf{d}} \mid \mathbf{S}, \mathbf{y}\} = \underset{\tilde{\mathbf{d}}}{\operatorname{argmax}} p_{\underline{\mathcal{Y}}|\tilde{\mathbf{d}}, \mathbf{S}}(\mathbf{y}) \cdot \Pr\{\tilde{\mathbf{d}}\} \quad (5.1.2)$$

where the second equality is obtained by applying Bayes rule and exploiting the fact that $p_{\underline{\mathcal{Y}}|\mathbf{S}}(\mathbf{y})$ is independent from the hypothesis $\tilde{\mathbf{d}}$ and, therefore, does not affect the decision. As already explained in Section 1.3, the hypotheses $\tilde{\mathbf{d}}$ are generally uniformly distributed or the probabilities $\Pr\{\tilde{\mathbf{d}}\}$ are not known a priori. In these cases, $\Pr\{\tilde{\mathbf{d}}\}$ is not available and the joint maximum likelihood detector has to be applied

$$\hat{\mathbf{d}}^{\text{mld}} = \underset{\tilde{\mathbf{d}}}{\operatorname{argmax}} p_{\underline{\mathcal{Y}}|\tilde{\mathbf{d}}, \mathbf{S}}(\mathbf{y}). \quad (5.1.3)$$

The conditional probability density function in (5.1.3) has the form

$$p_{\underline{\mathcal{Y}}|\tilde{\mathbf{d}}, \mathbf{S}}(\mathbf{y}) = \frac{1}{\det(\pi \Phi_{\underline{\mathcal{N}}\underline{\mathcal{N}}})} \cdot \exp\left(-[\mathbf{y} - \mathbf{S} \cdot \mathbf{a}(\tilde{\mathbf{d}})]^H \Phi_{\underline{\mathcal{N}}\underline{\mathcal{N}}}^{-1} [\mathbf{y} - \mathbf{S} \cdot \mathbf{a}(\tilde{\mathbf{d}})]\right) \quad (5.1.4)$$

where $\mathbf{a}(\tilde{\mathbf{d}})$ denotes the modulated sequence associated with the hypothesis $\tilde{\mathbf{d}}$. Inserting (5.1.4) into (5.1.3), neglecting all terms independent of the hypothesis $\tilde{\mathbf{d}}$ and applying the natural logarithm, we obtain with $\Phi_{\underline{\mathcal{N}}\underline{\mathcal{N}}} = \sigma_{\mathcal{N}}^2 \mathbf{I}$

$$\begin{aligned} \hat{\mathbf{d}}^{\text{mld}} &= \underset{\tilde{\mathbf{d}}}{\operatorname{argmax}} \ln \exp\left(-\frac{[\mathbf{y} - \mathbf{S} \cdot \mathbf{a}(\tilde{\mathbf{d}})]^H [\mathbf{y} - \mathbf{S} \cdot \mathbf{a}(\tilde{\mathbf{d}})]}{\sigma_{\mathcal{N}}^2}\right) \\ &= \underset{\tilde{\mathbf{d}}}{\operatorname{argmin}} \|\mathbf{y} - \mathbf{S} \cdot \mathbf{a}(\tilde{\mathbf{d}})\|^2. \end{aligned} \quad (5.1.5)$$

From (5.1.5) we recognize that the joint maximum likelihood detector searches for that hypothesis $\tilde{\mathbf{d}}$ that minimizes the squared Euclidian distance between the received sequence \mathbf{y} and $\mathbf{S} \cdot \mathbf{a}(\tilde{\mathbf{d}})$. Since \mathbf{d} consists of discrete values, gradient based methods cannot be applied and an exhaustive search is necessary. Obviously, even for medium size systems the required computational complexity is far too high for practical implementations because it grows exponentially with the number of users as well as the lengths of the sequences.

Contrarily to the joint detection, each user can also be individually detected [Ver98]. Individual MAP detection of a certain user u can be expressed by

$$\hat{\mathbf{d}}_u^{\text{map}} = \underset{\tilde{\mathbf{d}}_u}{\operatorname{argmax}} \Pr\{\tilde{\mathbf{d}}_u \mid \mathbf{S}, \mathbf{y}\} = \underset{\tilde{\mathbf{d}}_u}{\operatorname{argmax}} p_{\underline{\mathcal{Y}}|\tilde{\mathbf{d}}_u, \mathbf{S}}(\mathbf{y}) \cdot \Pr\{\tilde{\mathbf{d}}_u\}. \quad (5.1.6)$$

Equivalently to (5.1.3), the individual ML detector is obtained by

$$\hat{\mathbf{d}}_u^{\text{mld}} = \underset{\tilde{\mathbf{d}}_u}{\operatorname{argmax}} p_{\underline{\mathcal{Y}}|\tilde{\mathbf{d}}_u, \mathbf{S}}(\mathbf{y}). \quad (5.1.7)$$

Individual and joint detection do not always lead to the same result as the joint detector described in (5.1.2) what was already illuminated by a simple example on page 23. Before we come to the next subsection, an important difference between joint detection and individual detection has to be emphasized [Ver98].

5.1.2 Optimum Preprocessing and Subsequent Decoding

A first step towards a reduced complexity is to separate FEC decoding and multi-user detection. In order to exploit as much information as possible, a hard decision multi-user detector must be avoided. Instead, the joint preprocessor should deliver log-likelihood ratios $L(\hat{b}_u[\ell] \mid \mathbf{y})$ of the coded bits $b_u[\ell]$ for each user u that can be directly processed by the FEC decoders.

For the sake of notational simplicity, we restrict to synchronous frequency-nonselective environments and in OFDM-CDMA systems assuming a coarse synchronization [Küh03] (compare Section 4.3). In these scenarios, the system matrix \mathbf{S} is block diagonal and can be split into several $N_s \times N_U$ matrices $\mathbf{S}[\ell]$. Hence, symbol-wise preprocessing is optimal and we omit the time variable ℓ . However, the derivation can generally be extended to the asynchronous case. Furthermore, we only consider BPSK modulation so that no soft-output demodulation is required¹. In this case, $b_u \in \{0, 1\}$ and $a_u \in \{+1, -1\}$ can be used equivalently.

The resulting structure is shown in **Fig. 5.1.1**. The transmitters consist of FEC encoders including the BPSK mapping and user-specific interleavers Π_u [BSGS00].

¹In the case of QPSK, a soft-output demodulator demultiplexes inphase and quadrature components into a single data stream. For M -ary modulation schemes with $M > 4$, appropriate soft-output demodulation algorithms have to be employed.

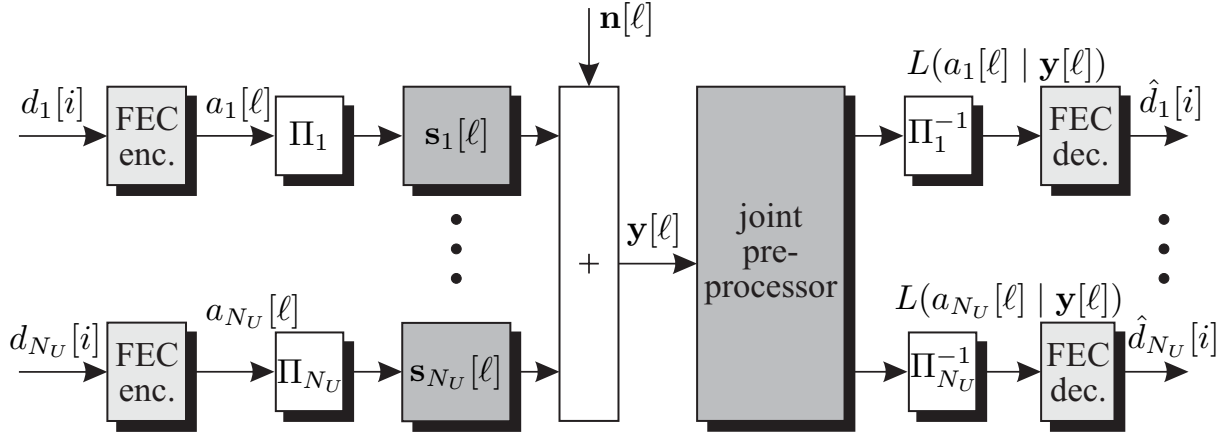


Figure 5.1.1: CDMA system with joint preprocessing and individual FEC decoding

Spreading with the codes $\mathbf{c}_u[\ell]$ and the transmission over the channels $\mathbf{h}_u[\ell]$ are embraced in the blocks denoted with the signature $\mathbf{s}_u[\ell]$. Finally, the received signal $\mathbf{y}[\ell]$ is obtained by summing all transmit signals and the background noise $\mathbf{n}[\ell]$.

At the receiver, the processing for $\mathbf{y} = \mathbf{y}[\ell]$ at time instance ℓ starts with the calculation of the log-likelihood ratios

$$\begin{aligned} L(\hat{a}_u \mid \mathbf{y}) &= \ln \frac{\Pr\{a_u = +1 \mid \mathbf{y}\}}{\Pr\{a_u = -1 \mid \mathbf{y}\}} = \ln \frac{p_{\underline{\mathbf{y}}|a_u=+1}(\mathbf{y}) \cdot \Pr\{a_u = +1\}}{p_{\underline{\mathbf{y}}|a_u=-1}(\mathbf{y}) \cdot \Pr\{a_u = -1\}} \quad (5.1.8) \\ &= L(\mathbf{y} \mid \hat{a}_u) + L_a(a_u). \end{aligned}$$

Extending a_u in nominator and denominator of $L(\mathbf{y} \mid \hat{a}_u)$ to \mathbf{a} and summing over all possible combinations of $a_{\nu \neq u}$ yields with $\Phi_{\underline{\mathcal{N}}\underline{\mathcal{N}}} = \sigma_{\mathcal{N}}^2 \cdot \mathbf{I}_{N_s}$

$$\begin{aligned} L(\hat{a}_u \mid \mathbf{y}) &= \ln \frac{\sum_{\mathbf{a}, a_u=+1} p_{\underline{\mathbf{y}}|\mathbf{a}}(\mathbf{y}) \cdot \Pr\{\mathbf{a}\}}{\sum_{\mathbf{a}, a_u=-1} p_{\underline{\mathbf{y}}|\mathbf{a}}(\mathbf{y}) \cdot \Pr\{\mathbf{a}\}} \\ &= \ln \frac{\sum_{\mathbf{a}, a_u=+1} \exp\left[-\|\mathbf{y} - \mathbf{S} \cdot \mathbf{a}\|^2 / \sigma_{\mathcal{N}}^2\right] \cdot \Pr\{\mathbf{a}\}}{\sum_{\mathbf{a}, a_u=-1} \exp\left[-\|\mathbf{y} - \mathbf{S} \cdot \mathbf{a}\|^2 / \sigma_{\mathcal{N}}^2\right] \cdot \Pr\{\mathbf{a}\}}. \quad (5.1.9) \end{aligned}$$

The probabilities $\Pr\{\mathbf{a}\}$ in (5.1.9) are generally not known a priori so that they are neglected for the moment. However, we will come back to this point when talking about iterative schemes. Performing some manipulations on the squared magnitudes in nominator and denominator and dropping all terms that do not depend on \mathbf{a} results in

$$\begin{aligned} -\|\mathbf{y} - \mathbf{S} \cdot \mathbf{a}\|^2 &\Rightarrow 2 \cdot \operatorname{Re}\{\mathbf{a}^H \cdot \mathbf{S}^H \cdot \mathbf{y}\} - \mathbf{a}^H \cdot \mathbf{S}^H \cdot \mathbf{S} \cdot \mathbf{a} \\ &= 2 \cdot \operatorname{Re}\{\mathbf{a}^H \cdot \mathbf{r}\} - \mathbf{a}^H \cdot \mathbf{R} \cdot \mathbf{a}. \quad (5.1.10) \end{aligned}$$

We recognize that the matched filtered signal $\mathbf{r} = \mathbf{S}^H \cdot \mathbf{y}$ is correlated with the hypothesis \mathbf{a} . In the case of BPSK, \mathbf{a} and $\mathbf{r}' = \text{Re}\{\mathbf{S}^H \cdot \mathbf{y}\}$ are real-valued and (5.1.10) simplifies to

$$-\|\mathbf{y} - \mathbf{S} \cdot \mathbf{a}\|^2 \Rightarrow 2\mathbf{a}^T \mathbf{r}' - \mathbf{a}^T \mathbf{R}' \mathbf{a} \quad (5.1.11)$$

with $\mathbf{R}' = \text{Re}\{\mathbf{R}\}$. The output of the matched filter represents a sufficient statistics, i.e. it contains the same information as the channel output \mathbf{y} , and subsequent post-processing can still provide optimal log-likelihood ratios. We obtain

$$L(\mathbf{r}' | \hat{a}_u) = \ln \frac{\sum_{\mathbf{a}, a_u=+1} \exp([2\mathbf{a}^T \mathbf{r}' - \mathbf{a}^T \mathbf{R}' \mathbf{a}] / (2\sigma_{N'}^2))}{\sum_{\mathbf{a}, a_u=-1} \exp([2\mathbf{a}^T \mathbf{r}' - \mathbf{a}^T \mathbf{R}' \mathbf{a}] / (2\sigma_{N'}^2))}. \quad (5.1.12)$$

Obviously, the computational complexity still depends exponentially on the number of users (and the alphabet size). A modest complexity reduction can be achieved by applying the already known approximation of (3.4.37). This results in

$$\begin{aligned} L(\mathbf{r}' | \hat{a}_u) &\approx \frac{1}{2\sigma_{N'}^2} \cdot \max_{\mathbf{a}, a_u=+1} [2\mathbf{a}^T \mathbf{r}' - \mathbf{a}^T \mathbf{R}' \mathbf{a}] \\ &\quad - \frac{1}{2\sigma_{N'}^2} \cdot \max_{\mathbf{a}, a_u=-1} [2\mathbf{a}^T \mathbf{r}' - \mathbf{a}^T \mathbf{R}' \mathbf{a}]. \end{aligned} \quad (5.1.13)$$

5.1.3 Turbo Detection with Optimum Preprocessing and Decoding

In the next step, individual de-interleaving and FEC decoding is performed. According to the turbo-principle, it is possible to feedback information to the preprocessor so that an iterative process arises [Hag96a, RSAA98, LH02]. If soft-output decoding algorithms like the BCJR algorithm explained in Section 3.4.3 are employed delivering the LLR's $L(\hat{a}_u) = L_a(a_u)$, these LLR's can be used to calculate a priori probabilities

$$\Pr\{a_u\} = \frac{e^{L_a(a_u)/2}}{1 + e^{L_a(a_u)}} \cdot e^{a_u L_a(a_u)/2} \quad (5.1.14)$$

that can be inserted into (5.1.9). Due to individual interleavers, the LLR's $L_a(a_u)$ are assumed to be statistically independent so that

$$\Pr\{\mathbf{a}\} = \prod_{u=1}^{N_U} \frac{e^{L_a(a_u)/2}}{1 + e^{L_a(a_u)}} \cdot e^{a_u L_a(a_u)/2} \quad (5.1.15)$$

holds. Using the results for BPSK from (5.1.11) and inserting (5.1.15) into (5.1.9) results in

$$\begin{aligned} L(\hat{a}_u \mid \mathbf{r}) &= \ln \frac{\sum_{\mathbf{a}, a_u=+1} e^{\left[2\mathbf{a}^T \mathbf{r}' - \mathbf{a}^T \mathbf{R}' \mathbf{a}\right]/(2\sigma_{N'}^2)} \cdot \prod_{\mu=1}^{N_U} \frac{e^{L_a(a_\mu)/2}}{1+e^{L_a(a_\mu)}} e^{a_u L_a(a_u)/2}}{\sum_{\mathbf{a}, a_u=-1} e^{\left[2\mathbf{a}^T \mathbf{r}' - \mathbf{a}^T \mathbf{R}' \mathbf{a}\right]/(2\sigma_{N'}^2)} \cdot \prod_{\mu=1}^{N_U} \frac{e^{L_a(a_\mu)/2}}{1+e^{L_a(a_\mu)}} e^{a_u L_a(a_u)/2}} \\ &= \ln \frac{\sum_{\mathbf{a}, a_u=+1} e^{\left[2\mathbf{a}^T \mathbf{r}' - \mathbf{a}^T \mathbf{R}' \mathbf{a}\right]/(2\sigma_{N'}^2) + \sum_{\mu=1}^{N_U} a_\mu L_a(a_\mu)/2}}{\sum_{\mathbf{a}, a_u=-1} e^{\left[2\mathbf{a}^T \mathbf{r}' - \mathbf{a}^T \mathbf{R}' \mathbf{a}\right]/(2\sigma_{N'}^2) + \sum_{\mu=1}^{N_U} a_\mu L_a(a_\mu)/2}}. \end{aligned} \quad (5.1.16)$$

The terms $e^{L_a(a_u)/2}/(1 + e^{L_a(a_\mu)})$ are independent of the hypotheses \mathbf{a} within the summations and, therefore, identical in nominator and denominator so that they can be neglected. Furthermore, the u -th contribution in the last sums of nominator and denominator is constant due to the restrictions of the outer summations over \mathbf{a} with $a_u = +1$ or $a_u = -1$. Hence, we can extract a common factor from the sums and obtain

$$L(\hat{a}_u \mid \mathbf{r}) = L_a(a_u) + L_e(\hat{a}_u) \quad (5.1.17a)$$

with

$$L_e(\hat{a}_u) = \ln \frac{\sum_{\mathbf{a}, a_u=+1} e^{\left[2\mathbf{a}^T \mathbf{r}' - \mathbf{a}^T \mathbf{R}' \mathbf{a}\right]/(2\sigma_{N'}^2) + \sum_{\substack{\mu=1 \\ \mu \neq u}}^{N_U} a_\mu L_a(a_\mu)/2}}{\sum_{\mathbf{a}, a_u=-1} e^{\left[2\mathbf{a}^T \mathbf{r}' - \mathbf{a}^T \mathbf{R}' \mathbf{a}\right]/(2\sigma_{N'}^2) + \sum_{\substack{\mu=1 \\ \mu \neq u}}^{N_U} a_\mu L_a(a_\mu)/2}}. \quad (5.1.17b)$$

The approximation already known from (5.1.13) becomes

$$\begin{aligned} L(\hat{a}_u \mid \mathbf{r}) &\approx L_a(a_u) + \max_{\mathbf{a}, a_u=+1} \left[\frac{2\mathbf{a}^T \mathbf{r}' - \mathbf{a}^T \mathbf{R}' \mathbf{a}}{2\sigma_{N'}^2} + \frac{1}{2} \sum_{\substack{\mu=1 \\ \mu \neq u}}^{N_U} a_\mu L_a(a_\mu) \right] \\ &\quad - \max_{\mathbf{a}, a_u=-1} \left[\frac{2\mathbf{a}^T \mathbf{r}' - \mathbf{a}^T \mathbf{R}' \mathbf{a}}{2\sigma_{N'}^2} + \frac{1}{2} \sum_{\substack{\mu=1 \\ \mu \neq u}}^{N_U} a_\mu L_a(a_\mu) \right]. \end{aligned} \quad (5.1.18)$$

The receiver structure depicted in **Fig. 5.1.2** illustrates the way how to calculate the solutions presented in (5.1.16) and (5.1.18). In the first iteration, no a priori information is available and only the terms given in (5.1.11) have to be calculated. They remain constant during subsequent iteration steps and are to be determined only once. After having performed the FEC decoding for the first time, the LLR's $L_a(b_u)$ can be used as a priori information according to (5.1.15) in order to improve the estimates $L(\hat{a}_u \mid \mathbf{r})$.

As already mentioned above, the complexity of the joint preprocessor still grows exponentially with the number of users while the decoding part depends linearly

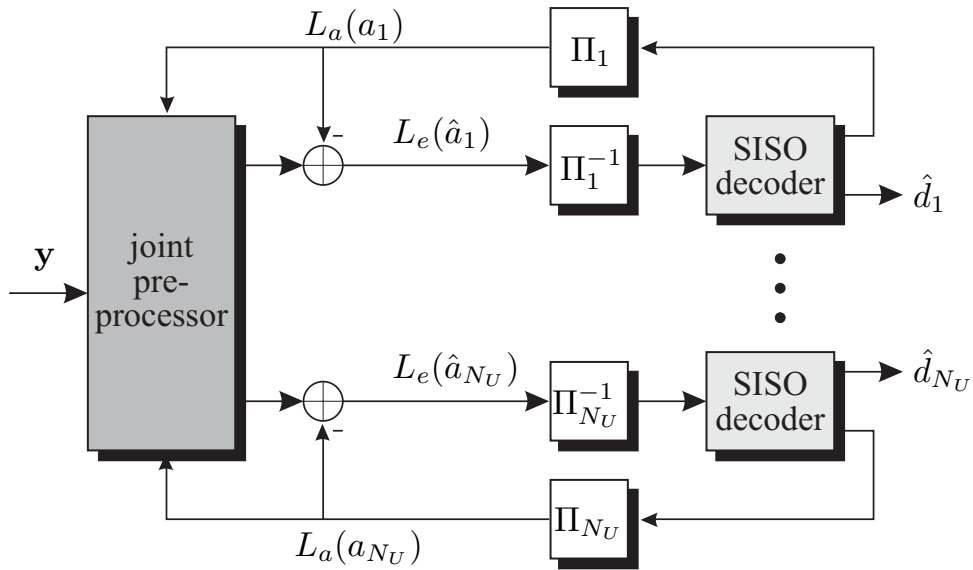


Figure 5.1.2: Turbo receiver for joint preprocessing and individual FEC decoding

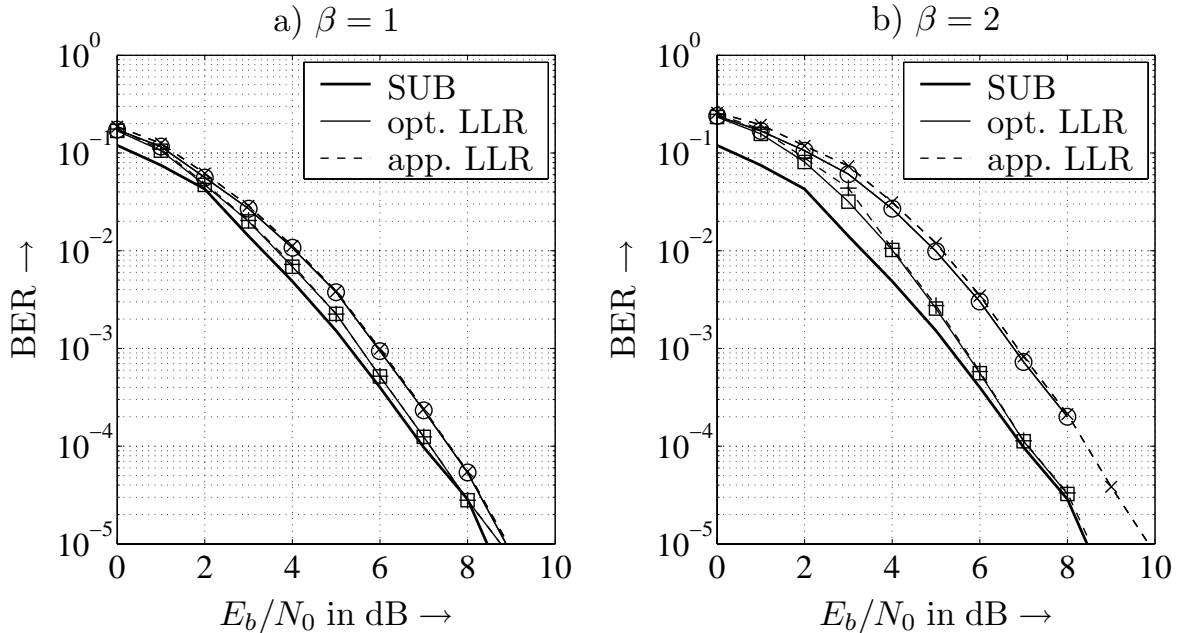


Figure 5.1.3: Performance of optimum multi-user detection with subsequent decoding for the first two iterations (1: \circ , \times and 2: \square , $+$)

on N_U . For a small OFDM-CDMA system with a spreading factor $N_s = 4$, some results are shown in **Fig. 5.1.3**. They have been obtained for a 4-paths Rayleigh fading channel with uniform power delay profile and random spreading codes. A half rate convolutional code with $L_c = 3$ and generators $g_1 = 5_8$, $g_2 = 7_8$ was employed. At the receiver, perfect LLR's from (5.1.16) as well as for the approximation of (5.1.18) have been used.

Obviously, the approximation (\times and $+$) performs nearly as good as the optimum solution. The error rate can be remarkably reduced with the second iteration. Subsequent iterations that are not shown here do not lead to substantial additional improvements because we are already close to the single-user bound. It is reached at a signal to noise ratio of 7 dB for $\beta = 1$ as well as $\beta = 2$. Only for small SNRs, the loss compared to the SUB amounts to 0.2 dB for $\beta = 1$ and 0.5 dB for $\beta = 2$.

5.2 Linear Multi-User Detection

A further reduction of the computational complexity can be achieved by applying only linear joint preprocessing. A common property of all linear techniques is that they do not exploit the knowledge of the finite signal alphabet but assume continuously distributed transmit signals. Therefore, we have only a polynomial complexity with respect to the number of active users instead of an exponential relationship. The following approaches are related to simple linear algebra, i.e. the linear equation system $\mathbf{y} = \mathbf{S}\mathbf{a} + \mathbf{n}$ has to be solved with respect to \mathbf{a} , i.e. we look for a matrix \mathbf{W} with $\hat{\mathbf{a}} = \mathbf{W} \cdot \mathbf{y}$. For simplicity, we first restrict to the uncoded case and the system matrix \mathbf{S} consists of N_U columns and N_s rows.

5.2.1 Decorrelator (Zero Forcing, ZF)

First, we consider the decorrelator being equivalent to the zero-forcing equalizer [Mos96, HT00]. It searches for the symbol vector $\hat{\mathbf{a}}_{\text{ZF}}$ that minimizes the squared Euclidean distance to the received vector \mathbf{y} according to

$$\hat{\mathbf{a}}_{\text{ZF}} = \underset{\tilde{\mathbf{a}} \in \mathbb{C}^{N_U}}{\operatorname{argmin}} \|\mathbf{y} - \mathbf{S}\tilde{\mathbf{a}}\|^2. \quad (5.2.1)$$

The solution $\hat{\mathbf{a}}_{\text{ZF}}$ leads to the best reconstruction of \mathbf{y} when multiplied from the left with \mathbf{S} .² This optimization problem is solved by calculating the derivative of the squared Euclidean distance in (5.2.1) with respect to $\tilde{\mathbf{a}}^H$ and setting it to zero. With the relation $\partial \tilde{\mathbf{a}} / \partial \tilde{\mathbf{a}}^H = \mathbf{0}$ [Fis02], we obtain

$$\begin{aligned} \frac{\partial}{\partial \tilde{\mathbf{a}}^H} (\mathbf{y} - \mathbf{S}\tilde{\mathbf{a}})^H \cdot (\mathbf{y} - \mathbf{S}\tilde{\mathbf{a}}) &= \frac{\partial}{\partial \tilde{\mathbf{a}}^H} (\mathbf{y}^H \mathbf{y} - \mathbf{y}^H \mathbf{S}\tilde{\mathbf{a}} - \tilde{\mathbf{a}}^H \mathbf{S}^H \mathbf{y} + \tilde{\mathbf{a}}^H \mathbf{S}^H \mathbf{S}\tilde{\mathbf{a}}) \\ &= -\mathbf{S}^H \mathbf{y} + \mathbf{S}^H \mathbf{S}\tilde{\mathbf{a}} \stackrel{!}{=} \mathbf{0} \end{aligned} \quad (5.2.2)$$

whose solution is obviously [Ver98]

$$\hat{\mathbf{a}}_{\text{ZF}} = \mathbf{W}_{\text{ZF}} \cdot \mathbf{y} = (\mathbf{S}^H \mathbf{S})^{-1} \cdot \mathbf{S}^H \cdot \mathbf{y} = \mathbf{R}^{-1} \cdot \mathbf{r}. \quad (5.2.3)$$

²It is interesting to note that the decorrelator represents the joint maximum likelihood detector for continuously distributed signal alphabets.

We recognize that the decorrelator starts again with a bank of matched filters (multiplying \mathbf{y} with \mathbf{S}^H). Afterwards, the intermediate results in \mathbf{r} are *decorrelated* with \mathbf{R}^{-1} , i.e. the correlations between the matched filter outputs are removed. If \mathbf{S} consists of linear independent columns what is generally fulfilled for $N_U \leq N_s$, the correlation matrix $\mathbf{R} = \mathbf{S}^H \mathbf{S}$ has full rank and its inverse exists. Inserting the structure of \mathbf{y} into (5.2.3) leads to

$$\hat{\mathbf{a}}_{\text{ZF}} = \mathbf{R}^{-1} \mathbf{S}^H \cdot (\mathbf{S}\mathbf{a} + \mathbf{n}) = \mathbf{a} + \mathbf{R}^{-1} \mathbf{S}^H \cdot \mathbf{n} = \mathbf{a} + \mathbf{W}_{\text{ZF}} \cdot \mathbf{n}. \quad (5.2.4)$$

The output of the decorrelator consists of the desired symbol vector \mathbf{a} and a modified noise term. Therefore, as already mentioned in Section 4.5.3, the interference can be totally suppressed. However, the background noise is multiplied with the inverse of the correlation matrix \mathbf{R} leading especially for high loads β to a strong noise amplification and, hence, to low SNRs. This drawback is also indicated by the error covariance matrix

$$\begin{aligned} \Phi_{\text{ZF}} &= E \left\{ (\hat{\mathbf{a}}_{\text{ZF}} - \mathbf{a})(\hat{\mathbf{a}}_{\text{ZF}} - \mathbf{a})^H \right\} \\ &= E \left\{ (\mathbf{a} + \mathbf{W}_{\text{ZF}} \mathbf{n} - \mathbf{a})(\mathbf{a} + \mathbf{W}_{\text{ZF}} \mathbf{n} - \mathbf{a})^H \right\} = \mathbf{W}_{\text{ZF}} E \left\{ \mathbf{n} \mathbf{n}^H \right\} \mathbf{W}_{\text{ZF}}^H \\ &= \sigma_{\mathcal{N}}^2 \mathbf{W}_{\text{ZF}} \mathbf{W}_{\text{ZF}}^H = \sigma_{\mathcal{N}}^2 \mathbf{R}^{-1} \mathbf{S}^H \mathbf{S} \mathbf{R}^{-1} = \sigma_{\mathcal{N}}^2 \mathbf{R}^{-1}. \end{aligned} \quad (5.2.5)$$

It contains on its diagonal the mean squared error (MSE) for each user and equals the inverse of the correlation matrix \mathbf{R} multiplied with the noise power $\sigma_{\mathcal{N}}^2$.

For real-valued modulation schemes like BPSK or M -ary ASK, significant improvements can be achieved by the following modification. Since we know that real symbols have been transmitted, only the real part of the matched filter outputs $\mathbf{r}' = \text{Re} \{ \mathbf{S}^H \mathbf{y} \}$ is of interest. Consequently, the inverse has to be determined only from $\mathbf{R}' = \text{Re} \{ \mathbf{S}^H \mathbf{S} \}$ and we obtain

$$\hat{\mathbf{a}}_{\text{ZF}} = \text{Re} \{ \mathbf{S}^H \mathbf{S} \}^{-1} \cdot \text{Re} \{ \mathbf{S}^H \cdot \mathbf{y} \} = \mathbf{R}'^{-1} \cdot \mathbf{r}'. \quad (5.2.6)$$

The advantage of (5.2.6) becomes obvious when the received signal is only described by real matrices.

$$\mathbf{y}^r = \begin{bmatrix} \mathbf{y}' \\ \mathbf{y}'' \end{bmatrix} = \begin{bmatrix} \mathbf{S}' & -\mathbf{S}'' \\ \mathbf{S}'' & \mathbf{S}' \end{bmatrix} \cdot \begin{bmatrix} \mathbf{a}' \\ \mathbf{a}'' \end{bmatrix} + \begin{bmatrix} \mathbf{n}' \\ \mathbf{n}'' \end{bmatrix} = \begin{bmatrix} \mathbf{S}' \\ \mathbf{S}'' \end{bmatrix} \cdot \mathbf{a}' + \begin{bmatrix} \mathbf{n}' \\ \mathbf{n}'' \end{bmatrix} = \tilde{\mathbf{S}}^r \mathbf{a}' + \mathbf{n}^r \quad (5.2.7)$$

Splitting up real and imaginary parts doubles the sizes of all vectors and matrices. Since $\mathbf{a}'' = \mathbf{0}$ holds for real-valued modulation schemes, only the first N_U columns of the real system matrix influence the channel output. This halves the effective interference so that $\tilde{\mathbf{S}}^r$ is better conditioned than \mathbf{S}^r and the background noise is less amplified.

Next, we have to discuss the case when \mathbf{R} is singular and its inverse does not exist. This often occurs for $N_U > N_s$ and requires the pseudo inverse or Moore-Penrose

inverse. It is obtained from the singular value decomposition [GvL93] of \mathbf{S} (see also Appendix C)

$$\mathbf{S} = \mathbf{U}\Sigma\mathbf{V}^H = \mathbf{U} \begin{bmatrix} \Sigma_0 & \mathbf{0} \\ \mathbf{0} & \mathbf{0} \end{bmatrix} \mathbf{V}^H \Rightarrow \mathbf{R} = \mathbf{U} \begin{bmatrix} \Sigma_0^2 & \mathbf{0} \\ \mathbf{0} & \mathbf{0} \end{bmatrix} \mathbf{U}^H = \mathbf{U}\Lambda\mathbf{U}^H \quad (5.2.8)$$

where $\mathbf{U} \in \mathbb{C}^{N_s \times N_s}$ and $\mathbf{V} \in \mathbb{C}^{N_U \times N_U}$ are unitary matrices. The diagonal matrix Σ_0 contains all nonzero singular values of \mathbf{S} . With this definition, we obtain the pseudo inverses that include also the nonsingular case

$$\mathbf{S}^\dagger = \mathbf{V}\Sigma^\dagger\mathbf{U}^H = \mathbf{V} \begin{bmatrix} \Sigma_0^{-1} & \mathbf{0} \\ \mathbf{0} & \mathbf{0} \end{bmatrix} \mathbf{U}^H = \begin{cases} (\mathbf{S}^H\mathbf{S})^{-1}\mathbf{S}^H & \text{rank}(\mathbf{S}) = N_U \\ \mathbf{S}^H(\mathbf{S}\mathbf{S}^H)^{-1} & \text{rank}(\mathbf{S}) = N_s \end{cases} \quad (5.2.9)$$

and

$$\mathbf{R}^\dagger = \mathbf{S}^\dagger\mathbf{S}^{H\dagger} = \mathbf{V} \begin{bmatrix} \Sigma_0^{-2} & \mathbf{0} \\ \mathbf{0} & \mathbf{0} \end{bmatrix} \mathbf{V}^H = \begin{cases} (\mathbf{S}^H\mathbf{S})^{-1} & \text{rank}(\mathbf{S}) = N_U \\ \mathbf{S}^H(\mathbf{S}\mathbf{S}^H)^{-2}\mathbf{S} & \text{rank}(\mathbf{S}) = N_s \end{cases}. \quad (5.2.10)$$

Using (5.2.9) and (5.2.10), we obtain the general result $\mathbf{W}_{\text{ZF}} = \mathbf{S}^\dagger$. In scenarios with near far effects (compare page 178), the received signal can be expressed as

$$\mathbf{y} = \mathbf{SP}^{1/2}\mathbf{a} + \mathbf{n}.$$

The corresponding decorrelating filter is

$$\mathbf{W}_{\text{ZF}} = \mathbf{P}^{-1/2}\mathbf{S}^\dagger, \quad (5.2.11)$$

i.e. it consists of the already known decorrelator with successive scalar weighting of the filter outputs. Since the decorrelator totally removes the interference, weak users do not suffer from strong users and the decorrelator is called *near-far resistant*.

Fig. 5.2.1a shows the bit error rate performance of the decorrelator for BPSK. Although multiple-access interference can be totally suppressed, the performance degrades with increased load. Only for very low β the single-user bound (SUB) can be reached. The reason for this behavior is the amplification of the background noise that becomes larger with growing load. For $\beta = 2$, a reliable transmission is not possible at all. However, except for low SNR and extremely high loads, the decorrelator performs better than the simple matched filter represented by dashed lines.

This can also be observed in **Fig. 5.2.1b** showing the error rate performance versus β for different signal-to-noise ratios E_s/N_0 . While the error rate degrades dramatically for the matched filter even for moderate loads, the BER increases more slowly for the decorrelator. Nevertheless, the noise amplification leads to a

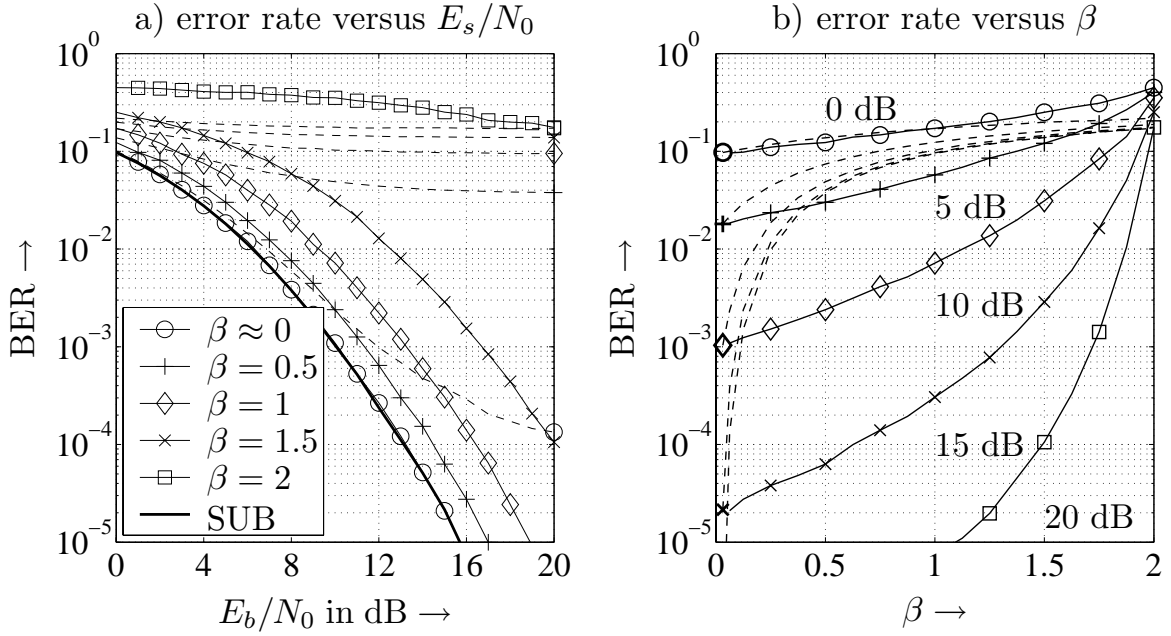


Figure 5.2.1: Error rate performance of decorrelator for different loads and uncoded OFDM-CDMA system with BPSK, 4-paths Rayleigh fading channel (dashed lines: matched filter)

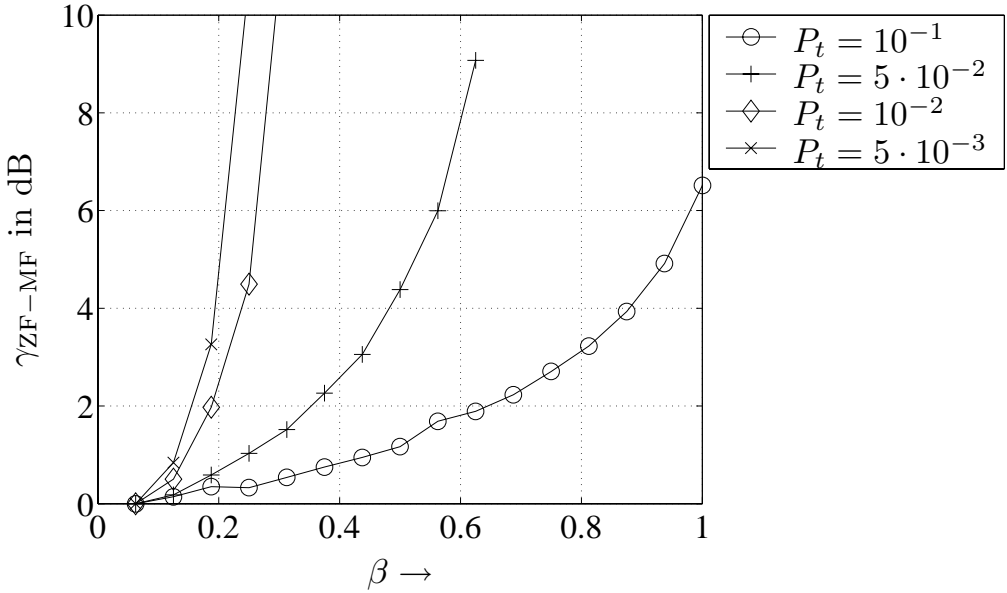


Figure 5.2.2: Gain of decorrelator compared to MF for different loads and uncoded OFDM-CDMA system with BPSK, 4-paths Rayleigh fading channel

weak performance at high SNRs, the error rate performance degrades dramatically when β approaches 2. It has to be emphasized that the example assumes independent fading channels for all users (see uplink transmission in Section 4.3) so that the interference is distributed in the complex plane. Since we use real-valued BPSK, only half of the interference power affects the transmission. Otherwise, the point of intersection in Fig. 5.2.1b would have been reached already for $\beta = 1$.

Fig. 5.2.2 compares the performance of the decorrelator with that of a simple matched filter. It depicts the gain of the decorrelator for different target error rates P_t , i.e.

$$\gamma_{\text{ZF-MF}} = 10 \log_{10} \frac{E_b/N_0|_{\text{MF}}}{E_b/N_0|_{\text{ZF}}} \quad (5.2.12)$$

the logarithmic ratio of required signal to noise ratios in order to achieve the bit error rate P_t . Obviously, $\gamma_{\text{ZF-MF}}$ grows with β and the slope becomes higher for low target error rates. For small SNRs and if β approaches 2, the decorrelator performs worse than the matched filter as can be seen from Fig. 5.2.1.

5.2.2 Minimum Mean Squared Error Receiver (MMSE)

So far, we considered two extreme linear detectors: The matched filter in Chapter 4 that addresses only the background noise and, therefore, suffers severely from multi-user interference and the decorrelator of the preceding section that concentrates only on the interference neglecting the influence of the noise. A compromise between both is obtained with the MMSE detector \mathbf{W}_{MMSE} minimizing the average squared Euclidean distance between the estimate $\hat{\mathbf{a}}_{\text{MMSE}} = \mathbf{W}_{\text{MMSE}} \cdot \mathbf{y}$ and the true data vector \mathbf{a} .

$$\hat{\mathbf{a}}_{\text{MMSE}} = \mathbf{W}_{\text{MMSE}} \cdot \mathbf{y} \quad \text{with} \quad \mathbf{W}_{\text{MMSE}} = \underset{\widetilde{\mathbf{W}} \in \mathbb{C}^{N_U \times N_s}}{\operatorname{argmin}} E \left\{ \|\widetilde{\mathbf{W}}\mathbf{y} - \mathbf{a}\|^2 \right\}. \quad (5.2.13)$$

Again, a solution of the problem defined in (5.2.13) is found by setting the partial derivative of the squared Euclidean distance with respect to $\widetilde{\mathbf{W}}^H$ to zero. With the relation $\partial \widetilde{\mathbf{W}} / \partial \widetilde{\mathbf{W}}^H = 0$ [Fis02], we obtain

$$\begin{aligned} & \frac{\partial}{\partial \widetilde{\mathbf{W}}^H} E \left\{ \operatorname{tr} [(\widetilde{\mathbf{W}}\mathbf{y} - \mathbf{a})(\widetilde{\mathbf{W}}\mathbf{y} - \mathbf{a})^H] \right\} \\ &= \operatorname{tr} \left[\frac{\partial}{\partial \widetilde{\mathbf{W}}^H} \left(\widetilde{\mathbf{W}}\Phi_{\underline{\mathcal{Y}}\underline{\mathcal{Y}}} \widetilde{\mathbf{W}}^H - \widetilde{\mathbf{W}}\Phi_{\underline{\mathcal{A}}\underline{\mathcal{Y}}} - \Phi_{\underline{\mathcal{A}}\underline{\mathcal{Y}}} \widetilde{\mathbf{W}}^H + \Phi_{\underline{\mathcal{A}}\underline{\mathcal{A}}} \right) \right] \\ &= \operatorname{tr} \left[\widetilde{\mathbf{W}}\Phi_{\underline{\mathcal{Y}}\underline{\mathcal{Y}}} - \Phi_{\underline{\mathcal{A}}\underline{\mathcal{Y}}} \right] \stackrel{!}{=} 0 \end{aligned} \quad (5.2.14)$$

leading to the well-known Wiener solution

$$\mathbf{W}_{\text{MMSE}} = \Phi_{\underline{\mathcal{A}}\underline{\mathcal{Y}}} \cdot \Phi_{\underline{\mathcal{Y}}\underline{\mathcal{Y}}}^{-1}. \quad (5.2.15)$$

In order to determine the covariance matrices in (5.2.15), some general assumptions are made that are fulfilled in most practical communication systems. First, the AWGN channel adds white noise, i.e. successive noise samples are uncorrelated. Second, the data symbols a_u of different users are statistically independent.

Furthermore, the data symbols are independent from the noise samples leading to the following set of equations.

$$\Phi_{\underline{\mathcal{N}}\underline{\mathcal{N}}} = E\{\mathbf{n}\mathbf{n}^H\} = \sigma_{\mathcal{N}}^2 \cdot \mathbf{I}_{N_s} \quad (5.2.16a)$$

$$\Phi_{\underline{\mathcal{A}}\underline{\mathcal{A}}} = E\{\mathbf{a}\mathbf{a}^H\} = \sigma_{\mathcal{A}}^2 \cdot \mathbf{I}_{N_U} \quad (5.2.16b)$$

$$\Phi_{\underline{\mathcal{A}}\underline{\mathcal{N}}} = E\{\mathbf{a}\mathbf{n}^H\} = \mathbf{0} \quad (5.2.16c)$$

These results deliver the covariance matrix of the received samples

$$\Phi_{\underline{\mathcal{Y}}\underline{\mathcal{Y}}} = E\{\mathbf{y}\mathbf{y}^H\} = \mathbf{S}\Phi_{\underline{\mathcal{A}}\underline{\mathcal{A}}}\mathbf{S}^H + \Phi_{\underline{\mathcal{N}}\underline{\mathcal{N}}} = \sigma_{\mathcal{A}}^2 \cdot \mathbf{S}\mathbf{S}^H + \sigma_{\mathcal{N}}^2 \cdot \mathbf{I}_{N_s} \quad (5.2.17)$$

and the crosscovariance matrix

$$\Phi_{\underline{\mathcal{A}}\underline{\mathcal{Y}}} = E\{\mathbf{a}\mathbf{y}^H\} = \Phi_{\underline{\mathcal{A}}\underline{\mathcal{A}}}\mathbf{S}^H + \Phi_{\underline{\mathcal{A}}\underline{\mathcal{N}}} = \sigma_{\mathcal{A}}^2 \cdot \mathbf{S}^H. \quad (5.2.18)$$

We obtain the MMSE filter

$$\mathbf{W}_{\text{MMSE}} = \sigma_{\mathcal{A}}^2 \mathbf{S}^H (\sigma_{\mathcal{A}}^2 \mathbf{S}\mathbf{S}^H + \sigma_{\mathcal{N}}^2 \mathbf{I}_{N_s})^{-1} = \mathbf{S}^H (\mathbf{S}\mathbf{S}^H + \frac{\sigma_{\mathcal{N}}^2}{\sigma_{\mathcal{A}}^2} \mathbf{I}_{N_s})^{-1} \quad (5.2.19)$$

which can be shown to be equivalent to³.

$$\mathbf{W}_{\text{MMSE}} = (\mathbf{S}^H \mathbf{S} + \frac{\sigma_{\mathcal{N}}^2}{\sigma_{\mathcal{A}}^2} \mathbf{I}_{N_U})^{-1} \cdot \mathbf{S}^H = (\mathbf{R} + \frac{N_0}{E_s} \mathbf{I}_{N_U})^{-1} \cdot \mathbf{S}^H. \quad (5.2.20)$$

Analyzing the result in (5.2.20), we see that the MMSE detector starts like the decorrelator with a matched filter bank. Moreover, \mathbf{W}_{MMSE} really represents a compromise between matched filter and decorrelator. For $\sigma_{\mathcal{N}}^2 \rightarrow 0$, i.e. infinitely large SNR, the identity matrix in the inverse is cancelled and we obtain the decorrelator in (5.2.3) suppressing the interference perfectly. Contrarily, the identity matrix dominates the inverse for $\sigma_{\mathcal{N}}^2 \rightarrow \infty$ so that \mathbf{R} can be neglected. In this case, we simply obtain the matched filter that addresses only the noise [Mü198].

However, the MMSE detector does not suppress the multi-user interference perfectly and some residual interference still disturbs the transmission. Moreover, the detector is biased. The error covariance matrix now becomes

$$\begin{aligned} \Phi_{\text{MMSE}} &= E\left\{(\hat{\mathbf{a}}_{\text{MMSE}} - \mathbf{a})(\hat{\mathbf{a}}_{\text{MMSE}} - \mathbf{a})^H\right\} \\ &= \sigma_{\mathcal{A}}^2 \left[\mathbf{I}_{N_U} - (\mathbf{R} + \frac{\sigma_{\mathcal{N}}^2}{\sigma_{\mathcal{A}}^2} \mathbf{I}_{N_U})^{-1} \mathbf{R} \right] = \sigma_{\mathcal{N}}^2 (\mathbf{R} + \frac{\sigma_{\mathcal{N}}^2}{\sigma_{\mathcal{A}}^2} \mathbf{I}_{N_U})^{-1}. \end{aligned} \quad (5.2.21)$$

³A simple way to derive (5.2.20) is to start with a matched filter bank and minimizing $\|\mathbf{W}\mathbf{S}^H \mathbf{y} - \mathbf{a}\|^2 = \|\mathbf{W}\mathbf{r} - \mathbf{a}\|^2$.

The normalized mean squared error per user can be easily calculated and amounts to

$$\begin{aligned} \frac{1}{\sigma_A^2 N_U} \text{tr} [\Phi_{\text{MMSE}}] &= \frac{1}{N_U} \text{tr} \left[\frac{\sigma_N^2}{\sigma_A^2} (\mathbf{U} \boldsymbol{\Lambda} \mathbf{U}^H + \frac{\sigma_N^2}{\sigma_A^2} \mathbf{I}_{N_U})^{-1} \right] \\ &= \frac{1}{N_U} \sum_{\mu=1}^{\text{rank}(\mathbf{S})} \frac{N_0/E_s}{\lambda_\mu + N_0/E_s} \end{aligned} \quad (5.2.22)$$

where λ_μ denotes the μ -th nonzero eigenvalue of the correlation matrix \mathbf{R} . Hence, the average error depends on the singular-value distribution of \mathbf{S} . For large signal to noise ratio $E_s/N_0 \rightarrow \infty$, the error diminishes, for $E_s/N_0 \rightarrow 0$, it becomes 1.

Looking again at a BPSK transmission, the performance can be improved by concentrating on the important real parts. We obtain similar to the derivation for the decorrelator

$$\hat{\mathbf{a}}_{\text{MMSE}} = \left(\mathbf{R}' + \frac{N_0}{2E_s} \mathbf{I}_{N_U} \right)^{-1} \cdot \mathbf{r}' . \quad (5.2.23)$$

Note that the noise power in (5.2.23) is halved compared to the complex-valued case!

In near-far scenarios, the MMSE filter has to be adapted to the different power levels among the users and becomes

$$\mathbf{W}_{\text{MMSE}} = \mathbf{P}^{1/2} \mathbf{S}^H (\mathbf{S} \mathbf{P} \mathbf{S}^H + \sigma_N^2 \mathbf{I}_{N_s})^{-1} \quad (5.2.24a)$$

$$= \mathbf{P}^{1/2} (\mathbf{S}^H \mathbf{S} \mathbf{P} + \sigma_N^2 \mathbf{I}_{N_U})^{-1} \mathbf{S}^H . \quad (5.2.24b)$$

From (5.2.24a) and (5.2.24b) we observe that the power levels affect the behavior of the MMSE filter. If the signal to noise ratio grows without bound, the influence of the background noise vanishes and the MMSE filter concentrates on the interference suppression. Hence, the MMSE detector approaches the decorrelator and is **asymptotically** near-far resistant [Ver98]. However, for finite SNR, weak users suffer more from strong users than in the case of the decorrelator, i.e. near-far resistance is not generally given.

Fig. 5.2.3a shows the bit error rate performance of the MMSE detector for an OFDM-CDMA system and a 4-paths Rayleigh fading channel. Similar to the decorrelator, performance degrades for increased system load β . However, the comparison with the decorrelator in **Fig. 5.2.3b** illustrates that the degradation is much smaller than for the zero-forcing solution. The MMSE filter outperforms the decorrelator for all loads β and all signal to noise ratios and the gain grows with the system load. This is also confirmed in **Fig. 5.2.4**.

Concluding, we can state that the linear MUD techniques reduce multiple access interference efficiently. Especially the MMSE filter outperforms the simple

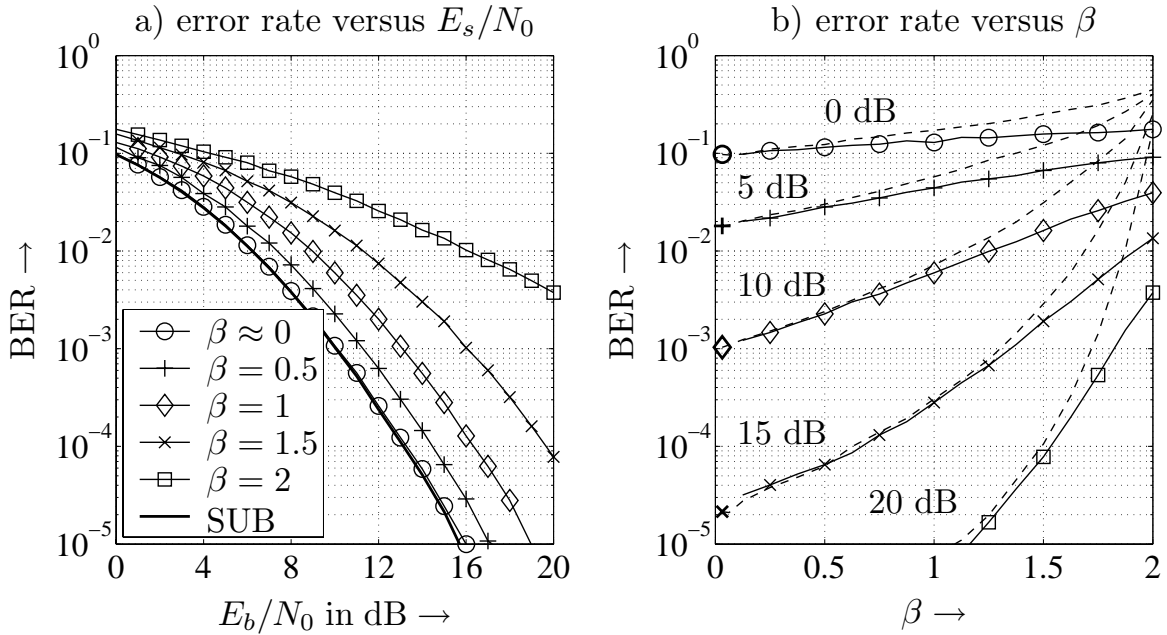


Figure 5.2.3: Error rate performance of MMSE filter for different loads and OFDM-CDMA system with 4-paths Rayleigh fading channel (dashed line: decorrelator)

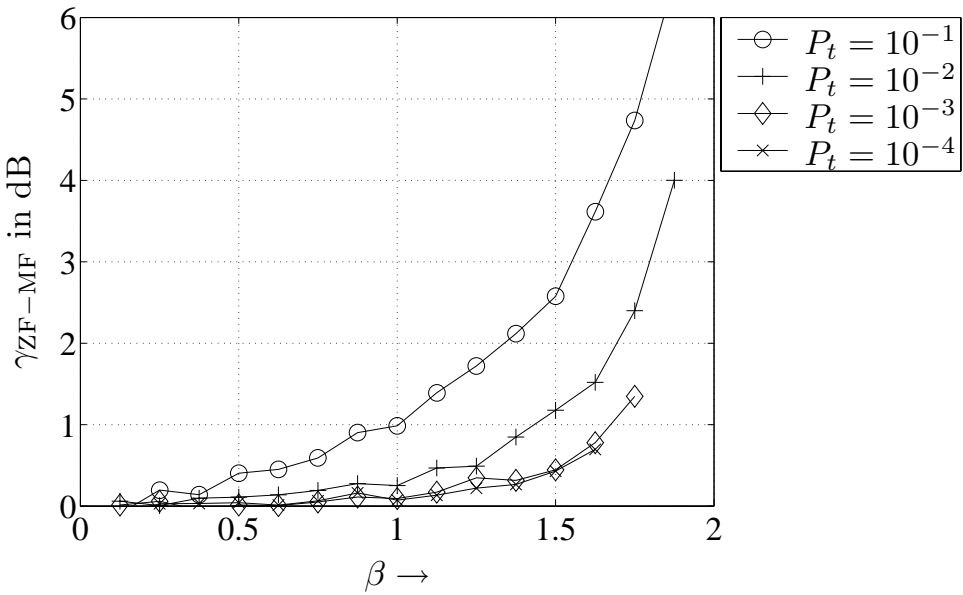


Figure 5.2.4: Gain of MMSE filter compared to decorrelator for different loads and an uncoded OFDM-CDMA system with BPSK, 4-paths Rayleigh fading channel

matched filter for all signal to noise ratios. Although the computational complexity of the described linear detectors is much lower than that of the optimum multi-user detector, it still grows cubically with the system size. Hence, calculating the pseudo inverse of \mathbf{S} is a demanding task. The next subsections describe

some iterative schemes approximating the zero-forcing and MMSE solutions with lower computational costs.

5.2.3 Linear Parallel Interference Cancellation

By calculating the (pseudo) inverse of the system matrix \mathbf{S} we basically solve a linear equation system. From mathematics [GvL93] we know that the solution can be obtained iteratively. Starting with a matched filter bank, we have to process the signal

$$\mathbf{r} = \mathbf{R}\mathbf{a} + \mathbf{S}^H\mathbf{n} \quad \Rightarrow \quad \hat{\mathbf{a}} = \mathbf{W} \cdot \mathbf{r} \quad \Leftrightarrow \quad \mathbf{M} \cdot \hat{\mathbf{a}} = \mathbf{r}. \quad (5.2.25)$$

Instead of looking in (5.2.25) for a matrix \mathbf{W} that leads to a good estimate $\hat{\mathbf{a}}$, we can describe the problem as solving the linear equation system $\mathbf{M} \cdot \hat{\mathbf{a}} = \mathbf{r}$. The matrix \mathbf{M} will be determined later. A single row of this linear equation system can be presented in the form

$$r_u = M_{u,u}\hat{a}_u + \sum_{v=1}^{u-1} M_{u,v}\hat{a}_v + \sum_{v=u+1}^{N_U} M_{u,v}\hat{a}_v, \quad (5.2.26)$$

i.e. the received value r_u consists of the superposition of the scaled desired symbol \hat{a}_u and the weighted interfering symbols $\hat{a}_{v \neq u}$. An iterative solution of the equation system is obtained by using the weighted matched filter outputs of the interfering symbols as initial estimates $\hat{a}_{v \neq u}^{(0)} = r_{v \neq u}/M_{v,v}$. Subtracting them from r_u leads to an improved estimate $\hat{a}_u^{(1)}$ after the first iteration. The interference cancellation is simultaneously applied to all users and repeated with updated estimates $\hat{a}_u^{(\mu)}$ in subsequent iterations. In the μ -th iteration, the u -th symbol becomes

$$\hat{a}_u^{(\mu)} = M_{u,u}^{-1} \cdot \left[r_u - \sum_{v=1}^{u-1} M_{u,v}\hat{a}_v^{(\mu-1)} - \sum_{v=u+1}^{N_U} M_{u,v}\hat{a}_v^{(\mu-1)} \right]. \quad (5.2.27)$$

The simultaneous application of (5.2.27) on all symbols a_u , $1 \leq u \leq N_U$, is also called Jacobi algorithm and known as linear parallel interference cancellation (PIC). An implementation leads directly to a multi-stage detector depicted in **Fig. 5.2.5** [Mos96, HT00]. Several identical modules highlighted by the gray shaded areas are serially concatenated. Each module represents one iteration step so that we need m stages for m iterations.

The choice of the matrix \mathbf{M} determines the kind of detector that is approximated. For $\mathbf{M} = \mathbf{R}$, we approximate the decorrelator, and the coefficients $M_{u,v} = R_{u,v}$ used in (5.2.27) equal the elements of the correlation matrix. The approximation of the MMSE filter is obtained for $\mathbf{M} = \mathbf{R} + \sigma_N^2/\sigma_A^2 \cdot \mathbf{I}_{N_U}$. Hence, the diagonal elements of \mathbf{M} have to be replaced by $M_{u,u} = R_{u,u} + N_0/E_s$.

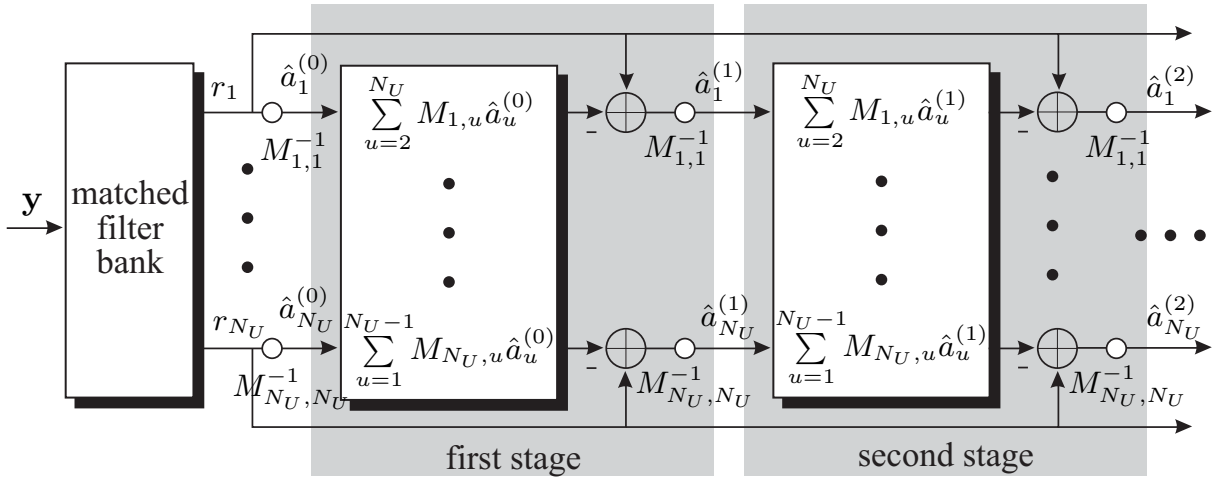


Figure 5.2.5: Structure of multi-stage detector for iterative parallel interference cancellation

Convergence Behavior of Decorrelator Approximation

The convergence properties of this iterative algorithm depend on the eigenvalue distribution of \mathbf{M} . Therefore, we describe (5.2.27) using vector notations. The matrix $\mathbf{A} = \text{diag}(\text{diag}(\mathbf{R}))$ is diagonal and contains the diagonal elements of the correlation matrix \mathbf{R} . The parallel interference cancellation approximating the decorrelator delivers

$$\begin{aligned}
\hat{\mathbf{a}}_{\text{ZF}}^{(0)} &= \mathbf{A}^{-1} \cdot \mathbf{r} \\
\hat{\mathbf{a}}_{\text{ZF}}^{(1)} &= \mathbf{A}^{-1} \left[\mathbf{r} - (\mathbf{R} - \mathbf{A}) \hat{\mathbf{a}}_{\text{ZF}}^{(0)} \right] = \mathbf{A}^{-1/2} \left[\mathbf{I}_{N_U} - \mathbf{A}^{-1/2} (\mathbf{R} - \mathbf{A}) \mathbf{A}^{-1/2} \right] \mathbf{A}^{-1/2} \mathbf{r} \\
\hat{\mathbf{a}}_{\text{ZF}}^{(2)} &= \mathbf{A}^{-1} \left[\mathbf{r} - (\mathbf{R} - \mathbf{A}) \hat{\mathbf{a}}_{\text{ZF}}^{(1)} \right] \\
&= \mathbf{A}^{-1/2} \left[\mathbf{I}_{N_U} - \mathbf{A}^{-1/2} (\mathbf{R} - \mathbf{A}) \mathbf{A}^{-1/2} + \left(\mathbf{A}^{-1/2} (\mathbf{R} - \mathbf{A}) \mathbf{A}^{-1/2} \right)^2 \right] \mathbf{A}^{-1/2} \mathbf{r} \\
&\vdots \\
\hat{\mathbf{a}}_{\text{ZF}}^{(m)} &= \mathbf{A}^{-1/2} \sum_{\mu=0}^m \left[\mathbf{A}^{-1/2} (\mathbf{A} - \mathbf{R}) \mathbf{A}^{-1/2} \right]^{\mu} \mathbf{A}^{-1/2} \mathbf{r}. \tag{5.2.28}
\end{aligned}$$

The output after the m -th iteration in (5.2.28) represents the m -th order Taylor series approximation of \mathbf{R}^{-1} [MV01]. Rewriting it with the normalized correlation matrix $\bar{\mathbf{R}} = \mathbf{A}^{-1/2} \mathbf{R} \mathbf{A}^{-1/2}$ yields

$$\hat{\mathbf{a}}_{\text{ZF}}^{(m)} = \mathbf{A}^{-1/2} \sum_{\mu=0}^m \left(\mathbf{I}_{N_U} - \bar{\mathbf{R}} \right)^{\mu} \mathbf{A}^{-1/2} \mathbf{r}. \tag{5.2.29}$$

This series only converges to the true inverse of \mathbf{R} if the magnitudes of all eigenvalues of $\mathbf{I}_{N_U} - \bar{\mathbf{R}}$ are smaller than 1. This condition is equivalent to $\lambda_{\max}(\bar{\mathbf{R}}) < 2$. Since λ_{\max} tends asymptotically to $(1 + \sqrt{\beta})^2$ [Mül98], we obtain an approximation of the maximum load below which the Jacobi algorithm will converge.

$$\beta_{\max} = \frac{N_{U,\max}}{N_s} < (\sqrt{2} - 1)^2 \approx 0.17 \quad (5.2.30)$$

Obviously, the Jacobi algorithm or, equivalently, the linear parallel interference cancellation converge towards the true decorrelator only for very low loads. Hence, this technique is not suited for highly loaded systems.

Convergence Behavior of MMSE Approximation

According to the last section, we have to replace the diagonal matrix \mathbf{A} by the matrix $\mathbf{D} = \mathbf{A} + \sigma_{\mathcal{N}}^2 / \sigma_{\mathcal{A}}^2 \mathbf{I}_{N_U}$ in order to approximate the MMSE detector. With this substitution, we obtain the following estimates after different iterations.

$$\begin{aligned} \hat{\mathbf{a}}_{\text{MMSE}}^{(0)} &= \mathbf{D}^{-1} \cdot \mathbf{r} \\ \hat{\mathbf{a}}_{\text{MMSE}}^{(1)} &= \mathbf{D}^{-1} \left[\mathbf{r} - (\mathbf{R} - \mathbf{A}) \hat{\mathbf{a}}_{\text{MMSE}}^{(0)} \right] \\ &= \mathbf{D}^{-1/2} \left[\mathbf{I}_{N_U} - \mathbf{D}^{-1/2} (\mathbf{R} - \mathbf{A}) \mathbf{D}^{-1/2} \right] \mathbf{D}^{-1/2} \mathbf{r} \\ \hat{\mathbf{a}}_{\text{MMSE}}^{(2)} &= \mathbf{D}^{-1} \left[\mathbf{r} - (\mathbf{R} - \mathbf{A}) \hat{\mathbf{a}}_{\text{MMSE}}^{(1)} \right] \\ &= \mathbf{D}^{-1/2} \left[\mathbf{I}_{N_U} - \mathbf{D}^{-1/2} (\mathbf{R} - \mathbf{A}) \mathbf{D}^{-1/2} + \left(\mathbf{D}^{-1/2} (\mathbf{R} - \mathbf{A}) \mathbf{D}^{-1/2} \right)^2 \right] \mathbf{D}^{-1/2} \mathbf{r} \\ &\vdots \\ \hat{\mathbf{a}}_{\text{MMSE}}^{(m)} &= \mathbf{D}^{-1/2} \sum_{\mu=0}^m \left[\mathbf{D}^{-1/2} (\mathbf{A} - \mathbf{R}) \mathbf{D}^{-1/2} \right]^{\mu} \mathbf{D}^{-1/2} \mathbf{r}. \end{aligned} \quad (5.2.31)$$

In order to determine the convergence properties concerning the MMSE filter, (5.2.31) can be transformed into the form of (5.2.29)

$$\hat{\mathbf{a}}_{\text{MMSE}}^{(m)} = \mathbf{D}^{-1/2} \sum_{\mu=0}^m \left[\mathbf{I}_{N_U} - \mathbf{D}^{-1/2} \left(\mathbf{R} + \frac{\sigma_{\mathcal{N}}^2}{\sigma_{\mathcal{A}}^2} \mathbf{I}_{N_U} \right) \mathbf{D}^{-1/2} \right]^{\mu} \mathbf{D}^{-1/2} \mathbf{r}. \quad (5.2.32)$$

Now, the same argumentation as for the decorrelator can be applied and the condition for convergence becomes [GS01]

$$\max_{u=1 \dots N_U} \frac{A_{u,u}^2 \lambda_u + \sigma_{\mathcal{N}}^2 / \sigma_{\mathcal{A}}^2}{A_{u,u}^2 + \sigma_{\mathcal{N}}^2 / \sigma_{\mathcal{A}}^2} < 2 \quad \Rightarrow \quad \beta < \min_{u=1 \dots N_U} \left(\sqrt{2 + \frac{\sigma_{\mathcal{N}}^2}{A_{u,u}^2 \sigma_{\mathcal{A}}^2}} - 1 \right)^2.$$

The first difference compared to the decorrelator is that the maximum load β depends on the signal to noise ratio $\sigma_{\mathcal{N}}^2/\sigma_{\mathcal{A}}^2 = N_0/E_s$. This term increases the convergence area a little bit. However, for high SNR, $\sigma_{\mathcal{N}}^2/\sigma_{\mathcal{A}}^2$ becomes small and both, decorrelator and MMSE filter are only approached for low loads.

This behavior is illustrated in **Fig. 5.2.6a** showing the results for the first five iterations and a load $\beta = 0.5$. Only for very low SNR (large $\sigma_{\mathcal{N}}^2/\sigma_{\mathcal{A}}^2$) the iterative approximation reaches the true MMSE filter. For higher signal to noise ratios, $\beta = 0.5$ is beyond the convergence region and the parallel interference cancellation performs even worse than the matched filter. Figure 5.2.6b shows the results for $E_b/N_0 = 10$ dB versus β . Again, it is confirmed that convergence can only be ensured for low load.

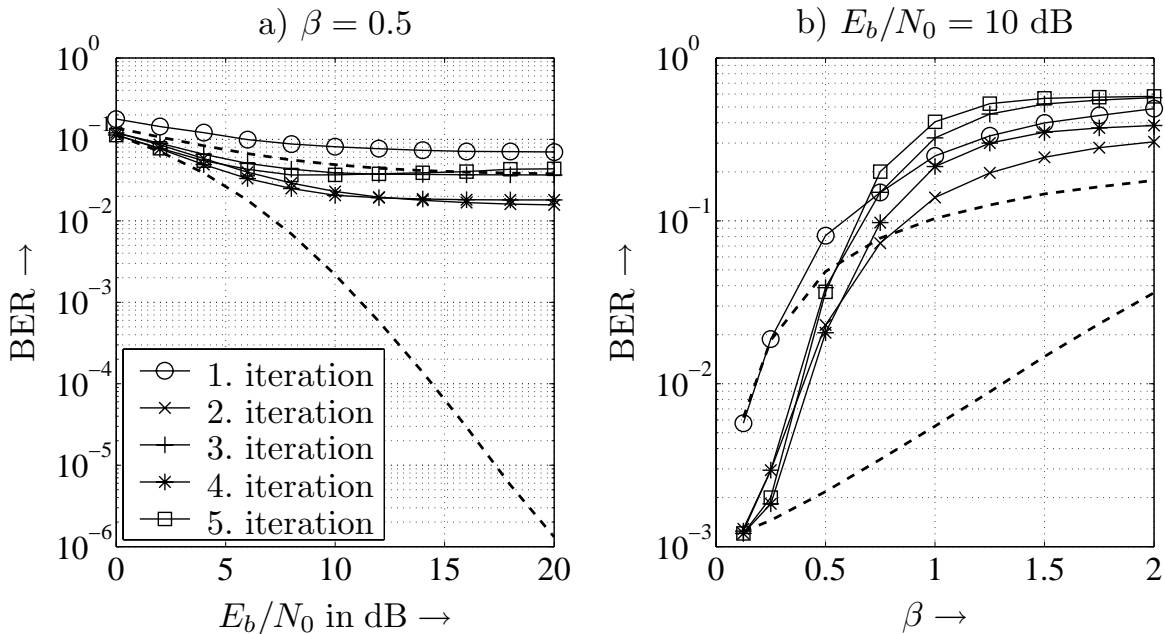


Figure 5.2.6: Performance of PIC approximating the MMSE filter (upper dashed line: matched filter, lower dashed line: true MMSE filter)

5.2.4 Linear Successive Interference Cancellation

The poor convergence properties of the linear parallel interference cancellation can be substantially improved. Imagine that the interference cancellation described in (5.2.27) is carried out successively for different users starting with $u = 1$ and ending with $u = N_U$. Considering the μ -th iteration for user u , only estimates $\hat{a}_{v \neq u}^{\mu-1}$ of the previous iteration $\mu - 1$ are used. However, updated estimates $\hat{a}_{v < u}^{(\mu)}$ of the μ -th iteration are already available for users $1 \leq v < u$. Replacing all old estimates $\hat{a}_{v < u}^{(\mu-1)}$ in (5.2.27) by their updated versions $\hat{a}_{v < u}^{(\mu)}$ results in the Gauss-Seidel algorithm

$$a_u^{(\mu)} = M_{u,u}^{-1} \cdot \left[r_u - \sum_{v=1}^{u-1} M_{u,v} \hat{a}_v^{(\mu)} - \sum_{v=u+1}^{N_U} M_{u,v} \hat{a}_v^{(\mu-1)} \right]. \quad (5.2.33)$$

Besides improved convergence properties another advantage is the *in-place* implementation, i.e. updated estimates can directly overwrite old values because they are not used any longer saving valuable memory.

The analysis of the convergence behavior is not as easy as for the parallel interference cancellation. In [GvL93] it is shown that the algorithm always converges for Hermitian positive definite matrices \mathbf{M} . Fortunately, \mathbf{M} represents in the context of our CDMA system the correlation matrix \mathbf{R} or $\mathbf{R} + \sigma_{\mathcal{N}}^2 / \sigma_{\mathcal{A}}^2 \mathbf{I}_{N_U}$. Hence, \mathbf{M} can be assumed to be Hermitian and positive definite so that the Gauss-Seidel algorithm always converges.

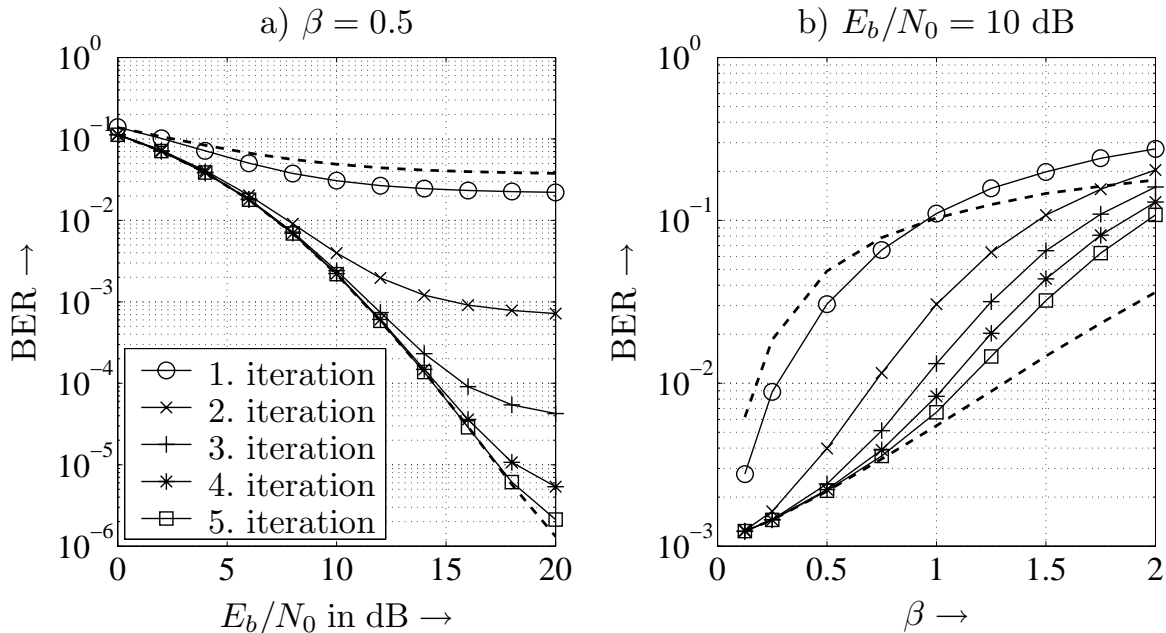


Figure 5.2.7: Performance of linear SIC approximating the MMSE filter (upper dashed line: matched filter, lower dashed line: true MMSE filter)

Fig. 5.2.7a confirms the promised convergence properties. Considering a half-loaded system, five iterations suffice to approach the true MMSE filter. At low signal to noise ratios, the performance of the MMSE filter is reached with even less iterations. Fig. 5.2.7b shows that with increasing load more iterations are needed. For loads above $\beta = 1$, the first iteration can perform even worse than the matched filter. However, successive iterations substantially improve the performance.

A major difference between parallel and successive interference cancellation is the influence of the order of detection. While the PIC treats all users simultaneously and performs well for identical SNRs for all users, the performance of SIC highly depends on the order of detection due to the risk of error propagation. Hence,

unequal power levels among the users are advantageous and the iteration should start with the strongest user.

Comparing now the computational costs of a direct matrix inversion with the iterative approximations in terms of number of multiplications, we see from (5.2.33) that N_U multiplications per iteration and user are needed. For m iterations, this leads to mN_U^2 multiplications compared to a complexity of $\mathcal{O}(N_U^3)$ for the direct matrix inversion. Hence, as long as the number of iterations is smaller than N_U , we save computational costs.

Besides parallel and successive interference cancellation strategies, there exist further iterative approaches like the conjugate gradient method and a general polynomial series expansion of the inverse [Mül98]. These approaches are not pursued in this thesis.

All linear techniques described so far do not reach the single-user bound, i.e. there remains interference in the system after filtering. From the information theoretic analysis in Section 4.4 we know that the optimum detector performs much better than linear techniques. Therefore, we have to look for nonlinear approaches coming closer to the optimum solution. These techniques exploit the finite signal alphabet in order to improve the multi-user detection.

5.3 Nonlinear Iterative Multi-User Detection

A major drawback of the previously introduced linear detectors is not to exploit the finite nature of the transmit signals. This shortcoming can be easily overcome by introducing nonlinear devices into the iterative structure in order to exploit the discrete alphabets. This means that the signals $\hat{a}_{v \neq u}^\mu$ in (5.2.27) or (5.2.33) are passed through a suited nonlinear device before they are used for interference cancellation. For simplicity we restrict the analysis to a normalized BPSK, i.e. we transmit $x = \pm 1$. An extension to QPSK that treats real and imaginary parts separately is straightforward while schemes with more levels need more sophisticated methods.

5.3.1 Nonlinear Devices

The simplest nonlinearity is naturally a hard decision, i.e. determining the sign of a signal

$$\mathcal{Q}_{\text{HD}}(y) = \text{sgn}(y) . \quad (5.3.1)$$

If the decision is correct, the interference can be cancelled perfectly. However, if the decision is wrong what may be very likely in early stages of the detection process, especially for large β , interference is not reduced but even increased and

the situation becomes worse. Therefore, more sophisticated functions taking into account the reliability of the signals should be preferred. A selection is depicted in **Fig. 5.3.1**.

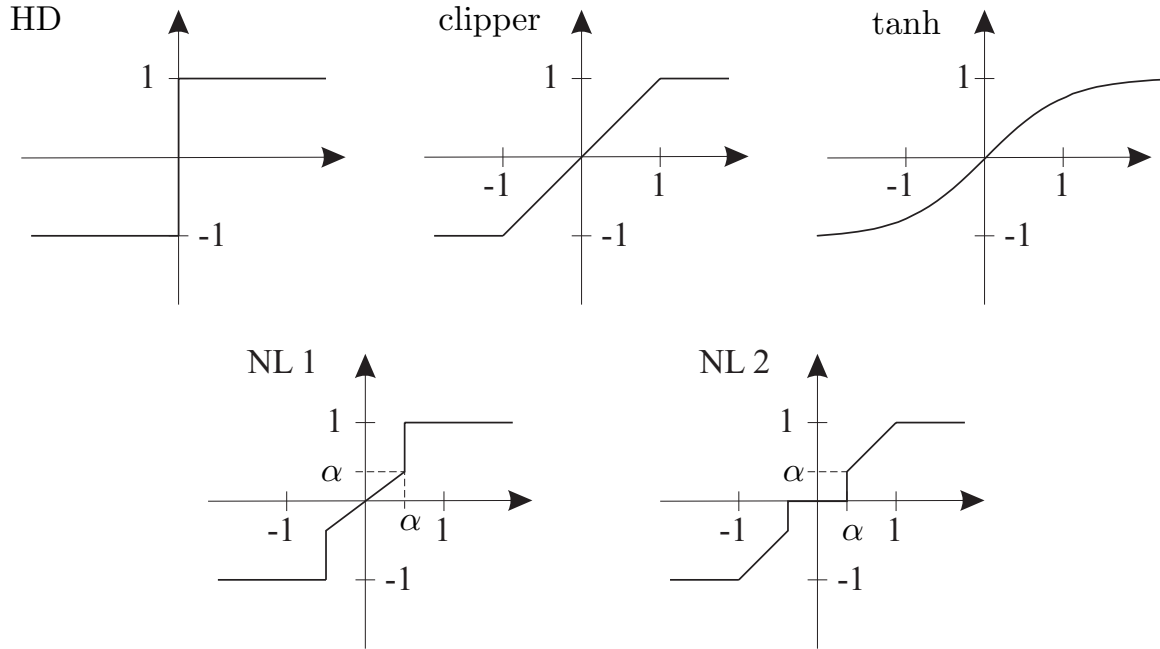


Figure 5.3.1: Examples for nonlinear devices

In order to keep the influence of wrong decisions as small as possible, it is advantageous not to decide unreliable (small) samples but to leave them small. Obviously, interference is generally not perfectly cancelled by these approaches, but the error made with wrong decision is remarkably reduced. The simplest form that follows this strategy is the clipper or limiter. It has a linear shape for $|y| \leq 1$ and outputs ± 1 for larger inputs $|y| > 1$

$$Q_{\text{clip}}(y) = \begin{cases} -1 & \text{for } y < -1 \\ y & \text{for } |y| \leq 1 \\ +1 & \text{for } y > +1 \end{cases}. \quad (5.3.2)$$

Hence, the clipper exploits the fact that the transmitted signals cannot be larger than one⁴. Interference is totally cancelled if the signal has the correct sign and a magnitude larger than one. For small values, the reliability is low and the interference can only be partly reduced. In case of a wrong sign, the degradation is not as large as for the hard decision.

A smooth version of the clipper is obtained with the tanh-function avoiding sharp edges. We know already from Section 3.4 on page 108 that the expectation of a bit

⁴For notational simplicity, we assume the normalization to $E_s/T_s = 1$.

is obtained from its log-likelihood ratio L by $\tanh(L/2)$. However, the LLR can be determined only if the SINR is perfectly known. This represents a big difficulty because we do not know the exact interference level in each iteration. Therefore, we introduce a parameter α according to

$$Q_{\tanh}(y) = \tanh(\alpha y) \quad (5.3.3)$$

that depends on the SNR as well as the effective interference and has to be optimized with respect to a minimum error rate. **Fig. 5.3.2** compares the tanh-function for different α with the hard decision and the clipper. For small α , the tanh is very smooth and its output is pretended to be unreliable even for large inputs. Contrarily, $\alpha = 1$ comes close to the clipper in the nearly linear regime and large $\alpha > 1$ leads to the hard decision.

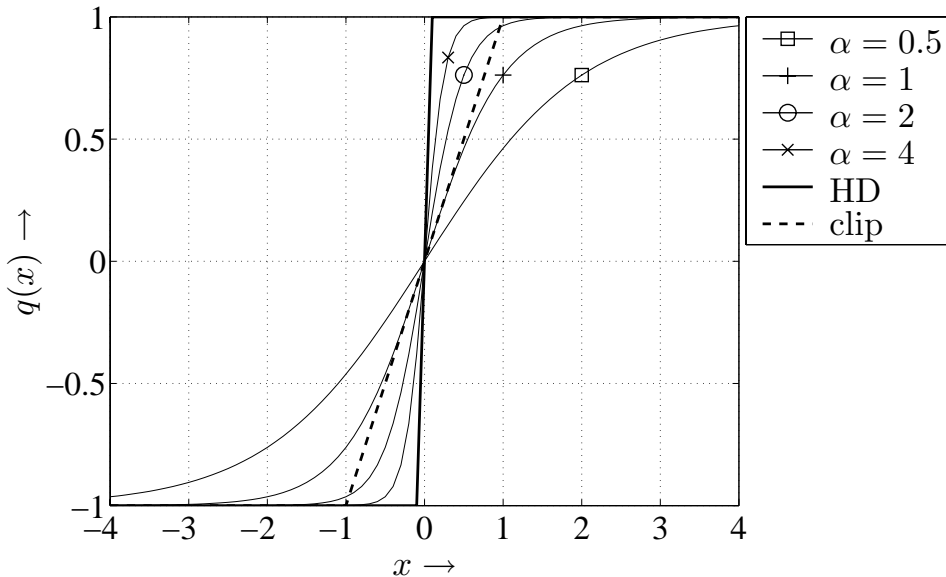


Figure 5.3.2: Comparison of tanh for different α with hard decision and clipper

Next, two further nonlinear functions are proposed. The first one (NL 1) has a linear shape around the origin and hops to ± 1 for values larger than a certain threshold α

$$Q_{\text{NL1}}(y) = \begin{cases} -1 & \text{for } y < -\alpha \\ y & \text{for } |y| \leq \alpha \\ +1 & \text{for } y > \alpha \end{cases} . \quad (5.3.4)$$

The difference to the clipper is that this nonlinearity starts for smaller values to totally remove the interference. The parameter α has to be optimized according to the load and the signal to noise ratio. The second function (NL 2) avoids any

cancellation for unreliable values and allows interference reduction only above a threshold α

$$\mathcal{Q}_{\text{NL2}}(y) = \begin{cases} -1 & \text{for } y < -1 \\ y & \text{for } -1 \leq y \leq -\alpha \\ 0 & \text{for } |\alpha| < \alpha \\ y & \text{for } \alpha \leq y \leq +1 \\ +1 & \text{for } y > +1 \end{cases}. \quad (5.3.5)$$

Obviously, it reduces to a simple clipper for $\alpha = 0$.

Finally, we look at coded CDMA systems. If the computational costs do not represent a restriction, the channel decoder can be used as a nonlinear device [Hag96a]. Since it exploits the redundancy of the code, it can increase the reliability of the estimates remarkably. Again, we have to distinguish between hard-output and soft-output decoding. For convolutional codes presented in Chapter 3, hard-output decoding can be performed by the Viterbi algorithm while soft-output decoding can be carried out by the BCJR or Max-Log-MAP algorithms.

5.3.2 Uncoded Nonlinear Interference Cancellation

Uncoded Parallel Interference Cancellation

First, we have to optimize the parameter α for the nonlinear functions NL 1, NL 2 and tanh. We start the analysis with the parallel interference cancellation whose structure – depicted in Fig. 5.2.5 for the linear case – has to be extended. **Fig. 5.3.3** shows the μ -th stage of the resulting multistage receiver. Prior to the interference cancellation, the interference reduced signals $\tilde{r}_{v \neq u}^{(\mu-1)}$ of the previous iteration are scaled with $M_{v,v}^{-1}$. The application of the nonlinear function now yields estimates for the interfering signal of user v

$$\hat{a}_v^{(\mu-1)} = \mathcal{Q}\left(M_{v,v}^{-1} \cdot \tilde{r}_v^{(\mu-1)}\right). \quad (5.3.6)$$

Next, these estimates are weighted with the correlation coefficients $M_{u,v}$, summed and subtracted from the matched filter output r_u

$$\tilde{r}_u^{(\mu)} = r_u - \sum_{v \neq u} M_{u,v} \cdot \hat{a}_v^{(\mu-1)}. \quad (5.3.7)$$

After subtracting the estimated interference for all users, the procedure is repeated again. If the iterative scheme converges and the global optimum is reached, the interference is more and more cancelled until the single-user performance is obtained. However, the iterative algorithm can get stuck in a local optimum.

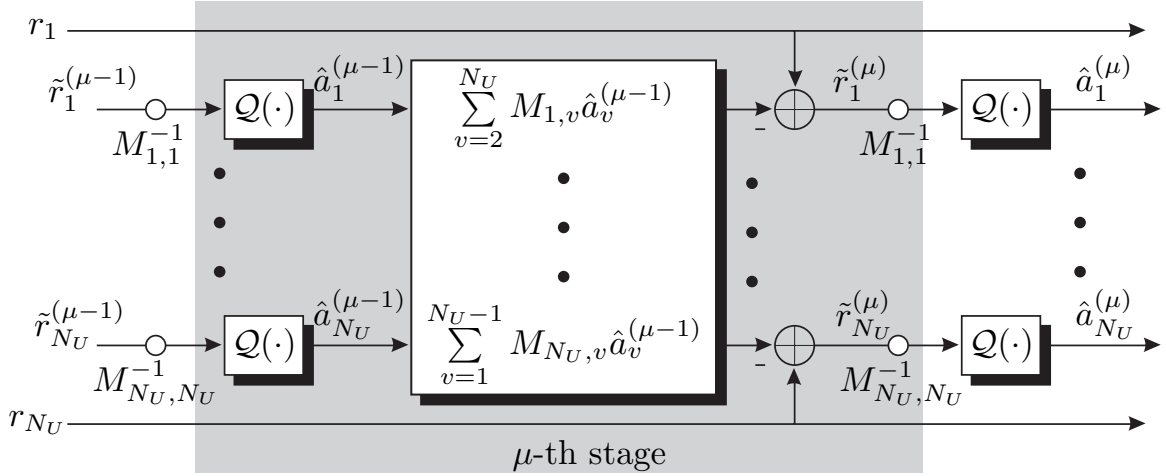


Figure 5.3.3: μ -th stage of a multi-stage detector for nonlinear parallel interference cancellation

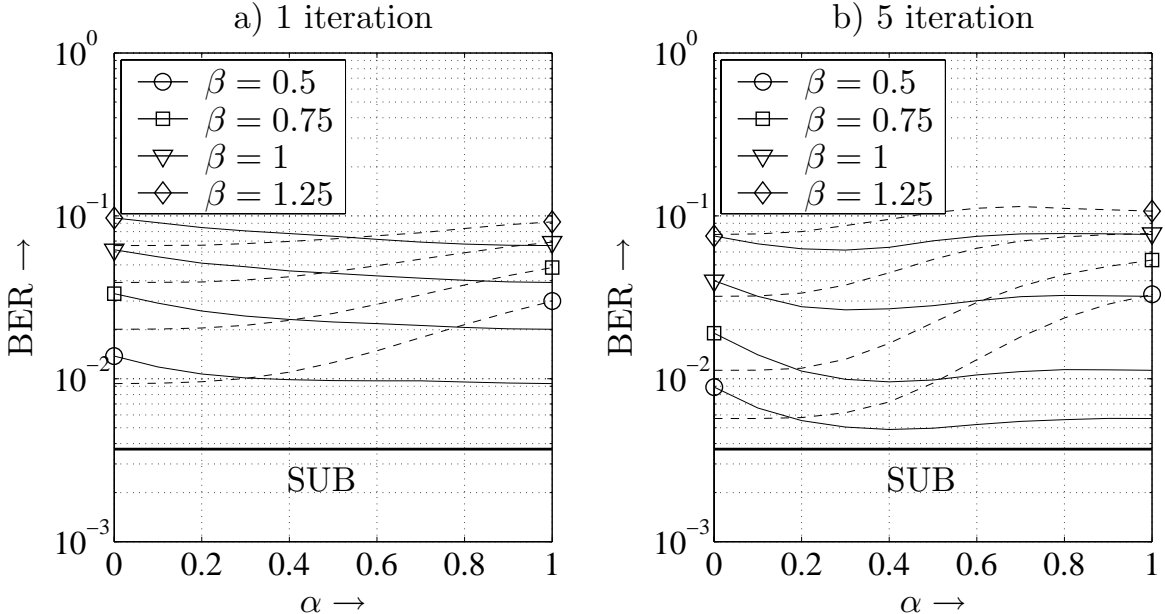


Figure 5.3.4: PIC-optimization for NL 1 and NL 2 in an OFDM-CDMA system with a 4-paths Rayleigh fading channel and $E_b/N_0 = 8$ dB
solid lines: NL 1, dashed lines: NL 2

Fig. 5.3.4 shows the performance of the nonlinearities NL 1 and NL 2 versus the design parameter α . Looking at NL 2, we observe that $\alpha_{\text{opt}}^{\text{NL } 2} = 0$ is always the best choice regardless of the number of iterations. Hence, NL 2 reduces to a simple clipper. Concerning NL 1, the optimum α depends on the iteration. In the first stage, the minimum bit error rate is also delivered by a clipper obtained with $\alpha_{\text{opt}}^{\text{NL } 1} = 1$. For the fifth stage, $0.3 \leq \alpha_{\text{opt}}^{\text{NL } 1} \leq 0.4$ is the best choice. Moreover, the comparison of NL 2 with NL 1 shows that NL 1 is at least as good as NL 2 and generally outperforms NL 2 [ZB03].

The same analysis has been performed for the tanh-function. From **Fig. 5.3.5** we recognize that $1 \leq \alpha \leq 2$ is an appropriate choice for a large variety of loads. With growing β , the optimum α becomes smaller and approaches one for $\beta = 1.25$. However, the differences are rather small in this interval. Only very low values of α result in a severe degradation because no interference is cancelled for $\alpha = 0$ leading to the matched filter performance. If α is chosen too large, the tanh-function saturates for most inputs and the error rate performance equals that of a hard decision.

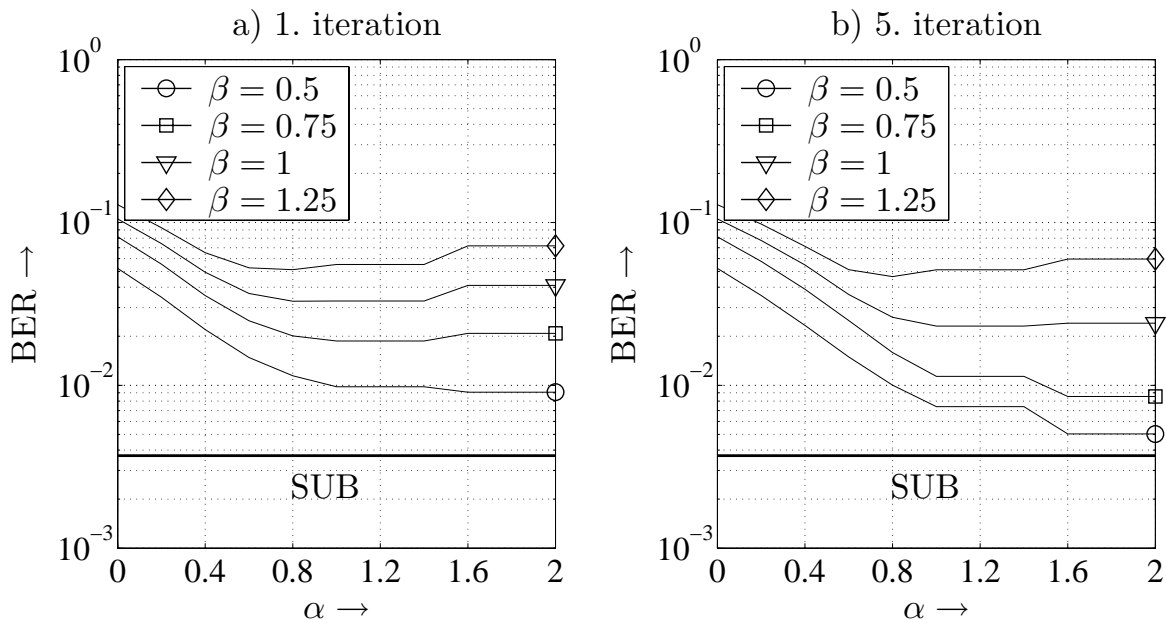


Figure 5.3.5: PIC -optimization for tanh and in an OFDM-CDMA system with a 4-paths Rayleigh fading channel and $E_b/N_0 = 8$ dB

Fig. 5.3.6a now compares all proposed nonlinearities for a fully loaded OFDM-CDMA system with $\beta = 1$ and 5 iterations. The tanh-function with optimized α shows the best performance among all schemes. NL 1 and clipping come closest to the tanh. The hard decision loses already 2 dB compared to the tanh. Although the nonlinearities consider the finite nature of the signal alphabet and all nonlinearities clearly outperform the matched filter, we observe an error floor and the single-user bound cannot be reached. **Fig. 5.3.6b** illustrates this loss versus β . At a load of $\beta = 1$, the error rate is increased by one decade compared to the single-user case, for $\beta = 1.5$, only the tanh can achieve a slight improvement compared to a simple matched filter. Therefore, we can conclude that nonlinear devices taking into account the finite nature of the signal alphabet improve the convergence behavior of PIC. The single-user bound is approximately reached up to loads of $\beta = 0.5$. For higher loads, performance degrades dramatically until no benefit to the matched filter can be observed.

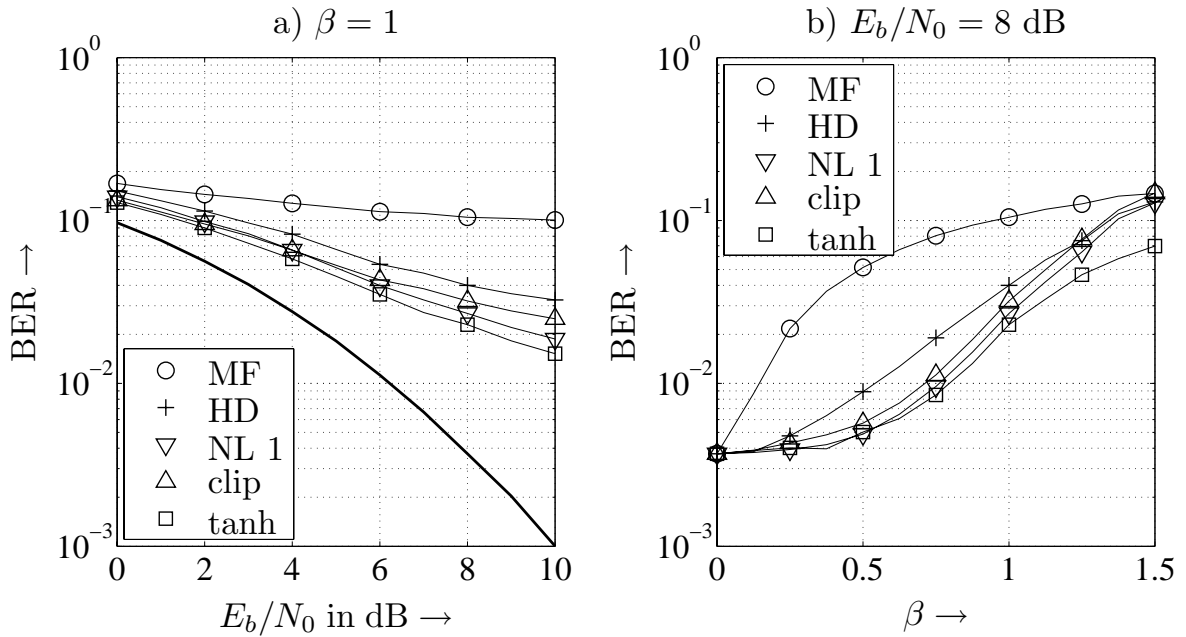


Figure 5.3.6: PIC -performance comparison of different nonlinearities with optimized α in an OFDM-CDMA system with 4-paths Rayleigh fading channel

Uncoded Successive Interference Cancellation

From linear interference cancellation techniques we know already that successive interference cancellation according to the Gauss-Seidel algorithm converges much better than the PIC. Consequently, we analyze now on the nonlinear SIC. **Fig. 5.3.7** analyzes the influence of the parameter α for NL 1 and NL 2 on the SIC performance. As already observed for PIC, $\alpha_{\text{opt}}^{\text{NL } 2} = 0$ reduces nonlinearity NL 2 to a simple clipper regardless of the load and the considered iteration. However, the influence of α on the error rate performance is much larger than for PIC. For $\alpha^{\text{NL } 2} \rightarrow 1$ which leads to a large interval of magnitudes where no interference is cancelled at all, the error rate tends to 0.5 for all iterations while the loss was quite moderate for the PIC.

Regarding NL 1, α has nearly no influence at the first iteration. In subsequent stages, e.g. the 5th iteration, the influence increases with growing load β and the lowest error rate is obtained for $\alpha_{\text{opt}}^{\text{NL } 1} = 0.4$. Again, NL 1 with optimum α shows a better performance than NL 2.

Fig. 5.3.8 depicts the optimization for the tanh-function. Astonishingly, the results in the first iteration differ from those of the parallel interference cancellation. The lowest error probability is obtained for $\alpha_{\text{opt}}^{\text{tanh}} = 2$ regardless of the load β . Also in subsequent stages, this choice of α represents a very good solution and it coincides with the results of the PIC.

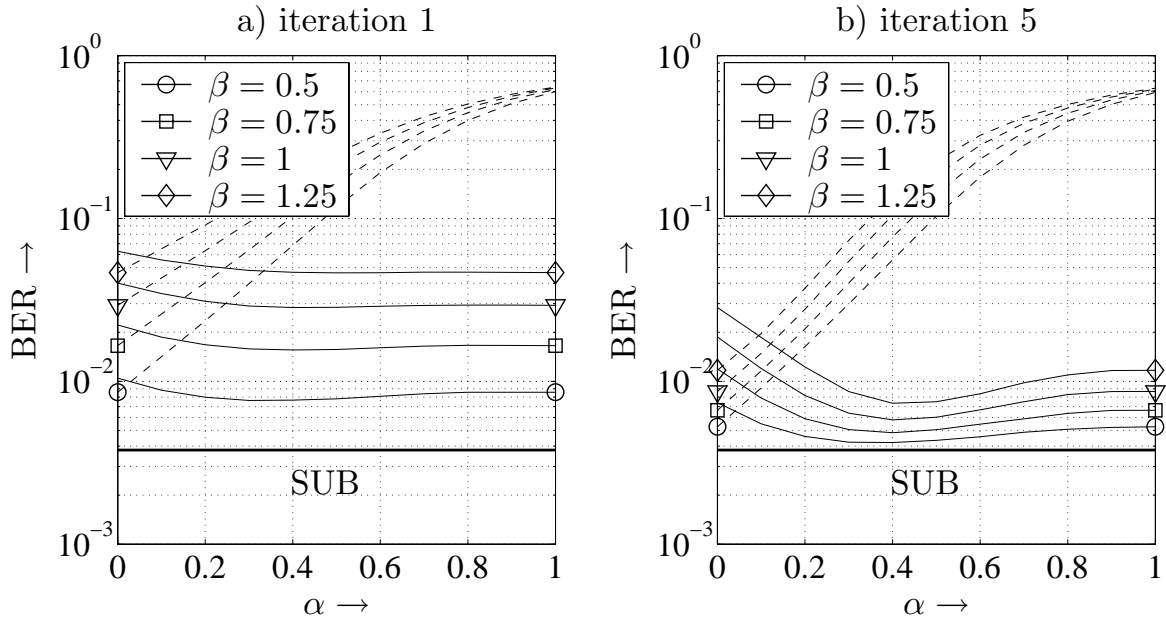


Figure 5.3.7: SIC-optimization for NL 1 and NL 2 in an OFDM-CDMA system with a 4-paths Rayleigh fading channel and $E_b/N_0 = 8$ dB
 solid lines: NL 1, dashed lines: NL 2

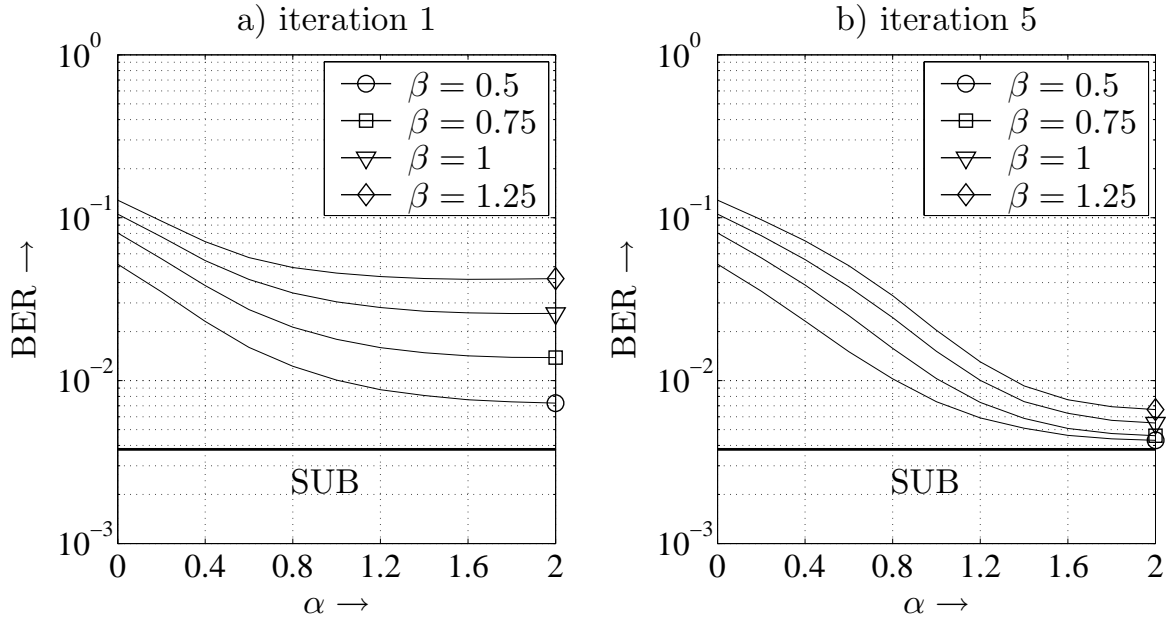


Figure 5.3.8: SIC-optimization for tanh in an OFDM-CDMA system with a 4-paths Rayleigh fading channel and $E_b/N_0 = 8$ dB

As can be seen from **Fig. 5.3.9**, NL 1 outperforms all other schemes and represents the best nonlinearity under consideration. For $\beta = 1$, the single-user bound is reached within a gap of 0.5 dB for all signal to noise ratios. The clipper (NL 2 with $\alpha = 0$) and the tanh come closest to NL 1 while hard decisions lose remarkably.

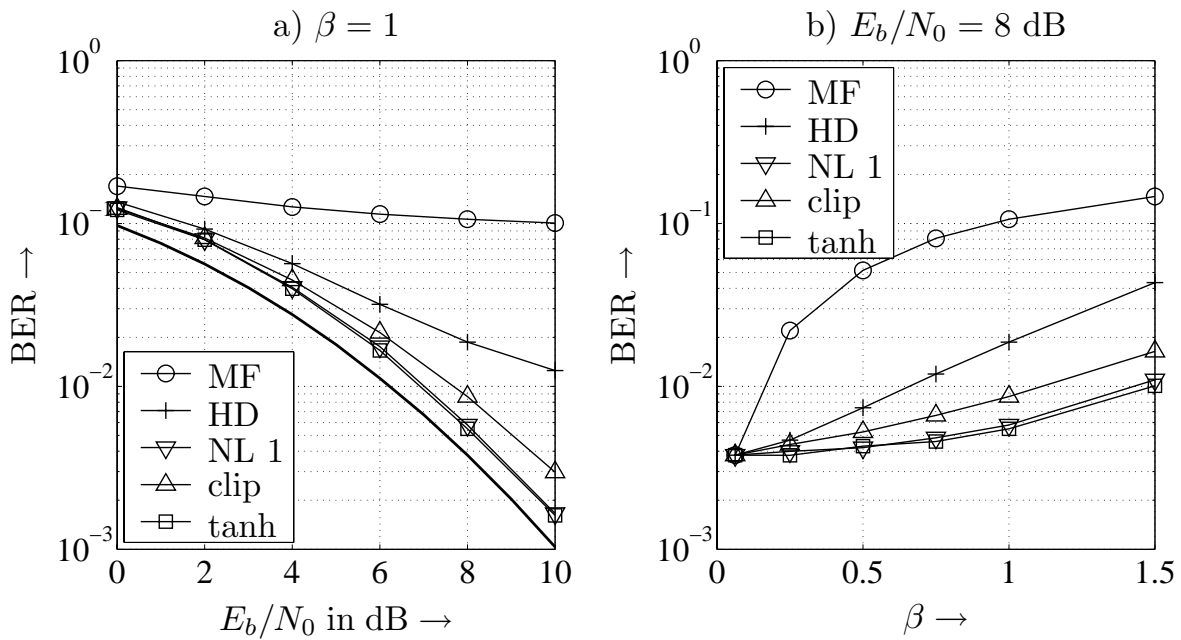


Figure 5.3.9: Performance comparison of different nonlinearities with optimized α for SIC in OFDM-CDMA system with 4-paths Rayleigh fading channel (5 iterations)

From **Fig. 5.3.9b** we see that NL 1 and the tanh are able to keep the loss compared to the single-user bound quite low up to a load of $\beta = 1.5$. Even for this high load, the gain over the matched filter is significant. Hence, we can conclude that the considered nonlinearities with optimum design parameters perform similar for PIC and SIC. However, SIC still shows a better convergence behaviour and comes close to the single-user user bound even for high loads.

Performance of Nonlinear SIC for QPSK Modulation

If we change from BPSK to QPSK, the effective interference is doubled (compare Chapter 4). Only slight changes are necessary in order to adapt the presented algorithms to QPSK. All nonlinearities have to be applied separately to real and imaginary parts of the signals. Due to the doubled interference, we obtain for $\beta = 0.75$ and QPSK nearly the same results as for $\beta = 1.5$ and BPSK.

Fig. 5.3.10 analyzes the influence of the parameter α of the nonlinearities for an OFDM-CDMA system with $\beta = 1$ and a 4-paths Rayleigh fading channel. For medium signal to noise ratios like $E_b/N_0 = 8$ dB, the results coincide with those already obtained for BPSK. Nearly no influence can be observed in the first stage. For further iterations and larger SNR, e.g. 20 dB, NL 1 requires a larger α to perform optimal. Due to the high interference, the estimates are less reliable and the step towards ± 1 occurs at higher amplitudes. Concerning the tanh, $\alpha_{\text{opt}}^{\text{tanh}} = 2$ still represents the a very good choice.

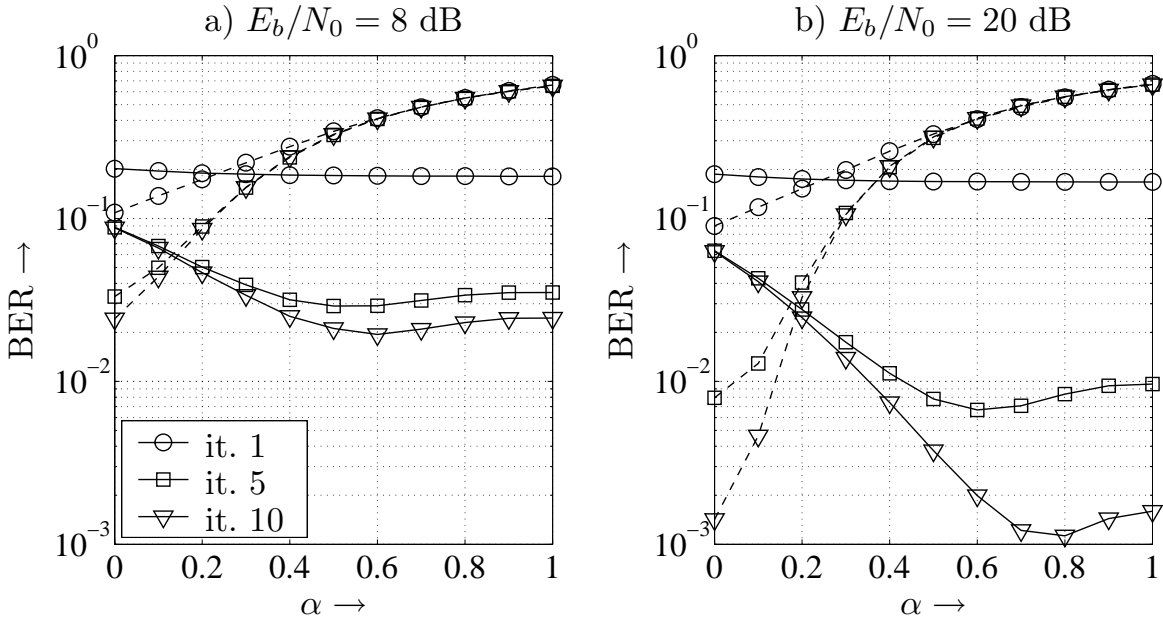


Figure 5.3.10: SIC-optimization for NL 1 and NL 2 in an OFDM-CDMA system with $\beta = 1$, QPSK and a 4-paths Rayleigh fading channel
 solid lines: NL 1, dashed lines: NL 2

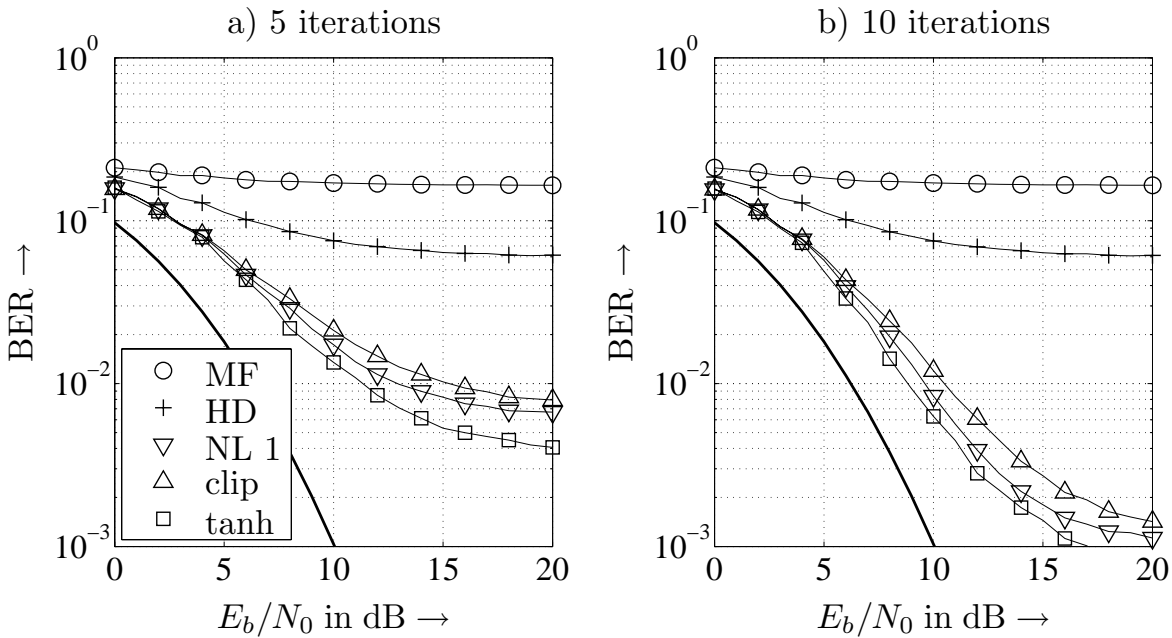


Figure 5.3.11: SIC-performance for nonlinearities with optimized α in an OFDM-CDMA system with QPSK and 4-paths Rayleigh fading channel ($\beta = 1$)

Fig. 5.3.11 shows the bit error rate performance for five and ten iterations and optimized α for NL 1 and tanh. While the hard decision does not gain from additional iterations, the nonlinear function NL 1, the tanh function and the clipper enhance the error rate remarkably. The tanh with optimized α is still the best

choice. However, for this high load there remains a large gap to the single user bound (bold line) that roughly amounts to 4 dB at an error rate of $2 \cdot 10^{-3}$.

5.3.3 Nonlinear Coded Interference Cancellation

Resuming the way from linear multi-stage receivers to nonlinear interference cancellation schemes it is straightforward to incorporate the channel decoder into the iterative structures in coded CDMA systems. Again, we restrict to BPSK and QPSK schemes for notational simplicity. The structure of the transmitter is already known from Fig. 5.1.1. The corresponding receiver for parallel interference cancellation is depicted in **Fig. 5.3.12**. After the matched filter bank, the obtained signals r_u , $1 \leq u \leq N_U$, are de-interleaved and FEC decoded. The decoder delivers either soft-outputs $L(\hat{b}_u)$ of the code bits or hard estimates \hat{b}_u . Soft-outputs can be generated by the BCJR or the Max-Log-MAP decoder while hard-outputs are obtained by the Viterbi algorithm.

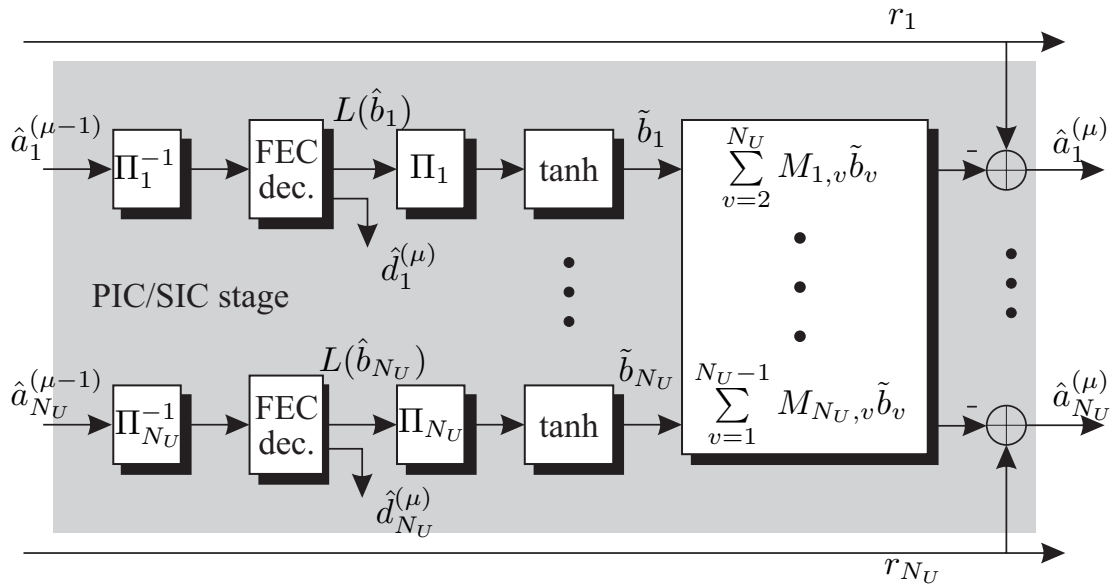


Figure 5.3.12: Single stage of a nonlinear PIC receiver in coded CDMA systems

Next, the outputs are interleaved and processed by a nonlinear function. This is necessary for soft-outputs because log-likelihoods are generally not limited in magnitude while the true code bits are either $+1$ or -1 . From Chapter 3 we know that the expectation of a bit can be calculated with its log-likelihood ratio by $\tanh(L/2)$ (see (3.4.4) on page 108). This is exactly the reason for using the tanh. Finally, the interfering signals are weighted with the correlation coefficients $M_{u,v}$, summed, and subtracted from the matched filter output r_u . The obtained estimate represents the input of the next stage.

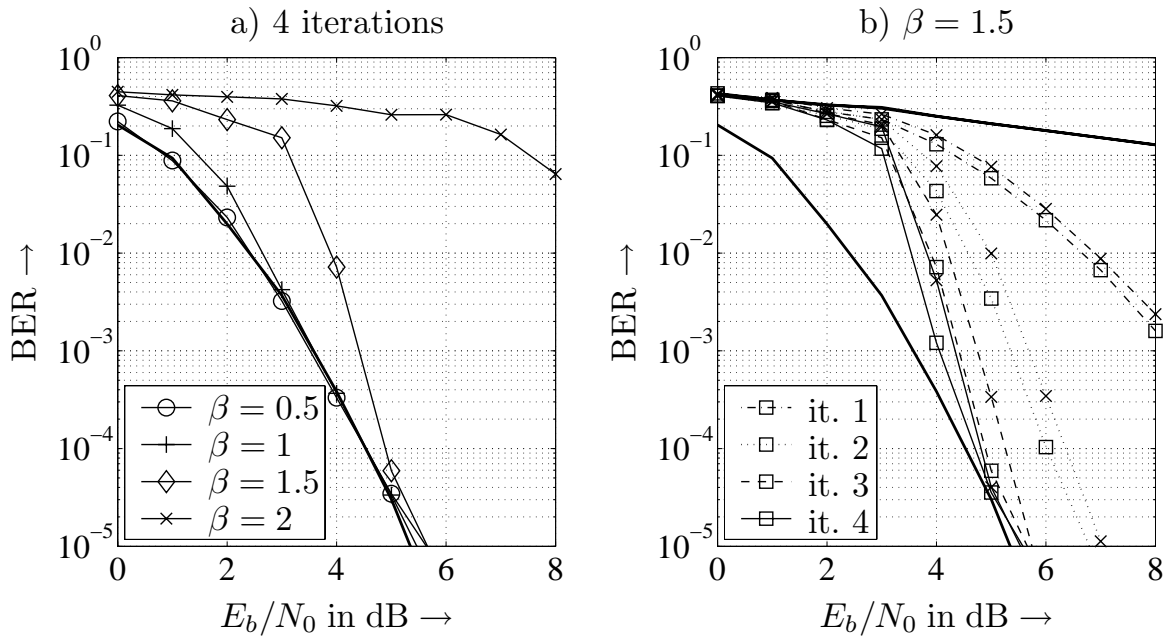


Figure 5.3.13: PIC-performance of coded OFDM-CDMA system with 4-paths Rayleigh fading channel (bold line: single-user bound)
a) comparing various loads,
b) comparing hard output (\times) and soft-output (\square) decoding

Fig. 5.3.13a shows the performance of an OFDM-CDMA system with a half-rate convolutional code of constraint length $L_c = 7$ and BPSK. As mobile radio channel, a 4-paths Rayleigh fading channel with uniform power delay profile was employed. Moreover, each user has in the average the same SNR. After 4 PIC iterations, the single-user bound (SUB) is obtained even for $\beta = 1.5$ what is equivalent to a spectral efficiency of $\eta = R_c \cdot \beta = 0.75$. We see that coding helps to improve the convergence of iterative interference cancellation schemes. The reliability of the estimated interference is enhanced leading to a better interference suppression. At low SNR, a gap to the SUB occurs that grows for increasing load. For $\beta = 2$, the PIC scheme does not converge anymore.

Fig. 5.3.13b compares hard and soft-decision outputs at the decoder. The upper bold solid line denotes the matched filter performance and the lower bold solid curve represents the SUB. Naturally, the performance after the first decoding (SUMF, upper solid line) is the same. For subsequent iterations, the soft-output always outperforms the hard-decision output. However, the differences are rather small and amount at most to 0.5 dB. For this example, both, hard and soft-output decoding reach the SUB at error rates below 10^{-4} . Nevertheless, for extremely high loads, convergence may be maintained with soft-output decoding while hard-decision decoding will fail.

Next, parallel and successive interference cancellation are compared in **Fig. 5.3.14a**. The upper bold solid line represents the matched filter performance, the lower bold solid curve the single-user bound. After 3 PIC iterations, both, SIC

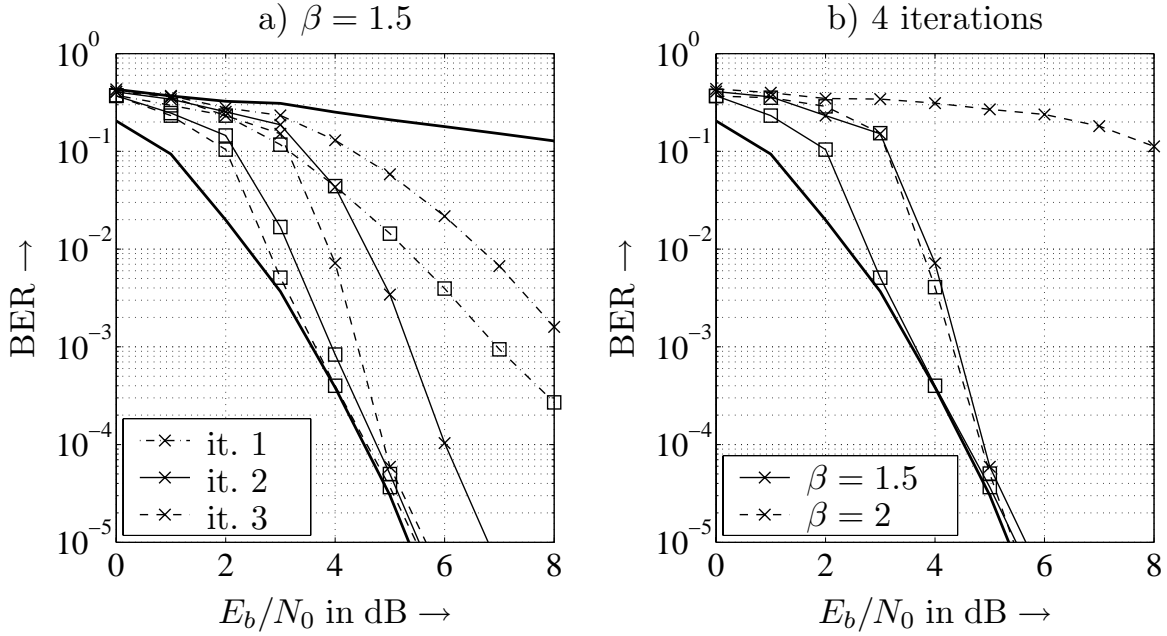


Figure 5.3.14: Performance of coded PIC (\times) and SIC (\square) for OFDM-CDMA system with 4-paths Rayleigh fading channel (bold line: single-user bound)
a) comparing convergence of PIC and SIC,
b) comparing PIC and SIC for various loads

and PIC reach the SUB. However, successive interference cancellation converges faster and needs in this example one iteration less than the PIC scheme. Hence, the benefits of SIC are preserved when coding is applied. In **Fig. 5.3.14b**, the load is increased to $\beta = 2$, i.e. the spectral efficiency $\eta = 1$ bit/s/Hz of such a system is twice as high as for half-rate coded TDMA or FDMA systems [Küh01d, Küh01a]. We see that the SIC scheme performs as good for $\beta = 2$ as the PIC approach for $\beta = 1.5$. For a doubly loaded system, the PIC scheme does not converge anymore.

As already explained for the uncoded system, there exist a major difference between parallel and successive interference cancellation. Due to the problem of error propagation, the order of detection is crucial for SIC. This dependency is illustrated in **Fig. 5.3.15** comparing sorted and unsorted SIC. Sorting is implemented by calculating the average magnitude of the decoder output and starting with the strongest user. This is probably not the best strategy, but it can be easily implemented. Obviously, sorting leads to a faster convergence. Especially at low SNR, the gap to the single-user bound can be decreased. Therefore, sorting is always applied for SIC in subsequent parts.

Fig. 5.3.16 now compares the performance of SIC for BPSK and QPSK modulation. We know from Section 4.2 that the use of QPSK in the uplink doubles the effective interference. Since, the spectral efficiency is also doubled because we transmit twice as many bits per symbol as for BPSK, $\eta_{\text{QPSK}} = 2\eta_{\text{BPSK}}$ holds. After 4 PIC iterations, we observe that the single-user bound has been reached

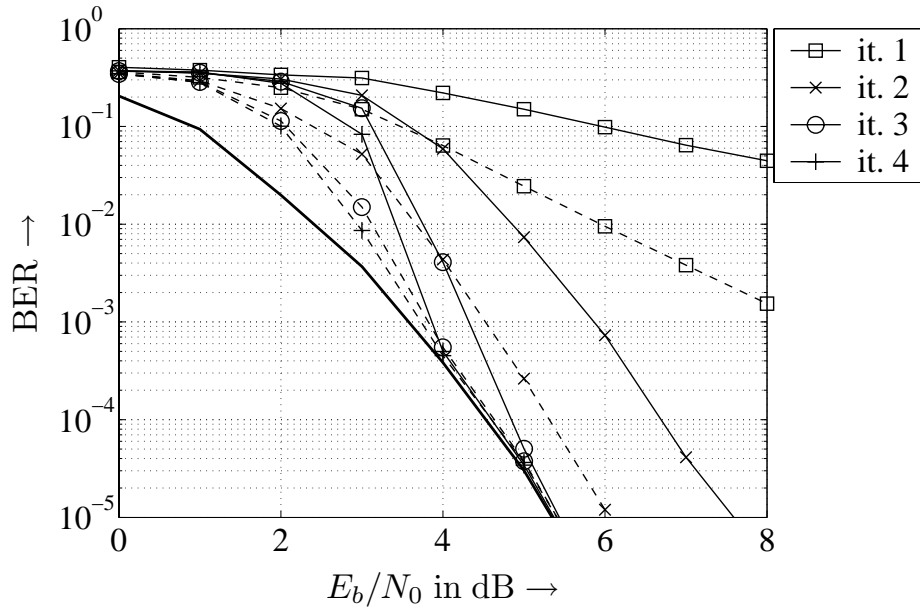


Figure 5.3.15: SIC-performance (solid: unsorted, dashed: sorted) for coded OFDM-CDMA system with 4-paths Rayleigh fading channel and $\beta = 2$. (bold line: single-user bound)

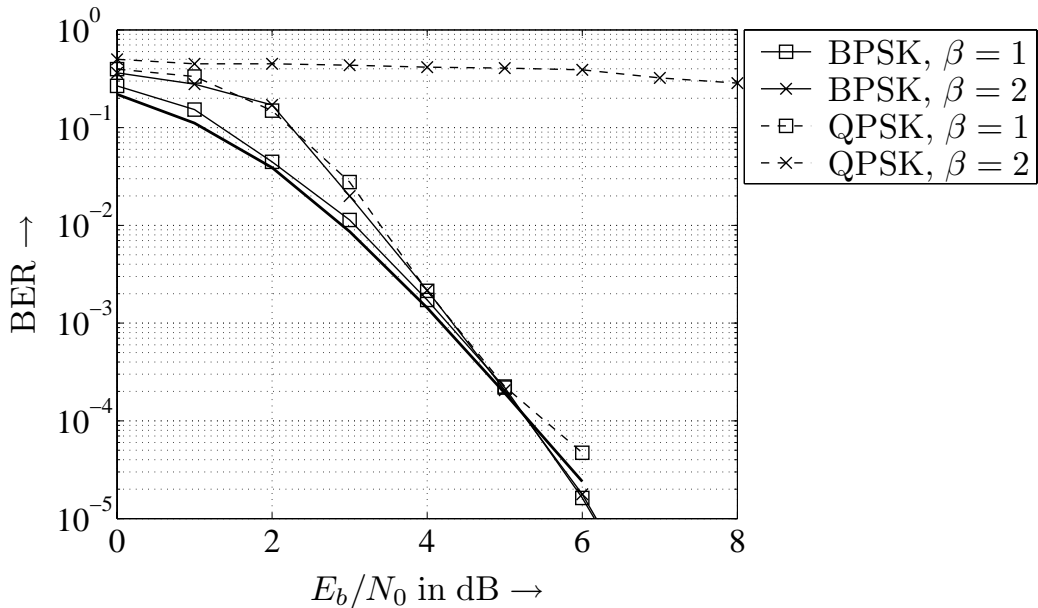


Figure 5.3.16: Performance of SIC for OFDM-CDMA system with a half-rate convolutional code ($L_c = 7$) and 4-paths Rayleigh fading channel, (bold line: single-user bound)

for QPSK and $\beta = 1$. This is equivalent to $\beta = 2$ for BPSK. No convergence is obtained for $\beta = 2$ and QPSK because the initial SINR is too low for achieving reliable estimates from the decoders.

Finally, the influence of different convolutional codes is analyzed. **Fig. 5.3.17** compares two half-rate convolutional codes: the already used $L_c = 7$ code and a weaker $L_c = 3$ code. Looking at Fig. a), we see that three or four iterations suffice to reach the SUB for BPSK. Concerning QPSK, even ten iterations cannot close the gap of approximately 4 dB. Contrarily, convergence starts earlier with the weak $L_c = 3$ code in Fig. b). Although the $L_c = 3$ code has a worse single-user bound, it performs better than the strong convolutional code and reaches its SUB even for $\beta = 2$ and QPSK. Taking into account the difference of 2 dB between the two SUB's, there still remains a gain of 2 dB compared to the $L_c = 7$ code.

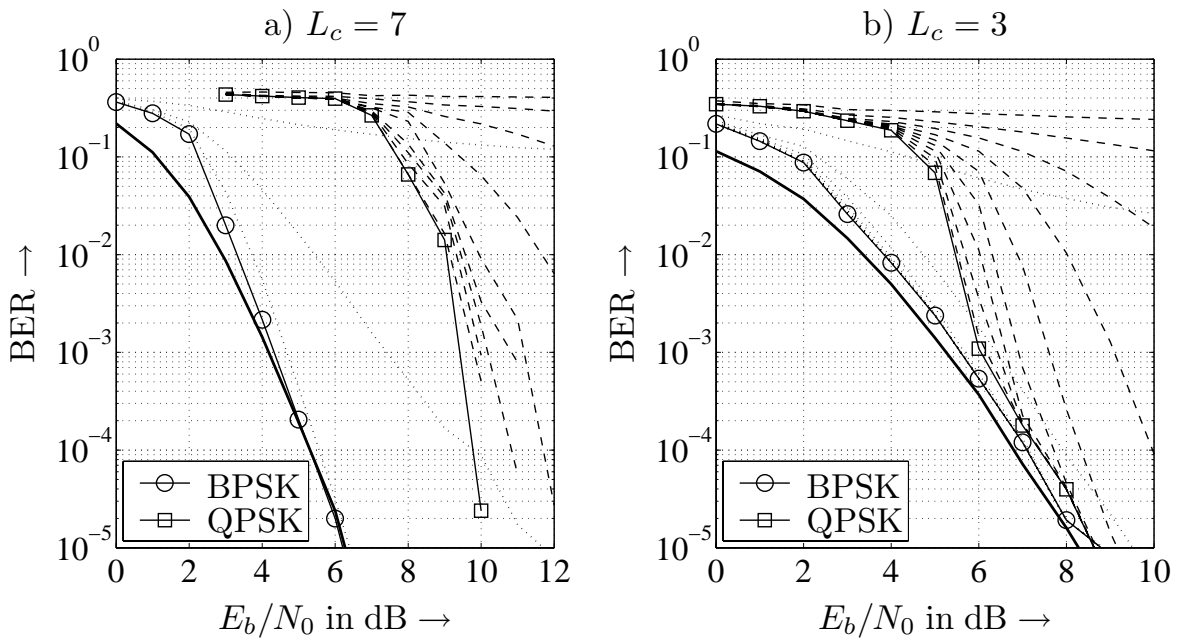


Figure 5.3.17: Performance of half-rate coded OFDM-CDMA system with $\beta = 2$, a 4-paths Rayleigh fading channel and different convolutional codes (bold line: single-user bound)

The explanation of this behavior can be found by observing the SUB curves for both codes in Fig. 5.3.17. We see that the $L_c = 3$ code has a slightly better performance at low SNR. For larger SNR, the curves intersect and the $L_c = 7$ code has a better performance. However, the first interference cancellation stage suffers from noise as well as severe interference that was not yet cancelled. For increasing loads, the SINR at the decoder inputs becomes smaller and smaller until it reaches the intersection of both curves. For higher loads, the weak code now performs better. In our example, parameters were chosen such that the strong code cannot achieve convergence while the $L_c = 3$ code still reaches its SUB. Therefore, we can conclude that strong error control codes are not always the best choice.⁵

⁵It has to be mentioned that this conclusion holds for uniform power distribution among the users. If different power levels occur (near-far effects), strong codes can have a better performance

5.4 Combining Linear MUD and Nonlinear SIC

5.4.1 BLAST Detection

As we saw from the previous results, the first detection stage suffers severely from multi-user interference. Hence, its error rate will dominate the performance of subsequent detection steps due to error propagation. The overall performance and the convergence speed can be improved by a linear suppression of the interference prior to the first detection stage. The BLAST (Bell Labs Layered Space Time) detection of the Bell Labs [Fos96, FG98, GFWV98, WFGV98] pursues this approach for multiple antenna systems. It can be directly applied to CDMA systems since both systems have similar structures and the same mathematical description $\mathbf{y} = \mathbf{S}\mathbf{a} + \mathbf{n}$.

In a first step, a linear filter \mathbf{w}_1 is applied suppressing the interference for user 1. The filter can be designed according to the zero-forcing or MMSE criterion, i.e. $\underline{\mathbf{w}}_1$ denotes the first row of $\mathbf{W}_1 = \mathbf{W}_{\text{ZF}}$ or $\mathbf{W}_1 = \mathbf{W}_{\text{MMSE}}$ according to Section 5.2 yielding

$$\tilde{a}_1 = \underline{\mathbf{w}}_1 \cdot \mathbf{y} . \quad (5.4.1)$$

Next, the symbol $\hat{a}_1 = \mathcal{Q}(\tilde{a}_1)$ can be decided with improved reliability because less interference disturbs this decision⁶. After detecting \hat{a}_1 , its influence onto the remaining signals can be removed by subtracting its contribution $\mathbf{s}_1\hat{a}_1$ from the received vector \mathbf{y} (interference cancellation)

$$\tilde{\mathbf{y}}_2 = \mathbf{y} - \mathbf{s}_1\hat{a}_1 , \quad (5.4.2)$$

where the vector \mathbf{s}_1 represents the first column of the system matrix \mathbf{S} (see Fig. 4.2.7 or (4.3.26)). The residual signal $\tilde{\mathbf{y}}_2$ is then processed by a second filter $\underline{\mathbf{w}}_2$. It is obtained by removing \mathbf{s}_1 from \mathbf{S} and calculating the zero-forcing or MMSE filter \mathbf{W}_2 for the reduced system matrix $\tilde{\mathbf{S}}_2 = [\mathbf{s}_2 \ \cdots \ \mathbf{s}_{N_U}]$. The first row of \mathbf{W}_2 denotes the filter $\underline{\mathbf{w}}_2$ that is used for suppressing the interference of the second user. This procedure is repeated until all users have been detected.

In order to determine the linear filters in the different detection steps, the system matrices describing the reduced systems have to be inverted. This causes high implementation costs. However, a much more convenient way exists that avoids multiple matrix inversions. This approach leads to identical results and is presented in the next section.

than weak codes [CMT04].

⁶Instead of performing a hard decision, other nonlinear functions as analyzed in Section 5.3 can be used.

5.4.2 QL Decomposition for Zero-Forcing Solution

In this subsection an alternative implementation of the BLAST detector is introduced. It saves computational complexity compared to the original detector introduced in the last section. As for the linear multi-user detectors, we can distinguish the zero-forcing and the MMSE solution. We start with the derivation of the QL decomposition for the linear zero-forcing solution⁷.

Going back to the model $\mathbf{y} = \mathbf{Sa} + \mathbf{n}$, the system matrix \mathbf{S} can be decomposed into an $N_s \times N_U$ matrix \mathbf{Q} with orthogonal columns \mathbf{q}_u of unit lengths and an $N_U \times N_U$ lower triangular matrix $\tilde{\mathbf{L}}$ [GvL93]

$$\mathbf{y} = \mathbf{Q}\mathbf{La} + \mathbf{n}. \quad (5.4.3)$$

Due to $\mathbf{Q}^H\mathbf{Q} = \mathbf{I}_{N_U}$, the multiplication of \mathbf{y} with \mathbf{Q}^H yields

$$\tilde{\mathbf{y}} = \mathbf{Q}^H \cdot \mathbf{y} = \mathbf{La} + \mathbf{Q}^H \mathbf{n} = \begin{bmatrix} L_{1,1} & 0 & & \\ L_{2,1} & L_{2,2} & & \mathbf{0} \\ \vdots & \vdots & \ddots & \\ L_{N_U,1} & L_{N_U,2} & \cdots & L_{N_U,N_U} \end{bmatrix} \cdot \mathbf{a} + \tilde{\mathbf{n}} \quad (5.4.4)$$

with $\tilde{\mathbf{n}}$ representing still white Gaussian noise because \mathbf{Q} is unitary. In order to clarify the effect of multiplying with \mathbf{Q}^H , we consider the matched filter outputs $\mathbf{r} = \mathbf{S}^H \mathbf{y} = \mathbf{Ra} + \mathbf{S}^H \mathbf{n}$. Performing a Cholesky decomposition [GvL93] of $\mathbf{R} = \mathbf{L}^H \mathbf{L}$ with the lower triangular matrix \mathbf{L} results in

$$\mathbf{r} = \mathbf{L}^H \mathbf{La} + \mathbf{S}^H \mathbf{n} \Rightarrow \tilde{\mathbf{r}} = \mathbf{La} + \mathbf{L}^{-H} \mathbf{S}^H \mathbf{n}. \quad (5.4.5)$$

Comparing (5.4.4) with (5.4.5) illustrates that the multiplication of \mathbf{y} with \mathbf{Q}^H can be split into two steps. First, a matched filter is applied providing the colored noise vector $\mathbf{S}^H \mathbf{n}$. Since the covariance matrix of the modified noise vector is $\Phi = \sigma_N^2 \mathbf{R} = \sigma_N^2 \mathbf{L}^H \mathbf{L}$, the second multiplication with $\Phi^{-1/2} = \mathbf{L}^{-H}$ can be interpreted as whitening.

Due to the triangular structure of \mathbf{L} in (5.4.4), the received vector $\tilde{\mathbf{y}}$ has been partly freed of interference, e.g. \tilde{y}_1 does only depend on a_1 disturbed by the noise term \tilde{n}_1 . Hence, it can be directly estimated by appropriate scaling and the application of a nonlinearity $\mathcal{Q}(\cdot)$

$$\hat{a}_1 = \mathcal{Q}(L_{1,1}^{-1} \cdot \tilde{y}_1). \quad (5.4.6)$$

The obtained estimate can be inserted in the second row to subtract interference from \tilde{y}_2 and so on. We obtain the u -th estimate by

$$\hat{a}_u = \mathcal{Q} \left(\frac{1}{L_{u,u}} \cdot \left[\tilde{y}_u - \sum_{v=1}^{u-1} L_{u,v} \cdot \hat{a}_v \right] \right). \quad (5.4.7)$$

⁷Throughout the subsequent derivation, the QL decomposition can be used equivalently.

This procedure termed QL-SIC can be continued until the last symbol a_{N_u} has been estimated so that a successive interference cancellation as depicted in **Fig. 5.3.6** is carried out. With this recursive procedure, the matrix inversions of the original BLAST detection can be circumvented and only a single QL decomposition has to be carried out. Furthermore, we have exploited the finite nature of the signal alphabet by introducing $\mathcal{Q}(\cdot)$.

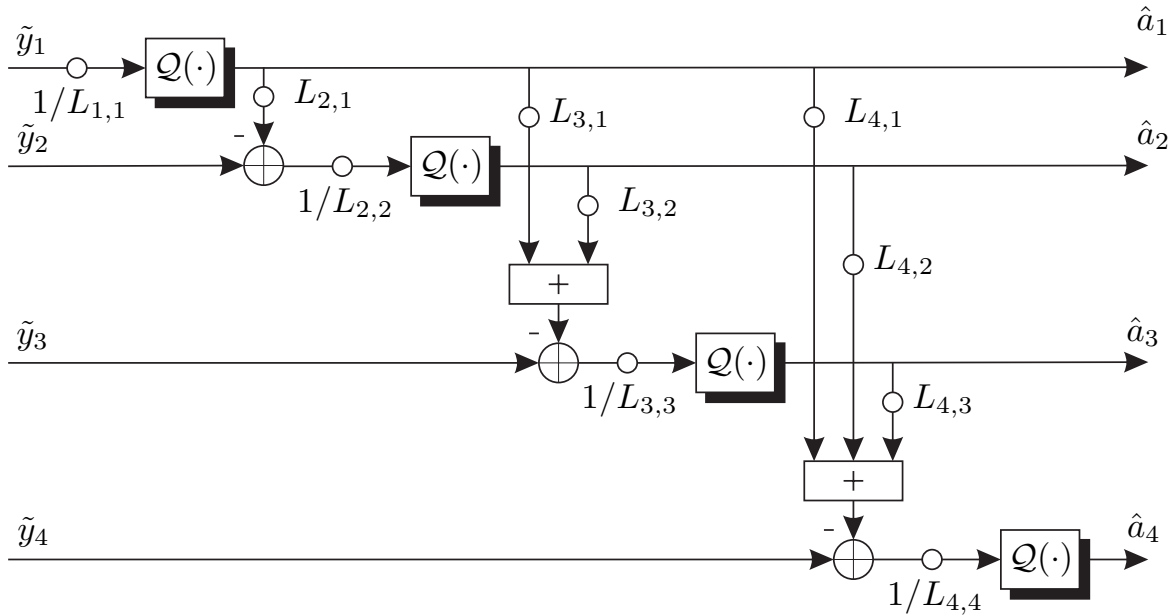


Figure 5.4.1: Illustration of interference cancellation after decomposing \mathbf{S} into \mathbf{Q} and \mathbf{L} and filtering \mathbf{y} with \mathbf{Q}^H

The linear filtering with \mathbf{Q} has to cope partly with the same problems as decorrelator. For the first user, all other users have to be linearly suppressed. Since all columns of \mathbf{Q} have unit length, the noise is not amplified but the desired signal may be very weak. This result in a small diagonal element in \mathbf{L} and, hence, a low signal to noise ratio. In successive steps, more interference is already cancelled and the columns of \mathbf{Q} tend more and more towards a matched filter. In multiple antenna systems, this affects also the achievable diversity gain as shown in Section 6.3.

From the above explanation we can also conclude that the proposed scheme cannot be directly applied to systems with a load $\beta > 1$. For $N_U > N_S$, the system matrix \mathbf{S} has more columns than rows. Since only N_s orthogonal columns exist that span the N_s dimensional space, \mathbf{Q} is an $N_s \times N_s$ matrix. Consequently, \mathbf{L} would not be a lower triangular matrix but has the form

$$\mathbf{L} = \left[\begin{array}{cccc|ccc} L_{1,1} & & & & L_{1,N_s+1} & \dots & L_{1,N_U} \\ L_{2,1} & L_{2,2} & & & L_{2,N_s+1} & \dots & L_{2,N_U} \\ \vdots & \vdots & \ddots & & \vdots & & \vdots \\ L_{N_U,1} & L_{N_U,2} & \dots & L_{N_U,N_s} & L_{N_U,N_s+1} & \dots & L_{N_U,N_U} \end{array} \right].$$

We recognize that all layers – even the first – now suffer from interference. Further information about overloaded systems in the context of multiple antenna systems can be found in [DGC03]. Concerning the MMSE solution, a direct implementation is possible even for $\beta > 1$ (see Section 5.4.3).

Improvement for Real Modulation Schemes

From linear detectors like decorrelator and MMSE filter we know already that remarkable improvements can be achieved by taking into account that the imaginary part of the transmitted symbols does not contain information for real-valued modulation schemes. In order to exploit this knowledge also for the QL decomposition, we have to separate real and imaginary parts for all terms of the equation $\mathbf{y} = \mathbf{S}\mathbf{a} + \mathbf{n}$. With \mathbf{y}' , \mathbf{S}' , \mathbf{a}' and \mathbf{n}' denoting real parts and \mathbf{y}'' , \mathbf{S}'' , \mathbf{a}'' and \mathbf{n}'' representing the imaginary parts, we obtain

$$\begin{bmatrix} \mathbf{y}' \\ \mathbf{y}'' \end{bmatrix} = \begin{bmatrix} \mathbf{S}' & -\mathbf{S}'' \\ \mathbf{S}'' & \mathbf{S}' \end{bmatrix} \cdot \begin{bmatrix} \mathbf{a}' \\ \mathbf{a}'' \end{bmatrix} + \begin{bmatrix} \mathbf{n}' \\ \mathbf{n}'' \end{bmatrix}. \quad (5.4.8)$$

Since $\mathbf{a}'' = \mathbf{0}$ for real modulation schemes, $\mathbf{a}' = \mathbf{a}$ holds and (5.4.8) reduces to

$$\begin{bmatrix} \mathbf{y}' \\ \mathbf{y}'' \end{bmatrix} = \begin{bmatrix} \mathbf{S}' \\ \mathbf{S}'' \end{bmatrix} \cdot \mathbf{a}' + \begin{bmatrix} \mathbf{n}' \\ \mathbf{n}'' \end{bmatrix} = \mathbf{S}^r \cdot \mathbf{a} + \mathbf{n}^r. \quad (5.4.9)$$

From (5.4.9), we see that the real system matrix has twice as many rows as \mathbf{S} . This leads generally to a better condition and, therefore, a lower noise amplification in the zero-forcing case. Representing the received symbols by separated real and imaginary parts, we simply have to decompose \mathbf{S}^r . The obtained real matrices \mathbf{Q}^r and \mathbf{L}^r are then used for the subsequent detection procedure as described above. Next, we consider a possible implementation of the QL decomposition.

Modified Gram-Schmidt Algorithm

The unsorted QL decomposition

$$\begin{aligned} \mathbf{S} &= [\mathbf{s}_1 \cdots \mathbf{s}_{N_U-1} \mathbf{s}_{N_U}] = \mathbf{Q}\mathbf{L} \\ &= [\mathbf{q}_1 \cdots \mathbf{q}_{N_U-1} \mathbf{q}_{N_U}] \cdot \begin{bmatrix} L_{1,1} & & & \\ \vdots & \ddots & & \\ L_{N_U-1,1} & L_{N_U-1,2} & L_{N_U-1,N_U-1} & \\ L_{N_U,1} & L_{N_U,2} & L_{N_U,N_U-1} & L_{N_U,N_U} \end{bmatrix} \end{aligned} \quad (5.4.10)$$

can be implemented by the modified Gram-Schmidt procedure [GvL93]. The orthonormal columns \mathbf{q}_u are determined successively one after the other. Neglecting for the moment an appropriate sorting, we start with the last column $\mathbf{q}_{N_U} = \mathbf{s}_{N_U} / \|\mathbf{s}_{N_U}\|$, i.e. \mathbf{q}_{N_U} points into the same direction as the last signature \mathbf{s}_{N_U} and has unit norm. Due to $\mathbf{s}_{N_U} = L_{N_U,N_U} \cdot \mathbf{q}_{N_U}$, $L_{N_U,N_U} = \|\mathbf{s}_{N_U}\|$ holds. The next column vector \mathbf{q}_{N_U-1} must be orthogonal to \mathbf{q}_{N_U} . Hence, we first subtract the projection of \mathbf{s}_{N_U-1} onto \mathbf{q}_{N_U}

$$L_{N_U,N_U-1} = \mathbf{q}_{N_U}^H \mathbf{s}_{N_U-1} \Rightarrow \tilde{\mathbf{q}}_{N_U-1} = \mathbf{s}_{N_U-1} - L_{N_U,N_U-1} \cdot \mathbf{q}_{N_U} \quad (5.4.11a)$$

and normalize the rest with L_{N_U-1,N_U-1} to length one.

$$L_{N_U-1,N_U-1} = \|\tilde{\mathbf{q}}_{N_U-1}\| \Rightarrow \mathbf{q}_{N_U-1} = \tilde{\mathbf{q}}_{N_U-1} / L_{N_U-1,N_U-1} \quad (5.4.11b)$$

The third column \mathbf{q}_{N_U-2} has to be perpendicular to the plane spanned by \mathbf{q}_{N_U} and \mathbf{q}_{N_U-1} . Hence, the above procedure has to be repeated and we obtain the general construction of the u -th column \mathbf{q}_u .

$$L_{v,u} = \mathbf{q}_v^H \cdot \mathbf{s}_u \text{ for } u \leq v < N_U \Rightarrow \tilde{\mathbf{q}}_u = \mathbf{s}_u - \sum_{v=u+1}^{N_U} L_{v,u} \cdot \mathbf{q}_v \quad (5.4.12a)$$

$$L_{u,u} = \|\tilde{\mathbf{q}}_u\| \Rightarrow \mathbf{q}_u = \tilde{\mathbf{q}}_u / L_{u,u} \quad (5.4.12b)$$

This procedure develops \mathbf{Q} and \mathbf{L} from right to left and has to be continued until all N_U columns in \mathbf{Q} and the corresponding elements in \mathbf{L} have been determined. Subtracting the projections of the unprocessed columns $\mathbf{s}_{v < u}$ onto the new orthonormal column \mathbf{q}_u immediately after fixing \mathbf{q}_u (steps (5) to (8)), we obtain the algorithm summarized in Table 5.4.1.

Optimum Post-Sorting Algorithm

Obviously, successive processing always leads to the problem of error propagation. Hence, we have to find the optimum order of detection that minimizes the risk of

Table 5.4.1: Pseudo code for modified Gram-Schmidt algorithm

```

(1) Initialize with  $\mathbf{L} = \mathbf{0}$ ,  $\mathbf{Q} = \mathbf{S}$ 
(2) for  $u = N_U, \dots, 1$ 
(3)   determine diagonal element  $L_{u,u} = \|\mathbf{q}_u\|$ 
(4)   normalize  $\mathbf{q}_u = \mathbf{q}_u / L_{u,u}$  to unit length
(5)   for  $v = 1, \dots, u - 1$ 
(6)     calculate projections  $L_{u,v} = \mathbf{q}_u^H \cdot \mathbf{q}_v$ 
(7)      $\mathbf{q}_v = \mathbf{q}_v - L_{u,v} \cdot \mathbf{q}_u$ 
(8)   end
(9) end

```

error propagation [WBR⁺01]. Therefore, we should certainly start with the user u that has the smallest probability of error, i.e. its estimate \hat{a}_u has the smallest mean squared error to the true symbol a_u . The user corresponds to the smallest diagonal element of the error covariance matrix Φ_{ZF} derived in (5.2.5). Inserting the QL decomposition into (5.2.5) yields

$$\Phi_{\text{ZF}} = \sigma_{\mathcal{N}}^2 \cdot \mathbf{W}_{\text{ZF}} \mathbf{W}_{\text{ZF}}^H = \sigma_{\mathcal{N}}^2 \cdot \mathbf{L}^{-1} \mathbf{L}^{-H}. \quad (5.4.13)$$

Hence, the smallest diagonal element of Φ_{ZF} corresponds to the smallest row norm of \mathbf{L}^{-1} . The order of detection can be optimized after the QL decomposition by an algorithm proposed in [Has00] and termed Post-Sorting Algorithm (PSA). Starting with the unsorted QL decomposition according to the modified Gram-Schmidt algorithm, we have to permute the rows of \mathbf{L}^{-1} according to a certain sorting criterion. However, permutations destroy the triangular structure of \mathbf{L} . The structure can be restored by applying Householder reflections [GvL93], i.e. we multiply with a unitary matrix Θ that forces certain elements of a row to zero (see also Appendix C).

Fig. 5.4.2 illustrates the principle of the post-sorting algorithm. In the first step, we have to find the row with the smallest norm (dark gray). It is exchanged with the first row of \mathbf{L} – this can be described by a permutation matrix \mathbf{P}_1 . Next, we apply the Householder reflection (matrix Θ_1) to force zeros in the new first row in order to restore the triangular structure. Note that Householder reflections do not affect the row norm so that the norm of the considered row is concentrated in a single nonzero element.

Now, we have generated a row in \mathbf{L} with a single nonzero element, i.e. no interference disturbs the corresponding symbol. Assuming that this symbol is decided correctly (it has the lowest error probability of all symbols), its interference on the remaining symbols can be perfectly cancelled. Hence, it has no influence on subsequent cancellation steps so that the first row and the first column in \mathbf{L} can

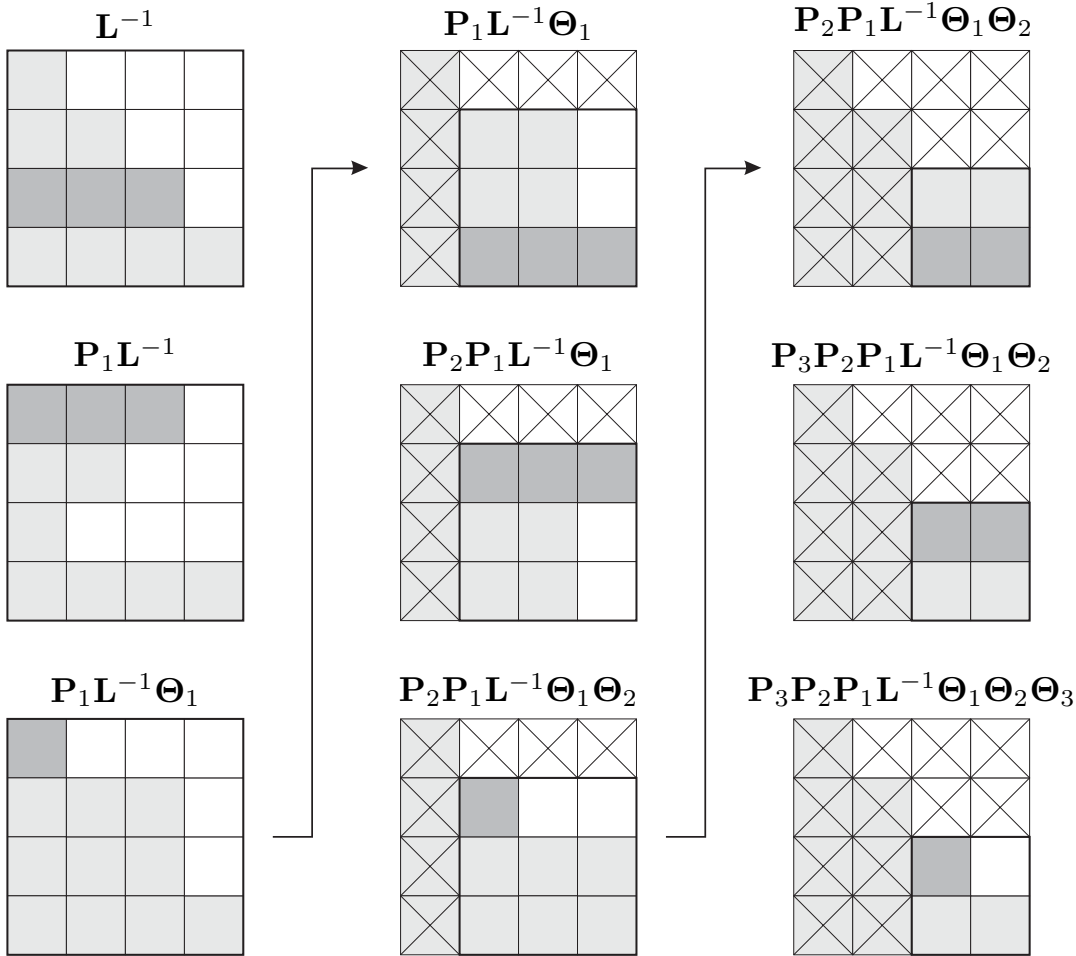


Figure 5.4.2: Illustration of post-sorting algorithm (white squares indicate zeros, light gray squares indicate nonzero elements, dark gray squares indicate row with minimum norm, crossed squares are neglected subsequent steps)

be removed. The whole procedure is now repeated for the reduced triangular matrix until the optimum order is obtained. We have to carry out at most N_U permutations and Householder reflections so that we finally obtain

$$\mathbf{L}_{\text{opt}}^{-1} = \mathbf{P}_{N_U} \cdots \mathbf{P}_1 \mathbf{L}^{-1} \Theta_1 \cdots \Theta_{N_U} \quad \Leftrightarrow \quad \mathbf{L}_{\text{opt}} = \Theta_{N_U}^H \cdots \Theta_1^H \mathbf{L} \mathbf{P}_1^H \cdots \mathbf{P}_{N_U}^H \quad (5.4.14)$$

and

$$\mathbf{Q}_{\text{opt}} = \mathbf{Q} \Theta_1 \cdots \Theta_{N_U} . \quad (5.4.15)$$

With the permuted symbol vector $\mathbf{a}_{\text{opt}} = \mathbf{P}_{N_U} \cdots \mathbf{P}_1 \mathbf{a}$, it is easy to show that permutations and Householder reflections do not change the system because the received signal can be expressed as

$$\begin{aligned} \mathbf{y} &= \mathbf{S}_{\text{opt}} \cdot \mathbf{a}_{\text{opt}} + \mathbf{n} = \mathbf{Q}_{\text{opt}} \cdot \mathbf{L}_{\text{opt}} \cdot \mathbf{a}_{\text{opt}} + \mathbf{n} \\ &= \underbrace{\mathbf{Q} \Theta_1 \cdots \Theta_{N_U} \cdot \Theta_{N_U}^H \cdots \Theta_1^H}_{\mathbf{I}_{N_U}} \underbrace{\mathbf{L} \mathbf{P}_1^H \cdots \mathbf{P}_{N_U}^H \cdot \mathbf{P}_{N_U} \cdots \mathbf{P}_1}_{\mathbf{I}_{N_U}} \mathbf{a} + \mathbf{n} = \mathbf{Q} \mathbf{L} \mathbf{a} + \mathbf{n} . \end{aligned}$$

After filtering with $\mathbf{Q}_{\text{opt}}^H$ and nonlinear interference cancellation with respect to \mathbf{L} , the estimated symbols in $\hat{\mathbf{a}}_{\text{opt}}$ have to be re-sorted into the original order

$$\hat{\mathbf{a}} = \mathbf{P}_1^H \cdots \mathbf{P}_{N_U}^H \cdot \hat{\mathbf{a}}_{\text{opt}} . \quad (5.4.16)$$

Besides the QL decomposition of \mathbf{S} , the optimum sorting requires a matrix inversion of \mathbf{L} and several permutations and Householder reflections. In order to reduce the computational costs, the next subsection introduces a sub-optimum algorithm performing very close to the optimum solution.

Sorted QL Decomposition

A sub-optimum but very efficient solution to the sorting problem is presented in [WBR⁺01] that directly affects the QL decomposition. The main problem to be solved is that the Gram-Schmidt algorithm starts with L_{N_U, N_U} in the lower right corner and proceeds up to $L_{1,1}$ while we would like to fix the largest possible $L_{1,1}$ first and continue down to the shortest row at the bottom. In other words, the order of detection is reverse to the order of decomposition.

We saw from the post-sorting algorithm that the order of detection can be adapted by permuting the columns \mathbf{q}_u of \mathbf{Q} as well as the rows of \mathbf{L} . This leads to a different sorting of the column vectors \mathbf{s}_u and the data symbols a_u in \mathbf{a} . A suboptimum permutation can be carried out during the QL decomposition itself. The algorithm proposed in [WBR⁺01] is based on a QR decomposition but can be directly adapted to the QL decomposition considered here. The basic idea behind the algorithm is that the determinant of a triangular matrix equals the product of the diagonal elements and is invariant with respect to permutations of rows or columns. The SQLD (Sorted QL Decomposition) now assumes that starting with the smallest possible L_{N_u, N_U} will finally lead to large values in the upper left part of \mathbf{L} since the product is constant. It is summarized as pseudo code in Table 5.4.2.

After the initialization $\mathbf{Q} = \mathbf{S}$, the column \mathbf{q}_{k_u} with the smallest norm is determined and exchanged with the most right unprocessed vector. Since the projections of the remaining columns onto a new vector are immediately subtracted in each step, no Householder reflections are explicitly necessary. At the end of the procedure, we obtain the orthonormal matrix \mathbf{Q} , the triangular matrix \mathbf{L} as well as the set of permutation matrices \mathbf{P}_u .

It has to be mentioned that the proposed SQLD does not always lead to the optimum detection order. Problems occur especially in situations where two column vectors have large lengths but point into similar directions. In this case, these large vectors are among the latest columns to be orthogonalized but the projection of one vector onto the other vector is very large so that the orthogonal component becomes very small. Hence, we obtain very small diagonal elements in the upper left corner of \mathbf{L} .

Table 5.4.2: Pseudo code for sorted QL decomposition

```

(1) Initialize with  $\mathbf{L} = \mathbf{0}$ ,  $\mathbf{Q} = \mathbf{S}$ 
(2) for  $u = N_U, \dots, 1$ 
(3)   search for minimum norm among remaining columns in  $\mathbf{Q}$ 
         $k_u = \operatorname{argmin}_{v=1, \dots, u} \|\mathbf{q}_v\|^2$ 
(4)   exchange columns  $u$  and  $k_u$  in  $\mathbf{Q}$ , and determine  $\mathbf{P}_u$ 
(5)   determine diagonal element  $L_{u,u} = \|\mathbf{q}_u\|$ 
(6)   normalize  $\mathbf{q}_u = \mathbf{q}_u / L_{u,u}$  to unit length
(7)   for  $v = 1, \dots, u - 1$ 
        calculate projections  $L_{u,v} = \mathbf{q}_u^H \cdot \mathbf{q}_v$ 
         $\mathbf{q}_v = \mathbf{q}_v - L_{u,v} \cdot \mathbf{q}_u$ 
(8)   end
(9) end
(10) end
(11) end

```

However, those events leading to sub-optimum sorting are very rare and the SQLD represents an appropriate pre-sorting algorithm. For the aforementioned situations, the presented post-sorting algorithm can be applied for further improvements. It then requires only a few additional permutations (low complexity) due to the pre-sorting and can still achieve the optimum order of detection. The whole receiver structure is depicted in **Fig. 5.4.3**. First, the system matrix \mathbf{S} – either ideally known or estimated – is decomposed according to the SQLD algorithm and post processed by the post-sorting algorithm (PSA). The latter delivers the matrices \mathbf{Q} for linear pre-filtering the received vector \mathbf{y} resulting in $\tilde{\mathbf{y}}$, \mathbf{L} for the successive interference cancellation providing $\hat{\mathbf{a}}_{\text{opt}}$ and \mathbf{P} for the inverse permutation leading to the final estimate $\hat{\mathbf{a}}$.

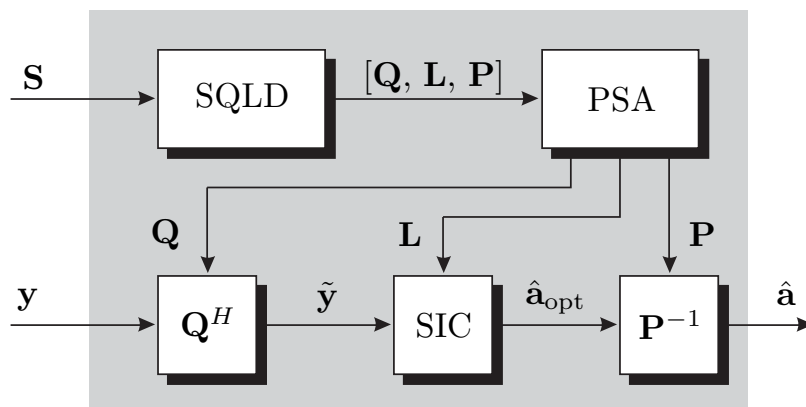
**Figure 5.4.3:** Block diagram of SQLD-SIC detector with post-sorting algorithm (PSA)

Fig. 5.4.4a analyzes the influence of α for NL 1 on the error rate performance. Obviously, there is only a slight dependency for QPSK and small values of α should be preferred. Although the average bit error rate over all users is considered, similar results are obtained for user specific error probabilities. Fig. b) compares different nonlinearities. Their performances are nearly identical because the average error rate is dominated by the first layer where no interference cancellation was applied. Due to the higher effective interference, the SQLD-SIC performs worse for QPSK. For BPSK, the SUB is reached asymptotically.

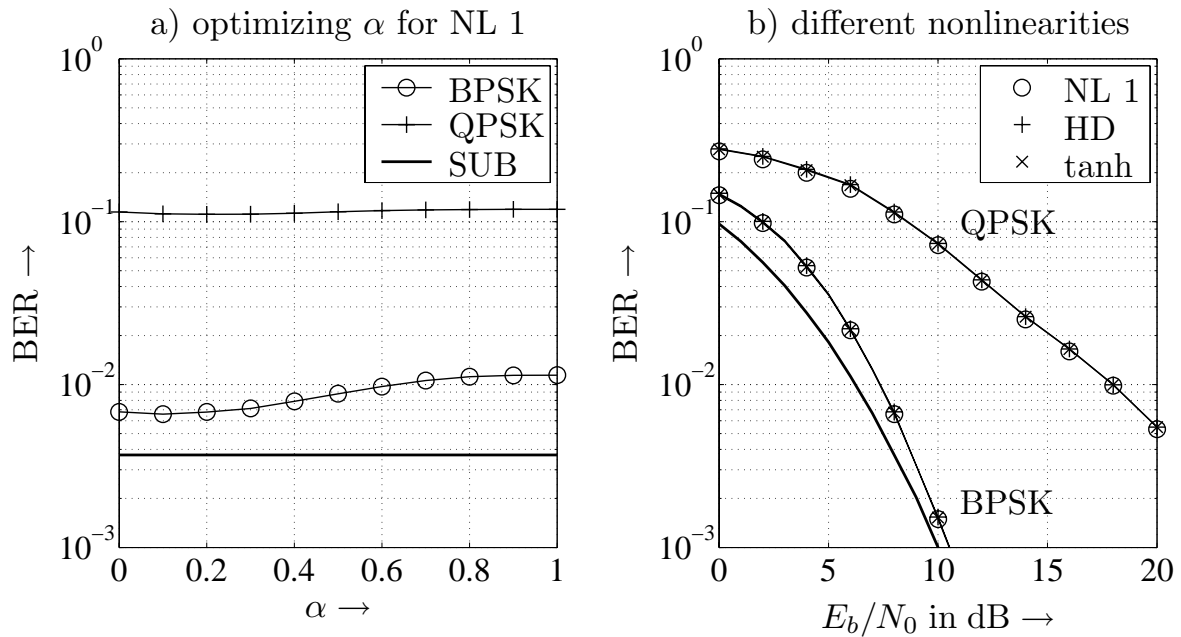


Figure 5.4.4: Performance of ZF-SQLD-SIC for uncoded OFDM-CDMA system, 4-paths Rayleigh fading channel, $\beta = 1$; **a)** $E_b/N_0 = 8$ dB, **b)** optimized α

Fig. 5.4.5a illustrates the performance improvement obtained by linear pre-processing with \mathbf{Q}^H . Comparing the error rate performance of the SQLD-SIC approach with that of a sole successive interference cancellation (SIC) after the first detection stage, we observe that linear pre-filtering enhances the performance significantly. While it approaches the SUB, the pure SIC saturates at $P_b = 10^{-2}$. Only at very low SNR, the performances are comparable. Additionally, the dashed line emphasizes the loss that occurs for SQLD-SIC when the real nature of BPSK is not considered in the QL decomposition. At an error rate of 10^{-2} , the loss amounts to 7 dB.

Fig. 5.4.5b depicts the results for QPSK. The gain of SQLD-SIC compared to SIC becomes larger for growing interference as the difference between BPSK and QPSK shows. However, for both detection schemes a large loss compared to the SUB can be observed. Moreover, it is demonstrated that even suboptimum sorting for the SQLD-SIC improves the performance compared to unsorted QLD-SIC. Applying

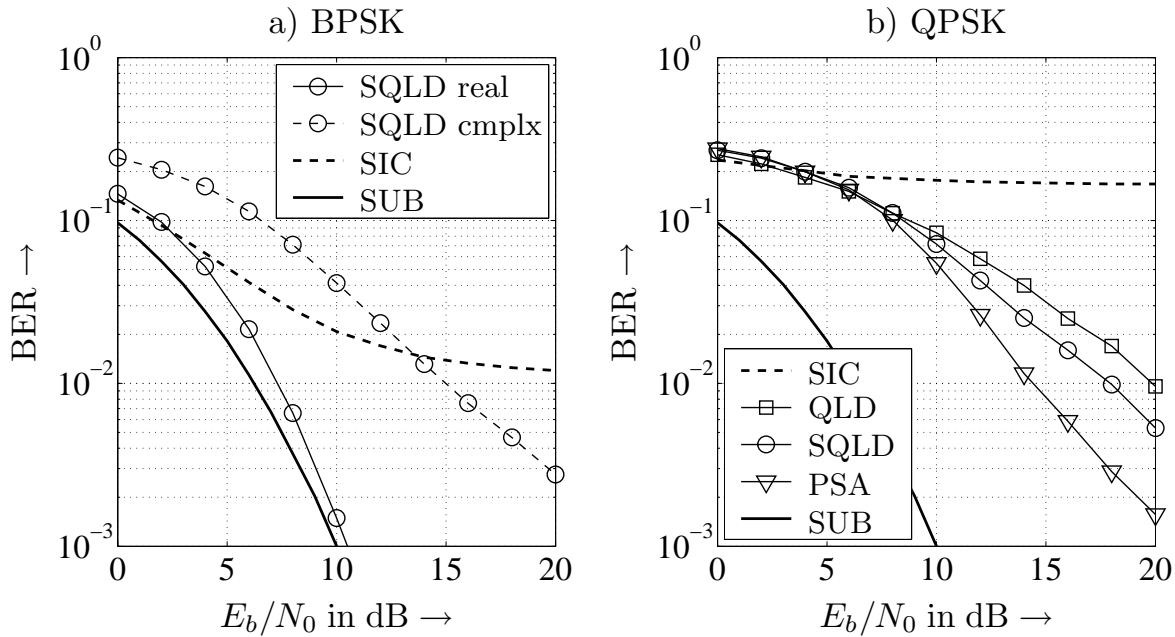


Figure 5.4.5: Performance of different detection schemes with NL 1 for uncoded OFDM-CDMA system, 4-paths Rayleigh fading channel, $\beta = 1$

the optimum PSA yields an additional gain of more than 3 dB over the SQLD-SIC. From Subsection 5.2.1 we know that the decorrelator totally suppresses multi-user interference at the expense of a noise amplification. Moreover, it was already mentioned that the first row of \mathbf{Q}^H also suppresses perfectly the interference but may suffer from small signal to noise ratios⁸ while the last row represents a matched filter dealing perfectly with the background noise. Hence, the SNRs of the remaining rows are somewhere in between. This is illustrated in **Fig. 5.4.6** showing the minimum, the maximum and the average error rates.

In order to improve especially the weak users, two possibilities exist that can also be combined. First, we can replace the zero-forcing approach by an MMSE solution as presented in the next subsection. Second, iterative turbo processing with an initial QL detection stage as explained in Subsection 5.4.4 can significantly improve the performance of a CDMA system.

5.4.3 QL Decomposition for MMSE Solution

From Subsection 5.2.2 we know already the linear MMSE detector

$$\mathbf{W}_{\text{MMSE}} = \left(\mathbf{S}^H \mathbf{S} + \frac{N_0}{E_s} \mathbf{I}_{N_U} \right)^{-1} \cdot \mathbf{S}^H$$

⁸The noise power is not influenced but the signal power may be very small.

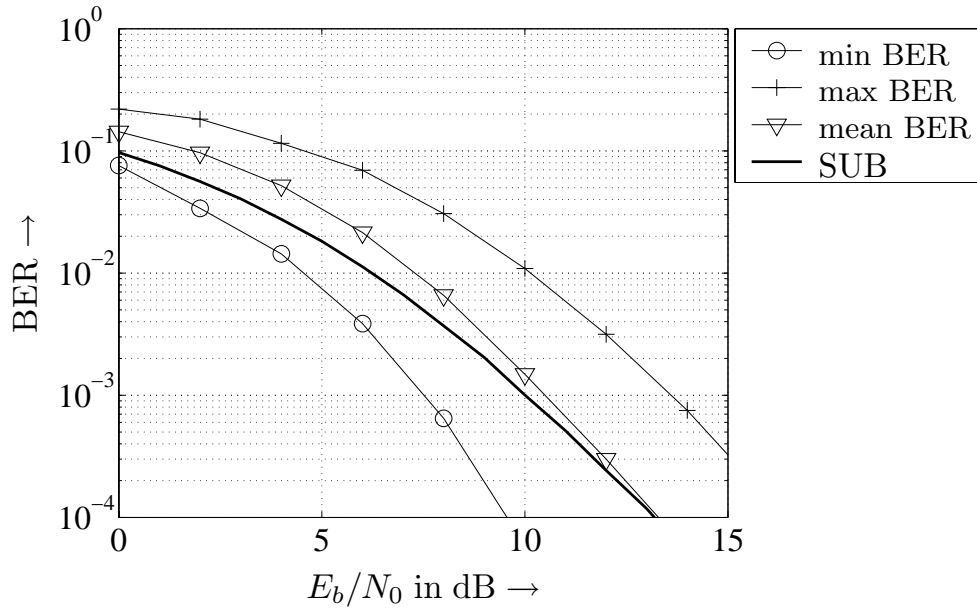


Figure 5.4.6: Error rates for weakest, strongest and average user after ZF-SQLD-SIC for uncoded OFDM-CDMA system with BPSK, 4-paths Rayleigh fading channel, $\beta = 1$

that looks for a compromise between interference suppression and noise enhancement. Hence, some residual interference remains in all outputs. In order to find the QL decomposition according to the MMSE criterion and an appropriate order of detection, the MMSE solution is now described as the zero-forcing solution of a modified system [BWKK03, WBKK03]. This modification is obtained by extending the received vector \mathbf{y} and the system matrix \mathbf{S} according to

$$\underline{\mathbf{y}} = \begin{bmatrix} \mathbf{y} \\ \mathbf{0}_{N_U \times 1} \end{bmatrix}, \quad \underline{\mathbf{S}} = \begin{bmatrix} \mathbf{S} \\ \frac{\sigma_N}{\sigma_A} \cdot \mathbf{I}_{N_U} \end{bmatrix}. \quad (5.4.17)$$

Applying now the the decorrelator to the modified system yields

$$\hat{\mathbf{a}}_{\text{MMSE}} = (\underline{\mathbf{S}}^H \underline{\mathbf{S}})^{-1} \underline{\mathbf{S}}^H \cdot \underline{\mathbf{y}} \quad (5.4.18a)$$

$$\begin{aligned} &= \left([\mathbf{S}^H \frac{\sigma_N}{\sigma_A} \cdot \mathbf{I}_{N_U}] \cdot \begin{bmatrix} \mathbf{S} \\ \frac{\sigma_N}{\sigma_A} \cdot \mathbf{I}_{N_U} \end{bmatrix} \right)^{-1} [\mathbf{S} \frac{\sigma_N}{\sigma_A} \cdot \mathbf{I}_{N_U}] \cdot \begin{bmatrix} \mathbf{y} \\ \mathbf{0}_{N_U \times 1} \end{bmatrix} \\ &= (\mathbf{S}^H \mathbf{S} + \frac{\sigma_N^2}{\sigma_A^2} \cdot \mathbf{I}_{N_U})^{-1} \cdot \mathbf{S}^H \mathbf{y}. \end{aligned} \quad (5.4.18b)$$

We recognize from (5.4.18b) that the zero-forcing approach of the modified system leads directly to the MMSE solution for the original system. Hence, we can apply the same QL decomposition as derived in the previous section to $\underline{\mathbf{S}}$ instead of \mathbf{S} . We obtain

$$\underline{\mathbf{S}} = \begin{bmatrix} \mathbf{S} \\ \frac{\sigma_N}{\sigma_A} \cdot \mathbf{I}_{N_U} \end{bmatrix} = \underline{\mathbf{Q}} \cdot \underline{\mathbf{L}} = \begin{bmatrix} \mathbf{Q}_1 \\ \mathbf{Q}_2 \end{bmatrix} \cdot \underline{\mathbf{L}} = \begin{bmatrix} \mathbf{Q}_1 \cdot \underline{\mathbf{L}} \\ \mathbf{Q}_2 \cdot \underline{\mathbf{L}} \end{bmatrix} \quad (5.4.19)$$

where $\underline{\mathbf{Q}}$ is now a unitary $(N_s + N_U) \times N_U$ matrix and $\underline{\mathbf{L}}$ a lower triangular $N_U \times N_U$ matrix. Obviously, they are different from \mathbf{Q} and \mathbf{L} of the zero-forcing solution. The matrices \mathbf{Q}_1 and \mathbf{Q}_2 divide the matrix $\underline{\mathbf{Q}}$ into the upper N_s and the lower N_U rows. Although $\underline{\mathbf{Q}}$ has orthogonal columns of unit length, this does certainly not hold for \mathbf{Q}_1 and \mathbf{Q}_2 .

An important difference to the zero-forcing solution has to be mentioned now. Since the extended system matrix $\underline{\mathbf{S}}$ consists of $N_s + N_U$ rows and N_U columns, it can always be QL decomposed regardless of the load β . Hence, the MMSE approach is also applicable for overloaded systems.

Looking at the filtered received vector

$$\tilde{\mathbf{y}} = \underline{\mathbf{Q}}^H \underline{\mathbf{y}} = \mathbf{Q}_1^H \mathbf{y} + \mathbf{Q}_2^H \mathbf{0} = \mathbf{Q}_1^H \mathbf{y} = \mathbf{Q}_1^H \mathbf{S} \mathbf{a} + \mathbf{Q}_1^H \mathbf{n}, \quad (5.4.20)$$

we observe that only the first part \mathbf{Q}_1 of $\underline{\mathbf{Q}}$ contributes to $\tilde{\mathbf{y}}$ because \mathbf{y} was extended by appending zeros. Multiplying only with \mathbf{Q}_1 slightly reduces the computational costs. Inserting $\mathbf{S} = \mathbf{Q}\mathbf{L}$ into (5.4.20) results in

$$\tilde{\mathbf{y}} = \mathbf{Q}_1^H \mathbf{Q} \mathbf{L} \mathbf{a} + \mathbf{Q}_1^H \mathbf{n}. \quad (5.4.21)$$

Since the columns in \mathbf{Q}_1 and \mathbf{Q} are not orthogonal, $\mathbf{Q}_1^H \cdot \mathbf{Q} \neq \mathbf{I}_{N_U}$ holds and the interference between two neighboring rows is not totally suppressed. This represents the known trade-off between interference suppression and noise amplification. With

$$\underline{\mathbf{Q}}^H \underline{\mathbf{S}} = \mathbf{Q}_1^H \mathbf{S} + \frac{\sigma_{\mathcal{N}}}{\sigma_{\mathcal{A}}} \cdot \mathbf{Q}_2^H \stackrel{!}{=} \underline{\mathbf{L}} \Rightarrow \mathbf{Q}_1^H \mathbf{S} = \underline{\mathbf{L}} - \frac{\sigma_{\mathcal{N}}}{\sigma_{\mathcal{A}}} \cdot \mathbf{Q}_2^H, \quad (5.4.22)$$

we can replace the term $\mathbf{Q}_1^H \cdot \mathbf{S}$ in (5.4.20) and obtain

$$\tilde{\mathbf{y}} = \underline{\mathbf{L}} \cdot \mathbf{a} - \frac{\sigma_{\mathcal{N}}}{\sigma_{\mathcal{A}}} \cdot \mathbf{Q}_2^H \mathbf{a} + \mathbf{Q}_1^H \mathbf{n} \quad (5.4.23)$$

for the filtered received signal. The second term in (5.4.23) represents the residual interference after filtering with \mathbf{Q}_1^H . The smaller the noise power $\sigma_{\mathcal{N}}^2$, the less interference remains in the system. For $\sigma_{\mathcal{N}}^2 \rightarrow 0$, the MMSE solution tends to the zero-forcing solution as already known from Section 5.2.

As in the case of the ZF-QL decomposition, the order of detection has to be determined with respect to the error covariance matrix Φ_{MMSE} . Using the extended system model with $\underline{\mathbf{S}}$, the zero-forcing criterion delivers with the results of Subsection 5.2.1

$$\Phi_{\text{MMSE}} = \Phi_{\text{ZF}} = \sigma_{\mathcal{N}}^2 \cdot (\underline{\mathbf{S}}^H \underline{\mathbf{S}})^{-1} = \sigma_{\mathcal{N}}^2 \cdot \underline{\mathbf{L}}^{-1} \underline{\mathbf{L}}^{-H}. \quad (5.4.24)$$

Hence, the row norms of $\underline{\mathbf{L}}^{-1}$ determine the optimum sorting. In the MMSE case, the inverse of $\underline{\mathbf{L}}$ need not to be calculated explicitly because it is already contained in (5.4.19).

$$\frac{\sigma_{\mathcal{N}}}{\sigma_{\mathcal{A}}} \cdot \mathbf{I}_{N_U} = \mathbf{Q}_2 \cdot \underline{\mathbf{L}} \Rightarrow \underline{\mathbf{L}}^{-1} = \frac{\sigma_{\mathcal{A}}}{\sigma_{\mathcal{N}}} \cdot \mathbf{Q}_2 \quad (5.4.25)$$

Therefore, the inverse of $\underline{\mathbf{L}}$ is obtained as a byproduct of the initial QL decomposition. We simply have to consider the norm of the rows in the lower part of $\underline{\mathbf{Q}}$. This compensates the higher computational costs for QL decomposing the extended matrix $\underline{\mathbf{S}}$.

Fig. 5.4.7a depicts the results obtained for ZF- and MMSE-SQLD-SIC for a fully loaded BPSK modulated system with $\beta = 1$. Both approaches show similar performances and reach the SUB above 10 dB. The real-valued nature of BPSK has been exploited so that the background noise amplification of the zero-forcing solution has not such a severe influence. However, 5 iterations of the nonlinear SIC without linear preprocessing (only shown in Fig. 5.3.9) achieve the same performance with lower computational complexity. Hence, filtering with $\underline{\mathbf{Q}}^H$ is not necessary for moderate SINR.

For QPSK with a twice as high effective interference, the situation changes. From **Fig. 5.4.7b** we see that the simple nonlinear SIC (bold dashed line) has a comparable performance only at low SNR and saturates after 10 iterations at 10^{-3} while the SQLD-SIC shows no error floor down to 10^{-4} . Moreover, the advantage of the MMSE approach compared to the zero-forcing solution becomes obvious. At an error rate of 10^{-2} , the gain amounts to 8 dB. The sorted ZF-QL decomposition gains 2 dB over the unsorted algorithm, 4 dB are gained for the MMSE solution. None of the schemes reaches the single-user bound.

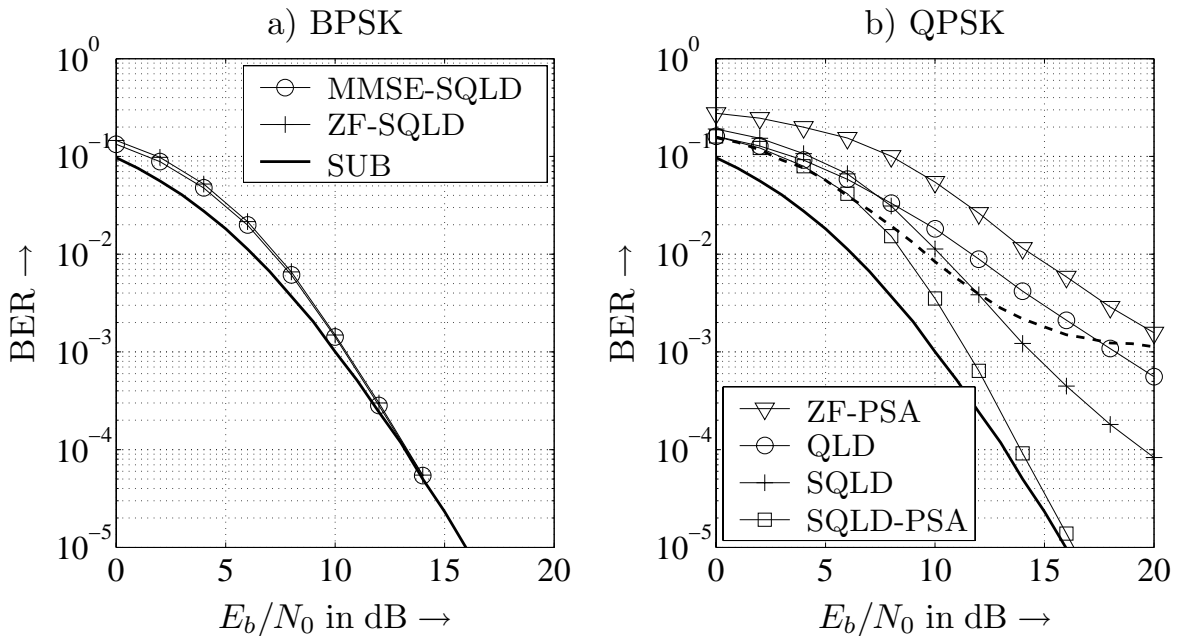


Figure 5.4.7: Performance of MMSE-SQLD-SIC and SIC for uncoded OFDM-CDMA system, a 4-paths Rayleigh fading channel, $\beta = 1$

5.4.4 Turbo Processing

In order to improve the performance of the SQLD-SIC schemes, iterative turbo detection can be applied. Once all signals have been detected, the filter \mathbf{Q}^H has to be substituted by a bank of matched filters and successive interference cancellation as described in Section 5.3 is carried out. Hence, the linear filter is just used as a catalyst improving the performance of the first stage and then dropped.

The reasons for this approach are twofold: First, the interference has been already partly cancelled after filtering with \mathbf{Q}^H . Due to the triangular structure of \mathbf{L} , the signal \tilde{y}_1 in the first row does not suffer from interference of $a_2 \cdots a_{N_U}$ and, hence, its decision cannot be improved by the knowledge of the other signals.

Second, suppressing interference by zero-forcing leads to a strong noise amplification, the MMSE solution represents a trade-off between interference suppression and noise amplification. The optimum receiver in the absence of interference, e.g. after a perfect cancellation, would be the matched filter performing simply maximum ratio combining. Hence, after the QL decomposition and a first successive interference cancellation stage delivering $\hat{\mathbf{a}}^{(1)}$, we use the output of the matched filter bank to apply the already introduced SIC.

Fig. 5.4.8a shows the obtained results for a load $\beta = 1$ and the zero-forcing criterion. Both, SQLD-SIC with and without PSA gain significantly by subsequent detection stages and outperform the pure SIC at high SNRs. Only at very low SNR, the performance of SIC is the same. Optimum post sorting of the initial SQLD improves the performance even after several iterations whereby the gain becomes smaller with each stage.

Fig. 5.4.8b compares the same detection schemes for the MMSE criterion. Contrarily to the ZF case, the PSA provides already in the initial detection stage a performance close to the SUB. Hence, subsequent iterations are not necessary saving valuable computational resources. Even without PSA, the MMSE approach performs much better than ZF and the gains due to additional iterations are smaller. At an error rate of 10^{-2} , the MMSE solution gains about 1 dB compared to the ZF approach, at 10^{-3} , the gain has increased to 2 dB.

From **Fig. 5.4.9** we see that for higher loads, e.g. $\beta = 1.5$, there is still a small improvement achievable by iterations. However, a convergence towards the SUB cannot be obtained anymore. Nevertheless, optimum sorting still provides a remarkable gain over the suboptimum sorting of the SQLD.

If channel coding is applied, we can obviously incorporate the decoder in the interference cancellation steps as described in Subsection 5.3.3. However, long codes for spreading or variations of the channels during one coded frame would lead to various system matrices $\mathbf{S}[k]$ which have to be QL decomposed. The sorted version of the QL decomposition would deliver with high probability different detection

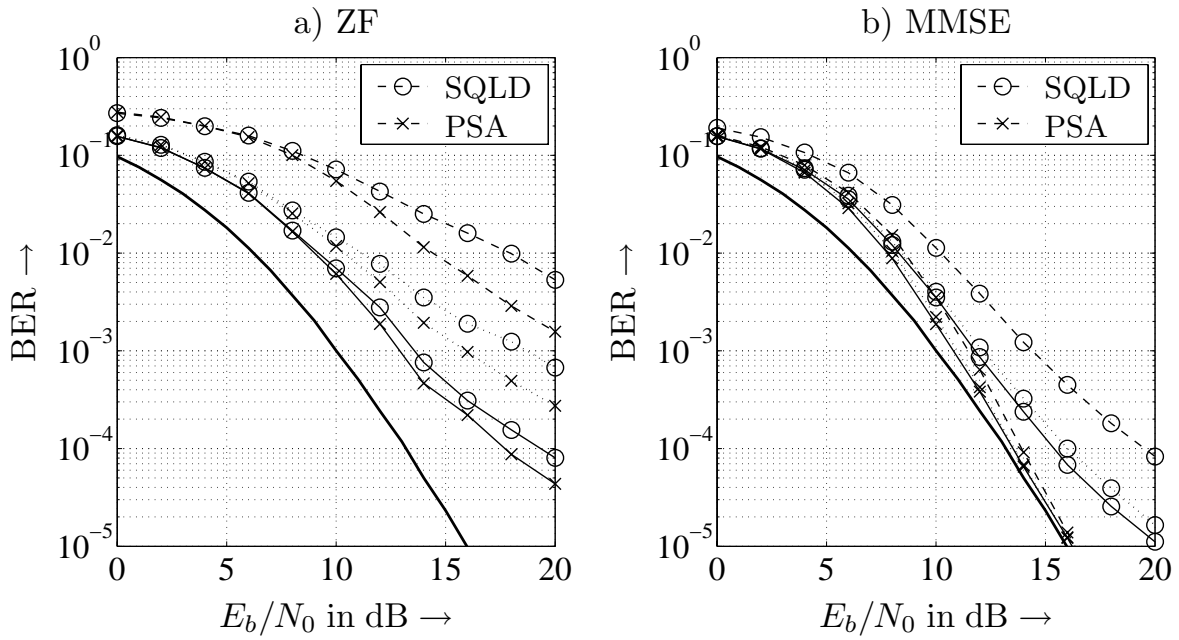


Figure 5.4.8: Performance of iterative SQLD-SIC and SIC for uncoded OFDM-CDMA system, QPSK and a 4-paths Rayleigh fading channel, $\beta = 1$ (dashed lines: initial stage, dotted lines: 3 subsequent stages, solid lines: 10 subsequent stages)

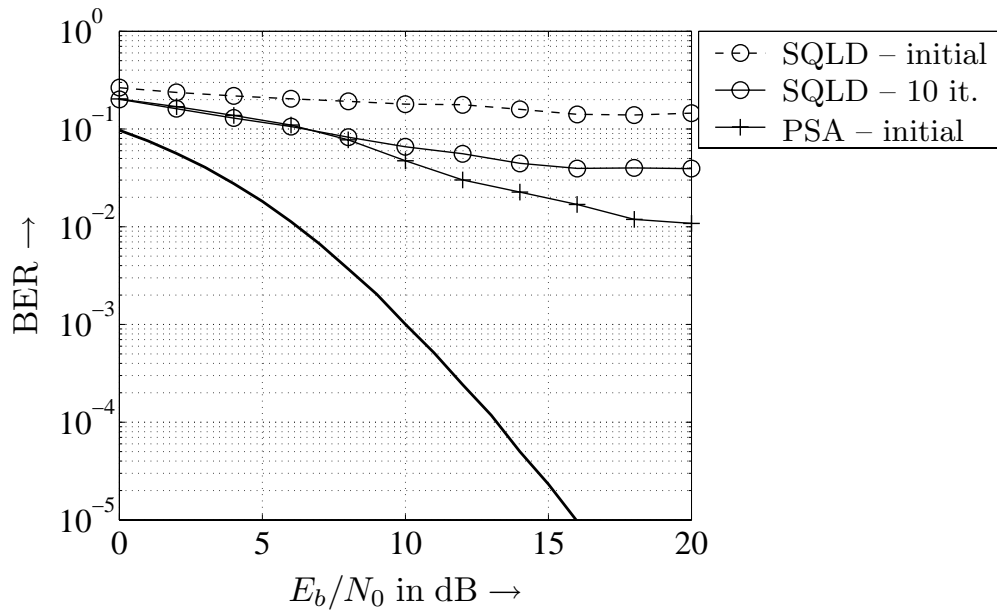


Figure 5.4.9: Performance of iterative MMSE-SQLD-SIC for uncoded OFDM-CDMA system, QPSK and a 4-paths Rayleigh fading channel, $\beta = 1.5$

orders. Therefore, the interference cancellation would start with a different user for each block. This causes problems for the channel decoding because decoding can start only if a complete frame of a certain user is processed.

Since the SIC in Subsection 5.3.3 was evaluated for a coded OFDM-CDMA system with seven fading blocks per frame, we now use the unsorted version of the QL decomposition allowing the same permutation for all blocks. Hence, after filtering with \mathbf{Q}^H , the coded frame of user 1 is totally freed from interference, can be decoded and the estimated coded bits are used to cancel interference from subsequent signals. Then, the procedure is continued for user 2 and so on.

Fig. 5.4.10a shows the results for a half-rate convolutional code with constraint length $L_c = 3$, QPSK and a load of $\beta = 2$. The dashed lines between the initial stage and the final stage indicate the error rate performance after different iterations. With the iterative approach, it is possible to approach the SUB within a gap of 1 dB for signal to noise ratios above 6 dB. Comparing the results with those of Fig. 5.3.17 (bold dashed line), it becomes obvious that the linear prefilter improves the performance at low SNR while both schemes have approximately the same performance for higher SNR.

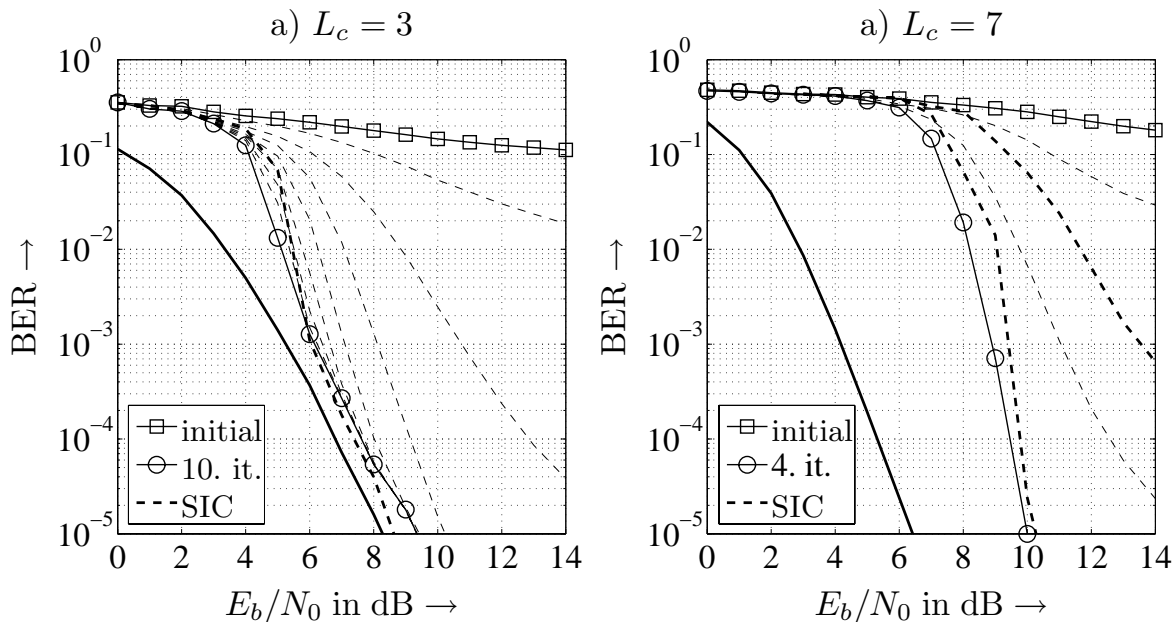


Figure 5.4.10: Performance of iterative MMSE-SQLD-SIC and SIC for coded OFDM-CDMA system, QPSK and a 4-paths Rayleigh fading channel, $\beta = 2$

Results for a convolutional code with $L_c = 7$ are shown in **Fig. 5.4.10b**. The two bold dashed lines represent the SIC performance after four and ten iterations (compare Fig. 5.3.17). Obviously, the SQLD-SIC scheme provides a much faster convergence. After four iterations, the simple SIC with ten iterations is outperformed. Nevertheless, there remains a large gap of 4 dB to the SUB that cannot be closed. A comparison with the $L_c = 3$ code shows that the performance is slightly worse although the computational costs are much higher. Four iterations for the $L_c = 7$ code require a complexity that is more than six times higher than the complexity for ten iterations of the $L_c = 3$ code.

Chapter 6

Multiple Antenna Systems

6.1 Introduction

There exist a multitude of reasons for using multiple antenna systems. This section gives a brief overview of different strategies without claiming to be comprehensive. Principally, two different categories can be distinguished. The first objective is to improve the link reliability, i.e. the ergodic error probability or the outage probability are reduced. This can be accomplished by enhancing the instantaneous SNR (beamforming) or by decreasing the variations of the SNR (diversity). If multiple access or cochannel interference in cellular networks disturbs the transmission, interferers that are separable in space can be suppressed with multiple antennas resulting in an improved signal to interference plus noise ratio (SINR). In Section 6.2, we will restrict only on diversity techniques reducing SNR variations.

The second objective is to multiply the data rate by transmitting several data streams simultaneously over different antennas. This approach is denoted as Space Division Multiple Access (SDMA) and can certainly be combined with other multiple access schemes. Since bandwidth became a very valuable and expensive resource, using the space for increasing data rates without expanding the bandwidth is very attractive. Moreover, we will see in Section 6.4 that the potential capacity gain of multiple antenna systems is much larger than the gain obtained by simply increasing the transmit power.

The way how multiple antennas should be used depends on the properties of the channel, especially on the rank r of \mathbf{H} or its covariance matrix $\Phi_{\mathcal{H}\mathcal{H}}$. As an example we know from Section 1.5 that correlation among the subchannels reduces the diversity gain. In case of a strong line-of-sight component (Rice fading) diversity is also not an appropriate means because fading is not a severe problem.

If we can exploit other sources of diversity, e.g. frequency diversity with the Rake receiver or time diversity due to coding over time varying channels, we probably are already close to the AWGN performance and little can be gained by a further increase of the diversity degree. In each of these cases, multiple antennas should be used in a different way.

If we look for spatial multiplexing, we know from Section 2.3 that we need a channel whose rank is larger than one. Otherwise, we cannot reliably transmit parallel data streams. Hence, for highly correlated channels with a rank $r = 1$, beamforming that exploits only the strongest eigenmode of a channel would be an appropriate choice instead of multi-layer transmission. Therefore, the way multiple antennas are used has to be properly adapted to the general propagation conditions.

In order to simplify notation, we restrict in this chapter to frequency-nonselective channels. Hence, the impulse response $h_{\nu,\mu}[\ell, \kappa]$ between transmit antenna μ and receive antenna ν reduces to scalar coefficients $h_{\nu,\mu}[\ell]$ and the channel matrix in (1.2.32) of Section 1.2.4 becomes $\mathbf{H}[\ell] = \mathbf{H}[\ell, 0]$. **Fig. 6.1.1** illustrates the resulting structure of the communication system. The received signal can be described by

$$\mathbf{y}[\ell] = \mathbf{H}[\ell] \cdot \mathbf{x}[\ell] + \mathbf{n}[\ell]. \quad (6.1.1)$$

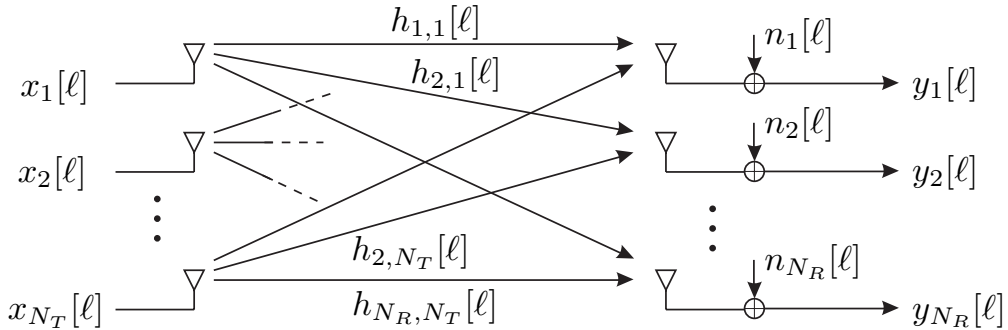


Figure 6.1.1: Structure of MIMO channel

The next section introduces diversity concepts for multiple antenna systems. Section 6.3 deals with multi-layer transmission and Section 6.4 summarizes some results from information theory.

6.2 Multiple Antenna Diversity

This section addresses the application of multiple antennas at receiver and / or transmitter for the purpose of increasing the diversity degree. As already mentioned, we restrict to frequency-nonselective channels for notational as well as

conceptual simplicity. Another reason is that diversity concepts are best suited for channels that do not provide diversity on their own. Moreover, only Rayleigh fading channels without a line of sight component are considered. For Rice fading channels refer to the theoretical results presented in Section 1.5. Since we know that correlations among the contributing channels reduce the diversity gain (see Section 1.5) we further assume that the channels are totally uncorrelated.

This can be accomplished by an appropriate antenna spacing that depends on the spatial channel characteristics, e.g. the angle spread. Assuming a uniform linear array with equidistantly arranged antennas and an isotropic scattering environment where signals are impinging from all directions with the same probability, a small distance $d = \lambda/2$ between neighboring elements may be sufficient. The parameter λ denotes the wavelength and is related to the carrier frequency f_0 by $\lambda = c/f_0$ where c describes the speed of light. Contrarily, $d \gg \lambda/2$ must hold in scenarios with small angle spread and d can take values up to 10λ . This obviously requires a device large enough to host several antennas with appropriate distances.

This section is divided into three parts: First, receive diversity is shortly explained. Next, orthogonal space-time block codes are addressed. Nonorthogonal block codes are not considered here and the interested reader is referred to [GBL00, BGL00, LGB01, LSB02, BGL02, LGB03]. In the last subsection, space-time trellis codes providing additionally a coding gain are introduced.

6.2.1 Receive Diversity

The simplest method to achieve space diversity is to use multiple antennas at the receiver. The structure of the system is depicted in **Fig. 6.2.1**. It can be mathematically described with

$$\mathbf{y}[\ell] = \mathbf{h}[\ell] \cdot \mathbf{x}[\ell] + \mathbf{n}[\ell] \quad (6.2.1)$$

where $\mathbf{h}[\ell] = [h_1[\ell] \quad \dots \quad h_{N_R}[\ell]]^T$ comprises all contributing channel coefficients. Since there is no interference, a simple matched filter performing maximum ratio combining represents the optimum receiver and we obtain

$$\mathbf{r}[\ell] = \mathbf{h}[\ell]^H \cdot \mathbf{y}[\ell] = \mathbf{x}[\ell] \cdot \sum_{\mu=1}^{N_R} |h_\mu[\ell]|^2 + \tilde{n}[\ell] \quad (6.2.2)$$

where $\tilde{n}[\ell] = \mathbf{h}[\ell]^H \cdot \mathbf{n}[\ell]$ denotes the noise at the matched filter output. Comparing (6.2.2) with the theoretical result from Section 1.5 we recognize that the full diversity degree $D = N_R$ is achieved as long as the channel coefficients remain uncorrelated. The single-input multiple output (SIMO) channel is transformed by matched filtering into an equivalent SISO channel with smaller variations of the

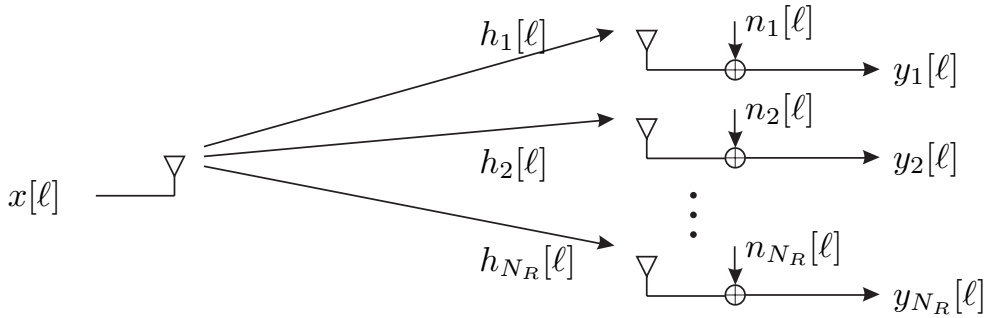


Figure 6.2.1: Structure of receive diversity system

SNR. Two differences occur between (6.2.2) and (1.5.3). First, the scaling with $\|\mathbf{h}\|^{-2}$ was not applied yet resulting in

$$\mathbf{r}[\ell] = \frac{1}{\|\mathbf{h}\|^2} \mathbf{h}[\ell]^H \cdot \mathbf{y}[\ell] = x[\ell] + \frac{1}{\|\mathbf{h}\|^2} \sum_{\mu=1}^{N_R} h_\mu[\ell]^* n_\mu[\ell]. \quad (6.2.3)$$

It is only important for multi-amplitude signalling and does not influence the SNR. Second, the total received power has not been normalized to E_s/T_s (missing factor $\sqrt{D} = \sqrt{N_R}$). The reason for this is that the application of multiple receive antennas does not only yield a diversity gain but also an array gain because the N_R -fold power is collected leading to a gain of $10 \log_{10}(N_R)$ dB. This gain is independent of diversity considerations and also available for totally correlated channels. Since Section 1.5 wanted to illustrate only the diversity effect, this array gain was suppressed by normalizing the received power. Hence, we always have to look carefully at the definition of the SNR when multiple antennas are applied.

Fig. 6.2.2 illustrates this difference by showing the results already known from Section 1.5. In Figure a), we fixed the total transmitted energy per information bit to E_b . Hence, it is independent of N_R and equally distributed onto the diversity paths so that only the N_R -th part of E_b can be exploited at each receive antenna. In this scenario, the gain solely obtained by diversity can be observed. Contrarily, Fig. b) depicts the error rate versus the average E_s/N_0 at each receive antenna. Therefore, the total transmit power increases linearly with N_R and the entire SNR after maximum ratio combining becomes N_R times larger indicating the additional array gain. Comparing the difference between adjacent curves in both plots, we recognize a difference of 3 dB that exactly represents the gain obtained by doubling the number of receive antennas.

We can conclude that receive diversity is an efficient and simple possibility to increase the link reliability. However, its applicability becomes immediately limited if the size of the receiving terminal is very small. Cell phones for mobile radio communications have become smaller and smaller in recent years so that it is a difficult task to place several antennas on such small devices. Even if we succeed,

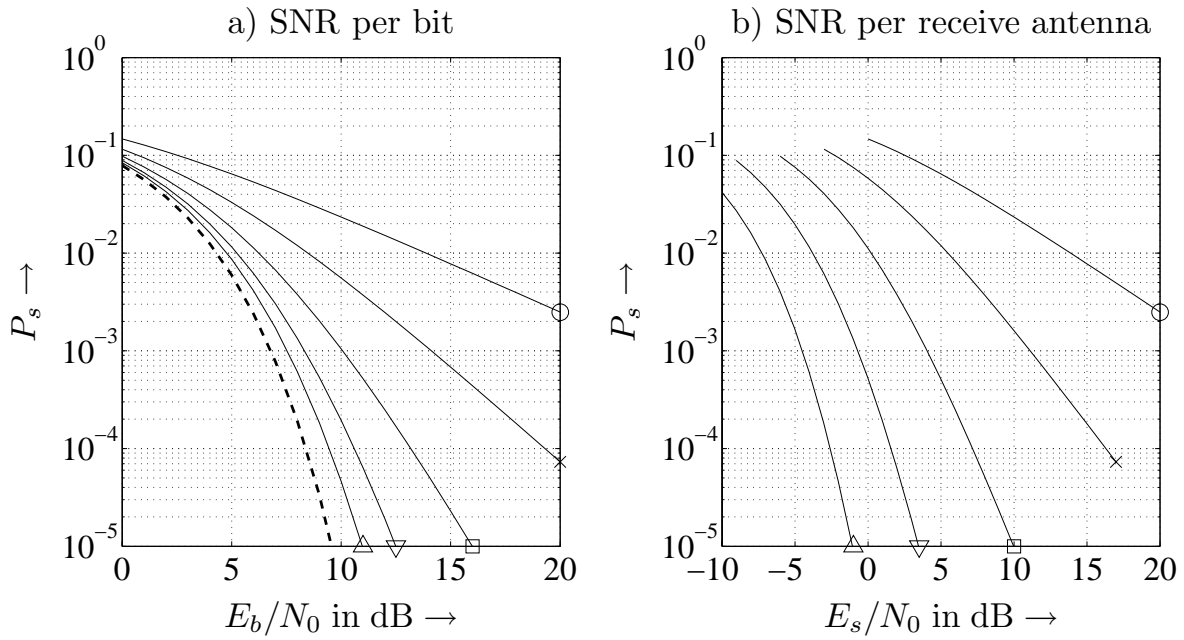


Figure 6.2.2: Performance of receive diversity for BPSK and uncorrelated Rayleigh fading channels, bold dashed line denotes AWGN channel ('o': $N_R = 1$, 'x': $N_R = 2$, '□': $N_R = 4$, '▽': $N_R = 8$, '△': $N_R = 16$)

it is questionable if the spacing is large enough to guarantee uncorrelated channels. In this situation, the question arises if diversity can also be exploited with multiple antennas at the transmitter.

6.2.2 Space-Time Transmit Diversity

In this subsection we address the general concept of space-time transmit diversity, i.e. using multiple antennas at the transmitter. A straight forward implementation where a signal $x[\ell]$ is transmitted simultaneously over several antennas will not provide the desired diversity gain. Looking at the received signal

$$y[\ell] = x[\ell] \cdot \sum_{\nu=1}^{N_T} h_{\nu} + n[\ell] \quad (6.2.4)$$

we see that an incoherent superposition is obtained resulting in a new Rayleigh distributed channel. Hence, the equivalent SISO channel still has as large SNR variations as the original single-input single-output system and no diversity has been gained. To overcome this dilemma, appropriate coding is required at the transmitter. This coding is performed in the dimensions space and time leading to the name *space-time codes* (STC). First, this subsection discusses the potential of STCs and derives some guidelines concerning the code construction. In the next two subsections, concrete codes, namely orthogonal space-time block codes (oSTBC) and space-time trellis codes (STTC) are introduced.

The general structure of the considered system is depicted in **Fig. 6.2.3**. The data bits $d[i]$ are fed into the space-time encoder that outputs the vectors $\mathbf{x}[k] = [x_1[k] \cdots x_{N_T}[k]]^T$. They are transmitted over a MIMO channel according to (6.1.1). The channel coefficients $h_{\mu,\nu}[k] = h_{\mu,\nu}$ are assumed to be constant during one encoded frame so that the received signal becomes

$$\mathbf{y}[k] = \mathbf{H} \cdot \mathbf{x}[k] + \mathbf{n}[k]. \quad (6.2.5)$$

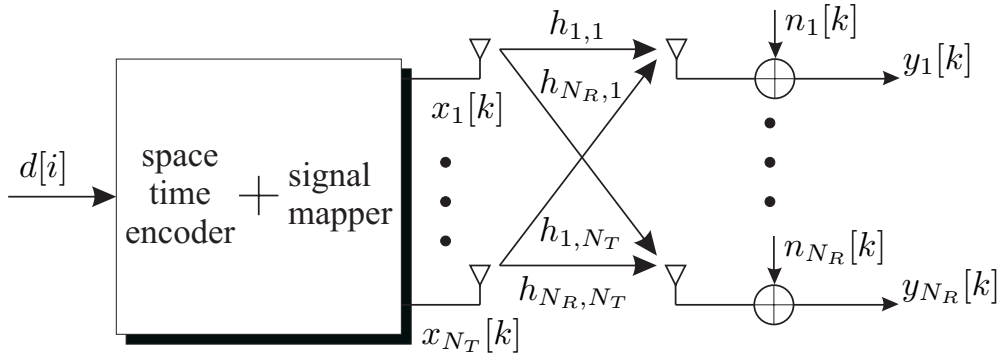


Figure 6.2.3: Structure of transmit diversity system with N_R receive antennas

Comprising all vectors $\mathbf{x}[k]$, $\mathbf{y}[k]$ and $\mathbf{n}[k]$ within one coded frame of length L as column vectors into the matrices \mathbf{X} , \mathbf{Y} and \mathbf{N} , respectively, results in

$$\mathbf{Y} = \mathbf{H} \cdot \mathbf{X} + \mathbf{N}, \quad (6.2.6)$$

where the $N_T \times L$ matrix

$$\mathbf{X} = [\mathbf{x}[0] \mathbf{x}[1] \cdots \mathbf{x}[L-1]] = \begin{bmatrix} x_1[0] & x_1[1] & \cdots & x_1[L-1] \\ x_2[0] & x_2[1] & \cdots & x_2[L-1] \\ \vdots & & \ddots & \vdots \\ x_{N_T}[0] & x_{N_T}[1] & \cdots & x_{N_T}[L-1] \end{bmatrix} \quad (6.2.7)$$

denotes the entire data frame encoded in space and time. The matrices \mathbf{N} and \mathbf{Y} have the dimensions $N_R \times L$.

Next, we derive some general results concerning the achievable diversity and coding gains that can be used for the code design. We assume an optimum maximum likelihood decision and a perfectly known channel matrix \mathbf{H} at the receiver. We start with the pairwise error probability between two competing codewords \mathbf{X} and $\tilde{\mathbf{X}}$ already known from Section 1.3. Contrarily to Section 1.3, we now receive a mixture of all transmit signals at each receive antenna. Therefore, we have to look at the squared Euclidean distance of the noiseless received signals $\|\mathbf{H}\mathbf{X} - \mathbf{H}\tilde{\mathbf{X}}\|^2$ of

both codewords instead of $\|\mathbf{X} - \tilde{\mathbf{X}}\|^2$. The conditional pairwise error probability of (1.3.15) then becomes

$$\Pr \left\{ \mathbf{X} \rightarrow \tilde{\mathbf{X}} \mid \mathbf{H} \right\} = \frac{1}{2} \cdot \operatorname{erfc} \left(\sqrt{\frac{\|\mathbf{H}\mathbf{X} - \mathbf{H}\tilde{\mathbf{X}}\|^2}{4\sigma_{\mathcal{N}}^2}} \right). \quad (6.2.8)$$

We now normalize the space-time codewords to $\mathbf{B} = \mathbf{X}/\sqrt{E_s/T_s}$ and $\tilde{\mathbf{B}} = \tilde{\mathbf{X}}/\sqrt{E_s/T_s}$ in the same way as done in Section 1.3. This changes the squared Euclidean distance to

$$\|\mathbf{H} \cdot (\mathbf{X} - \tilde{\mathbf{X}})\|^2 = \|\mathbf{H} \cdot (\mathbf{B} - \tilde{\mathbf{B}})\|^2 \cdot \frac{E_s}{T_s} \quad (6.2.9)$$

and (6.2.8) becomes with $\sigma_{\mathcal{N}}^2 = N_0/T_s$ for complex-valued signals

$$\Pr \left\{ \mathbf{X} \rightarrow \tilde{\mathbf{X}} \mid \mathbf{H} \right\} = \frac{1}{2} \cdot \operatorname{erfc} \left(\sqrt{\|\mathbf{H}(\mathbf{B} - \tilde{\mathbf{B}})\|^2 \cdot \frac{E_s}{4N_0}} \right). \quad (6.2.10)$$

The complementary error function can be upper bounded by $\operatorname{erfc}(\sqrt{x}) < e^{-x}$. Denoting the μ -th row of \mathbf{H} with $\underline{\mathbf{h}}_\mu$ leads to an upper bound

$$\begin{aligned} \Pr \left\{ \mathbf{B} \rightarrow \tilde{\mathbf{B}} \mid \mathbf{H} \right\} &\leq \frac{1}{2} \cdot \exp \left[-\|\mathbf{H}(\mathbf{B} - \tilde{\mathbf{B}})\|^2 \cdot \frac{E_s}{4N_0} \right] \\ &\leq \frac{1}{2} \cdot \exp \left[-\sum_{\mu=1}^{N_R} \|\underline{\mathbf{h}}_\mu(\mathbf{B} - \tilde{\mathbf{B}})\|^2 \cdot \frac{E_s}{4N_0} \right] \\ &\leq \frac{1}{2} \cdot \prod_{\mu=1}^{N_R} \exp \left[-(\underline{\mathbf{h}}_\mu(\mathbf{B} - \tilde{\mathbf{B}})(\mathbf{B} - \tilde{\mathbf{B}})^H \underline{\mathbf{h}}_\mu^H) \cdot \frac{E_s}{4N_0} \right]. \end{aligned} \quad (6.2.11)$$

Obviously, the matrix $\mathbf{A} = (\mathbf{B} - \tilde{\mathbf{B}})(\mathbf{B} - \tilde{\mathbf{B}})^H$ is Hermitian and its rank r equals that of $\mathbf{B} - \tilde{\mathbf{B}}$. Moreover, it is positive semidefinite and its r nonzero eigenvalues λ_ν obtained by an eigenvalue decomposition $\mathbf{A} = \mathbf{U}\boldsymbol{\Lambda}\mathbf{U}^H$ are real and positive. The pairwise error probability can now be expressed as

$$\begin{aligned} \Pr \left\{ \mathbf{B} \rightarrow \tilde{\mathbf{B}} \mid \mathbf{H} \right\} &\leq \frac{1}{2} \cdot \prod_{\mu=1}^{N_R} \exp \left[-(\underline{\mathbf{h}}_\mu \mathbf{U} \boldsymbol{\Lambda} \mathbf{U}^H \underline{\mathbf{h}}_\mu^H) \cdot \frac{E_s}{4N_0} \right] \\ &\leq \frac{1}{2} \cdot \prod_{\mu=1}^{N_R} \exp \left[-\underline{\boldsymbol{\beta}}_\mu \boldsymbol{\Lambda} \underline{\boldsymbol{\beta}}_\mu^H \cdot \frac{E_s}{4N_0} \right]. \end{aligned} \quad (6.2.12)$$

The new row vectors $\underline{\boldsymbol{\beta}}_\mu = \underline{\mathbf{h}}_\mu \mathbf{U} = [\beta_{\mu,1} \cdots \beta_{\mu,N_T}]$ still consist of complex rotationally invariant Gaussian distributed random variables $\beta_{\mu,\nu}$ because \mathbf{U} is unitary

[NTSC97]. Hence, their squared magnitudes are chi-square distributed with two degrees of freedom. In order to obtain a pairwise error probability that is independent of the instantaneous channel matrix \mathbf{H} , we have to calculate the expectation of (6.2.12) with respect to \mathbf{H} . We obtain

$$\begin{aligned} \Pr \{ \mathbf{B} \rightarrow \tilde{\mathbf{B}} \} &= \mathbb{E}_{\underline{\mathcal{H}}} \left\{ \Pr \{ \mathbf{B} \rightarrow \tilde{\mathbf{B}} \mid \mathbf{H} \} \right\} \\ &\leq \frac{1}{2} \cdot \prod_{\mu=1}^{N_R} \prod_{\nu=1}^r \mathbb{E}_{\beta} \left\{ \exp \left[-\lambda_{\nu} \cdot |\beta_{\mu,\nu}|^2 \cdot \frac{E_s}{4N_0} \right] \right\} \\ &\leq \frac{1}{2} \cdot \prod_{\mu=1}^{N_R} \prod_{\nu=1}^r \int_0^{\infty} e^{-\xi} \cdot \exp \left[-\xi \cdot \lambda_{\nu} \frac{E_s}{4N_0} \right] d\xi \\ &\leq \frac{1}{2} \cdot \left[\prod_{\nu=1}^r \frac{1}{1 + \lambda_{\nu} \cdot \frac{E_s}{4N_0}} \right]^{N_R}. \end{aligned} \quad (6.2.13)$$

A further upper bound that is tight for large SNR is obtained by dropping the $+1$ in the denominator. Rewriting (6.2.13) finally leads to the expression

$$\Pr \{ \mathbf{B} \rightarrow \tilde{\mathbf{B}} \} < \frac{1}{2} \cdot \left[\frac{E_s}{4N_0} \cdot \left(\prod_{\nu=1}^r \lambda_{\nu} \right)^{1/r} \right]^{-rN_R}. \quad (6.2.14)$$

From (6.2.14), the following conclusions can be drawn. Due to the similarity with (1.5.9) where the reciprocal of the signal to noise ratio is taken to the power of D , the exponent rN_R is called diversity gain. Hence, in order to achieve the maximum possible diversity degree, the minimum rank r among all pairwise differences $\mathbf{B} - \tilde{\mathbf{B}}$ should be maximized leading to the diversity gain

$$g_d = N_R \cdot \min_{(\mathbf{B}, \tilde{\mathbf{B}})} \text{rank} (\mathbf{B} - \tilde{\mathbf{B}}). \quad (6.2.15)$$

On the other hand, the coding gain leading to a horizontal shift of the error rate curves can be described by

$$g_c = \min_{(\mathbf{B}, \tilde{\mathbf{B}})} \left(\prod_{\nu=1}^r \lambda_{\nu} \right)^{1/r}. \quad (6.2.16)$$

If the code design ensures full rank differences, the product of the eigenvalues equals the determinant of $\mathbf{B} - \tilde{\mathbf{B}}$

$$g_c = \min_{(\mathbf{B}, \tilde{\mathbf{B}})} \left(\prod_{\nu=1}^{N_T} \lambda_{\nu} \right)^{1/N_T} = \min_{(\mathbf{B}, \tilde{\mathbf{B}})} \left(\det(\mathbf{B} - \tilde{\mathbf{B}}) \right)^{1/N_T}. \quad (6.2.17)$$

We obtain the code design criteria according to [TSC98]:

- **rank criterion:** In order to obtain the maximum diversity gain, the first design goal is to maximize the minimum rank r of all matrices $\mathbf{X} - \tilde{\mathbf{X}}$. The diversity degree equals rN_R , its maximum is $N_R N_T$.
- **determinant criterion:** For a diversity gain of rN_R , the coding gain is maximized if the minimum of $(\prod_{\nu=1}^r \lambda_\nu)^{1/r}$ is maximized over all codeword pairs.

A code optimization according to these criteria cannot be performed analytically but has to be carried out computer based code search. The next two subsections introduce examples for space-time coding schemes. First, orthogonal space-time block codes are presented. Since their codewords are obtained by orthogonal matrix design, the determinant is always one and no coding gain is obtained. However, full diversity gains are achievable and the receiver structures are very simple. Afterwards, space-time trellis codes are briefly described providing additional coding gains at the expense of much higher decoding complexity.

6.2.3 Orthogonal Space-Time Block Codes

Fig. 6.2.4 shows the principle structure of a space-time block coding system for $N_R = 1$ receive antenna. The subsequent derivation includes more generally the application of an arbitrary number of receive antennas. As a difference to the general concept of space-time coding depicted in Fig. 6.2.3, signal mapper and space-time encoder are separated. First, the data bits are mapped onto symbols $a[\ell]$ that are elements of a finite signal constellation according to the linear modulation schemes presented in Section 1.4. Next, the space-time block encoder collects a block of K successive symbols $a[\ell]$ and maps them onto a sequence of L consecutive vectors $\mathbf{x}[k] = [x_1[k] \cdots x_{N_T}[k]]^T$, $0 \leq k < L$. Hence, the generated symbols $a[\ell]$ are encoded in two dimensions, namely in space and time explaining the name *space-time coding*. The code rate amounts to

$$R_c = \frac{K}{L} . \quad (6.2.18)$$

Certainly, the system can be improved by an outer FEC coding scheme. In the sequel we make the widely used assumption that the channel remains constant during one coding block. Therefore, we can drop the time indices of the channel coefficients ($h_\mu[k] \rightarrow h_\mu$) in subsequent derivations.

Alamouti's Scheme

In order to illustrate how orthogonal Space-Time Block Codes (STBC) work, we start with a simple example introduced by Alamouti [Ala98]. Originally, it employs

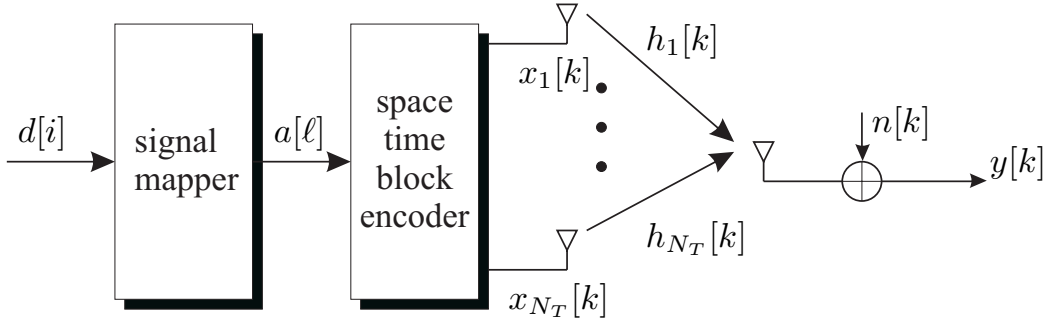


Figure 6.2.4: System structure for space-time block codes with $N_R = 1$ receive antenna

$N_T = 2$ transmit antennas and $N_R = 1$ receive antenna. However, it can be easily extended to more receive antennas. To be precise, we have to consider blocks of $K = 2$ consecutive symbols, say $a_1 = a[2\ell]$ and $a_2 = a[2\ell + 1]$. These two symbols are now encoded in the following way. At time instance $k = 2\ell$, symbol $x_1[k] = a_1$ is transmitted at antenna 1 and $x_2[k] = a_2$ at antenna 2. At the next time instance, the symbols are flipped and $x_1[k + 1] = -a_2^*$ as well as $x_2[k + 1] = a_1^*$ hold. The whole codeword arranged in space and time can be described using vector notations

$$\mathbf{X}_2 = [\mathbf{x}[2\ell] \quad \mathbf{x}[2\ell + 1]] = \begin{bmatrix} a_1 & -a_2^* \\ a_2 & a_1^* \end{bmatrix}. \quad (6.2.19)$$

The columns comprise the symbols transmitted at a certain time instance while the rows represent the symbols transmitted over a certain antenna. Since $K = 2$ symbols a_1 and a_2 are transmitted during $L = 2$ time instances, the rate of this code is $R_c = K/L = 1$. It is important to mention that the columns in \mathbf{X}_2 are orthogonal so that Alamouti's scheme does not provide a coding gain.

A different implementation was chosen in the UMTS standard [TS 99] without changing the achievable diversity gain. Here, the code matrix has the form

$$\mathbf{X}_2 = [\mathbf{x}[2\ell] \quad \mathbf{x}[2\ell + 1]] = \begin{bmatrix} a_1 & a_2 \\ -a_2^* & a_1^* \end{bmatrix}. \quad (6.2.20)$$

The advantage of this implementation is that the original symbols a_1 and a_2 are transmitted over the same antenna. Therefore, the first antenna is used as without space-time coding and only the second antenna has to be added without influencing the data stream $x_1[\ell]$. Nevertheless, we will restrict in our analysis on the first notation of (6.2.19).

The two received symbols can then be expressed by

$$y[2\ell] = h_1 a_1 + h_2 a_2 + n[2\ell] \quad (6.2.21a)$$

$$y[2\ell + 1] = h_1 (-a_2^*) + h_2 a_1^* + n[2\ell + 1]. \quad (6.2.21b)$$

Using vector notations, we can comprise the two received symbols and the two noise samples into vectors $\mathbf{y} = [y[2\ell] \ y[2\ell + 1]]^T$ and $\mathbf{n} = [n[2\ell] \ n[2\ell + 1]]^T$, respectively. This yields the compact description

$$\mathbf{y} = \begin{bmatrix} y_1 \\ y_2 \end{bmatrix} = \begin{bmatrix} a_1 & a_2 \\ -a_2^* & a_1^* \end{bmatrix} \cdot \begin{bmatrix} h_1 \\ h_2 \end{bmatrix} + \begin{bmatrix} n_1 \\ n_2 \end{bmatrix} = \mathbb{X}_2 \cdot \mathbf{h} + \mathbf{n}. \quad (6.2.22)$$

Rewriting (6.2.22) by taking the conjugate complex of the second line, we obtain

$$\tilde{\mathbf{y}} = \begin{bmatrix} y_1 \\ y_2^* \end{bmatrix} = \begin{bmatrix} h_1 & h_2 \\ h_2^* & -h_1^* \end{bmatrix} \cdot \begin{bmatrix} a_1 \\ a_2 \end{bmatrix} + \begin{bmatrix} n_1 \\ n_2^* \end{bmatrix} = \mathbf{H}[\mathbb{X}_2] \cdot \mathbf{a} + \tilde{\mathbf{n}}. \quad (6.2.23)$$

With this slight modification, we have transformed the multiple-input single-output (MISO) channel \mathbf{h} into an equivalent MIMO channel $\mathbf{H}[\mathbb{X}_2]$. The matrix describing this equivalent channel has orthogonal columns. In this case, we know already from Chapter 4 that the matched filter represents the optimum detector according to the maximum likelihood principle. The matched filter output becomes

$$\tilde{\mathbf{r}} = \mathbf{H}^H[\mathbb{X}_2] \cdot \tilde{\mathbf{y}} = \begin{bmatrix} |h_1|^2 + |h_2|^2 & 0 \\ 0 & |h_1|^2 + |h_2|^2 \end{bmatrix} \cdot \mathbf{a} + \mathbf{H}^H[\mathbb{X}_2] \cdot \tilde{\mathbf{n}}. \quad (6.2.24)$$

Looking at the diagonal elements, we observe that the Alamouti scheme provides the full diversity degree $D = N_T = 2$ that can be achieved with two transmit antennas. Moreover, no interference between a_1 and a_2 disturbs the transmission because $\mathbf{H}^H[\mathbb{X}_2]\mathbf{H}[\mathbb{X}_2]$ is a diagonal matrix. Due to this reason and the fact that the noise remains white when multiplied with a matrix consisting of orthogonal columns, the ML decision with respect to the vector \mathbf{a} can be split into element-wise decisions

$$\hat{a}_\mu = \operatorname{argmin}_{\tilde{a}} |\tilde{r}_\mu - (|h_1|^2 + |h_2|^2)\tilde{a}|^2. \quad (6.2.25)$$

As all space-time coding schemes, the Alamouti scheme can be easily combined with multiple receive antennas. According to (6.2.23), we obtain a vector

$$\tilde{\mathbf{y}}_\mu = \mathbf{H}_\mu[\mathbb{X}_2]\mathbf{a} + \tilde{\mathbf{n}}_\mu \quad (6.2.26)$$

containing two successive symbols at each receive antenna $1 \leq \mu \leq N_R$. They are now comprised in the vector

$$\tilde{\mathbf{y}} = [\tilde{\mathbf{y}}_1^T \ \cdots \ \tilde{\mathbf{y}}_{N_R}^T]^T.$$

Consequently, the equivalent channel matrix $\mathbf{H}[\mathbb{X}_2]$ also has to be extended. Following the notation in (6.2.23) it becomes

$$\mathbf{H}[\mathbb{X}_2] = \begin{bmatrix} \mathbf{H}_1[\mathbb{X}_2] \\ \vdots \\ \mathbf{H}_{N_R}[\mathbb{X}_2] \end{bmatrix} = \begin{bmatrix} h_{1,1} & h_{1,2} \\ h_{1,2}^* & -h_{1,1}^* \\ \vdots & \vdots \\ h_{N_R,1} & h_{N_R,2} \\ h_{N_R,2}^* & -h_{N_R,1}^* \end{bmatrix}. \quad (6.2.27)$$

The receiver now consists of a bank of matched filters, one for each receive antenna. Their outputs are simply summed yielding

$$\tilde{\mathbf{r}} = \mathbf{H}^H[\mathbb{X}_2] \cdot \tilde{\mathbf{y}} = \sum_{\mu=1}^{N_R} \mathbf{H}_\mu^H[\mathbb{X}_2] \cdot \tilde{\mathbf{y}}_\mu = \sum_{\mu=1}^{N_R} (|h_{\mu,1}|^2 + |h_{\mu,2}|^2) \cdot \mathbf{a} + \mathbf{H}^H[\mathbb{X}_2] \cdot \tilde{\mathbf{n}} \quad (6.2.28)$$

As long as all channels remain uncorrelated, a maximum diversity degree of $D = 2N_R$ can be achieved.

Extension to more than two Transmit Antennas

Using some basic results from matrix theory one can show that Alamouti's scheme is the only orthogonal space-time code with rate one. For more than two transmit antennas, several orthogonal codes have been found with lower rates, so that spectral efficiency is lost. The code matrix \mathbb{X}_{N_T} generally consists of N_T rows and L columns and contains the symbols a_1, \dots, a_K as well as the conjugate complex counterparts a_1^*, \dots, a_K^* . The construction of \mathbb{X}_{N_T} has to be performed such that \mathbb{X}_{N_T} has orthogonal rows, i.e.

$$\mathbb{X}_{N_T} \mathbb{X}_{N_T}^H = C \cdot \mathbf{I}_{N_T} \quad (6.2.29)$$

holds where C is a constant depending on the symbol powers.

In [TJC99a] it is shown that there exist half-rate codes for an arbitrary number of transmit antennas. The code matrices for $N_T = 3$ and $N_T = 4$ are presented as examples. For $N_T = 3$, we obtain

$$\mathbb{X}_3 = \begin{bmatrix} a_1 & -a_2 & -a_3 & -a_4 & a_1^* & -a_2^* & -a_3^* & -a_4^* \\ a_2 & a_1 & a_4 & -a_3 & a_2^* & a_1^* & a_4^* & -a_3^* \\ a_3 & -a_4 & a_1 & a_2 & a_3^* & -a_4^* & a_1^* & a_2^* \end{bmatrix} \quad (6.2.30)$$

providing a diversity degree of $D = N_T = 3$. Obviously, \mathbb{X}_3 consists of $L = 8$ columns and $K = 4$ different symbols a_1, \dots, a_4 are encoded leading to the rate $R_c = K/L = 1/2$. From (6.2.30), we can write the received vector as

$$\mathbf{y} = \begin{bmatrix} h_1 & h_2 & h_3 & 0 & 0 & 0 & 0 & 0 \\ h_2 & -h_1 & 0 & -h_3 & 0 & 0 & 0 & 0 \\ h_3 & 0 & -h_1 & h_2 & 0 & 0 & 0 & 0 \\ 0 & h_3 & -h_2 & -h_1 & 0 & 0 & 0 & 0 \\ 0 & 0 & 0 & 0 & h_1 & h_2 & h_3 & 0 \\ 0 & 0 & 0 & 0 & h_2 & -h_1 & 0 & -h_3 \\ 0 & 0 & 0 & 0 & h_3 & 0 & -h_1 & h_2 \\ 0 & 0 & 0 & 0 & 0 & h_3 & -h_2 & -h_1 \end{bmatrix} \begin{bmatrix} a_1 \\ a_2 \\ a_3 \\ a_4 \\ a_1^* \\ a_2^* \\ a_3^* \\ a_4^* \end{bmatrix} + \mathbf{n}. \quad (6.2.31)$$

We observe in (6.2.31) that the last four symbols in \mathbf{y} only depend on the conjugate complex transmit symbols. Hence, conjugating the last four rows similar to the procedure for Alamouti's scheme in (6.2.23) results in

$$\tilde{\mathbf{y}} = \mathbf{H}[\mathbb{X}_3]\mathbf{a} + \tilde{\mathbf{n}} \Rightarrow \begin{bmatrix} y_1 \\ y_2 \\ y_3 \\ y_4 \\ y_5^* \\ y_6^* \\ y_7^* \\ y_8^* \end{bmatrix} = \begin{bmatrix} h_1 & h_2 & h_3 & 0 \\ h_2 & -h_1 & 0 & -h_3 \\ h_3 & 0 & -h_1 & h_2 \\ 0 & h_3 & -h_2 & -h_1 \\ h_1^* & h_2^* & h_3^* & 0 \\ h_2^* & -h_1^* & 0 & -h_3^* \\ h_3^* & 0 & -h_1^* & h_2^* \\ 0 & h_3^* & -h_2^* & -h_1^* \end{bmatrix} \begin{bmatrix} a_1 \\ a_2 \\ a_3 \\ a_4 \end{bmatrix} + \begin{bmatrix} n_1 \\ n_2 \\ n_3 \\ n_4 \\ n_5^* \\ n_6^* \\ n_7^* \\ n_8^* \end{bmatrix}. \quad (6.2.32)$$

Obviously, (6.2.32) uses only the original symbols $\mathbf{a} = [a_1 \cdots a_4]^T$ and not their conjugate complex versions. Moreover, the columns in $\mathbf{H}[\mathbb{X}_3]$ are orthogonal so that

$$\mathbf{H}^H[\mathbb{X}_3] \cdot \mathbf{H}[\mathbb{X}_3] = 2 \cdot \sum_{\mu=1}^{N_T} |h_\mu|^2 \cdot \mathbf{I}_4 = 2 \cdot (|h_1|^2 + |h_2|^2 + |h_3|^2) \cdot \mathbf{I}_4 \quad (6.2.33)$$

holds. Therefore, the optimum receiver is again a matched filter that multiplies the modified received vector $\tilde{\mathbf{y}}$ with $\mathbf{H}^H[\mathbb{X}_3]$. In case of multi-amplitude modulation, an appropriate scaling with $(2 \cdot \sum_{\mu=1}^{N_T} |h_\mu|^2)^{-1}$ prior to the hard decision is necessary.

For $N_T = 4$, a diversity gain of $D = N_T = 4$ is achieved with the code matrix

$$\mathbb{X}_4 = \begin{bmatrix} a_1 & -a_2 & -a_3 & -a_4 & a_1^* & -a_2^* & -a_3^* & -a_4^* \\ a_2 & a_1 & a_4 & -a_3 & a_2^* & a_1^* & a_4^* & -a_3^* \\ a_3 & -a_4 & a_1 & a_2 & a_3^* & -a_4^* & a_1^* & a_2^* \\ a_4 & a_3 & -a_2 & a_1 & a_4^* & a_3^* & -a_2^* & a_1^* \end{bmatrix}. \quad (6.2.34)$$

Equivalently to the case of $N_T = 3$, we obtain a received vector \mathbf{y} according to

$$\mathbf{y} = \begin{bmatrix} h_1 & h_2 & h_3 & h_4 & 0 & 0 & 0 & 0 \\ h_2 & -h_1 & h_4 & -h_3 & 0 & 0 & 0 & 0 \\ h_3 & -h_4 & -h_1 & h_2 & 0 & 0 & 0 & 0 \\ h_4 & h_3 & -h_2 & -h_1 & 0 & 0 & 0 & 0 \\ 0 & 0 & 0 & 0 & h_1 & h_2 & h_3 & h_4 \\ 0 & 0 & 0 & 0 & h_2 & -h_1 & h_4 & -h_3 \\ 0 & 0 & 0 & 0 & h_3 & -h_4 & -h_1 & h_2 \\ 0 & 0 & 0 & 0 & h_4 & h_3 & -h_2 & -h_1 \end{bmatrix} \begin{bmatrix} a_1 \\ a_2 \\ a_3 \\ a_4 \\ a_1^* \\ a_2^* \\ a_3^* \\ a_4^* \end{bmatrix} + \mathbf{n}. \quad (6.2.35)$$

Complex conjugation of the last four elements in \mathbf{y} leads to $\tilde{\mathbf{y}} = \mathbf{H}[\mathbb{X}_4] \cdot \mathbf{a} + \tilde{\mathbf{n}}$ with

$$\mathbf{H}[\mathbb{X}_4] = \begin{bmatrix} h_1 & h_2 & h_3 & h_4 \\ h_2 & -h_1 & h_4 & -h_3 \\ h_3 & -h_4 & -h_1 & h_2 \\ h_4 & h_3 & -h_2 & -h_1 \\ h_1^* & h_2^* & h_3^* & h_4^* \\ h_2^* & -h_1^* & h_4^* & -h_3^* \\ h_3^* & -h_4^* & -h_1^* & h_2^* \\ h_4^* & h_3^* & -h_2^* & -h_1^* \end{bmatrix}. \quad (6.2.36)$$

Again, the columns of $\mathbf{H}[\mathbb{X}_4]$ are mutually orthogonal and estimates $\hat{\mathbf{a}}$ are obtained by multiplying $\tilde{\mathbf{y}}$ with $\mathbf{H}^H[\mathbb{X}_4]$ and appropriate scaling with $(2 \cdot \sum_{\mu=1}^{N_T} |h_\mu|^2)^{-1}$.

Looking towards higher spectral efficiencies, only two codes with $N_T = 3$ and $N_T = 4$ have yet been found for $R_c > 1/2$ [TJC99a, TJC99b]. In order to distinguish them from the codes presented so far, we use the notation \mathbb{T}_3 and \mathbb{T}_4 . For $N_T = 3$, the orthogonal space-time codeword is

$$\mathbb{T}_3 = \frac{1}{2} \cdot \begin{bmatrix} 2a_1 & -2a_2^* & \sqrt{2}a_3^* & \sqrt{2}a_3^* \\ 2a_2 & 2a_1^* & \sqrt{2}a_3^* & -\sqrt{2}a_3^* \\ \sqrt{2}a_3 & \sqrt{2}a_3 & -a_1 - a_1^* + a_2 - a_2^* & a_1 - a_1^* + a_2 + a_2^* \end{bmatrix}. \quad (6.2.37)$$

Since it comprises four time instances for transmitting three symbols, the code rate amounts to $R_c = 3/4$. Using (6.2.37), the received vector can be written as

$$\mathbf{y} = \begin{bmatrix} h_1 & h_2 & \frac{h_3}{\sqrt{2}} & 0 & 0 & 0 \\ 0 & 0 & \frac{h_3}{\sqrt{2}} & h_2 & -h_1 & 0 \\ -\frac{h_3}{\sqrt{2}} & \frac{h_3}{\sqrt{2}} & 0 & -\frac{h_3}{\sqrt{2}} & -\frac{h_3}{\sqrt{2}} & \frac{h_1+h_2}{\sqrt{2}} \\ \frac{h_3}{\sqrt{2}} & \frac{h_3}{\sqrt{2}} & 0 & -\frac{h_3}{\sqrt{2}} & \frac{h_3}{\sqrt{2}} & \frac{h_1-h_2}{\sqrt{2}} \end{bmatrix} \begin{bmatrix} a_1 \\ a_2 \\ a_3 \\ a_1^* \\ a_2^* \\ a_3^* \end{bmatrix} + \mathbf{n}. \quad (6.2.38)$$

Unfortunately, the channel matrix in (6.2.38) has not the block diagonal structure so that a separation into rows associated only with the original symbols a_1, \dots, a_3

and those associated with their complex conjugate versions is not possible. Hence, a direct construction of an equivalent matrix $\mathbf{H}[\mathbb{T}_3]$ containing the complex channel coefficients is not possible. However, we can separate real and imaginary parts of all components and stack them into vectors and matrices similar to the approach applied to linear multi-user detectors for real-valued modulation schemes discussed in Sections 5.2.1, 5.2.2 and 5.4.2. Denoting the real part of a complex symbol y with y' and the imaginary part with y'' , we define the real-valued vectors

$$\mathbf{y}^r = [y'_1 \quad \cdots \quad y'_L \quad y''_1 \quad \cdots \quad y''_L]^T \quad (6.2.39a)$$

$$\mathbf{n}^r = [n'_1 \quad \cdots \quad n'_L \quad n''_1 \quad \cdots \quad n''_L]^T \quad (6.2.39b)$$

$$\mathbf{a}^r = [a'_1 \quad \cdots \quad a'_K \quad a''_1 \quad \cdots \quad a''_K]^T. \quad (6.2.39c)$$

The received vector can now be expressed by $\mathbf{y}^r = \mathbf{H}^r[\mathbb{T}_3]\mathbf{a}^r + \mathbf{n}^r$ with

$$\mathbf{H}^r[\mathbb{T}_3] = \begin{bmatrix} h'_1 & h'_2 & \frac{h'_3}{\sqrt{2}} & -h''_1 & -h''_2 & -\frac{h''_3}{\sqrt{2}} \\ h'_2 & -h'_1 & \frac{h'_3}{\sqrt{2}} & h''_2 & -h''_1 & -\frac{h''_3}{\sqrt{2}} \\ -h'_3 & 0 & \frac{h'_1+h'_2}{\sqrt{2}} & 0 & -h''_3 & \frac{h''_1+h''_2}{\sqrt{2}} \\ 0 & h'_3 & \frac{h'_1-h'_2}{\sqrt{2}} & -h''_3 & 0 & \frac{h''_1-h''_2}{\sqrt{2}} \\ h''_1 & h''_2 & \frac{h''_3}{\sqrt{2}} & h'_1 & h'_2 & \frac{h'_3}{\sqrt{2}} \\ h''_2 & -h''_1 & \frac{h''_3}{\sqrt{2}} & -h'_2 & h'_1 & \frac{h'_3}{\sqrt{2}} \\ -h''_3 & 0 & \frac{h''_1+h''_2}{\sqrt{2}} & 0 & h'_3 & -\frac{h'_1+h'_2}{\sqrt{2}} \\ 0 & h''_3 & \frac{h''_1-h''_2}{\sqrt{2}} & h'_3 & 0 & -\frac{h'_1-h'_2}{\sqrt{2}} \end{bmatrix}. \quad (6.2.40)$$

Due to the separation of real and imaginary parts, we have again obtained a matrix with orthogonal columns

$$(\mathbf{H}^r[\mathbb{T}_3])^T \cdot \mathbf{H}[\mathbb{T}_3] = 2 \sum_{\mu=1}^{N_T} |h_\mu|^2 \cdot \mathbf{I}_3 = 2 \cdot (|h_1|^2 + |h_2|^2 + |h_3|^2) \cdot \mathbf{I}_3.$$

After multiplying \mathbf{y}^r with $(\mathbf{H}^r[\mathbb{T}_3])^T$, real and imaginary parts of each symbol experience a diversity gain of N_T . For multi-amplitude modulation, they have to be normalized and combined to a complex symbol again allowing the demodulation.

Finally, a space-time coding scheme with $N_T = 4$ transmit antennas shall be presented. The space-time code word is

$$\mathbb{T}_4 = \frac{1}{2} \cdot \begin{bmatrix} 2a_1 & -2a_2^* & \sqrt{2}a_3^* & \sqrt{2}a_3^* \\ 2a_2 & 2a_1^* & \sqrt{2}a_3^* & -\sqrt{2}a_3^* \\ \sqrt{2}a_3 & \sqrt{2}a_3 & -a_1 - a_1^* + a_2 - a_2^* & a_1 - a_1^* + a_2 + a_2^* \\ \sqrt{2}a_3 & -\sqrt{2}a_3 & -a_1 - a_1^* - a_2 - a_2^* & -(a_1 + a_1^* + a_2 + a_2^*) \end{bmatrix}. \quad (6.2.41)$$

Again, three symbols are transmitted within a block covering four time instances leading to $R_c = 3/4$. The received vector can be described using (6.2.41) yielding

$$\mathbf{y} = \begin{bmatrix} h_1 & h_2 & \frac{h_3+h_4}{\sqrt{2}} & 0 & 0 & 0 \\ 0 & 0 & \frac{h_3-h_4}{\sqrt{2}} & h_2 & -h_1 & 0 \\ \frac{-h_3+h_4}{2} & \frac{h_3-h_2}{2} & 0 & -\frac{h_3+h_4}{2} & -\frac{h_3+h_4}{2} & \frac{h_1+h_2}{\sqrt{2}} \\ \frac{h_3-h_4}{2} & \frac{h_3-h_4}{2} & 0 & -\frac{h_3+h_4}{2} & \frac{h_3+h_4}{2} & \frac{h_1-h_2}{\sqrt{2}} \end{bmatrix} \begin{bmatrix} a_1 \\ a_2 \\ a_3 \\ a_1^* \\ a_2^* \\ a_3^* \end{bmatrix} + \mathbf{n}. \quad (6.2.42)$$

The channel matrix for the real-valued received vector can now be expressed by

$$\mathbf{H}^r[\mathbb{T}_4] = \begin{bmatrix} h'_1 & h'_2 & \frac{h'_3+h_4}{\sqrt{2}} & -h''_1 & -h''_2 & -\frac{h''_3+h''_4}{\sqrt{2}} \\ h'_2 & -h'_1 & \frac{h'_3-h'_4}{\sqrt{2}} & h''_2 & -h''_1 & -\frac{h''_3+h''_4}{\sqrt{2}} \\ -h'_3 & -h'_4 & \frac{h'_1+h'_2}{\sqrt{2}} & -h''_4 & -h''_3 & \frac{h''_1+h''_2}{\sqrt{2}} \\ -h'_4 & h'_3 & \frac{h'_1-h'_2}{\sqrt{2}} & -h''_3 & h''_4 & \frac{h''_1-h''_2}{\sqrt{2}} \\ h''_1 & h''_2 & \frac{h''_3+h''_4}{\sqrt{2}} & h'_1 & h'_2 & \frac{h'_3+h'_4}{\sqrt{2}} \\ h''_2 & -h''_1 & \frac{h''_3-h''_4}{\sqrt{2}} & -h'_2 & h'_1 & \frac{h'_3-h'_4}{\sqrt{2}} \\ -h''_3 & -h''_4 & \frac{h''_1+h''_2}{\sqrt{2}} & h'_4 & h'_3 & -\frac{h'_1+h'_2}{\sqrt{2}} \\ -h''_4 & h''_3 & \frac{h''_1-h''_2}{\sqrt{2}} & h'_3 & -h'_4 & -\frac{h'_1-h'_2}{\sqrt{2}} \end{bmatrix}. \quad (6.2.43)$$

Due to the separation of real and imaginary parts, we have again obtained a matrix with orthogonal columns.

Certainly, the real-valued description can also be applied to Alamouti's scheme and to the codes \mathbb{X}_3 and \mathbb{X}_4 . Therefore, it is more general and can exploit more degrees of freedom because it is not restricted to use complex symbols and their conjugate versions. Linear space-time block codes constructed with real-valued notations are called *linear dispersion codes* [HH02].

As already explained for Alamouti's scheme, each of the discussed STBCs can be combined with several receive antennas. In this case, we obtain several equivalent channel matrices which are stacked into a large matrix according to (6.2.27). The receiver consists of a bank of N_R matched filters and simply sums their outputs. This leads to an overall diversity degree of $D = N_T \cdot N_R$.

Although orthogonal space-time block codes do not provide a coding gain, they have the great advantage that decoding simply requires some linear combinations of the received symbols. Moreover, they provide the full diversity degree achievable with a certain number of transmit and receive antennas.

Normalizing the Transmit Power

We now have to consider the transmit power of the presented STBCs in more detail. Starting with Alamouti's scheme, each of the two symbols a_1 and a_2 (including their complex conjugate versions) is transmitted twice during one block. For the code \mathbb{X}_3 on page 290, each symbol is transmitted $N_{\text{sym}} = 6$ times while $N_{\text{sym}} = 8$ holds for \mathbb{X}_4 . Last but not least, $N_{\text{sym}} = 3$ and $N_{\text{sym}} = 4$ hold for the schemes \mathbb{T}_3 and \mathbb{T}_4 , respectively. In order to draw a fair comparison among different schemes, we fix the total energy per symbol and block to E_s , i.e. the energy per symbol and transmission amounts to E_s/N_{sym} .

Moreover, a comparison of schemes with different spectral efficiencies is generally drawn with respect to E_b/N_0 . Taking also into account the number of receive antennas so that no array gain is measured, we obtain the following relationship between the average energy E_b per information bit and the symbol energy E_s

$$E_s = \frac{m \cdot R_c}{N_{\text{sym}} \cdot N_R} \cdot E_b = \frac{m \cdot K}{L \cdot N_{\text{sym}} \cdot N_R} \cdot E_b , \quad (6.2.44)$$

where m denotes the number of bits per symbol. N_{sym} describes how many times a symbol is transmitted with full energy per block. Alternatively, the SNR at each receive antenna can also be used so that the array gain of the receiver becomes obvious. However, this must be explicitly mentioned.

Simulation Results

We now look at the error rate performance of the space-time block coding schemes explained so far. First, **Fig. 6.2.5a** depicts the error rates of Alamouti's scheme with different number of receive antennas. Since \mathbb{X}_2 provides a diversity degree of $D = 2$, additional receive antennas multiply this degree leading to $D = 4$, $D = 6$ and $D = 8$ for $N_R = 2$, $N_R = 3$ and $N_R = 4$, respectively. A comparison between theoretical results from Section 1.5 (lines) and simulation results (symbols) illustrates that the both perfectly coincide. Hence, as long as the channel is ideally known to the receiver, optimum diversity performance is achieved. **Fig. 6.2.5b** shows the performance of \mathbb{X}_2 for different modulation schemes. Both, QPSK and 8-PSK, profit by an increased diversity degree.

Next, different space-time coding schemes are compared for BPSK and a single receive antenna. From **Fig. 6.2.6a** it becomes obvious that \mathbb{X}_3 and \mathbb{T}_3 have identical diversity degrees as well as \mathbb{X}_4 and \mathbb{T}_4 . The results are identical with those obtained from Section 1.5. However, the codes have different rates R_c leading to different spectral efficiencies. Therefore, we have to depict the error rates versus E_b/N_0 instead of E_s/N_0 . **Fig. 6.2.6b** shows the corresponding relations. The slopes of all curves are still the same as in Fig. a) but they are shifted horizontally

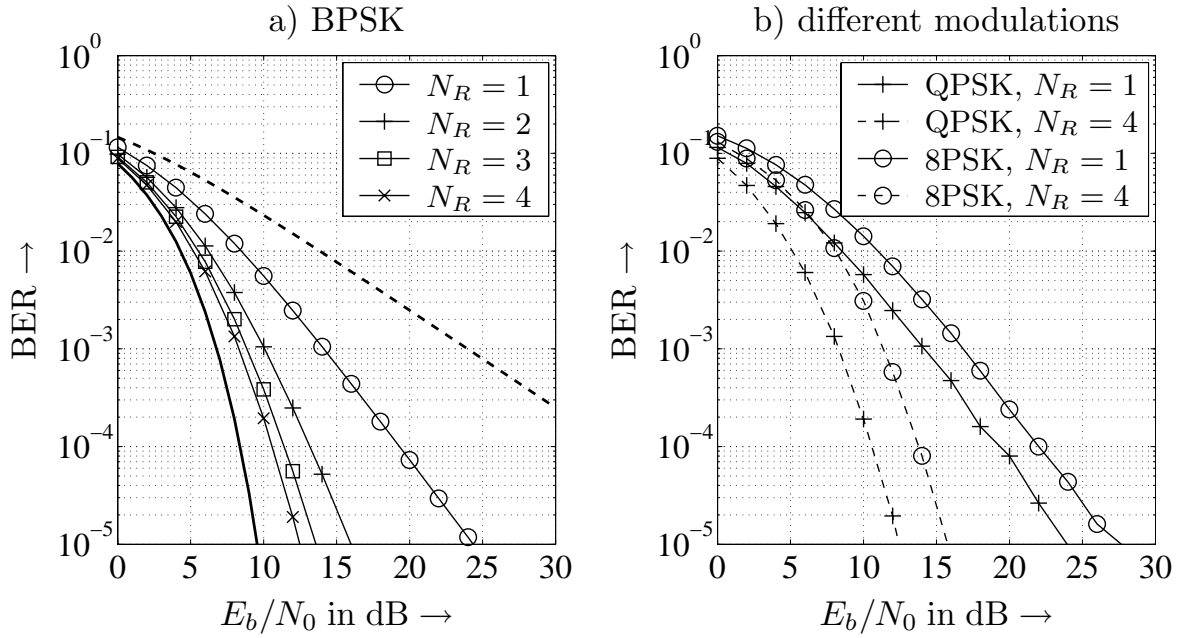


Figure 6.2.5: Bit error rate of Alamouti's scheme for different modulation types and number of receive antennas, (solid bold line: AWGN channel, solid dashed line: Rayleigh fading channel without diversity)

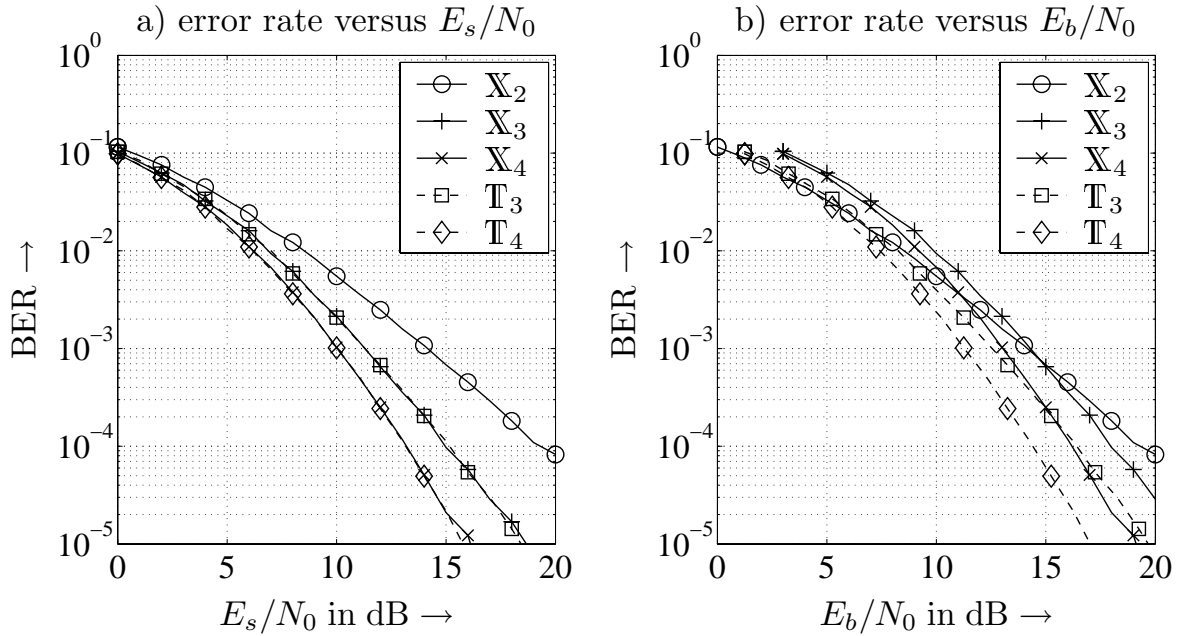


Figure 6.2.6: Bit error rate for different orthogonal STBCs, BPSK and $N_R = 1$ receive antenna

by $10 \log_{10}(R_c)$. The half rate codes X_3 and X_4 lose especially at small signal to noise ratios compared to T_3 and T_4 . Despite its higher diversity degree, X_3 outperforms Alamouti's scheme only for SNRs above 15 dB. The same holds for X_4 and T_3 .

A fair comparison between different space-time coding schemes can be guaranteed if it is drawn for identical spectral efficiencies. This can be achieved by choosing an appropriate modulation scheme for each STC. Table 6.2.1 summarizes some constellations considered here. For $\eta = 2$ bits/s/Hz, Alamouti's scheme employs a QPSK while \mathbb{X}_3 and \mathbb{X}_4 have to use a 16-QAM or 16-PSK due to their lower code rate of $R_c = 1/2$. For $\eta = 3$ bits/s/Hz, we use the 8-PSK for \mathbb{X}_2 and 16-QAM for \mathbb{T}_3 and \mathbb{T}_4 .

Table 6.2.1: Combinations of space-time codes and modulation schemes for different overall spectral efficiencies

η	\mathbb{X}_2	\mathbb{X}_3	\mathbb{X}_4	\mathbb{T}_3	\mathbb{T}_4
1 bit/s/Hz	BPSK	QPSK	QPSK	—	—
2 bits/s/Hz	QPSK	16-QAM	16-QAM	—	—
3 bits/s/Hz	8-PSK	—	—	16-QAM	16-QAM

The results for $\eta = 1$ bit/s/Hz are depicted in **Fig. 6.2.7a**. Since BPSK and QPSK show the same bit error rate performance versus E_b/N_0 , \mathbb{X}_3 and \mathbb{X}_4 do not suffer from a higher sensitivity of the modulation scheme and can fully exploit the larger diversity degree. In **Fig. 6.2.7b**, we observe different results for $\eta = 2$ bit/s/Hz. QPSK is much more robust than 16-QAM against the influence of noise. Hence, the higher diversity degree becomes obvious only for high signal to noise ratios. At low SNR, Alamouti's scheme with QPSK still performs best.

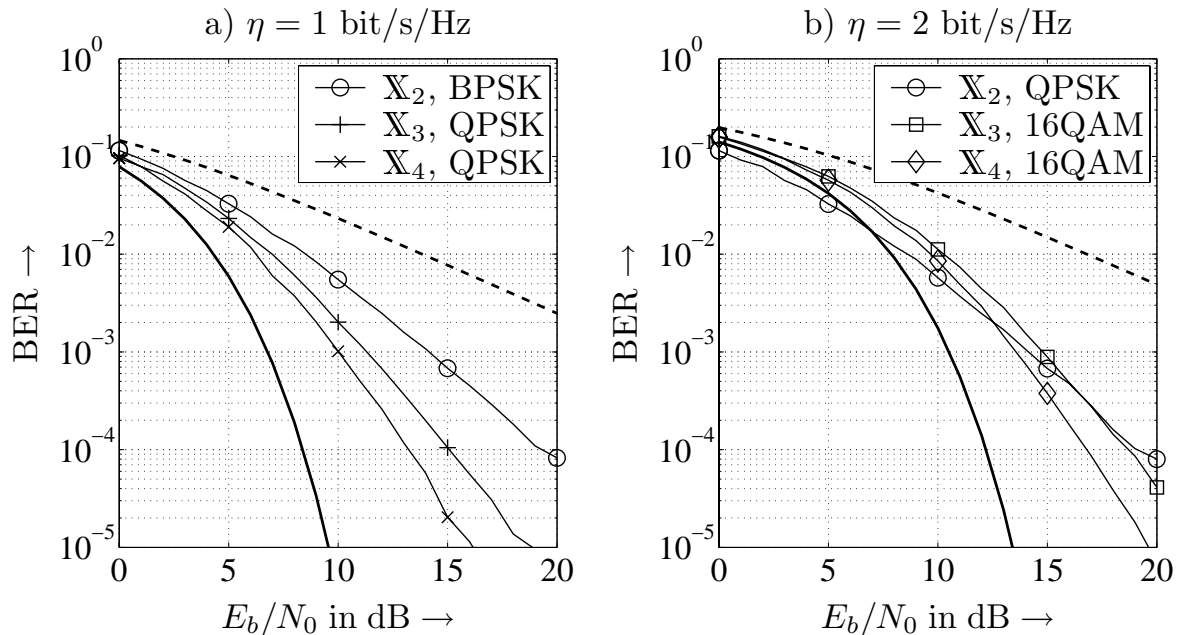


Figure 6.2.7: Bit error rate for different orthogonal STCs, $N_R = 1$ receive antenna and different spectral efficiencies (solid bold line: AWGN, dashed bold line: flat Rayleigh fading; in Fig. b) both for 16-QAM)

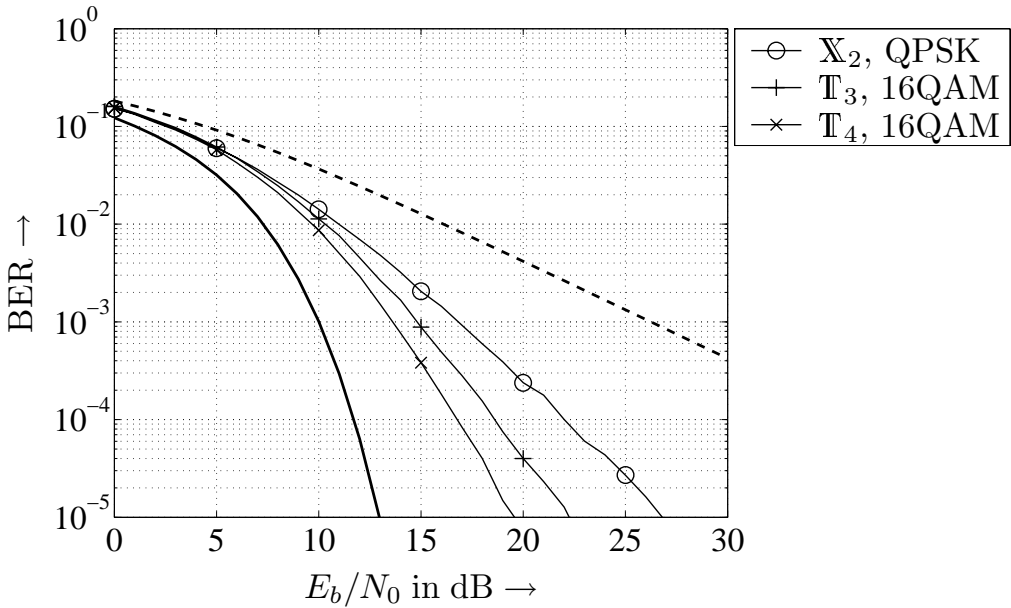


Figure 6.2.8: Bit error rate for different orthogonal STCs and $N_R = 1$ receive antenna, spectral efficiency $\eta = 3$ bit/s/Hz

Finally, **Fig. 6.2.8** illustrates the results obtained for a spectral efficiency of $\eta = 3$ bit/s/Hz. Due to the relative high code rate of $R_c = 0.75$, we have just to switch between 8-PSK and 16-QAM. However, 16-QAM performs nearly as good as 8-PSK because it exploits the signal space more efficiently (compare Section 1.4). Therefore, the loss obtained by changing from 8-PSK to 16-QAM is rather low and the diversity gain dominates the bit error rate for T_3 and T_4 .

The following conclusion can be drawn concerning the trade-off between diversity degree and modulation type for a fixed spectral efficiency η . In the high SNR regime, diversity is most important and overcompensate the larger sensitivity of high order modulation schemes. At low SNR, robust modulation schemes like QPSK should be preferred because the diversity gain is smaller than the loss associated with a change of the modulations scheme.

6.2.4 Space-Time Trellis Codes

Contrarily to the previously presented orthogonal STBCs, space-time trellis codes (STTC) can also provide a coding gain. First optimization criteria and some handmade codes have been presented in [STC97, TSC97, TSC98]. Results of a systematic computer based code search can be found in [BBH00a, BBH00b] and some implementation aspects in [NTSC97, NTSC98].

Fig. 6.2.9 shows the general structure of an encoder with $N_T = 2$ transmit antennas. Obviously, STTCs are related to convolutional codes explained in Section 3.3. At each time instance ℓ , a vector $\mathbf{d}[\ell] = [d_1[\ell] \cdots d_K[\ell]]^T$ is fed into the linear shift

register consisting of L_c blocks each comprising K bits. The old content is shifted by K positions to the right. Hence, the total length of the register is $L_c K$ bits and L_c represents the constraint length as for convolutional codes. The variable $Q = L_c - 1$ denotes the memory of the register.

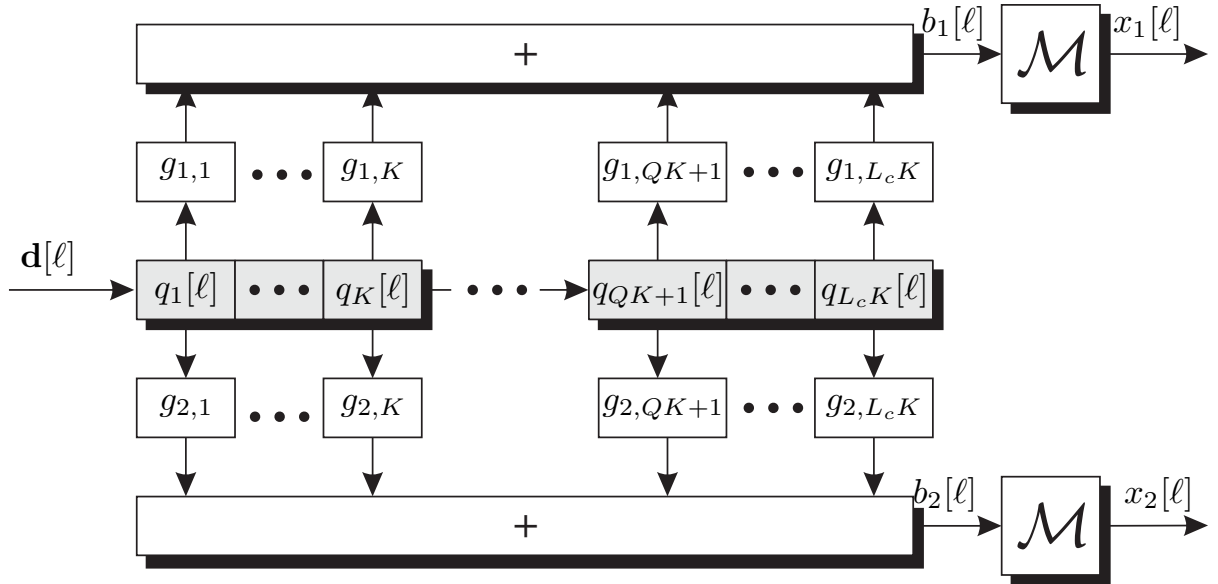


Figure 6.2.9: General structure of space-time trellis encoder for $N_T = 2$ transmit antennas ($Q = L_c - 1$)

The major difference to binary convolutional codes is the way how the register content

$$\mathbf{q}[\ell] = \begin{bmatrix} \mathbf{d}[\ell] \\ \vdots \\ \mathbf{d}[\ell - Q] \end{bmatrix} = \underbrace{\begin{bmatrix} q_1[\ell] & \cdots & q_K[\ell] \end{bmatrix}}_{\text{input vector } \mathbf{d}[\ell]} \underbrace{\begin{bmatrix} q_{K+1}[\ell] & \cdots & q_{L_c K}[\ell] \end{bmatrix}}_{\text{state}}^T \quad (6.2.45)$$

is combined to form the outputs $b_1[\ell]$ and $b_2[\ell]$. Assuming an M -ary linear modulation scheme according to Section 1.4, the generator coefficients $g_{i,j}$ are generally nonbinary with $g_{i,j} \in \{0, 1, \dots, M-1\}$. They can be comprised in the generator matrix

$$\mathbf{G} = \begin{bmatrix} g_{1,1} & g_{1,2} & \cdots & g_{1,L_c K} \\ g_{2,1} & g_{2,2} & \cdots & g_{2,L_c K} \\ \vdots & \vdots & \ddots & \vdots \\ g_{N_T,1} & g_{N_T,2} & \cdots & g_{N_T,L_c K} \end{bmatrix} \quad (6.2.46)$$

with which the output vector $\mathbf{b}[\ell] = [b_1[\ell] \dots b_{N_T}[\ell]]$ can be described by

$$\mathbf{b}[\ell] = (\mathbf{G} \cdot \mathbf{q}[\ell]) \bmod M. \quad (6.2.47)$$

The N_T integers $b_\mu[\ell] \in \{0, \dots, M-1\}$ are then mapped onto M -ary PSK or QAM symbols by N_T independent signal mappers.

In [TSC98] it is shown that the maximum K is restricted by the modulation scheme if maximum diversity degree of $N_T N_R$ should be achieved. Hence, $K = \log_2(M)$ holds for M -ary modulation schemes. The number of states naturally depends on the memory of the register. However, it may happen that the most left and the most right bit tuples $\mathbf{d}[\ell]$ and $\mathbf{d}[\ell - Q]$ are not fully connected to the generators. Assuming that the last τ elements of $\mathbf{a}[\ell]$ are not connected to the generators, only $QK - \tau$ memory elements are used the number of states reduces to $2^{QK - \tau}$. In this case, the generator matrix is not fully loaded [Blu00].

Similar to convolutional codes, space-time trellis codes can also be graphically described with a trellis diagram. An example with four states and $N_T = 2$ transmit antennas is depicted in **Fig. 6.2.10** where $K = 2$ and $L_c = 2$ hold resulting in $2^2 = 4$ states. At each time instance, two input bits $d_1[\ell]$ and $d_2[\ell]$ are encoded in a register with memory $Q = 1$ resulting in four branches leaving each state. On the left hand side, the binary representation of each state, i.e. the register content, is depicted. On the right hand side, the output symbols $x_1[\ell]$ and $x_2[\ell]$ belonging to different branches are listed whereby the first symbol pair belongs to the most upper branch leaving a state and the last to the lowest branch. Generally, natural mapping (see Section 1.4) is applied as can be seen from the signal space of QPSK.

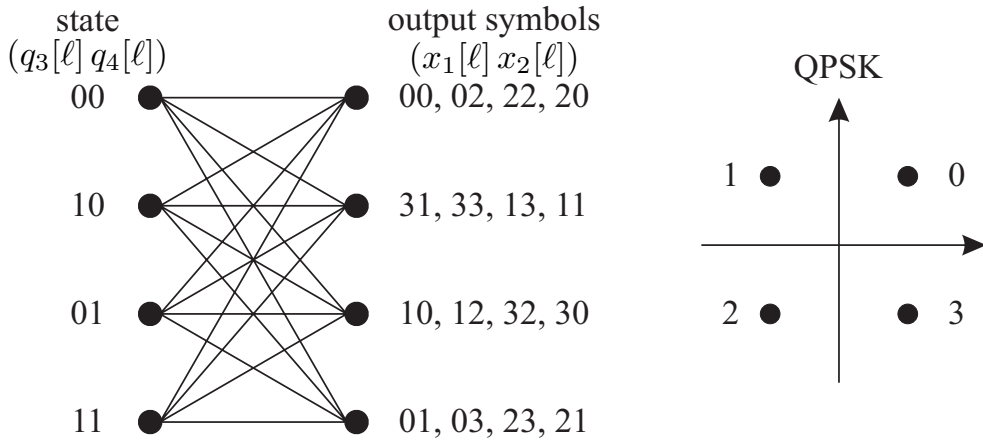


Figure 6.2.10: Trellis diagrams for space-time code with $2^{QK} = 2^K = 4$ states, QPSK and $N_T = 2$ transmit antennas

Decoding Space-Time Trellis Codes

Due to the equivalence between convolutional codes and space-time trellis codes, we can use the Viterbi algorithm for decoding. However, there exists a major difference. In the case of binary convolutional codes, the n bits $b_1[i], \dots, b_n[i]$

belonging to one codeword $\mathbf{b}[i]$ are received successively. Contrarily, the N_T symbols $x_1[\ell]$ up to $x_{N_T}[\ell]$ at the output of the STC encoder interfere incoherently at the receiver and are not obtained in a separate form. For the general case of N_R receive antennas

$$\mathbf{y}[\ell] = \mathbf{H} \cdot \mathbf{x}[\ell] + \mathbf{n}[\ell] \quad (6.2.48)$$

with the μ -th received signal

$$y_\mu[\ell] = \underline{\mathbf{h}}_\mu \cdot \mathbf{x}[\ell] + n_\mu[\ell] = \sum_{\nu=1}^{N_T} h_{\mu,\nu} \cdot x_\nu[\ell] + n_\mu[\ell] \quad (6.2.49)$$

holds. This modification has to be considered when calculating the incremental metrics $\gamma^{(s' \rightarrow s)}[\ell]$ given in (3.3.11). Since all interfering symbols are outputs of the STC encoder at the time instance ℓ they originate all from the same state s' . The incremental metric between the states s' and s becomes

$$\gamma^{(s' \rightarrow s)}[\ell] = \left\| \mathbf{y}[\ell] - \mathbf{H} \cdot \mathbf{z}^{(s' \rightarrow s)} \right\|^2 = \sum_{\mu=1}^{N_R} \sum_{\nu=1}^{N_T} \left| y_\mu[\ell] - h_{\mu,\nu} \cdot z_\nu^{(s' \rightarrow s)} \right|^2 \quad (6.2.50)$$

where $z_\nu^{(s' \rightarrow s)}$ denotes the hypothesis of the symbol transmitted over antenna ν for the transition between states s' and s . Consequently, $\mathbf{z}^{(s' \rightarrow s)}$ comprises all N_T hypotheses. The remaining parts of the Viterbi algorithm are identical to that of convolutional codes.

Examples for Space-Time Trellis Codes

In the sequel, we present some codes derived by Wittneben, Tarokh, Yan and Bäro [Wit91, Wit93, TSC98, YB00]. This list claims of course not to be comprehensive. In order to distinguish the codes, we use the following notation. The codes from Wittneben, Tarokh, Yan and Bäro are denoted by $\mathbb{W}(M, Z, N_T)$, $\mathbb{T}(M, Z, N_T)$, $\mathbb{Y}(M, Z, N_T)$ and $\mathbb{B}(M, Z, N_T)$, respectively. The three parameters describe the constellation size M of the linear modulation, the number of states Z in the trellis and the number of transmit antennas N_T . All codes achieve the maximum diversity gain $N_T N_R$ so that only the coding gain has to be considered.

Delay Diversity by Wittneben

The delay diversity scheme proposed by Wittneben [Wit91, Wit93] represents an exception because it provides no coding gain. However, it can be interpreted as the simplest STTC and is illustrated in **Fig. 6.2.11**. For the general case of M -ary modulation schemes, $K = \log_2(M)$ bits are fed into the shift register at each time instance. In our example, we use QPSK resulting in $K = 2$. The number of transmit antennas equals the constraint length $L_c = N_T$ because each K bit block

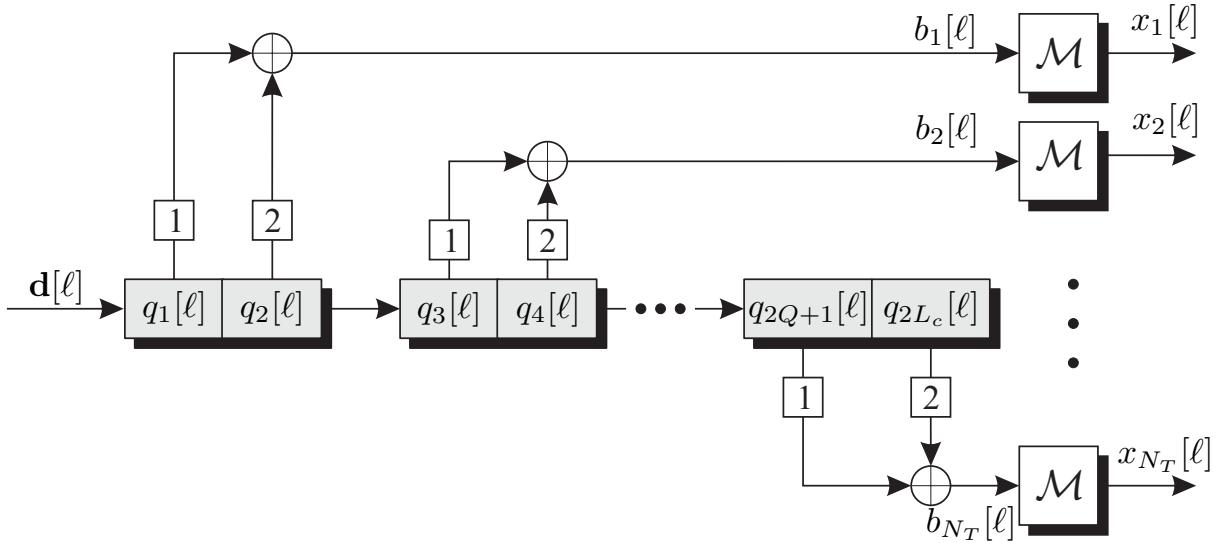


Figure 6.2.11: Structure of delay diversity scheme by Wittneben with QPSK

is connected to a mapper of only one antenna. This leads to the general structure of the generator matrix

$$\mathbf{G} = \begin{bmatrix} 1 & 2 & \dots & 2^{K-1} & 0 & \dots & 0 & \dots & 0 & \dots & 0 \\ 0 & \dots & 0 & 1 & 2 & \dots & 2^{K-1} & \dots & 0 & \dots & 0 \\ \vdots & & & & & & & & \vdots & & \\ 1 & 2 & \dots & 2^{K-1} \end{bmatrix} \quad (6.2.51)$$

and the number of states grows exponentially with the number of transmit antennas.

Obviously, the transmit antennas emit delayed versions of the same information. As a consequence, the signal at receive antenna μ becomes

$$y_\mu[\ell] = \sum_{\nu=1}^{N_T} h_{\mu,\nu} \cdot x_\nu[\ell] + n_\mu[\ell] = \sum_{\nu=1}^{N_T} h_{\mu,\nu} \cdot x_1[\ell - \nu + 1] + n_\mu[\ell]. \quad (6.2.52)$$

We recognize that (6.2.52) describes the convolution of a symbol sequence $x_1[\ell]$ with a frequency-selective channel $\underline{\mathbf{h}}_\mu = [h_{\mu,1} \dots h_{\mu,N_T}]$. Therefore, the flat MISO channel is transformed by the delay diversity scheme into a frequency-selective single-input single-output channel providing the full diversity degree of $D = N_T = L_c$. Decoding is identical to the equalization of intersymbol interference channels and can be performed by a Viterbi equalizer [Pro95, Kam96].

For the example $W(4, 4, 2)$ of $N_T = 2$ transmit antennas, QPSK and four states, we obtain a trellis segment depicted in Fig. 6.2.12. While the first antenna transmits in the ν -th state always symbol ν , the second antenna transmits a symbol μ identifying the successive state $s = \mu$. The generator matrix has the form

$$\mathbf{W}(4, 4, 2) = \begin{bmatrix} 1 & 2 & 0 & 0 \\ 0 & 0 & 1 & 2 \end{bmatrix}. \quad (6.2.53)$$

Due to the simplicity of this scheme, it can be easily extended to an arbitrary number of transmit antennas and, therefore, to a very high diversity gain. However, the decoding or detection complexity grows exponentially with N_T and limits the potential due to practical restrictions.

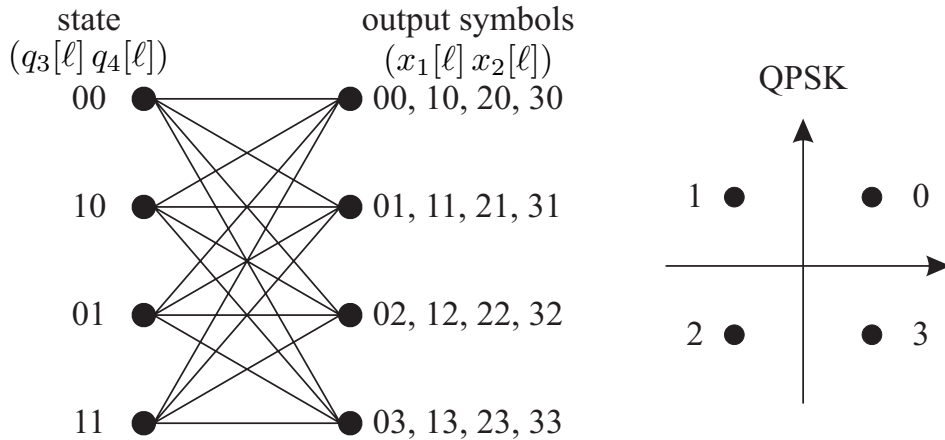


Figure 6.2.12: Structure of delay diversity scheme by Wittneben with memory $Q = 1$, $N_T = 2$ and QPSK

Space-Time Trellis Codes with $N_T = 2$ Transmit Antennas

Next, we focus on schemes providing a coding gain G_c with only two transmit antennas. Table 6.2.2 lists the codes $\mathbb{T}(4, Z, 2)$ and $\mathbb{Y}(4, Z, 2)$ by Tarokh and Yan [TSC98, YB00] for Z states and QPSK, Table 6.2.3 the codes $\mathbb{B}(4, Z, 2)$ by Bäro [BBH00a, BBH00b]. As an example, the encoder structure of $\mathbb{T}(4, 8, 2)$ is shown in **Fig. 6.2.13**. The corresponding generator matrix is not fully loaded due to $\tau = 1$ leading to $2^{KQ-1} = 8$ states.

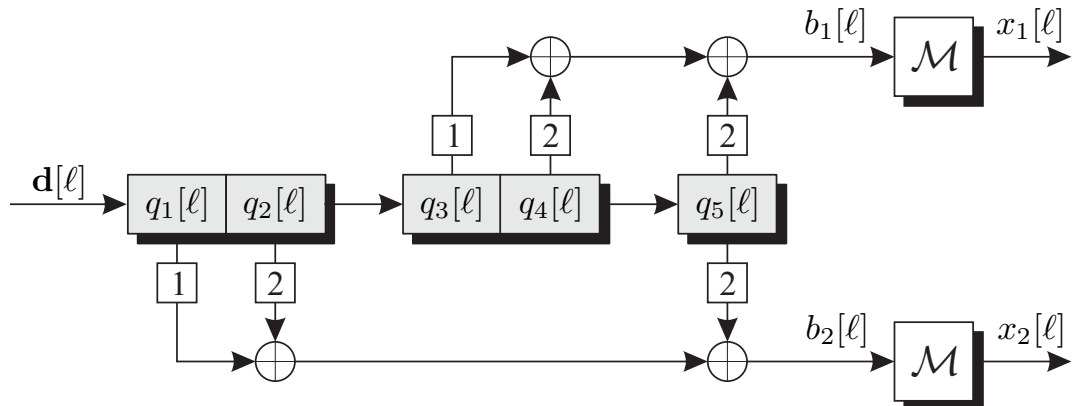


Figure 6.2.13: Structure of encoder for $\mathbb{T}(4, 8, 2)$ for $N_T = 2$ and QPSK

Table 6.2.2: List of space-time trellis codes taken from [TSC98, YB00] for $N_T = 2$, QPSK, $\eta = 2$ bits/s/Hz and diversity degree $D = 2$

Z	$\mathbb{T}(4, Z, 2)$	g_c	$\mathbb{Y}(4, Z, 2)$	g_c
4	$\begin{bmatrix} 1 & 2 & 0 & 0 \\ 0 & 0 & 1 & 2 \end{bmatrix}$	2	$\begin{bmatrix} 2 & 0 & 1 & 2 \\ 2 & 2 & 2 & 1 \end{bmatrix}$	$\sqrt{8}$
8	$\begin{bmatrix} 0 & 0 & 1 & 2 & 2 \\ 1 & 2 & 0 & 0 & 2 \end{bmatrix}$	$\sqrt{12}$	$\begin{bmatrix} 0 & 2 & 1 & 0 & 2 \\ 2 & 1 & 0 & 2 & 2 \end{bmatrix}$	4
16	$\begin{bmatrix} 0 & 0 & 1 & 2 & 2 & 0 \\ 1 & 2 & 2 & 0 & 0 & 2 \end{bmatrix}$	$\sqrt{12}$	$\begin{bmatrix} 0 & 2 & 1 & 1 & 2 & 0 \\ 2 & 2 & 1 & 2 & 0 & 2 \end{bmatrix}$	$\sqrt{32}$
32	$\begin{bmatrix} 0 & 0 & 1 & 2 & 2 & 3 & 2 \\ 1 & 2 & 1 & 2 & 0 & 3 & 2 \end{bmatrix}$	$\sqrt{12}$	$\begin{bmatrix} 0 & 2 & 3 & 1 & 2 & 0 & 2 \\ 2 & 0 & 1 & 2 & 1 & 2 & 2 \end{bmatrix}$	$\sqrt{40}$

Table 6.2.3: List of space-time trellis codes taken from [BBH00a, BBH00b] for $N_T = 2$, QPSK, $\eta = 2$ bits/s/Hz and diversity degree $D = 2$

Z	$\mathbb{B}(4, Z, 2)$	g_c
4	$\begin{bmatrix} 0 & 2 & 3 & 1 \\ 2 & 2 & 1 & 0 \end{bmatrix}$	$\sqrt{8}$
8	$\begin{bmatrix} 0 & 2 & 1 & 2 & 2 \\ 1 & 2 & 0 & 0 & 2 \end{bmatrix}$	$\sqrt{12}$
16	$\begin{bmatrix} 2 & 1 & 0 & 2 & 2 & 0 \\ 0 & 2 & 2 & 1 & 0 & 2 \end{bmatrix}$	$\sqrt{20}$

The coding gains G_c listed in the tables have been obtained by analyzing the pairwise differences $\mathbf{X} - \hat{\mathbf{X}}$ as described in Subsection 6.2.2. The codes by Yan achieve the highest coding gains while those of Tarokh show no improvement for more than eight states. These theoretical results are now evaluated by simulations.

First, we analyze the achievable coding gains of the codes $\mathbb{Y}(4, Z, 2)$ for different number of states Z . The frame error rate has been determined by transmitting code frames of length 130 symbols over time-invariant channels so that diversity is only gained by the resource space. The obtained frame and bit error rates for $N_R = 1$ receive antenna are depicted in Fig. 6.2.14. It can be observed that the frame error rate decreases with growing Z . For an FER of 10^{-2} , the code with 32 states gains a little bit less than 3 dB compared to $\mathbb{T}(4, 4, 2)$. Since all codes provide the full diversity gain of $D = N_T = 2$, the slopes of all curves are identical and only the coding gain is observed. According to Table 6.2.2, we should have achieved a gain of

$$10 \cdot \log_{10} \frac{g_c(\mathbb{Y}(4, 32, 2))}{g_c(\mathbb{Y}(4, 4, 2))} = 10 \cdot \log_{10} \frac{\sqrt{40}}{\sqrt{8}} = 3.5 \text{ dB} . \quad (6.2.54)$$

Contrarily, the bit error rate depicted in Fig. 6.2.14b) shows only minor differences. At very low SNR, the weak codes with low memory perform slightly better; a result that we know already from Chapter 3. At high SNR, the codes with higher memory close the gap but can not significantly outperform the weak codes. Moreover, the theoretical bit error rate curve for $N_T = 2$ -fold diversity is not reached and a gap of 2 dB remains. This observation can be explained by the fact that some frames cannot be correctly decoded and the decoding process itself artificially generates additional errors increasing the BER. This specifically happens for bad instantaneous channels. Concerning the FER, the number of errors within one frame is not important so that it is not affected. Therefore, we will focus on the FER in the sequel. It has to be mentioned that things will change if the channel varies during one frame. In this case, the decoder exploits time diversity and especially the bit error rate can be improved remarkably.

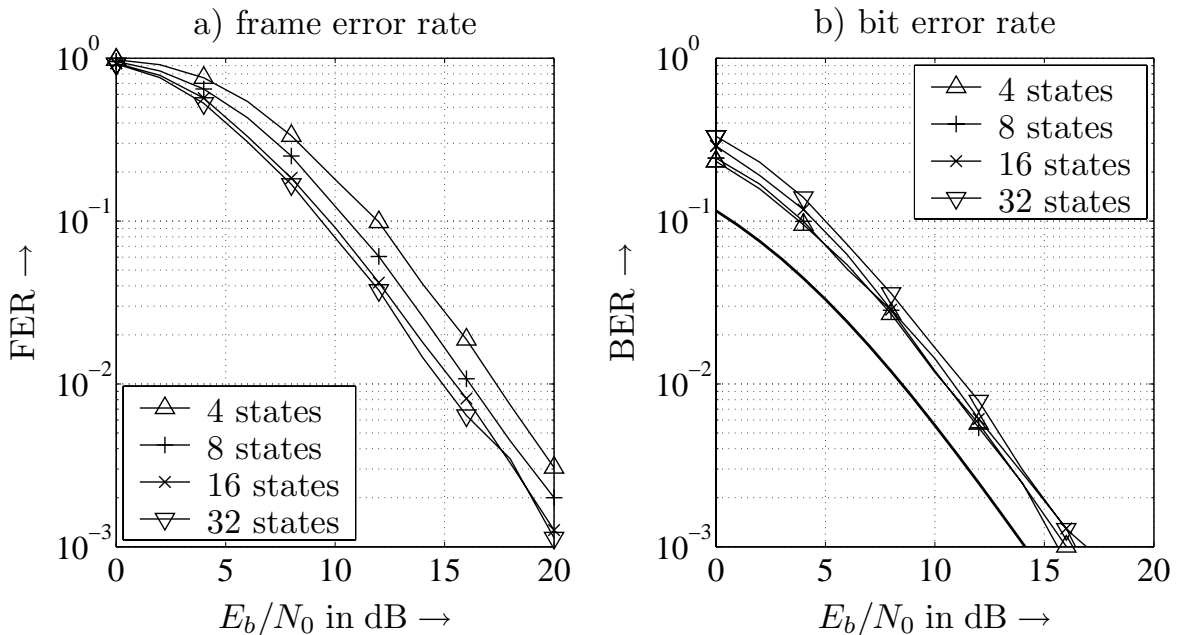


Figure 6.2.14: Error rate performance of code $\mathbb{Y}(4, Z, 2)$ by Yan for QPSK and $N_R = 1$ receive antenna (bold line: theoretical error rate for diversity $D = 2$)

A higher diversity degree is also obtained if the number of receive antennas is increased. **Fig. 6.2.15** shows the corresponding results for $N_R = 2$. Looking at the FER, all codes profit from the increased diversity degree and gain between 5 dB and 6 dB at an FER of 10^{-2} . However, the differences between them become smaller and the gain of $\mathbb{Y}(4, 32, 2)$ compared to $\mathbb{Y}(4, 4, 2)$ reduces to only 2 dB. The bit error rate is also improved by approximately 3 dB but all codes still perform very similar so that no coding gain can be observed. The gap to the theoretical diversity curve is closed.

Fig. 6.2.16a compares the performances of the codes $\mathbb{W}(4, 4, 2)$, $\mathbb{T}(4, Z, 2)$, $\mathbb{Y}(4, Z, 2)$ and $\mathbb{B}(4, Z, 2)$ for $N_R = 1$ receive antenna and four or sixteen states.

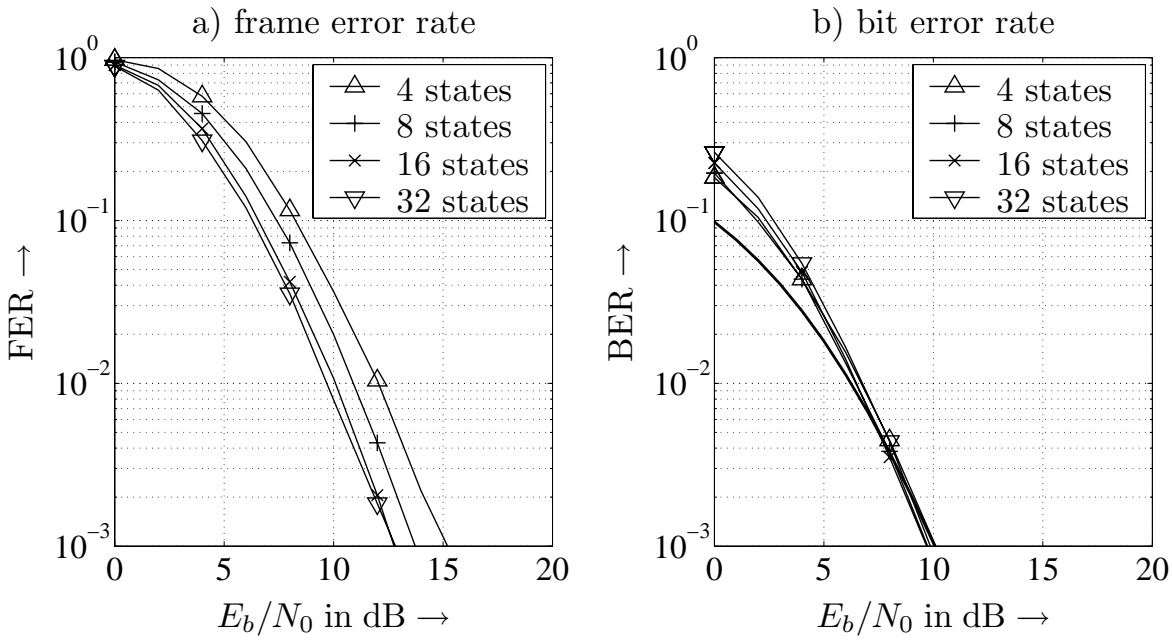


Figure 6.2.15: Error rate performance of code $\mathbb{Y}(4, Z, 2)$ by Yan for QPSK and $N_R = 2$ receive antennas (bold line: theoretical error rate for diversity $D = 4$)

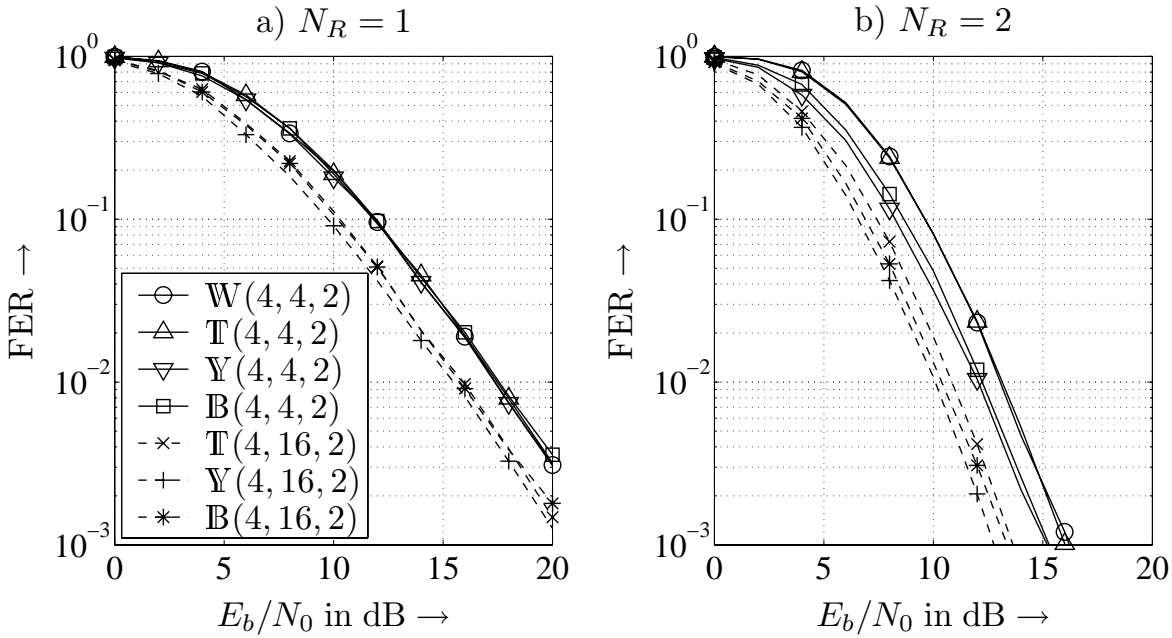


Figure 6.2.16: Frame error rate performance of different codes for QPSK

The theoretical differences indicated in Tables 6.2.2 and 6.2.3 cannot be confirmed. For example, there should occur a gain of

$$10 \cdot \log_{10} \frac{g_c(\mathbb{Y}(4, 16, 2))}{g_c(\mathbb{T}(4, 16, 2))} = 10 \cdot \log_{10} \frac{\sqrt{32}}{\sqrt{12}} = 2.13 \text{ dB} \quad (6.2.55)$$

between $\mathbb{T}(4, 16, 2)$ and $\mathbb{Y}(4, 16, 2)$. However, all codes with four states show a similar performance as well as all codes with sixteen states. For $\mathbb{W}(4, 4, 2)$ and $\mathbb{T}(4, 4, 2)$, this is not astonishing because Tarokh's four state code is identical to the delay diversity scheme with two transmit antennas. The code proposed by Yan shows no significant performance improvement. The only observable difference is the improvement of 2 dB obtained by increasing the number of states to sixteen.

For $N_R = 2$ receive antennas, larger differences between the curves can be observed although the promised gains are not achieved. The codes from Yan performs best closely followed by those of Bäro. However, the differences remain small. The reason for this behaviour is the fact the coding gain was calculated only with respect to the minimum determinant of the difference matrices described in Subsection 6.2.2. This criterion is comparable to the minimum Hamming distance of a code that dominates the error rate only asymptotically for large signal to noise ratios. In low or medium SNR regions, also sequence pairs with larger distance influence the performance what is not considered in the theoretical derivation.

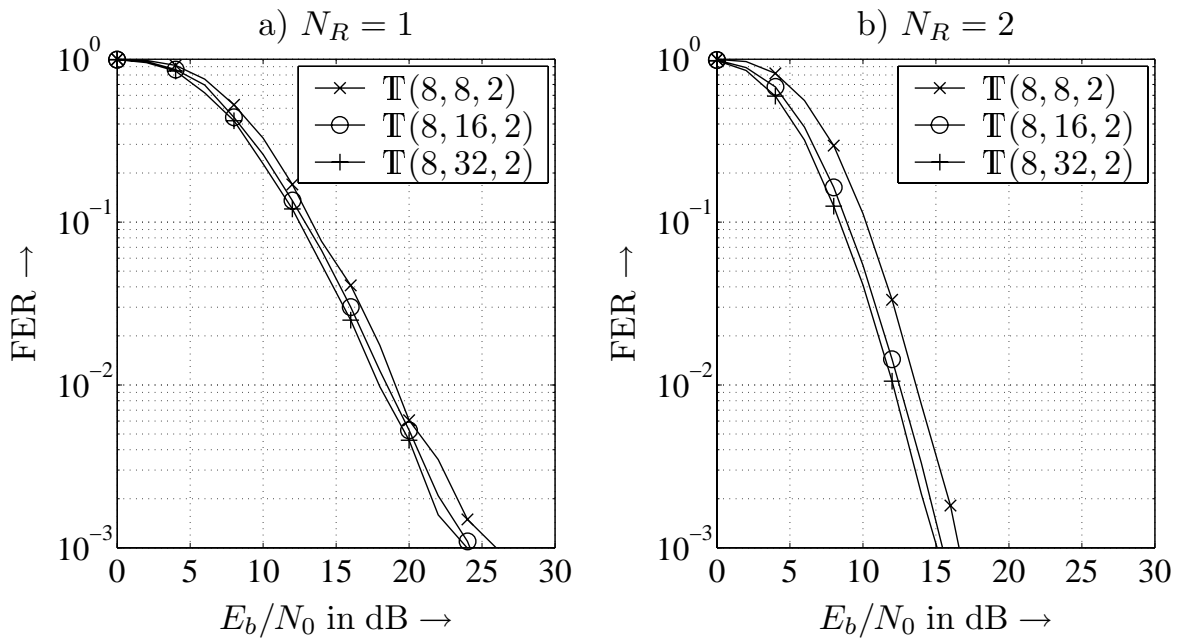


Figure 6.2.17: Frame error rate performance for codes by Tarokh for 8-PSK and different number of states

So far, only QPSK modulation has been used. For 8-PSK, 3 bits can be transmitted per time instance resulting in a higher spectral efficiency $\eta = 3$ bits/s/Hz. Tarokh presented in [TSC98] some space-time trellis codes for 8-PSK. The generator matrices are given in Table 6.2.4. Due to the high computational costs, no results on the coding gains exist. **Fig. 6.2.17** shows the corresponding simulation results. Only very small gains can be obtained by increasing the number of states, and, therefore, the decoding complexity. Moreover, the relations between the curves hardly changes for different number of receive antennas.

Table 6.2.4: List of space-time trellis codes taken from [TSC98] for $N_T = 2$, 8-PSK, $\eta = 3$ bits/s/Hz and diversity degree $D = 2$

$\mathbb{T}(8, 8, 2)$	$\mathbb{T}(8, 16, 2)$	$\mathbb{T}(8, 32, 2)$
$\begin{bmatrix} 0 & 0 & 0 & 5 & 2 & 4 \\ 1 & 2 & 4 & 0 & 0 & 0 \end{bmatrix}$	$\begin{bmatrix} 0 & 0 & 0 & 5 & 2 & 4 & 1 \\ 1 & 2 & 4 & 1 & 2 & 4 & 5 \end{bmatrix}$	$\begin{bmatrix} 0 & 0 & 0 & 5 & 2 & 4 & 3 & 2 \\ 1 & 2 & 4 & 1 & 2 & 4 & 7 & 2 \end{bmatrix}$

Space-Time Codes for more than Two Transmit Antennas

For more than $N_T = 2$ transmit antennas and BPSK modulation, Yan presented in [YB00] some codes for $N_T = 3$ and $N_T = 4$ transmit antennas. They are listed in Table 6.2.5. Again, coding gains between 2 dB up to 2.4 dB are promised by the determinant criterion of Subsection 6.2.2 between two and four states for $N_T = 3$ and between four and eight states for $N_T = 4$.

Table 6.2.5: List of space-time trellis codes taken from [YB00] for $N_T = 3$ and $N_T = 4$, BPSK, $\eta = 1$ bits/s/Hz

Z	$\mathbb{Y}(2, Z, 3)$	g_c	$\mathbb{Y}(2, Z, 4)$	g_c
2	$\begin{bmatrix} 0 & 1 \\ 1 & 1 \end{bmatrix}$	4		
4	$\begin{bmatrix} 0 & 1 & 1 \\ 1 & 0 & 1 \end{bmatrix}$	$\sqrt{48}$	$\begin{bmatrix} 0 & 1 & 1 \\ 1 & 0 & 1 \\ 1 & 1 & 1 \end{bmatrix}$	4
8	$\begin{bmatrix} 1 & 0 & 1 & 1 \\ 1 & 1 & 0 & 1 \end{bmatrix}$	$\sqrt{80}$	$\begin{bmatrix} 1 & 0 & 0 & 1 \\ 1 & 0 & 1 & 0 \\ 1 & 1 & 1 & 1 \end{bmatrix}$	$256^{1/3}$
16	$\begin{bmatrix} 0 & 1 & 0 & 1 & 1 \\ 1 & 0 & 1 & 0 & 1 \end{bmatrix}$	$\sqrt{128}$	$\begin{bmatrix} 1 & 0 & 0 & 1 & 1 \\ 1 & 1 & 0 & 1 & 0 \\ 1 & 1 & 1 & 0 & 1 \end{bmatrix}$	8

The corresponding simulation results are shown in **Fig. 6.2.18** for $N_T = 1$ receive antenna. Due to the higher diversity degree of $D = N_T = 3$ or $D = N_T = 4$, an increase in the number of states really leads to a measurable coding gain. The theoretical differences can be approximately confirmed. The same holds for the case of $N_R = 2$ receive antennas depicted in **Fig. 6.2.19**. These diagrams show additionally the theoretical frame error rates (bold dashed curves) for D -fold diversity.

They can be calculated by looking first at the instantaneous frame error probability $P_f(\mathbf{H})$ as a function of the symbol error probability $P_s(\mathbf{H})$. For a frame of length L , we assume that the channel \mathbf{H} remains constant. A frame error occurs if at least one symbol is wrong. In other words, the whole sequence is only correct if all

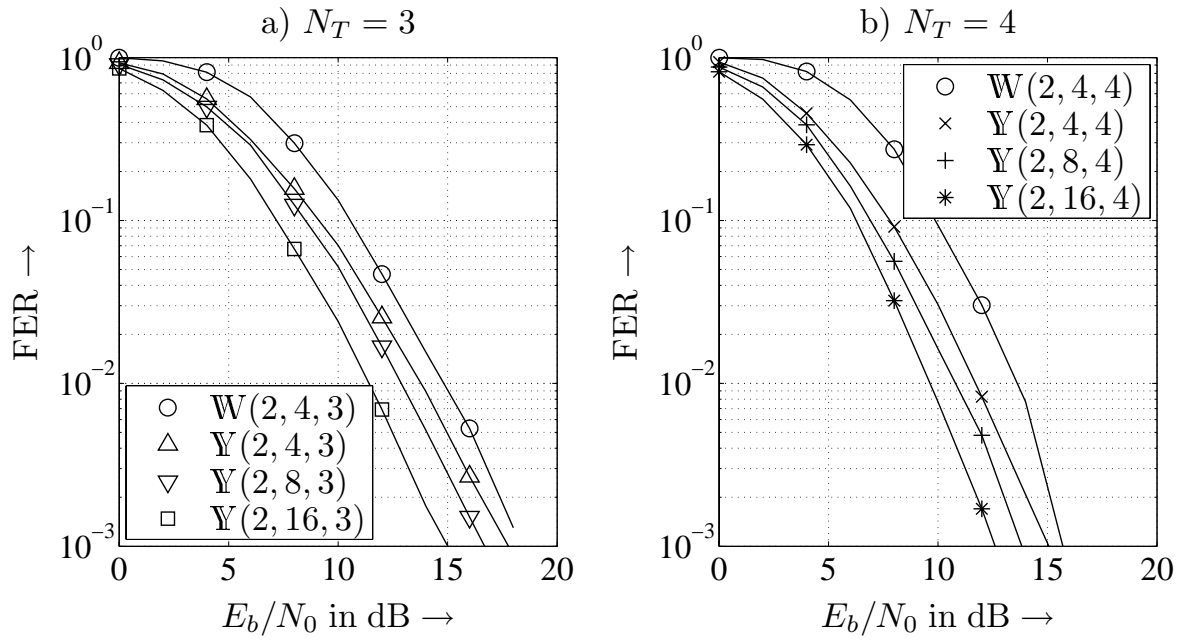


Figure 6.2.18: Frame error rate performance for Codes by Yan for BPSK, different number of transmit antennas and $N_R = 1$ receive antenna

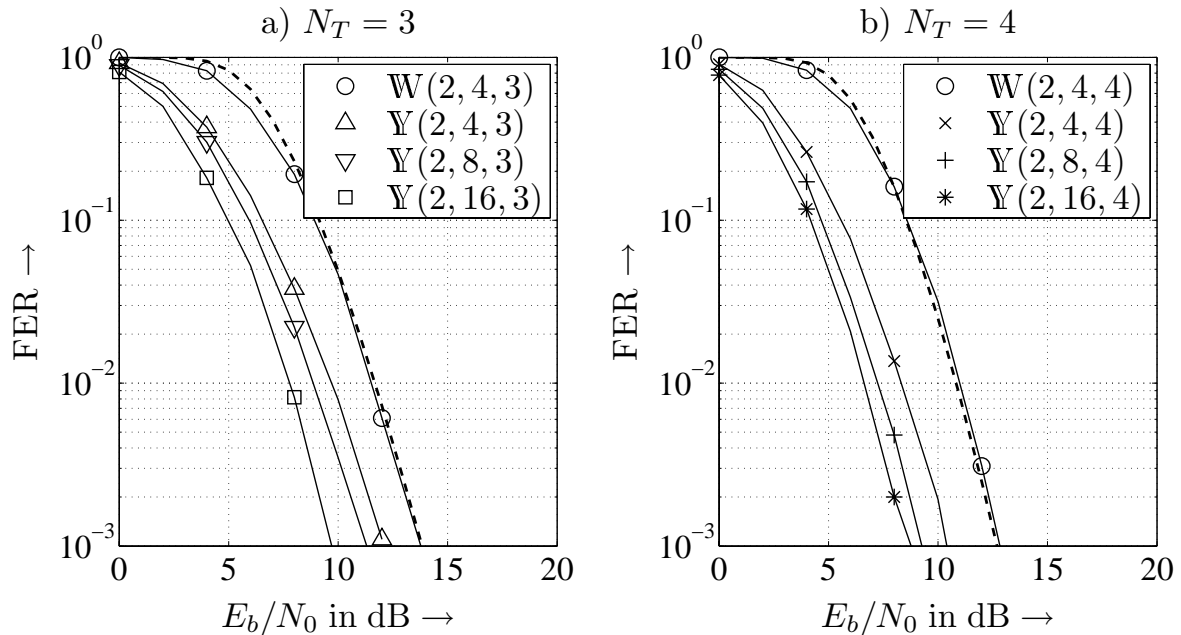


Figure 6.2.19: Frame error rate performance for Codes by Yan for BPSK, different number of transmit antennas and $N_R = 2$ receive antennas (bold dashed line: theoretical frame error rate)

L symbols are correct. Since the noise is white, the error probabilities $P_s(\mathbf{H})$ of successive symbols are identical and independent and the probability that a frame is received correctly amounts to $(1 - P_s(\mathbf{H}))^L$. Hence, the frame error probability is

$$P_f(\mathbf{H}) = 1 - (1 - P_s(\mathbf{H}))^L. \quad (6.2.56)$$

The ergodic probability is now obtained by calculating the expectation of (6.2.56)

$$P_f = \mathbb{E} \{P_f(\mathbf{H})\} = \mathbb{E} \left\{ 1 - (1 - P_s(\mathbf{H}))^L \right\} \quad (6.2.57)$$

which is not easy because expectations over powers of $P_s(\mathbf{H})$ have to be calculated. A tight approximation applies a series expansion to the L -th power and considers only the linear terms. This yields

$$P_f \approx \mathbb{E} \{ 1 - (1 - L \cdot P_s(\mathbf{H})) \} \approx L \cdot P_s. \quad (6.2.58)$$

We recognize from Fig. 6.2.19 that the delay diversity scheme fully exploits the diversity degree of $D = N_R \cdot N_T$ while the codes by Yan additionally profit from the coding gain.

Generally, we can conclude that the coding gains of space-time trellis codes promised by the determinant criterion can be hardly achieved in practice. Only for high diversity degrees that require either time-selective channels or many antennas at transmitter or receiver, coding gains become visible. Naturally, space-time block codes as well as space-time trellis codes can be combined with classical error correction coding schemes [Bau99, BHS00]. This leads to concatenated schemes that can be processed iteratively according to the turbo principle introduced in Section 3.6.

6.3 Multi-Layer Transmission

6.3.1 Channel Knowledge at Transmitter and Receiver

The diversity techniques discussed so far improve the link reliability, mainly by using multiple antennas at the transmitter and one or more receive antennas. Contrarily, we now try to enhance the data rate by transmitting parallel data streams over the antennas and, thus, perform spatial multiplexing. Therefore, we remember the general MIMO concept illustrated in Fig. 6.1.1 with the channel output $\mathbf{y} = \mathbf{Hx} + \mathbf{n}$ given in (6.1.1). First, we focus on the case where transmitter and receiver both have perfect channel knowledge. In this case, we know from Chapter 2 that we have to exploit the eigenmodes of the channel. Hence, a singular value decomposition

$$\mathbf{H} = \mathbf{U} \cdot \boldsymbol{\Sigma} \cdot \mathbf{V}^H \quad (6.3.1)$$

of the channel matrix \mathbf{H} has to be performed at transmitter and receiver. Remember that \mathbf{U} and \mathbf{V} are unitary matrices of size $N_R \times N_R$ and $N_T \times N_T$, respectively.

If $r \leq \min(N_T, N_R)$ denotes the rank of the channel, Σ becomes

$$\Sigma = \begin{bmatrix} \Sigma_0 & \mathbf{0} \\ \mathbf{0} & \mathbf{0} \end{bmatrix} \quad (6.3.2)$$

where the $r \times r$ matrix Σ_0 contains on its diagonal all r nonzero singular values of \mathbf{H} . We can transmit at most r independent data streams. This number may be even smaller if the chosen power distribution excludes some layers and spends power only to the strongest modes (compare waterfilling principle in Section 2.3). If linear modulation schemes like PSK or QAM are employed, waterfilling does not represent the optimum choice as in the case of a Gaussian distributed signal. Here, finding the optimum power distribution is still an unsolved problem.

In the sequel, we assume that r independent data streams a_ν are transmitted as shown in **Fig. 6.3.1**. We first adjust their power levels according to an appropriate criterion by multiplying $\mathbf{a} = [a_1, \dots, a_r]^T$ with the square root of the diagonal matrix $\Lambda = \text{diag}[\lambda_1 \dots \lambda_r]$. Next, each layer is coupled into a certain eigenmode of the channel by using a distinct eigenvector in \mathbf{V} . If \mathbf{V}_X comprises those columns of \mathbf{V} that correspond to the used eigenmodes (nonzero singular values), the transmit vector has the form

$$\mathbf{x} = \mathbf{V}_X \cdot \Lambda_X^{1/2} \cdot \mathbf{a}. \quad (6.3.3)$$

Generally, \mathbf{a} consists of r i.i.d. symbols a_μ and we obtain with $\Phi_{\mathcal{A}\mathcal{A}} = E\{\mathbf{a}\mathbf{a}^H\} = E_s/T_s \cdot \mathbf{I}_r$ the covariance matrix of the transmit vector

$$\Phi_{\mathcal{X}\mathcal{X}} = E\{\mathbf{x}\mathbf{x}^H\} = \mathbf{V}_X \Lambda_X^{1/2} \Phi_{\mathcal{A}\mathcal{A}} \Lambda_X^{1/2} \mathbf{V}_X^H = \frac{E_s}{T_s} \cdot \mathbf{V}_X \Lambda_X \mathbf{V}_X^H. \quad (6.3.4)$$

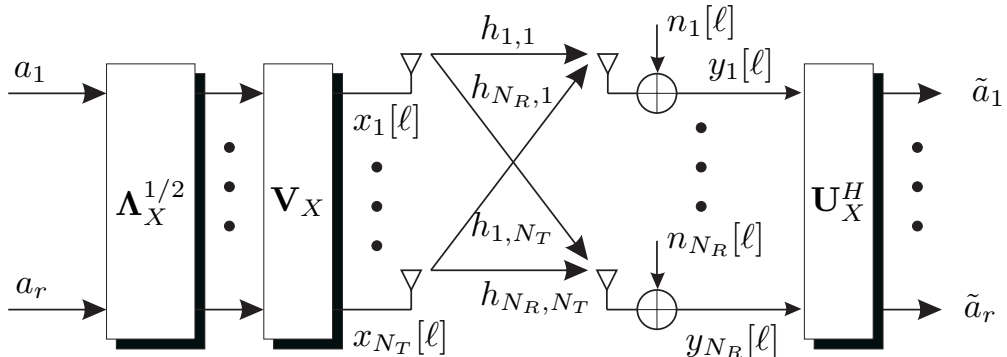


Figure 6.3.1: Multi-layer transmission with perfect channel knowledge at transmitter and receiver

The receiver applies an $r \times N_R$ matrix \mathbf{U}_X^H to $\mathbf{y} = \mathbf{Hx} + \mathbf{n}$ that comprises those r columns of \mathbf{U} corresponding to the used eigenmodes. With the definitions of \mathbf{U} and \mathbf{V} we obtain

$$\mathbf{V}^H \cdot \mathbf{V}_X = \begin{bmatrix} \mathbf{I}_r \\ \mathbf{0}_{N_T-r \times r} \end{bmatrix} \quad \text{and} \quad \mathbf{U}_X^H \cdot \mathbf{U} = \begin{bmatrix} \mathbf{I}_r & \mathbf{0}_{r \times N_T-r} \end{bmatrix} \quad (6.3.5)$$

and the output signal $\tilde{\mathbf{a}}$ can be described by

$$\tilde{\mathbf{a}} = \mathbf{U}_X^H \cdot (\mathbf{H}\mathbf{x} + \mathbf{n}) = \mathbf{U}_X^H \mathbf{U} \cdot \Sigma \cdot \mathbf{V}^H \mathbf{V}_X \cdot \Lambda_X^{1/2} \cdot \mathbf{a} + \mathbf{U}^H \cdot \mathbf{n} = \Sigma_0 \cdot \Lambda_X^{1/2} \cdot \mathbf{a} + \tilde{\mathbf{n}} . \quad (6.3.6)$$

Since the matrices Σ_0 and Λ_X are diagonal, (6.3.6) describes a set of decoupled scalar equations and no interference disturbs the transmission. The ν -th symbol can be detected from

$$\tilde{a}_\nu = \sigma_\nu \cdot \sqrt{\lambda_\nu} \cdot a_\nu + \tilde{n}_\nu . \quad (6.3.7)$$

The signal to noise ratio of this eigenmode amounts to

$$\gamma_\nu = \sigma_\nu^2 \cdot \lambda_\nu \cdot \frac{E_s/T_s}{\sigma_N^2} = \sigma_\nu^2 \cdot \lambda_\nu \cdot \frac{E_S}{N_0} \quad (6.3.8)$$

and depends on the singular value σ_ν of the channel as well as the chosen transmit power level λ_ν .

Beamforming

If only a single eigenmode of the channel is exploited, we call this *beamforming*. Beamforming is beneficial if the channel matrix is rank deficient and has only one dominating nonzero eigenvalue. In this case, the transmit power is concentrated on this strong eigenmode and only a single data stream is transmitted. Denoting with σ_{\max} the strongest singular value of \mathbf{H} and with \mathbf{u}_{\max} and \mathbf{v}_{\max} the associated columns of the unitary matrices \mathbf{U} and \mathbf{V} , we obtain the transmitted signal $\mathbf{x} = \mathbf{v}_{\max} \cdot a$. Filtering the received vector \mathbf{y} with \mathbf{u}_{\max}^H results in

$$\mathbf{u}_{\max}^H \cdot \mathbf{y} = \mathbf{u}_{\max}^H \mathbf{U} \cdot \Sigma \cdot \mathbf{V}^H \mathbf{v}_{\max} \cdot a + \tilde{n} = \sigma_{\max} \cdot a + \tilde{n} . \quad (6.3.9)$$

Since the columns in \mathbf{U} as well as in \mathbf{V} are mutually orthogonal, the products $\mathbf{u}_{\max}^H \mathbf{U}$ and $\mathbf{V}^H \mathbf{v}_{\max}$ deliver vectors that have only a single one exactly at that position belonging to the maximum singular value σ_{\max} in Σ .

Certainly, beamforming can also be applied when multiple antennas are only present either at the transmitter or the receiver. For those scenarios, the channel matrix \mathbf{H} reduces to a vector \mathbf{h} and we obtain $\mathbf{v} = \mathbf{h}^H / \|\mathbf{h}\|$ or $\mathbf{u}^H = \mathbf{h} / \|\mathbf{h}\|$, respectively. Hence, beamforming either at transmitter or receiver ensures maximum ratio combining for perfect channel knowledge.

In practical systems, the channel matrix \mathbf{H} has to be estimated. Besides estimation unavoidable errors, there is also the problem to estimate the channel at transmitter and receiver, i.e. in the uplink and the downlink. Unfortunately, both channels need not to be identical. For Frequency Division Duplex (FDD), uplink and downlink are separated into different frequency bands so that the short-term statistics are different. However, long-term statistics like directions of arrival or

departure can be assumed to be identical. Hence, an eigenvalue analysis can be performed on the basis of the long-term statistics, i.e. the covariance matrices measured at transmitter and receiver [BUN01]. In Time Division Duplex (TDD) systems, the frequency range of uplink and downlink is the same as they are separated into different time slots. If the channel varies slowly in time, estimates at the transmitter and receiver describe mainly the same channel and instantaneous channel knowledge (short-term statistics) can be used.

6.3.2 Channel Knowledge only at Receiver

If the transmitter has no channel knowledge, we can still exploit the high potential of multiple antenna systems with only a moderate loss in capacity (see next section). The missing channel knowledge has to be compensated by more sophisticated signal processing at the receiver. This leads to the well-known vertical Bell Labs Layered Space-Time (V-BLAST) architecture [Fos96, FG98, FGVW99] depicted in **Fig. 6.3.2**. We see that the parallel data streams are transmitted with identical power levels over different antennas without further pre-processing. Neglecting the interleaver, each data stream is transmitted over a single antenna leading to a vertical arrangement of the layers (see V-BLAST in **Fig. 6.3.3**). Due to N_R receive antennas, the maximum diversity degree amounts to $D = N_R^1$.

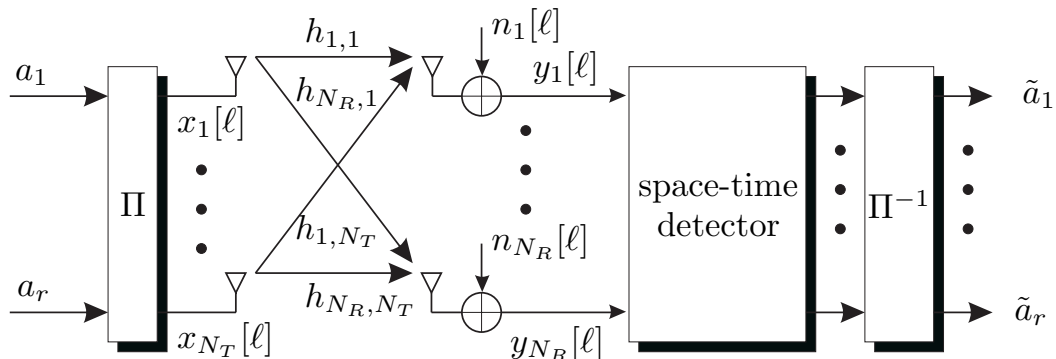


Figure 6.3.2: Multi-layer transmission with perfect channel knowledge only at receiver (BLAST)

An alternative implementation that increases the diversity degree for each layer is the diagonal BLAST (D-BLAST) architecture. It employs an interleaver in front of the transmit antennas and a corresponding de-interleaver at the receiver. According to Fig. 6.3.3, interleaving is performed such that the antenna index $\nu = (\ell \bmod N_T) + 1$ is increased modulo N_T with time index ℓ so that N_T consecutive symbols of a certain layer are switched successively onto all transmit antennas

¹It depends on the kind of detection algorithm if the full diversity degree can be exploited. For MLD, full diversity is obtained for all layers while the QL-based SIC provides different diversity degrees for the layers (compare Fig. 6.3.7).

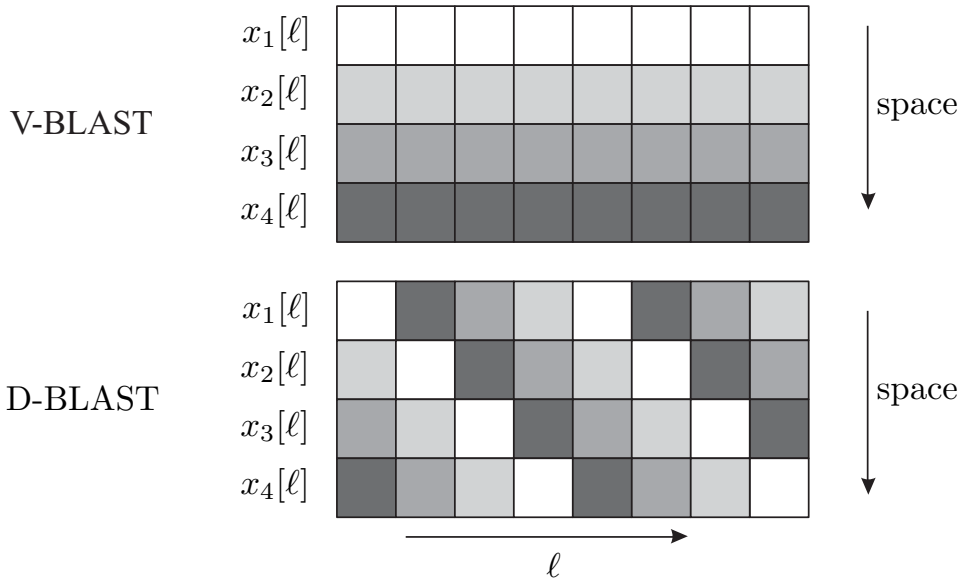


Figure 6.3.3: Data streams of V-BLAST and D-BLAST for $N_T = 4$ transmit antennas

resulting in a diagonal space-time arrangement. Therefore, each data stream is spread over all transmit antennas increasing the achievable diversity degree from N_R to $N_T \cdot N_R$ ¹. In both systems, a superposition of all layers is obtained at each receive antenna requiring sophisticated space-time signal processing. For notational simplicity, we restrict in the sequel to the simpler V-BLAST.

Similarity of CDMA and Multi-Layer Architectures

Next, the similarity of the considered multi-layer architectures and the uplink of CDMA systems should be briefly discussed. Therefore, we have a look at Fig. 6.3.2 and the received vector $\mathbf{y} = \mathbf{H}\mathbf{x} + \mathbf{n} = \mathbf{H}\mathbf{a} + \mathbf{n}$. A comparison with the results from Chapters 4 and 5, especially (5.1.1) on page 227, demonstrates the equivalence of multiple antenna systems and the uplink of a CDMA system whose output vector can be described by $\mathbf{y} = \mathbf{S}\mathbf{a} + \mathbf{n}$. Since \mathbf{a} contain in both systems symbols of a finite modulation alphabet, differences between both scenarios are restricted to the properties of the system matrix \mathbf{S} and the channel matrix \mathbf{H} . If the data layers are assigned to different users, BLAST is identical to the uplink of an ordinary space-division multiple access scheme.

In OFDM-CDMA systems or single-carrier CDMA systems with flat fading channels, \mathbf{S} has the dimensions $N_s \times N_U$ and its columns represent the signatures of all users. Remember that the signature was obtained by convolving the spreading code with the channel impulse response. Concerning multiple antenna schemes, \mathbf{H} is a $N_R \times N_T$ matrix containing the pure channel coefficients $h_{\mu,\nu}$. Hence, the spreading factor N_S is similar to the number of receive antennas while the number

of users N_U is equivalent to the number of layers N_T ². Consequently, the load of a CDMA system $\beta = N_U/N_s$ becomes N_T/N_R in multi-layer architectures. The larger the difference between N_T and N_R with $N_R > N_T$, the easier becomes the detection at the receiver.

Due to this similarity, the multi-user detection algorithms described in Chapter 5 can also be applied to BLAST-like architectures. Strategies like parallel or successive interference cancellation described in Section 5.3 can be used as well as linear filters like decorrelator and MMSE filter derived in Section 5.2. The next subsection compares their error rate performances under the specific conditions of multiple antenna systems and flat Rayleigh fading channels.

6.3.3 Performance of Multi-Layer Detection Schemes

We will focus in this section on the combination of linear and nonlinear techniques as analyzed in Section 5.4. Since we look only at the first detection stage (no turbo detection), simple hard decisions are used as nonlinearities. The QLD-SIC strategies are compared with optimum maximum likelihood detection³ for different combinations of N_T and N_R as well as different modulation schemes. Moreover, the influences of sorting and error propagation are illuminated.

Fig. 6.3.4 shows the results obtained for an uncoded QPSK system with $N_T = 4$ transmit antennas, $N_R = 6$ receive antennas and i.i.d. Rayleigh fading channels between them. Diagram a) depicts the results for the zero-forcing criterion while diagram b) those for the MMSE criterion. First, we see that the linear approaches lose about 1 dB compared to the unsorted interference cancellation schemes (QLD) because they do not consider the finite nature of the signal alphabet. Applying the SQLD with suboptimum sorting, a gain of 3.3 dB is obtained for the zero-forcing as well as the MMSE solution at an error rate of 10^{-3} . The loss compared to the algorithm with optimum post-sorting (SQLD+PSA) known as V-BLAST detection [FGVW99] and described in Section 5.4.2 is neglectable. This performance is obtained with only a fraction of the computational costs of the V-BLAST. The MMSE criterion outperforms the ZF approach by 0.6 - 0.7 dB at an error rate of 10^{-3} so that the SQLD+PSA algorithm approaches the ML detector up to a gap of 1 dB.

Next, we increase the *load* of the system by choosing only $N_R = 4$ receive antennas. **Fig. 6.3.5** illustrates the QPSK signal spaces after each detection step of the SQLD-SIC algorithm. After filtering with \mathbf{Q}^H , we have to start the successive

²Despite this similarity, both systems differ in that the diversity degree increases with the number of receive antennas while it does not for growing N_s and constant bandwidth.

³Besides the brute force approach that calculates $\hat{\mathbf{x}} = \operatorname{argmin}_{\tilde{\mathbf{x}}} \|\mathbf{y} - \mathbf{H}\tilde{\mathbf{x}}\|^2$ for each hypothesis $\tilde{\mathbf{x}}$, MLD can also be accomplished by means of sphere detection [FP85, SE94, AEVZ02] with lower computational costs.

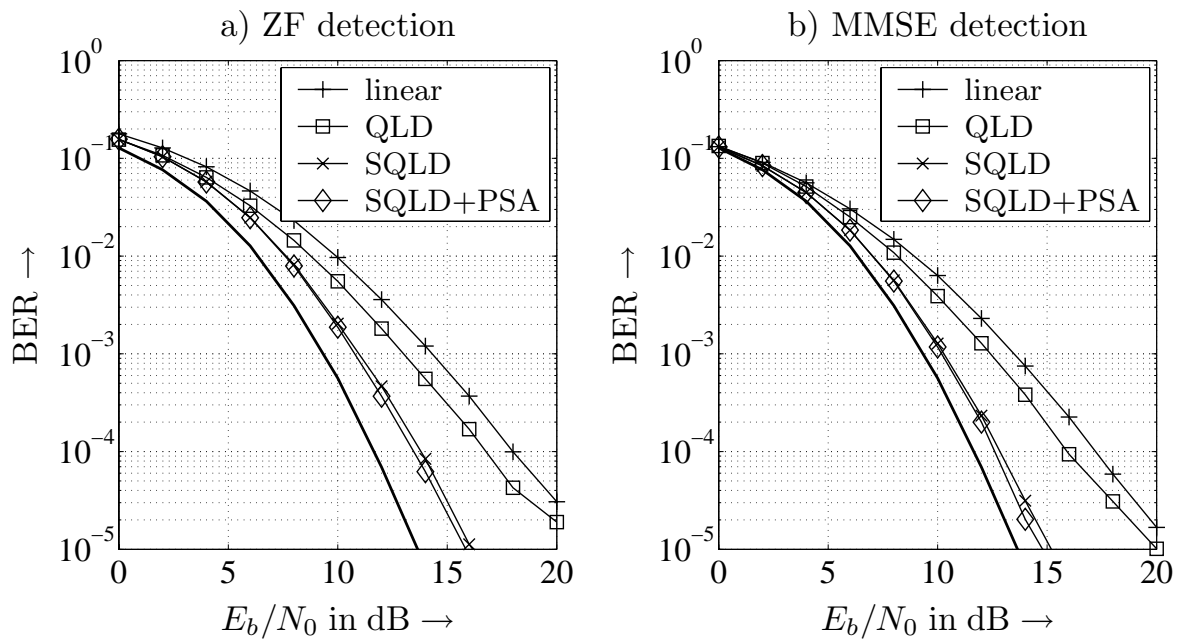


Figure 6.3.4: Bit error rate performance of **a)** ZF and **b)** MMSE detectors for QPSK system with $N_T = 4$ and $N_R = 6$ antennas (bold line: maximum likelihood detection)

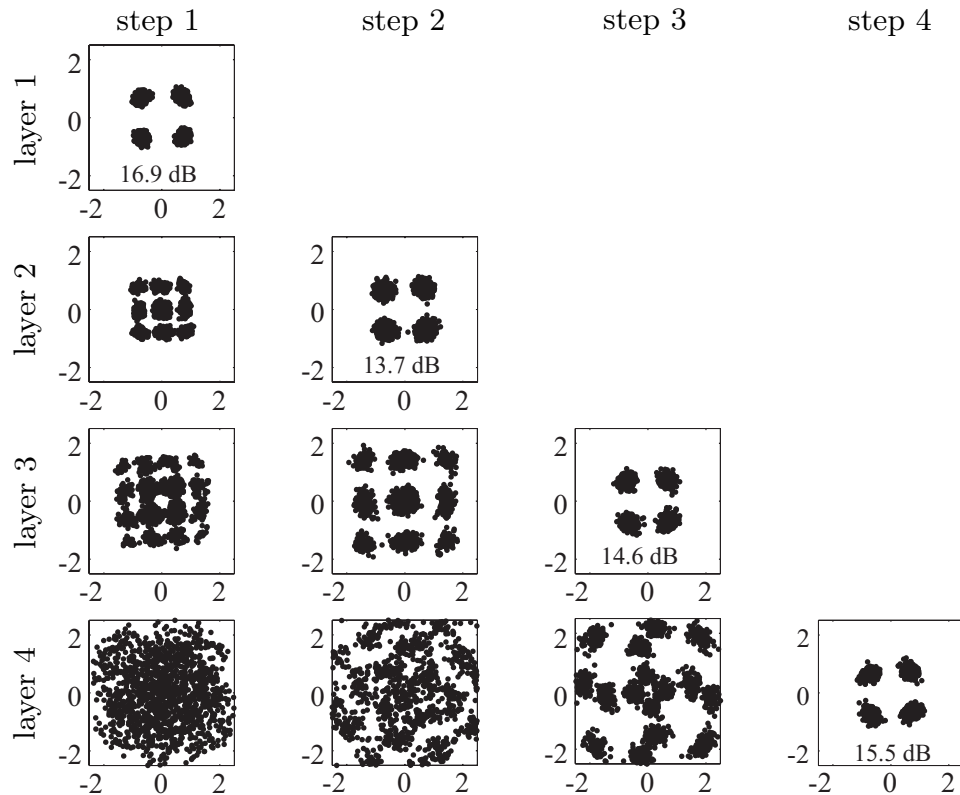


Figure 6.3.5: Signal spaces per layer after different detection steps of S(QLD)-SIC for $N_T = 4$ transmit and $N_R = 4$ receive antennas with QPSK modulation

detection from top to bottom. The first layer does not suffer from interference and its symbols can be directly detected. For this scenario, a signal to noise ratio of 16.9 dB was achieved. Before the interference cancellation step, we can clearly recognize the superposition of two QPSK constellations in the second layer. The QPSK constellation with an SNR of 13.7 dB is obtained only after subtracting the contribution of the first layer. In all subsequent layers, the signal constellations become more obvious after each cancellation step.

Due to the higher load, it can be expected that both, the error rates and the gap to the maximum likelihood detector will increase. The results in **Fig. 6.3.6** confirm these predictions. The relations between the curves in Figs. a) and b) are similar to the case of six receive antennas. However, the algorithms based on the zero-forcing criterion do not work satisfactory since the gap to the MLD amounts to more than 10 dB even with optimum post sorting. The MMSE variants perform much better because they avoid the noise amplification. The loss of the SQLD with PSA compared to the MLD grows up to 2.8 dB. Moreover, the difference between the SQLD with and without post sorting becomes larger at high SNR.

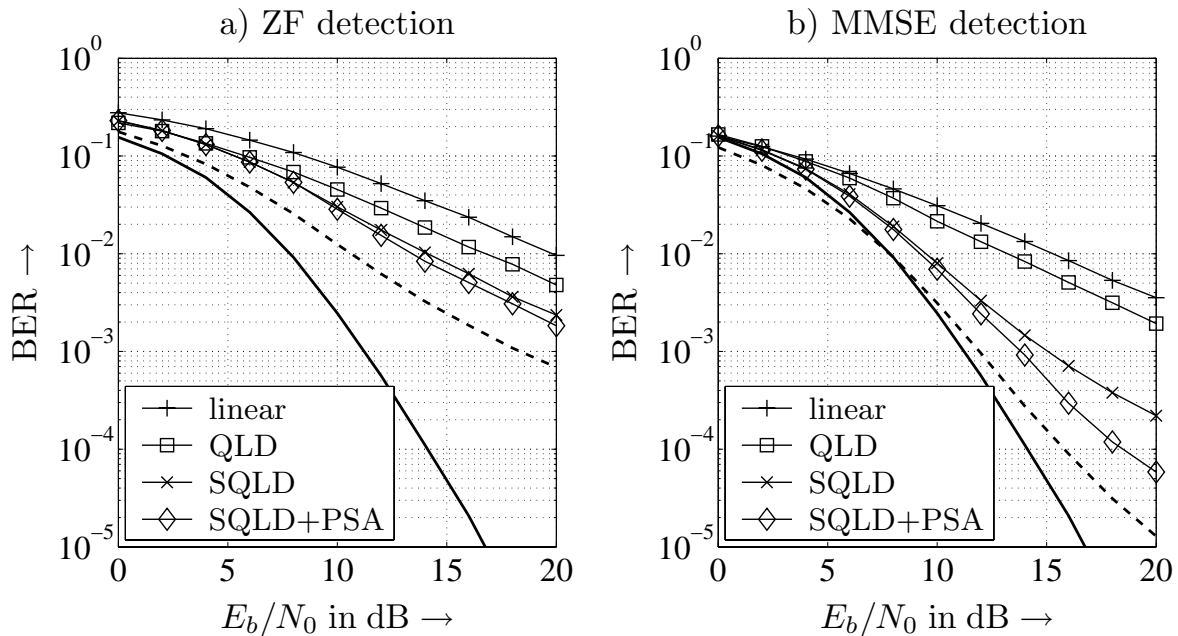


Figure 6.3.6: Bit error rate performance of **a)** ZF and **b)** MMSE detectors for $N_T = N_R = 4$ antennas and QPSK (bold solid line: maximum likelihood detection, bold dashed line: genie aided detector)

Additionally, we have illustrated the curves for a theoretical device called genie aided detector indicated by the bold dashed lines. It allows a perfect interference cancellation and, therefore, avoids error propagation. Nevertheless, detection errors occur in each layer. Even with optimum post sorting, error propagation is a severe problem. At an error rate of $2 \cdot 10^{-3}$, the loss amounts to 4 dB for the ZF solution and approximately 2 dB at 10^{-3} in the MMSE case.

This effect shall be further examined in **Fig. 6.3.7** showing layer-specific error rates for ZF-SQLD-SIC with and without a genie aided detector. With the genie aided detector, substantial improvements are achieved with each cancellation step. Layer 4 does not suffer from interference at all and comes very close to the MLD performance. As we know from Section 1.5, the different slopes of the curves indicate that each layer experiences a different diversity degree. In the first layer, the main purpose of \mathbf{Q}^H is to suppress interference so that only a diversity degree of $N_R - N_T + 1 = 1$ is achievable [WRB⁺02]. With each SIC step, we gain a degree of freedom because less layers have to be suppressed so that the linear filter tends towards a matched filter and collects more and more diversity. Hence, the diversity degree grows up to $N_R = 4$ for the last layer. Without genie, the performance of all layers is dominated by the first one due to error propagation.

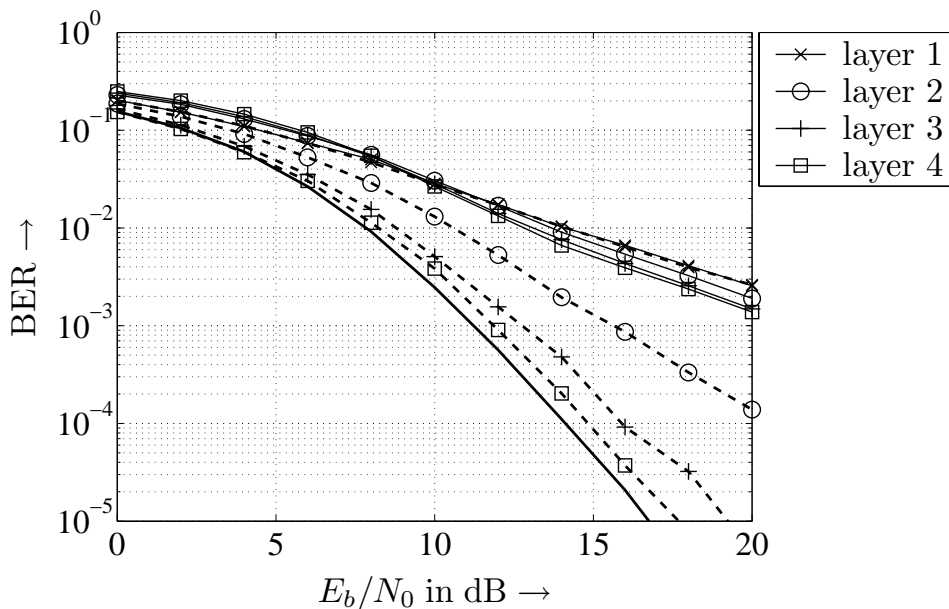


Figure 6.3.7: Demonstration of error propagation for QPSK system with ZF-SQLD-SIC and $N_T = N_R = 4$ (bold solid line: maximum likelihood detection, bold dashed line: genie aided detector)

In order to achieve higher spectral efficiencies, we can employ modulation schemes with more bits per symbol. **Fig. 6.3.8** illustrates the results for 16-QAM. Since it is more sensitive to noise and interference than QPSK, larger SNRs are required to obtain the similar error rates. Moreover, the SQLD-SIC even with optimum post sorting loses a lot compared to the MLD bound.

For approximately the same number of receive antennas as transmit antennas, the matrix describing the MIMO channel is generally badly conditioned. In this case, the noise amplification of the zero-forcing approach is very high and also the MMSE filter performs weak. A significant improvement coming close to the MLD performance even under these severe conditions is described in the next

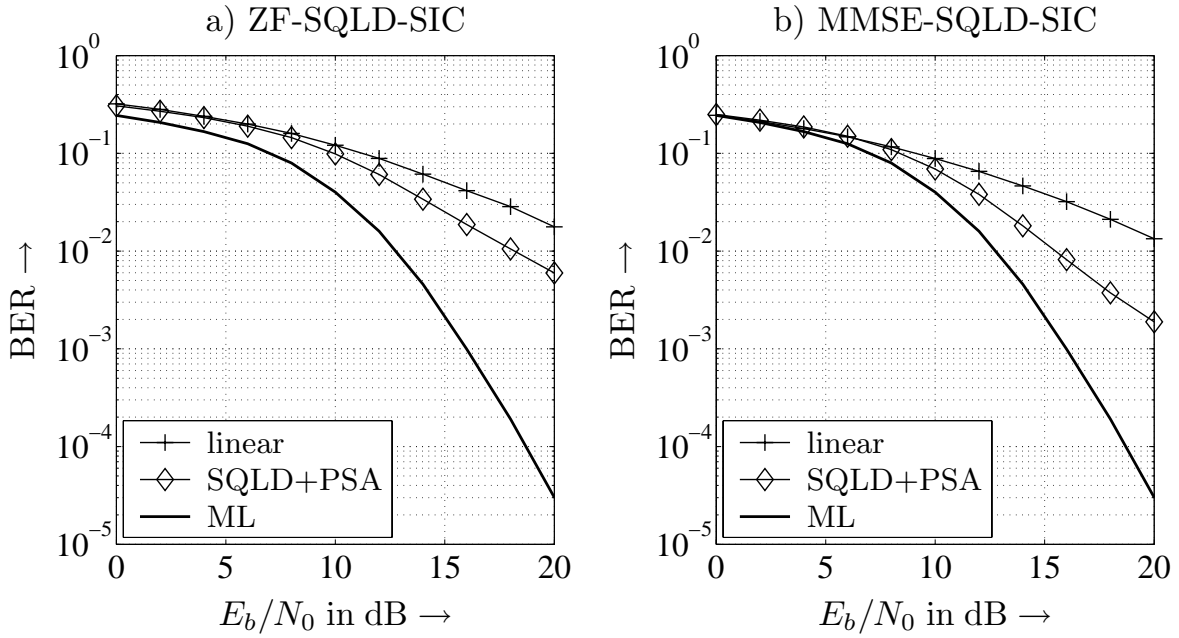


Figure 6.3.8: Performance of a) ZF-SQLD-SIC and b) MMSE-SQLD-SIC detectors and system with $N_T = 4$ and $N_R = 4$, 16-QAM

subsection. It was not already presented in the context of MUD techniques in Chapter 5 because the considered algorithm works best for small matrices and the system matrix \mathbf{S} of a CDMA system is generally larger than \mathbf{H} .

6.3.4 Lattice Reduction aided Detection

The aforementioned techniques have severe problems if the channel matrix \mathbf{H} is badly conditioned. The condition number of a matrix \mathbf{H} is defined as

$$\kappa(\mathbf{H}) = \frac{\sigma_{\max}}{\sigma_{\min}} \geq 1 , \quad (6.3.10)$$

i.e. it equals the ratio of largest and smallest singular value [Str88]. With $\|\mathbf{H}\|_2$ as the spectral norm of \mathbf{H} , the condition number becomes

$$\kappa(\mathbf{H}) = \|\mathbf{H}\|_2 \cdot \|\mathbf{H}^{-1}\|_2 . \quad (6.3.11)$$

For orthogonal matrices with $\mathbf{H}^{-1} = \mathbf{H}^T$, the condition number is one and no noise amplification occurs for linear detectors. Hence, matched filter and decorrelator are identical and optimum receivers. Contrarily, ill-conditioned matrices with large $\kappa(\mathbf{H})$ lead to high noise enhancements and, therefore, to severe detection problems especially for the decorrelator. Concluding, we can state that it would be desirable to have a roughly orthogonal matrix with a condition number close to one⁴.

⁴It is sufficient that the columns in \mathbf{H} are orthogonal but have different norms. In this case, $\kappa(\mathbf{H}) \neq 1$ holds and $\mathbf{H}^H \mathbf{H}$ would result in a diagonal but not the identity matrix.

This goal can be accomplished with the so-called *lattice reduction* (LR) technique [WF03a, WF03b, WBKK04b, WKK04]. For the derivation, we use the real-valued description of a communication link as described in (5.4.8) on page 265

$$\mathbf{y}^r = \mathbf{H}^r \mathbf{x}^r + \mathbf{n}^r \Leftrightarrow \begin{bmatrix} \mathbf{y}' \\ \mathbf{y}'' \end{bmatrix} = \begin{bmatrix} \mathbf{H}' & -\mathbf{H}'' \\ \mathbf{H}'' & \mathbf{H}' \end{bmatrix} \cdot \begin{bmatrix} \mathbf{x}' \\ \mathbf{x}'' \end{bmatrix} + \begin{bmatrix} \mathbf{n}' \\ \mathbf{n}'' \end{bmatrix}.$$

Restricting ourselves to multi-amplitude signalling like M -ASK or M -QAM, the data symbols $x'_v, x''_v \in \mathbb{X}$ can be expressed as integers with appropriate scaling. From Section 1.4, we know that the set \mathbb{X} can be chosen according to

$$\mathbb{X}_{\text{ASK}} = \{ \pm e, \pm 3e, \dots, \pm (M-1)e \} \quad \text{with} \quad e = \sqrt{\frac{3}{(M^2-1)E_s/T_s}} \quad (6.3.12a)$$

$$\mathbb{X}_{\text{QAM}} = \{ \pm e, \pm 3e, \dots, \pm (\sqrt{M}-1)e \} \quad \text{with} \quad e = \sqrt{\frac{3}{2(M-1)E_s/T_s}} \quad (6.3.12b)$$

containing all odd multiples of e in a certain interval whose size depends on M . PSK modulation is explicitly excluded from this derivation. Instead of using only odd numbers, the transformation

$$x = (2b-1) \cdot e \quad (6.3.13)$$

with consecutive integers $b \in \mathbb{B} = \{-M/2+1, \dots, M/2\}$ delivers the same set \mathbb{X}_{ASK} ⁵. Considering for the moment a generalization such that all integers $b \in \mathbb{Z}$ (set of all integer numbers) are considered, the $2N_T$ columns \mathbf{h}_v^r in \mathbf{H}^r span an infinite lattice as depicted in **Fig. 6.3.9** for the case of $N_T = 1$. All points in this lattice can be reached by linear combinations of the vectors \mathbf{h}_1^r and \mathbf{h}_2^r .

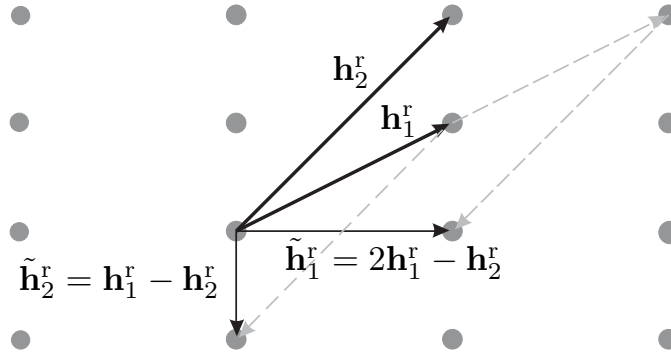


Figure 6.3.9: Illustration of the principle of lattice reduction for $N_T = 1$ with $\mathbf{h}_1^r = [2 \ 1]^T$ and $\mathbf{h}_2^r = [2 \ 2]^T$

In our example, the vectors $\mathbf{h}_1^r = [2 \ 1]^T$ and $\mathbf{h}_2^r = [2 \ 2]^T$ are obviously not orthogonal to each other but highly correlated so that a multiplication with the

⁵An equivalent expression is obtained for QAM by exchanging M with \sqrt{M} .

Moore-Penrose inverse of \mathbf{H}^r would lead to an amplification of the background noise. The basic principle behind the lattice reduction is to find vectors $\tilde{\mathbf{h}}_1^r$ and $\tilde{\mathbf{h}}_2^r$ that generate the same lattice and are roughly orthogonal. For our example, we can find

$$\tilde{\mathbf{h}}_1^r = 2\mathbf{h}_1^r - \mathbf{h}_2^r = \begin{bmatrix} 2 \\ 0 \end{bmatrix} \quad (6.3.14a)$$

$$\tilde{\mathbf{h}}_2^r = \mathbf{h}_1^r - \mathbf{h}_2^r = \begin{bmatrix} 0 \\ -1 \end{bmatrix} \quad (6.3.14b)$$

which are exactly orthogonal. The new matrix

$$\mathbf{H}_{\text{red}} = [\tilde{\mathbf{h}}_1^r \quad \tilde{\mathbf{h}}_2^r] = \begin{bmatrix} 2 & 0 \\ 0 & -1 \end{bmatrix} \quad (6.3.15)$$

has been obtained by subtracting integer multiples of one column from the other. It has a condition number $\kappa(\mathbf{H}_{\text{red}}) = 2$ instead of $\kappa(\mathbf{H}^r) = 6.32$ for the original matrix. Generally, any matrix $\tilde{\mathbf{H}}^r$ generated from \mathbf{H}^r by exchanging columns, multiplying columns with -1 and adding integer multiples of one column to another spans the same lattice. These linear operations can be expressed by an $2N_T \times 2N_T$ unimodular matrix \mathbf{T} , i.e. \mathbf{T} consists only of integers and its determinant takes only the values ± 1 [SE94]. Therefore, the inverse of \mathbf{T} always exists, it also contains only integers and allows the operation $\mathbf{T} \cdot \mathbf{T}^{-1} = \mathbf{I}_{2N_T}$. The reduced channel matrix is obtained by

$$\mathbf{H}_{\text{red}} = \mathbf{H}^r \cdot \mathbf{T}. \quad (6.3.16)$$

For the above example, $\mathbf{T} = \begin{bmatrix} 2 & 0 \\ 0 & -1 \end{bmatrix}$ holds. This result is explained in more detail In Appendix C.3.

The goal is now to find a transformation matrix \mathbf{T} such that the condition number of \mathbf{H}_{red} is as small as possible, especially $\kappa(\mathbf{H}_{\text{red}}) < \kappa(\mathbf{H}^r)$ should hold. Finding a nearly orthogonal basis is equivalent to the problem of finding vectors of minimum length. This can be easily seen from **Fig. 6.3.9**. Only if none of the two vectors has a significant projection onto the other, both have a small length and are nearly perpendicular. A first step towards this goal is the QL decomposition of \mathbf{H}^r since it already determines a set of orthogonal vectors \mathbf{q}_ν with $\nu = 1, \dots, 2N_T$. However, their linear combination is given by \mathbf{L} whose elements are generally real numbers and no integers. Nevertheless, this decomposition allows an efficient lattice reduction especially if appropriate sorting is applied. The exact definition of a reduced lattice and a detailed description of the LLL algorithm as one example for a lattice reduction can be found in the Appendix C.3.

Once we found a transformation matrix \mathbf{T} and, thus, the reduced matrix \mathbf{H}_{red} , we can rewrite the received signal as

$$\mathbf{y}^r = \mathbf{H}^r \mathbf{x}^r + \mathbf{n}^r = \mathbf{H}^r \mathbf{T} \cdot \mathbf{T}^{-1} \mathbf{x}^r + \mathbf{n}^r = \mathbf{H}_{\text{red}} \cdot \mathbf{T}^{-1} \mathbf{x}^r + \mathbf{n}^r. \quad (6.3.17)$$

Applying the transformation in (6.3.13) to the whole vector $\mathbf{b} = [b_1, \dots, b_{2N_T}]^T$, the product $\mathbf{T}^{-1}\mathbf{x}^r$ can be expressed by

$$\mathbf{T}^{-1}\mathbf{x}^r = \mathbf{T}^{-1}(2\mathbf{b} - \mathbf{1}_{2N_t \times 1})e = (2\mathbf{z} - \mathbf{T}^{-1}\mathbf{1}_{2N_t \times 1})e \quad (6.3.18)$$

where $\mathbf{z} = \mathbf{T}^{-1}\mathbf{b}$ contains only integer numbers according to the properties of \mathbf{T} . The received signal becomes

$$\mathbf{y}^r = 2e\mathbf{H}_{\text{red}}\mathbf{z} - e\mathbf{H}_{\text{red}}\mathbf{T}^{-1}\mathbf{1}_{2N_T \times 1} + \mathbf{n}^r. \quad (6.3.19)$$

Since the modified channel matrix \mathbf{H}_{red} is generally better conditioned, we can apply linear detectors as well as SQLD-SIC based approaches known from Chapter 5 without suffering much from the noise amplification. The main difference to the conventional detection is that the decision is made with respect to the integer variable \mathbf{z} instead of \mathbf{x}^r . Assuming for simplicity the decorrelator as detector, we obtain with $\mathbf{H}_{\text{red}}^\dagger \cdot \mathbf{H}_{\text{red}} = \mathbf{I}_{2N_T}$

$$\frac{1}{2e} \cdot \mathbf{H}_{\text{red}}^\dagger \mathbf{y}^r = \mathbf{z} - \frac{1}{2} \cdot \mathbf{T}^{-1}\mathbf{1}_{2N_T \times 1} + \frac{1}{2e} \cdot \mathbf{H}_{\text{red}}^\dagger \mathbf{n}^r. \quad (6.3.20)$$

Moving the constant offset to the left hand side of (6.3.20) and performing an element-wise integer decision $\mathcal{Q}(\cdot)$ delivers the estimate

$$\hat{\mathbf{z}} = \mathcal{Q}\left(\frac{1}{2e} \cdot \mathbf{H}_{\text{red}}^\dagger \mathbf{y}^r + \frac{1}{2} \cdot \mathbf{T}^{-1}\mathbf{1}_{2N_T \times 1}\right). \quad (6.3.21)$$

Due to this decision, the lattice reduction aided detection is a nonlinear technique although the decorrelator itself is linear. Finally, the estimate $\hat{\mathbf{z}}$ has to be transformed back into the original domain by $\hat{\mathbf{b}} = \mathbf{T}\hat{\mathbf{z}}$ leading with (6.3.13) to

$$\hat{\mathbf{x}}^r = (2\hat{\mathbf{b}} - \mathbf{1}_{2N_t \times 1})e. \quad (6.3.22)$$

Certainly, the MMSE detector or the SQLD-SIC schemes can also be applied instead of the decorrelator. The whole receiver structure is depicted in **Fig. 6.3.10**. Starting with the QL decomposition of \mathbf{H}^r already known from Section 5.4, the matrices \mathbf{Q} , \mathbf{L} and \mathbf{P} are obtained. They are fed into the block termed *lattice reduction* that provides a QL representation of a reduced matrix \mathbf{H}_{red} consisting of a unitary matrix \mathbf{Q}_{red} , a lower triangular matrix \mathbf{L}_{red} and a transformation matrix \mathbf{T} . They are subsequently used for the detection process, e.g. linear filtering or SQLD-SIC, as well as the transformation back into the original signal space.

Contrarily to the lattice theory we have only finite signal spaces \mathbb{X} and \mathbb{B} in the original domain, and, therefore, also in the transformed domain. Moreover, it is very important to realize that the signal space of the new variable \mathbf{z} is not identical to the original space \mathbb{B}^{2N_T} as is illustrated in **Fig. 6.3.11**. The dimensions are

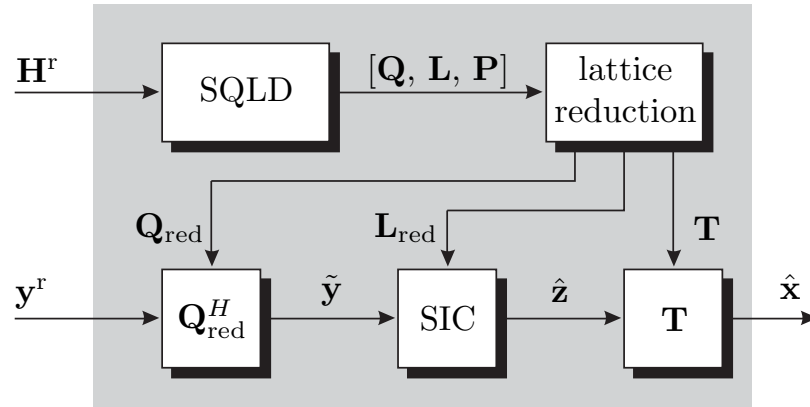


Figure 6.3.10: Structure of lattice reduction aided QLD-SIC detector

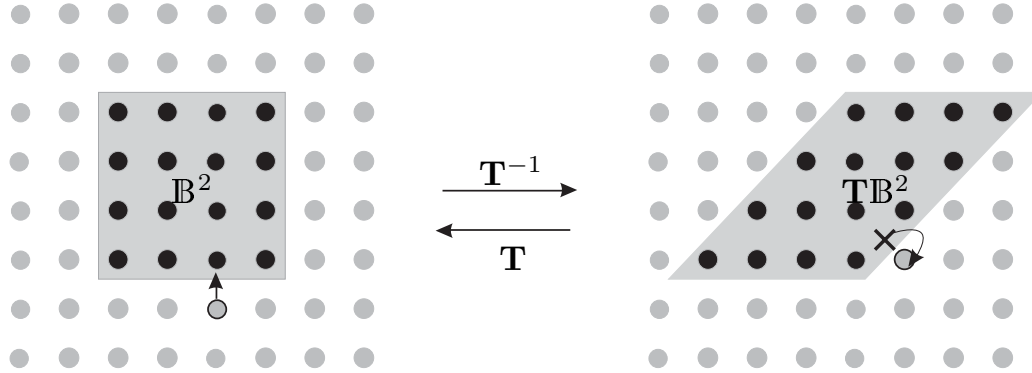


Figure 6.3.11: Original and transformed signal spaces for $N_T = 1$

no longer linear independent so that an optimum decision would require a vector quantization providing an estimate of the entire vector $\hat{\mathbf{z}}$. In order to keep the computational costs as low as possible, we apply instead a scalar quantization that separately delivers estimates $\hat{z}_\mu \in \mathbb{Z}$, i.e. we look for the integer closest to our decision variable. Hence, it may happen that $\hat{\mathbf{z}}$ lies outside the transformed alphabet so that the backward transformation $\hat{\mathbf{b}} = \mathbf{T}\hat{\mathbf{z}}$ also delivers a result outside of \mathbb{B}^{2N_T} . In this case, we have to apply a quantization again so that valid symbols are obtained. Although this procedure is not optimum, we will see that a performance close to the optimum maximum likelihood detector can be achieved.

Concerning the application of the LR based detection in coded systems, it has to be mentioned that the hard decision in the transformed domain makes the calculation of LLRs for the original domain difficult. This is of special interest because hard decisions prior to decoding lead to a loss in performance. Extensions of the lattice reduction aided detection providing soft information are still a current research topic.

Extension to MMSE Solution

So far, we just described the zero-forcing implementation of the lattice reduction. A better performance can be obtained with the MMSE criterion. Remembering Section 5.4 on page 273, the QL decomposition for the MMSE solution was obtained by extending the system matrix \mathbf{S} according to

$$\underline{\mathbf{S}} = \begin{bmatrix} \mathbf{S} \\ \frac{\sigma_{\mathcal{N}}}{\sigma_{\mathcal{X}}} \mathbf{I}_{N_U} \end{bmatrix}.$$

A direct implementation of this approach would extend the reduced channel matrix \mathbf{H}_{red} obtained from the previous derivation in the same way resulting in

$$\begin{bmatrix} \mathbf{H}_{\text{red}} \\ \frac{\sigma_{\mathcal{N}}}{\sigma_{\mathcal{X}}} \cdot \mathbf{I}_{N_T} \end{bmatrix} = \underline{\mathbf{Q}}_{\text{red}} \cdot \underline{\mathbf{L}}_{\text{red}} \cdot \underline{\mathbf{P}}_{\text{red}} \quad (6.3.23)$$

where a subsequent QL decomposition would deliver \mathbf{Q}_{red} , \mathbf{L}_{red} and \mathbf{P}_{red} . However, this does not yield the best performance because the MMSE solution inverts the matrix $[(\mathbf{H}^r)^H \mathbf{H}^r + \sigma_{\mathcal{N}}^2 / \sigma_{\mathcal{X}}^2 \mathbf{I}_{2N_T}]$ so that we need a roughly orthogonal basis of $\underline{\mathbf{H}}$ and not of \mathbf{H} . Instead, the channel matrix \mathbf{H} should be directly extended to

$$\underline{\mathbf{H}} = \begin{bmatrix} \mathbf{H} \\ \frac{\sigma_{\mathcal{N}}}{\sigma_{\mathcal{X}}} \cdot \mathbf{I}_{N_T} \end{bmatrix} \quad (6.3.24)$$

and the QL decomposition as well as the lattice reduction are applied to $\underline{\mathbf{H}}$. This results in $\underline{\mathbf{H}}_{\text{red}} = \underline{\mathbf{H}} \mathbf{T}$ [WBKK04b].

Simulation Results

Now, we want to compare the performance of the introduced lattice reduction approach to the detection techniques already described in Chapter 5. We consider multiple antenna systems with identical number of receive and transmit antennas. Moreover, uncorrelated flat Rayleigh fading channels between different pairs of transmit and receive antennas are assumed. Note that no iterations according to the turbo principle are carried out so that we regard a one-stage-detector. If the loss compared to the maximum likelihood detector is large, the performance can be improved by iterative schemes as shown in Chapter 5.

Fig. 6.3.12 compares the bit error rate performance of an uncoded QPSK⁶ system with $N_T = N_R = 4$ antennas at transmitter and receiver. The left diagram summarizes the zero-forcing results. The simple decorrelator (bold dashed curve) based on the original channel matrix \mathbf{H} shows the worst performance. It severely

⁶Although PSK was explicitly excluded, QPSK is an exception because it is equivalent to 4-QAM.

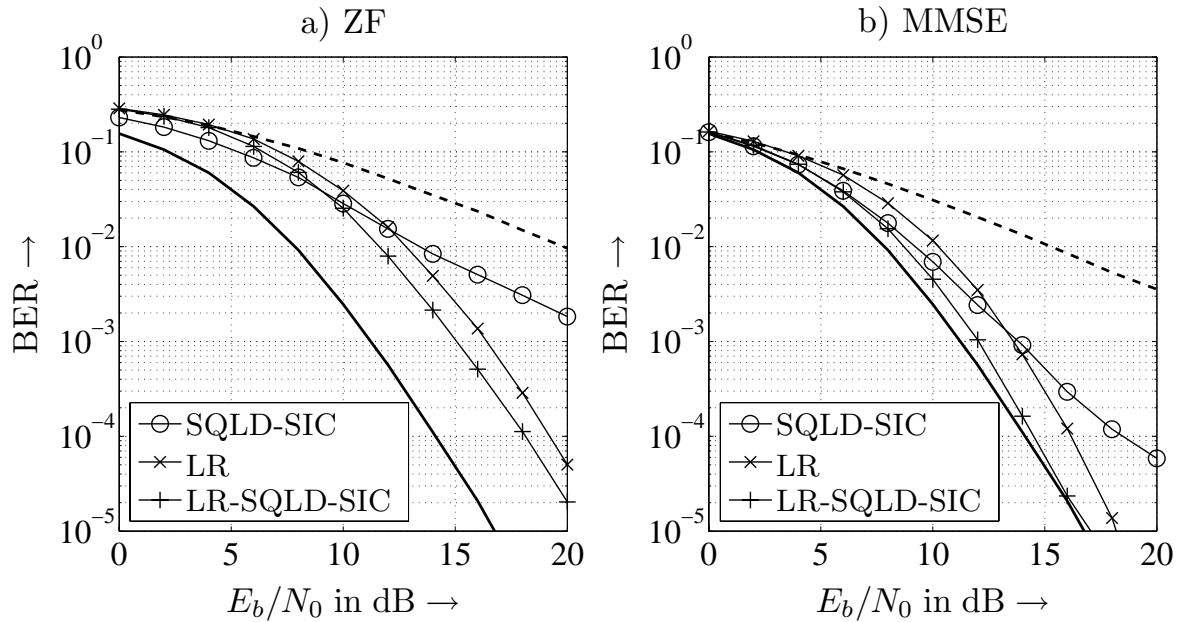


Figure 6.3.12: Performance of lattice reduction aided detection for QPSK system with $N_T = N_R = 4$ (solid bold line: MLD performance, dashed bold line: linear detectors)

amplifies the background noise and cannot exploit diversity so that the slope of the curve corresponds to a diversity degree of $D = N_R - N_T + 1 = 1$. The ZF-S QLD-SIC detection gains about 7 dB at 10^{-2} compared to the decorrelator but is still far away from the maximum likelihood performance. It can only partly exploit diversity as will be shown later in Fig. 6.3.13. The decorrelator based on the reduced channel matrix \mathbf{H}_{red} ⁷ labelled LR performs slightly worse than the ZF-S QLD-SIC at low SNRs and much better at high signal to noise ratios. At an error rate of $2 \cdot 10^{-3}$, the gain already amounts to 4 dB. On the one hand, the lattice reduction aided decorrelator does not enhance the background noise very much due to the nearly orthogonal structure. On the other hand, it fully exploits diversity as indicated by the higher slope of the error rate curve.

Since the reduced channel matrix \mathbf{H}_{red} is not perfectly orthogonal, multi-layer interference still disturbs the decision. Hence, a subsequent nonlinear successive interference cancellation applying hard decisions (ZF-S QLD-SIC) can improve the performance by 1 dB. The gain is not as high as for the conventional QLD-SIC due to the good condition of \mathbf{H}_{red} .

Looking at the MMSE solutions depicted in Fig. 6.3.12b), we recognize that all curves are coming closer to the MLD performance. The linear MMSE filter based on \mathbf{H} performs worst, the lattice reduction based counterpart (LR) outperforms

⁷As already mentioned, the system representation by a reduced channel matrix requires a decision in the transformed domain and a subsequent inverse transformation. Therefore, the whole detector is nonlinear although a linear device was employed in the transformed domain.

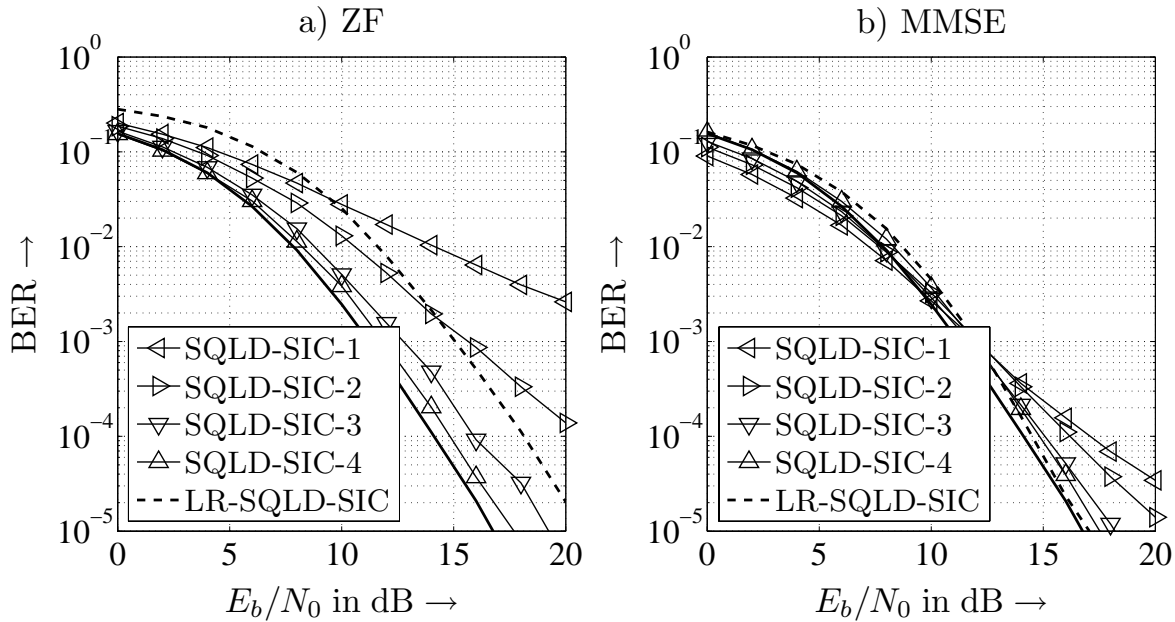


Figure 6.3.13: Illustration of diversity degree per layer for SQLD and lattice reduction aided detection for QPSK system with $N_T = N_R = 4$ (solid bold line: MLD performance)

the MMSE-SQLD-SIC at high SNR. The LR-SQLD-SIC improves the performance such that the MLD curve is reached. Thus, we can conclude that the lattice reduction technique improves the performance significantly and that it is well suited for enhancing the signal detection in environments with severe multiple access interference. For the considered scenario, near-maximum likelihood performance is achieved with much lower computational costs.

Next, we analyze how the different detectors exploit diversity. From Fig. 6.3.7 we know already that each layer experiences a different diversity degree for QLD-SIC based approaches. This is again illustrated in **Fig. 6.3.13** for ZF and MMSE criteria. The curves have been obtained by employing a genie aided detector that perfectly avoids error propagation. Hence, the error rates truly represent the different diversity degrees and do not suffer from errors made in previous detection steps.

The results for the LR-based detection are depicted with only one curve because the error rates of all layers are nearly identical. Hence, all layers experience the same diversity degree of $D = 4$ (compare slope with SQLD-4) so that even the first layer can be detected with high reliability. Since this layer dominates the average error rate especially in the absence of a genie, this represents a major benefit compared to QLD-SIC schemes.

Concerning the MMSE solution, the differences are not as large but still observable. At very low SNRs, the genie aided MMSE-SQLD-SIC even outperforms the maximum likelihood detector because no layer suffers from interference and decisions are made layer by layer while the MLD has to cope with all layers simultaneously.

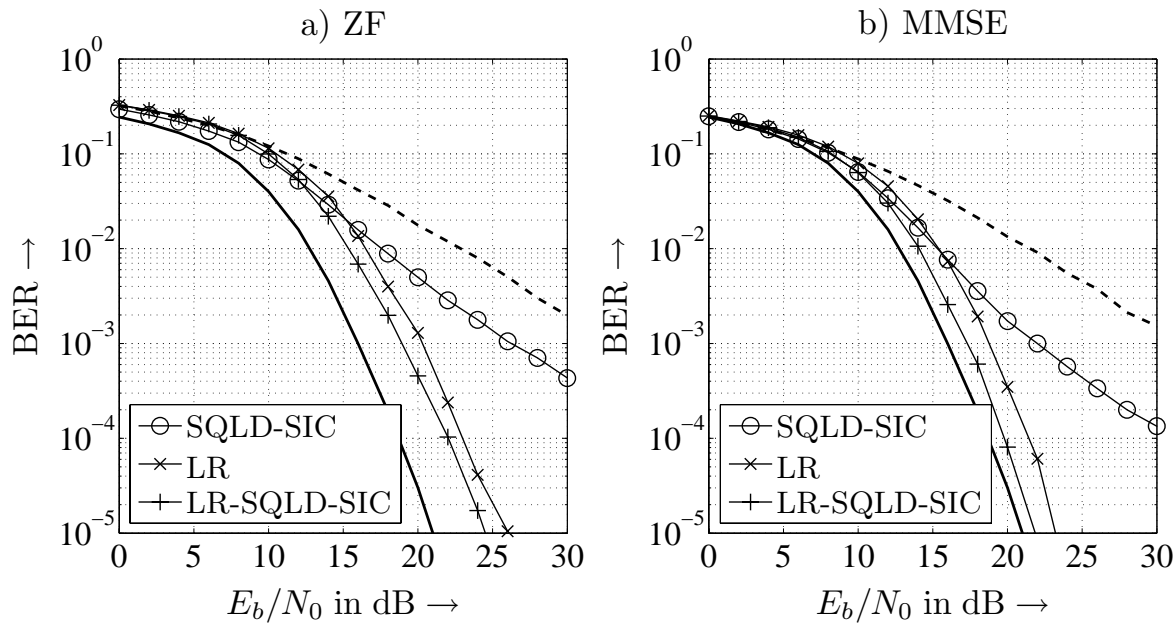


Figure 6.3.14: Performance of lattice reduction aided detection for 16-QAM system with $N_T = N_R = 4$ (solid bold line: MLD performance, dashed bold line: linear detector)

Fig. 6.3.14 shows the performance of the same system for 16-QAM. First, it has to be mentioned that the computational complexity of lattice reduction itself is totally independent of the size of the modulation alphabet. This is a major advantage compared to the ML detector because its complexity grows exponentially with the alphabet size. Compared to QPSK, larger SNRs are needed to achieve the same error rates. However, the relations between the curves are qualitatively still the same. The LR based SQLD-SIC gains 1 dB compared to the LR based decorrelator of 2 dB for the MMSE solution. The SQLD-SIC approach based on the original channel matrix is clearly outperformed but the MLD performance is not obtained anymore and a gap of approximately 1 dB remains for the MMSE approach.

Finally, a larger system with $N_T = N_R = 6$ and 16-QAM is considered. **Fig. 6.3.15** shows that the LR based SQLD-SIC still outperforms the detector based on \mathbf{H} but the gap to the maximum likelihood detector becomes larger. The reason is the efficient but suboptimum LLL algorithm (see Appendix C.3) used for the lattice reduction. It loses in performance for large matrices because the inherent sorting gets worse. This is also the reason why the lattice reduction aided detector was not introduced in the context of multi-user detection in CDMA systems in Chapter 5. The considered CDMA systems have much more inputs and outputs (larger system matrices \mathbf{S}) than the multiple antenna systems analyzed here so that no advantage can be observed compared to the conventional SQLD-SIC.

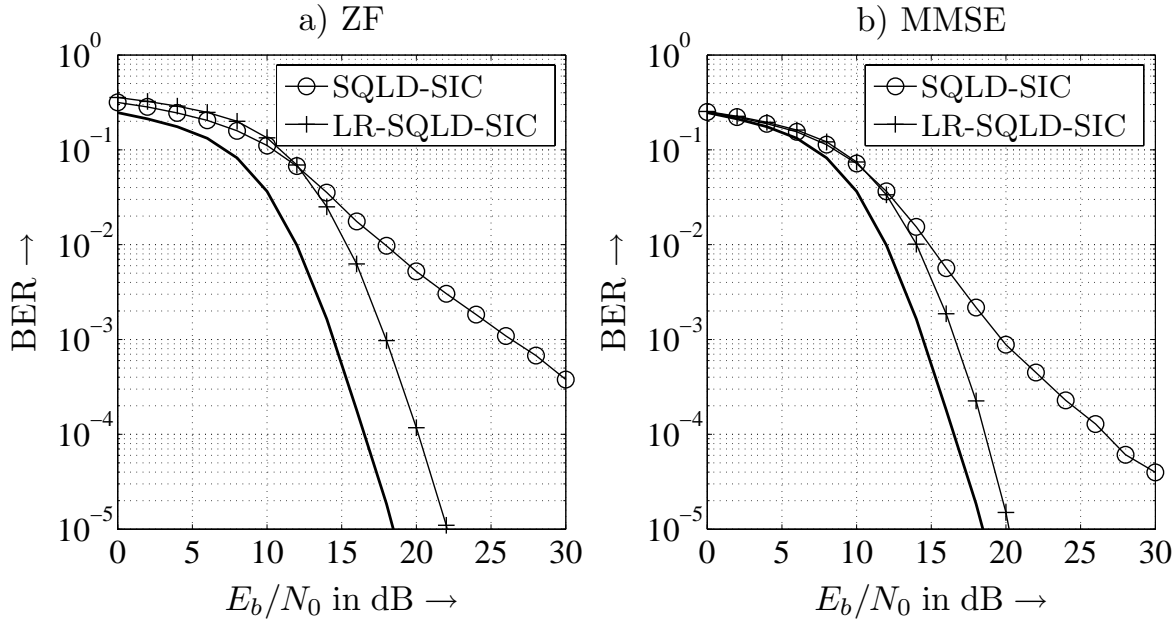


Figure 6.3.15: Performance of lattice reduction aided detection 16-QAM system with $N_T = N_R = 6$ (solid bold line: MLD performance)

6.4 Information Theoretic Analysis

In this section, we illustrate the theoretical results of Section 2.3 for multiple antenna systems. We consider uncorrelated as well as correlated frequency-nonselective MIMO channels and determine the channel capacities for Gaussian distributed input signals for different levels of channel knowledge at the transmitter. Perfect channel knowledge at the receiver is always assumed.

Uncorrelated MIMO Channels

First, **Fig. 6.4.1a** shows the capacity for an uncorrelated SIMO channel with up to four outputs versus the SNR per receive antenna. We observe that the ergodic capacity increases with growing number of receive antennas due to the higher diversity degree and the array gain. The latter one shifts the curves by $10 \log_{10}(N_R)$ to the left, i.e. doubling the number of receive antennas leads to an array gain of 3 dB. Concentrating only on the diversity gain, we have to depict the curves versus the SNR after maximum ratio combining as shown in **Fig. 6.4.1b**. We recognize that the capacity gains due to diversity are rather small and the slope of the curves is independent of N_R . Hence, the capacity enhancement depends mainly logarithmically on the signal to noise ratio because the channel vector \mathbf{h} has obviously rank $r = 1$ due to $N_T = 1$, i.e. only one nonzero eigenvalue exists so that only one data stream can be transmitted at a time. In this scenario, multiple receive antennas can only increase the link reliability leading to moderate capacity

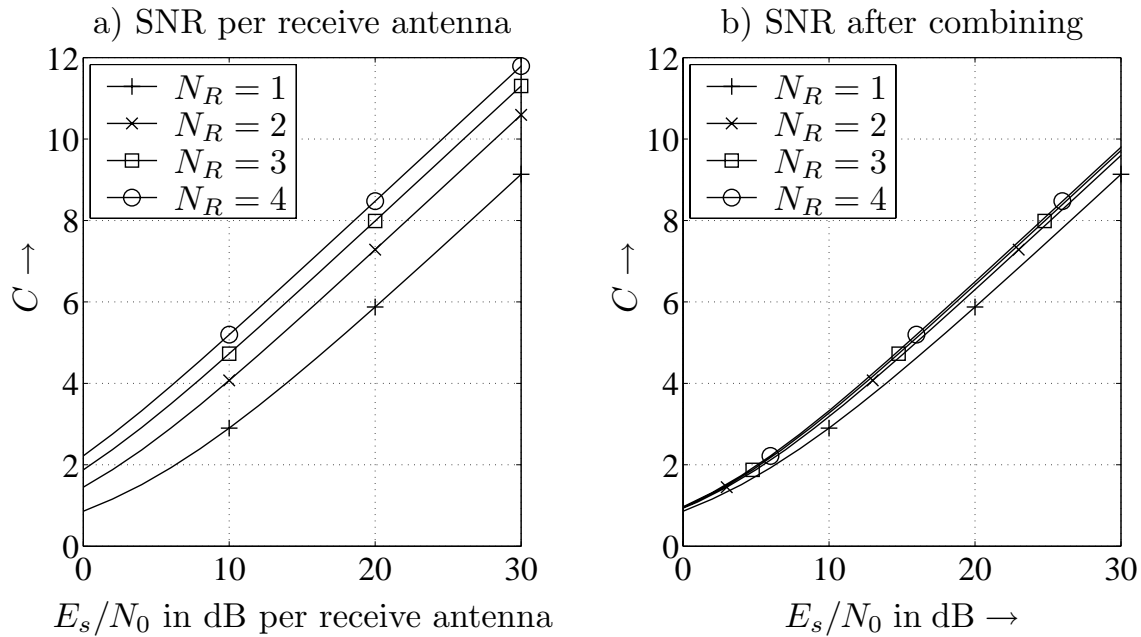


Figure 6.4.1: Channel capacity versus SNR for i.i.d. Rayleigh fading channels, $N_T = 1$ transmit antenna and N_R receive antennas

enhancements. Nevertheless, the outage probability can be significantly decreased by diversity techniques (compare Section 1.5).

Contrarily, **Fig. 6.4.2a** shows the capacity for a system with $N_T = 4$ transmit antennas and different number of receive antennas with i.i.d. channels where the total transmit power is fixed to E_s/T_s . First, a comparison with Fig. 6.4.1 shows that the combinations $N_R = 4$, $N_T = 1$ and $N_R = 1$, $N_T = 4$ provide identical results, i.e. the system is symmetric. Moreover, with increasing N_T the slope of the curve grows according to the parameter $m = \min[N_R, N_T]$. This indicates that m parallel virtual channels exist over which parallel data streams can be transmitted. Hence, the data rate is multiplied by m so that multiple antenna systems may increase the capacity linearly with m while it grows only logarithmically with the SNR. This emphasizes the high potential of multiple antennas at transmitter and receiver.

Fig. 6.4.2b demonstrates the influence of perfect channel knowledge at the transmitter allowing the application of the waterfilling principle introduced in Section 2.3. A comparison with Fig. 6.4.2a) shows that the capacity is improved only for $N_T > N_R$ and high SNR. If we have more receive than transmit antennas, the best strategy for high signal to noise ratios is to distribute the power equally over all antennas. Since, this is automatically done in the absence of channel knowledge, waterfilling provides no additional gain for $N_R = N_T = 4$.

Similar to Section 1.5, we can analyze the outage probability of multiple antenna systems, i.e. the probability P_{out} that a certain rate R is not achieved. From Chap-

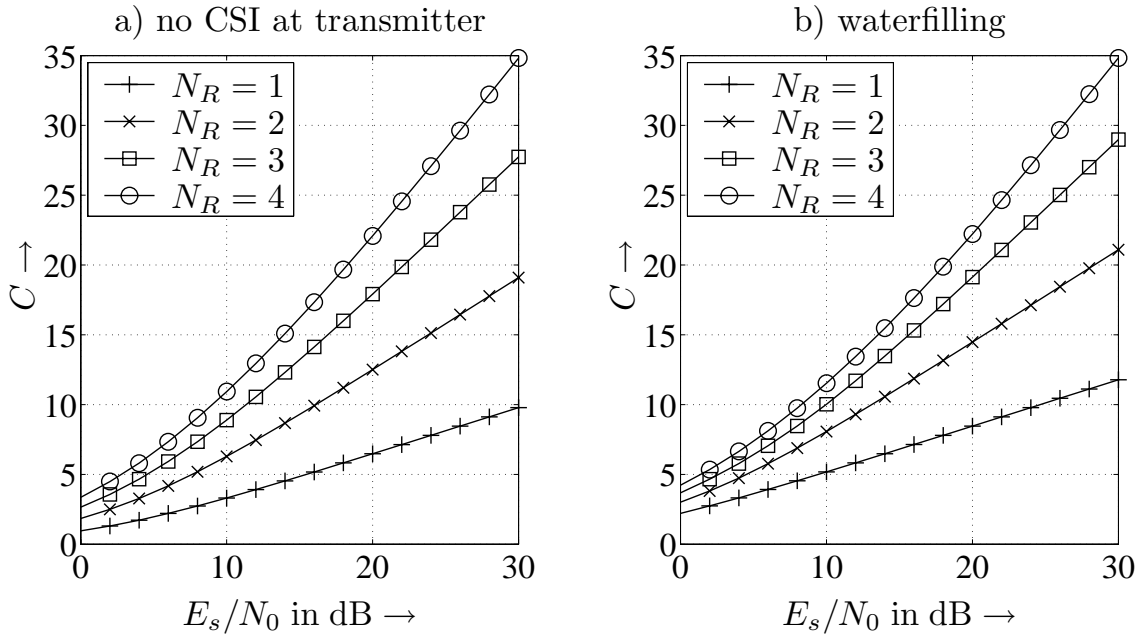


Figure 6.4.2: Channel capacity versus SNR for i.i.d. Rayleigh fading channels, $N_T = 4$ transmit antennas and N_R receive antennas (SNR per receive antenna)

ter 2 we know already that diversity decreases the outage probability because the SNR variations are reduced. This behavior can also be observed from **Fig. 6.4.3**. Especially diagram a) emphasizes that diversity reduces the outage probability, the rapid growth of the curves starts later at higher rates R . However, they also become steeper, i.e. a link becomes quickly unreliable if a certain rate is exceeded. Generally, increasing $\max[N_T, N_R]$ while keeping the minimum constant does not lead to an additional eigenmode and diversity increases the link reliability. Contrarily, increasing $\min[N_T, N_R]$ shifts the curves to the right because the number of virtual channels and, therefore, the data rate is enlarged.

A strange behavior can be observed in **Fig. 6.4.4** for high rates R above the ergodic capacity C . Here, increasing the number of transmit antennas, and, thus the diversity degree, does not lead to a reduction of P_{out} . Comparing directly the curves for $N_R = 1$ and $N_T = 1, 2, 3, 4$ (MISO channels), we recognize that P_{out} even increases with N_T . The reason is that the variations of the SNR are reduced so that very low, but also very high instantaneous values occur more rarely. Therefore, very high rates are obtained less frequently than for low diversity degrees.

Correlated MIMO Channels

We now consider correlated MIMO systems. This scenario occurs if the antenna elements are arranged very close to each other and the impinging waves arrive from a few dominant directions. Hence, we do not have a diffuse electromagnetic

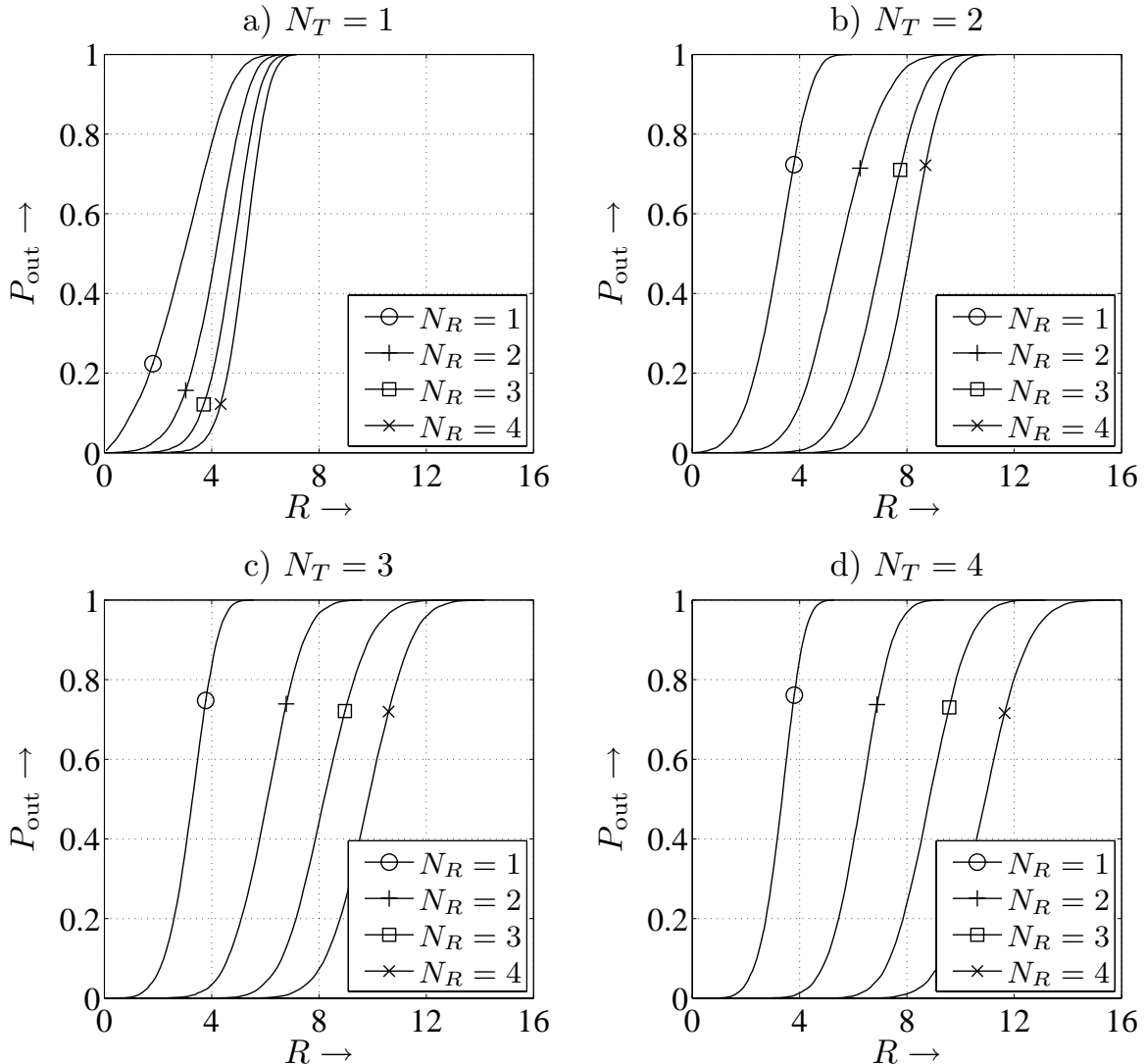


Figure 6.4.3: Outage probability versus rate R in bits/s/Hz for i.i.d. Rayleigh fading channels and a signal to noise ratio of 10 dB

field with a uniform distribution of the angles of arrival, but preferred directions θ_μ with a certain angle spread $\Delta\theta_\mu$.

Fig. 6.4.5 compares the ergodic capacity of i.i.d. and correlated 4×4 MIMO channels for different levels of channel knowledge at the transmitter. First, it can be seen that perfect channel knowledge (CSI) at the transmitter does not increase the capacity of uncorrelated channels except for very low SNR. Hence, the best strategy over a wide range of signal to noise ratios is to transmit four independent data streams.

Concerning the correlated MIMO channel, we can state that channel knowledge at the transmitter increases the capacity. Hence, it is necessary to have channel state information at the transmitter for correlated channels. Moreover, the ergodic

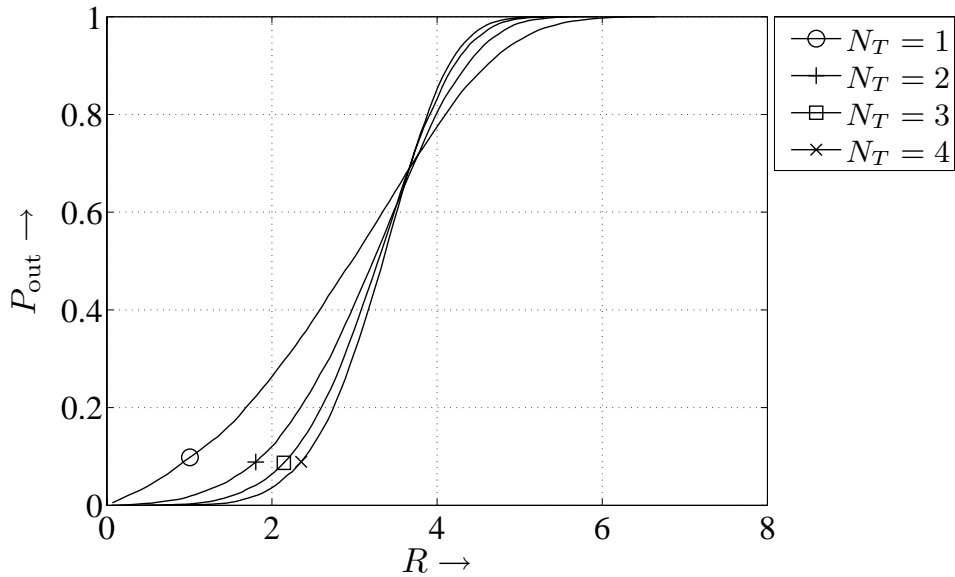


Figure 6.4.4: Outage probability versus rate R in bits/s/Hz for $N_R = 1$ and i.i.d. Rayleigh fading channels and a signal to noise ratio of 10 dB

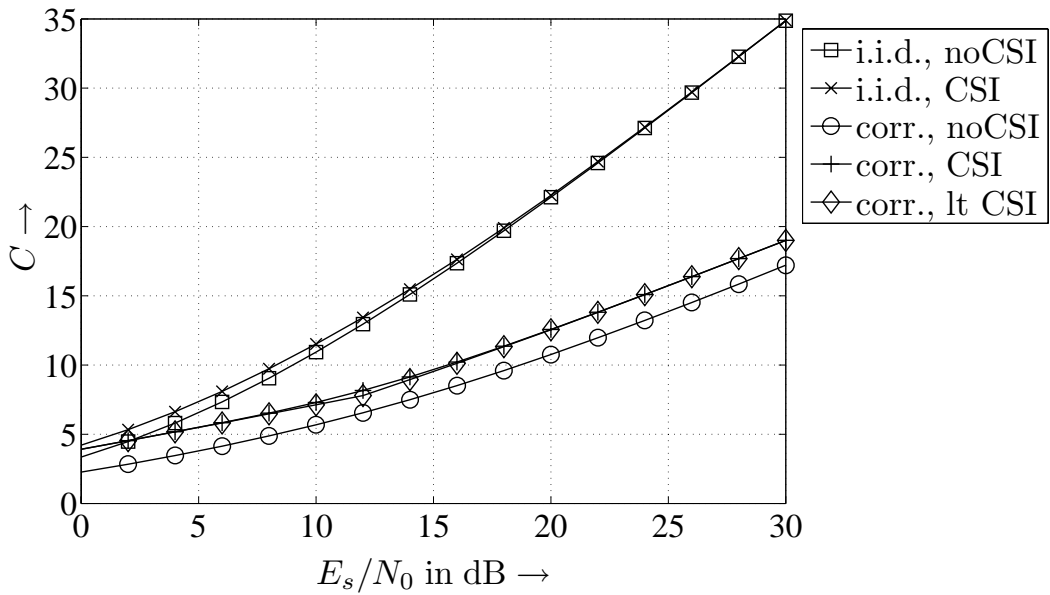


Figure 6.4.5: Channel capacity versus SNR for i.i.d. and correlated Rayleigh fading channels, $N_T = 4$ transmit and $N_R = 4$ receive antennas

capacity is greatly reduced due to correlations. Only for extremely low SNR, correlations can slightly improve capacity because in this specific scenario, increasing the SNR by beamforming is better than transmitting parallel data streams.

Finally, we analyze the performance when only long-term channel knowledge is available at the transmitter. This means that we do not know the instantaneous channel matrix $\mathbf{H}[k]$ but its covariance matrix $\Phi_{\mathcal{H}\mathcal{H}} = \mathbb{E}\{\mathbf{H}^H \mathbf{H}\}$. This approach

is motivated by the fact that long-term statistics like angle of arrivals remain constant for a relatively large duration and can therefore be accurately estimated. Moreover, it is often assumed that these long-term properties are identical for uplink and downlink allowing the application of $\hat{\Phi}_{\mathcal{H}\mathcal{H}}$ measured in the downlink for the uplink transmission.

From Fig. 6.4.5 we see that the knowledge of the covariance matrix (lt CSI) leads to the same performance as optimal channel state information for correlated channels. In the absence of correlations, only instantaneous channel information can improve capacity and long-term statistics do not help at all.

Appendix A

Channel Models

A.1 Equivalent Baseband Representation

The output of the receive filter $g_R(t)$ can be expressed by

$$y(t) = g_R(t) * \left(y_{\text{BP}}^+(t) \frac{1}{\sqrt{2}} e^{-j\omega_0 t} \right) \quad (\text{A.1.1})$$

$$\begin{aligned} &= g_R(t) * \left([y_{\text{BP}}(t) + j\mathcal{H}\{y_{\text{BP}}(t)\}] \frac{1}{\sqrt{2}} e^{-j\omega_0 t} \right) \\ &= g_R(t) * \left([h_{\text{BP}}(t, \tau) * x_{\text{BP}}(t) + n_{\text{BP}}(t) \right. \\ &\quad \left. + j\mathcal{H}\{h_{\text{BP}}(t, \tau) * x_{\text{BP}}(t) + n_{\text{BP}}(t)\}] \frac{1}{\sqrt{2}} e^{-j\omega_0 t} \right). \quad (\text{A.1.2}) \end{aligned}$$

The convolution in (A.1.2) is defined in (1.2.7)

$$h(t, \tau) * x(t) = \int_0^\infty h(t, \tau) x(t - \tau) d\tau.$$

Exploiting the linearity of the Hilbert transform and the property $\mathcal{H}\{a(t) * b(t)\} = a(t) * \mathcal{H}\{b(t)\}$ yields

$$\begin{aligned} y(t) &= g_R(t) * \left([h_{\text{BP}}(t, \tau) * x_{\text{BP}}(t) + jh_{\text{BP}}(t, \tau) * \mathcal{H}\{x_{\text{BP}}(t)\} \right. \\ &\quad \left. + n^+(t)] \frac{1}{\sqrt{2}} e^{-j\omega_0 t} \right) \\ &= g_R(t) * (h_{\text{BP}}(t, \tau) e^{-j\omega_0 t}) * x(t) + n(t) \quad (\text{A.1.3}) \end{aligned}$$

with $x(t) = x^+(t) \frac{1}{\sqrt{2}} e^{-j\omega_0 t}$ equivalent to (1.2.1) and

$$n(t) = g_R(t) * \left(n^+(t) \frac{1}{\sqrt{2}} \cdot e^{-j\omega_0 t} \right). \quad (\text{A.1.4})$$

Due to $G_R(j\omega) = 0$ for $|\omega| > B$, $B \ll f_0$ and property (1.2.9) of the analytical signal,

$$\begin{aligned} g_R(t) * (h_{\text{BP}}(t, \tau) e^{-j\omega_0 t}) &= \mathcal{F}^{-1} \{ G_R(j\omega) \cdot H_{\text{BP}}(t, j\omega - j\omega_0) \} \\ &= \mathcal{F}^{-1} \left\{ G_R(j\omega) \cdot \frac{1}{2} H_{\text{BP}}^+(t, j\omega - j\omega_0) \right\} \\ &= g_R(t) * \left(\frac{1}{2} h_{\text{BP}}^+(t, \tau) e^{-j\omega_0 t} \right) \\ &= g_R(t) * h(t, \tau) \end{aligned} \quad (\text{A.1.5})$$

holds. Thus, we get

$$y(t) = g_R(t) * h(t, \tau) * x(t) + n(t) \quad (\text{A.1.6})$$

$$= \sum_k x[k] (g_R(t) * h(t, \tau) * g_T(t - kT_s)) + n(t). \quad (\text{A.1.7})$$

The twofold convolution can be interpreted as a single filter

$$\tilde{h}(t, kT_s) = g_R(t) * h(t, \tau) * g_T(t - kT_s) \quad (\text{A.1.8})$$

and (A.1.7) becomes

$$y(t) = \sum_k x[k] \cdot \tilde{h}(t, kT_s) + n(t). \quad (\text{A.1.9})$$

A.2 Typical Propagation Profiles for Outdoor Mobile Radio Channels

In order to receive realistic parameters of mobile radio channels, extensive measurements have been carried out by COST 207 (*European Cooperation in the Fields of Scientific and Technical Research*) [COS89] for the GSM system. The obtained power delay profiles are listed in **Table A.2.1** and represent typical propagation scenarios.

Equivalent results were obtained for the Doppler power spectra listed in **Table A.2.2**. Principally, the statistical characteristics of the Doppler power spectra are affected by the delay τ . For delays smaller than $0.5 \mu\text{s}$, $\Phi_{hh}(f_d)$ has a distribution according to the Jakes spectrum, while for larger τ Gaussian distributions

Table A.2.1: Power delay profile of COST 207 [COS89] (delays τ in μs)

profile	power delay profile $\Phi_{h,h}(\tau)$
Rural Area (RA)	$9.21 \cdot \exp(-9.2\tau) \quad 0 \leq \tau < 0.7$ 0 else
Typical Urban (TU)	$\exp(-\tau) \quad 0 \leq \tau < 7$ 0 else
Bad Urban (BU)	$0.67 \cdot \exp(-\tau) \quad 0 \leq \tau < 5$ $0.335 \cdot \exp(5 - \tau) \quad 5 \leq \tau < 10$ 0 else
Hilly Terrain (HT)	$3.08 \cdot \exp(-3.5\tau) \quad 0 \leq \tau < 2$ $0.1232 \cdot \exp(15 - \tau) \quad 15 \leq \tau < 20$ 0 else

Table A.2.2: Doppler power spectrum of COST 207 [COS89]

delay	Doppler power spectrum $\Phi_{hh}(f_d)$
$0 < \tau < 0.5 \mu\text{s}$	$\frac{A}{\sqrt{1-(f_d/f_{d \max})^2}} \quad f_d \leq f_{d \max}$ 0 else ,
$0.5 < \tau < 2 \mu\text{s}$	$A \cdot \exp\left(-\frac{(f_d+0.8f_{d \max})^2}{2(0.05f_{d \max})^2}\right) + \frac{A}{10} \cdot \exp\left(-\frac{(f_d-0.4f_{d \max})^2}{2(0.1f_{d \max})^2}\right)$
$\tau > 2 \mu\text{s}$	$B \cdot \exp\left(-\frac{(f_d-0.7f_{d \max})^2}{2(0.1f_{d \max})^2}\right) + \frac{B}{31.6} \cdot \exp\left(-\frac{(f_d+0.4f_{d \max})^2}{2(0.15f_{d \max})^2}\right)$
Rural Area ($\tau = 0$)	$\frac{0.41}{2\pi f_{d \max} \sqrt{1-(f_d/f_{d \max})^2}} + 0.91 \cdot \delta(f_d - 0.7f_{d \max})$

Table A.2.3: Propagation conditions for UMTS in multi-path fading environments [TS2], delays τ in ns and rel. powers $|h|^2$ in dB, f_d classically distributed

$v = 3 \text{ km/h}$	$v = 3 \text{ km/h}$	$v = 120 \text{ km/h}$	$v = 3 \text{ km/h}$	$v = 250 \text{ km/h}$					
τ	$ h ^2$	τ	$ h ^2$	τ	$ h ^2$	τ	$ h ^2$	τ	$ h ^2$
0	0	0	0	0	0	0	0	0	0
976	-10	976	0	260	-3	976	0	260	-3
		20000	0	521	-6			521	-6
				781	-9			781	-9

with different means and variances occur. The *Rural Area* scenario represents a special case because it is characterized by a line of sight link (Rice fading).

According to the requirements for the UMTS standard, different propagation scenarios were defined. They are summarized in **Table A.2.3**. Five cases are distinguished that differ with respect to velocity and the number of taps.

A.3 Moment Generating Function for Ricean Fading

The channel coefficient h of a frequency-nonselective Ricean fading channel with average power P and Rice factor K has the form given in (1.2.27)

$$h = \sqrt{\frac{P}{K+1}} \cdot \left(\sqrt{K} + \alpha \right) .$$

It consists of two parts, a constant line-of-sight component and a fading component represented by the factor α whose real and imaginary parts are statistically independent zero-mean Gaussian processes each with variance $1/2$. Hence, the real part \mathcal{H}' of \mathcal{H} is Gaussian distributed

$$\begin{aligned} p_{\mathcal{H}'}(\xi) &= \frac{1}{\sqrt{2\pi\sigma_{\mathcal{H}'}^2}} \cdot \exp \left[-\frac{\left(\xi - \sqrt{\frac{PK}{K+1}} \right)^2}{2\sigma_{\mathcal{H}'}^2} \right] \\ &= \sqrt{\frac{K+1}{\pi P}} \cdot \exp \left[-\left(\xi \sqrt{\frac{K+1}{P}} - \sqrt{K} \right)^2 \right] \end{aligned} \quad (\text{A.3.1a})$$

with mean $\sqrt{PK/(1+K)}$ and variance $\sigma_{\mathcal{H}'}^2 = P/[2(K+1)]$ while the imaginary part \mathcal{H}'' is Gaussian distributed with the same variance but zero-mean.

$$p_{\mathcal{H}''}(\xi) = \frac{1}{\sqrt{2\pi\sigma_{\mathcal{H}''}^2}} \cdot \exp \left[-\frac{\xi^2}{2\sigma_{\mathcal{H}''}^2} \right] = \sqrt{\frac{K+1}{\pi P}} \cdot \exp \left[-\frac{(K+1)\xi^2}{P} \right] \quad (\text{A.3.1b})$$

In order to calculate the density of $|\mathcal{H}|^2$, we have to deal with the densities of $(\mathcal{H}')^2$ and $(\mathcal{H}'')^2$. In [Pap65] the general condition

$$p_{\mathcal{X}^2}(\xi) = \frac{1}{2\sqrt{\xi}} \cdot \left[p_{\mathcal{X}}(\sqrt{\xi}) + p_{\mathcal{X}}(-\sqrt{\xi}) \right] \quad (\text{A.3.2})$$

between the pdf of a process \mathcal{X} and the pdf of \mathcal{X}^2 is given. With (A.3.2), we obtain for the squared real part a non-central chi-square distribution with 1 degree of freedom

$$p_{\mathcal{H}'^2}(\xi) = \sqrt{\frac{K+1}{\pi P \xi}} \cdot \exp\left[-\frac{\xi(K+1)}{P} - K\right] \cdot \cosh\left[2\sqrt{\frac{\xi K(K+1)}{P}}\right] \quad (\text{A.3.3a})$$

and for the squared imaginary part a central chi-square distribution with 1 degree of freedom

$$p_{\mathcal{H}''^2}(\xi) = \sqrt{\frac{K+1}{\pi P \xi}} \cdot \exp\left[-\frac{\xi(K+1)}{P}\right]. \quad (\text{A.3.3b})$$

Since the squared magnitude of \mathcal{H} is obtained by adding the squared magnitudes of real and imaginary part, their probability densities have to be convolved. This is equivalent with multiplying the corresponding moment generating functions. They have the form [Pro95]

$$\mathcal{M}_{\mathcal{H}'^2}(s) = \sqrt{\frac{K+1}{K+1-sP}} \cdot \exp\left[\frac{sKP}{(K+1)-sP}\right] \quad (\text{A.3.4a})$$

and

$$\mathcal{M}_{\mathcal{H}''^2}(s) = \sqrt{\frac{K+1}{K+1-sP}}. \quad (\text{A.3.4b})$$

Consequently, we obtain the overall moment generating function

$$\mathcal{M}_{|\mathcal{H}|^2}(s) = \frac{K+1}{K+1-sP} \cdot \exp\left[\frac{sKP}{(K+1)-sP}\right]. \quad (\text{A.3.5})$$

Appendix B

Derivations for Information Theory

B.1 Chain Rule for Entropies

Let $\mathcal{X}_1, \mathcal{X}_2, \dots, \mathcal{X}_n$ be random variables belonging to a joint probability $\Pr\{\mathcal{X}_1, \mathcal{X}_2, \dots, \mathcal{X}_n\}$, the chain rule for entropy has the form:

$$\bar{I}(\mathcal{X}_1, \mathcal{X}_2, \dots, \mathcal{X}_n) = \sum_{i=1}^n \bar{I}(\mathcal{X}_i | \mathcal{X}_{i-1}, \dots, \mathcal{X}_1) \quad (\text{B.1.1})$$

Proof: We simply repeat the application of the chain rule for two random variables.

$$\begin{aligned} \bar{I}(\mathcal{X}_1, \mathcal{X}_2) &= \bar{I}(\mathcal{X}_1) + \bar{I}(\mathcal{X}_2 | \mathcal{X}_1) \\ \bar{I}(\mathcal{X}_1, \mathcal{X}_2, \mathcal{X}_3) &= \bar{I}(\mathcal{X}_1) + \bar{I}(\mathcal{X}_2, \mathcal{X}_3 | \mathcal{X}_1) \\ &= \bar{I}(\mathcal{X}_1) + \bar{I}(\mathcal{X}_2 | \mathcal{X}_1) + \bar{I}(\mathcal{X}_3 | \mathcal{X}_1, \mathcal{X}_2) \\ &\vdots \\ \bar{I}(\mathcal{X}_1, \mathcal{X}_2, \dots, \mathcal{X}_n) &= \bar{I}(\mathcal{X}_1) + \bar{I}(\mathcal{X}_2, \dots, \mathcal{X}_n | \mathcal{X}_1) \\ &= \bar{I}(\mathcal{X}_1) + \bar{I}(\mathcal{X}_2 | \mathcal{X}_1) + \bar{I}(\mathcal{X}_3, \dots, \mathcal{X}_n | \mathcal{X}_1, \mathcal{X}_2) \\ &= \sum_{i=1}^n \bar{I}(\mathcal{X}_i | \mathcal{X}_{i-1}, \dots, \mathcal{X}_1) \end{aligned}$$

B.2 Chain Rule for Information

General chain rule for information [CT91]:

$$\bar{I}(\mathcal{X}_1, \dots, \mathcal{X}_n; \mathcal{Z}) = \sum_{i=1}^n \bar{I}(\mathcal{X}_i; \mathcal{Z} \mid \bar{I}(\mathcal{X}_{i-1}, \dots, \mathcal{X}_1)) \quad (\text{B.2.1})$$

Prof: Applying chain rule for entropies

$$\begin{aligned} \bar{I}(\mathcal{X}_1, \dots, \mathcal{X}_n; \mathcal{Z}) &= \bar{I}(\mathcal{X}_1, \dots, \mathcal{X}_n) - \bar{I}(\mathcal{X}_1, \dots, \mathcal{X}_n \mid \mathcal{Z}) \\ &= \sum_{i=1}^n \bar{I}(\mathcal{X}_i \mid \mathcal{X}_{i-1} \dots \mathcal{X}_1) - \sum_{i=1}^n \bar{I}(\mathcal{X}_i \mid \mathcal{X}_{i-1} \dots \mathcal{X}_1, \mathcal{Z}) \\ &= \sum_{i=1}^n \bar{I}(\mathcal{X}_i \mid \mathcal{X}_{i-1} \dots \mathcal{X}_1) - \bar{I}(\mathcal{X}_i \mid \mathcal{X}_{i-1} \dots \mathcal{X}_1, \mathcal{Z}) \\ &= \sum_{i=1}^n \bar{I}(\mathcal{X}_i; \mathcal{Z} \mid \mathcal{X}_{i-1} \dots \mathcal{X}_1) \end{aligned}$$

B.3 Data Processing Theorem

Data processing theorem: We consider a Markovian chain $\mathcal{X} \rightarrow \mathcal{Y} \rightarrow \mathcal{Z}$ where \mathcal{X} and \mathcal{Z} are independent given \mathcal{Y} , i.e. $\bar{I}(\mathcal{X}; \mathcal{Z} \mid \mathcal{Y}) = 0$. The data processing theorem states:

$$\bar{I}(\mathcal{X}; \mathcal{Y}) \geq \bar{I}(\mathcal{X}; \mathcal{Z}). \quad (\text{B.3.1})$$

Proof:

The mutual information $\bar{I}(\mathcal{X}; \mathcal{Y}, \mathcal{Z})$ can be extended with the chain rule in two different ways:

$$\bar{I}(\mathcal{X}; \mathcal{Y}, \mathcal{Z}) = \bar{I}(\mathcal{X}; \mathcal{Z}) + \bar{I}(\mathcal{X}; \mathcal{Y} \mid \mathcal{Z}) = \bar{I}(\mathcal{X}; \mathcal{Y}) + \bar{I}(\mathcal{X}; \mathcal{Z} \mid \mathcal{Y}). \quad (\text{B.3.2})$$

Due to the condition $\bar{I}(\mathcal{X}; \mathcal{Z} \mid \mathcal{Y}) = 0$, we see from (B.3.2)

$$\bar{I}(\mathcal{X}; \mathcal{Y}) = \bar{I}(\mathcal{X} \mid \mathcal{Z}) + \underbrace{\bar{I}(\mathcal{X}; \mathcal{Y} \mid \mathcal{Z})}_{\geq 0}. \quad (\text{B.3.3})$$

Since entropies are always nonnegative, $\bar{I}(\mathcal{X}; \mathcal{Y} \mid \mathcal{Z}) \geq 0$ holds and we obtain the inequality

$$\bar{I}(\mathcal{X}; \mathcal{Y}) \geq \bar{I}(\mathcal{X} \mid \mathcal{Z}). \quad (\text{B.3.4})$$

Appendix C

Linear Algebra

C.1 Selected Basics

This appendix summarizes some basic results of linear algebra. It is not comprehensive and focusses only on topics needed in this thesis. Unless otherwise stated, we consider complex vectors and matrices. An $N \times N$ identity matrix is denoted by \mathbf{I}_N , $\mathbf{0}_{N \times M}$ is an $N \times M$ matrix containing only zeros and $\mathbf{1}_{N \times M}$ a matrix of same size consisting only of ones.

Definition C.1 (Determinant). *A determinant uniquely assigns a real or complex-valued number $\det(\mathbf{A})$ to an $N \times N$ matrix \mathbf{A} . The determinant is zero if a row (column) only consists of zeros or if it can be represented as a linear combination of other rows (columns). The determinant of a product of square matrices is identical to the product of the corresponding determinants*

$$\det(\mathbf{AB}) = \det(\mathbf{A}) \cdot \det(\mathbf{B}) . \quad (\text{C.1.1})$$

According to [Tel95], we can rewrite (C.1.1) as

$$\det(\mathbf{I} + \mathbf{AB}) = \det(\mathbf{I} + \mathbf{BA}) . \quad (\text{C.1.2})$$

Definition C.2 (Hermitian Operation). *The Hermitian of a matrix (vector) is defined as the transposed matrix (vector) with complex conjugate elements*

$$\mathbf{A}^H = (\mathbf{A}^*)^T \quad \text{and} \quad \mathbf{x}^H = (\mathbf{x}^*)^T \quad (\text{C.1.3})$$

The following rules exist:

- $(\mu\mathbf{A} + \nu\mathbf{B})^H = \mu^*\mathbf{A}^H + \nu^*\mathbf{B}^H$

- $(\mathbf{AB})^H = \mathbf{B}^H \mathbf{A}^H$
- $(\mathbf{A}^H)^H = \mathbf{A}$
- $(\mathbf{A}^{-1})^H = (\mathbf{A}^H)^{-1}$
- concerning real-valued matrices, the Hermitian form equals the transposed: $\mathbf{A}^H = \mathbf{A}^T$.

Definition C.3 (Inner Product). *The inner product (dot-product [GvL93]) of two complex $N \times 1$ vectors $\mathbf{x} = [x_1, x_2, \dots, x_N]^T$ and $\mathbf{y} = [y_1, y_2, \dots, y_N]^T$ is defined by*

$$\mathbf{x}^H \mathbf{y} = \sum_{i=1}^N x_i^* y_i \quad (\text{C.1.4})$$

where x_i^* denotes the complex conjugate value of x_i .

The definition of the inner product allows the calculation of the length of a vector consisting of complex elements:

$$\|\mathbf{x}\| = \sqrt{\mathbf{x}^H \mathbf{x}} = \sqrt{|x_1|^2 + |x_2|^2 + \dots + |x_N|^2}. \quad (\text{C.1.5})$$

Two vectors \mathbf{x} and \mathbf{y} are called unitary, if their inner product is zero ($\mathbf{x}^H \mathbf{y} = 0$). This is a complex generalization of the orthogonality of real-valued vectors ($\mathbf{x}^T \mathbf{y} = 0$) and sometimes called conjugated orthogonality [ZF92]. For real vectors, the properties unitary and orthogonal are identical.

Definition C.4 (Rank). *For an arbitrary matrix \mathbf{A} , the largest number r of linearly independent columns equals always the largest number of linearly independent rows. This number r is called rank of a matrix and denoted by $r = \text{rank}(\mathbf{A})$.*

From this definition it follows directly that the rank of an $N \times M$ matrix is always less or equal to the minimum of N and M :

$$r = \text{rank}(\mathbf{A}) \leq \min(N, M). \quad (\text{C.1.6})$$

We can derive the following properties with the definition of $\text{rank}(\mathbf{A})$:

- An $N \times N$ matrix \mathbf{A} is called regular if its determinant is nonzero and, therefore, $r = \text{rank}(\mathbf{A}) = N$ holds. For regular matrices, the inverse \mathbf{A}^{-1} with $\mathbf{A}^{-1} \mathbf{A} = \mathbf{I}_{N \times N}$ exists.
- If the determinant is zero, $r = \text{rank}(\mathbf{A}) < N$ holds and the matrix is called singular. The inverse does not exist for singular matrices.

- For each $N \times N$ matrix \mathbf{A} of rank r , there exist at least one $r \times r$ submatrix whose determinant is nonzero. The determinants of all $(r+1) \times (r+1)$ sub-matrices of \mathbf{A} are zero.
- The rank of the product \mathbf{AA}^H is

$$\text{rank}(\mathbf{AA}^H) = \text{rank}(\mathbf{A}) . \quad (\text{C.1.7})$$

Definition C.5 (Eigenvalue Problem). *The calculation of the eigenvalues λ_i and the eigenvectors \mathbf{x}_i of a square $N \times N$ matrix \mathbf{A} is called eigenvalue problem. The goal is to find a vector \mathbf{x} that is proportional to \mathbf{Ax} and, therefore, fulfills the eigenvalue equation*

$$\mathbf{A} \cdot \mathbf{x} = \lambda \cdot \mathbf{x} . \quad (\text{C.1.8})$$

This equation can be rewritten in $(\mathbf{A} - \lambda \mathbf{I}_N) \mathbf{x} = 0$. Since we are looking for the nontrivial solution $\mathbf{x} \neq \mathbf{0}$, the columns of $(\mathbf{A} - \lambda \mathbf{I}_N)$ have to be linearly dependent, i.e. $\det(\mathbf{A} - \lambda \mathbf{I}_N) = 0$ holds. Hence, the eigenvalues λ_i represent the zeros of the characteristic polynomial $p_N(\lambda) = \det(\mathbf{A} - \lambda \mathbf{I}_N)$ of rank N . Each $N \times N$ matrix has exactly N eigenvalues that need not to be different.

For each eigenvalue λ_i , the equation $(\mathbf{A} - \lambda_i \mathbf{I}_N) \mathbf{x}_i = 0$ has to be solved with respect to the eigenvector \mathbf{x}_i . There always exist solutions $\mathbf{x}_i \neq \mathbf{0}$. Besides \mathbf{x}_i , also $c \cdot \mathbf{x}_i$ is an eigenvector corresponding to λ_i . Hence, we can normalize the eigenvectors to unit length.

The eigenvectors $\mathbf{x}_1, \dots, \mathbf{x}_k$ belonging to different eigenvalues $\lambda_1, \dots, \lambda_k$ are linear independent of each other [Str88, HJ85].

There exist the following relationships between the matrix \mathbf{A} and its eigenvalues:

- The sum of all eigenvalues is identical to the sum of all N diagonal elements called trace of a square matrix \mathbf{A}

$$\text{tr}(\mathbf{A}) = \sum_{i=1}^{r=N} A_{i,i} = \sum_{i=1}^{r=N} \lambda_i . \quad (\text{C.1.9})$$

- If a square matrix \mathbf{A} has full rank $r = N$, the product of its eigenvalues equals the determinant of \mathbf{A} :

$$\prod_{i=1}^{r=N} \lambda_i = \det(\mathbf{A}) \quad (\text{C.1.10})$$

If the matrix is rank deficient with $r < N$, the product of the nonzero eigenvalues equals the determinant of the $r \times r$ submatrix of rank r .

- An eigenvalue $\lambda_i = 0$ exists if and only if the matrix is singular, i.e. $\det(\mathbf{A}) = 0$ holds.

Definition C.6 (Orthogonality). A real-valued matrix is called orthogonal, if its columns are mutually orthogonal. Therefore, the inner product between different columns becomes $\mathbf{q}_i^T \mathbf{q}_j = 0$. If all columns of an orthogonal matrix have unit length,

$$\mathbf{q}_i^T \mathbf{q}_j = \delta(i, j) \quad (\text{C.1.11})$$

holds and the matrix is called orthonormal. Orthonormal matrices are generally denoted by \mathbf{Q} and have the properties

$$\mathbf{Q}^T \mathbf{Q} = \mathbf{I}_N \quad \Leftrightarrow \quad \mathbf{Q}^T = \mathbf{Q}^{-1}. \quad (\text{C.1.12})$$

Definition C.7 (Unitary Matrix). A complex $N \times N$ matrix with orthonormal columns is called a unitary matrix \mathbf{U} with the properties

$$\mathbf{U}^H \mathbf{U} = \mathbf{U} \mathbf{U}^H = \mathbf{I}_N \quad \Leftrightarrow \quad \mathbf{U}^H = \mathbf{U}^{-1} \quad (\text{C.1.13})$$

The columns of \mathbf{U} span an N -dimensional orthonormal vector space.

From the definition of a unitary matrix \mathbf{U} , it follows:

- all eigenvalues of \mathbf{U} have unit length ($|\lambda_i| = 1$),
- unitary matrices are normal because $\mathbf{U} \mathbf{U}^H = \mathbf{U}^H \mathbf{U} = \mathbf{I}_N$ holds,
- eigenvectors belonging to different eigenvalues are orthogonal to each other,
- the inner product $\mathbf{x}^H \mathbf{y}$ between two vectors remains unchanged if each vector is multiplied with a unitary matrix \mathbf{U} because $(\mathbf{U}\mathbf{x})^H(\mathbf{U}\mathbf{y}) = \mathbf{x}^H \mathbf{U}^H \mathbf{U}\mathbf{y} = \mathbf{x}^H \mathbf{y}$ holds,
- the length of a vector does not change when multiplied with \mathbf{U} : $\|\mathbf{U}\mathbf{x}\| = \|\mathbf{x}\|$,
- a random matrix \mathbf{B} has the same statistical properties as the matrices $\mathbf{B}\mathbf{U}$ and $\mathbf{U}\mathbf{B}$
- the determinant of a unitary matrix amounts to $\det(\mathbf{U}) = 1$ [Blu00].

Definition C.8 (Hermitian Matrix). A square matrix \mathbf{A} is called Hermitian if it equals its complex conjugate transposed version.

$$\mathbf{A} = \mathbf{A}^H \quad (\text{C.1.14})$$

The real part of an Hermitian matrix is symmetric and the imaginary part is antisymmetric:

$$\operatorname{Re}\{\mathbf{A}\} = \operatorname{Re}\{\mathbf{A}\}^T \quad \text{and} \quad \operatorname{Im}\{\mathbf{A}\} = -\operatorname{Im}\{\mathbf{A}^T\}. \quad (\text{C.1.15})$$

Obviously, the properties symmetric and Hermitian are identical for real matrices.

Hermitian matrices have the following properties [Str88]:

- all diagonal elements $A_{i,i}$ are real,
- for each element, $A_{i,j} = A_{j,i}^*$ holds,
- for all complex vectors \mathbf{x} , the number $\mathbf{x}^H \mathbf{A} \mathbf{x}$ is real,
- $\mathbf{A} \mathbf{A}^H = \mathbf{A}^H \mathbf{A}$ holds because the matrix \mathbf{A} is *normal*,
- the determinant $\det(\mathbf{A})$ is real,
- all eigenvalues λ_i of an Hermitian matrix are real,
- the eigenvectors \mathbf{x}_i of a real symmetric matrix or an Hermitian matrix are orthogonal to each other, if they belong to different eigenvalues λ_i .

Definition C.9 (Eigenvalue Decomposition). Every $N \times N$ matrix \mathbf{A} with N linear independent eigenvectors \mathbf{x}_i can be transformed into a diagonal matrix [HJ85]. This can be accomplished by generating the matrix \mathbf{U} whose columns comprise all all eigenvectors of \mathbf{A} . It follows:

$$\mathbf{U}^{-1} \mathbf{A} \mathbf{U} = \Lambda = \begin{pmatrix} \lambda_1 & & & \\ & \lambda_2 & & \\ & & \ddots & \\ & & & \lambda_N \end{pmatrix} \quad (\text{C.1.16})$$

with $\mathbf{U} = (\mathbf{x}_1, \mathbf{x}_2, \dots, \mathbf{x}_N)$. The eigenvalue matrix Λ is diagonal and contains the eigenvalues of \mathbf{A} on its diagonal.

From definition C.9 it follows directly that each matrix \mathbf{A} can be expressed as $\mathbf{A} = \mathbf{U} \Lambda \mathbf{U}^{-1} = \mathbf{U} \Lambda \mathbf{U}^H$ (eigenvalue decomposition).

Definition C.10 (Singular Value Decomposition). A generalization of definition (C.9) for arbitrary $N \times M$ matrices \mathbf{A} is called singular value decomposition (SVD). A matrix \mathbf{A} with rank r can be expressed with

$$\mathbf{A} = \mathbf{U} \Sigma \mathbf{V}^H \quad (\text{C.1.17})$$

with the unitary $N \times N$ matrix \mathbf{U} and the unitary $M \times M$ matrix \mathbf{V} . The columns of \mathbf{U} contain the eigenvectors of $\mathbf{A} \mathbf{A}^H$ and the columns of \mathbf{V} the eigenvectors of $\mathbf{A}^H \mathbf{A}$. The matrix Σ is an $N \times M$ diagonal matrix with nonnegative, real-valued elements σ_k on its diagonal. Denoting the eigenvalues of $\mathbf{A} \mathbf{A}^H$ and, therefore, also of $\mathbf{A}^H \mathbf{A}$ with λ_k , $1 \leq k \leq r$, the diagonal elements σ_k are the positive square roots of λ_k

$$\sigma_k = \sqrt{\lambda_k} \quad 1 \leq k \leq r . \quad (\text{C.1.18})$$

They are called singular values of \mathbf{A} . For the matrix containing the singular values, we obtain

$$\Sigma = \left(\begin{array}{cccc|ccc} \sigma_1 & 0 & \dots & 0 & 0 & \dots & 0 \\ 0 & \sigma_2 & & 0 & 0 & & 0 \\ \vdots & & \ddots & \vdots & \vdots & & \vdots \\ 0 & 0 & \dots & \sigma_r & 0 & \dots & 0 \\ \hline 0 & 0 & \dots & 0 & 0 & \dots & 0 \\ \vdots & & \ddots & \vdots & \vdots & & \vdots \\ 0 & 0 & \dots & 0 & 0 & \dots & 0 \end{array} \right) \quad \left. \begin{array}{l} r \text{ rows} \\ M-r \text{ rows} \end{array} \right\} \quad (\text{C.1.19})$$

$\underbrace{\hspace{10em}}_{r \text{ columns}} \quad \underbrace{\hspace{10em}}_{N-r \text{ columns}}$

Definition C.11 (Spectral Theorem). Every real symmetric matrix can be transformed into a diagonal matrix by multiplying with an orthogonal matrix

$$\mathbf{A} = \mathbf{Q}\Lambda\mathbf{Q}^{-1} = \mathbf{Q}\Lambda\mathbf{Q}^T \quad (\text{C.1.20})$$

and every Hermitian matrix can be transformed into a diagonal matrix by multiplying with a unitary matrix:

$$\mathbf{A} = \mathbf{U}\Lambda\mathbf{U}^{-1} = \mathbf{U}\Lambda\mathbf{U}^H. \quad (\text{C.1.21})$$

Due to definitions C.1 and C.7, the determinant of \mathbf{A} becomes

$$\det(\mathbf{A}) = \det(\mathbf{U}) \det(\Lambda) \det(\mathbf{U}^{-1}) = \det(\Lambda). \quad (\text{C.1.22})$$

Definition C.12 (Square Root of a Matrix). An $N \times M$ matrix \mathbf{B} is called square root of an $N \times N$ matrix \mathbf{A} , if

$$\mathbf{B}\mathbf{B}^H = \mathbf{A} \quad (\text{C.1.23})$$

holds. From

$$\mathbf{A}^H = (\mathbf{B}\mathbf{B}^H)^H = (\mathbf{B}^H)^H \mathbf{B}^H = \mathbf{A} \quad (\text{C.1.24})$$

we see that \mathbf{A} is always Hermitian and from definition C.4) it follows that the rank of \mathbf{A} is

$$\text{rank}(\mathbf{A}) = \text{rank}(\mathbf{B}\mathbf{B}^H) = \text{rank}(\mathbf{B}). \quad (\text{C.1.25})$$

Definition C.13 (Positive Semidefinite Matrix). An Hermitian $N \times N$ matrix \mathbf{A} is called positive semidefinite, if

$$\mathbf{x}^H \mathbf{A} \mathbf{x} \geq 0 \quad (\text{C.1.26})$$

holds for each vector $\mathbf{x} \in \mathbb{C}^N$.

The following rules are valid:

- A matrix \mathbf{A} is positive semidefinite, if its square root \mathbf{B} according to definition C.12 exists, so that it is always Hermitian.
- An Hermitian matrix is positive semidefinite if and only if all eigenvalues are real and nonnegative, so that $\lambda_i \geq 0$ for $1 \leq i \leq N$ holds.

C.2 Householder Reflections and Givens Rotation

Householder Reflections

Householder reflections are used to reflect a vector \mathbf{x} at a plain surface or line onto a vector \mathbf{y} of same length by multiplying with a unitary matrix Θ . If \mathbf{x} and \mathbf{y} are column vectors with $\|\mathbf{x}\| = \|\mathbf{y}\|$, we obtain $\mathbf{y} = \Theta \cdot \mathbf{x}$ with the unitary matrix

$$\Theta = \mathbf{I}_N - (1 + w) \cdot \mathbf{u} \mathbf{u}^H \quad (\text{C.2.1})$$

and

$$\mathbf{u} = \frac{\mathbf{x} - \mathbf{y}}{\|\mathbf{x} - \mathbf{y}\|} \quad \text{and} \quad w = \frac{\mathbf{x}^H \mathbf{u}}{\mathbf{u}^H \mathbf{x}}. \quad (\text{C.2.2})$$

In the real-valued case, $w = 1$ holds and (C.2.1) becomes

$$\Theta = \mathbf{I}_N - 2 \cdot \mathbf{u} \mathbf{u}^H. \quad (\text{C.2.3})$$

The reflection is graphically illustrated in **Fig. C.2.1** for real-valued vectors. The vector $\mathbf{u} \mathbf{u}^H \mathbf{x}$ is a projection of \mathbf{x} onto the vector \mathbf{u} . Subtracting this projection twice from the vector \mathbf{x} results in a reflection at the line perpendicular to \mathbf{u} .

As a special example, the Householder reflection can be used to force certain elements of a matrix to zero. This is applied in the Post Sorting Algorithm (PSA) in Section 5.4. In this case the target vector becomes $\mathbf{y} = [\|\mathbf{0} \mathbf{x}\|]^T$, i.e. the last element equals the norm of \mathbf{x} while the remaining part of \mathbf{y} is zero. In the same way Householder reflections can be used to QL decompose an $M \times N$ matrix \mathbf{A} with $M \geq N$ as is shown with the pseudo code in **Table C.2.1**.

If a row vector $\underline{\mathbf{x}}$ instead of a column vector has to be reflected, w and Θ become

$$\Theta = \mathbf{I}_N - (1 + w) \cdot \underline{\mathbf{u}}^H \underline{\mathbf{u}} \quad \text{and} \quad w = \frac{\underline{\mathbf{u}} \underline{\mathbf{x}}^H}{\underline{\mathbf{x}} \underline{\mathbf{u}}^H}. \quad (\text{C.2.4})$$

The reflection is performed by $\underline{\mathbf{y}} = \underline{\mathbf{x}} \cdot \Theta$.

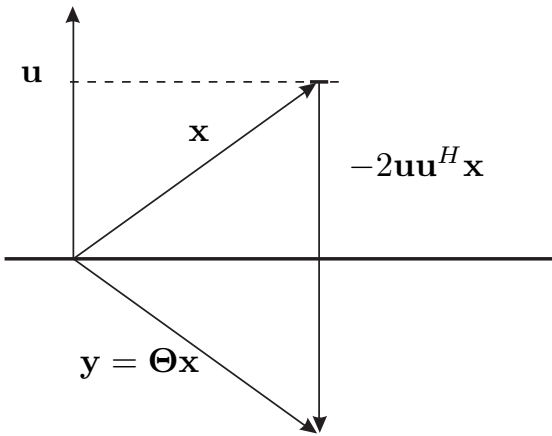


Figure C.2.1: Illustration of Householder reflection

Table C.2.1: Pseudo code for QL decomposition via Householder reflections

- (1) Initialize with $\mathbf{L} = \mathbf{A}$ and $\mathbf{Q} = \mathbf{I}_M$
- (2) for $k = N, \dots, 1$
- (3) $\mathbf{x} = \mathbf{L}[1 : M - N + k, k]$
- (4) $\mathbf{y} = [\mathbf{0} \ \| \mathbf{x} \|]^T$
- (5) calculate \mathbf{u} , w and Θ
- (6) $\mathbf{L}[1 : M - N + k, 1 : k] = \Theta \cdot \mathbf{L}[1 : M - N + k, 1 : k]$
- (7) $\mathbf{Q}[:, 1 : M - N + k] = \mathbf{Q}[:, 1 : M - N + k] \cdot \Theta^H$
- (8) end

Givens Rotation

Let $\mathbf{G}(i, k, \theta)$ be an $N \times N$ identity matrix except for $G_{i,i}^* = G_{k,k} = \cos \theta = \alpha$ and $-G_{i,k}^* = G_{k,i} = \sin \theta = \beta$. Hence, $\mathbf{G}(i, k, \theta)$ has the form

$$\mathbf{G}(i, k, \theta) = \begin{bmatrix} 1 & & & & \\ & \ddots & & & \\ & & \alpha & \cdots & -\beta \\ & & \vdots & \ddots & \vdots \\ & & \beta^* & \cdots & \alpha^* \\ & & & & \ddots \\ & & & & 1 \end{bmatrix}, \quad (\text{C.2.5})$$

it is unitary and describes a rotation by θ in the N -dimensional vector space. If the angle θ is chosen appropriately, $\mathbf{G}(i, k, \theta)$ can be used to force the i -th element

of a vector to zero. Considering an arbitrary column vector $\mathbf{x} = [x_1, \dots, x_N]^T$, we choose

$$\alpha = \cos \theta = \frac{x_k}{\sqrt{|x_i|^2 + |x_k|^2}} \quad \text{and} \quad \beta = \sin \theta = \frac{x_i}{\sqrt{|x_i|^2 + |x_k|^2}}, \quad (\text{C.2.6})$$

and obtain the new vector $\mathbf{y} = \mathbf{G}(i, k, \theta)\mathbf{x}$.

$$\begin{bmatrix} 1 & & & & \\ & \ddots & & & \\ & & \frac{x_k}{\sqrt{|x_i|^2 + |x_k|^2}} & \cdots & \frac{-x_i}{\sqrt{|x_i|^2 + |x_k|^2}} \\ & & \vdots & \ddots & \vdots \\ & & \frac{x_i^*}{\sqrt{|x_i|^2 + |x_k|^2}} & \cdots & \frac{x_k^*}{\sqrt{|x_i|^2 + |x_k|^2}} \\ & & & & \ddots \\ & & & & 1 \end{bmatrix} \cdot \begin{bmatrix} x_1 \\ \vdots \\ x_i \\ \vdots \\ x_k \\ \vdots \\ x_N \end{bmatrix} = \begin{bmatrix} x_1 \\ \vdots \\ 0 \\ \vdots \\ \sqrt{|x_i|^2 + |x_k|^2} \\ \vdots \\ x_N \end{bmatrix}.$$

Obviously, \mathbf{x} and \mathbf{y} are identical except two elements: $y_i = 0$ and $y_k = \sqrt{|x_i|^2 + |x_k|^2}$. The Givens rotation can also be used to perform QL decompositions similar to the application of Householder reflections.

C.3 LLL Lattice-Reduction

This appendix describes the LLL algorithm developed by Lenstra, Lenstra and Lovász [LLL82] for the reduction of a lattice basis. The LLL algorithm does not deliver the optimum solution, i.e. the minimum basis, but performs pretty good for the considered multiple antenna systems and has a moderate computational complexity. Remember, that all vectors and matrices have been defined with real elements. This doubles their sizes so that the channel matrix has $m = 2N_T$ columns and $n = 2N_R$ rows. First, we have to define a reduced lattice.

Definition C.14 (Reduced Lattice by Lenstra-Lenstra-Lovász). A basis \mathbf{H}_{red} with QL decomposition $\mathbf{H}_{\text{red}} = \mathbf{Q}_{\text{red}} \cdot \mathbf{L}_{\text{red}}$ is called LLL-reduced with parameter δ , $1/4 < \delta \leq 1$, if

$$|L_{\ell,k}| \leq \frac{1}{2} \cdot |L_{\ell,\ell}| \quad \text{for } 1 \leq k < \ell \leq m \quad (\text{C.3.1})$$

and

$$\delta L_{k+1,k+1}^2 \leq L_{k,k}^2 + L_{k+1,k}^2 \quad \text{for } 1 \leq k \leq m-1 \quad (\text{C.3.2})$$

hold.

If only (C.3.1) is fulfilled, i.e. the diagonal elements of the lower triangular matrix \mathbf{L}_{red} are at least twice as large as the off-diagonal elements of the same row, the basis is called *size reduced*. This condition guarantees that no column in \mathbf{Q} has a significant projection onto another column. Therefore, (C.3.1) coincides with the basic explanation given in Section 6.3. If it is violated for a pair (ℓ, k) , we subtract an integer multiple of the ℓ -th column from the k -th one such that (C.3.1) is fulfilled.

However, (C.3.1) alone does not guarantee a minimum basis of the lattice. This effect will be illustrated by a small example at the end of this section. Additionally, the columns have to be sorted according to their lengths, i.e. we have to start from right to left with the shortest column and end with the largest column. This condition coincides with the sorted QL decomposition that also starts from the right hand side with the shortest column. Since column exchanges represent the main effort of the lattice reduction algorithm, a pre-sorted QL decomposition can greatly reduce the computational costs [WBKK04a, WBKK04b].

Condition (C.3.2) of the LLL algorithm just approximates the correct sorting because the lengths of columns are only compared on the basis of a small 2×2 submatrix as depicted in **Fig. C.3.1**. The square of the diagonal element $L_{k+1,k+1}$ weighted with δ must be smaller than the sum of $L_{k,k}^2$ and $L_{k+1,k}^2$. The parameter δ affects the quality of the reduced basis and is generally chosen to $\delta = 3/4$ [LLL82]. If condition (C.3.2) is not fulfilled, columns have to be exchanged. The consideration of only small submatrices reduces the computational costs at the expense of a degraded performance especially for large matrices. Therefore, the LLL algorithm shows a limited performance in CDMA systems although the general concept to use a reduced basis of a lattice may lead to encouraging results.

$$\left[\begin{array}{ccccc} L_{1,1} & & & & \\ L_{2,1} & L_{2,2} & & & \\ L_{3,1} & L_{3,2} & L_{3,3} & & \\ L_{4,1} & L_{4,2} & L_{4,3} & L_{4,4} & \\ L_{5,1} & L_{5,2} & L_{5,3} & L_{5,4} & L_{5,5} \end{array} \right]$$

Figure C.3.1: LLL-algorithm for lattice reduction

Concluding, we first have to perform a QL decomposition of the channel matrix \mathbf{H} or the extended version $\underline{\mathbf{H}}$. Using the sorted QL decomposition reduces the computational costs of the subsequent lattice reduction remarkably [WBKK04a, WBKK04b] because the number of required column exchanges is decreased. Afterwards, the LLL algorithm determines a new reduced basis \mathbf{H}_{red} of the lattice. The whole algorithm is described via a pseudo code in Table C.3.1

[LLL82, FP85]. Within the algorithm, $\mathbf{A}[a : b, c : d]$ denotes the submatrix of \mathbf{A} with elements from rows a, \dots, b and columns c, \dots, d . With $\lceil x \rceil$ we denote the integer closest to x .

The algorithm processes the matrices column-wise. In steps (3)-(10), the size is reduced by subtracting integer multiples of already processed columns to the right (column index ℓ) from the column k under consideration. Steps (11)-(16) perform the sorting. If condition (C.3.2) is violated, two columns are exchanged and the triangular structure of \mathbf{L} is restored by the application of a Givens rotation.

Table C.3.1: LLL Lattice-Reduction Algorithm [LLL82]

INPUT: $\mathbf{Q}, \mathbf{L}, \mathbf{P}$ (default: $\mathbf{P} = \mathbf{I}_m$)

OUTPUT: $\mathbf{Q}_{\text{red}}, \mathbf{L}_{\text{red}}, \mathbf{T}$

- (1) Initialization: $\mathbf{Q}_{\text{red}} := \mathbf{Q}, \mathbf{L}_{\text{red}} := \mathbf{L}, \mathbf{T} := \mathbf{P}$
 - (2) $k = m - 1$
 - (3) while $k \geq 1$
 - (4) for $\ell = k + 1, \dots, m$
 - (5) $\mu = \lceil \mathbf{L}_{\text{red}}[\ell, k] / \mathbf{L}_{\text{red}}[\ell, \ell] \rceil$
 - (6) if $\mu \neq 0$
 - (7) $\mathbf{L}_{\text{red}}[\ell : m, k] = \mathbf{L}_{\text{red}}[\ell : m, k] - \mu \mathbf{L}_{\text{red}}[\ell : m, \ell]$
 - (8) $\mathbf{T}[:, k] = \mathbf{T}[:, k] - \mu \mathbf{T}[:, \ell]$
 - (9) end
 - (10) end
 - (11) if $\delta \mathbf{L}_{\text{red}}[k + 1, k + 1]^2 > \mathbf{L}_{\text{red}}[k, k]^2 + \mathbf{L}_{\text{red}}[k + 1, k]^2$
 - (12) Exchange columns k and $k + 1$ in \mathbf{L}_{red} and \mathbf{T}
 - (13) Calculate Givens rotation matrix Θ such that
element $\mathbf{L}_{\text{red}}[k, k + 1]$ becomes zero:

$$\Theta = \begin{bmatrix} \alpha & -\beta \\ \beta & \alpha \end{bmatrix} \text{ with } \alpha = \frac{\mathbf{L}_{\text{red}}[k+1, k+1]}{\|\mathbf{L}_{\text{red}}[k:k+1, k+1]\|} \quad \beta = \frac{\mathbf{L}_{\text{red}}[k, k+1]}{\|\mathbf{L}_{\text{red}}[k:k+1, k+1]\|}$$
 - (14) $\mathbf{L}_{\text{red}}[k : k + 1, 1 : k + 1] = \Theta \cdot \mathbf{L}_{\text{red}}[k : k + 1, 1 : k + 1]$
 - (15) $\mathbf{Q}_{\text{red}}[:, k : k + 1] = \mathbf{Q}_{\text{red}}[:, k : k + 1] \cdot \Theta^T$
 - (16) $k = \min\{k + 1, m - 1\}$
 - (17) else
 - (18) $k := k - 1$
 - (19) end
 - (20) end
-

Example for Lattice Reduction

In order to illustrate the lattice reduction, we look at the example of Section 6.3.4 and consider the 2×2 channel matrix $\mathbf{H} = [\begin{smallmatrix} 2 & 2 \\ 1 & 2 \end{smallmatrix}]$. Obviously, its columns are not orthogonal and we can probably find a reduced basis. A QL decomposition leads to $\mathbf{H} = \mathbf{Q}\mathbf{L}$ with

$$\mathbf{Q} = \frac{1}{\sqrt{2}} \cdot \begin{bmatrix} 1 & 1 \\ -1 & 1 \end{bmatrix} \quad \text{and} \quad \mathbf{L} = \frac{1}{\sqrt{2}} \cdot \begin{bmatrix} 1 & 0 \\ 3 & 4 \end{bmatrix} .$$

The transformation matrix \mathbf{T} is initialized as identity matrix $\mathbf{T} = \mathbf{I}_2$. Now, we start with the size reduction and look at the elements $L_{2,2}$ and $L_{2,1}$ of \mathbf{L} . Since $\mu = \lceil 3/4 \rceil = 1$, we have to subtract the second columns of \mathbf{L} and \mathbf{T} from the corresponding first columns and obtain

$$\mathbf{L}_{\text{red}} = \frac{1}{\sqrt{2}} \cdot \begin{bmatrix} 1 & 0 \\ -1 & 4 \end{bmatrix} \quad \text{and} \quad \mathbf{T} = \begin{bmatrix} 1 & 0 \\ -1 & 1 \end{bmatrix} .$$

After steps (3)-(10) in Table C.3.1, we obtain the intermediate result

$$\mathbf{H}_{\text{red}} = \mathbf{HT} = \mathbf{QL}_{\text{red}} = \begin{bmatrix} 0 & 2 \\ -1 & 2 \end{bmatrix} .$$

Obviously, a size reduction does not lead to the minimum basis already given in Section 6.3.4 because the second column contains integer multiples of the first column. Therefore, it is essential to proceed with the sorting part of the algorithm. Condition (C.3.2) is violated due to

$$\frac{3}{4} \cdot \left(\frac{4}{\sqrt{2}} \right)^2 = 6 > \left(\frac{1}{\sqrt{2}} \right)^2 + \left(\frac{3}{\sqrt{2}} \right)^2 = 5$$

so that the columns in \mathbf{L}_{red} have to be exchanged. This yields

$$\mathbf{L}_{\text{red}} = \frac{1}{\sqrt{2}} \cdot \begin{bmatrix} 0 & 1 \\ 4 & -1 \end{bmatrix} \quad \text{and} \quad \mathbf{T} = \begin{bmatrix} 0 & 1 \\ 1 & -1 \end{bmatrix} .$$

Next, the triangular structure of \mathbf{L}_{red} has to be restored by applying the Givens rotation. With

$$\Theta = \frac{1}{\sqrt{2}} \cdot \begin{bmatrix} -1 & -1 \\ 1 & -1 \end{bmatrix} ,$$

we obtain

$$\mathbf{L}_{\text{red}} = \Theta \cdot \mathbf{L}_{\text{red}} = \begin{bmatrix} -2 & 0 \\ -2 & 1 \end{bmatrix} \quad \text{and} \quad \mathbf{Q}_{\text{red}} = \mathbf{Q} \cdot \Theta^T = \begin{bmatrix} -1 & 0 \\ 0 & -1 \end{bmatrix} .$$

The next intermediate result is

$$\mathbf{H}_{\text{red}} = \mathbf{H}_{\text{red}} \mathbf{T} = \mathbf{Q}_{\text{red}} \mathbf{L}_{\text{red}} = \begin{bmatrix} 2 & 0 \\ 2 & 1 \end{bmatrix}$$

which still does not represent the minimum basis. We use \mathbf{L}_{red} for a new length reduction. With $\mu = \lceil -2/1 \rceil = -2$, this leads to

$$\mathbf{L}_{\text{red}} = \begin{bmatrix} -2 & 0 \\ 0 & 1 \end{bmatrix} \quad \text{and} \quad \mathbf{T} = \begin{bmatrix} 2 & 1 \\ -1 & -1 \end{bmatrix}.$$

We finally obtain the reduced basis

$$\mathbf{H}_{\text{red}} = \mathbf{H} \mathbf{T} = \mathbf{Q}_{\text{red}} \mathbf{L}_{\text{red}} = \begin{bmatrix} 2 & 0 \\ 0 & -1 \end{bmatrix}.$$

Abbreviations

ARQ	Automatic Repeat on Request
ASK	Amplitude Shift Keying
AWGN	Additive White Gaussian Noise
BCJR	Bahl, Cocke, Jelinek, Raviv
BER	Bit Error Rate
BLAST	Bell Labs Layered Space Time
BPSK	Binary Phase Shift Keying
BSC	Binary Symmetric Channel
CC	Convolutional Code
CCS	Conventional Coding Scheme
CDMA	Code Division Multiple Access
COST	European Cooperation in the field of Scientific and Technical Research
CSS	Code-Spread System
DAB	Digital Audio Broadcast
D-BLAST	Diagonal BLAST
DFT	Discrete Fourier Transform
DS-CDMA	Direct Sequence CDMA
EGC	Equal Gain Combining
EVD	Eigenvalue Decomposition
EXIT	EXtrinsic Information Transfer
FDD	Frequency Division Duplex
FDMA	Frequency Division Multiple Access
FEC	Forward Error Correction
FER	Frame Error Rate
FFT	Fast Fourier Transform
FIR	Finite Impulse Response
GF	Galois Field

GSM	Global System for Mobile communications
HSDPA	High Speed Downlink Packet Access
ICI	Inter-Carrier Interference
IDFT	Inverse Discrete Fourier Transform
IFFT	Inverse Fast Fourier Transform
IIR	Infinite Impulse Response
IOWEF	Input Output Weight Enumerating Function
IPC	Information Processing Characteristic
ISI	Inter-Symbol Interference
LLR	Log-Likelihood Ratio
LoS	Line of Sight
LR	Lattice Reduction
LSB	Least Significant Bit
MAI	Multiple Access Interference
MAP	Maximum A Posteriori
MC	Multi-Carrier
MF	Matched Filter
MGF	Moment Generating Function
MIMO	Multiple Input Multiple Output
MISO	Multiple Input Single Output
ML	Maximum Likelihood
MLD	Maximum Likelihood Decoding
MMSE	Minimum Mean Square Error
MRC	Maximum Ratio Combining
MSB	Most Significant Bit
MUD	Multi-User Detection
MUI	Multi-User Interference
NSC	Nonrecursive Nonsystematic Convolutional
OFDM	Orthogonal Frequency Division Multiplexing
ORC	Orthogonal Restoring Combining
PAM	Pulse Amplitude Modulation
PCCS	Parallel Concatenated Coding Scheme
PIC	Parallel Interference Cancellation
PSA	Post-Sorting Algorithm
PSK	Phase Shift Keying
QAM	Quadrature Amplitude Modulation
QLD	QL Decomposition
QPSK	Quaternary Phase Shift Keying

RSC	Recursive Systematic Convolutional
SC	Selection Combining
SCCS	Serially Concatenated Coding Scheme
SDMA	Space Division Multiple Access
SIC	Successive Interference Cancellation
SIMO	Single Input Multiple Output
SINR	Signal to Interference plus Noise Ratio
SISO	Single Input Single Output
SLC	Square Law Combining
SNR	Signal to Noise Ratio
SOVA	Soft-Output Viterbi Algorithm
SPC	Single Parity Check Code
SQLD	Sorted QL Decomposition
STBC	Space-Time Block Code
STC	Space-Time Code
STTC	Space-Time Trellis Code
SUMF	Single-User Matched Filter
SUB	Single-User Bound
SVD	Singular Value Decomposition
TDMA	Time Division Multiple Access
TDD	Time Division Duplex
UEP	Unequal Error Protection
UMTS	Universal Mobile Telecommunications System
V-BLAST	Vertical BLAST
WSSUS	wide sense stationary uncorrelated scattering
ZF	Zero Forcing

Bibliography

- [AEVZ02] E. Agrell, T. Eriksson, A. Vardy, and K. Zeger. Closest Point Search in Lattices. *IEEE Trans. on Information Theory*, 48(8):2201–2214, August 2002.
- [Ala98] S.M. Alamouti. A Simple Transmit Diversity Technique for Wireless Communications. *IEEE Journal on Selected Areas in Communications*, 16(8):1451–1458, October 1998.
- [ARAS99] P.D. Alexander, M.C. Reed, J.A. Asenstorfer, and C.B. Schlegel. Iterative Multiuser Interference Reduction: Turbo CDMA. *IEEE Trans. on Communications*, 47(7):1008–1014, July 1999.
- [Bau99] G. Bauch. Concatenation of Space-Time Block Codes and Turbo-TCM. In *IEEE Proc. International Conference on Communications*, pages 1202–1206, Vancouver, British Columbia, Kanada, June 1999.
- [BB99] S. Benedetto and E. Biglieri. *Principles of Digital Transmission with Wireless Applications*. Kluwer-Academic/Plenum Publishers, New York, 1999.
- [BBH00a] S. Bäro, G. Bauch, and A. Hansmann. Improved Codes for Space-Time Trellis Coded Modulation. *IEEE Communications Letters*, 4(1):20–22, January 2000.
- [BBH00b] S. Bäro, G. Bauch, and A. Hansmann. New Trellis Codes for Space-Sime Coded Modulation. In *Source and Channel Coding*, ITG Conference, pages 147–150, Munich, January 2000.
- [BCJR72] L.R. Bahl, J. Cocke, F. Jelinek, and J. Raviv. Optimal Decoding of Linear Codes for Minimizing Symbol Error Rate. In *International Symposium on Information Theory, Asilomar*, page 90, January 1972.
- [BCJR74] L.R. Bahl, J. Cocke, F. Jelinek, and J. Raviv. Optimal Decoding of Linear Codes for Minimizing Symbol Error Rate. *IEEE Trans. on Information Theory*, 20:248–287, March 1974.
- [BDMP98] S. Benedetto, D. Divsalar, G. Montorsi, and F. Pollara. Serial Concatenation of Interleaved Codes: Performance Analysis, Design, and Iterative Decoding. *IEEE Trans. on Information Theory*, 44(3):909–926, May 1998.
- [BDMS91] E. Biglieri, D. Divsalar, P. McLane, and M. Simon. *Introduction to Trellis-Coded Modulation with Applications*. Macmillan Publishing Company, New York, 1991.

- [Ben96] M. Benthin. *Vergleich kohärenter und inkohärenter Codemultiplex-Übertragungskonzepte für zellulare Mobilfunksysteme*. PhD thesis, Universität Hamburg-Harburg, 1996.
- [BF98] G. Bauch and V. Franz. Iterative Equalization and Decoding for the GSM-System. In *IEEE Proc. Vehicular Technology Conference*, Ottawa, 1998.
- [BG93] C. Berrou and A. Glavieux. Turbo-Codes: General Principles Applications. In *Proceedings of the 6th Tirrenia International Workshop on Digital Communications*, pages 215–226, Tirrenia, 1993.
- [BGL00] M. Bossert, E.M. Gabidulin, and P. Lusina. Space-time codes based on hadamard matrices. In *IEEE Proc. International Symposium on Information Theory*, page 283, 25-30 June 2000.
- [BGL02] M. Bossert, E.M. Gabidulin, and P. Lusina. Space-time codes based on Gaussian integers. In *IEEE Proc. International Symposium on Information Theory*, page 273, 2002.
- [BGT93] C. Berrou, A. Glavieux, and P. Thitimajshima. Near Shannon Limit Error-Correcting Coding and Decoding: Turbo-Codes (1). In *IEEE Proc. International Conference on Communications*, pages 1064–1070, Geneva, 1993.
- [BH02] J.S. Blogh and L. Hanzo. *Third-Generation Systems and Intelligent Wireless Networking: Smart Antennas and Adaptive Modulation*. IEEE-Press, John Wiley, 2002.
- [BHS00] G. Bauch, J. Hagenauer, and N. Seshadri. Turbo-TCM and Transmit Antenna Diversity in Multipath Fading Channels. In *Proc. International Symposium on Turbo Codes*, Brest, France, September 2000.
- [Bin90] J.A.C. Bingham. Multicarrier Modulation for Data Transmission: An idea whose time has come. *IEEE Communications Magazine*, pages 5–14, 1990.
- [BKK04a] R. Böhnke, V. Kühn, and K.-D. Kammeyer. Efficient Near Maximum-Likelihood Decoding of Multistratum Space-Time Codes. In *IEEE Semianual Vehicular Technology Conference (VTC2004-Fall)*, Los Angeles, USA, September 2004.
- [BKK04b] R. Böhnke, V. Kühn, and K.-D. Kammeyer. Multistratum Space-Time Codes for the Asynchronous Uplink of MIMO-CDMA Systems. In *International Symposium on Spread Spectrum Techniques and Applications (ISSSTA'04)*, Sydney, Australia, September 2004.
- [BKK04c] R. Böhnke, V. Kühn, and K.-D. Kammeyer. Quasi-Orthogonal Multistratum Space-Time Codes. In *IEEE Global Conference on Communications (Globecom'04)*, Dallas, USA, September 2004.
- [Bla83] R.E. Blahut. *Theory and Practice of Error Control Codes*. Addison-Wesley, Reading (MA), 1983.
- [Blu00] R.S. Blum. Analytical Tools for the Design of Space-Time Convolutional Codes. In *Conference on Information Sciences and Systems*, Princeton University, NJ, March 2000.

- [BM96a] S. Benedetto and G. Montorsi. Design of Parallel Concatenated Convolutional Codes. *IEEE Trans. on Communications*, 44(5):591–600, May 1996.
- [BM96b] S. Benedetto and G. Montorsi. Unveiling Turbo-Codes: Some Results on Parallel Concatenated Coding Schemes. *IEEE Trans. on Information Theory*, 42(2):409–428, March 1996.
- [BMDP96] S. Benedetto, G. Montorsi, D. Divsalar, and F. Pollara. Serial Concatenation of Interleaved Codes: Performance Analysis, Design, and Iterative Decoding. *TDA Report*, 42(126), August 1996.
- [Bos99] M. Bossert. *Channel Coding for Telecommunications*. John Wiley & Sons, New York, 1999.
- [BP95] A.S. Barbulescu and S.S. Pietrobon. Interleaver Design for Three Dimensional Turbo Codes. In *IEEE Proc. International Symposium on Information Theory*, page 37, 17-22 September 1995.
- [BSGS00] S. Bruck, U. Sorger, S. Gligorevic, and N. Stolte. Interleaving for Outer Convolutional Codes in DS-CDMA Systems. *IEEE Trans. on Communications*, 48(7):1100–1107, July 2000.
- [BSMM00] I.N. Bronstein, K.A. Semendjajew, G. Musiol, and H. Mühlig. *Taschenbuch der Mathematik*. Harri Deutsch Verlag, 5th edition, 2000.
- [BUN01] C. Brunner, W. Utschick, and J.A. Nossek. Exploiting the short-term and long-term channel properties in space and time: eigenbeamforming concepts for the bs in wcdma. *European Transactions on Telecommunications*, 12(5):365–378, 2001.
- [BWKK03] R. Böhnke, D. Wübben, V. Kühn, and K.-D. Kammeyer. Reduced Complexity MMSE Detection for BLAST Architectures. In *IEEE Proc. Global Conference on Telecommunications*, San Francisco, California, USA, December 2003.
- [CC81] G.C. Clark and J.B. Cain. *Error-Correcting Coding for Digital Communications*. Plenum Press, New York, 1981.
- [CFV99] A.R. Calderbank, G.D. Forney, and A. Vard. Minimal Tail-Biting Trellises: The Golay Code and More. *IEEE Trans. on Information Theory*, 45(5):1435–1455, July 1999.
- [CM88] G.R. Cooper and C.D. McGillem. *Modern Communications and Spread Spectrum*. McGraw-Hill, second edition, 1988.
- [CMCT00] D.J. Costello, P.C. Massey, O.M. Collins, and O.Y. Takeshita. Some reflections on the mythology of turbo codes. In *3rd ITG Conference Source and Channel Coding*, pages 157–160, Januar 2000.
- [CMT04] G. Caire, R.R. Müller, and T. Tanaka. Iterative Multiuser Joint Decoding: Optimum Power Allocation and Low-Complexity Implementation. *IEEE Transactions on Information Theory*, 50(9):1950–1973, September 2004.
- [COS89] *Final Report COST 207*, 1989.

- [Cra91] J.W. Craig. A new, simple and exact result for calculating the probability of error for two-dimensional signal constellations. In *IEEE MILCOMM'91*, pages 25.5.1–25.5.5, Boston, 1991.
- [CT91] T.M. Cover and J.A. Thomas. *Elements of Information Theory*. Wiley & Sons, New York, 1991.
- [DDP01] D. Divsalar, S. Dolinar, and F. Pollara. Iterative Turbo Decoder Analysis Based on Density Evolution. *IEEE Journal on Selectes Areas in Communications*, 19(5):891–907, May 2001.
- [Dek00] A. Dekorsy. *Kanalcodierungskonzepte für Mehrträger-Codemultiplex in Mobilfunksystemen*. Forschungsberichte aus dem Arbeitsbereich Nachrichtentechnik der Universität Bremen, Nr. 6. Shaker-Verlag, July 2000. Hrsg. K.-D. Kammeyer.
- [DGC03] M.O. Damen, H.E. Gamal, and G. Caire. On Maximum Likelihood Detection and the Search for the Closest Lattice Point. *IEEE Trans. on Information Theory*, 49(10):2389–2402, October 2003.
- [DGNS98] E. Dahlman, B. Gudmundson, M. Nilsson, and J. Sköld. UMTS/IMT-2000 Based on Wideband CDMA. *IEEE Communications Magazine*, pages 70–80, September 1998.
- [DJB95] C. Douillard, M. Jézéquel, and C. Berrou. Iterative Correction of Intersymbol Interference: Turbo-Equalization. *European Transactions on Telecommunications*, 6, 1995.
- [DK96] A. Dekorsy and V. Kühn. Applicability of Importance Sampling for Rayleigh Fading Mobile Radio Channels. In *IEEE Proc. International Symposium on Spread Spectrum Techniques and Applications*, volume 1, pages 224–228, Mainz, Germany, January 1996.
- [DKK99a] A. Dekorsy, V. Kühn, and K.-D. Kammeyer. Exploiting Time and Frequency Diversity by Iterative Decoding in OFDM-CDMA Systems. In *IEEE Proc. Global Conference on Telecommunications*, Rio de Janeiro, Brazil, December 1999.
- [DKK99b] A. Dekorsy, V. Kühn, and K.-D. Kammeyer. Iterative Decoding with Mary Orthogonal Walsh Modulation in OFDM-CDMA Systems. In *Proc. 1st International OFDM-Workshop*, Hamburg-Harburg, Germany, January 1999.
- [DKK03] A. Dekorsy, V. Kühn, and K.-D. Kammeyer. Low Rate Channel Coding with Complex Valued Block Codes. *IEEE Transactions on Communications*, 51(5):800–809, 2003.
- [DS93] V.M. DaSilva and E.S. Sousa. Performance of Orthogonal CDMA for Quasi-synchronous Communication Systems. In *IEEE Proc. International Conference on Universal Personal Communications*, pages 995–999, October 1993.
- [FBZS01] J. Freudbergerand, M. Bossert, V.V. Zyablov, and S. Shavgulidze. Woven Codes with Outer Warp: Variations, Design, and Distance Properties. *IEEE Journal on Selectes Areas in Commununications*, 19(5):813–824, 2001.

- [FG98] G.J. Foschini and M.J. Gans. On Limits of Wireless Communications in a Fading Environment when Using Multiple Antennas. *Wireless Personal Communications*, 6(3):311–335, March 1998.
- [FGVW99] G.J. Foschini, G.D. Golden, A. Valenzela, and P.W. Wolniansky. Simplified Processing for High Spectral Efficiency Wireless Communications Employing Multi-Element Arrays. *IEEE Journal on Selected Areas in Communications*, 17(11):1841–1852, November 1999.
- [FHW98] R.F.H. Fischer, J. Huber, and U. Wachsmann. On the Combination of Multilevel Coding and Signal Shaping. In *2nd ITG Conference Source and Channel Coding*, pages 273–278, March 1998.
- [Fis02] R.F.H. Fischer. *Precoding and Signal Shaping for Digital Transmission*. John Wiley & Sons, Inc., 2002.
- [FK01] M. Feuersänger and V. Kühn. Combating Near Far Effects of linear MMSE Multiuser Detection in coded OFDM-CDMA. In *Third International Workshop on Multi-Carrier Spread-Spectrum (MC-SS 2001) & Related Topics*, Oberpfaffenhofen, Germany, September 2001.
- [FK03] K. Fazel and S. Kaiser. *Multi Carrier and Spread Spectrum Systems*. Wiley, 2003.
- [FKK01a] S. Fischer, V. Kühn, and K.-D. Kammeyer. Analysis of Diversity Effects for Satellite Communication Systems. In *IEEE Proc. Global Conference on Telecommunications*, San Antonio, USA, November 2001.
- [FKK01b] S. Fischer, V. Kühn, and K.-D. Kammeyer. Comparison of Diversity Schemes for LEO Satellite Communication Systems. In *Proc. CSCC Multi-Conference 2001*, Rethymnon, Crete, July 2001.
- [FKK01c] S. Fischer, V. Kühn, and K.-D. Kammeyer. Diversitätsuntersuchung bei LEO-Satellitensystemen. In *Proc. URSI Kleinheubacher Tagung*, Kleinheubach, Germany, September 2001.
- [FKK01d] S. Fischer, V. Kühn, and K.-D. Kammeyer. Satellite Diversity for a LEO Satellite System with CDMA Technology. *ASSI Satellite Communication Letter*, 1(1):5–13, March 2001.
- [FKKK02] S. Fischer, K. Knoche, V. Kühn, and K.-D. Kammeyer. Efficient linear multiuser detection for leo satellite systems with long codes. In *SoftCOM 2002*, volume 1, pages 471–475, Split, Croatia, October 2002.
- [FOO98] P. Frenger, P. Orten, and T. Ottosson. Code-Spread CDMA using Low-Rate Convolutional Codes. In *IEEE Proc. International Symposium on Spread Spectrum Techniques and Applications*, pages 374–378, Sun City, South Africa, September 1998.
- [FOOS98] P. Frenger, P. Orten, T. Ottosson, and A. Svensson. Multi-Rate Convolutional Codes. Technical Report 21, Göteborg, March 1998.
- [For66] G.D. Forney. *Concatenated Codes*. The M.I.T. Press, Cambridge, Massachusetts, 1966.

- [For72] G.D. Forney. Maximum-likelihood sequence estimation for digital sequences in the presence of intersymbol interference. *IEEE Trans. on Information Theory*, IT-18:363–378, 1972.
- [Fos96] G.J. Foschini. Layered Space-Time Architecture for Wireless Communication in a Fading Environment when Using Multiple Antennas. *Bell Labs Technical Journal*, 1(2):41–59, Autumn 1996.
- [FP85] U. Fincke and M. Pohst. Improved Methods for Calculating Vectors of Short Length in a Lattice, Including a Complexity Analysis. *Math. Comp.*, 44:463–471, 1985.
- [FP93] K. Fazel and L. Papke. On the performance of convolutionally-coded CDMA/OFDM for mobile radio communications systems. In *IEEE Proc. IEEE Int. Symp. on Personal, Indoor and Mobile Radio Communications*, pages D.3.2.1–D.3.2.5, September 1993.
- [Fri96] B. Friedrichs. *Kanalcodierung*. Springer Verlag, Berlin, 1996.
- [FWKK02] S. Fischer, B.L. Wenning, V. Kühn, and K.-D. Kammeyer. Blind interference suppression for ds-cdma leo satellite communication systems. In *European Wireless 2002*, Florence, Italy, February 2002.
- [Gal63] R. Gallager. *Low-Density Parity-Check Codes*. PhD thesis, Cambridge, Massachussatts, 1963.
- [GBL00] E.M. Gabidulin, M. Bossert, and P. Lusina. Space-time codes based on rank codes. In *IEEE Proc. International Symposium on Information Theory*, page 284, 25-30 June 2000.
- [GFWV98] G.D. Golden, G.J. Foschini, P.W. Wolniansky, and R.A. Valenzuela. V-BLAST: A High Capacity Space-Time Architecture for the Rich-Scattering Wireless Channel. *Proc. International Symposium on Advanced Radio Technologies*, September 1998.
- [GJP⁺91] K. Gilhousen, I. Jacobs, R. Padovani, A.J. Viterbi, L. Weaver, and C. Wheatley. On the Capacity of a Cellular CDMA System. *IEEE Trans. on Vehicular Technology*, 40:57–62, 1991.
- [Gol67] R. Gold. Optimal binary sequences for spread spectrum multiplexing. *IEEE Trans. on Information Theory*, IT-13:619–621, 1967.
- [Gra00] I.M. Gradshteyn, I.S. Ryzhik. *Table of Integrals, Series and Products*. Academic Press, San Diego, CA, 6th edition, 2000.
- [GS01] A. Grant and C. Schlegel. Iterative Implementations for Linear Multiuser Detectors. *IEEE Trans. on Communications*, 49(10):1824–1834, October 2001.
- [GV97] S. Glisic and B. Vucetic. *Spread Spectrum CDMA Systems for Wireless Communications*. Artec House Publishers, Boston, 1997.
- [GvL93] G.H. Golub and C.F. van Loan. *Matrix Computations*. The John Hopkins University Press, London, second edition, 1993.

- [Hag88] J. Hagenauer. Rate-Compatible Punctured Convolutional Codes (RCPC-Codes and their Applications. *IEEE Trans. on Communications*, 36(4):389–400, April 1988.
- [Hag89] J. Hagenauer. Unequal Error Protection (UEP) for Statistically Time-Varying Channels. In *Proceedings ITG-Conference 'Stochastic Models and Methods in Information Technology'*, pages 253–262, April 1989. ITG-Bericht 107.
- [Hag96a] J. Hagenauer. Forward Error Correcting for CDMA Systems. In *IEEE Proc. International Symposium on Spread Spectrum Techniques and Applications*, pages 566–569, September 1996.
- [Hag96b] J. Hagenauer. Source-controlled channel decoding. *IEEE Trans. on Communications*, 43(9):2449–2457, September 1996.
- [Har64] H.-F. Harmuth. Die Orthogonalteilung als Verallgemeinerung der Zeit- und Frequenzteilung. *Archiv elektronische Übertragung*, 18:43–50, 1964.
- [Har71] H.-F. Harmuth. *Transmission of Information by Orthogonal Functions*. Springer-Verlag, New York, 1971.
- [Has00] B. Hassibi. An Efficient Square-Root Algorithm for BLAST. In *IEEE Proc. International Conference on Acoustics, Speech and Signal Processing*, pages 5–9, Istanbul, June 2000.
- [HCS01] L. Hanzo, P. Cherriman, and J. Streit. *Wireless Video Communications: Second to Third Generation Systems and Beyond*. IEEE-PRess, John Wiley, 2001.
- [HH89] J. Hagenauer and P. Höher. A Viterbi Algorithm with Soft-Decision Output and its Applications. In *IEEE Proc. Global Conference on Telecommunications*, pages 47.1.1–47.1.7, November 1989.
- [Höh92] P. Höher. A statistical discrete-time model for WSSUS multipath channels. *IEEE Trans. on Vehicular Technology*, 41(4):461–468, 1992.
- [HH02] B. Hassibi and B.H. Hochwald. High Rate Codes That Are Linear in Space and Time. *IEEE Trans. on Information Theory*, 48(7):1804–1824, July 2002.
- [HHFJ02] S. Hüttinger, J. Huber, R.F.H. Fischer, and R. Johannesson. Soft-Output-Decoding: Some Aspects from Information Theory. In *4th ITG Conference on Source and Channel Coding*, pages 81–89, Berlin, January 2002.
- [Hip99] HiperLAN2 Global Forum, 1999.
- [HJ71] J.A. Heller and I.M. Jacobs. Viterbi Decoding for Satellite and Space Communication. *IEEE Trans. on Communications*, 19(5):835–848, October 1971.
- [HJ85] R.A. Horn and C.B. Johnson. *Matrix Analysis*. Cambridge University Press, 1985.
- [HL99] P. Höher and J. Lodge. Turbo DPSK: Iterative differential PSK demodulation and channel decoding. *IEEE Trans. on Communications*, 47(6):837–843, Juni 1999.

- [HL01] W. Hoeg and T. Lauterbach. *Digital Audio Broadcasting*. Wiley, 2001.
- [HLY02] L. Hanzo, T.H. Liew, and B.L. Yeap. *Turbo Coding, Turbo Equalisation and Space-Time Coding*. IEEE-Press, John Wiley, 2002.
- [HMCK03] L. Hanzo, M. Münster, B.J. Choi, and T. Keller. *OFDM and MC-CDMA for Broadband Multi-user Communications, WLANs and Broadcasting*. IEEE-Press, John Wiley, 2003.
- [HSW01] L. Hanzo, F.C.A. Somerville, and J.P. Woodard. *Voice Compression and Communications - Principles and Applications for Fixed and Wireless Channels*. IEEE-Press, John Wiley, 2001.
- [HT00] M. Honig and M.K. Tsatsanis. Multiuser CDMA Receivers. *IEEE Signal Processing Magazine*, pages 49–61, May 2000.
- [HT02] H. Holma and A. Toskala. *WCDMA for UMTS*. Wiley, 2002.
- [HtB03] B.H. Hochwald and S. ten Brink. Achieving Near-Capacity on a Multiple-Antenna Channel. *IEEE Trans. on Communications Technology*, 51(3):389–399, March 2003.
- [HTZ03] A. Hübner, D.V. Truhachev, and K. Zigangirov. On cycle-based permutor designs for serially concatenated convolutional codes. In *IEEE Proc. International Symposium on Information Theory*, page 279, 29 June-04 July 2003.
- [HTZ04] A. Hübner, D.V. Truhachev, and K. Zigangirov. On Permutor Designs Based on Cycles for Serially Concatenated Convolutional Codes. *IEEE Trans. on Communications*, 52(9):1494–1503, September 2004.
- [HWK00] L. Hanzo, W.T. Webb, and T. Keller. *Single- and Multi-carrier Quadrature Amplitude Modulation – Principles and Applications for Personal Communications WLANs Broadcasting*. IEEE-Press, John Wiley, second edition, 2000.
- [HWY02] L. Hanzo, C.H. Wong, and M.S. Yee. *Adaptive Wireless Transceivers: Turbo-Coded, Space-Time Coded TDMA, CDMA and OFDM Systems*. IEEE-Press, John Wiley, 2002.
- [HYKY03] L. Hanzo, L-L. Yang, E-L. Kuan, and K. Yen. *Single- and Multi-Carrier DS-CDMA: Multi-User Detection, Space-Time Spreading, Synchronisation, Networking and Standards*. IEEE-Press, John Wiley, 2003.
- [JHJ01] R. Jordan, R. Host, and R. Johannesson. On Interleaver Design for Serially Concatenated Convolutional Codes. In *IEEE Proc. International Symposium on Information Theory*, page 212, 24-29 June 2001.
- [JJB04] R. Jordan, R. Johannesson, and M. Bossert. On Nested Convolutional Codes and Their Application to Woven Codes. *IEEE Trans. on Information Theory*, 50(2):380–384, 2004.
- [Jor00] Frank Jordan. *Ein Beitrag zur Optimierung von Empfängern unter GSM-Randbedingungen*. PhD thesis, Universität Bremen, May 2000.
- [JZ98] R. Johannesson and K. Zigangirov. *Fundamentals of Convolutional Coding*. IEEE Digital & Mobile Communications, Piscataway, USA, 1998.

- [Kai98] S. Kaiser. *Multi-Carrier CDMA Mobile Radio Systems – Analysis and Optimization of Detection, Decoding and Channel Estimation*. VDI, January 1998.
- [Kam96] K.-D. Kammeyer. *Nachrichtenübertragung*. Teubner, Stuttgart, second edition, 1996.
- [KBK02] V. Kühn, R. Böhnke, and K.-D. Kammeyer. Multi-User Detection in Multicarrier-CDMA Systems. *e&i journal*, 11:395–402, 2002.
- [KDK00a] V. Kühn, A. Dekorsy, and K.-D. Kammeyer. Channel Coding Aspects in an OFDM-CDMA System. In *3-rd ITG Conference Source and Channel Coding*, pages 31–36, Munich, Germany, January 2000.
- [KDK00b] V. Kühn, A. Dekorsy, and K.-D. Kammeyer. Low Rate Channel Coding for CDMA Systems. *International Journal of Electronics and Communications (AEÜ)*, 54 (2000)(6):353–363, October 2000.
- [KF02] V. Kühn and M. Feuersänger. Multi-User Detection for Coded Multirate OFDM-CDMA Systems. In *4th International ITG Conference on Source and Channel Coding*, Berlin, Germany, January 2002.
- [Küh97] V. Kühn. Applying List Output Viterbi Algorithms to a GSM-based Mobile Cellular Radio System. In *IEEE Proc. International Conference on Universal Personal Communications*, pages 878–882, San Diego, California, USA, January 1997.
- [Küh98a] V. Kühn. Turbo-Codes and Turbo-Coded Modulation in CDMA Mobile Radio Systems for Short Frame Transmission. In *IEEE Proc. International Symposium on Spread Spectrum Techniques and Applications*, volume 2, pages 364–368, Sun City, South Africa, January 1998.
- [Küh98b] V. Kühn. *Turbo-Codes und Turbo-Codierte Modulation in Codemultiplex-Mobilfunksystemen*. PhD thesis, Dept. of Telecommunications, University of Paderborn, Aachen, February 1998.
- [Küh99] V. Kühn. Evaluating the Performance of Turbo-Codes and Turbo-Coded Modulation in a DS-CDMA Environment. *IEEE Journal on Selectes Areas in Commununications*, 17(12):2139–2147, December 1999.
- [Küh01a] V. Kühn. Combined Linear and Nonlinear Multi-User Detection for Coded OFDM-CDMA. In *International Symposium on Theoretical Electrical Engineering (ISTET) 2001*, Linz, Austria, August 2001.
- [Küh01b] V. Kühn. Combined MMSE-PIC in Coded OFDM-CDMA Systems. In *IEEE Proc. Global Conference on Telecommunications*, San Antonio, USA, November 2001.
- [Küh01c] V. Kühn. Linear and Nonlinear Multi-User Detection in Coded OFDM-CDMA Systems. In *International Conference on Telecommunications*, Bucharest, Romania, July 2001.
- [Küh01d] V. Kühn. Parallel Interference Cancellation in Coded DS-CDMA Systems. In *COST 262 Workshop on Multiuser Detection in Spread Spectrum Communications*, pages 31–38, Schloss Reisensburg, Germany, January 2001.

- [Küh03] V. Kühn. Iterative-Interference Cancellation and Channel Estimation for Coded OFDM-CDMA. In *International Conference on Communications (ICC03)*, Anchorage, Alaska, USA, May 2003.
- [Küh04] V. Kühn. Analysis of Iterative Multi-User Detection Schemes with EXIT Charts. In *International Symposium on Spread Spectrum Techniques and Applications (ISSSTA '04)*, Sydney, Australia, September 2004.
- [KK01] K.-D. Kammeyer and V. Kühn. *Matlab in der Nachrichtentechnik*. J. Schlembach Fachbuchverlag, Weil der Stadt, Germany, November 2001.
- [KK04] V. Kühn and K.-D. Kammeyer. Multiple Antennas in Mobile Communications: Concepts and Algorithms. In *International Symposium on Electromagnetic Theory (URSI 2004)*, Pisa, Italy, May 2004.
- [KKP01] K.-D. Kammeyer, V. Kühn, and T. Petermann. Blind and Non-Blind Turbo Estimation for Fast Fading GSM Channels. *IEEE Journal on Selectes Areas in Commununications*, 19(9):1718–1728, September 2001.
- [Kle96] A. Klein. *Multi-user detection of CDMA signals - algorithms and their application to cellular mobile radio*. PhD thesis, Universität Kaiserslautern, 1996.
- [KM95] V. Kühn and M. Meyer. Correlative Channel Estimation in DS-CDMA Systems. In *Proc. Third Annual Wireless Symposium*, pages 279–284, Santa Clara, California, USA, January 1995.
- [KSTB92] K.-D. Kammeyer, H. Schulze, U. Tuisel, and H. Bochmann. Digital multicarrier-transmission of audio signals over mobile radio channels. *European Transactions on Telecommunications*, 3(3):23–33, 1992.
- [LBB98] R. Lucas, M. Bossert, and M. Breitbach. On Iterative Soft-Decision Decoding of Linear Binary Block Codes and Product Codes. *IEEE Journal on Selectes Areas in Commununications*, 16(2):276–296, 1998.
- [LC04] S. Lin and D. Costello. *Error Control Coding*. Pearson Prentice-Hall, second edition, 2004.
- [LGB01] P. Lusina, E.M. Gabidulin, and M. Bossert. Efficient decoding of space-time Hadamard codes using the Hadamard transform. In *IPISIT*, page 243, 2001.
- [LGB03] P. Lusina, E.M. Gabidulin, and M. Bossert. Maximum rank distance codes as space-time codes. *IEEE Trans. on Information Theory*, 49(10):2757–2760, October 2003.
- [LH02] A. Lampe and J. Huber. Iterative Interference Cancellation for DS-CDMA Systems with High System Loads Using Reliability-Dependent Feedback. *IEEE Trans. on Vehicular Technology*, 51(3):445–452, May 2002.
- [LHH04] I. Land, P. Höher, and J. Huber. Bounds on Information Combining for Parity-Check Equations. In *International Zurich Seminar on Communications (IZS)*, pages 68–71, Zurich, Switzerland, February 2004.
- [LHHH03] I. Land, S. Hüttlinger, P. Höher, and J. Huber. Bounds on Information Combining. In *International Symposium on Turbo Codes & Related Topics*, pages 39–42, Brest, France, September 2003.

- [LLL82] A.K. Lenstra, H.W. Lenstra, and L. Lovàsz. Factoring Polynomials with Rational Coefficients. *Math. Ann.*, 261:515–534, 1982.
- [LSB02] P. Lusina, S. Shavgulidze, and M. Bossert. Space time block code construction based on cyclotomic coset factorization. In *IEEE Proc. International Symposium on Information Theory*, page 135, 2002.
- [LVS95] X. Li, B. Vucetic, and Y. Sato. Optimum Soft-Output Detection for Channels with Intersymbol Interference. *IEEE Trans. on Information Theory*, 41(3):704–713, May 1995.
- [LWN02] J. Laiho, A. Wacker, and T. (ed.) Novosad. *Radio Network Planning and Optimisation for UMTS*. Wiley, 2002.
- [Mas84] J.L. Massey. The How and Why of Channel Coding. In *IEEE Proc. International Zürich Seminar on Digital Communications*, pages 67–73, 1984.
- [Mer99] A. Mertins. *Signal Analysis - Wavelets, Filter Banks, Time-Frequency Transforms and Applications*. Wiley, 1999.
- [Mül98] R.R. Müller. *Power and Bandwidth Efficiency of Multiuser Systems with Random Spreading*. PhD thesis, Universität Erlangen-Nurenberg, 1998.
- [Mos96] S. Moshavi. Multi-User Detection for DS-CDMA Communications. *IEEE Communications Magazine*, pages 124–136, October 1996.
- [MP92] M. Mouly and M.B. Pautet. *The GSM-System for Mobile Communications*. Eigenverlag, 1992.
- [MV01] R.R. Müller and S. Verdu. Design and Analysis for Low Complexity Interference Mitigation on Vector Channels. *IEEE Journal on Selectes Areas in Commununications*, 19(8):1429–1441, 2001.
- [NTSC97] A.F. Naguib, V. Tarokh, N. Seshadri, and A.R. Calderbank. Space-Time Coded Modulation for High Data Rate Wireless Communications. In *IEEE Proc. Global Conference on Telecommunications*, volume 1, pages 102–109, November 1997.
- [NTSC98] A.F. Naguib, V. Tarokh, N. Seshadri, and A.R. Calderbank. A Space-Time Coding Modem for High-Data-Rate Wireless Communications. *IEEE Journal on Selected Areas in Communications*, 16(8):1459–1478, October 1998.
- [Nyg28] H. Nyquist. Certain topics in telegraph transmission theory. *Trans. AIEE*, 47:617–644, 1928.
- [Off96] E. Offer. *Decodierung mit Qualitätsinformation bei verketteten Codiersystemen*. Deutsche Forschungsanstalt für Luft- und Raumfahrt (DLR). VDI Fortschrittsberichte, June 1996.
- [OP98a] T. Ojanperä and R. Prasad. An Overview of Air Interface Multiple Access for IMT-2000/UMTS. *IEEE Communications Magazine*, pages 82–95, September 1998.
- [OP98b] T. Ojanperæ and R. Prasad. *Wideband CDMA for Third Generation Mobile Communications*. Artec House Publishers, Boston, 1998.

- [Pap65] A. Papoulis. *Probability, Random Variables and Statistic Processes*. McGraw-Hill, New York, 1965.
- [PG58] R. Price and P.E. Greene. A Communication Technique for Multipath Channels. In *Proceedings IRE*, volume 46, pages 555–570, March 1958.
- [PKK00] T. Petermann, V. Kühn, and K.-D. Kammeyer. Iterative Blind and Non-blind Channel Estimation in GSM Receivers. In *IEEE Proc. IEEE Int. Symp. on Personal, Indoor and Mobile Radio Communications*, pages 554–559, London, UK, September 2000.
- [PMS91] R.L. Pickholtz, L.B. Milstein, and D.L. Schilling. Spread spectrum for mobile communications. *IEEE Trans. on Vehicular Technology*, 40(2):313–321, May 1991.
- [Pro95] J.G. Proakis. *Digital Communications*. McGraw-Hill, third edition, 1995.
- [PSM82] R.L. Pickholtz, D.L. Schilling, and L.B. Milstein. Theory of spread spectrum communications - a tutorial. *IEEE Trans. on Communications*, 30(5):855–884, May 1982.
- [PW72] W.W. Peterson and E.J. Weldon. *Error-Correcting Codes*. MIT-Press, Cambridge (MA), 1972.
- [Rei95] U. Reimers. *Digitale Fernsehtechnik*. Springer-Verlag, 1995.
- [RHV97] P. Robertson, P. Höher, and E. Villebrun. Optimal and sub-optimal maximum a posteriori algorithms suitable for turbo-decoding. *European Transactions on Telecommunications*, 8(2):119–125, March/April 1997.
- [RM94] M. Rupf and J.L. Massey. Optimum sequences Multisets for Synchronous Code-Division Multiple-Access Channels. *IEEE Trans. on Information Theory*, 40:1261–1266, July 1994.
- [RSAA98] M.C. Reed, C.B. Schlegel, P.D. Alexander, and J.A. Asenstorfer. Iterative Multiuser Detection for CDMA with FEC: Near-Single-User Performance. *IEEE Trans. on Communications*, 46(12):1693–1699, December 1998.
- [RVH95] P. Robertson, E. Villebrun, and P. Hoher. A Comparison of Optimal and Sub-Optimal MAP Decoding Algorithms Operating in the Log-Domain. In *IEEE Proc. International Conference on Communications*, pages 1009–1013, Seattle, USA, June 1995.
- [SA00] M.K. Simon and M.-S. Alouini. *Digital Communication over Fading Channels*. John Wiley, New York, 2000.
- [Sal67] B.R. Saltzberg. Performance of an efficient parallel data transmission system. *IEEE Trans. on Communications Technology*, COM-15:805–811, 1967.
- [Sch89] H. Schulze. Stochastische Modelle und digitale Simulation von Mobilfunkkanälen. *Kleinheubacher Berichte*, Nr. 32:473–483, 1989.
- [Sch98] H. Schulze. Möglichkeiten und Grenzen des Mobilempfang von DVB-T. In *3. OFDM Fachgespräch*, Braunschweig, September 1998.
- [SE94] C.P. Schnoor and M. Euchner. Lattice Basis Reduction: Improved Practical Algorithms and Solving Subset Sum Problems. *Mathematical Programming*, 66:181–191, 1994.

- [SG91] A. Salmasi and K. Gilhousen. On the system design aspects of code division multiple access (CDMA) applied to digital cellular and personal communication networks. *IEEE Proc. Vehicular Technology Conference*, pages 57–62, May 1991.
- [SH99] R. Steele and L. Hanzo. *Mobile Radio Communications*. Wiley, second edition, 1999.
- [Sha48] C.E. Shannon. *A Mathematical Theory of Communication*, volume 27, pages 379–423 (part 1), pages 623–656 (part 2). Bell System Technical Journal, 1948.
- [SKK⁺01] H. Schmidt, V. Kühn, K.-D. Kammeyer, R. Rückriem, and S. Fechtel. Channel Tracking in Wireless OFDM Systems. In *SCI 2001*, Orlando, Florida, USA, July 2001.
- [SKK02] A. Scherb, V. Kühn, and K.-D. Kammeyer. Pilot aided channel estimation for short-code ds-cdma. In *International Symposium on Spread Spectrum Techniques and Applications (ISSSTA 2002)*, Prague, Czech Republic, September 2002.
- [SKK03a] A. Scherb, V. Kühn, and K.-D. Kammeyer. Comparison of Intelligent Code Acquisition for Sectorized Multi-Antenna CDMA in Downlink Mode. In *IEEE Proc. Global Conference on Telecommunications*, San Francisco, California, USA, December 2003.
- [SKK03b] A. Scherb, V. Kuehn, and K.-D. Kammeyer. On Phase Correct Blind Deconvolution exploiting Channel Coding. In *IEEE International Symposium on Signal Processing and Information Technology (ISSPIT'03)*, Darmstadt, Germany, December 2003.
- [SKK04] A. Scherb, V. Kühn, and K.-D. Kammeyer. Comparison of Methods for Joint Data Detection and Channel Estimation. In *Semiannual Vehicular Technology Conference 2004 (VTC Spring 2004)*, Milano, Italy, May 2004.
- [SM99] P. Schramm and R.R. Müller. Spectral Efficiency of CDMA Systems with Linear MMSE Interference Suppression. *IEEE Trans. on Communications*, 47(5):722–731, May 1999.
- [SP80] D.V. Sarvate and M.B. Pursley. Crosscorrelation Properties of Pseudorandom and Related Sequences. *IEEE Proceedings*, 68(5):593–619, May 1980.
- [STC97] N. Seshadri, V. Tarokh, and A.R. Calderbank. Space-Time Codes for Wireless Communication: Code Construction. In *IEEE Proc. Vehicular Technology Conference*, volume 2-A, pages 637–641, Phoenix, AZ, May 1997.
- [Str88] G. Strang. *Linear Algebra and its Applications*. Harcourt Brace Jovanovich College Publishers, Orlando, Florida, 3rd edition, 1988.
- [SW93] N.J. Sloane and A.D. Wyner. *Claude Elwood SHANNON: Collected Papers*. IEEE Press, first edition, 1993.
- [SW94] N. Seshadri and J.H. Winters. Two Signaling Schemes for Improving the Error Performance of Frequency Division (FDD) Transmission Systems Using Transmitter Antenna Diversity. *International Journal of Wireless Networks*, 1(1):49–60, 1994.

- [SWBK03] A. Sezgin, D. Wübben, R. Böhnke, and V. Kühn. On Exit Charts for Space Time Block Codes. In *IEEE Proc. International Symposium on Information Theory*, Yokohama, Japan, June 2003.
- [SWK03] A. Sezgin, D. Wübben, and V. Kühn. Analysis of Mapping Strategies for Turbo Coded Space-Time Block Codes. In *IEEE Information Theory Workshop (ITW03)*, Paris, France, March 2003.
- [tB00a] S. ten Brink. Iterative Decoding Trajectories of Parallel Concatenated Codes. In *IEEE/ITG Conference on Source and Channel Coding*, pages 75–80, Munich, January 2000.
- [tB00b] S. ten Brink. Rate one-half code for approaching the Shannon limit by 0.1 dB. *Electronics letters*, 36(15):1293–1294, July 2000.
- [tB01a] S. ten Brink. Code Characteristic Matching for Iterative Decoding of Serially Concatenated Codes. In *Ann. des Telecommunication*, pages 100–110, 2001.
- [tB01b] S. ten Brink. Code doping for triggering iterative decoding convergence. In *IEEE Proc. International Symposium on Information Theory*, pages 235–235, 2001.
- [tB01c] S. ten Brink. Convergence Behavior of Iteratively Decoded Parallel Concatenated Codes. *IEEE Trans. on Communications*, 49(10):1727–1737, October 2001.
- [TCD⁺98] A. Toskala, J. Castro, E. Dahlman, M. Latva-Aho, and T. Ojanperä. Frames FMA2 Wideband-CDMA for UMTS. *European Transactions on Telecommunications*, 9(4):325–335, August 1998.
- [Tel95] E. Telatar. Capacity of Multi-antenna Gaussian Channels. *ATT-Bell Labs Internal Tech. Memo*, June 1995.
- [TH99] D. Tse and S.V. Hanly. Linear Multiuser Receivers: Effective Interference, Effective Bandwidth and User Capacity. *IEEE Trans. on Information Theory*, 45(2):641–657, March 1999.
- [TJC99a] V. Tarokh, H. Jafarkhani, and A.R. Calderbank. Space-Time Block Codes from Orthogonal Designs. *IEEE Trans. on Information Theory*, 45(5):1456–1467, July 1999.
- [TJC99b] V. Tarokh, H. Jafarkhani, and A.R. Calderbank. Space-Time Block Coding for Wireless Communications: Performance Results. *IEEE Journal on Selected Areas in Communications*, 17(3):451–460, March 1999.
- [TS 99] 3rd Generation Partnership Project. *TS 25.211 Physical channels and mapping of transport channels onto physical channels (FDD)*, October 1999.
- [TS2] 3rd Generation Partnership Project. *User Equipment (UE) radio transmission and reception (FDD)*.
- [TSC97] V. Tarokh, N. Seshadri, and A.R. Calderbank. Space-Time Codes for High Data Rate Wireless Communication: Performance Criteria. In *IEEE Proc. International Conference on Communications*, volume 1, pages 299–303, Montreal, Canada, May 1997.

- [TSC98] V. Tarokh, N. Seshadri, and A.R. Calderbank. Space-Time Codes for High Data Rate Wireless Communication: Performance Criterion and Code Construction. *IEEE Trans. on Information Theory*, 44(2):744–765, March 1998.
- [Ung82] G. Ungerboeck. Channel Coding with Multilevel Phase Signaling. *IEEE Trans. on Information Theory*, IT-25:55–67, 1982.
- [Van95] L. Vandendorpe. Multitone spread spectrum multiple-access communications system in a multipath ricean fading channel. *IEEE Trans. on Vehicular Technology*, 44(2):327–337, May 1995.
- [Ver98] S. Verdu. *Multiuser Detection*. Cambridge University Press, New York, 1998.
- [Vit67] A.J. Viterbi. Error-bounds for convolutional codes and an asymptotically optimum decoding algorithm. *IEEE Trans. on Information Theory*, IT-13:260–269, 1967.
- [Vit90] A.J. Viterbi. Very Low Rate Convolutional Codes for Maximum Theoretical Performance of Spread-Spectrum Multiple-Access Channels. *IEEE Journal on Selected Areas in Comms*, 8(4):641–649, May 1990.
- [Vit95] A.J. Viterbi. *CDMA Principles of Spread Spectrum Communication*. Addison-Wesley Wireless Communication Series, Reading, Massachusetts, 1995.
- [VO79] A.J. Viterbi and J.K. Omura. *Principles of Digital Communication and Coding*. McGraw-Hill, New York, 1979.
- [VS99] S. Verdu and S. Shamai. Spectral Efficiency of CDMA with Random Spreading. *IEEE Trans. on Information Theory*, 45(2):622–640, March 1999.
- [vWL98] D.J. van Wyk and L.P. Linde. A Turbo Coded DS/CDMA System with Embedded Walsh-Hadamard Codewords. In *IEEE Proc. International Symposium on Spread Spectrum Techniques and Applications*, pages 359–363, Sun City, RSA, 1998.
- [Wal23] J. Walsh. A closed set of orthogonal functions. *American Journal of Mathematics*, 45:5–24, 1923.
- [WBKK03] D. Wübben, R. Böhnke, V. Kühn, and K.-D. Kammeyer. MMSE Extension of V-BLAST based on Sorted QR Decomposition. In *IEEE Semiannual Vehicular Technology Conference (VTC2003-Fall)*, Orlando, Florida, USA, October 2003.
- [WBKK04a] D. Wübben, R. Böhnke, V. Kühn, and K.-D. Kammeyer. MMSE-Based Lattice-Reduction for Near-ML Detection of MIMO Systems. In *ITG Workshop on Smart Antennas*, Munich, Germany, March 2004.
- [WBKK04b] D. Wübben, R. Böhnke, V. Kühn, and K.-D. Kammeyer. Near-Maximum-Likelihood Detection of MIMO Systems using MMSE-Based Lattice Reduction. In *IEEE International Conference on Communications (ICC'2004)*, Paris, France, June 2004.

- [WBR⁺01] D. Wübben, R. Böhnke, J. Rinas, V. Kühn, and K.-D. Kammeyer. Efficient Algorithm for Decoding Layered Space-Time Codes. *IEE Electronic Letters*, 37(22):1348–1350, November 2001.
- [Wei94] S.B. Weinstein. Data transmission by frequency division multiplexing using the discrete fourier transform. *IEEE Personal Communications*, 1(1):18–24, 1994.
- [WF03a] C. Windpassinger and R.F.H. Fischer. Low-Complexity Near-Maximum-Likelihood Detection and Precoding for MIMO Systems using Lattice Reduction. In *IEEE Information Theory Workshop (ITW 2003)*, Paris, France, March 2003.
- [WF03b] C. Windpassinger and R.F.H. Fischer. Optimum and Sub-Optimum Lattice-Reduction-Aided Detection and Precoding for MIMO Communications. In *Canadian Workshop on Information Theory*, pages 88–91, Waterloo, Ontario, Canada, May 2003.
- [WFGV98] P.W. Wolniansky, G.J. Foschini, G.D. Golden, and R.A. Valenzuela. V-BLAST: An Architecture for Realizing Very High Data Rates Over the Rich-Scattering Wireless Channel. *invited paper, Proc. ISSSE-98*, 29. September 1998.
- [Wit91] A. Wittneben. Basestation Modulation Diversity for digital SIMUL-CAST. In *IEEE Proc. Vehicular Technology Conference*, pages 848–853, St. Louis, USA, May 1991.
- [Wit93] A. Wittneben. A New Bandwidth Efficient Transmit Antenna Modulation Diversity Scheme for Linear Digital Modulation. In *IEEE Proc. International Conference on Communications*, pages 1630–1634, Geneva, Switzerland, 1993.
- [WKK03] D. Wübben, V. Kühn, and K.-D. Kammeyer. Successive Detection Algorithm for Frequency Selective Layered Space-Time Receiver. In *International Conference on Communications (ICC03)*, Anchorage, Alaska, USA, May 2003.
- [WKK04] D. Wübben, V. Kühn, and K.-D. Kammeyer. On the Robustness of Lattice-Reduction Aided Detectors in Correlated MIMO Systems. In *IEEE Semianual Vehicular Technology Conference (VTC2004-Fall)*, Los Angeles, USA, September 2004.
- [Wol78] J.K. Wolf. Efficient Maximum Likelihood Decoding of Linear Block Codes Using a Trellis. *IEEE Trans. on Information Theory*, IT-24:76–80, 1978.
- [WRB⁺02] D. Wübben, J. Rinas, R. Böhnke, V. Kühn, and K.-D. Kammeyer. Efficient Algorithm for Detecting Layered Space-Time Codes. In *4th International ITG Conference on Source and Channel Coding*, Berlin, Germany, January 2002.
- [YB00] Q. Yan and R. S. Blum. Optimum Space-Time Convolutional Codes. In *WCNC 2000*, 2000.
- [YLF93] N. Yee, J.-P. Linnartz, and G. Fettweis. Multicarrier CDMA in Indoor Wireless Radio Networks. In *IEEE Proc. IEEE Int. Symp. on Personal,*

- Indoor and Mobile Radio Communications*, pages D.1.3.1–D.1.3.5, September 1993.
- [ZB03] W. Zha and S.D. Blostein. Soft-Decision Multistage Multiuser Interference Cancellation. *IEEE Trans. on Vehicular Technology*, 52(2):380–389, March 2003.
- [ZF92] R. Zurmühl and S. Falk. *Matrizen und ihre Anwendungen 1*. Springer-Verlag, Berlin, Heidelberg, 1992.
- [ZP85] R.E. Ziemer and R.L. Peterson. *Digital Communications and Spread Spectrum Systems*. Macmillan Publishing Company, 1985.

Index

A

a priori information, 111, 114, 119, 150, 153, 157, 232
additive white Gaussian noise, *see* AWGN
Alamouti, 287
amplitude shift keying, *see* ASK
analytical signal, 11
ASK, 30
autocorrelation function, 187
Automatic Repeat Request, 103
AWGN, 12, 31, 33, 48, 125, 181
 channel capacity, 69

B

Bayes rule, 22
BCJR algorithm
 for binary block codes, 113
 for convolutional codes, 116
 in logarithmic domain, 118
 initialization, 115
beamforming, 2, 312
Bhattacharyya
 bound, 65
 error exponent, 66
binary entropy function, 56
binary symmetric channel, 72
bit error probability, 37
BLAST, 313
BLAST detection, 262
BSC, *see* binary symmetric channel

C

carrier frequency, 10
CDMA, 4, 20, 22, 167, 227
chain rule
 for entropy, 58, 341

for information, 59, 342
of information, 133
channel capacity, 59, 63, 219, 328
 for CDMA uplink, 218
 for diversity reception, 76
 for multiple antenna systems, 328
 of AWGN channel, 69
 of MIMO systems, 79
 of Rayleigh fading channel, 74
channel coding, 87
channel coding theorem, 64, 69
channel state information, 26
Chi squared distribution, 16
Cholesky decomposition, 263
code division multiple access, *see* CDMA
code rate, 62, 89
code-spread system, 208
coding gain for STC, 286
coherence bandwidth, 15
coherence time, 14
complementary error function, 25, 26
complex envelope, 9
concatenated codes, 136
 parallel concatenation, 137, 144, 149, 152, 164
 serial concatenation, 137, 139, 141, 149, 150, 161
convolutional code
 RSC encoder, 100
convolutional code, 97, 210
 catastrophic code, 104
 constraint length, 98
 finite state diagram, 101
 NSC encoder, 99
 puncturing, 102

tailbiting code, 101
 terminated code, 101
 trellis diagram, 102
 truncated code, 101
 correlated channels, 330
 correlation function, 186
 COST 207, 337
 crosscorrelation function, 187
 CSI, *see* channel state information
 cut-off rate, 66
 cyclic convolution, 195

D

D-BLAST, 314
 data processing theorem, 60, 342
 decision region, 24
 decorrelator, 223, 235, 243
 delay diversity, 301, 303
 determinant, 343
 determinant criterion, 287
 differential entropy, 60
 Digital Audio Broadcasting (DAB), 192
 Digital Video Broadcasting (DVB), 192
 direct-sequence spread spectrum, 168
 discrete multi-tone, 192
 distance spectrum of codes, 121
 diversity, 2, 39

- frequency diversity, 15, 40
- gain for STC, 286
- polarization diversity, 41
- receive diversity, 281
- space diversity, 41, 280
- space-time transmit diversity, 283
- time diversity, 14, 40, 89

Doppler

- bandwidth, 14
- frequency, 14, 16
- power spectrum, 14

 Doppler power profile, 337
 downlink, 2, 176, 199
 downlink transmission, 181
 dual code, 92

E

effective distance, 140
 eigenvalue decomposition, 347
 entropy, 56

equal gain combining, 42, 201
 equalizer, 22
 equivalent baseband representation, 9
 equivalent code, 91
 equivocation, 58
 error covariance matrix, 235, 239
 error function, 25
 even correlation function, 186, 187
 extended Battail algorithm, 116
 extrinsic information, 111

F

Fast Hadamard Transform, 96
 Fast Hadamard transform, 210
 FDMA, 4, 20
 FEC, *see* forward error correction
 finite field, 88
 finite impulse response filter, 15
 flat fading, 15, 128
 forward error correction, 87
 frame error probability, 22
 free distance, 97
 frequency division duplex, 312
 frequency division multiple access, *see* FDMA
 frequency-selective channel, 15
 frequency-selective fading channels, 13
 fully loaded system, 176

G

Gallager

- bound, 67
- exponent, 67
- function, 67

 Gauss-Seidel algorithm, 246
 Gaussian distribution, 13
 Gaussian normal form, 92
 generator matrix, 91
 Givens rotation, 350
 Global System for Mobile Communications (GSM), 5
 Gold codes, 189
 Gray mapping, 30
 guard interval, 4, 194

H

Hadamard code, 95, 188

Hadamard matrix, 95

Hamming

bound, 93

code, 94

distance, 90

weight, 121

Hamming distance

minimum distance, 90

Hermitian, 343

Hilbert transformation, 11

Householder reflection, 349

I

ICI, *see* intercarrier interference

IDFT, 193

IFFT, 193

information, 89

information content, 56

information processing characteristic, 131

input output weight enumerating function, 121

intercarrier interference, 193

interference cancellation, 217

interleaving, 7

block interleaver, 7

convolutional interleaver, 8

interleaving depth, 8

random interleaver, 8

uniform interleaver, 138

intersymbol interference, 13, 15, 175, 193

intrinsic information, 111

inverse Discrete Fourier Transform, *see* IDFT

inverse Fast Fourier Transform, *see* IFFT

IOWEF, *see* input output weight enumerating function

of serial concatenated codes, 139

IPC, *see* information processing characteristic

irrelevance, 59

ISI, *see* intersymbol interference, 193

J

Jacobi algorithm, 242

joint entropy, 57

K

Karhunen-Loève transformation, 51

L

L-Algebra, 109

lattice reduction, 320, 351

line of sight, 338

linear block codes, 90

linear multi-user detection, 234

linear successive interference cancellation, 246

LLL algorithm, 352

LLR, *see* log-likelihood ratio

log-likelihood ratio, 107

Log-MAP, *see* BCJR algorithm

long spreading codes, 169

M

m-sequences, 188

MAP

probability, 22

sequence detection, 22

symbol-by-symbol detection, 23

symbol-wise detection, 24

MAP criterion, 108

matched filter, 13, 89, 171, 172, 263

Max-Log-MAP algorithm, 120

maximum a posteriori, *see* MAP

maximum length sequences, 188

maximum likelihood

sequence detection, 22

symbol-by-symbol detection, 23

symbol-wise detection, 24

maximum ratio combining, 41, 172, 199

MC-CDMA, 197

MIMO, *see* multiple-input multiple-output system

MISO, *see* multiple-input single-output

ML, *see* maximum likelihood

MMSE detector, 201, 223, 244

modified Gram-Schmidt algorithm, 266

Moore-Pensore inverse, 236

MUD, 227

multi-carrier, 191, 197

multi-layer transmission, 227, 311

multi-rate CDMA systems, 179
 multi-stage detector, 242
 multi-user communications, 1
 multi-user detection, *see* MUD
 multiple access, 3
 multiple access interference, 3
 multiple antennas, 310
 multiple-input multiple-output system,
 1, 18
 multiple-input single-output system, 1,
 18
 mutual information, 59

N

natural mapping, 30, 300
 near-far effect, 178
 near-far resistance, 178, 236
 non-periodic correlations function, 187
 nonsystematic encoder, 89
 Nyquist, first criterion, 13

O

odd correlation function, 187
 OFDM, 20, 22, 192
 OFDM-CDMA, 197
 OFDMA, 20
 Orthogonal Frequency Division Multiple Access, *see* OFDMA
 Orthogonal Frequency Division Multiplexing, *see* OFDM, *see* OFDMA
 orthogonal matrix, 346
 orthogonal restoring combining, 200
 orthogonal space-time block codes, 287
 orthogonal spreading codes, 188, 219
 outage capacity, 76
 outage probability, 27, 28, 35, 38, 76

P

PAM, 30
 parallel concatenated coding scheme,
 214
 parallel interference cancellation, *see*
 PIC
 parity check codes, 94
 parity check matrix, 92
 path crosstalk, 175

perfect codes, 95
 periodic correlation function, 186
 phase shift keying, *see* PSK
 PIC, 242
 positive semidefinite , 348
 post-sorting algorithm, 268
 power delay profile, 14, 337
 preferred pairs, 189
 processing gain, 169
 PSK, 35
 pulse amplitude modulation, *see* PAM
 punctured codes, 106

Q

QAM, 32
 QL decomposition, 263, 272
 quadrature amplitude modulation, *see*
 QAM

R

Rake receiver, 172
 random spreading, 220
 rank criterion, 287
 rank of a matrix, 344
 Rayleigh distribution, 16
 Rayleigh fading, 31, 34, 47, 73
 redundancy, 56, 89
 repetition code, 94
 Rice distribution, 17
 Rice factor, 17
 Rice fading, 48, 338

S

scattering function, 14
 scrambling code, 188, 206
 SDMA, 5, 20, 279
 selection combining, 42
 serial concatenated coding scheme, 210
 short spreading codes, 169
 signal shaping, 71
 signal to interference plus noise ratio,
 see SINR
 signal to noise ratio, 13
 SIMO, *see* single-input multiple-output
 Simplex code, 95
 single-input multiple-output system, 1
 single-input single-output channel, 9

single-input single-output system, 1, 18
 single-user matched filter, 180
 singular value decomposition, 80, 236, 310, 347
 SINR, 181
 SISO, *see* single-input single-output
 soft-in soft-out decoding, 107
 soft-output decoding, 110
 of block codes, 116
 of convolutional codes, 116
 of Walsh codes, 118
 sorted QL decomposition, *see* SQLD
 source coding, 56
 SOVA, 120
 space division multiple access, *see*
 SDMA
 spatial multiplexing, 311
 spectral efficiency, 4, 219
 sphere packing bound, 93
 SQLD, 269
 square law combining, 42
 standard array decoding, 94
 sufficient statistics, 60, 231
 SUMF, *see* single-user matched filter
 super-orthogonal codes, 214
 SVD, *see* singluar value decomposition
 symbol error probability
 ASK and AWGN, 31
 ASK and flat Rayleigh fading, 32
 BPSK and AWGN, 37
 QAM and AWGN, 33
 QAM and flat Rayleigh fading, 35
 QPSK and AWGN, 37
 symbol-by-symbol MAP decoder, 113
 syndrome, 93
 syndrome decoding, 94
 system load, 176
 systematic encoder, 89

T

TDMA, 3, *see* time division multiple access, 20
 time diversity, 130
 time division duplex, 313
 time division multiple access, *see*
 TDMA

time-selective channel, 14
 trellis diagram
 for block codes, 96
 for convolutional codes, 101
 turbo codes, 146
 turbo decoding, 149, 150, 154
 turbo detection, 231

U

UMTS, 5, 337
 union bound, 24, 126, 138
 unitary matrix, 346
 Universal Mobile Telecommunications System, *see* UMTS
 uplink, 3, 178, 184, 204

V

V-BLAST, 313
 vector channel, 1
 Viterbi algorithm, 104, 105
 decision depth, 106
 incremental metric, 105
 survivor, 106

W

Walsh codes, 210
 Walsh sequence, 96, 188
 waterfilling, 83
 whitening, 263
 wide sense stationary uncorrelated scattering, 15
 Wiener solution, 238
 WSSUS, *see* wide sense stationary uncorrelated scattering

Z

zero-forcing, 223, 235, 243